



MONASH University

The Structural Basis Of Kidney Oxygenation

Jennifer Principal Ngo

Bachelor of Biomedical Science

A thesis submitted for the degree of Doctor of Philosophy at
Monash University in 2016
Department of Physiology

*You don't write because you want to say something; you write
because you've got something to say.*

F. Scott Fitzgerald
The Crack-Up, ed. Edmund Wilson

Copyright notice

© Jennifer Principal Ngo (2016). Except as provided in the Copyright Act 1968, this thesis may not be reproduced in any form without the written permission of the author.

I certify that I have made all reasonable efforts to secure copyright permissions for third-party content included in this thesis and have not knowingly added copyright content to my work without the owner's permission.

TABLE OF CONTENTS

| | |
|--|------|
| LIST OF FIGURES | I |
| LIST OF TABLES..... | V |
| ABSTRACT | VI |
| DECLARATION..... | VIII |
| GENERAL DECLARATION: THESIS INCLUDING PUBLISHED WORKS..... | IX |
| ACKNOWLEDGEMENTS..... | X |
| PUBLICATIONS | XII |
| CONFERENCE ABSTRACTS | XII |
| PRESENTATIONS & AWARDS | XIII |
| SYMBOLS AND ABBREVIATIONS | XIV |

CHAPTER 1: INTRODUCTION

| | |
|---|----|
| 1.1 OVERVIEW | 1 |
| 1.2 HYPOXIA AND THE PATHOGENESIS OF ACUTE KIDNEY INJURY AND CHRONIC KIDNEY DISEASE | 3 |
| 1.3 THE RENAL CIRCULATION | 6 |
| 1.4 CORTICAL AND MEDULLARY OXYGENATION: IS ONE DEPENDENT ON THE OTHER? | 10 |
| 1.5 CURRENT KNOWLEDGE OF THE STRUCTURE OF THE RENAL CIRCULATION IN THE RAT | 12 |
| 1.5.1 <i>Qualitative information on the renal circulation</i> | 12 |
| 1.5.2 <i>Quantitative information on the renal circulation</i> | 13 |
| 1.6 PHYSIOLOGICAL REGULATION OF KIDNEY OXYGENATION | 13 |
| 1.7 STRUCTURAL DETERMINANTS OF KIDNEY OXYGENATION | 15 |
| 1.7.1 <i>A mathematical model of oxygen transport in the kidney</i> | 18 |
| 1.7.2 <i>Conceptual basis of the mathematical model</i> | 19 |
| 1.7.3 <i>Structural basis of the mathematical model</i> | 19 |
| 1.7.4 <i>Limitations of the mathematical model</i> | 19 |
| 1.8 COUNTER-CURRENT TRANSPORT OF GASES AND OTHER MOLECULES IN THE RENAL CIRCULATION | 20 |
| 1.9 EXPERIMENTAL APPROACH | 20 |
| 1.9.1 <i>Overview</i> | 20 |
| 1.10 AIMS AND HYPOTHESES | 21 |
| REFERENCES | 22 |

CHAPTER 2: REVIEW – DIFFUSIVE SHUNTING OF GASES AND OTHER MOLECULES IN THE RENAL VASCULATURE: PHYSIOLOGICAL AND EVOLUTIONARY SIGNIFICANCE

| | |
|--|----|
| 2.1 ABSTRACT | 26 |
| 2.2 INTRODUCTION | 26 |
| 2.3 COUNTER-CURRENT EXCHANGE IN ORGANS OTHER THAN THE KIDNEY | 27 |
| 2.3.1 <i>Heat exchange</i> | 27 |
| 2.3.2 <i>Gas exchange</i> | 29 |
| 2.4 POTENTIAL LOCATIONS OF COUNTER-CURRENT DIFFUSION IN THE RENAL CIRCULATION | 29 |
| 2.4.1 <i>Renal cortex</i> | 30 |
| 2.4.2 <i>Renal medulla</i> | 31 |
| 2.5 PROPERTIES THAT INFLUENCE COUNTER-CURRENT DIFFUSION OF MOLECULES AND GASES IN THE RENAL CIRCULATION | 34 |
| 2.6 COUNTER-CURRENT DIFFUSION OF EXOGENOUS LIPID SOLUBLE SUBSTANCES IN THE RENAL CIRCULATION | 38 |
| 2.7 OXYGEN | 38 |

| | | |
|---|---|----|
| 2.7.1 | <i>Generation of oxygen gradients in the renal circulation</i> | 38 |
| 2.7.2 | <i>Evidence of diffusive oxygen shunting</i> | 39 |
| 2.8 | CARBON DIOXIDE | 41 |
| 2.8.1 | <i>Generation of carbon dioxide gradients in the renal circulation</i> | 41 |
| 2.8.2 | <i>Evidence of diffusive carbon dioxide shunting</i> | 41 |
| 2.9 | AMMONIA | 42 |
| 2.9.1 | <i>Generation of ammonia gradients in the renal circulation</i> | 42 |
| 2.9.2 | <i>Is there evidence of diffusive ammonia shunting in the renal circulation?</i> | 43 |
| 2.10 | NITRIC OXIDE AND SUPEROXIDE | 44 |
| 2.10.1 | <i>Are there gradients in the concentrations of nitric oxide and superoxide in the renal circulation?</i> | 44 |
| 2.10.2 | <i>Is there evidence of diffusive shunting of nitric oxide and superoxide in the renal circulation?</i> | 45 |
| 2.11 | WHAT FACTORS HAVE DRIVEN EVOLUTION OF THE VASCULAR ARCHITECTURE OF THE MAMMALIAN KIDNEY? | 46 |
| 2.11.1 | <i>Renal cortex</i> | 46 |
| 2.11.2 | <i>Renal medulla</i> | 48 |
| 2.12 | PERSPECTIVES AND SIGNIFICANCE | 49 |
| | REFERENCES | 50 |
| CHAPTER 3: GENERAL METHODS | | |
| 3.1 | ANIMALS | 58 |
| 3.2 | PERFUSION FIXATION PROTOCOL | 58 |
| 3.3 | HEMATOXYLIN AND EOSIN STAINING | 59 |
| 3.4 | LIGHT MICROSCOPY VS. SYNCHROTRON-BASED MICRO-COMPUTED TOMOGRAPHY | 60 |
| 3.4.1 | <i>Advantages and limitations of light microscopy</i> | 60 |
| 3.4.2 | <i>Technical basis of micro-computed tomography</i> | 61 |
| 3.4.3 | <i>3D Imaging techniques</i> | 64 |
| | REFERENCES | 68 |
| CHAPTER 4: A PILOT STUDY OF THE UTILITY OF IMMUNOHISTOCHEMICAL METHODS FOR IDENTIFICATION OF THE RENAL VASCULATURE | | |
| 4.1 | ABSTRACT | 70 |
| 4.2 | INTRODUCTION | 70 |
| 4.3 | METHODS | 71 |
| 4.3.1 | <i>Experimental approach</i> | 71 |
| 4.3.2 | <i>Animals</i> | 72 |
| 4.3.3 | <i>Kidney Perfusion protocol</i> | 72 |
| 4.3.4 | <i>Kidney sectioning</i> | 72 |
| 4.3.5 | <i>Microscopy and photomicrography</i> | 72 |
| 4.3.6 | <i>Hematoxylin and eosin staining</i> | 73 |
| 4.3.7 | <i>Immunohistochemistry</i> | 74 |
| 4.4 | RESULTS | 80 |
| 4.4.1 | <i>Detection of renal blood vessels</i> | 80 |
| 4.5 | DISCUSSION | 86 |
| 4.5.1 | <i>Major findings</i> | 86 |
| 4.5.2 | <i>Immunohistochemistry as a technique to distinguish renal arteries, veins and capillaries ..</i> | 86 |
| 4.6 | CONCLUSIONS AND ALTERNATIVE APPROACHES TO IDENTIFY THE RENAL VASCULATURE ... | 88 |
| | REFERENCES | 90 |
| CHAPTER 5: ANALYSIS OF THE SPATIAL GEOMETRY OF ARTERY-VEIN PAIRS IN THE KIDNEY | | |
| 5.1 | ABSTRACT | 92 |
| 5.2 | INTRODUCTION | 93 |
| 5.3 | METHODS | 95 |
| 5.3.1 | <i>Experimental approach</i> | 95 |
| 5.3.2 | <i>Hematoxylin and eosin stained tissue</i> | 95 |
| 5.3.3 | <i>Microfil® - filled tissue</i> | 98 |

| | | |
|---|--|------------|
| 5.4 | RESULTS | 103 |
| 5.4.1 | <i>Typical arrangement of arteries and veins vary according to arterial diameter</i> | <i>103</i> |
| 5.4.2 | <i>The relationship between arterial caliber and separation distance and wrapping</i> | <i>107</i> |
| 5.4.3 | <i>Capillary density around AV pairs varies by arterial caliber</i> | <i>108</i> |
| 5.5 | DISCUSSION | 110 |
| 5.5.1 | <i>Major findings</i> | <i>110</i> |
| 5.5.2 | <i>Analysis of the characteristic association of arteries and veins using hematoxylin and eosin stained sections</i> | <i>111</i> |
| 5.5.3 | <i>Analysis of data generated by micro-CT</i> | <i>111</i> |
| 5.5.4 | <i>Analysis of peritubular capillary density in the vicinity of arteries</i> | <i>114</i> |
| 5.5.5 | <i>Potential sites of AV oxygen shunting</i> | <i>115</i> |
| 5.5.6 | <i>Strengths and limitations of the light microscope and micro-CT methods</i> | <i>120</i> |
| 5.5.7 | <i>Implications for a mathematical model of oxygen transport in the kidney</i> | <i>122</i> |
| 5.6 | SUMMARY AND CONCLUSIONS | 122 |
| | REFERENCES | 123 |
| CHAPTER 6: VASCULAR GEOMETRY AND OXYGEN DIFFUSION IN THE VICINITY OF ARTERY-VEIN PAIRS IN THE KIDNEY | | 124 |
| CHAPTER 7: POTENTIAL IMPACT OF VASCULAR GEOMETRY ON ARTERIAL-TO-VEIN OXYGEN SHUNTING ACROSS THE BRANCHING LEVELS OF THE RENAL CORTICAL CIRCULATION | | |
| 7.1 | ABSTRACT | 136 |
| 7.2 | INTRODUCTION | 137 |
| 7.3 | METHODS | 138 |
| 7.3.1 | <i>Overview</i> | <i>138</i> |
| 7.3.2 | <i>Shrinkage of Microfil® following exposure to ethanol, glycerol and acetone</i> | <i>139</i> |
| 7.3.3 | <i>Estimation of the shrinkage of Microfil®</i> | <i>140</i> |
| 7.3.4 | <i>Methods for assigning arteries to Strahler orders</i> | <i>140</i> |
| 7.3.5 | <i>Calculation of mass-transfer coefficients</i> | <i>142</i> |
| 7.3.6 | <i>Effective mass transfer area</i> | <i>146</i> |
| 7.3.7 | <i>Statistical analysis</i> | <i>146</i> |
| 7.4 | RESULTS | 147 |
| 7.4.1 | <i>Shrinkage of Microfil®</i> | <i>147</i> |
| 7.4.2 | <i>Frequency distribution patterns for the characteristics of arteries binned into Strahler orders</i> | <i>147</i> |
| 7.4.3 | <i>Mean and median separation distance, and wrapping</i> | <i>150</i> |
| 7.4.4 | <i>The impact of vascular geometry on barriers to oxygen diffusion across Strahler orders</i> | <i>153</i> |
| 7.5 | DISCUSSION | 158 |
| 7.5.1 | <i>Main findings</i> | <i>158</i> |
| 7.5.2 | <i>Analysis of shrinkage of Microfil®</i> | <i>158</i> |
| 7.5.3 | <i>Categorizing light microscopic data into Strahler orders</i> | <i>159</i> |
| 7.5.4 | <i>Two different approaches for calculating mass transfer coefficients</i> | <i>160</i> |
| 7.5.5 | <i>Impact of vascular geometry on the barriers to diffusion of oxygen</i> | <i>160</i> |
| 7.5.6 | <i>Future perspectives</i> | <i>161</i> |
| 7.5.7 | <i>Strengths and limitations</i> | <i>162</i> |
| 7.6 | CONCLUSIONS | 162 |
| | REFERENCES | 164 |
| CHAPTER 8: SURFACE AREA OF PERITUBULAR CAPILLARIES IN THE RAT RENAL CORTEX | | |
| 8.1 | ABSTRACT | 166 |
| 8.2 | INTRODUCTION | 166 |
| 8.3 | METHODS | 166 |
| 8.3.1 | <i>Tissue preparation</i> | <i>166</i> |
| 8.3.2 | <i>Sampling</i> | <i>167</i> |
| 8.3.3 | <i>Estimation of surface area</i> | <i>167</i> |
| 8.4 | RESULTS | 168 |
| 8.5 | DISCUSSION | 169 |

| | |
|---|------------|
| REFERENCES | 170 |
| CHAPTER 9: MICRO-COMPUTED TOMOGRAPHIC ANALYSIS OF THE RADIAL GEOMETRY OF ARTERY-VEIN PAIRS IN THE KIDNEY OF THE RAT | |
| 9.1 ABSTRACT | 171 |
| 9.2 INTRODUCTION | 171 |
| 9.3 METHODS..... | 173 |
| 9.3.1 Overview | 173 |
| 9.3.2 Animal ethics | 173 |
| 9.3.3 Preparation of tissues for morphometric analyses | 173 |
| 9.3.4 Micro-CT scanning and imaging | 174 |
| 9.3.5 Three-dimensional volume reconstruction of whole kidneys..... | 174 |
| 9.3.6 Selection of artery-vein pairs and image analysis | 175 |
| 9.3.7 Histological tissue sections | 176 |
| 9.3.8 Qualitative analysis: matching histological sections with corresponding micro-CT slices | 177 |
| 9.3.9 Quantitative analysis: Comparison of vascular geometry generated by micro-CT and light microscopy | 177 |
| 9.3.10 Automated analysis of the radial geometry of artery-vein pairs | 177 |
| 9.3.11 Statistics | 180 |
| 9.4 RESULTS | 181 |
| 9.4.1 Quality of Micro-CT reconstructions | 181 |
| 9.4.2 Shrinkage of Microfil | 182 |
| 9.4.3 Qualitative comparison of vessel geometry using micro-CT and light microscopy | 185 |
| 9.4.4 Quantitative comparison of light microscopy and micro-CT using manual analyses..... | 185 |
| 9.4.5 Quantitative comparison of light microscopy and automated analyses via micro-CT ... | 189 |
| 9.4.6 Automated analysis of vessel geometry | 190 |
| 9.5 DISCUSSION | 193 |
| 9.5.1 Main findings | 193 |
| 9.5.2 Analysis of the quality of cured and non-cured Microfil® | 193 |
| 9.5.3 Analysis of shrinkage of Microfil®..... | 194 |
| 9.5.4 The validity of manual analysis of renal vascular geometry from micro-CT | 194 |
| 9.5.5 Automated analysis of micro-CT volumes | 196 |
| 9.5.6 Conclusions | 200 |
| REFERENCES..... | 201 |
| CHAPTER 10: FINAL DISCUSSION AND CONCLUSIONS | |
| 10.1. DO THE SPATIAL RELATIONSHIPS BETWEEN ARTERIES, VEINS AND BARRIERS TO DIFFUSION CHANGE ALONG THE COURSE OF THE RENAL CIRCULATION? | 203 |
| 10.2. PERITUBULAR CAPILLARIES ACT AS BOTH OXYGEN SOURCES AND SINKS | 204 |
| 10.3. MICRO-COMPUTED TOMOGRAPHY AS A POTENTIAL AUTOMATED ANALYSIS APPROACH FOR DETERMINING THE SPATIAL RELATIONSHIPS OF THE CORTICAL CIRCULATION | 205 |
| 10.4. USE OF STRUCTURAL INFORMATION IN MATHEMATICAL MODELS | 206 |
| 10.5. CLINICAL IMPLICATIONS | 206 |
| 10.6. FUTURE DIRECTIONS..... | 207 |
| REFERENCES..... | 209 |
| APPENDIX 1: DIFFUSIVE OXYGEN SHUNTING BETWEEN VESSELS IN THE PREGLOMERULAR RENAL VASCULATURE – ANATOMIC OBSERVATIONS AND COMPUTATIONAL MODELING..... | |
| | 211 |
| APPENDIX 2: BASAL RENAL O₂ CONSUMPTION AND THE EFFICIENCY OF O₂ UTILIZATION FOR NA⁺ REABSORPTION..... | |
| | 225 |
| APPENDIX 3: LETTER TO THE EDITOR: "THE PLAUSIBILITY OF ARTERIAL-TO-VENOUS OXYGEN SHUNTING IN THE KIDNEY: IT ALL DEPENDS ON RADIAL GEOMETRY" | |
| | 235 |
| APPENDIX 4: PROTOCOLS | |
| | 237 |

List of figures

CHAPTER 1

| | | |
|-------------------|--|----|
| Figure 1.1 | The arrangement of the arteries and veins at the corticomedullary border | 2 |
| Figure 1.2 | A schematic diagram demonstrating a proposed vicious cycle of hypoxia and cellular damage and dysfunction in the progression of chronic kidney disease | 4 |
| Figure 1.3 | The two different types of mammalian kidneys | 7 |
| Figure 1.4 | A schematic demonstrating the vascular organization of the kidney | 9 |
| Figure 1.5 | Two hypothetical effects of cortical ischemia in the kidney | 11 |
| Figure 1.6 | A schematic diagram of the mechanisms controlling renal oxygen tension (PO_2) | 16 |
| Figure 1.7 | Quantification of renal cortical vascular structure by Nordsletten <i>et al</i> | 17 |
| Figure 1.8 | The pathways for oxygen diffusion from a renal artery | 18 |

CHAPTER 2

| | | |
|-------------------|--|----|
| Figure 2.1 | Examples of artery-vein arrangements that allow for the preservation of heat | 28 |
| Figure 2.2 | Changes in artery-vein associations in the renal cortex of the rat | 32 |
| Figure 2.3 | Images of the close spatial association of descending (DVR) and ascending vasa recta (AVR)..... | 33 |
| Figure 2.4 | The likely direction of diffusion for oxygen, carbon dioxide, nitric oxide, superoxide, and ammonia between afferent and efferent vessels of the renal cortex (A) and medulla (B)..... | 47 |

CHAPTER 3

| | | |
|-------------------|---|----|
| Figure 3.1 | A schematic of two typical setups used in micro-computed tomographic (micro-CT) imaging | 62 |
| Figure 3.2 | The setup at the Imaging and Medical Therapy Beam Line (IMBL) | 63 |

CHAPTER 4

| | | |
|-------------------|---|----|
| Figure 4.1 | Schematic diagram of the three different planes in which the kidneys were sectioned | 73 |
| Figure 4.2 | A schematic diagram of the serial section method | 79 |
| Figure 4.3 | Photomicrographs of diaminobenzidine (DAB) staining for von Willebrand factor in sections of the rat kidney | 80 |
| Figure 4.4 | Photomicrographs of (A) immunofluorescence for von Willebrand factor (vWF) in sections of the rat kidney and (B) a light micrograph of the same section | 81 |
| Figure 4.5 | Photomicrographs of double-labeling immunofluorescence for (A) smooth muscle actin, and (B) von Willebrand factor (vWF), and also a light micrograph of the same section (C)..... | 83 |
| Figure 4.6 | Photomicrographs of serial sections. (A) immunofluorescence for von Willebrand factor (vWF), (B) smooth muscle actin, and (C) a photomicrograph of a section stained with hematoxylin and eosin | 84 |
| Figure 4.7 | Photomicrographs of immunofluorescence for von Willebrand factor (vWF) in sections of the rat kidney..... | 85 |

CHAPTER 5

| | | |
|--------------------|--|-----|
| Figure 5.1 | Schematic diagram of the three different planes in which the kidneys were sectioned | 95 |
| Figure 5.2 | A section of rat kidney stained with toluidine blue and examples of concentric zones used for the three different capillary analyses | 101 |
| Figure 5.3 | Photomicrographs of hematoxylin and eosin stained sections displaying large arteries in the renal cortex of the rat | 104 |
| Figure 5.4 | Photomicrographs of hematoxylin and eosin stained sections displaying small arteries in the renal cortex of the rat | 105 |
| Figure 5.5 | Arrangements of artery and veins in hematoxylin and eosin stained sections of biceps femoris tissue of the rat | 106 |
| Figure 5.6 | Scatter plot of arterial diameter against diffusion distance (lumen-to-lumen) | 107 |
| Figure 5.7 | Peritubular capillary density around arteries of varying diameters | 109 |
| Figure 5.8 | Critical error in the method used to measure diffusion distances in the data analysis of Nordsletten <i>et al</i> | 112 |
| Figure 5.9 | Scatter plots illustrating the relationship between arterial diameter and diffusion distance in terms of Strahler order, generated from the data-set of Nordsletten <i>et al</i> | 113 |
| Figure 5.10 | Frequency histograms of diffusion distances of (A) our data based on light microscopy and (B) data generated by micro-computed tomography (micro-CT) | 116 |
| Figure 5.11 | Relationships between arterial order and diffusion distance | 118 |
| Figure 5.12 | A schematic of the renal circulation | 119 |

CHAPTER 6

| | | |
|------------------|--|-------------|
| Figure 1 | Representative micrographs of renal tissue in which the vasculature was visualized by Microfil | 125 (F1112) |
| Figure 2 | Characteristic cross sections of tissue in the vicinity of an artery | 126 (F1113) |
| Figure 3 | Theoretical effects of the plane of sectioning on estimation of the metabolic oxygen demand of tubules | 127 (F1114) |
| Figure 4 | Distance between the arterial and venous lumens as a function of arterial diameter in various regions of the kidney | 129 (F1116) |
| Figure 5 | Distance between the arterial and venous lumens as a function of arterial diameter | 129 (F1116) |
| Figure 6 | Proportion of the arterial lumen wrapped by the venous wall in various regions of the kidney | 130 (F1117) |
| Figure 7 | Proportion of the arterial lumen wrapped by the venous wall as a function of arterial diameter | 130 (F1117) |
| Figure 8 | Diffusion distance for not-wrapped (A and C) and wrapped (B and D) arteries of various sizes and regions of the kidney | 131 (F1118) |
| Figure 9 | Scattergram of diffusion distance against proportion of wrapping (%) for arteries in various regions of the kidney | 131 (F1118) |
| Figure 10 | Variation in tissue oxygen tension (PO_2) and oxygen fluxes for artery-vein pairs of different length scales (based on D_A) and spatial configurations (wrapped/not wrapped) | 132 (F1119) |
| Figure 11 | Quantification of oxygen diffusion in the vicinity of the 4 typical arteries shown in Figs 2 and 10 | 133 (F1120) |

Chapter 7

| | | |
|-------------------|--|-----|
| FIGURE 7.1 | A simplified geometrical schematic of a vascular (arterial or venous) compartment corresponding to a specific branching level in the renal cortical circulation..... | 143 |
| FIGURE 7.2 | Degree of Microfil® shrinkage | 148 |
| FIGURE 7.3 | Mean separation distance and wrapping according to Strahler order..... | 151 |
| FIGURE 7.4 | Median separation distance and wrapping according to Strahler order..... | 152 |
| FIGURE 7.5 | Mean mass transfer coefficients and mean effective mass transfer areas across Strahler orders..... | 156 |
| FIGURE 7.6 | Median mass transfer coefficients and median effective mass transfer areas across Strahler orders | 156 |
| FIGURE 7.7 | Mean total mass flux per unit driving force across Strahler orders..... | 157 |
| FIGURE 7.8 | Median total mass flux per unit driving force across Strahler orders..... | 157 |

CHAPTER 9

| | | |
|--------------------|--|-----|
| FIGURE 9.1 | Selection of artery-vein pairs for determining shrinkage after 24 hours of tissue preparation | 175 |
| FIGURE 9.2 | Sampling of renal tissue | 176 |
| FIGURE 9.3 | Generating automated analyses of artery-vein geometry via MATLAB | 179 |
| FIGURE 9.4 | A schematic representing the method determining wrapping for an artery | 180 |
| FIGURE 9.5 | A comparison of kidneys with and without curing agent added to Microfil® | 181 |
| FIGURE 9.6 | Vessel diameters from scans generated immediately after and 24 hours after tissue preparation | 183 |
| FIGURE 9.7 | Ordinary least products regression analyses of the diameters of vessels determined from scans generated immediately after sample preparation and 24 hours later..... | 184 |
| FIGURE 9.8 | Sections of rat cortical tissue as observed by light microscopy and in corresponding micro-computed tomographic slices | 187 |
| FIGURE 9.9 | Relationships between measures of renal vascular geometry determined by light microscopy and micro-computed tomography (micro-CT) when the ring artifact was included and excluded | 188 |
| FIGURE 9.10 | Relationships between manual and automated measures of renal vascular geometry determined by light microscopy and micro-computed tomography (micro-CT)..... | 191 |
| FIGURE 9.11 | Scatter plots of the relationships of diffusion distance (A) and proportion of wrapping (B) with arterial diameter | 192 |
| FIGURE 9.12 | A schematic of artery-vein pairs with ring artifacts and a possible explanation for the results observed in Figure 9.9C..... | 196 |
| FIGURE 9.13 | Schematic of the concept of propagation-based imaging | 198 |

APPENDIX 1

| | | |
|-----------------|--|------------|
| FIGURE 1 | A slice through the data set of Nordsletten <i>et al</i> | 212 (F606) |
| FIGURE 2 | Micrographs of hemotoxylin and eosin stained rat renal cortex | 213 (F607) |
| FIGURE 3 | Relationship between arterial diameter and the distance between the arterial and venous wall (lumen separation)..... | 214 (F608) |

| | |
|---|------------|
| FIGURE 4 Capillary density in concentric zones around arteries of various calibres | 214 (F608) |
| FIGURE 5 Circular and wrapped idealized geometries showing variations in PO_2 (A and B) and diffusive flux magnitude (C and D) | 216 (F610) |
| FIGURE 6 Incorporating the capillary switch (CS) into the models (B and D) creates a larger PO_2 exclusion zone around the vessels compared with the idealized models (A and C)..... | 216 (F610) |
| FIGURE 7 Effect of applying (CS) or not applying (NCS) the capillary switch on arterial-to-venous (AV) shunting | 217 (F611) |
| FIGURE 8 PO_2 profiles of vessels in the parametric study | 218 (F612) |
| FIGURE 9 Diffusive flux magnitude profiles corresponding to the geometries used in Fig. 8 for PO_2 | 219 (F613) |
| FIGURE 10 Effect on flux of altering LS from $0.1R_A$ to $1.3R_A$ in the circular (A-C) and wrapped (D-F) configurations | 220 (F614) |
| FIGURE 11 Effect of R_A/R_V ratio on AV shunting | 221 (F615) |
| FIGURE 12 Effect of vessel orientation on flux..... | 221 (F615) |
| FIGURE 13 Effect of the ratio of arterial to venous PO_2 on AV shunting (A and D), VT flux (B and E), and AT flux (C and F) in circular (A-C) and wrapped (D-F) configurations | 222 (F616) |

APPENDIX 2

| | |
|--|------------|
| FIGURE 1 Relationship between the fractional excretion of Na^+ (FE_{Na^+}) under control conditions and the estimate of basal renal O_2 consumption (VO_2^{basal}) as a percentage of total renal VO_2 (VO_2^{total})(basal percent renal VO_2)..... | 229 (F555) |
| FIGURE 2 Predicted effects of altered VO_2^{basal} in the rat kidney on the relationships between FE_{Na^+} and basal percent renal VO_2 | 229 (F555) |
| FIGURE 3 Relationship between FE_{Na^+} and T_{Na^+}/VO_2^{total} | 230 (F556) |
| FIGURE 4 Relationship between percent changes in T_{Na^+} and percent changes in T_{Na^+}/VO_2^{total} | 230 (F556) |
| FIGURE 5 Predicted effects of altered VO_2^{basal} in the kidney of the rat on the relationship between T_{Na^+} and the quotient of T_{Na^+}/VO_2^{total} | 231 (F557) |
| FIGURE 6 Predicted effects of altered T_{Na^+} on VO_2^{total} when VO_2 for functions other than T_{Na^+} varies as a linear function of T_{Na^+} | 231 (F557) |

APPENDIX 3

| | |
|---|------------|
| FIGURE 1 Effects of the close association between arteries and veins (wrapping) on oxygen flux between artery-vein pairs | 235 (F179) |
|---|------------|

List of Tables

CHAPTER 2

| | |
|--|----|
| TABLE 2.1 The solubilities and diffusivities of the five molecules reviewed | 36 |
| TABLE 2.2 Lipid membrane permeabilities of the five molecules reviewed | 37 |

CHAPTER 4

| | |
|--|----|
| TABLE 4.1 Primary and secondary antisera used for immunohistochemical protocols | 76 |
|--|----|

CHAPTER 5

| | |
|---|-----|
| TABLE 5.1 The varying zone widths for each arterial diameter group across the four different analyses | 102 |
| TABLE 5.2 The mean minimum distance from the arterial lumen to the adventitia for the arterial diameter groups, and the corresponding zone width assigned to the arterial diameter | 102 |

CHAPTER 6

| | |
|---|-------------|
| TABLE 1 Model parameters | 100 (F1114) |
| TABLE 2 Characteristics of arteries according to internal diameter and anatomic region ... | 121 (F1115) |

CHAPTER 7

| | |
|---|-----|
| TABLE 7.1 Arterial radii corrected for shrinkage and the range of arterial radii used for categorizing data into Strahler orders via the ‘statistical’ and ‘mid-point’ methods | 149 |
|---|-----|

CHAPTER 8

| | |
|---|-----|
| TABLE 8.1 Calculated total surface area (mean \pm SEM) of cortical peritubular capillaries | 168 |
|---|-----|

APPENDIX 1

| | |
|--|------------|
| TABLE 1 Variables used in the formulation of the diffusive oxygen transport model | 212 (F606) |
| TABLE 2 Results from the mathematical analysis of the 3D (micro-CT) model of rat renal vasculature of Nordsletten et al | 214 (F609) |

APPENDIX 2

| | |
|---|--------------------|
| TABLE 1 Available estimates of $\text{VO}_2^{\text{basal}}$ as a percentage of $\text{VO}_2^{\text{total}}$ (basal percent renal VO_2) | 226-227 (F552-553) |
|---|--------------------|

Abstract

The kidneys receive ~25% of the cardiac output but weigh ~1% of total body weight. Yet the kidney is susceptible to hypoxia. One mechanism that may contribute to this susceptibility is the countercurrent shunting of oxygen, both in the cortex between arteries and veins and in the medulla between descending and ascending vasa recta. The susceptibility of the kidney, and in particular the renal medulla, to hypoxia may contribute to the pathogenesis of acute kidney injury. The physiology of renal oxygenation is further complicated by the arrangement of the renal circulation. That is, arterial blood destined for the medulla travels with blood destined for the cortex, to the level of the proximal interlobular arteries, where the afferent arterioles of juxtamedullary glomeruli originate. Thus, arterial-to-venous (AV) oxygen shunting in the renal cortex could reduce oxygen delivery to both the cortex and medulla. This proposition is consistent with experimental findings suggesting that oxygenation of the renal medulla is dependent on cortical perfusion and oxygenation. This PhD project was aimed towards developing a better understanding of the impact of renal vascular architecture and structure on kidney oxygenation. Both light microscopy and micro-computed tomography were used to characterize the radial geometry of individual artery-vein pairs in the renal cortex of the rat. We determined the separation distance between artery-vein pairs and the proportion of the arterial wall surrounded by the wall of a vein (wrapping). We observed that there are both wrapped and non-wrapped arteries in the renal cortical circulation. However, the proportion of wrapped arteries was found to change along the course of the cortical circulation. Larger arteries were more often wrapped than were smaller arteries. Consequently, the mean proportion of the arterial wall surrounded by its paired vein gradually decreased, while mean diffusion distance increased, along the course of the preglomerular circulation. Thus our data indicate that AV oxygen shunting should be favored in larger vessels, such as interlobar and arcuate vessels. However, because of the branching nature of the renal circulation, there are many more smaller vessels than larger vessels. When this was

taken into account in an analysis of the preglomerular circulation as a network, AV oxygen shunting was found to be most significant between paired interlobular arteries and veins. We then showed that synchrotron-based micro-computed tomography is a valid approach for analysis of the geometry of the preglomerular vasculature. We also developed an automated method for performing such analyses. However, in its current form this method does not generate valid information regarding the geometry of artery-vein pairs. In conclusion, using light microscopy and synchrotron-based micro-computed tomography, we were able to demonstrate that the architecture of the renal cortical circulation is arranged in such a way that likely favors the diffusional shunting of oxygen (and perhaps other gases) in the interlobular vessels of the preglomerular circulation. The data presented in this thesis can be incorporated into computational models of oxygen transport in the kidney. Our approach could also be applied to models of renal disease and various species.

Declaration

This thesis contains no material which has been accepted for the award of any other degree or diploma at any university or equivalent institution and that, to the best of my knowledge and belief, this thesis contains no material previously published or written by another person, except where due reference is made in the text of the thesis.

Chapters 2, 7, 8 & 9 are unpublished manuscripts, and have not been submitted, accepted for submission, or published.

The following co-authors contributed to the work in:

Chapter 2:

My contribution = 75%

Co-authors: Connie PC Ow, Michelle M Kett, Bruce S Gardiner, James T Pearson, David W Smith, Saptarshi Kar & Roger G Evans

Chapter 7:

My contribution = 65%

Co-authors: Saptarshi Kar, David W Smith, Bruce S Gardiner & Roger G Evans

Chapter 8:

My contribution = 75%

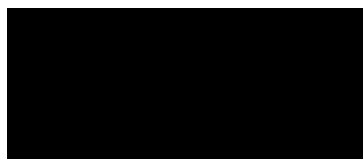
Co-authors: Michelle M Kett, John F Bertram, David W Smith, Bruce S Gardiner & Roger G Evans

Chapter 9:

My contribution = 60%

Co-authors: Michelle M Kett, Zohaib Khan, James T Pearson, Mayer M Melhem, David W Smith, Bruce S Gardiner & Roger G Evans

Signature:

A solid black rectangular box used to redact the signature of the author.

Print Name: JENNIFER PRINCIPAL NGO

Date:24/04/2016.....

Publications during enrolment

Thesis including published works declaration

I hereby declare that this thesis contains no material which has been accepted for the award of any other degree or diploma at any university or equivalent institution and that, to the best of my knowledge and belief, this thesis contains no material previously published or written by another person, except where due reference is made in the text of the thesis.

This thesis includes 4 original papers published in peer reviewed journals and 0 unpublished publications. The core theme of the thesis is oxygen transport in the kidney. The ideas, development and writing up of all the papers in the thesis were the principal responsibility of myself, the candidate, working within the Department of Physiology under the supervision of Associate Professor Roger G Evans.

(The inclusion of co-authors reflects the fact that the work came from active collaboration between researchers and acknowledges input into team-based research.)

In the case of *Chapter 6, Appendix 1, Appendix 2 and Appendix 3*, my contribution to the work involved the following:


(If this is a laboratory-based discipline, a paragraph outlining the assistance given during the experiments, the nature of the experiments and an attribution to the contributors could follow.)

| Thesis chapter | Publication title | Publication status* | Nature and extent (%) of students contribution |
|----------------|--|---------------------|--|
| 6 | Vascular geometry and oxygen diffusion in the vicinity of artery-vein pairs in the kidney | Published | 60% |
| Appendix 1 | Diffusive oxygen shunting between vessels in the preglomerular renal vasculature: anatomic observations and computational modeling | Published | 10% |
| Appendix 2 | Basal renal O ₂ consumption and the efficiency of O ₂ utilization for Na ⁺ reabsorption | Published | 5% |
| Appendix 3 | Letter to the editor: "The plausibility of arterial-to-venous oxygen shunting in the kidney: it all depends on radial geometry" | Published | 10% |
| | | | |

* e.g. 'published' / 'in press' / 'accepted' / 'returned for revision'

I have not renumbered sections of submitted or published papers in order to generate a consistent presentation within the thesis.

Student signature:



Date: 24/04/2016

The undersigned hereby certify that the above declaration correctly reflects the nature and extent of the student and co-authors' contributions to this work.

Main Supervisor signature:



Date: 24/04/2016

Acknowledgements

I've done it!! I've finally completed my thesis!! It took a total of 6 years, but I've reached the finish line!

First and foremost I would like to thank my supervisors.

Roger, thank you for your wisdom and advice. I know it wasn't the smoothest ride, and it wasn't without its fair share of blood, sweat and tears, but you have supported me until the end of this journey. One of my favorite moments of this experience was seeing you sing and dance at FASEB. I saw a different side to you and that was awesome haha. Also a huge thank you for the departmental scholarship you helped set up for me. This support was greatly appreciated.

To Michelle, thank you for all your help with my experimental and written work. Your advice was invaluable. I most definitely have to thank you for coming to the rescue when I had an emotional break down. I didn't know whom else to turn to, and even though you had plans, you still made a huge effort to come save a blubbering Jen.

Thank you James for all your expertise and help with the synchrotron imaging side of this project. To all of my supervisors, thank you for your guidance regarding my seminar presentations, you all made it less nerve-racking as I was more confident with my presentations following your advice. I have learnt so much from all of you.

Thank you to John Bertram and John Ludbrook for sharing your expertise in stereology and statistics. This project would have been stuck if it weren't for your help. Also a thank you to Rebecca and Victor for helping me with some staining in my first study.

I would like to thank those who assisted my learning of techniques throughout this project. Thank you Amany for always being kind and helpful when I asked questions. Thank you for also showing me how to perfusion fix. Thank you Priya for showing me the ropes around the lab when I first started. Thank you Brad at Pharmacology for always being happy to assist me with my histochemical and immunofluorescence protocols. Thank you Stef, Camilla, Jonathan, Sue and Julie at the Monash histology and resin lab. I appreciate all your time and effort in training me, and for all your advice with my kidney tissue, whether it be staining or sectioning. Thank you Anton at the Australian Synchrotron for helping me with micro-CT reconstructions and for teaching me how to use X-TRACT and Drishti.

A huge thanks to the team in Perth. You modeling gurus!! Thank you for always being welcoming when I visited UWA. Thank you Sarah, Bruce, David, Saptarshi, Zohaib and

Chang-Joon. Special thanks to Saptarshi and Zohaib for being patient with me and for always answering my (sometimes silly) questions. Thank you Zohaib for teaching me how to use AVIZO and MATLAB. Thank you Saptarshi for the Skype sessions, these were really helpful in understanding the maths and modeling.

I also need to thank the honors and Masters students who enriched my PhD experience. Thank you Sera, Mayer, and Bianca for being great students. Instead of me being the one being taught something, I got to teach you guys a little something (hopefully)!

I'd like to thank the staff and students in the Cardiovascular and renal laboratory. You guys made the lab a nicer place to be in. Also, your advice for sprucing up my seminar presentations was always appreciated. Special thanks to Lisa and Bec for being the mums of the lab and for always being happy to answer my questions.

Thank you to Helena and the HDR coordinators for their help and advice during my PhD milestones. Thank you also to the Department of Physiology for attending my seminars. Turning up to HDR seminars can become draining, so thank you for showing your support to us HDR students.

A massive thank you to my family away from home: Debra, Connie, Peggy and Melissa. You guys made the lab much more fun. I will miss our lunchtime talks and coffee breaks. Special thanks to Debra who has somehow become my mum when I'm at uni (how did this even start? Hahaha). Your care and support has not gone unnoticed. Our strange imagination was most memorable: Remember the ghost of physiology? Hahahaha. Love you to bits! Thanks Connie for being my travel buddy when we jetted off around the world to attend conferences and lab visits. From Boston to Amsterdam, Aarhus to Tokyo, you were awesome company and I won't forget the nights we watched the World Cup on TV while having a few drinks and nibbles! Thank you all for attending my seminar presentations and showing your support! Seeing your faces in the crowd made the experience much better without a doubt.

I am also grateful for the Monash University Postgraduate Research travel grant, ERA-EDTA travel grant, and Roger for funding my conference travels.

Finally, thank you to my family at home: Mum, Dad and Vi. Thank you mum and dad for the roof over my head, for the lovely home-cooked meals waiting for me when I got home from a long day at uni, for the unconditional love you have for me. Thanks Vi for reading through this thesis and for accompanying me on brunch and lunch dates. And thanks for all those gym sessions, even though my body gets sore the day after. It has been a long and sometimes stressful experience, but now that it is over it was all worth it!

Publications included in this PhD thesis

1. Gardiner BS, Thompson SL, **Ngo JP**, Smith DW, Abdelkader A, Broughton BR, Bertram JF, Evans RG. Diffusive oxygen shunting between vessels in the preglomerular renal vasculature: anatomic observations and computational modeling. *Am J Physiol Renal Physiol* 303: F605-618, 2012.
2. Evans RG, Harrop GK, **Ngo JP**, Ow CP, O'Connor PM. Basal renal O₂ consumption and the efficiency of O₂ utilization for Na⁺ reabsorption. *Am J Physiol Renal Physiol* 306: F551-560, 2014.
3. **Ngo JP**, Kar S, Kett MM, Gardiner BS, Pearson JT, Smith DW, Ludbrook J, Bertram JF, Evans RG. Vascular geometry and oxygen diffusion in the vicinity of artery-vein pairs in the kidney. *Am J Physiol Renal Physiol* 307: F1111-1122, 2014.
4. Evans RG, Smith DW, Khan Z, **Ngo JP**, Gardiner BS. Letter to the editor: "The plausibility of arterial-to-venous oxygen shunting in the kidney: it all depends on radial geometry". *Am J Physiol Renal Physiol* 309: F179-180, 2015

Conference abstracts

1. Kar S, Gardiner BS, Smith DW, Evans RG, **Ngo JP**. A computational-experimental protocol for investigating the quantity and anatomical location of pre-glomerular oxygen shunting

Conference: FASEB (Federation of American Societies for Experimental Biology) – Renal hemodynamics – 2013

The FASEB Journal, vol 28, no. 1, Supplement 890.13 (2014)

2. **Ngo JP**, Kett MM, Pearson JT, Smith DW, Abdelkader A, Kar S, Bertram JF, Gardiner BS, Evans RG. The influence of renal vascular geometry on oxygen delivery to renal tissue.

Conference: 51st ERA-EDTA Congress (European Renal Association-European Dialysis and Transplant Association) – 2014

Nephrology Dialysis Transplantation (2014), vol 29 (suppl 3): iii56-iii57

Presentations and awards

1. Awarded a travel grant and certificate for presenting at the 51st ERA-EDTA Congress:

Ngo JP, Kett MM, Pearson JT, Smith DW, Abdelkader A, Kar S, Bertram JF, Gardiner BS & Evans RG. The influence of renal vascular geometry on oxygen delivery to renal tissue, *European Renal Association-European Dialysis and Transplant Association (ERA-EDTA)*, Amsterdam, The Netherlands (2014)

2. Presentation at CARPE DIEM satellite meeting:

Ngo JP, Kett MM, Pearson JT, Smith DW, Abdelkader A, Kar S, Bertram JF, Gardiner BS & Evans RG. Assessment and Prediction of Kidney Oxygenation in Health and Disease: The road to a 3D model of oxygen transport in the cortex, *CARPE DIEM (Cardio Renal Paradigms Elucidated through an International Exchange Scheme)*, Amsterdam, The Netherlands (2014)

3. Poster presentation at HBPRCA:

Ngo JP, Kett MM, Pearson JT, Gardiner BS, Smith DW, Abdelkader A, Kar S, Bertram JF & Evans RG. A quantitative analysis of the factors influencing oxygen diffusion in the vicinity of artery-vein pairs in the kidney, *High Blood Pressure Research Council of Australia (HBPRCA)*, Melbourne, Australia (2013)

4. Poster presentation at FASEB:

Ngo JP, Kett MM, Pearson JT, Gardiner BS, Smith DW, Abdelkader A, Kar S, Bertram JF & Evans RG. A quantitative analysis of the factors influencing oxygen diffusion in the vicinity of artery-vein pairs in the kidney, *Federation of American Societies of Experimental Biology (FASEB) – Renal hemodynamics*, Vermont, USA (2013)

Symbols and abbreviations

SYMBOLS

| | |
|--------------------|--------------------------|
| \pm | plus or minus |
| \times | times or multiplied by |
| \leq | at least or less than |
| \geq | at least or greater than |
| $<$ | less than |
| $>$ | greater than |
| % | percent |
| \sim | approximately |
| μ | micro |
| cm | centimeter |
| L | liters |
| M | molar |
| mol | moles |
| $^{\circ}$ | degrees |
| $^{\circ}\text{C}$ | degrees Celsius |

ABBREVIATIONS

| | |
|---------------|---|
| 1D | one-dimensional |
| 2D | two-dimensional |
| 3D | three-dimensional |
| AKI | acute kidney injury |
| ANOVA | analysis of variance |
| AQP1 | aquaporin-1 |
| AQP2 | aquaporin-2 |
| ATP | adenosine triphosphate |
| AV | arterial-to-venous or arteriovenous |
| BSA | bovine serum albumin |
| CCD | charge-couple device |
| CD31 | cluster of differentiation 31 |
| CKD | chronic kidney disease |
| CMOS | complementary metal-oxide semiconductor |
| CO_2 | carbon dioxide |
| CT | computed tomography |
| DAB | diaminobenzidine |
| DAPI | 4', 6-diamidino-2-phenylindole |
| DO_2 | oxygen delivery |
| DPX | dibutyl phthalate in xylene |
| FITC | fluoresceinisothiocyanate |

| | |
|-------------------------------|---|
| g | grams |
| GMA | glycolmethacrylate |
| H & E | hematoxylin and eosin |
| H ₂ O ₂ | hydrogen peroxide |
| HRP | horseradish peroxidase |
| i.p | intraperitoneal |
| ID | inner diameter |
| IgG | immunoglobulin |
| K ⁺ | potassium |
| KeV | kiloelectron volt |
| MARP | Monash animal research platform |
| MASSIVE | Multi-modal Australian ScienceS Imaging and Visualization Environment |
| micro-CT | micro-computed tomography |
| mm | millimeter |
| mmHg | millimeters of mercury |
| MRA | magnetic resonance angiography |
| MRI | magnetic resonance imaging |
| MTC(s) | mass transfer coefficient(s) |
| Na ⁺ | sodium |
| NaCl | sodium chloride |
| NADPH | nicotinamide adenine dinucleotide phosphate oxidase |
| NH ₃ | ammonia |
| NH ₄ ⁺ | ammonium |
| NO | nitric oxide |
| O ₂ | oxygen |
| O ₂ ⁻ | superoxide |
| OD | outer diameter |
| OH ⁻ | hydroxyl |
| ONOO ⁻ | peroxynitrite |
| PBI | propagation based imaging |
| PBS | phosphate buffered saline |
| PE | polyethylene |
| PET | positron emission tomography |
| PFA | paraformaldehyde |
| PO ₂ | oxygen tension or partial pressure of oxygen |
| ROS | reactive oxygen species |
| SD | standard deviation |
| SEM | standard error of the mean |
| SM | smooth muscle |
| TIFF | tag image file format |

| | |
|-----------------|-----------------------|
| TSA | total surface area |
| v/v | volume per volume |
| VO ₂ | oxygen consumption |
| vWF | von Willebrand factor |

1 | INTRODUCTION

1.1 OVERVIEW

Acute kidney injury (AKI) and chronic kidney disease (CKD) are major causes of morbidity and mortality worldwide (2, 43). Hypoxia is the deficiency in the availability of oxygen in organs, tissues, and cells of the body. Hypoxia can result from a reduction in oxygen supply to tissue or increase in oxygen consumption, or some combination of these factors. Tissue hypoxia is a common characteristic of both AKI (4, 61) and CKD (52). Indeed there is accumulating evidence that tissue hypoxia is a critical pathogenic event in multiple forms of renal disease. However, the causes of renal hypoxia, and therefore the possible treatments for hypoxic injury, have still not been clearly defined. This deficiency in our knowledge provides the impetus for further study of kidney oxygenation and hypoxia. Importantly, there are virtually no quantitative data on the structural aspects of the kidney that influence renal oxygenation, despite the strong evidence that tissue hypoxia is a crucial factor in the pathogenesis of many forms of renal disease (11, 24, 33, 47, 73).

This PhD project focuses on the structural basis of kidney oxygenation. Using histological and imaging techniques, quantitative information on the pathways for oxygen diffusion between arteries, veins, capillaries and tissue were obtained. Convection is the movement of molecules in fluids and involves advection. Diffusion, a type of passive transport, involves the spontaneous net movement of molecules down their concentration gradient. Oxygen flows from arteries to capillaries by convection, but it also diffuses to tissue from arteries, capillaries, and even veins (13, 29). It may also diffuse from arteries to intimately associated veins, so that some of the oxygen transported to the kidney in the arteries may bypass renal tissue (55, 71). Diffusive oxygen shunting occurs in both the renal cortex (between the arteries and veins) and the renal medulla (between descending and ascending vasa recta) (71, 74). This phenomenon of diffusive oxygen shunting complicates our understanding of renal oxygenation because the amount of oxygen shunted is likely not constant, but rather dependent on blood flow and oxygen consumption (7, 8, 21). Furthermore, the nature of the pathways for diffusion of oxygen from arteries to veins likely differs as the renal cortical circulation gradually branches en route to the glomeruli. Our qualitative and quantitative analysis of the spatial association between arteries and veins of the kidney enabled us to determine how the pathways and barriers to diffusion of oxygen change along the renal arterial vasculature. This information can then be used to generate computational models of oxygen transport in the kidney.

A limiting factor in our understanding of the physiology and pathophysiology of intra-renal oxygenation is the complexity of renal oxygen transport. Our understanding of the regulation of oxygenation of both the cortex and medulla is also complicated by the unusual arrangement of the blood vessels in these two vascular territories. That is, arterial blood destined for the medulla travels with blood destined for the cortex, to the level of the proximal interlobular arteries, where the afferent arterioles of juxtamedullary glomeruli originate (Fig. 1.1). Thus, diffusive shunting of oxygen from arteries to veins in the cortex could reduce oxygen delivery to the medulla, as well as the cortex.

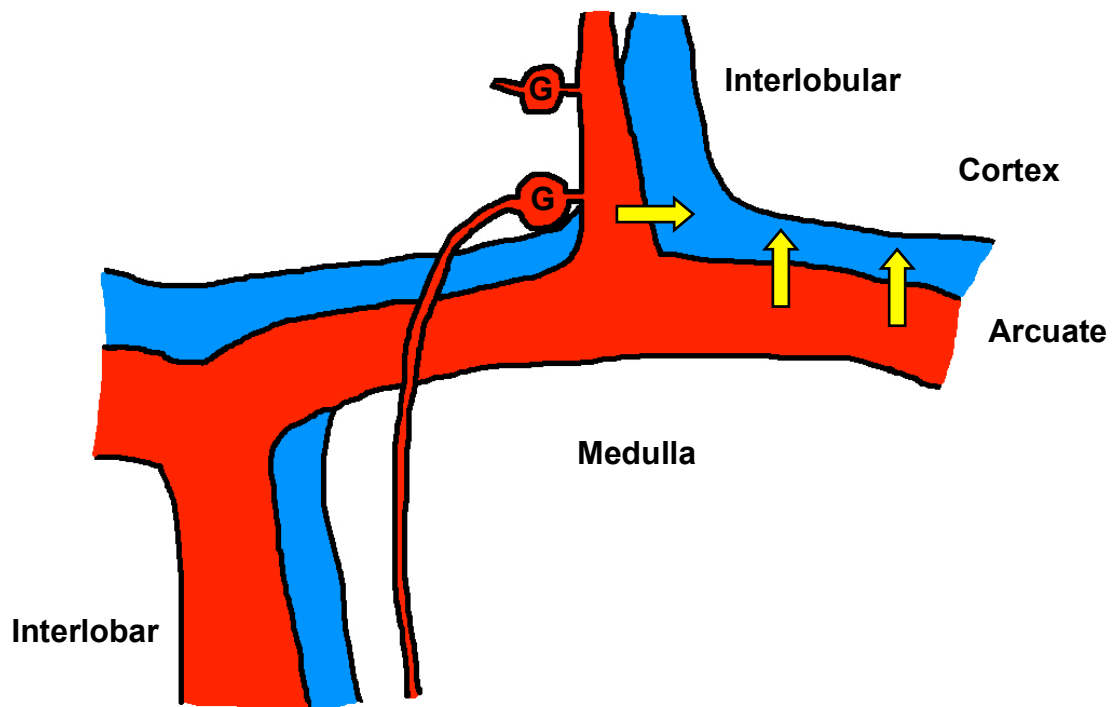


Figure 1.1. The arrangement of the arteries and veins at the corticomedullary border. Arterial blood destined for the medulla travels with blood destined for the cortex. Putative diffusive shunting of oxygen is indicated by the directional arrows. This shunting could reduce oxygen delivery to both the cortex and medulla. Arteries are in red, veins in blue, and 'G' represents glomeruli.

In order to improve our understanding of renal oxygenation, our group developed a mathematical model of oxygen transport in the renal cortex (21). However, the limitation of this model is that it did not include quantitative information regarding the radial geometry of vascular elements in the renal cortex, or of the relationships between capillaries and tissue in the cortex or medulla. Therefore, the aim of this PhD project was to obtain this information in the healthy rat kidney through quantitative analyses of the rat renal circulation.

There is experimental evidence of oxygenation being linked in the cortical and medullary circulations (56). A study by O'Connor *et al* provided evidence that tissue oxygenation of the cortex is independent of medullary perfusion, while medullary oxygenation is dependent on both cortical and medullary perfusion (56). Medullary oxygenation was reduced as expected when medullary perfusion was reduced. Interestingly, reduced cortical blood flow also resulted in reduced medullary oxygenation, even when medullary perfusion was maintained. Reductions in medullary perfusion were found to have no significant effect on cortical oxygenation. O'Connor *et al* proposed that the observed dependence of medullary oxygenation on cortical perfusion reflected the ability of deoxygenated venous blood in cortical veins to 'steal' oxygen from arteries containing blood destined for the medullary circulation (56). This proposition is also consistent with simulations generated by Gardiner *et al* using computational models of oxygen transport in the preglomerular circulation (21, 22).

Medullary hypoxia is likely to be an important factor in the pathogenesis of AKI (24, 33, 61). Because of the dependence of medullary oxygenation on cortical oxygenation, possibly due to the impact of arterial-to-venous (AV) oxygen shunting in the cortical circulation, it is imperative that we improve our understanding of diffusion of oxygen from preglomerular arteries and arterioles.

1.2 HYPOXIA AND THE PATHOGENESIS OF ACUTE KIDNEY INJURY AND CHRONIC KIDNEY DISEASE

There is accumulating evidence that hypoxia is a critical mediator of kidney injury (67). The tubulointerstitium includes the renal tubules and interstitial tissue of the kidney. Tubulointerstitial hypoxia in the kidney is a common pathological characteristic in a number of renal diseases, including AKI and CKD. Hypoxia limits oxygen availability for the production of adenosine triphosphate (ATP). Aerobic respiration requires oxygen to produce energy, with 36-38 mol of ATP generated per mol of glucose (49). In contrast, only 2 mol of ATP is produced per mol of glucose through anaerobic respiration under hypoxic conditions (49). It is thus inevitable that the severe depletion of energy in renal cells exposed to hypoxia leads to cell death (66). Hypoxia is also a mediator of fibrosis, and cellular fibrosis enhances hypoxia in the kidney by impeding the diffusion of oxygen from blood to renal tissue, leading to further kidney damage (50). It also appears to drive capillary rarefaction (6). This has led to the proposition that a vicious cycle of hypoxia and cellular damage contributes to the progression of both CKD and AKI (Fig. 1.2).

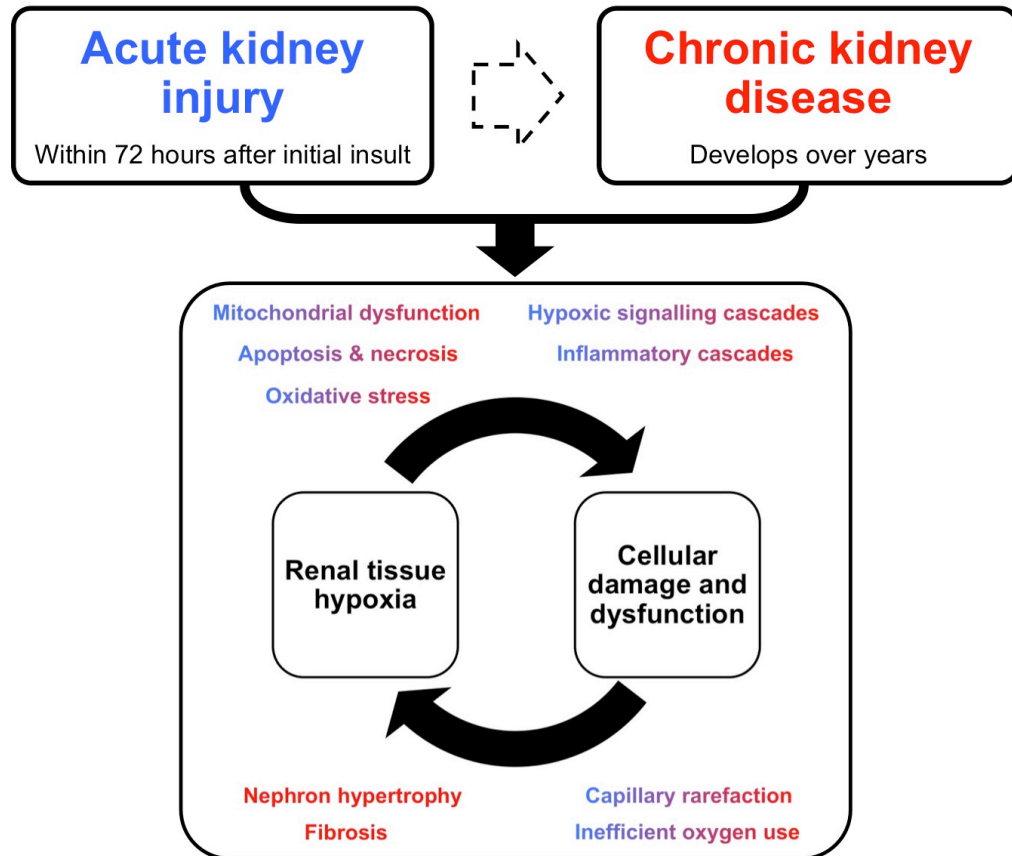


Figure 1.2. A schematic diagram demonstrating a proposed vicious cycle of hypoxia and cellular damage and dysfunction in the progression of chronic kidney disease. There is considerable evidence that the progression of acute kidney injury and chronic kidney disease is at least partly driven by renal tissue hypoxia and cellular damage and dysfunction. Tissue hypoxia drives cellular damage and dysfunction. There is also evidence that cellular damage can lead to hypoxia. The factors in red are exclusive to chronic kidney disease (CKD). The factors in both blue and red are common to both acute kidney injury (AKI) and CKD. Note also that AKI can progress to CKD and that CKD increases the susceptibility of individuals to AKI (26).

Multiple factors mediate renal dysfunction in AKI and CKD. These include inflammatory cascades, endothelial damage and dysfunction, oxidative stress and mitochondrial dysfunction (11, 24). These factors either increase renal oxygen consumption (VO_2) or reduce renal oxygen delivery (DO_2), and can thus promote tissue hypoxia (Fig. 1.2). Evidence of hypoxic damage in renal tissue has been observed in all forms of AKI and CKD studied thus far (24). For example, in CKD, often due to endothelial dysfunction, renal tissue perfusion and therefore renal DO_2 are impaired (33). Furthermore, there is also strong evidence for a reduction in the efficiency of oxygen utilization for sodium reabsorption in some forms of AKI (33, 46). For example, the efficiency of oxygen utilization for the reabsorption of sodium is reduced when there is a loss of Na^+/K^+ -ATPase polarity and tight junctions between renal tubular cells, which can be a consequence of renal ischemia reperfusion injury (46). Epithelial

cells, including renal tubule cells, are polarized, in the sense that membrane-bound proteins such as cell adhesion molecules, co-transporters, ion channels, and pumps are preferentially localized to either the apical or basolateral surface of the cell membrane (9, 72). This enables the coordinated transport of ions and solutes through the cell membrane. A loss of Na^+/K^+ -ATPase polarity results from the Na^+/K^+ -ATPase pump being mislocated to the apical membrane from its normal location of the basolateral membrane. The mislocation of the pump results in a decrease in fluid reabsorption, reducing the efficiency of oxygen use in the kidney for Na^+ reabsorption. This would be expected to promote hypoxic injury in the kidney. Furthermore, a loss of tight junctions produces gaps in the tubular wall, leading to back-leak of ions. That is, sodium and water are reabsorbed transcellularly, but then re-enters the tubule through the gaps between epithelial cells. In CKD, and when AKI progresses to permanent renal damage, it is possible that interstitial fibrosis increases the diffusion distances between blood and tissue (18, 33). Tissue hypoxia can cause further progression of kidney disease, and this progression can then exacerbate tissue hypoxia (47) (Fig. 1.2). Thus, not only is tissue hypoxia an outcome of renal disease, it also is likely involved in the pathogenesis of AKI and CKD (17).

Oxidative stress is a consequence of increased production of reactive oxygen species (ROS) and/or a decrease in the activation of anti-oxidant defense mechanisms (37). ROS are by-products of normal oxygen metabolism (68). Hydrogen peroxide (H_2O_2), hydroxyl radicals (OH^\cdot) and superoxide (O_2^\cdot) are the major ROS in biological systems (28). In the kidneys, O_2^\cdot is predominantly produced from nicotinamide adenine dinucleotide phosphate oxidase (NADPH) (23). Under healthy conditions, ROS have an important role in defending against invading microorganisms and also participate in renal vascular and tubular regulation (62). In contrast, under conditions of oxidative stress, the associated increase in ROS bioavailability is linked to the pathogenesis of CKD (62, 68). One way ROS promote CKD may be through promoting renal tissue hypoxia (60, 70, 71). Nitric oxide inhibits sodium reabsorption, the major oxygen consuming process within the kidney (58). It also normally competes with oxygen in the mitochondrial respiratory chain, thus acting to suppress tissue oxygen consumption (30) and so enhance the efficiency of oxygen utilization for sodium reabsorption (60, 71). Superoxide avidly reacts with nitric oxide, resulting in the formation of peroxynitrite (ONOO^\cdot). The consequent reduction in the bioavailability of nitric oxide leads to an increase in VO_2 and therefore increased risk of renal tissue hypoxia (60, 70).

Histopathological analyses have demonstrated that, in patients with CKD, functional impairment of the kidney is more closely associated to the degree of tubulointerstitial damage

than to glomerular injury (39, 47, 49). This discovery underlies the proposition that the final common pathway of kidney failure in CKD occurs primarily in the tubulointerstitium (47, 48), with accumulating evidence suggesting a critical role for chronic hypoxia in the tubulointerstitium as the final common pathway to end-stage kidney injury (47). Renal tissue hypoxia has been demonstrated in CKD through the use of a variety of methods. For example pimonidazole adduct immunohistochemistry has been used to demonstrate renal hypoxia in association with a reduction in peritubular capillary blood flow at an early stage of disease in a rat model of progressive glomerulonephritis (40).

AV oxygen shunting is thought to limit oxygen delivery to the renal tissue (54, 56, 63). However, this could also render the kidney susceptible to hypoxia. The impact of AV oxygen shunting on medullary oxygenation must depend on the sites, along the pre-glomerular circulation, where shunting occurs. For example, the interlobar and arcuate arteries and veins of the cortical circulation are organized in close arrangement (63). These vessels are also proximal to the divergence of the cortical and medullary circulations. Thus, if AV oxygen shunting occurs at this location, it likely impairs medullary oxygenation. A principle aim of the studies described in this thesis, therefore, was to increase our understanding of the locations of AV shunting in the renal circulation. To do this we need to first understand the anatomy of the renal vasculature, since the structure of the renal circulation complicates our understanding of medullary oxygenation.

1.3 THE RENAL CIRCULATION

In order to understand the regulation of oxygen by the kidney, we need to first understand its structure and the organization of its blood supply. Human kidneys are multilobar (Fig. 1.3B) and are thus more complicated in structure than the kidneys of common laboratory animals, such as the rat, mouse, and rabbit, which have unilobar kidneys. A longitudinal section through a unilobular kidney (Fig. 1.3A) demonstrates two clear sections: the cortex and medulla. Most commonly, each kidney receives its blood supply from a single renal artery, which arises from the abdominal aorta. However, ‘accessory’ vessels may arise from an early division of the renal artery (64, 65). These additional arteries often supply the lower poles of the kidney (3, 44).

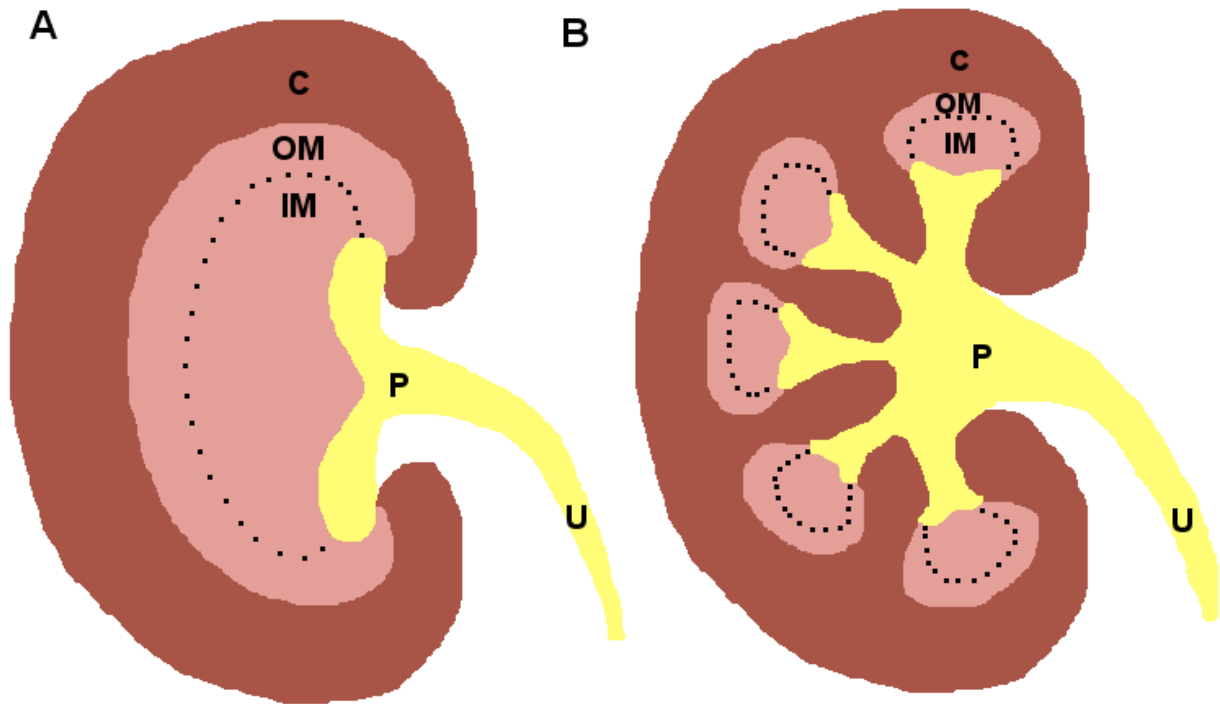


Figure 1.3. The two different types of mammalian kidneys. ‘A’ shows a unilobar or unipapillary kidney demonstrating the two main sections: the cortex (C) and the medulla, which is further divided into the outer medulla (OM) and inner medulla (IM). The renal pelvis (P) and ureter (U) are also included. ‘B’ is a multilobar or multipapillary kidney showing the cortex, medulla, pelvis and ureter.

The renal artery then divides into interlobar arteries, which then divide into arcuate arteries (45). These arcuate arteries run across the cortico-medullary border (45) (Fig. 1.4B & C). The arcuate arteries diverge into interlobular arteries that run radially through the renal cortex toward the surface of the kidney. From the interlobular arteries arise the afferent arterioles that supply the glomeruli. The afferent arterioles branch into a capillary network (glomerulus), which in turn converge into an efferent arteriole. Efferent arterioles lead to the peritubular capillaries. There are two types of peritubular circulations: cortical and medullary (Fig. 1.4C).

Efferent arterioles from the cortical nephrons divide to form an elaborate peritubular capillary network in the cortex (Fig. 1.4C). The medullary circulation arises from the efferent arterioles of juxtamedullary glomeruli, whose afferent arterioles arise from the proximal interlobular arteries, near their junction with arcuate arteries, or from the arcuate arteries themselves (1, 16, 41, 59). This means that all blood that flows through the cortex and medulla, must first flow through the proximal portion of the cortical circulation. Most of the efferent arterioles

from the juxtamedullary glomeruli divide to form the vasa recta. The vasa recta travel down into the medulla and return to the corticomedullary junction and empty into the arcuate vein (Fig. 1.4C). There are no arteries present within the renal medulla.

Accompanying the renal arteries are the veins. Superficial and stellate veins lie within the superficial cortex and drain the areas located at the surface of the kidney. Interlobular veins arise from peritubular capillaries (Fig. 1.4C) and drain the majority of the renal cortex before forming the arcuate veins, which like the arcuate arteries, run along the cortico-medullary border (Fig. 1.4B & C). The arcuate veins then lead to the interlobar veins and finally the renal vein.

It has been noted that the architecture of the renal arterial circulation is broadly similar across various mammalian species used in experimental renal physiology (1, 27, 31, 45). Thus, the nomenclature that is used is also similar. An example is the interlobar arteries, called as such even in animals with unilobar kidneys. Contrastingly, the venous circulation displays evident differences between species. For example, superficial and stellate veins are present in the kidneys of humans, cats, and dogs, whereas they are absent in the hamster, mouse, and rat, where blood is drained from the cortex simply by the interlobular veins (19, 32).

Blood flow to the renal medulla can be regulated, at least partially, independently of the cortical circulation (14). However, an unusual feature of the renal circulation is that the cortical and medullary circulations share a common path before they diverge at the level of the proximal interlobular arteries. Thus diffusion of oxygen from arteries prior to the divergence of the two circulations would be expected to limit oxygen delivery to both the cortex and medulla. In contrast, diffusion of oxygen from more distal arteries and arterioles would be expected to limit oxygen delivery only to the renal cortex. Thus, to fully understand the mechanisms that influence oxygenation of the renal medulla (and the cortex), we must develop a better understanding of the diffusion of oxygen from the pre-glomerular circulation in the renal cortex.

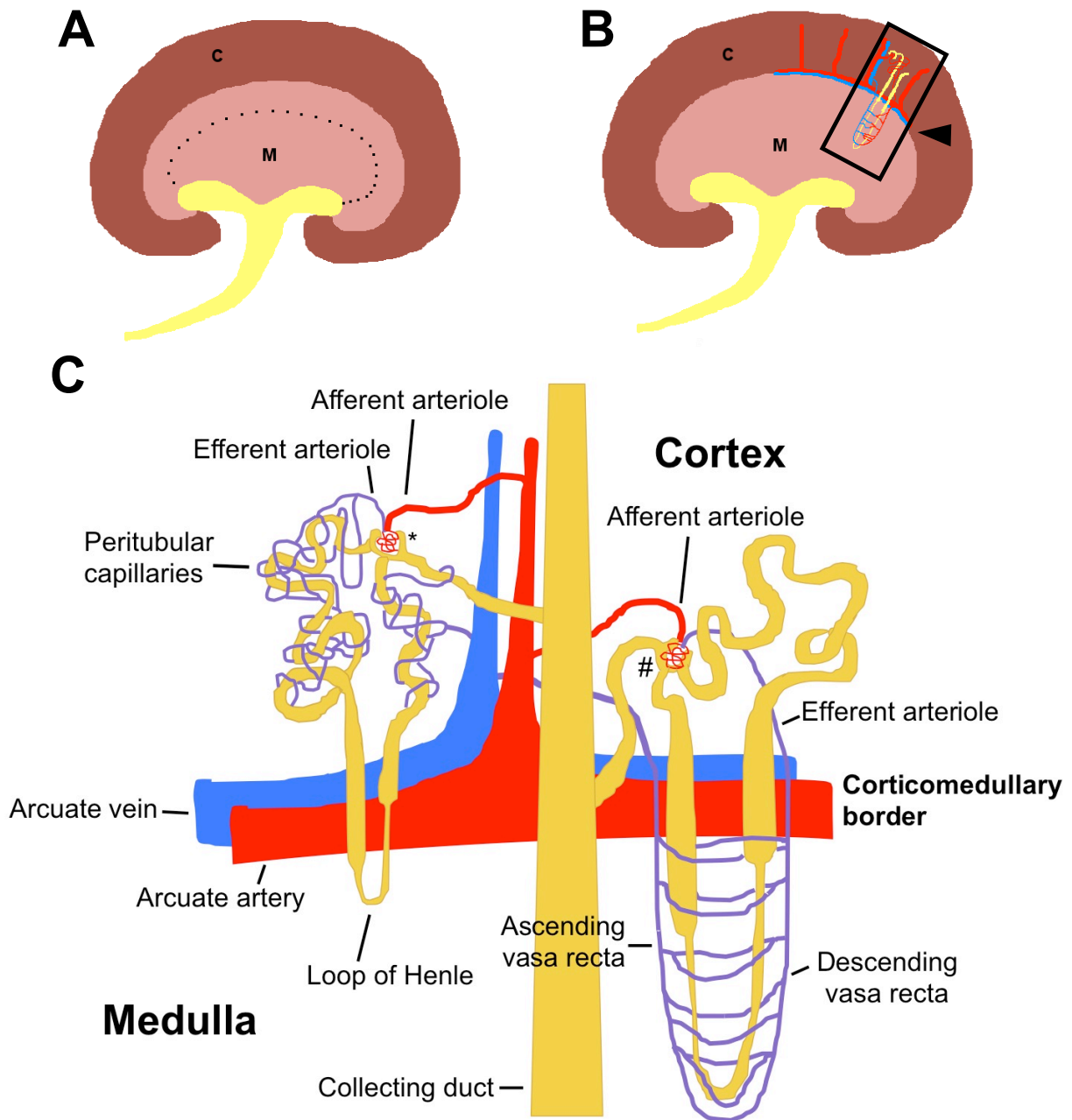


Figure 1.4. A schematic demonstrating the vascular organization of the kidney. ‘A’ demonstrates the two distinct divisions of the kidney: the cortex (C) and the medulla (M). A simplified schematic of the circulation is shown in ‘B’. An enlarged representation of the circulation inside the black rectangle in ‘B’ is shown in ‘C’. Arteries are shown in red, while the veins are in blue and capillaries in purple. The arcuate arteries and veins run along the corticomedullary border (arrow head in B & image C) where interlobular arteries form and taper towards the surface of the kidney (C). From the interlobular arteries arise the afferent arterioles, which lead to a cortical glomerulus (*, C) and its capillary network before becoming an efferent arteriole. The efferent arterioles form peritubular capillaries. Afferent arterioles at the juxtamedullary region lead to juxtamedullary nephrons (#, C). The glomerular capillaries exit the glomerulus to form vasa recta, which supply blood to the medulla before returning to the juxtamedullary area and emptying into the interlobular and arcuate veins.

1.4 CORTICAL AND MEDULLARY OXYGENATION: IS ONE DEPENDENT ON THE OTHER?

The mechanisms that render medullary oxygenation dependent on cortical blood flow remain unknown. However, AV oxygen shunting is a prime candidate. Due to the unique arrangement of the renal vasculature, where the medullary circulation arises from a small population of efferent arterioles in the juxtaglomerular cortex, medullary blood flow can be independently regulated from the vast bulk of that of the cortex (14). Thus, in theory, stimuli that cause vasoconstriction in vascular elements that regulate cortical blood flow, but not those that regulate medullary blood flow, should only cause hypoxia in the cortex. However, experimental evidence indicates that cortical oxygenation has a profound influence on oxygenation of the medulla. O'Connor *et al* used a variety of vasoactive stimuli to induce ischemia in either the renal cortex or medulla (56). They found that medullary oxygenation is dependent on not only medullary perfusion, but also cortical perfusion. Thus, medullary hypoxia may occur during cortical ischemia despite medullary perfusion being maintained. A potential explanation for these findings is that, during cortical ischemia and hypoxia, venous blood effectively ‘steals’ oxygen from arterial blood somewhere upstream from the divergence of the cortical and medullary circulations. This PhD project focuses on understanding and explaining the phenomena observed by O'Connor *et al* (56).

Let us consider the potential impact of AV oxygen shunting on medullary oxygenation from a theoretical perspective. The first scenario to consider is the possible effect of cortical ischemia if AV shunting occurs predominantly in the distal preglomerular circulation (Fig. 1.5A). These vessels include distal interlobular arteries and veins. In this situation, medullary oxygenation and perfusion remain relatively independent of cortical oxygenation during cortical ischemia. The second scenario is the expected outcome of cortical ischemia if AV shunting occurs predominantly in the proximal preglomerular circulation (Fig. 1.5B). These vessels comprise of proximal interlobular and arcuate arteries and veins. Under such conditions, the blood draining the cortex will be low in oxygen due to cortical hypoxia. The relative deoxygenation of this venous blood would increase the gradient in the partial pressure of oxygen (PO_2) between arteries and veins in the proximal sub-divisions of the cortical vasculature. This augmented PO_2 would thus promote AV oxygen shunting between these arteries and veins. As mentioned above, this theoretical scenario appears to be consistent with experimental observations (56).

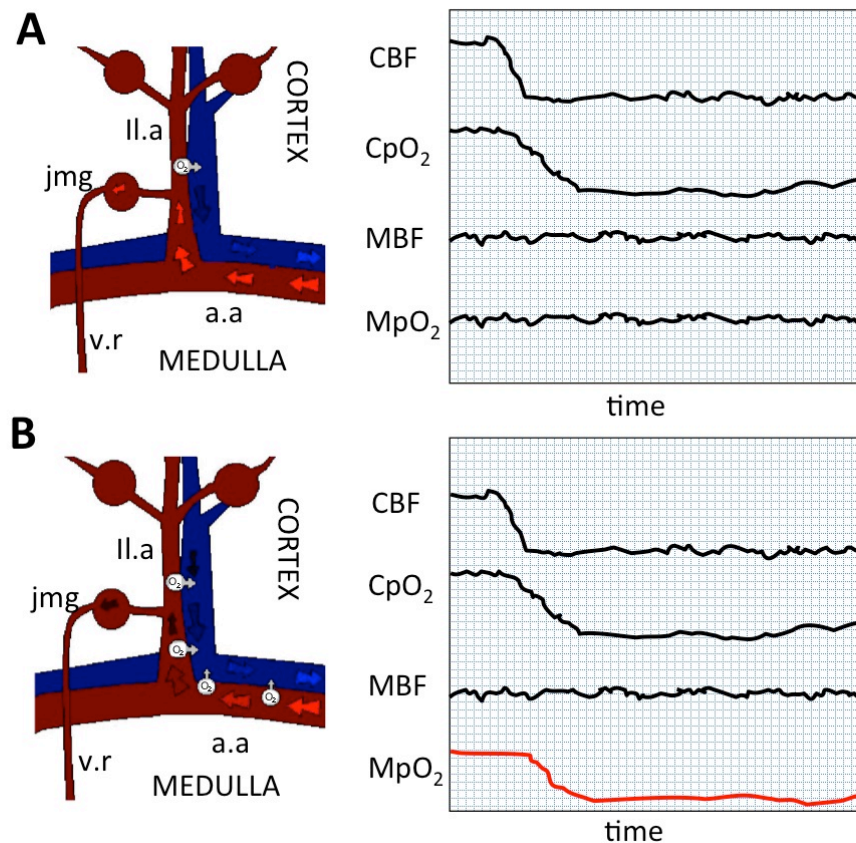


Figure 1.5. Two hypothetical effects of cortical ischemia in the kidney. (A) The effects of cortical ischemia if AV oxygen shunting occurs predominantly in the distal interlobular vessels. In this scenario, cortical perfusion and oxygenation is reduced, but medullary perfusion and oxygenation is maintained. (B) The effects of cortical ischemia if AV shunting occurs predominantly in vessels proximal to the divergence of the medullary and cortical circulations. Under these conditions, medullary oxygenation would be reduced despite medullary perfusion being maintained. Reproduced, with permission, from Evans *et al* (15). Hypothetical scenario B was reproduced in experimental studies by O'Connor *et al* (56). Il.a = interlobular artery; jmg = juxtamedullary glomeruli; v.r = vasa recta; a.a = arcuate artery; CBF = cortical blood flow; CpO₂ = cortical PO₂; MBF = medullary blood flow; MpO₂ = medullary PO₂.

AV oxygen shunting in the kidney is difficult to study experimentally. However, it is amenable to study through computational modeling. In order to generate a model of oxygen transport in the rat kidney, accurate quantitative data on the geometry of arteries and veins in the rat kidney are required. Thus, we need to examine current knowledge of the anatomy of the rat renal vasculature and how its geometry may affect oxygen transport.

1.5 CURRENT KNOWLEDGE OF THE STRUCTURE OF THE RENAL CIRCULATION IN THE RAT

1.5.1 Qualitative information on the renal circulation

1.5.1.1 Vascular patterns

Moffat and Fourman described the vascular pattern of the rat kidney back in the early 1960s (45). There are four clearly distinguished zones in the rat kidney: cortical, subcortical, outer medullary, and inner medullary. The cortical zone contains the interlobular arteries and veins, glomeruli, and a network of peritubular capillaries. In the subcortical zone juxtamedullary efferent arterioles are present. Also, vasa recta ascending from the outer medulla are evident. Efferent arterioles of glomeruli begin to divide into vasa recta and there are no obvious vascular bundles observed. The outer medullary zone contains both descending and ascending vasa recta. The inner medulla consists of a branching network of capillary loops. These observations, while important in our understanding of the anatomy of the kidney, are only qualitative. Quantitative information is required for modeling renal oxygenation. Therefore a chief aim of this PhD project is to obtain the quantitative data required for such modeling.

1.5.1.2 The renal interstitium

In the renal parenchyma, the extravascular and peritubular regions are termed the interstitial space, or interstitium. Lemley and Kriz have defined the interstitium as being enclosed completely by the basement membranes of tubules and vascular elements (34). There are various divisions of the renal interstitium; the peritubular and periarterial divisions belong to the cortical region of the kidney. The medulla is characterized by three types of interstitial space: the outer stripe, inner stripe, and inner medulla.

The peritubular interstitium in the cortex is the spaces between the capillaries, glomeruli, and tubules (34). This type of interstitium is distinguished from periarterial connective tissue. Surrounding renal arteries is periarterial connective tissue, which is a loose sheath of connective tissue that contains lymphatic vessels. This sheath of connective tissue predominantly surrounds the larger arteries, including the arcuate and interlobular arteries. Indeed, the sheath travels along the renal arteries to the afferent arteriole (34). Here, the sheath diminishes in density. Notably the approach we have taken to modeling oxygen transport in the kidney, described herein, has taken into consideration the thickness of this connective tissue and whether it acts as a barrier to the diffusion of oxygen.

1.5.2 Quantitative information on the renal circulation

Quantitative information regarding the renal circulation has been limited. As mentioned in detail in a later section of this thesis (section 1.7 of this chapter, as well as Chapters 5 – 7), Nordsletten *et al* have provided quantitative information regarding the renal circulation of the rat (51). However these data also have limitations. They provide quantitative information on axial geometry, but quantitative information on the radial geometry is also required for a three dimensional (3D) model of kidney oxygen transport to be generated. The studies described in Chapters 4 – 8 of this thesis represent a program of research aimed at provision of this information.

1.6 PHYSIOLOGICAL REGULATION OF KIDNEY OXYGENATION

In relation to their size and weight, the kidneys are one of the most perfused organs in the body. They receive almost 25% of the cardiac output at rest (49), yet they make up less than 1% of the total body weight. Oxygen delivered by renal blood flow (RBF) greatly exceeds the level needed to meet the kidney's metabolic demand (53, 55). Yet, although renal DO_2 greatly exceeds VO_2 , the kidney is still susceptible to hypoxia, which, as described above, appears to be a critical event in the pathogenesis of both AKI and CKD (11, 24).

Since the kidney extracts only ~10-20% of the oxygen delivered to it (53), relatively high oxygen tension (PO_2) in the renal tissue, especially the cortex, might be expected (55). However, the kidney is not hyperoxic, with tissue PO_2 in the cortex lower than expected (54). This inconsistency, between high oxygen supply and relatively low oxygen tension of kidney tissue, might be partly explained by the unique arrangement of the kidney's vasculature (11). In the cortex and medulla, the renal arteries and veins run parallel with each other (49, 54). Furthermore, the vessels are also in close contact with one another over long distances (54). This arrangement appears to promote the diffusion of oxygen from the arteries into the veins. The veins thus effectively 'steal' oxygen that would otherwise enter the capillary bed. Hence, a countercurrent gas exchange system appears to exist between the arterial and venous components of the renal cortical circulation (54). Moreover, a second countercurrent system appears to exist between the major medullary vessels, the ascending and descending vasa recta. This system is analogous to the countercurrent arrangement of arteries and veins in the cortex. Mathematical models predict that oxygen from the blood flowing into the medulla in the descending vasa recta diffuses into the blood flowing out of the medulla in the ascending vasa recta (74). In the renal medulla, the countercurrent arrangement of vasa recta helps maintain the cortico-medullary osmotic gradient, which in turn is thought to facilitate the

concentration of urine (12). However this anatomical arrangement also renders the medulla vulnerable to hypoxic damage (50).

It has been suggested that as much as 50% of the oxygen entering the kidney may be shunted from arteries to veins (42). Results from a mathematical model recently developed by our research group (21) suggest that cortical oxygen shunting is of the same order of magnitude as renal VO_2 under normal conditions (~5-10% of DO_2). Other models have generated smaller estimates (57). Thus the quantitative importance of renal AV oxygen shunting remains a matter of considerable controversy. AV oxygen shunting occurs where arteries and veins are aligned in a countercurrent manner. It is driven by renal VO_2 , which generates the AV difference in PO_2 that drives oxygen diffusion. Thus, resolution of this controversy will be dependent on generation of accurate information on renal vascular geometry.

The renal medulla is often considered to be a hypoxic environment where VO_2 is relatively high compared to DO_2 (53). The inner medulla has one of the lowest oxygen tensions in the body (11). Two major factors are responsible for renal medullary hypoxia. The first is diffusional shunting of oxygen from descending and ascending vasa recta (described above). The second major factor is the metabolic requirement of oxygen for sodium reabsorption in medullary tubular elements, particularly the thick ascending limbs of Henle's loop. Most renal VO_2 is used for sodium reabsorption (51), since a considerable amount of energy is needed by the kidney tubules for the activity of Na^+/K^+ -ATPase (50). The high metabolic activity of basolateral Na^+/K^+ -ATPase, which facilitates the reabsorption of 99% of the glomerular filtrate under normal physiological conditions (50), has a particularly profound impact on medullary oxygenation.

Kidney tissue PO_2 is sensitive to changes in both oxygen delivery and oxygen demand. This sensitivity enables the kidneys to act as the body's 'critmeter' (10). That is, the kidneys regulate the production of erythropoietin and thus hematocrit. However it also makes the kidneys more prone to hypoxic damage (49). The medulla is particularly susceptible to hypoxia due to high oxygen demand and limited oxygen supply (5, 25). The impact of these factors is particularly profound in the outer medulla, where the thick ascending limbs of the loops of Henle have a large energy requirement, yet the supply of oxygenated blood to this section of the kidney is particularly poor (25). Consequently, the outer medulla is a major site of renal damage in AKI of multiple etiologies (25).

From the discussion above, it is clear that a full understanding of the determinants of kidney oxygenation requires the consideration of the interplay between the structural and functional

determinants of tissue perfusion, tissue VO_2 , and countercurrent oxygen shunting. Our group has developed a mathematical model of kidney oxygenation (21). In the section below, I will outline the biophysics of oxygen transport in the kidney and the theoretical basis of the model. I will also outline the strengths and weaknesses of the model. A principal aim of this PhD project was to provide the structural information required to overcome these weaknesses.

1.7 STRUCTURAL DETERMINANTS OF KIDNEY OXYGENATION

Multiple processes enable oxygen to be delivered to the renal tissue via the renal circulation. These include the processes of convection of oxygen bound to hemoglobin and dissolved in plasma, the distribution of red blood cells during convection, and the diffusion of unbound oxygen (15). Under normal physiological conditions, the aforementioned processes function in concert in a manner that provides adequate oxygen delivery to meet renal metabolic requirements. Renal oxygen tension is heterogeneous (38), and is dependent on several factors including the rate and spatial distribution of oxygen metabolism, blood flow, the distance of the tissue to the closest blood supply, tissue permeability to oxygen, and, most importantly, the partial pressure of oxygen and oxygen saturation of hemoglobin in blood within the renal circulation (15).

It has been proposed that oxygen shunting from arteries to veins in the cortex of the kidney limits oxygen supply to renal tissue (Fig. 1.6) (15, 21, 54). In order to aid our understanding of renal oxygenation, a mathematical model of kidney oxygenation was developed (21). It incorporates AV oxygen shunting, and so allows interrogation of the potential impact on kidney oxygenation of the complex interactions between tissue perfusion, VO_2 and AV oxygen shunting.

In order to model renal oxygenation and AV oxygen shunting, we need to know about convection (axial information) and diffusion (radial information). Nordsletten *et al* (51) have provided the information required on convection, at least for the kidney of the rat (Fig. 1.7). Using high-resolution computed tomography of the renal vasculature of the rat, Nordsletten *et al* (51) identified the average radius, length, number, and total cross sectional area of vessels for each of the 11 representative branching levels (Strahler orders) of the arterial and venous vasculatures. These data were then used as the basis of the mathematical model of oxygen transport in the kidney (21). Importantly, these data allowed prediction of oxygen convection in the renal circulation (21). However, the current model is limited due to the fact that there is a lack of information regarding the radial geometry of the vessels, and also because the model does not incorporate capillaries.

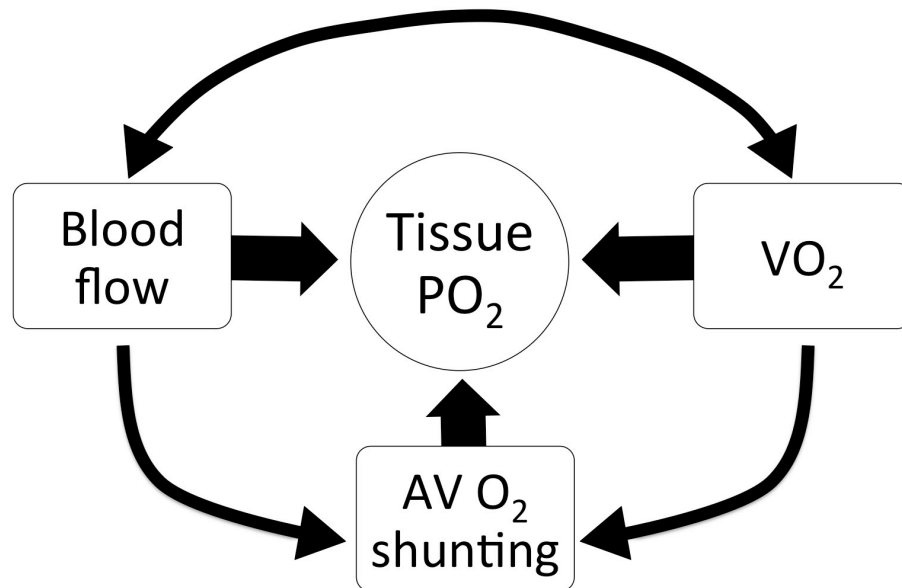


Figure 1.6. A schematic diagram of the mechanisms controlling renal oxygen tension (PO_2). Changes in blood flow affect tissue PO_2 directly via changes in oxygen supply. Alterations in blood flow also affect renal PO_2 due to changes in glomerular filtration rate (GFR) and the reabsorption of sodium. That is, a change in GFR and sodium reabsorption affects the consumption of oxygen (VO_2) by changing the Na^+/K^+ -ATPase activity. Arterial-venous (AV) shunting likely limits oxygen delivery to kidney tissue. Furthermore, the driving force of AV oxygen shunting, the AV PO_2 gradient, is produced by tubular VO_2 . Thus an increase in VO_2 should increase oxygen shunting, which should in turn affect tissue PO_2 . Changes in blood flow would also be expected to influence AV oxygen shunting by altering the transit time of convected oxygen in the renal circulation.

Because there are no data available regarding the barriers to diffusion between arteries, veins and the renal tissue (Fig. 1.8), the model was calibrated against measurements of the difference between renal tissue PO_2 and renal venous PO_2 in the outer cortex generated by Welch *et al* (71). The outer cortex is the most well oxygenated region of the kidney (63, 71). Thus the model was based on a conservative estimate of the difference between tissue PO_2 and venous PO_2 . Therefore, the estimates of AV oxygen shunting in this mathematical model (21) are expected to be conservative. The calculated diffusion coefficient was then applied across all branches. We now aim to obtain accurate information on the diffusion barriers to oxygen and identify the diffusion coefficients and how they change along the course of the renal vasculature. This is the central aim of this PhD project.

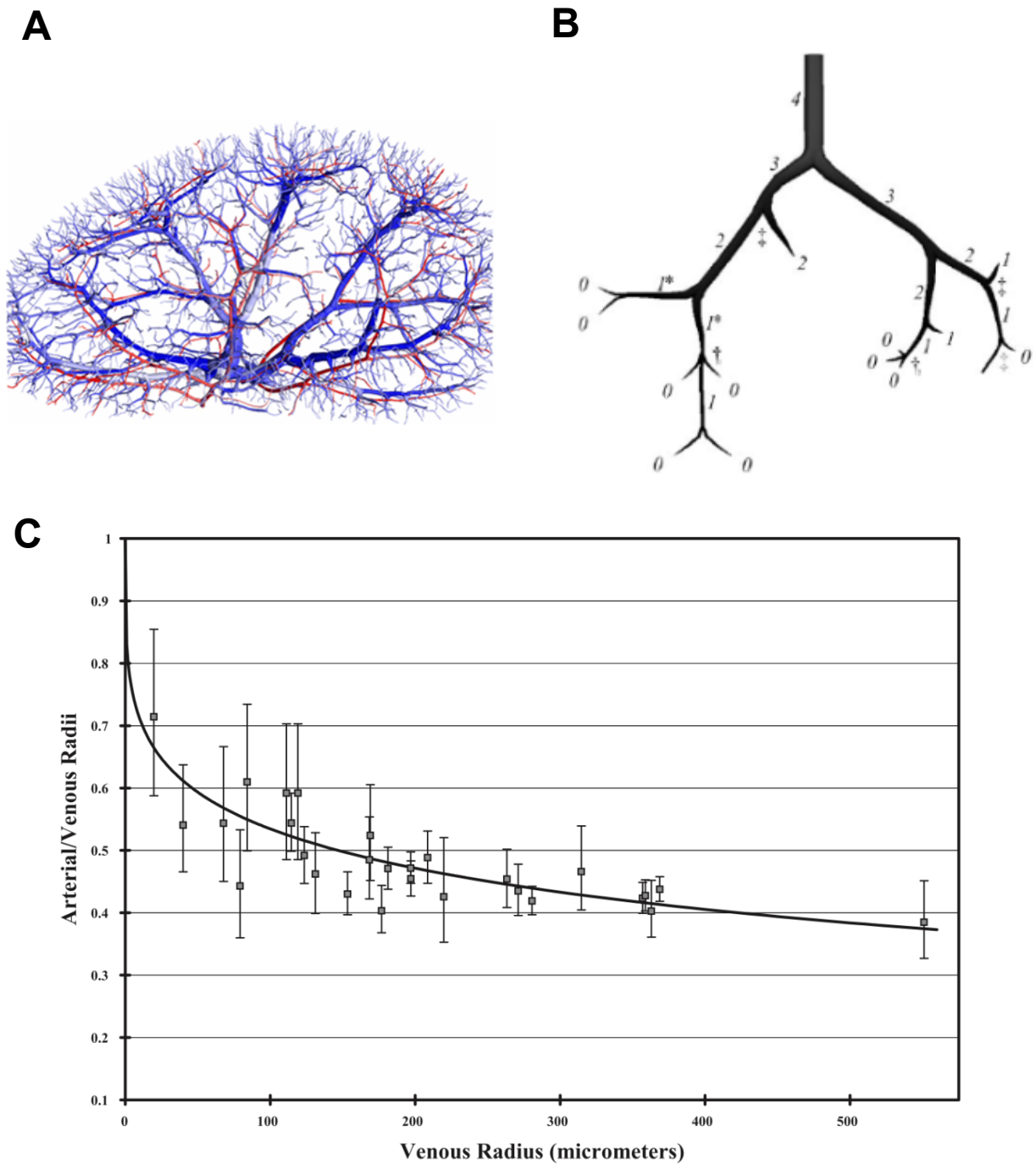


Figure 1.7. Quantification of renal cortical vascular structure by Nordsletten *et al* (51). Based on a high-resolution computer tomographic reconstruction of a renal vascular cast (A), the cortical circulation was divided into 11 representative levels, or Strahler orders (0-10) (B). The lengths and radii of arteries and veins of each order were then determined (C). These data provided the basis for modelling oxygen convection in the study by Gardiner *et al* (21), which assessed the potential contribution of arterial-venous oxygen shunting to kidney oxygen regulation. Images reproduced, with permission, from Nordsletten *et al* (51).

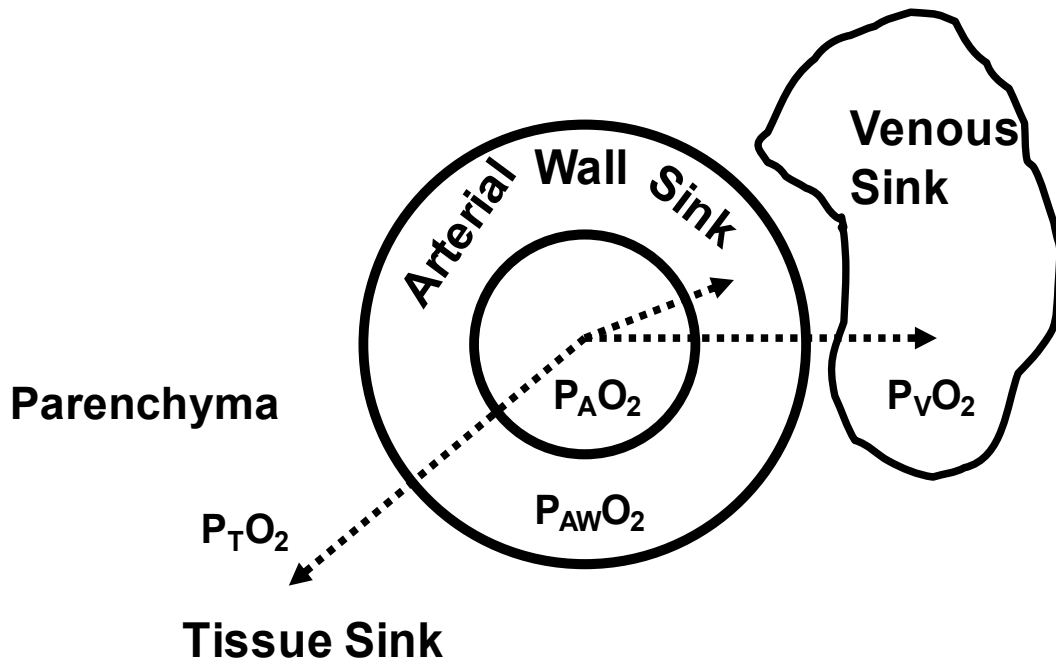


Figure 1.8. The pathways for oxygen diffusion from a renal artery. Oxygen diffuses from regions of high oxygen tension (PO_2) to regions of low PO_2 . A high PO_2 exists within the artery (arterial oxygen tension; P_{AO_2}), while lower PO_2 exists outside the artery (tissue oxygen tension, P_{TO_2} ; arterial wall oxygen tension, P_{AWO_2} ; and venous oxygen tension, P_{VO_2}). Due to these PO_2 gradients, oxygen can diffuse to these three oxygen ‘sinks’, the tissue, arterial wall, and venous sinks. A principal aim of this project was to quantify the barriers to diffusion of oxygen from arteries to these three oxygen sinks.

1.7.1 A mathematical model of oxygen transport in the kidney

The unique architecture of the renal vasculature (11, 54) provides a challenge in the understanding of renal oxygenation. Veins are generally in an intimate parallel arrangement to arteries (49, 54) and blood flows in a countercurrent manner in arteries and veins in the cortex, as well as in descending and ascending vasa recta in the medulla. This close association is hypothesized to aid in diffusive oxygen shunting in both the cortex and medulla (54). Due to the complex nature of the renal circulation, it is a challenge to generate a model of renal oxygen transport. Thus we needed to simplify the renal circulation so that we could develop a feasible and practical modeling approach without it being computationally expensive. Few models have been established for the study of blood flow and oxygen diffusion within the renal vasculature and tissues (7, 8, 69, 74). A model consisting of a hierarchy of countercurrent compartments connected in series was produced (21), with each compartment corresponding to a known level of cortical vascular branching. In this model, major processes in cortical oxygenation such as the arrangement of the cortical vasculature,

the effects of the variation in the sizes of renal vessels, variation in the velocity of blood, binding of oxygen to hemoglobin, and oxygen consumption and transport, were included.

1.7.2 Conceptual basis of the mathematical model

To simplify the model, it was streamlined to consist of countercurrent compartments. Each compartment contains an artery and a vein in parallel arrangement with contrasting fluid velocities. The cross-sectional area and length of the compartments directly relate to the average vessel dimensions of the eleven Strahler orders previously characterized by Nordsletten *et al* (51) (Fig. 1.7). One compartment therefore represents a branch level, which in the model is referred to as a “representative level”. Information on vessel architecture provided by Nordsletten *et al* (51) was then incorporated into the model.

1.7.3 Structural basis of the mathematical model

Through the use of high-resolution computed tomography (micro-CT) (20), the renal vasculature of the rat kidney was studied by Nordsletten *et al* (51). The average vessel radius, length, total cross-sectional area and number of vessels of each of the eleven known Strahler orders were identified. Moreover, the average radius of the arteries intimately associated with veins of each Strahler order was also reported (51) (Fig. 1.7). Nordsletten *et al* (51) presented the total cross-sectional area at each Strahler order, which allowed the estimation of average blood velocity from the volumetric flow rate in each branch level (51). The Strahler orders 0 – 10 were integrated into the model as representative levels ($i = 0-10$), where the largest vessels corresponded to the largest level (i.e. $i = 10$). Blood flow in arteries is in the direction of largest to smallest representative level number, and in veins, flow is from smaller representative level numbers to larger numbers (21). The model uses knowledge regarding physiological behavior and parameters, quantitative measurements of both renal arterial and venous geometry of the rat, and computer simulations of oxygen advection-diffusion.

1.7.4 Limitations of the mathematical model

In its existing form, the mathematical model of Gardiner *et al* (21) contains a few limitations. Firstly, this model only includes the cortical circulation, and groups the peritubular capillaries and medullary vasa recta together as a single oxygen sink.

The model allows for oxygen diffusion from arteries to veins, and also from both arteries and veins to the tissue (21). However, the model applies a single diffusion co-efficient across all levels of the circulation. Since it is possible that the nature of the diffusion barriers may change along the renal circulation, quantitative information regarding this factor will enable

the identification of the various diffusion coefficients at each representative level, which could then be incorporated into the model. These factors will determine the amount of AV oxygen shunting along the course of the renal circulation. Thus, an important area for improvement, which will require new data, would be to take into account the spatial association between arteries, veins and the renal tissue, as they might vary between the many branch levels of the renal circulation (21).

1.8 COUNTERCURRENT TRANSPORT OF GASES AND OTHER MOLECULES IN THE RENAL CIRCULATION

The focus in the literature on countercurrent shunting in the renal circulation has been on oxygen transport. This in turn has led to studies demonstrating how the unique spatial arrangement of arteries and veins in the kidney may facilitate the shunting of oxygen (35, 36). However, we should also recognize the potential for other molecules to diffuse between paired arteries and veins. Therefore, in Chapter 2 of this thesis, I review the evidence that oxygen and other molecules (e.g. carbon dioxide) can diffuse between arteries and veins in the kidney. I also consider the potential for diffusive shunting to have provided selection pressures to influence the evolution of the mammalian kidney.

1.9 EXPERIMENTAL APPROACH

1.9.1 Overview

Our ability to accurately model oxygen transport in the kidney is limited by the quality and quantity of available data regarding vessel geometry. To overcome such limitations, in the experiments described in this thesis, we used both light microscopic and micro-CT approaches. Studies using light microscopy enabled the generation of quantitative information regarding the spatial association between arteries and veins, as well as the relationships of these vessels to tissue oxygen sinks such as capillaries and tubules. Synchrotron-based micro-CT allowed us to create high-resolution 3D reconstructions of the renal vasculature. We used automated image analysis to convert these reconstructions into quantitative information to be used in the creation of models of renal oxygenation.

1.10 AIMS AND HYPOTHESES

The overall aim of this project was to develop new methods to quantify the radial geometry of arteries, veins and tissue in the renal cortex.

We hypothesize that:

- The spatial relationships between arteries, veins and the barriers to diffusion of oxygen from arteries to veins in the renal cortex, change along the course of the renal circulation.
- AV oxygen shunting is favored in vessels common to the cortical and medullary circulations.
- Oxygen is supplied to renal tissue by arteries, veins, and capillaries.
- Capillaries act as both sources of oxygen and oxygen sinks in the kidney.

To test these hypotheses, we aimed to

- Develop methods to identify arteries, veins and capillaries in the kidney (Chapters 4 & 5 of this thesis).
- Determine, qualitatively, the spatial relationships between arteries and veins of various calibers within the kidney (Chapter 5 of this thesis).
- Identify typical artery-vein arrangements as well as quantify the spatial relationships of artery-vein pairs in the cortex (Chapter 6 of this thesis).
- Quantify the spatial relationships between arteries and veins at the various representative levels of the renal cortical circulation (Chapter 7 of this thesis).
- Determine the surface area of peritubular capillaries in the renal cortex using stereological methods (Chapter 8 of this thesis).
- Use micro-CT methods to quantify how the radial geometry of arteries and veins changes along the course of the renal circulation (Chapter 9 of this thesis). These data can then be incorporated into a pseudo-3D model of the renal pre-glomerular circulation.

REFERENCES

1. **Bankir L, Kaissling B, de Rouffignac C, Kriz W.** The vascular organization of the kidney of *Psammomys obesus*. *Anat Embryol (Berl)* 155: 149-160, 1979.
2. **Bello AK, Nwankwo E, El Nahas AM.** Prevention of chronic kidney disease: A global challenge. *Kidney Int Suppl* 68: S11-S17, 2005.
3. **Boijesen E.** Angiographic studies of the anatomy of single and multiple renal arteries. *Acta Radiol Suppl* 183: 1-135, 1959.
4. **Bonventre JV, Weinberg JM.** Recent advances in the pathophysiology of ischemic acute renal failure. *J Am Soc Nephrol* 14: 2199-2210, 2003.
5. **Brezis M, Rosen S.** Hypoxia of the renal medulla-its implications for disease. *N Engl J Med* 332: 647-655, 1995.
6. **Chade AR.** Renal vascular structure and rarefaction. *Compr Physiol* 3: 817-831, 2013.
7. **Chen J, Edwards A, Layton AT.** A mathematical model of O₂ transport in the rat outer medulla. II. Impact of outer medullary architecture. *Am J Physiol Renal Physiol* 297: F537-F548, 2009.
8. **Chen J, Layton AT, Edwards A.** A mathematical model of O₂ transport in the rat outer medulla. I. Model formulation and baseline results. *Am J Physiol Renal Physiol* 297: F517-F536, 2009.
9. **Cibrian-Uhalte E, Abdelilah-Seyfried S.** Cell Polarity. In: *Encyclopedic Reference of Genomics and Proteomics in Molecular Medicine* Springer Berlin Heidelberg, 2006, p. 237-243.
10. **Donnelly S.** Why is erythropoietin made in the kidney? The kidney functions as a 'critmeter' to regulate the hematocrit. *Adv Exp Med Biol* 543: 73-87, 2003.
11. **Eckardt KU, Bernhardt WM, Weidemann A, Warnecke C, Rosenberger C, Wiesener MS, Willam C.** Role of hypoxia in the pathogenesis of renal disease. *Kidney Int* 68: S-46-S-51, 2005.
12. **Edwards A.** Modeling transport in the kidney: Investigating function and dysfunction. *Am J Physiol Renal Physiol* 298: F475-F484, 2010.
13. **Ellsworth ML, Pittman RN.** Arterioles supply oxygen to capillaries by diffusion as well as by convection. *Am J Physiol Heart Circ Physiol* 258: H1240-H1243, 1990.
14. **Evans RG, Eppel GA, Anderson WP, Denton KM.** Mechanisms underlying the differential control of blood flow in the renal medulla and cortex. *J Hypertens* 22: 1439-1451, 2004.
15. **Evans RG, Gardiner BS, Smith DW, O'Connor PM.** Intrarenal oxygenation: Unique challenges and the biophysical basis of homeostasis. *Am J Physiol Renal Physiol* 295: F1259-F1270, 2008.
16. **Evans RG, Head GA, Eppel GA, Burke SL, Rajapakse NW.** Angiotensin II and neurohumoral control of the renal medullary circulation. *Clin Exp Pharmacol Physiol* 37: e58-69, 2010.
17. **Evans RG, May CN.** Tissue hypoxia as a therapeutic target in acute kidney injury: Editorial commentary. *Clin Exp Pharmacol Physiol* 36: 867-869, 2009.
18. **Fine LG, Norman JT.** Chronic hypoxia as a mechanism of progression of chronic kidney diseases: from hypothesis to novel therapeutics. *Kidney Int* 74: 867-872, 2008.
19. **Fourman J, Moffat D, B.** *The blood vessels of the kidney*. London, UK: Blackwell Scientific Publications, 1971, p. 176.
20. **Garcia-Sanz A, Rodriguez-Barbero A, Bentley MD, Ritman EL, Romero JC.** Three-dimensional microcomputed tomography of renal vasculature in rats. *Hypertension* 31: 440-444, 1998.

21. **Gardiner BS, Smith DW, O'Connor PM, Evans RG.** A mathematical model of diffusional shunting of oxygen from arteries to veins in the kidney. *Am J Physiol Renal Physiol* 300: F1339-1352, 2011.
22. **Gardiner BS, Thompson SL, Ngo JP, Smith DW, Abdelkader A, Broughton BR, Bertram JF, Evans RG.** Diffusive oxygen shunting between vessels in the preglomerular renal vasculature: anatomic observations and computational modeling. *Am J Physiol Renal Physiol* 303: F605-618, 2012.
23. **Guay-Woodford LM.** Renal cystic diseases: Diverse phenotypes converge on the cilium/centrosome complex. *Pediatr Nephrol* 21: 1369-1376, 2006.
24. **Heyman SN, Khamaisi M, Rosen S, Rosenberger C.** Renal parenchymal hypoxia, hypoxia response and the progression of chronic kidney disease. *Am J Nephrol* 28: 998-1006, 2008.
25. **Heyman SN, Rosen S, Brezis M.** The renal medulla: Life at the edge of anoxia. *Blood Purif* 15: 232-242, 1997.
26. **Hsu CY, Ordonez JD, Chertow GM, Fan D, McCulloch CE, Go AS.** The risk of acute renal failure in patients with chronic kidney disease. *Kidney Int* 74: 101-107, 2008.
27. **Kaissling B, Kriz W.** Structural analysis of the rabbit kidney. *Adv Anat Embryol Cell Biol* 56: 1-123, 1979.
28. **Knight JA.** Free radicals: Their history and current status in aging and disease. *Ann Clin Lab Sci* 28: 331-346, 1998.
29. **Kobayashi H, Takizawa N.** Imaging of oxygen transfer among microvessels of rat cremaster muscle. *Circulation* 105: 1713-1719, 2002.
30. **Koivisto A, Pittner J, Froelich M, Erik A, Persson G.** Oxygen-dependent inhibition of respiration in isolated renal tubules by nitric oxide. *Kidney Int* 55: 2368-2375, 1999.
31. **Kriz W.** Structural organization of the renal medulla: comparative and functional aspects. *Am J Physiol* 241: R3-16, 1981.
32. **Kriz W, Koepsell H.** The structural organization of the mouse kidney. *Z Anat Entwicklungsgesch* 144: 137-163, 1974.
33. **Legrand M, Mik EG, Johannes T, Payen D, Ince C.** Renal hypoxia and dysoxia after reperfusion of the ischemic kidney. *Mol Med* 14: 502-516, 2008.
34. **Lemley KV, Kriz W.** Anatomy of the renal interstitium. *Kidney Int* 39: 370-381, 1991.
35. **Levy MN, Imperial ES.** Oxygen shunting in renal cortical and medullary capillaries. *Am J Physiol* 200: 159-162, 1961.
36. **Levy MN, Saucedo G.** Diffusion of oxygen from arterial to venous segments of renal capillaries. *Am J Physiol* 196: 1336-1339, 1959.
37. **Locatelli F, Canaud B, Eckardt KU, Stenvinkel P, Wanner C, Zoccali C.** Oxidative stress in end-stage renal disease: An emerging treat to patient outcome. *Nephrol Dial Transplant* 18: 1272-1280, 2003.
38. **Lübbers DW, Baumgärtl H.** Heterogeneities and profiles of oxygen pressure in brain and kidney as examples of the pO₂ distribution in the living tissue. *Kidney Int* 51: 372-380, 1997.
39. **Mackensen-Haen S, Bader R, Grund KE, Bohle A.** Correlations between renal cortical interstitial fibrosis, atrophy of the proximal tubules and impairment of the glomerular filtration rate. *Clin Nephrol* 15: 167-171, 1981.
40. **Matsumoto M, Tanaka T, Yamamoto T, Noiri E, Miyata T, Inagi R, Fujita T, Nangaku M.** Hypoperfusion of peritubular capillaries induces chronic hypoxia before progression of tubulointerstitial injury in a progressive model of rat glomerulonephritis. *J Am Soc Nephrol* 15: 1574-1581, 2004.
41. **Mattson DL.** Importance of the renal medullary circulation in the control of sodium excretion and blood pressure. *Am J Physiol Regul Integr Comp Physiol* 284: R13-27, 2003.

42. **Maxwell P.** HIF-1: An oxygen response system with special relevance to the kidney. *J Am Soc Nephrol* 14: 2712-2722, 2003.
43. **Mehta RL, Chertow GM.** Acute renal failure definitions and classification: Time for change? *J Am Soc Nephrol* 14: 2178-2187, 2003.
44. **Merklin RJ, Michels NA.** The variant renal and suprarenal blood supply with data on the inferior phrenic, ureteral and gonadal arteries: a statistical analysis based on 185 dissections and review of the literature. *J Int Coll Surg* 29: 41-76, 1958.
45. **Moffat DB, Fourman J.** The vascular pattern of the rat kidney. *J Anat* 97: 543-553, 1963.
46. **Molitoris BA, Wagner MC.** Surface membrane polarity of proximal tubular cells: alterations as a basis for malfunction. *Kidney Int* 49: 1592-1597, 1996.
47. **Nangaku M.** Chronic hypoxia and tubulointerstitial injury: A final common pathway to end-stage renal failure. *J Am Soc Nephrol* 17: 17-25, 2006.
48. **Nangaku M.** Mechanisms of tubulointerstitial injury in the kidney: Final common pathways to end-stage renal failure. *Intern Med* 43: 9-17, 2004.
49. **Nangaku M, Eckardt KU.** Hypoxia and the HIF system in kidney disease. *J Mol Med* 85: 1325-1330, 2007.
50. **Nangaku M, Nishi H, Miyata T.** Role of chronic hypoxia and hypoxia inducible factor in kidney disease. *Chin Med J* 121: 257-264, 2008.
51. **Nordsletten DA, Blackett S, Bentley MD, Ritman EL, Smith NP.** Structural morphology of renal vasculature. *Am J Physiol Heart Circ Physiol* 291: H296-H309, 2006.
52. **Norman JT, Fine LG.** Intrarenal oxygenation in chronic renal failure. *Clin Exp Pharmacol Physiol* 33: 989-996, 2006.
53. **O'Connor PM.** Renal oxygen delivery: Matching delivery to metabolic demand. *Clin Exp Pharmacol Physiol* 33: 961-967, 2006.
54. **O'Connor PM, Anderson WP, Kett MM, Evans RG.** Renal preglomerular arterial-venous O₂ shunting is a structural anti-oxidant defence mechanism of the renal cortex. *Clin Exp Pharmacol Physiol* 33: 637-641, 2006.
55. **O'Connor PM, Evans RG.** Structural antioxidant defense mechanisms in the mammalian and nonmammalian kidney: Different solutions to the same problem? *Am J Physiol Regul Integr Comp Physiol* 299: R723-R727, 2010.
56. **O'Connor PM, Kett MM, Anderson WP, Evans RG.** Renal medullary tissue oxygenation is dependent on both cortical and medullary blood flow. *Am J Physiol Renal Physiol* 290: F688-F694, 2006.
57. **Olgac U, Kurtcuoglu V.** Renal oxygenation: preglomerular vasculature is an unlikely contributor to renal oxygen shunting. *Am J Physiol Renal Physiol* 308: F671-688, 2015.
58. **Ortiz PA, Garvin JL.** Role of nitric oxide in the regulation of nephron transport. *Am J Physiol Renal Physiol* 282: F777-F784, 2002.
59. **Pallone TL, Zhang Z, Rhinehart K.** Physiology of the renal medullary microcirculation. *Am J Physiol Renal Physiol* 284: F253-266, 2003.
60. **Palm F.** Intrarenal oxygen in diabetes and a possible link to diabetic nephropathy. *Clin Exp Pharmacol Physiol* 33: 997-1001, 2006.
61. **Rosenberger C, Rosen S, Heyman SN.** Renal parenchymal oxygenation and hypoxia adaptation in acute kidney injury. *Clin Exp Pharmacol Physiol* 33: 980-988, 2006.
62. **Schnackenberg CG.** Physiological and pathophysiological roles of oxygen radicals in the renal microvasculature. *Am J Physiol Regul Integr Comp Physiol* 282: R335-R342, 2002.
63. **Schurek HJ, Jost U, Baumgartl H, Bertram H, Heckmann U.** Evidence for a preglomerular oxygen diffusion shunt in rat renal cortex. *Am J Physiol* 259: F910-915, 1990.
64. **Sykes D.** The arterial supply of the human kidney with special reference to accessory renal arteries. *Br J Surg* 50: 368-374, 1963.
65. **Sykes D.** The correlation between renal vascularisation and lobulation of the kidney. *Br J Urol* 36: 549-555, 1964.

66. **Tanaka T, Miyata T, Inagi R, Kurokawa K, Adler S, Fujita T, Nangaku M.** Hypoxia-induced apoptosis in cultured glomerular endothelial cells: Involvement of mitochondrial pathways. *Kidney Int* 64: 2020-2032, 2003.
67. **Tanaka T, Nangaku M.** The role of hypoxia, increased oxygen consumption, and hypoxia-inducible factor-1 alpha in progression of chronic kidney disease. *Curr Opin Nephrol Hypertens* 19: 43-50, 2010.
68. **Vaziri ND.** Roles of oxidative stress and antioxidant therapy in chronic kidney disease and hypertension. *Curr Opin Nephrol Hypertens* 13: 93-99, 2004.
69. **Walley KR.** Heterogeneity of oxygen delivery impairs oxygen extraction by peripheral tissues: Theory. *J Appl Physiol* 81: 885-894, 1996.
70. **Welch WJ.** Intrarenal oxygen and hypertension. *Clin Exp Pharmacol Physiol* 33: 1002-1005, 2006.
71. **Welch WJ, Baumgartl H, Lubbers D, Wilcox CS.** Nephron pO₂ and renal oxygen usage in the hypertensive rat kidney. *Kidney Int* 59: 230-237, 2001.
72. **Wilson PD.** Apico-basal polarity in polycystic kidney disease epithelia. *Biochim Biophys Acta* 1812: 1239-1248, 2011.
73. **Wilson PD.** Polycystic kidney disease. *N Engl J Med* 350: 151-164, 2004.
74. **Zhang W, Edwards A.** Oxygen transport across vasa recta in the renal medulla. *Am J Physiol Heart Circ Physiol* 283: H1042-H1055, 2002.

2 | REVIEW[†]

DIFFUSIVE SHUNTING OF GASES AND OTHER MOLECULES IN THE RENAL VASCULATURE: PHYSIOLOGICAL AND EVOLUTIONARY SIGNIFICANCE

[†] Note that this chapter, written in the form of a review article, includes some data from the candidate's thesis that were published at the time of writing.

2.1 ABSTRACT

Countercurrent systems have evolved in a variety of biological systems that allow transfer of heat, gases and solutes. For example, in the renal medulla, the countercurrent arrangement of vascular and tubular elements facilitates the trapping of urea and other solutes in the inner medulla, which in turn facilitates the formation of concentrated urine. Arteries and veins in the cortex are also arranged in a countercurrent fashion, as are descending and ascending vasa recta in the medulla. For countercurrent diffusion to occur, barriers to diffusion must be small. This appears to be particularly likely for the larger vessels in the renal cortex. There must also be gradients in the concentration of molecules between afferent and efferent vessels, with the transport of molecules possible in either direction (afferent to efferent vessels and vice versa). Such gradients exist for oxygen in both the cortex and medulla, but there is little evidence that they exist for other molecules such as carbon dioxide, nitric oxide, superoxide and ammonia. There is some experimental evidence for arterial-to-venous (AV) oxygen shunting. Mathematical models also provide evidence for oxygen shunting in both the cortex and medulla. However, the quantitative significance of AV oxygen shunting remains a matter of controversy. Thus, while the countercurrent arrangement of vasa recta in the medulla appears to have evolved as a consequence of the evolution of Henle's loop, the evolutionary significance of the intimate countercurrent arrangement of blood vessels in the renal cortex remains an enigma.

2.2 INTRODUCTION

Countercurrent systems in the kidney have long been associated with the arrangement of tubules in the renal medulla that is critical for urine concentration. However, countercurrent systems also exist in the renal vasculature. For example, the diffusional shunting of oxygen within the renal cortex has been proposed as a mechanism that might limit oxygen delivery to renal tissue (40). The intimate countercurrent arrangement of arteries and veins in the cortex (50), as well as that of the descending and ascending vasa recta in the medulla (158), may facilitate the exchange of certain gases and other highly diffusible molecules down their concentration gradients. The selection pressures that drove the evolution of these vascular arrangements have only partly been identified. For example, the countercurrent arrangement of descending and ascending vasa recta appears to be critical for urinary concentrating mechanisms (124). The countercurrent arrangement of arteries and veins in the renal cortex has been proposed to function as an antioxidant defense mechanism (103, 104). However, many molecules, including carbon dioxide, nitric oxide, superoxide and ammonia have the potential to diffuse between paired vessels in the renal circulation. Thus, it is possible that

diffusional shunting of one or more of these molecules provided the adaptive advantages that drove the evolution of countercurrent vascular arrangements in the mammalian kidney.

In this chapter, we assess the physiological significance of diffusive shunting of various molecular species in the renal circulation. We review published information regarding the kinetics and transport of oxygen (O_2), carbon dioxide (CO_2), ammonia and ammonium (NH_3 and NH_4^+), nitric oxide (NO), and superoxide (O_2^-) within the renal vasculature and renal parenchyma.

According to Fick's 1st law, the rate of transport of a specific molecular species diffusing in a specific medium depends on three factors; (i) the nature of the barriers to diffusion, (ii) the diffusivity of each molecule in the context of these barriers (defined by the diffusion coefficient), and (iii) the magnitude of the gradient in partial pressure/concentration driving diffusion. We address each of these factors in turn. We then attempt to place these observations in a physiological as well as an evolutionary perspective, to allow us to consider the selection-pressures that have driven the evolution of countercurrent arrangements in the renal vasculature. But first, we consider the importance of countercurrent exchange systems in biological systems in general.

2.3 COUNTERCURRENT EXCHANGE IN ORGANS OTHER THAN THE KIDNEY

2.3.1 Heat exchange

Countercurrent heat exchange is a common mechanism among marine animals. This mechanism allows such animals to maintain a warm body temperature in cold environments. For example, arteries and veins in the fins of whales are arranged in a manner that allows for the preservation of heat. A single artery is closely surrounded by multiple venous vessels (126) (Fig. 2.1A & B). Likewise, the arrangement of afferent and efferent vessels in the legs of aquatic birds also facilitates heat exchange (92, 93, 133) (Fig. 2.1C & D). The Iceland gull, an arctic seabird, has 3-4 veins in close association with a single artery in each leg (92). Cold venous blood returning to the body from the feet passes closely to warm arterial blood. Due to the close arrangement of the vessels, the warm arterial blood warms the cold venous blood. Anatomical and histological observations in sloths (125), leatherback turtles (58), and tuna (132) also suggest the existence of mechanisms for heat preservation via countercurrent heat exchange between afferent and efferent blood vessels. Thus, it seems clear that selection pressures for adaptations that allow regulation of tissue and body temperature have influenced

the evolution of vascular architecture across a range of species. Could the same be said for regulation or transport of gases and other molecules?

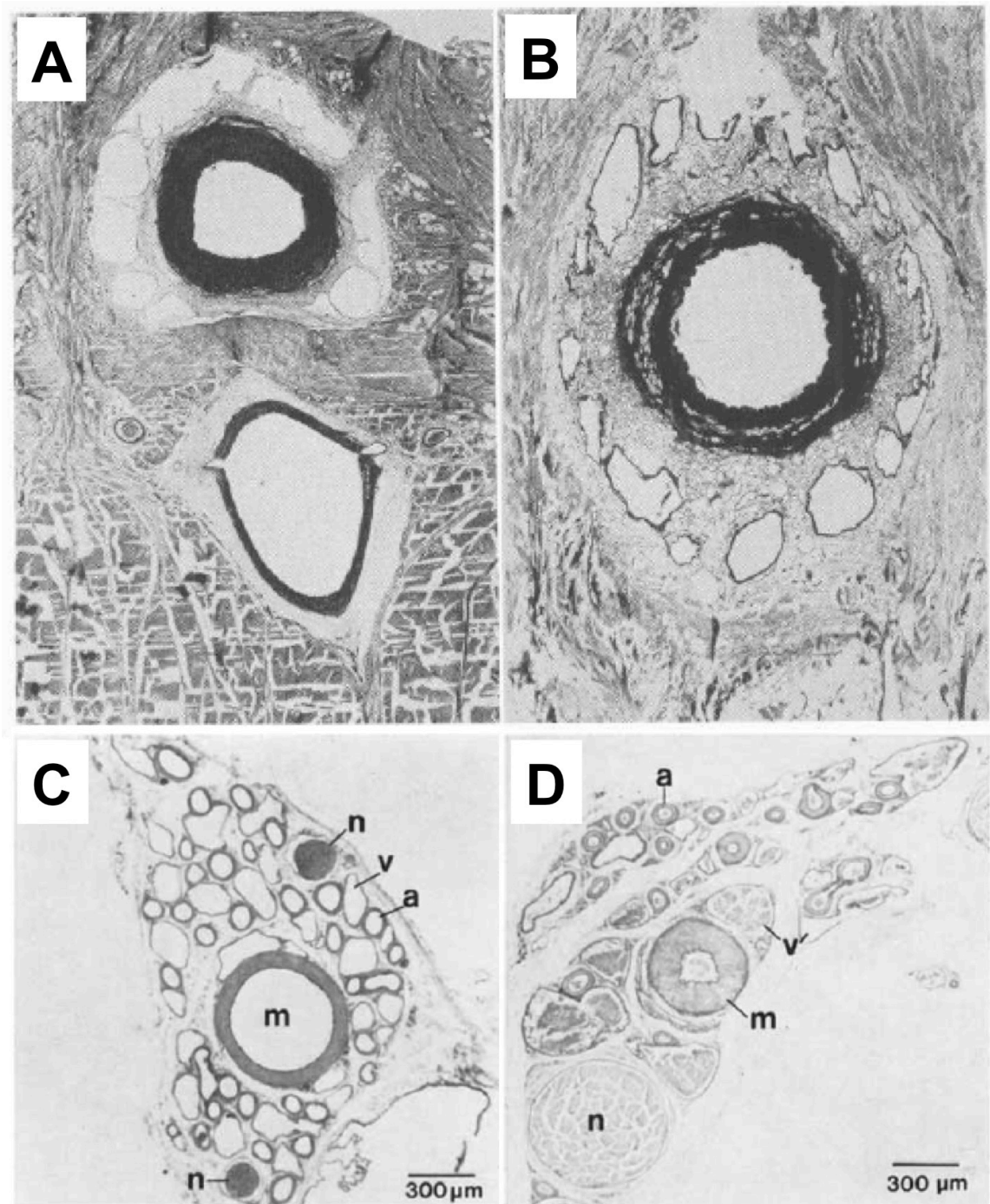


Figure 2.1. Examples of artery-vein arrangements that allow for the preservation of heat. **A & B** Cross sections of a whale fin displaying a single artery surrounded by multiple veins. **C & D** Cross sections of hind limbs of an aquatic bird. a=artery, m = main artery, v = vein, n = peroneal nerves. Images A and B reproduced, with permission, from Scholander and Schevill (126). Images C and D reproduced, with permission, from Midtgård (93).

2.3.2 Gas exchange

Diffusional shunting of gases has been demonstrated in a range of vascular beds including the stomach, small intestine, and skeletal muscle of cats (66, 68, 129), as well as in the canine heart (122). For example, the time required for oxygen to traverse the circulation of the stomach (66) and small intestine (68) was found to be less than that for erythrocytes, similar to findings by Levy and colleagues in the kidney (83, 84), as discussed later. These studies utilized boluses of blood enriched in oxygen beyond its physiological level, so the arteriovenous gradient of the partial pressure of oxygen was considerably greater than observed under physiological conditions. In skeletal muscle, Sejrsen *et al* examined the transit of ^{133}Xe , ^{51}Cr -labelled erythrocytes, as well as albumin conjugated with Evans blue dye across a skeletal muscle vascular bed, by measuring the concentration of these substances in the venous effluent (129). By using xenon, a highly diffusible molecule, Sejrsen *et al* maximized the likelihood of observing diffusion between afferent and efferent vessels in skeletal muscle. Furthermore, xenon is not naturally present in the body. Thus, although these experimental studies show the potential for highly soluble gases to diffuse between closely associated vessels, they do not provide direct evidence that countercurrent diffusion is quantitatively significant under physiological conditions. Nevertheless, countercurrent gas exchange is thought to occur in a range of vascular beds. Does the structure of the kidney allow for such shunting of molecules, and if so, where?

2.4 POTENTIAL LOCATIONS OF COUNTERCURRENT DIFFUSION IN THE RENAL CIRCULATION

Multiple computational models have provided insight into how countercurrent oxygen shunting might operate in the kidney and other vascular beds (16, 32, 49, 130). For example, Sharan and Popel created a mathematical model of oxygen transport between generic paired arterioles and venules (130). Their findings indicate that the separation distance between paired vessels is critical in determining the flux of oxygen from the arteriole to the venule. They predicted that a separation distance of $\leq 25\text{ }\mu\text{m}$ resulted in significant shunting between vessels (130). It is therefore imperative for such mathematical models to include accurate data regarding the separation distance of blood vessels. More recently, Ngo *et al* (101) generated quantitative information regarding the barriers to diffusion between arteries and veins in the renal cortex. Simulations generated using a computational model based on these data indicate that separation distance is an important factor in influencing oxygen flux between paired vessels in the kidney (50). That is, the shorter the distance, the greater the flux of oxygen between the vessels. Separation distance undoubtedly also strongly influences the flux of

other molecular species between paired renal blood vessels. Consequently, we must now consider the nature of barriers to countercurrent diffusion in the renal circulation.

2.4.1 Renal cortex

Arteries and veins in the renal cortex have an intimate relationship, particularly the large vessels found at the cortico-medullary border (47). There is some experimental evidence for diffusive shunting of oxygen from arteries to veins in the renal cortex (83, 127, 152). These will be described in detail later in this review. Importantly, Schurek *et al* were the first, to our knowledge, to suggest that AV oxygen shunting is facilitated by the intimate relationship between arteries and veins in the kidney (127). At the time, it was known that an intimate relationship existed between some intrarenal arteries and veins (at least in the rat). It was also recognized that intrarenal veins have an unusual structure, having very thin-walls similar to those of capillaries (47). These two features of the renal preglomerular circulation were proposed to facilitate diffusive shunting of oxygen and potentially other molecules (103, 104). However, there was little understanding of how these features change along the course of the renal circulation, and thus the relative quantities of oxygen (and other gases) that might diffuse between arteries and veins at various points along the renal circulation. Subsequently, Ngo *et al* found that the larger, proximal arteries of the renal cortical circulation, such as the interlobar and arcuate arteries, were more likely to be in close physical contact with corresponding veins than their smaller distal counterparts (101). Unfortunately, there are no available methods to directly measure diffusive shunting in the kidney, either across the entire vascular bed or at a segmental level. We have employed an alternative approach, combining experimental anatomy and physiology with computational modeling. That is, generation of quantitative information about the spatial relationships between arteries and veins in the renal circulation has formed the basis for mathematical models to predict how much shunting occurs and where it occurs.

Gardiner *et al* employed a two-dimensional (2D) model of countercurrent flow in idealized artery-vein pairs to identify four factors that likely have a critical impact on the quantity of oxygen (and thus other molecules) that diffuses between individual pairs of vessels (50). These are (i) the presence of capillaries or tubules between the walls of the artery and vein that could act as sources of, or sinks for, the gas (e.g. oxygen consumption by tubules), (ii) the distance between the lumen of the artery and vein (diffusion distance), (iii) the degree to which the wall of the vein envelops the wall of the artery (wrapping), and (iv) the gradients in partial pressure of gases and concentrations of other molecules between the arterial and venous blood (50). Note that three of these four factors depend upon the spatial relationships

between arteries, veins and the renal parenchyma. The findings of Gardiner *et al* accorded with those of previous modeling studies of oxygen diffusion between generic artery-vein pairs in other vascular territories (38, 55, 73, 130). The unique aspect of the relationship between arteries and veins in the renal circulation, which was not considered in these earlier studies, is the phenomenon of wrapping. That is, some arteries in the kidney are partially enveloped (venous lumen surrounds the arterial wall) by their paired vein.

Ngo *et al* hypothesized that the spatial relationships between arteries and veins change along the course of the vasculature, which in turn influences the quantities of oxygen (and so potentially other molecules) that diffuse between arterial and venous blood. To test this hypothesis, light microscopy was employed to measure arterial diameter, diffusion distance and degree of wrapping in a large sample ($n = 1628$) of artery-vein pairs in the kidneys of rats (101). They found that the intimacy of artery-vein pairs changes along the course of the cortical circulation, in a manner that likely favors oxygen shunting in vessels common to both the cortical and medullary circulations. That is, large arteries in the inner-cortex and juxtamedullary region were more likely, than smaller arteries in the mid- and outer-cortex, to (i) be devoid of capillaries and tubules in the space between the artery and its paired vein, (ii) have some proportion of the arterial wall wrapped by the wall of the vein, and (iii) have a short diffusion distance ($< 20 \mu\text{m}$) between the lumen of the artery and vein (Fig. 2.2). The 2D model of Gardiner *et al* (50) was then used to predict oxygen flux in the vicinity of typical artery-vein pairs, identified from the analysis of images generated by light microscopy. The model simulations indicated that significant diffusion of oxygen from an artery to a paired vein only occurs when the vein wall partially envelops the arterial wall. Collectively, these observations indicate that countercurrent shunting in the cortical vasculature is likely to be favored in vessels common to the cortical and medullary circulation.

2.4.2 Renal medulla

The vessels that supply the renal medulla are the vasa recta. These vessels arise from the efferent arterioles of juxtamedullary glomeruli. The descending and ascending vasa recta are arranged in a countercurrent manner. Thus one might expect countercurrent exchange to occur between these vessels. Indeed, exchange of water and solutes does occur between the ascending and descending vasa recta. Descending vasa recta lose water and gain solute while ascending vasa recta gain water and lose solute (124). This countercurrent arrangement potentially also allows for the diffusion of gases and other highly diffusive molecules between descending and ascending vasa recta (16, 17, 33).

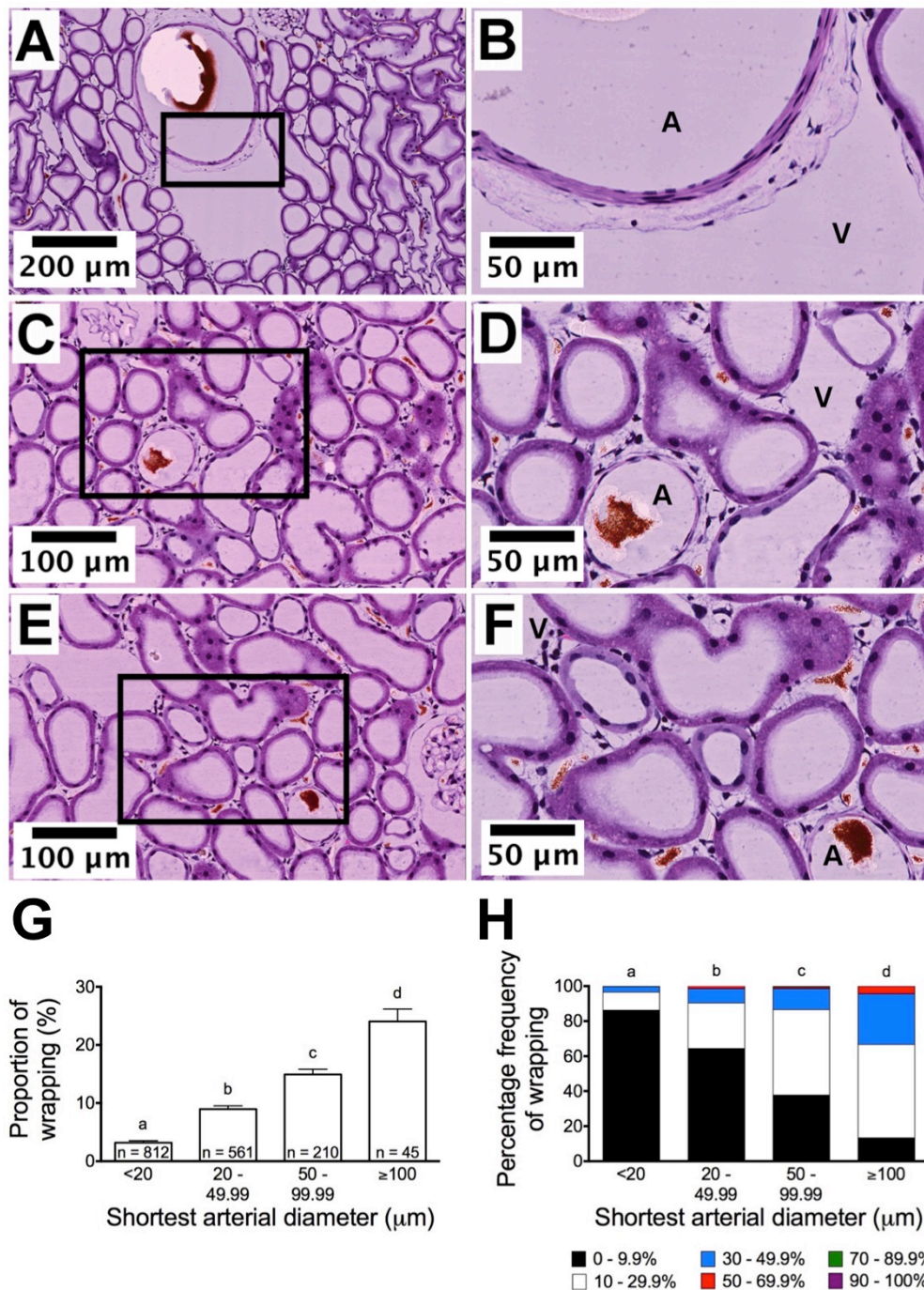


Figure 2.2. Changes in artery-vein associations in the renal cortex of the rat. (A) An interlobar artery (A) partially surrounded by a vein (V), demonstrating the phenomenon of ‘wrapping’. (C & E) Smaller arteries tend to be separated from the nearest vein. (B, D & F) represent magnified images of A, C & E respectively. (G) Changes in proportion of wrapping (%) with arterial diameter. (H) Relative frequencies of arterial profile wrapped by a vein binned into ranges of arterial diameter. The same lower case letters represent bins of arterial diameter for which wrapping (Tukey’s test; G) or percentage frequency of categories of wrapping (Cochran-Armitage test for trends; H) did not differ significantly. All images reproduced, with permission, from Ngo *et al* (101).

Descending and ascending vasa recta are closely associated (74, 75, 81). To the best of our knowledge, this association has not been quantified. Visual inspection of published histological, immunohistological images and electron micrographs (81, 111, 112, 156) shows that descending and ascending vasa recta can be as close as 5-10 μm , providing a short pathway for diffusion of soluble molecules between the vessels (Fig. 2.3).

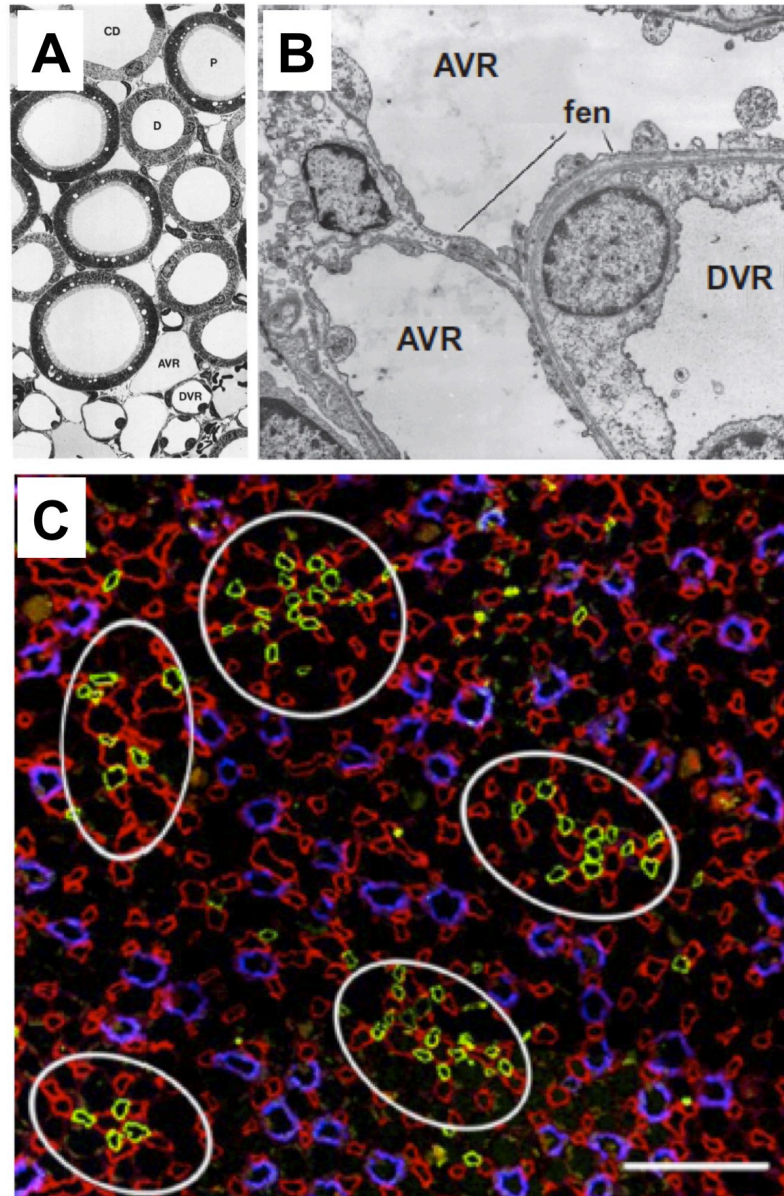


Figure 2.3. Images of the close spatial association of descending (DVR) and ascending vasa recta (AVR). (A) Transmission electron microscopy of rat renal medulla ($\sim \times 1000$ magnification). (B) Electron micrograph of DVR and AVR. Fenestrations (fen) are observed in the AVR, and the close contact of the vasa recta can be clearly seen ($\times 12,400$ magnification). (C) Vascular bundles of the medulla. DVR are represented by green fluorescent structures and AVR are represented by red fluorescent structures. Scale bar = 100 μm . Image A reproduced, with permission, from Lemley and Kriz (81). Image B reproduced, with permission, from Pallone *et al* (109) and Pallone *et al* (112), Copyright © American Physiological Society. Image C reproduced, with permission, from Yuan and Pannabecker (156). CD = collecting duct, P = proximal tubule, D = distal tubule.

The structural factors described above, chiefly in the context of putative oxygen shunting, will also influence diffusion of other molecules between the afferent and efferent vessels in the kidney. However, there are two other important sets of factors that must also be considered. Firstly, we must consider the physico-chemical properties of each molecule, which in turn defines its ability to diffuse through blood, the vessel walls and renal tissue. Secondly, we must consider the way in which each molecule is handled within the kidney, which in turn determines the nature of the gradients in partial pressure that could potentially drive countercurrent diffusion of each species in the vasculature.

2.5 PROPERTIES THAT INFLUENCE COUNTERCURRENT DIFFUSION OF MOLECULES AND GASES IN THE RENAL CIRCULATION

When we think about the transport of molecules within the kidney, we normally consider the processes of tubular reabsorption and secretion. Water-soluble molecules can pass through pores in the capillary wall by bulk flow, and across the gap between capillaries and tubules by passive diffusion. At the tubular epithelium, active and passive transport systems (including facilitated transport) regulate the magnitude of reabsorption and secretion of specific molecular species. Thus, many molecules that are unable to passively diffuse across cell membranes can nevertheless be reabsorbed or secreted.

It gets more complicated when we consider the transport of molecules across the wall of arteries, which are made up of multiple layers of cells. Thus, for any molecule to pass through the arterial wall, it must be lipid soluble. Consequently, we must consider both the diffusibility of substances in aqueous media and lipid membrane permeability.

The ability of a specific molecular species to diffuse through a specific medium is defined by Krogh's diffusion coefficient. Krogh's diffusion coefficient is the product of the diffusion coefficient of the molecule and its solubility in the medium through which it diffuses (117). Thus, Krogh's diffusion coefficient is determined largely by the solubility of the molecule in question. All molecules discussed in this review are highly diffusible in plasma and/or water (Table 2.1), making them very likely to diffuse within extracellular space. Table 2.1 also provides the relative solubilities of the molecules discussed in this review. Carbon dioxide is 24 times more soluble in water than oxygen (117) so diffuses more readily within the interstitium than oxygen. Oxygen and nitric oxide have similar diffusion coefficients (144, 157). The solubilities of oxygen, carbon dioxide and nitric oxide differ, but their diffusion coefficients are similar because these molecules have similar molecular weight (Table 2.1).

We now consider the permeability of these molecules in cellular membranes. Permeability is a measure of the ability of a liquid or gas to pass through a medium. It is thus defined as the rate at which a liquid or gas penetrates a medium. Even if a concentration gradient exists, a molecule will not diffuse between arteries and veins, or descending and ascending vasa recta, unless it is lipid permeable. Oxygen, carbon dioxide, and nitric oxide are highly lipid permeable (Table 2.2). In contrast, ammonia's ability to pass through lipid bilayers is limited. Indeed, the cell membranes of the colon, gastric cells and thick ascending limbs of the loop of Henle appear impermeable to ammonia (6, 72, 105, 131, 147). Theoretically, cell membranes should be impermeable to superoxide. Superoxide is negatively charged, and charged ions cannot passively pass through lipid membranes. Indeed, there is evidence that cell membranes are highly impermeable to superoxide (59, 85, 95, 123, 137). However, superoxide can pass through cell membranes via anion channels (85, 88, 95), so lipid permeability is not required.

In addition to the solubilities of the molecules in aqueous media and their permeabilities in lipid membranes, we must also consider the concentration gradients present between vessels. The magnitude of the concentration gradient undoubtedly has a profound effect on the diffusion of the molecule across the barrier. The greater the concentration difference between the afferent and efferent limb, the greater the drive for countercurrent diffusion. This concept is important for consideration of the interpretation of some of the earlier studies of diffusive shunting in the renal circulation. These studies, described in detail below, relied on injection of pulses of molecules that do not naturally occur in the kidney, or of supra-physiological amounts of naturally occurring molecules. Thus, such approaches maximize the gradients for countercurrent diffusion, so findings utilizing them should be interpreted with care.

Table 2.1. The solubilities and diffusivities of the five molecules reviewed.

| Gas | Solubility in plasma at 37°C (ml/dL) | Solubility in water (ml/dL) | α (<i>Solubility relative to oxygen</i>) | <i>D</i> Diffusivity ($\mu\text{m}^2/\text{s}$) | <i>D</i> (diffusion coefficient relative to oxygen) | | <i>K</i> = αD (Krogh's diffusion coefficient) |
|-----------------------------|---|-----------------------------------|---|--|---|--|--|
| | | | | | | | |
| O ₂ | 0.003 ¹ | 0.003 ¹ | 1 ($1.34 \times 10^{-3} \text{ mol.m}^{-3}.\text{mmHg}^{-1}$) ² | 2070-2550 ^{3,8} (water; 25°C) 2800 ⁹ (tissue) | 1 | | 1 |
| CO ₂ | 0.067 – 0.078 ¹⁰⁻¹² | 0.067 ⁵ | 24 ($3.21 \times 10^{-2} \text{ mol.m}^{-3}.\text{mmHg}^{-1}$) ¹³ | 1850-2110 ^{4,6,7,8} (water; 25°C) 2500 ^{19,20} (water; 37 °C) | 0.89 | | 21.40 |
| NO | ND | 0.035 – 0.04 ²¹ | 1.9 ($2.55 \times 10^{-3} \text{ mol.m}^{-3}.\text{mmHg}^{-1}$) ²² | 3300 ^{9,23} (tissue) 2210 ¹¹ (water; 25°C) | 1.18 | | 2.24 |
| O ₂ ⁻ | ND | ND | ND | 2800 ⁹ (tissue; assumed same as oxygen) | 1 | | ND |
| NH ₃ | 0.91 ²⁴ | 0.6-0.9 ²⁵ | 200 – 300 ²⁵ ($3.85 \times 10^4 \text{ mol.m}^{-3}.\text{mmHg}^{-1}$) ²⁶ | 1770 ²⁶ (water) | 0.63 | | 108 - 162 |

ND = information not available. Superscript numbers represent the source of the data presented in this table.

1. Marino and Suin (2007); reference (89)

2. Lamkin-Kennard *et al* (2004); reference (80)

3. Tse & Sandall (1979); reference (142)

4. Davidson & Cullen (1957); reference (19)

5. Baird & Davidson (1962); reference (4)

6. Vivian & King (1964); reference (145)

7. Ferrel & Himmelblau (1967); reference (44)

8. Duda & Vrentas (1968); reference (29).

9. Buerk *et al* (2003); reference (12)

10. Beachey (2013); reference (5)

11. Powell Jr (2003); reference (119)

12. Neuman & Thom (2008); reference (100)

13. Forster & Edsall (1969); reference (46)

14. Tang & Himmelblau (1965); reference (138)

15. Thomas & Adams (1965); reference (141)

16. Tham *et al* (1967); reference (140)

17. Perez & Sandall (1973); reference (116)

18. Unver & Himmelblau (1964); reference (143)

19. Geers & Gros (2000); reference (53)

20. Hulikova & Swietach (2014); reference (65)

21. Wise & Houghton (1968); reference (155)

22. Zacharia & Deen (2005); reference (157)

23. Malinski *et al* (1993); reference (87)

24. Jacques *et al* (1959); reference (67)

25. Taylor (1998); reference (139)

26. Cameron (1986); reference (15)

Table 2.2. Lipid membrane permeabilities of the five molecules reviewed.

| Molecule | Membrane type | Temperature (°C) | Permeability (cm/s) | Reference |
|-----------------------|---|------------------|------------------------------|-----------|
| Oxygen | EYPC (0 mol% cholesterol) | 20 | 67 | (136) |
| | EYPC (27.5 mol % cholesterol) | 20 | 48 | (136) |
| | L- α -Dimyristoyl-PC (0 mol% cholesterol) | 18 | 12.2 ± 0.4 | (135) |
| | | 29 | 125 ± 12.5 | (135) |
| | L- α -Dimyristoyl-PC (50 mol% cholesterol) | 18 | 10.4 ± 1.6 | (135) |
| | | 29 | 22.7 ± 4.1 | (135) |
| | L- α -Oleoyl-PC (0 mol% cholesterol) | 10 | 33 ± 1.9 | (135) |
| | | 30 | 114 ± 4.9 | (135) |
| | L- α -Oleoyl-PC (50 mol% cholesterol) | 10 | 13.7 ± 1.6 | (135) |
| | | 30 | 54.6 ± 5.6 | (135) |
| Carbon dioxide | Egg lecithin & cholesterol (1:1 mol ratio) | 22-24 | 0.35 | (60) |
| | Three types: | | 3.2 | |
| | - Pure diphytanoyl-PC (DPhPC) - 3:2:1 mixture of cholesterol, DPhPC, and egg sphingomyelin - EYPC, egg phosphatidylethanolamine, brain phosphatidylserine, cholesterol, and sphingomyelin | | | (94) |
| Ammonia | DPhPC | | $(48 \pm 5) \times 10^{-2}$ | |
| | 2:1 mixture of DPhPC and cholesterol | | $(21 \pm 10) \times 10^{-2}$ | |
| | PC from soybeans | | $(52 \pm 4) \times 10^{-2}$ | (1) |
| | 2:1 mixture of PC from soybeans and cholesterol | | $(16 \pm 5) \times 10^{-2}$ | |
| | EYPC | | 13×10^{-2} | (148) |
| Nitric oxide | Predicted from data of carbon dioxide permeability in phospholipid membrane and phospholipid-water partition coefficients | 25 | 4.6 | (39) |
| | EYPC (0 mol% cholesterol) | 20 | 93 | (136) |
| | EYPC (30 mol% cholesterol) | 20 | 77 | (136) |
| Superoxide | Soybean PC | 25 | 2.1×10^{-6} | (137) |
| | EYPC | 23 | 7.6×10^{-8} | (59) |

Permeability is defined as the rate at which a molecule passes through a medium.

PC = phosphatidylcholine, EYPC = Egg yolk phosphatidylcholine, DPhPC = diphytanoyl-phosphatidylcholine

2.6 COUNTERCURRENT DIFFUSION OF EXOGENOUS LIPID SOLUBLE SUBSTANCES IN THE RENAL CIRCULATION

Effros *et al* tested the hypothesis that lipid soluble substances are able to diffuse from arteries to veins in the kidney (37). They reasoned that this phenomenon would be evinced by the appearance of these substances in the renal vein at an earlier time point than non-lipid soluble substances, after administration via the renal artery (37). They performed transit-time, tissue distribution, and tissue equilibrium studies. Using perfused isolated kidneys from rabbits, they observed greater concentrations of [^{14}C]-butanol and $^3\text{H}_2\text{O}$ compared to ^{125}I -albumin in initial samples collected from venous outflow. Increasing flow resulted in earlier appearance of ^{125}I -albumin in the renal venous effluent compared to [^{14}C]-butanol and $^3\text{H}_2\text{O}$. Consistent with their hypothesis, these transit-time studies provided evidence that soluble [^{14}C]-butanol and $^3\text{H}_2\text{O}$ diffused from arteries to veins, at least at low rates of perfusion. Effros *et al* then used tissue distribution and equilibrium studies to determine the location of diffusion within the kidney. They discovered that the ratio of [^{14}C]-butanol to $^3\text{H}_2\text{O}$ was significantly greater in the deep cortex compared to the superficial cortex when these molecules were infused for 10 seconds. When these molecules were infused for a longer period of time (60 s to 2 h), this gradient in the ratio of [^{14}C]-butanol to $^3\text{H}_2\text{O}$ was less apparent. Thus, countercurrent diffusion may occur between interlobular arteries and veins in the renal cortex (37). Taken collectively, these observations indicate that lipid-soluble substances can diffuse from arteries-to-veins in the renal cortex. But can biologically relevant molecules also diffuse between these vascular elements, and if so, do these phenomena have significance in terms of the physiology of the kidney? We now discuss the existence of concentration gradients of oxygen, carbon dioxide, ammonia, nitric oxide and superoxide in the renal vasculature. We also examine experimental and/or theoretical evidence of countercurrent diffusion of these molecules in the renal vasculature.

2.7 OXYGEN

2.7.1 Generation of oxygen gradients in the renal circulation

The consumption of oxygen in the kidney generates the driving force for putative diffusion of oxygen from arteries to veins (49) and from descending to ascending vasa recta (16, 17). The majority of oxygen consumption in the kidney is used to drive sodium reabsorption (42). Under normal physiological conditions, the kidney extracts only 10-20% of the oxygen delivered to it. Consequently, when arterial oxygen tension (PO_2) is ~ 100 mmHg renal venous PO_2 is 50-60 mmHg (41), so an arteriovenous gradient of 40-50 mmHg exists. PO_2 in

descending and ascending vasa recta has not been measured directly, but has been estimated to be in the range of 45 to 65 mmHg (158). A baseline value of 55 mmHg, in the descending vasa recta at the corticomedullary junction, has been assumed for the purposes of computational modeling (158). Model simulations predict a PO_2 at the end of the ascending vasa recta of 40 to 45 mmHg, giving a gradient of 10 to 15 mmHg (158). As will be discussed in detail later, both experimental (83, 152) and computational studies (16, 17, 49, 50) have provided evidence that oxygen shunting occurs in both the cortex and medulla. However, the quantitative significance of these phenomena remains a matter of controversy (43, 106, 107).

2.7.2 Evidence of diffusive oxygen shunting

2.7.2.1 Renal cortex

Historically, most interest in the diffusive shunting of gases in the renal cortex has focused on the phenomenon of arterial-to-venous (AV) oxygen shunting. Levy and colleagues, in a set of ingenious experiments, provided evidence that the mean transit-time for oxygen across the renal circulation is less than that of erythrocytes (83, 84). The only satisfactory explanation for these observations was the existence of a diffusive shunt between the afferent (arterial) and efferent (venous) limbs of the renal circulation. However, an important caveat must be applied to the interpretation of these studies. As was the case for the studies of countercurrent shunting in the stomach (66) and small intestine (68) of the cat mentioned above, these studies were conducted under conditions in which the AV gradient in PO_2 was increased way beyond that present under physiological conditions.

Schurek *et al* provided further evidence for the existence of such shunt pathways by showing that the glomerular PO_2 in Wistar rats is lower than that in systemic arteries (an average of 46 mmHg vs 90 mmHg respectively) (127). These observations indicate that oxygen is lost from arteries in the preglomerular circulation, although they do not indicate the fate of this oxygen. Indeed, their findings could also be explained by diffusion of oxygen from arteries to the renal parenchyma. Delivery of oxygen to tissue by diffusion from arteries, as well as by convection of oxygen to capillaries, is well established in skeletal muscle (30, 38) and is supported in the kidney by the findings of a recent theoretical analysis (101, 106).

Perhaps the best evidence for the existence of AV oxygen shunting comes from the work of Welch *et al* (152). They used miniaturized Clark electrodes (outer tip diameter 3 – 5 μm) to measure the PO_2 of various segments along the nephron and in the vasculature of the superficial cortex. The PO_2 measured in efferent arterioles (average of 45 mmHg) was lower

than that in the renal vein (average of 52 mmHg). These observations indicate that some of the oxygen in renal arterial blood diffuses directly to adjacent veins, bypassing the peritubular capillaries.

The critical question is: how much of the oxygen supplied to the kidney in the renal artery is lost by diffusion to veins? Unfortunately, AV oxygen shunting cannot be quantified by experimental measurement, so it has been necessary to rely on computational models to try to answer this question. Based on the observations of Welch *et al* described above (152), Gardiner and colleagues calibrated their model to reflect the measured PO₂ observed by Welch *et al* (152). Then, they estimated that 5-10% of the total amount of oxygen delivered in the renal artery is shunted to the intrarenal veins under normal physiological conditions (49). Their simulations indicated that this proportion could increase considerably in pathological conditions associated with renal ischemia and/or anemia. However, Olgac and Kurtcuoglu (43, 106, 107) have developed an alternative model that predicts AV oxygen shunting is negligible. Both models were limited by the absence of precise information regarding the spatial relationships between arteries and veins in the kidney (43). Resolution of this controversy will require the development of more sophisticated models that incorporate this information.

2.7.2.2 Renal medulla

Modeling of oxygen transport across the vasa recta provided evidence that oxygen could be shunted from the descending to the ascending vasa recta (158) thus limiting delivery of oxygen to the renal papilla (158). Interestingly, modeling studies of the outer medulla have suggested that the manner in which blood vessels are arranged in the outer medulla sustains oxygen delivery to the inner medulla (16, 17). The long descending vasa recta are sequestered in the center of the vascular bundle, thus limiting loss of oxygen from descending vasa recta that penetrate the inner medulla (16, 17). This preserves oxygen delivery to the inner medulla but is predicted to impede the diffusion of oxygen to the thick ascending limbs (16). An important limitation of these models is that they do not incorporate quantitative information regarding the distances separating descending and ascending vasa recta, an important factor in determining the amount of oxygen shunted between countercurrent vessels, as demonstrated by Sharan and Popel (130) and Gardiner and colleagues (50).

2.8 CARBON DIOXIDE

2.8.1 Generation of carbon dioxide gradients in the renal circulation

Metabolism of fats, carbohydrates and proteins results in the production of carbon dioxide. Thus, catabolism contributes to the gradient of carbon dioxide between efferent and afferent vessels in all vascular beds. In the kidney, an additional process operates, since carbon dioxide and bicarbonate (HCO_3^-) are reabsorbed into peritubular capillaries from tubules (2). Furthermore, within peritubular blood the relative concentrations of carbon dioxide and bicarbonate are influenced by the activity of carbonic anhydrase and the buffering actions of proteins in the plasma and erythrocytes (including hemoglobin). In humans at rest, renal venous carbon dioxide tension (PCO_2) has been estimated to be ~ 1 mmHg greater than arterial PCO_2 , whereas mixed venous PCO_2 was ~ 4 mmHg greater than arterial PCO_2 (120). Thus, the arteriovenous gradients in the partial pressure of both oxygen and carbon dioxide are less for the kidney than the systemic circulation. Importantly, these observations do not provide support for a large AV gradient of PCO_2 that would drive venous-to-arterial shunting of carbon dioxide in the renal cortex.

The diffusive shunting of carbon dioxide from ascending to descending vasa recta in the renal medulla would require a greater PCO_2 in ascending than descending vasa recta. Available measurements indicate that such a gradient does not exist (76, 77). Thus, there is little evidence for the existence of a gradient to drive diffusive shunting of carbon dioxide in the medullary circulation. However it may be in the form of a bicarbonate or hydrogen ion gradient due to the bicarbonate buffer system. Carbonic anhydrase catalyzes the reaction between carbon dioxide and water to readily form carbonic acid. Carbonic acid then dissociates to bicarbonate and hydrogen ions. Thus, the inability to detect a gradient in carbon dioxide may be due to the bicarbonate buffer system. But what evidence is there to suggest that carbon dioxide can diffuse between countercurrent blood vessels?

2.8.2 Evidence of diffusive carbon dioxide shunting

2.8.2.1 Renal cortex

DuBose *et al* measured PCO_2 in the kidney (23, 25, 27, 28). Using pH-sensing microelectrodes, they found gradients of PCO_2 in the renal cortex (28). Similar findings were generated by four other research groups (7, 11, 54, 64). In the studies of Du Bose and colleagues, PCO_2 was approximately 65 mmHg in the distal tubules and stellate vessels (subcapsular vessels that form the interlobular veins) of the outer cortex, and was approximately 40 mmHg in the renal vein. These findings are consistent with the presence of

diffusive transfer of carbon dioxide from venules/veins to arterioles/arteries in the renal cortex. Bidani *et al* took a mathematical approach to examine the role of diffusive shunting of carbon dioxide in generating high PCO_2 in the outer cortex (8). They also compared the model's predictions of PCO_2 (8) with those measured by DuBose *et al* (27, 28). Their model could replicate the findings of Du Bose *et al*, provided both metabolic production of carbon dioxide by aerobic respiration and its diffusion from veins to arteries were accounted for. Modeling also predicted that the effect of countercurrent exchange can explain the high levels of PCO_2 in the superficial cortex (3). Taken together, these observations support the proposition that diffusive shunting of carbon dioxide generates a gradient of PCO_2 in the cortex. This proposition, however, was questioned by De Mello Aires *et al* (20) who were unable to detect a difference in PCO_2 between the renal cortex and systemic arterial blood. Three different types of Severinghaus PCO_2 microelectrodes were used in their studies, one of which was a 'glass bubble' pH electrode with some similarities as well as some differences to the 'glass membrane' electrode employed by Du Bose *et al*. The discrepancy between the findings from these different groups has not been resolved (24). Consequently, the presence of venous-to-arterial shunting of carbon dioxide in the renal cortex remains unresolved.

2.8.2.2 Renal medulla

Burke and colleagues (13) reasoned that, due to the countercurrent arrangement of the descending and ascending vasa recta, gradients in PCO_2 and pH should accompany gradients of PO_2 within the kidney (13). They developed a simple model to simulate the gradients of oxygen and carbon dioxide in the medulla (13). Their model indicates that there can be shunting of carbon dioxide between the vasa recta, provided there is a gradient in the partial pressure of carbon dioxide between descending and ascending vasa recta. Unfortunately, it has not been possible to measure the concentrations of any molecule at the beginning of the descending and end of the ascending vasa recta. The only available relevant data come from micropuncture studies of the renal papilla, in which no gradients in PCO_2 could be detected between ascending and descending vasa recta (76, 77). Thus the PCO_2 levels in the vasa recta of the outer medulla remain unknown. Consequently, the critical assumption, upon which the model of Burke and colleagues was based, remains to be tested.

2.9 AMMONIA

2.9.1 Generation of ammonia gradients in the renal circulation

Ammonia exists in two molecular forms, uncharged ammonia (NH_3) and charged ammonium (NH_4^+). These molecular species play an important role in maintenance of intracellular pH. In

this review, we define ‘ammonia’ as the total of both ammonia species. When referring to a specific species, we use either NH_3 or NH_4^+ . In most mammalian biological fluids of pH 7.4, total ammonia is mostly present as NH_4^+ and ~1% is present as NH_3 (151). Ammonia is produced by the kidney in the proximal tubule and is then transported to the renal vein or into urine. It is delivered to the renal medulla via the loops of Henle, and ammonia from the thick ascending limb is ‘recycled’ into the descending limb of the loop of Henle. This recycling therefore leads to accumulation of ammonia in the medullary interstitium and is reflected in the high concentrations of ammonia in the medulla (121, 134), resulting in a cortico-medullary gradient of ammonia. But could there also be gradients in the concentration of ammonia between the afferent and efferent limbs of the renal circulations?

Ammonia is unlikely to be shunted between blood vessels due to its impermeability across lipid bilayers. In particular, it is unlikely that ammonia can pass through the walls of arteries as they consist of many layers of cells. An exception would be the passage of ammonia through ascending vasa recta, which are highly fenestrated. Recent modeling indicates that the level of ammonia in ascending vasa recta might be ~1300% greater than that in descending vasa recta (102). High concentrations in ascending vasa recta probably reflect high levels in the interstitium. In conclusion, there is little evidence for large gradients in the concentration of ammonia between arteries and veins in the renal cortex. However there may be a significant gradient between ascending and descending vasa recta in the medulla.

2.9.2 Is there evidence of diffusive ammonia shunting in the renal circulation?

2.9.2.1 Renal cortex

Studies on ammonia transport have focused on the tubules, the site of ammonia production and consequent transport. There have been numerous studies that provide evidence for the active transport of ammonia between tubules via transporters (45, 51, 56, 57, 91, 96). The impermeability of lipid bilayers to ammonia provides theoretical evidence for the lack of shunting of ammonia between blood vessels in the renal cortex.

Due to its uncharged nature, NH_3 should theoretically diffuse through lipid bilayers (148). However, NH_3 appears to have limited lipid permeability (6, 105). Indeed, the cell membranes of the colon (131), gastric glands (147), and medullary thick ascending limb of Henle (72) have low permeability for NH_3 . Because of its charge, NH_4^+ requires channels, carriers, or transport proteins to pass through lipid layers. To the best of our knowledge, such

transporters are only present in tubules, not blood vessels. Thus, it is unlikely that NH_3 or NH_4^+ can diffuse between arteries and veins in the renal cortex.

2.9.2.2 Renal medulla

The ascending vasa recta are highly fenestrated (109, 110) and lie in close proximity to the ascending limb of the loop of Henle (82) and collecting duct (113, 114). Subsequently, some of the ammonia, as it diffuses from the loop of Henle into the collecting duct, will diffuse into the ascending vasa recta. However, it is unlikely that NH_3 diffuses between descending and ascending vasa recta due to the limited permeability of NH_3 and continuous epithelium of the descending vasa recta.

Collectively, there is little evidence of countercurrent shunting of ammonia in either the cortical or medullary circulations. Theoretically, ammonia would not be expected to diffuse between blood vessels due to its limited lipid permeability.

2.10 NITRIC OXIDE AND SUPEROXIDE

2.10.1 Are there gradients in the concentrations of nitric oxide and superoxide in the renal circulation?

Nitric oxide and its scavenger superoxide are involved in the regulation of vascular and tubular function (78, 149, 154). Nitric oxide is a vasoactive gas produced in the blood vessels and tubules of the kidney via nitric oxide synthase (90). Due to its high diffusibility but short half-life, it is possible for nitric oxide to only affect structures in the immediate vicinity of its site of production (108). Thus, it acts as a paracrine or autocrine factor. Superoxide is also highly diffusible and has a short half-life (35, 153). Indeed nitric oxide and superoxide avidly react to form peroxynitrite. Thus, they can be considered to operate as a system. Both nitric oxide and superoxide are involved in local control of sodium reabsorption and oxygenation. Nitric oxide inhibits sodium reabsorption by inhibiting the $\text{Na}^+/\text{K}^+/\text{2Cl}^-$ co-transporter (108). Superoxide has reciprocal effects and can augment sodium reabsorption via scavenging of nitric oxide as well as its direct cellular actions (52). Furthermore, nitric oxide and superoxide also affect tubular oxygen consumption, through the ability of nitric oxide to inhibit oxygen utilization by the mitochondria (9). There is evidence that metabolites of arachidonic acid can diffuse from venules to adjacent arterioles in skeletal muscle to induce vasodilatation (62, 63). Likewise, is it possible for nitric oxide, superoxide or other vasoactive free radicals to diffuse from a venule to an arteriole, so providing a mechanism for feedback control of vascular tone?

There is a theoretical argument against the presence of a nitric oxide gradient from venules to arterioles. Arterioles have a shear rate 4 – 6 times greater than venules (98). If release of nitric oxide by endothelial cells is proportional to shear stress (69), then the endothelium of the arteriole should release greater amounts of nitric oxide than the venular endothelium. These considerations predict a greater concentration of nitric oxide in the arteriole than the adjacent venule. On the other hand, it has been proposed that there are more endothelial cells in the venule wall due to its larger radial size than arterioles.

There are little direct observational data regarding the concentrations of nitric oxide and superoxide in the cortical circulation. Furthermore, in non-renal vascular beds, the presence of gradients in nitric oxide remains a matter of controversy. For example, higher levels of nitric oxide in the venular wall compared to the arteriolar wall were found in rat intestine (10), while others have found peri-arteriolar concentrations of nitric oxide to be mostly higher than peri-venular levels in rat intestine (97, 146). However, these putative gradients of nitric oxide between arteries/arterioles and veins/venules were mostly not statistically significant (10, 98, 146). The only exception is the observations of Nase *et al* (97) who found significantly greater peri-arteriolar than peri-venular concentrations of nitric oxide.

Although modeling predicts that radial concentration gradients for nitric oxide and superoxide are present in the medulla (35), we are not aware of theoretical or experimental evidence to support the presence of gradients in the concentrations of these molecules between veins and arteries in the cortex, or between ascending and descending vasa recta in the medulla.

2.10.2 Is there evidence of diffusive shunting of nitric oxide and superoxide in the renal circulation?

Due to the important roles of nitric oxide and superoxide in the regulation of microcirculatory function, the transport and interactions between these molecules has been extensively studied using computational models (14, 21, 22, 70, 71, 79, 80). Collectively, these modeling studies provide evidence that the diffusion of these molecules between paired vessels is possible.

The computational model of nitric oxide transport between a paired arteriole and venule developed by Kavdia and Popel provided support for the concept that venular release of nitric oxide could induce dilatation of adjacent arterioles (70). They presumed that the close countercurrent arrangement of these vessels might facilitate diffusion of nitric oxide. Veins are much more compliant than arteries. Thus, veins dilate if the volume of fluid they contain increases. On the other hand, arteries can dilate if acted upon by endothelium-derived relaxing

factors such as nitric oxide. So while such mediators diffusing from arteries to veins will have little or no effect on the venule, such mediators diffusing from the venule to the arteriole would be expected to dilate the arteriole. Hence, it is possible for these mediators to control arteriolar tone. Modeling predicts that diffusion of nitric oxide can only occur when there is a nitric oxide concentration gradient present and the paired vessels are close together (18, 70). These findings support the hypothesis that the spatial arrangement of the vessels aids the diffusion of nitric oxide between blood vessels, but does not provide evidence that diffusive shunting occurs under physiological conditions.

In summary, there is little evidence to suggest that significant gradients of nitric oxide (or superoxide) exist between afferent and efferent vessels in the renal circulation. Also, to the best of our knowledge, there are no experimental data or model simulations that provide evidence that diffusive shunting of nitric oxide (or superoxide) occurs in the renal cortical or medullary circulations.

2.11 WHAT FACTORS HAVE DRIVEN EVOLUTION OF THE VASCULAR ARCHITECTURE OF THE MAMMALIAN KIDNEY?

As a summary, Figure 2.4 depicts the likely direction of diffusion of the molecules discussed in this review. Below, we consider the potential adaptive consequences of such diffusion and speculate regarding the potential for these phenomena to contribute to the selection pressures that might have driven the evolution of vascular architecture in the mammalian kidney. Naturally, we must also consider the possibility that factors other than countercurrent diffusion have provided this selection pressure.

2.11.1 Renal cortex

A unique aspect of the mammalian kidney is the intimate association of arteries and veins. What selection pressures have driven evolution of this arrangement? O'Connor *et al* proposed that diffusional shunting of oxygen, from arteries to veins in the renal cortex, represents a structural anti-oxidant mechanism (103, 104). They argued that, by limiting oxygen delivery to the renal tissue, this mechanism would prevent excessive production of superoxide, and thus oxidative stress. An antioxidant defense mechanism of this nature, that inhibits formation of reactive oxygen species, would be more energetically efficient than one that relies on the chemical quenching of reactive oxygen species once they are formed. This argument is, of course, entirely dependent on the proposition that AV oxygen shunting is quantitatively significant. As discussed above, the jury is still out on this question.

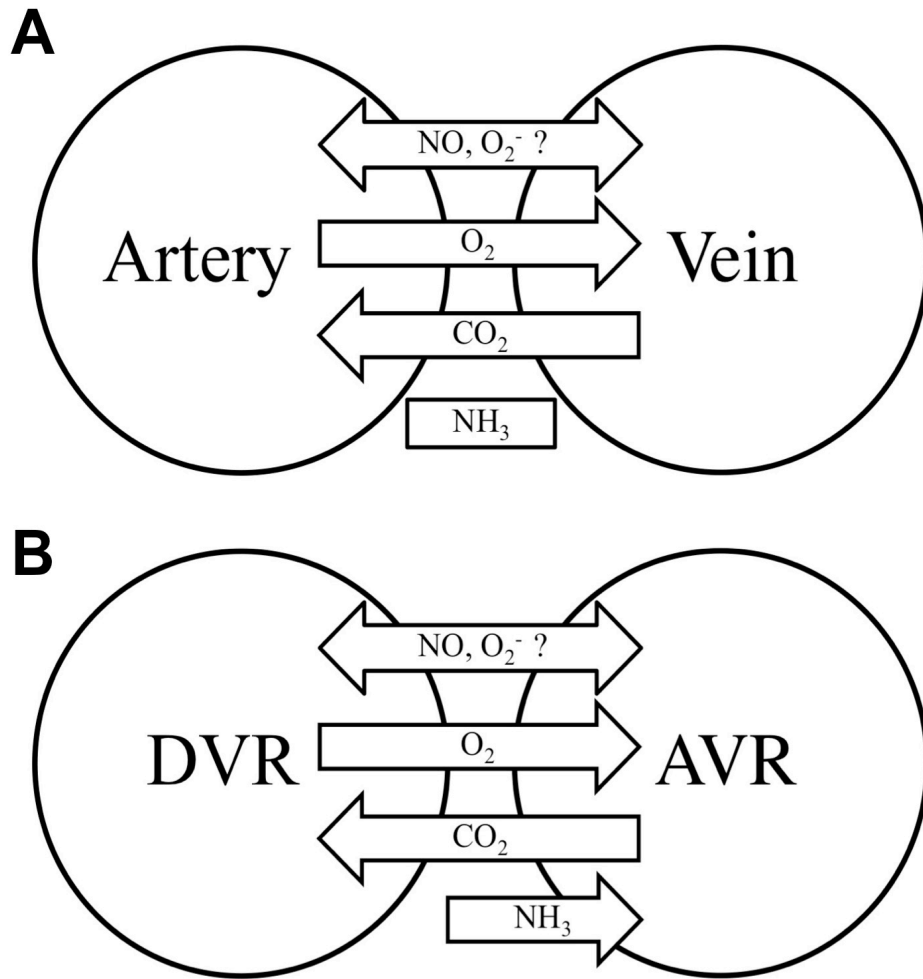


Figure 2.4. The likely direction of diffusion for oxygen, carbon dioxide, nitric oxide, superoxide, and ammonia between afferent and efferent vessels of the renal cortex (A) and medulla (B). DVR = descending vasa recta, AVR = ascending vasa recta, O₂ = oxygen, NO = nitric oxide, CO₂ = carbon dioxide, O₂⁻ = superoxide, NH₃ = ammonia. Note that blood vessels are relatively impermeable to ammonia, unless they are fenestrated, as is the case for ascending vasa recta.

Carbon dioxide is much more soluble than oxygen, so should diffuse more avidly. Venous-to-arterial shunting of carbon dioxide would be predicted to have two important effects. Firstly, it would be expected to lead to ‘trapping’ of carbon dioxide, particularly in the outer cortex (28, 86). This phenomenon would potentially enhance oxygen delivery to tissue by shifting the oxygen-hemoglobin dissociation curve to the right. Furthermore, it would potentially be enhanced when renal blood flow is reduced, thus providing a mechanism that sustains oxygen delivery to cortical tissue during renal ischemia. However, as reviewed above, it seems that the gradient in PCO₂ between veins and arteries in the renal cortex is relatively small (~1 mmHg), at least under normal physiological conditions, and so is unlikely to be sufficient to drive quantitatively significant shunting of carbon dioxide. A plausible explanation for the absence of a significant gradient is that the cortical structures have high permeability to carbon dioxide, so that its levels approach equilibrium. DuBose *et al* (28) observed that PCO₂

levels were similar across the proximal tubule, distal tubule, and stellate vessels. Thus their findings accord with those of others, of high tubular permeability to carbon dioxide (128, 150).

Theoretically, vasoactive paracrine factors could diffuse from intrarenal veins to intrarenal arteries, thus providing a mechanism for feedback regulation of arteriolar tone. Such mechanisms have been described in non-renal vascular beds (48, 118). However, we are not aware of any evidence that such mechanisms operate in the kidney.

It seems unlikely that countercurrent shunting of nitric oxide, superoxide or ammonia are quantitatively significant in the cortical vasculature. Thus, based on currently available information, shunting of oxygen seems to be the best candidate, with carbon dioxide less likely, for providing selection pressure for the evolution of the intimate spatial relationships between arteries and veins in the mammalian kidney.

2.11.2 Renal medulla

It is not currently feasible to quantify the concentration gradients of any molecule between descending and ascending vasa recta in the outer medulla. Therefore our current understanding of diffusive shunting in the medulla comes from theoretical studies underpinned by anatomical observations.

Our review of the literature indicates that countercurrent shunting of ammonia, nitric oxide and superoxide are unlikely to be important in the renal medulla. However, it remains feasible that the evolution of the architecture of the medullary vasculature has been influenced by adaptive advantages of diffusive countercurrent shunting of oxygen and/or carbon dioxide.

The countercurrent arrangement of the descending and ascending vasa recta is thought to be critical for the countercurrent trapping of solutes, and thus the mechanisms that allow generation of concentrated urine. It has been argued that this arrangement renders the renal medulla susceptible to hypoxia. The latter, would thus represent a counter-adaptive consequence of the evolutionary imperative for concentration of urine in terrestrial animals. But could the countercurrent arrangement of vasa recta also have additional functional consequences for the kidney?

Oxygen shunting could exacerbate medullary hypoxia, but the sequestration of long vasa recta into the core of vascular bundles may help preserve oxygen delivery to the inner medulla (17). This is of particular importance as the medulla is susceptible to hypoxia (31, 41, 61). Indeed,

medullary PO₂ is in the range of 10-20 mmHg (99). However, the preservation of oxygen delivery to the inner medulla is at the expense of limiting oxygen delivery to the thick ascending limb, a major site of sodium reabsorption.

Predictions from a computational model support the idea that the countercurrent shunting of carbon dioxide, from ascending to descending vasa recta, acts to ‘trap’ carbon dioxide in the inner medulla (13). This mechanism could potentially be augmented when oxygen delivery to the medulla is restricted or when medullary oxygen consumption is increased. It might be predicted that the resultant increase in PCO₂ and decrease in pH would enhance oxygen delivery to tissue under such circumstances, by shifting the oxygen-hemoglobin dissociation curve to the right. However, all of this rests on the assumption of a gradient in PCO₂, between ascending and descending vasa recta, which has yet to be verified experimentally.

2.12 PERSPECTIVES AND SIGNIFICANCE

Our discussion of the physiological and evolutionary significance of countercurrent diffusion in the renal vasculature has, if nothing else, identified the critical gaps in our knowledge that must be filled before we can fully understand the selection pressures that led to the unique countercurrent arrangements of afferent and efferent vessels in the renal cortex and medulla. Firstly, we require more detailed and quantitative information regarding the barriers to diffusion between arteries and veins and descending and ascending vasa recta. Some progress has been made in this field (101, 114, 115), but we still have a long way to go. Secondly, we require measurements of the concentrations of gases (e.g. oxygen, carbon dioxide, nitric oxide, superoxide) and other molecules (e.g. ammonia) within the renal vasculature. Currently, our knowledge is mostly limited to measurements in arterial and renal venous blood, and in some cases (e.g. oxygen) in vessels in the superficial cortex (152) or the tip of the papilla (26, 56, 76, 77, 134). The available information has allowed development of computational models of the transport of oxygen (16, 17, 49, 50, 106, 130, 158), carbon dioxide (13), nitric oxide (21, 22, 33-36, 70, 71, 79, 80) and superoxide (12, 34-36) in the renal cortex and/or medulla. Mathematical models can tell us what is theoretically possible, but we rely on experimental measurements to know what ‘is’. Consequently, development of methods to assess the concentrations of various molecules within the renal vasculature, at high temporal and spatial resolution, remains the field’s ‘Holy Grail’. Such methods represent the only way to quantify the concentration gradients that could drive diffusion of molecules between the afferent and efferent limbs of the countercurrent circulations in the renal cortex and medulla.

REFERENCES

1. **Antonenko YN, Pohl P, Denisov GA.** Permeation of ammonia across bilayer lipid membranes studied by ammonium ion selective microelectrodes. *Biophys J* 72: 2187-2195, 1997.
2. **Atherton LJ, Deen WM, Maddox DA, Gennari FJ.** Analysis of the factors influencing peritubular PCO₂ in the rat. *Am J Physiol* 247: F61-72, 1984.
3. **Atherton LJ, Maddox DA, Gennari FJ, Deen WM.** Analysis of PCO₂ variations in the renal cortex. II. Countercurrent exchange. *Am J Physiol* 255: F361-371, 1988.
4. **Baird MHI, Davidson JF.** Annular jets—II: Gas absorption. *Chem Eng Sci* 17: 473-480, 1962.
5. **Beachey W.** Respiratory Care Anatomy and Physiology: Foundations for Clinical Practice. St. Louis, Mo.: Elsevier, 2013, p. 159-167.
6. **Bell JM, Feild AL.** The distribution of ammonia between water and chloroform. *J Am Chem Soc* 33: 940-943, 1911.
7. **Bengele HH, McNamara ER, Alexander EA.** Effect of acute thyroparathyroidectomy on nephron acidification. *Am J Physiol* 246: F569-574, 1984.
8. **Bidani A, Crandall ED, DuBose TD, Jr.** Analysis of the determinants of renal cortical PCO₂. *Am J Physiol* 247: F466-474, 1984.
9. **Blantz RC, Weir MR.** Are the oxygen costs of kidney function highly regulated? *Curr Opin Nephrol Hypertens* 13: 67-71, 2004.
10. **Bohlen HG.** Mechanism of increased vessel wall nitric oxide concentrations during intestinal absorption. *Am J Physiol* 275: H542-550, 1998.
11. **Bomsztyk K, Calalb MB.** A new microelectrode method for simultaneous measurement of pH and PCO₂. *Am J Physiol* 251: F933-937, 1986.
12. **Buerk DG, Lamkin-Kennard K, Jaron D.** Modeling the influence of superoxide dismutase on superoxide and nitric oxide interactions, including reversible inhibition of oxygen consumption. *Free Radic Biol Med* 34: 1488-1503, 2003.
13. **Burke TJ, Malhotra D, Shapiro JI.** Factors maintaining a pH gradient within the kidney: role of the vasculature architecture. *Kidney Int* 56: 1826-1837, 1999.
14. **Butler AR, Megson IL, Wright PG.** Diffusion of nitric oxide and scavenging by blood in the vasculature. *Biochim Biophys Acta* 1425: 168-176, 1998.
15. **Cameron JN.** Ammonia. In: *Principles of Physiological Measurement*, edited by Cameron JN. Orlando, FL: Academic Press, 1986, p. 115-124.
16. **Chen J, Edwards A, Layton AT.** A mathematical model of O₂ transport in the rat outer medulla. II. Impact of outer medullary architecture. *Am J Physiol Renal Physiol* 297: F537-F548, 2009.
17. **Chen J, Layton AT, Edwards A.** A mathematical model of O₂ transport in the rat outer medulla. I. Model formulation and baseline results. *Am J Physiol Renal Physiol* 297: F517-F536, 2009.
18. **Chen X, Buerk DG, Barbee KA, Jaron D.** A model of NO/O₂ transport in capillary-perfused tissue containing an arteriole and venule pair. *Ann Biomed Eng* 35: 517-529, 2007.
19. **Davidson JF, Cullen EJ.** The determination of diffusion coefficients for sparingly soluble gases in liquids. *Trans Inst Chem Eng* 35: 51-60, 1957.
20. **De Mello Aires M, Lopes MJ, Malnic G.** PCO₂ in renal cortex. *Am J Physiol* 259: F357-365, 1990.
21. **Deonikar P, Abu-Soud HM, Kavdia M.** Computational analysis of nitric oxide biotransport to red blood cell in the presence of free hemoglobin and NO donor. *Microvasc Res* 95: 15-25, 2014.
22. **Deonikar P, Kavdia M.** A computational model for nitric oxide, nitrite and nitrate biotransport in the microcirculation: effect of reduced nitric oxide consumption by red blood cells and blood velocity. *Microvasc Res* 80: 464-476, 2010.

23. **DuBose TD, Jr., Bidani A.** Determinants of CO₂ generation and maintenance in the renal cortex: role of metabolic CO₂ production and diffusive CO₂ transfer. *Miner Electrolyte Metab* 11: 223-229, 1985.
24. **DuBose TD, Jr., Bidani A, Caflisch CR, Gennari FJ, Maddox DA, Deen WM.** Comment on PCO₂ in renal cortex. *Am J Physiol* 260: F608-612, 1991.
25. **DuBose TD, Jr., Caflisch CR, Bidani A.** Role of metabolic CO₂ production in the generation of elevated renal cortical PCO₂. *Am J Physiol* 246: F592-599, 1984.
26. **DuBose TD, Jr., Good DW.** Chronic hyperkalemia impairs ammonium transport and accumulation in the inner medulla of the rat. *J Clin Invest* 90: 1443-1449, 1992.
27. **DuBose TD, Jr., Pucacco LR, Lucci MS, Carter NW.** Micropuncture determination of pH, PCO₂, and total CO₂ concentration in accessible structures of the rat renal cortex. *J Clin Invest* 64: 476-482, 1979.
28. **DuBose TD, Jr., Pucacco LR, Seldin DW, Carter NW.** Direct determination of PCO₂ in the rat renal cortex. *J Clin Invest* 62: 338-348, 1978.
29. **Duda JL, Vrentas JS.** Laminar liquid jet diffusion studies. *AIChE J* 14: 286-294, 1968.
30. **Duling BR, Berne RM.** Longitudinal gradients in periarteriolar oxygen tension. A possible mechanism for the participation of oxygen in local regulation of blood flow. *Circ Res* 27: 669-678, 1970.
31. **Eckardt KU, Bernhardt WM, Weidemann A, Warnecke C, Rosenberger C, Wiesener MS, Willam C.** Role of hypoxia in the pathogenesis of renal disease. *Kidney Int* 68: S-46-S-51, 2005.
32. **Edwards A.** Modeling transport in the kidney: Investigating function and dysfunction. *Am J Physiol Renal Physiol* 298: F475-F484, 2010.
33. **Edwards A, Layton AT.** Impact of nitric oxide-mediated vasodilation on outer medullary NaCl transport and oxygenation. *Am J Physiol Renal Physiol* 303: F907-917, 2012.
34. **Edwards A, Layton AT.** Modulation of outer medullary NaCl transport and oxygenation by nitric oxide and superoxide. *Am J Physiol Renal Physiol* 301: F979-996, 2011.
35. **Edwards A, Layton AT.** Nitric oxide and superoxide transport in a cross section of the rat outer medulla. I. Effects of low medullary oxygen tension. *Am J Physiol Renal Physiol* 299: F616-633, 2010.
36. **Edwards A, Layton AT.** Nitric oxide and superoxide transport in a cross section of the rat outer medulla. II. Reciprocal interactions and tubulovascular cross talk. *Am J Physiol Renal Physiol* 299: F634-647, 2010.
37. **Effros RM, Taki K, Reid E, Silverman P.** Countercurrent diffusion in the renal cortex of the rabbit. *Circ Res* 55: 463-467, 1984.
38. **Ellsworth ML, Pittman RN.** Arterioles supply oxygen to capillaries by diffusion as well as by convection. *Am J Physiol Heart Circ Physiol* 258: H1240-H1243, 1990.
39. **Endeward V, Al-Samir S, Itel F, Gros G.** How does carbon dioxide permeate cell membranes? A discussion of concepts, results and methods. *Front Physiol* 4: 382, 2014.
40. **Evans RG, Gardiner BS, Smith DW, O'Connor PM.** Intrarenal oxygenation: Unique challenges and the biophysical basis of homeostasis. *Am J Physiol Renal Physiol* 295: F1259-F1270, 2008.
41. **Evans RG, Goddard D, Eppel GA, Connor PM.** Factors that render the kidney susceptible to tissue hypoxia in hypoxemia. *Am J Physiol Regul Integr Comp Physiol* 300: R931-R940, 2011.
42. **Evans RG, Harrop GK, Ngo JP, Ow CP, O'Connor PM.** Basal renal O₂ consumption and the efficiency of O₂ utilization for Na⁺ reabsorption. *Am J Physiol Renal Physiol* 306: F551-560, 2014.

43. **Evans RG, Smith DW, Khan Z, Ngo JP, Gardiner BS.** Letter to the editor: "The plausibility of arterial-to-venous oxygen shunting in the kidney: it all depends on radial geometry". *Am J Physiol Renal Physiol* 309: F179-180, 2015.
44. **Ferrell RT, Himmelblau DM.** Diffusion coefficients of nitrogen and oxygen in water. *J Chem Eng Data* 12: 111-115, 1967.
45. **Flessner MF, Mejia R, Knepper MA.** Ammonium and bicarbonate transport in isolated perfused rodent long-loop thin descending limbs. *Am J Physiol* 264: F388-396, 1993.
46. **Forster RE, Edsall JT.** Carbon dioxide: chemical, biological, and physiological aspects. *Science* 166: 410-413, 1969.
47. **Frank M, Kriz W.** The luminal aspect of intrarenal arteries and veins in the rat as revealed by scanning electron microscopy. *Anat Embryol (Berl)* 177: 371-376, 1988.
48. **Furchgott RF, Jothianandan D.** Endothelium-dependent and -independent vasodilation involving cyclic GMP: relaxation induced by nitric oxide, carbon monoxide and light. *Blood Vessels* 28: 52-61, 1991.
49. **Gardiner BS, Smith DW, O'Connor PM, Evans RG.** A mathematical model of diffusional shunting of oxygen from arteries to veins in the kidney. *Am J Physiol Renal Physiol* 300: F1339-1352, 2011.
50. **Gardiner BS, Thompson SL, Ngo JP, Smith DW, Abdelkader A, Broughton BR, Bertram JF, Evans RG.** Diffusive oxygen shunting between vessels in the preglomerular renal vasculature: anatomic observations and computational modeling. *Am J Physiol Renal Physiol* 303: F605-618, 2012.
51. **Garvin JL, Knepper MA.** Bicarbonate and ammonia transport in isolated perfused rat proximal straight tubules. *Am J Physiol* 253: F277-281, 1987.
52. **Garvin JL, Ortiz PA.** The role of reactive oxygen species in the regulation of tubular function. *Acta Physiol Scand* 179: 225-232, 2003.
53. **Geers C, Gros G.** Carbon dioxide transport and carbonic anhydrase in blood and muscle. *Physiol Rev* 80: 681-715, 2000.
54. **Gennari FJ, Caflisch CR, Johns C, Maddox DA, Cohen JJ.** PCO₂ measurements in surface proximal tubules and peritubular capillaries of the rat kidney. *Am J Physiol* 242: F78-85, 1982.
55. **Goldman D.** Theoretical models of microvascular oxygen transport to tissue. *Microcirculation* 15: 795-811, 2008.
56. **Good DW, Caflisch CR, DuBose TD, Jr.** Transepithelial ammonia concentration gradients in inner medulla of the rat. *Am J Physiol* 252: F491-500, 1987.
57. **Good DW, DuBose TD, Jr.** Ammonia transport by early and late proximal convoluted tubule of the rat. *J Clin Invest* 79: 684-691, 1987.
58. **Greer AE, Lazell JD, Wright RM.** Anatomical evidence for a counter-current heat exchanger in the leatherback turtle (*Dermochelys coriacea*). *Nature* 244: 181-181, 1973.
59. **Gus'kova RA, Ivanov, II, Kol'tover VK, Akhobadze VV, Rubin AB.** Permeability of bilayer lipid membranes for superoxide (O₂⁻) radicals. *Biochim Biophys Acta* 778: 579-585, 1984.
60. **Gutknecht J, Bisson MA, Tosteson FC.** Diffusion of carbon dioxide through lipid bilayer membranes: effects of carbonic anhydrase, bicarbonate, and unstirred layers. *J Gen Physiol* 69: 779-794, 1977.
61. **Haase VH.** Mechanisms of hypoxia responses in renal tissue. *J Am Soc Nephrol* 24: 537-541, 2013.
62. **Hammer LW, Ligon AL, Hester RL.** ATP-mediated release of arachidonic acid metabolites from venular endothelium causes arteriolar dilation. *Am J Physiol Heart Circ Physiol* 280: H2616-2622, 2001.
63. **Hammer LW, Overstreet CR, Choi J, Hester RL.** ATP stimulates the release of prostacyclin from perfused veins isolated from the hamster hindlimb. *Am J Physiol Regul Integr Comp Physiol* 285: R193-199, 2003.

64. **Hogg RJ, Pucacco LR, Carter NW, Laptook AR, Kokko JP.** In situ PCO₂ in the renal cortex, liver, muscle, and brain of the New Zealand white rabbit. *Am J Physiol* 247: F491-498, 1984.
65. **Hulikova A, Swietach P.** Rapid CO₂ permeation across biological membranes: implications for CO₂ venting from tissue. *FASEB J* 28: 2762-2774, 2014.
66. **Ivarsson L, Nilsson NJ, Lundgren O.** Extravascular arteriovenous oxygen shunting in the cat stomach. *Acta Physiol Scand* 135: 293-297, 1989.
67. **Jacquez JA, Poppell JW, Jeltsch R.** Solubility of ammonia in human plasma. *J Appl Physiol* 14: 255-258, 1959.
68. **Kampp M, Lundgren O, Nilsson NJ.** Extravascular shunting of oxygen in the small intestine of the cat. *Acta Physiol Scand* 72: 396-403, 1968.
69. **Kanai AJ, Strauss HC, Truskey GA, Crews AL, Grunfeld S, Malinski T.** Shear stress induces ATP-independent transient nitric oxide release from vascular endothelial cells, measured directly with a porphyrinic microsensor. *Circ Res* 77: 284-293, 1995.
70. **Kavdia M, Popel AS.** Venular endothelium-derived NO can affect paired arteriole: a computational model. *Am J Physiol Heart Circ Physiol* 290: H716-723, 2006.
71. **Kavdia M, Tsoukias NM, Popel AS.** Model of nitric oxide diffusion in an arteriole: impact of hemoglobin-based blood substitutes. *Am J Physiol Heart Circ Physiol* 282: H2245-2253, 2002.
72. **Kikeri D, Sun A, Zeidel ML, Hebert SC.** Cell membranes impermeable to NH₃. *Nature* 339: 478-480, 1989.
73. **Kobayashi H, Takizawa N.** Imaging of oxygen transfer among microvessels of rat cremaster muscle. *Circulation* 105: 1713-1719, 2002.
74. **Kriz W.** Structural organization of renal medullary circulation. *Nephron* 31: 290-295, 1982.
75. **Kriz W.** Structural organization of the renal medulla: comparative and functional aspects. *Am J Physiol* 241: R3-16, 1981.
76. **Kuramochi G, Gekle M, Silbernagl S.** Ochratoxin A disturbs pH homeostasis in the kidney: increases in pH and HCO₃⁻ in the tubules and vasa recta. *Pflugers Arch* 434: 392-397, 1997.
77. **Kuramochi G, Kersting U, Dantzler WH, Silbernagl S.** Changes in the countercurrent system in the renal papilla: diuresis increases pH and HCO₃⁻ gradients between collecting duct and vasa recta. *Pflugers Arch* 432: 1062-1068, 1996.
78. **Lahera V, Salom MG, Fiksen-Olsen MJ, Romero JC.** Mediatory role of endothelium-derived nitric oxide in renal vasodilatory and excretory effects of bradykinin. *Am J Hypertens* 4: 260-262, 1991.
79. **Lamkin-Kennard K, Jaron D, Buerk DG.** Modeling the regulation of oxygen consumption by nitric oxide. *Adv Exp Med Biol* 510: 145-149, 2003.
80. **Lamkin-Kennard KA, Buerk DG, Jaron D.** Interactions between NO and O₂ in the microcirculation: a mathematical analysis. *Microvasc Res* 68: 38-50, 2004.
81. **Lemley KV, Kriz W.** Anatomy of the renal interstitium. *Kidney Int* 39: 370-381, 1991.
82. **Lever AF, Kriz W.** Countercurrent exchange between the vasa recta and the loop of Henle. *Lancet* 1: 1057-1060, 1966.
83. **Levy MN, Imperial ES.** Oxygen shunting in renal cortical and medullary capillaries. *Am J Physiol* 200: 159-162, 1961.
84. **Levy MN, Saucedo G.** Diffusion of oxygen from arterial to venous segments of renal capillaries. *Am J Physiol* 196: 1336-1339, 1959.
85. **Lynch RE, Fridovich I.** Permeation of the erythrocyte stroma by superoxide radical. *J Biol Chem* 253: 4697-4699, 1978.
86. **Maddox DA, Gennari FJ.** Proximal tubular bicarbonate reabsorption and PCO₂ in chronic metabolic alkalosis in the rat. *J Clin Invest* 72: 1385-1395, 1983.

87. **Malinski T, Taha Z, Grunfeld S, Patton S, Kapturczak M, Tomboulia P.** Diffusion of nitric oxide in the aorta wall monitored in situ by porphyrinic microsensors. *Biochem Biophys Res Commun* 193: 1076-1082, 1993.
88. **Mao GD, Poznansky MJ.** Electron spin resonance study on the permeability of superoxide radicals in lipid bilayers and biological membranes. *FEBS Lett* 305: 233-236, 1992.
89. **Marino PL, Sutin KM.** *The ICU book*. Philadelphia: Lippincott Williams & Wilkins, 2007, 171-175.
90. **Markewitz BA, Michael JR, Kohan DE.** Cytokine-induced expression of a nitric oxide synthase in rat renal tubule cells. *J Clin Invest* 91: 2138-2143, 1993.
91. **Mejia R, Flessner MF, Knepper MA.** Model of ammonium and bicarbonate transport along LDL: implications for alkalinization of luminal fluid. *Am J Physiol* 264: F397-403, 1993.
92. **Midtgård U.** A morphometric study of structures important for cold resistance in the arctic iceland gull compared to herring gulls. *Comp Biochem Physiol Physiol* 93: 399-402, 1989.
93. **Midtgård U.** The Rete tibiotarsale and arteriovenous association in the hind limb of birds: A comparative morphological study on counter-current heat exchange systems. *Acta Zool* 62: 67-87, 1981.
94. **Missner A, Kugler P, Saparov SM, Sommer K, Mathai JC, Zeidel ML, Pohl P.** Carbon dioxide transport through membranes. *J Biol Chem* 283: 25340-25347, 2008.
95. **Mumbengegwi DR, Li Q, Li C, Bear CE, Engelhardt JF.** Evidence for a superoxide permeability pathway in endosomal membranes. *Mol Cell Biol* 28: 3700-3712, 2008.
96. **Nagami GT, Kurokawa K.** Regulation of ammonia production by mouse proximal tubules perfused in vitro. Effect of luminal perfusion. *J Clin Invest* 75: 844-849, 1985.
97. **Nase GP, Tuttle J, Bohlen HG.** Reduced perivascular PO₂ increases nitric oxide release from endothelial cells. *Am J Physiol Heart Circ Physiol* 285: H507-515, 2003.
98. **Nellore K, Harris NR.** Nitric oxide measurements in rat mesentery reveal disrupted venulo-arteriolar communication in diabetes. *Microcirculation* 11: 415-423, 2004.
99. **Neuhof W, Beck FX.** Cell survival in the hostile environment of the renal medulla. *Annu Rev Physiol* 67: 531-555, 2005.
100. **Neuman TS, Thom SR.** *Physiology and medicine of hyperbaric oxygen therapy*. Philadelphia: Saunders/Elsevier, 2008, 153-158.
101. **Ngo JP, Kar S, Kett MM, Gardiner BS, Pearson JT, Smith DW, Ludbrook J, Bertram JF, Evans RG.** Vascular geometry and oxygen diffusion in the vicinity of artery-vein pairs in the kidney. *Am J Physiol Renal Physiol* 307: F1111-1122, 2014.
102. **Noiret L, Baigent S, Jalan R, Thomas SR.** Mathematical model of ammonia handling in the rat renal medulla. *PLoS One* 10: e0134477, 2015.
103. **O'Connor PM, Anderson WP, Kett MM, Evans RG.** Renal preglomerular arterial-venous O₂ shunting is a structural anti-oxidant defence mechanism of the renal cortex. *Clin Exp Pharmacol Physiol* 33: 637-641, 2006.
104. **O'Connor PM, Evans RG.** Structural antioxidant defense mechanisms in the mammalian and nonmammalian kidney: Different solutions to the same problem? *Am J Physiol Regul Integr Comp Physiol* 299: R723-R727, 2010.
105. **Occleshaw VJ.** CXCV.-The distribution of ammonia between chloroform and water at 25°. *J Chem Soc* 1436-1438, 1931.
106. **Olgac U, Kurtcuoglu V.** Renal oxygenation: preglomerular vasculature is an unlikely contributor to renal oxygen shunting. *Am J Physiol Renal Physiol* 308: F671-688, 2015.
107. **Olgac U, Kurtcuoglu V.** Reply to "Letter to the editor: 'The plausibility of arterial-to-venous oxygen shunting in the kidney: it all depends on radial geometry'". *Am J Physiol Renal Physiol* 309: F181-182, 2015.

108. **Ortiz PA, Garvin JL.** Role of nitric oxide in the regulation of nephron transport. *Am J Physiol Renal Physiol* 282: F777-F784, 2002.
109. **Pallone TL, Edwards A, Mattson DL.** Renal medullary circulation. *Compr Physiol* 2: 97-140, 2012.
110. **Pallone TL, Robertson CR, Jamison RL.** Renal medullary microcirculation. *Physiol Rev* 70: 885-920, 1990.
111. **Pallone TL, Turner MR, Edwards A, Jamison RL.** Countercurrent exchange in the renal medulla. *Am J Physiol Regul Integr Comp Physiol* 284: R1153-1175, 2003.
112. **Pallone TL, Work J, Myers RL, Jamison RL.** Transport of sodium and urea in outer medullary descending vasa recta. *J Clin Invest* 93: 212-222, 1994.
113. **Pannabecker TL.** Structure and function of the thin limbs of the loop of Henle. *Compr Physiol* 2: 2063-2086, 2012.
114. **Pannabecker TL, Dantzler WH.** Three-dimensional architecture of inner medullary vasa recta. *Am J Physiol Renal Physiol* 290: F1355-1366, 2006.
115. **Pannabecker TL, Henderson CS, Dantzler WH.** Quantitative analysis of functional reconstructions reveals lateral and axial zonation in the renal inner medulla. *Am J Physiol Renal Physiol* 294: F1306-1314, 2008.
116. **Perez JF, Sandall OC.** Diffusivity measurements for gases in power law non-Newtonian. *AIChE J* 19: 1073-1075, 1973.
117. **Pittman RN.** Oxygen Transport. In: *Regulation of Tissue Oxygenation*. San Rafael (CA): Morgan & Claypool Life Sciences, 2011.
118. **Pollman MJ, Yamada T, Horiuchi M, Gibbons GH.** Vasoactive substances regulate vascular smooth muscle cell apoptosis. Countervailing influences of nitric oxide and angiotensin II. *Circ Res* 79: 748-756, 1996.
119. **Powell Jr FL.** Oxygen and carbon dioxide transport in the blood. In: *Essential medical physiology*, edited by Johnson LR. San Diego, CA: Elsevier Academic Press, 2003, p. 289-298.
120. **Rennie D, Lozano R, Monge C, Sime F, Whitembury J.** Renal oxygenation in male Peruvian natives living permanently at high altitude. *J Appl Physiol* 30: 450-456, 1971.
121. **Robinson RR, Owen EE.** Intrarenal distribution of ammonia during diuresis and antidiuresis. *Am J Physiol* 208: 1129-1134, 1965.
122. **Roth AC, Feigl EO.** Diffusional shunting in the canine myocardium. *Circ Res* 48: 470-480, 1981.
123. **Salvador A, Sousa J, Pinto RE.** Hydroperoxyl, superoxide and pH gradients in the mitochondrial matrix: a theoretical assessment. *Free Radic Biol Med* 31: 1208-1215, 2001.
124. **Sands JM, Layton HE.** The physiology of urinary concentration: an update. *Semin Nephrol* 29: 178-195, 2009.
125. **Scholander PF, Krog J.** Countercurrent heat exchange and vascular bundles in sloths. *J Appl Physiol* 10: 405-411, 1957.
126. **Scholander PF, Schevill WE.** Counter-current vascular heat exchange in the fins of whales. *J Appl Physiol* 8: 279-282, 1955.
127. **Schurek HJ, Jost U, Baumgartl H, Bertram H, Heckmann U.** Evidence for a preglomerular oxygen diffusion shunt in rat renal cortex. *Am J Physiol* 259: F910-915, 1990.
128. **Schwartz GJ, Weinstein AM, Steele RE, Stephenson JL, Burg MB.** Carbon dioxide permeability of rabbit proximal convoluted tubules. *Am J Physiol* 240: F231-244, 1981.
129. **Sejrsen P, Tonnesen KH.** Shunting by diffusion of inert gas in skeletal muscle. *Acta Physiol Scand* 86: 82-91, 1972.
130. **Sharan M, Popel AS.** A mathematical model of countercurrent exchange of oxygen between paired arterioles and venules. *Math Biosci* 91: 17-34, 1988.

131. **Singh SK, Binder HJ, Geibel JP, Boron WF.** An apical permeability barrier to $\text{NH}_3/\text{NH}_4^+$ in isolated, perfused colonic crypts. *Proc Natl Acad Sci U S A* 92: 11573-11577, 1995.
132. **Smeda JS, Lee RM, Forrest JB.** Structural and reactivity alterations of the renal vasculature of spontaneously hypertensive rats prior to and during established hypertension. *Circ Res* 63: 518-533, 1988.
133. **Steen I, Steen JB.** The importance of the legs in the thermoregulation of birds. *Acta Physiol Scand* 63: 285-291, 1965.
134. **Stern L, Backman KA, Hayslett JP.** Effect of cortical-medullary gradient for ammonia on urinary excretion of ammonia. *Kidney Int* 27: 652-661, 1985.
135. **Subczynski WK, Hyde JS, Kusumi A.** Oxygen permeability of phosphatidylcholine-cholesterol membranes. *Proc Natl Acad Sci U S A* 86: 4474-4478, 1989.
136. **Subczynski WK, Lomnicka M, Hyde JS.** Permeability of nitric oxide through lipid bilayer membranes. *Free Radic Res* 24: 343-349, 1996.
137. **Takahashi MA, Asada K.** Superoxide anion permeability of phospholipid membranes and chloroplast thylakoids. *Arch Biochem Biophys* 226: 558-566, 1983.
138. **Tang YP, Himmelblau DM.** Effect of solute concentration on the diffusivity of carbon dioxide in water. *Chem Eng Sci* 20: 7-14, 1965.
139. **Taylor EW.** Gills of water-breathers: structures with multiple functions. In: *Principles of animal design: the optimization and symmorphosis debate*, edited by Weibel ER, Taylor CR, and Bolis L. Cambridge, NY: Cambridge University Press, 1998, p. 186-194.
140. **Tham MJ, Bhatia KK, Gubbins KF.** Steady-state method for studying diffusion of gases in liquids. *Chem Eng Sci* 22: 309-311, 1967.
141. **Thomas WJ, Adams MJ.** Measurement of the diffusion coefficients of carbon dioxide and nitrous oxide in water and aqueous solutions of glycerol. *J Chem Soc Faraday Trans* 61: 668-673, 1965.
142. **Tse FC, Sandall OC.** Diffusion coefficients for oxygen and carbon dioxide in water at 25°C by unsteady state desorption from a quiescent liquid. *Chem Eng Commun* 3: 147-153, 1979.
143. **Unver AA, Himmelblau DM.** Diffusion Coefficients of CO_2 , C_2H_4 , C_3H_6 and C_4H_8 in water from 6° to 65°C. *J Chem Eng Data* 9: 428-431, 1964.
144. **Vanderkooi JM, Wright WW, Erecinska M.** Nitric oxide diffusion coefficients in solutions, proteins and membranes determined by phosphorescence. *Biochim Biophys Acta* 1207: 249-254, 1994.
145. **Vivian JE, King CJ.** Diffusivities of slightly soluble gases in water. *AIChE J* 10: 220-221, 1964.
146. **Vukosavljevic N, Jaron D, Barbee KA, Buerk DG.** Quantifying the L-arginine paradox in vivo. *Microvasc Res* 71: 48-54, 2006.
147. **Waisbren SJ, Geibel JP, Modlin IM, Boron WF.** Unusual permeability properties of gastric gland cells. *Nature* 368: 332-335, 1994.
148. **Walter A, Gutknecht J.** Permeability of small nonelectrolytes through lipid bilayer membranes. *J Membr Biol* 90: 207-217, 1986.
149. **Wang HD, Pagano PJ, Du Y, Cayatte AJ, Quinn MT, Brecher P, Cohen RA.** Superoxide anion from the adventitia of the rat thoracic aorta inactivates nitric oxide. *Circ Res* 82: 810-818, 1998.
150. **Warnock DG, Burg MB.** Urinary acidification: CO_2 transport by the rabbit proximal straight tubule. *Am J Physiol* 232: F20-25, 1977.
151. **Weiner ID, Hamm LL.** Molecular mechanisms of renal ammonia transport. *Annu Rev Physiol* 69: 317-340, 2007.
152. **Welch WJ, Baumgartl H, Lubbers D, Wilcox CS.** Nephron pO_2 and renal oxygen usage in the hypertensive rat kidney. *Kidney Int* 59: 230-237, 2001.

153. **Widlansky ME, Malik MA.** Vascular Endothelial Function. In: *PanVascular Medicine*, edited by Lanzer P. Berlin, Heidelberg: Springer Berlin Heidelberg, 2013, p. 1-37.
154. **Wilcox CS, Welch WJ.** Interaction between nitric oxide and oxygen radicals in regulation of tubuloglomerular feedback. *Acta Physiol Scand* 168: 119-124, 2000.
155. **Wise DL, Houghton G.** Diffusion coefficients of neon, krypton, xenon, carbon monoxide and nitric oxide in water at 10–60°C. *Chem Eng Sci* 23: 1211-1216, 1968.
156. **Yuan J, Pannabecker TL.** Architecture of inner medullary descending and ascending vasa recta: pathways for countercurrent exchange. *Am J Physiol Renal Physiol* 299: F265-272, 2010.
157. **Zacharia IG, Deen WM.** Diffusivity and solubility of nitric oxide in water and saline. *Ann Biomed Eng* 33: 214-222, 2005.
158. **Zhang W, Edwards A.** Oxygen transport across vasa recta in the renal medulla. *Am J Physiol Heart Circ Physiol* 283: H1042-H1055, 2002.

3 | GENERAL METHODS

3.1 ANIMALS

Male and female Sprague Dawley rats were used in the studies described in this thesis. Our previous modeling study (13) was based on data presented by Nordsletten *et al* in their structural analysis of the rat renal circulation (21). Nordsletten *et al* based their analysis on micro-computed tomographic data from the vascular casts of the rat renal vasculature produced by Garcia-Sanz *et al*. Thus, all rats weighed between 250 and 300 g to be consistent with the methods used by Garcia-Sanz *et al* (12). The animals were obtained from Monash Animal Research Platform (MARF, Clayton, VIC, Australia) and were housed in the Monash University Large Animal Facility in the Department of Physiology (Monash University, VIC, Australia) under a 12:12 hour light-dark cycle. The rats were given *ad libitum* access to standard chow (Barastoc diet, Irradiated Feed-Custom Mix Ration, Ridley AgriProducts Pty Ltd, High Performance Animal Nutrition, Pakenham, VIC, Australia) and tap water. All experimental protocols were approved by the Monash University School of Biomedical Sciences Animal Ethics Committee (ethics approval numbers SOBSA-P-2009-84 and MARF-2013-092).

3.2 PERFUSION FIXATION PROTOCOL

Perfusion fixation was used in the experiments described in Chapters 4 - 9. The perfusion fixation protocol differed slightly between the studies as we tailored and optimized the protocol of the studies. However, the methods common to all studies are described here.

After an initial bolus of pentobarbital (60 mg/kg. i.p; Sigma-Aldrich, St Louis, MO, USA), supplementary doses were administered, as required, until a surgical level of anesthesia was reached, as judged by abolition of the toe-pinch reflex. A midline incision was made to open the abdominal cavity and expose the abdominal aorta and inferior vena cava. Both the aorta and vena cava were exposed below the level of the renal arteries/veins and freed of adipose and connective tissue. A silk ligature (3/0, Dysilk, Dynek, South Australia) was placed around the aorta and vena cava. Another ligature was placed around the aorta above the level of the renal arteries. A polyethylene catheter (PE 160, ID = 1.14 mm, OD = 1.57 mm; Becton Dickinson and Company, NJ, USA) was inserted into the abdominal aorta, caudal to the renal arteries, and connected to a perfusion apparatus via a three-way valve. Solutions were perfused through the kidneys at a pressure of 150 mmHg. Buffer was first perfused through the kidneys to clear them of blood. Then, the fixative was perfused through the kidney. Following the perfusion fixation process, the kidneys were collected and decapsulated. This general method was employed in all of the experiments described in this thesis. Minor

differences between the protocols for the various experiments are detailed in the individual chapters.

3.3 HEMATOXYLIN AND EOSIN STAINING

Histological analyses, through the use of hematoxylin and eosin staining, were carried out to observe the structures surrounding the blood vessels in the kidney. Hematoxylin and eosin staining was carried out to distinguish the nuclear (blue) and cytoplasmic (pink) components respectively. Histological analyses were made to visualize the tubular and vascular elements of the rat kidney.

Hematoxylin originates from the wood of the logwood tree (16) and cannot stain tissues directly. It first must be oxidized to hematin, and then used in conjunction with chemicals called mordants (31, 32). Mordants are metallic ions and enable staining to occur by providing a link between the hematoxylin dye and the tissue (31, 32). Thus hematoxylin cannot stain tissue unless a mordant has been added (20). The most common mordants are salts of aluminum or iron. Hematoxylin coupled with a mordant can act as a dye. It is positively charged and can thus react with negatively charged cell components such as nucleic acids. The color of the stain is dependent on the composition of the solution and type of mordant used. A solution containing aluminum alum or potassium alum as the mordant leads to a blue nuclear staining. Solutions containing an iron mordant give a darker stain.

Alum hematoxylin solutions include Mayer's (18) and Harris' (27) hematoxylin. Harris' and Mayer's hematoxylin contain mercuric oxide and sodium iodate respectively, both of which oxidize hematoxylin to hematin. The mordants of iron hematoxylin are ferric chloride or ferric ammonium sulfate (2). These compounds also oxidize hematoxylin to hematin. Weigert's hematoxylin is an iron hematoxylin consisting of 1% alcoholic hematoxylin.

Both Harris' and Weigert's hematoxylin were used in studies described in this thesis.

Eosin is anionic and acts as an acidic dye. In contrast to the hematoxylin solution, it is negatively charged and will react with positively charged cell components such as amino groups in proteins. Positive staining results in a pink color.

3.4 LIGHT MICROSCOPY VS. SYNCHROTRON-BASED MICRO-COMPUTED TOMOGRAPHY

3.4.1 Advantages and limitations of light microscopy

Light microscopy is a common tool used for visualizing biological samples. Conventional compound light microscopes are relatively simple to use. Two-dimensional (2D) images are produced using transmitted light. Thus, tissue samples must be thin enough to be translucent (usually 1 - 20 μm in thickness). Consequently, only one 2D plane of the sample can be studied at any one time. Thus, if multiple planes are needed for analyses, multiple tissue sections (from one or multiple specimens) are required. We minimized this limitation in the experiments described in this thesis by sectioning kidney samples in two different planes, so as to sample as many artery-vein profiles as possible (see Chapters 4, 5, 6, 8 & 9). Light microscopy also suffers from the likely presence of superimposed structures. Thin sections of biological tissues are translucent under the microscope. Consequently, stains are often used to highlight specific structures. The thicker the tissue sections are, the greater the uptake of the stain, as well as the degree of superimposition. On the other hand, the thinner the tissue section the paler the staining. Thus, a balance is required between section thickness and stain intensity. In the experiments described in this thesis, we first performed pilot studies in which we sectioned kidney tissue at various thicknesses. This enabled us to select the optimum tissue thickness (3 or 5 μm) that thus allowed (i) visualization of structures without superimposition, and (ii) adequate uptake of tissue stains.

An additional challenge for histological analysis of the kidneys is the separate identification of the various tubular, vascular and interstitial elements that the kidney is comprised of. One approach to this problem is to use immunohistochemistry to label specific elements of the tissue. For example, much of our knowledge of the topography of vascular and tubular elements in the renal medulla has come from detailed immunohistochemical analyses using conventional light microscopy (25) and confocal/fluorescence microscopy (23, 24, 26, 33). In the studies described in this thesis, we aimed to specifically identify the vascular elements in the renal cortex so that their architecture and geometry could be characterized and quantified. In pilot studies (Chapter 4), we trialed the use of immunohistochemical approaches to solve this problem. Subsequently, we turned to a simpler approach, of filling the renal vascular with the silicone rubber polymer Microfil®, which appears brown in sections stained with hematoxylin and eosin. This method was used in experiments described in Chapters 5-9 of this thesis.

3.4.2 Technical basis of micro-computed tomography

Three-dimensional (3D) images can be obtained through the use of micro-computed tomography (micro-CT) (4, 11, 12, 22). Commercial CT imaging systems have a rotating X-ray source and a stationary stage. In contrast, for synchrotron-based micro-CT, the X-ray source remains stationary, so the sample must be rotated. Thus, a typical synchrotron radiation-based X-ray micro-tomographic scanner consists of a synchrotron X-ray source, a rotating stage, an X-ray-to-light converting scintillator, a light imaging device (usually a charge-coupled device (CCD)-based video camera), and a computer (14). Specimens are first placed on the rotatable stage. While the specimen is in the path of the X-ray beam, the stage is rotated in angular increments during image acquisition (Fig. 3.1). An X-ray transmission image is obtained at each increment in angle.

In CT-imaging, tissue structure is visualized through differences in the ability of various tissues to absorb X-rays. For example, bone is more radio-opaque than soft tissues like the kidney. In order to visualize the microvasculature of various organs, including the kidney, the radio-opaque polymer Microfil® is commonly used (14). In the experiments described in Chapter 9 of this thesis, kidneys were perfusion fixed and the vasculature was filled with Microfil® to allow the vasculature to be distinguished from the renal parenchyma.

The equipment used for our studies is presented in Fig. 3.1B and Fig. 3.2. We used the Ruby Detector at the Imaging and Medical Therapy Beam Line at the Australian Synchrotron. The sensor is a CMOS (complementary metal-oxide-semiconductor) device rather than a CCD-based device. The camera provides a full frame of 2560 by 2160 pixels (PCO.edge, PCO, Kelheim, Germany) and is equipped with a Nikon Micro-Nikkor 105 mm f/2.8 macro lens. A phosphor plate is placed orthogonal to the direction of the beam and a mirror is used to view this plate. The scintillator is a 200 μm thick terbium doped gadolinium oxy-sulfide (also known as Gadox or P43) screen coated in aluminum powder.

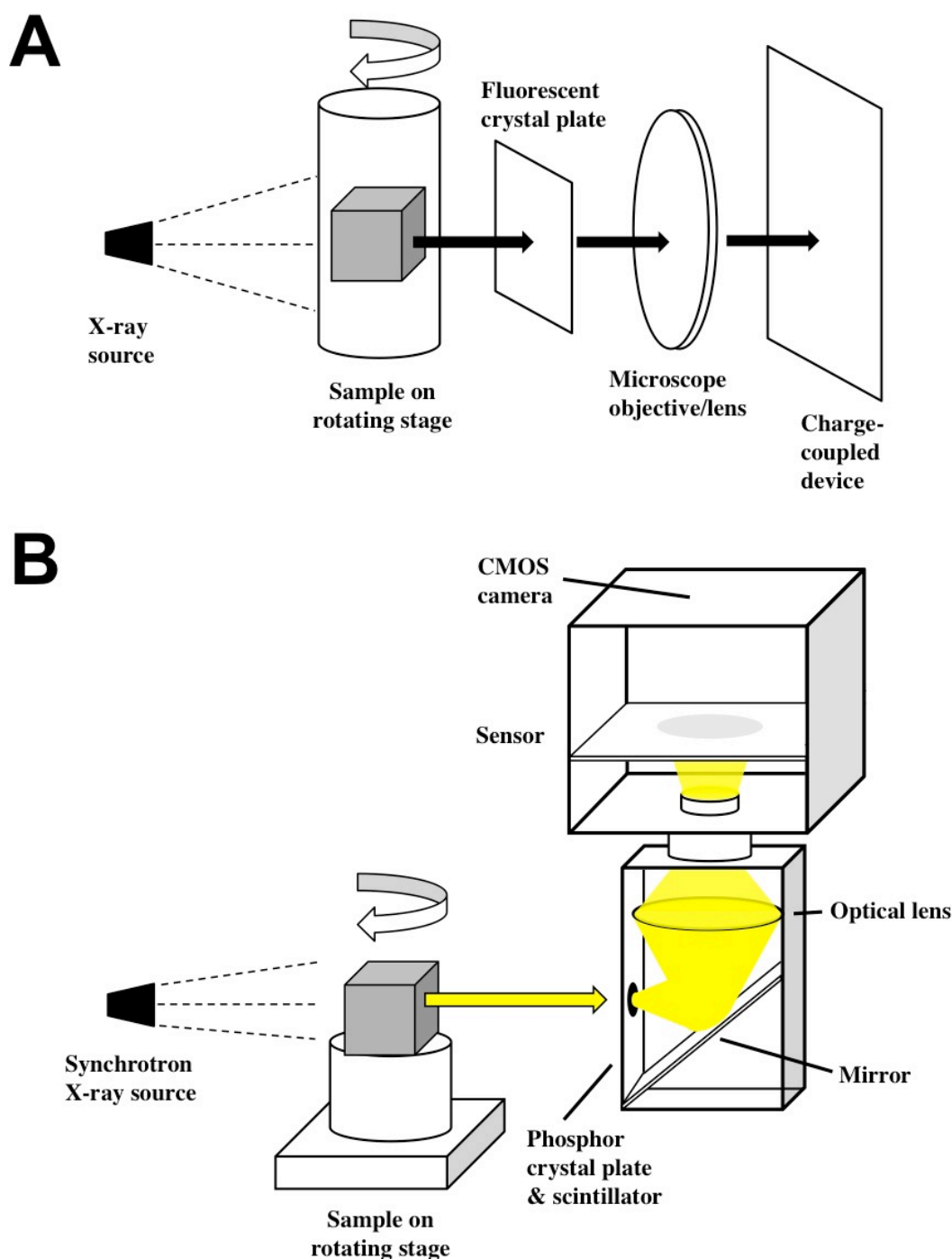


Figure 3.1. A schematic of two typical setups used in micro-computed tomographic (micro-CT) imaging. In both setups, the sample is placed on a rotating stage. The sample is illuminated by the X-ray source. This X-ray energy is then converted to visible light energy by a fluorescent scintillating crystal plate. A typical micro-CT setup utilises a charge-coupled device (CCD)-based camera (**A**). This setup is unable to tolerate synchrotron X-rays. A typical setup of synchrotron radiation-based micro-CT consists of a complementary metal-oxide-semiconductor (CMOS) device as the camera (**B**). However, a CCD-based camera can also be used. The setup described in (**B**) is indicative of the setup of the Ruby Detector at the Imaging and Medical Therapy Beam Line. This equipment was used in studies described in this thesis.

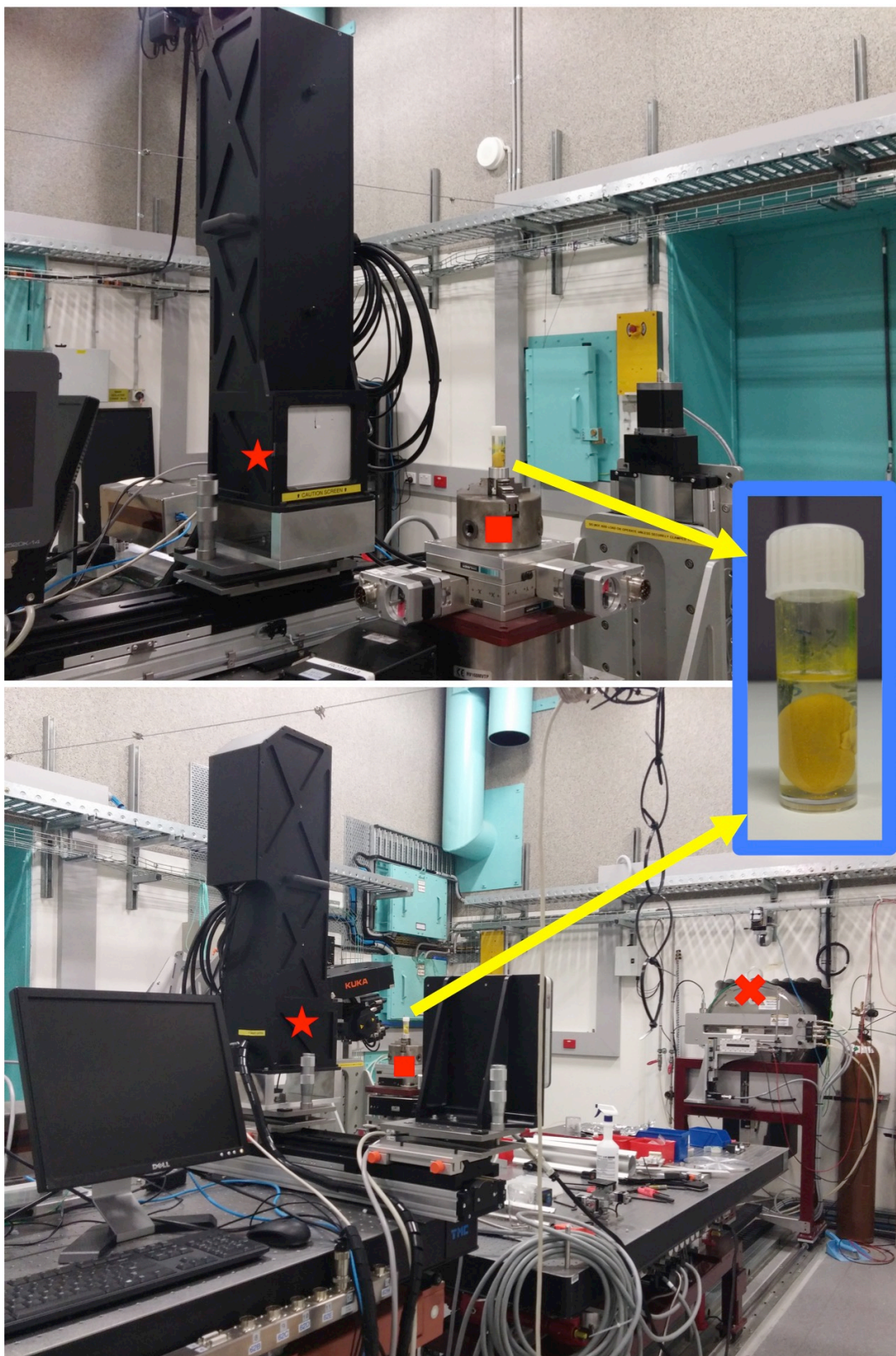


Figure 3.2. The setup at the Imaging and Medical Therapy Beam Line (IMBL). The kidney was placed in a cylindrical tube and covered in phosphate buffered saline. The tube was then placed on the rotating stage (■). Synchrotron X-rays from the source (✕) passed through the specimen and were detected by the phosphor plate (★). The image inset is of a Microfil®-filled rat kidney inside a tube that was placed on the rotating stage.

3.4.3 Three-dimensional imaging techniques

3.4.3.1 *The advantages and limitations of PET vs MRI vs CT imaging*

Positron emission tomography (PET) enables the visualization of organs and their functionality. PET scans utilize positron-emitting radioactive materials called radioisotopes (also known as radionuclides). Common radioisotopes and their respective half-lives include ^{11}C arbon (~20 minutes), ^{13}N itrogen (~10 minutes), ^{15}O xygen (~2 minutes), and ^{18}F luorine (~110 minutes). These radioisotopes can be incorporated into radiopharmaceuticals (also known as radiotracers) to detect diseases and disorders. These radioisotopes enable the detection of differences in both metabolic and chemical activity in the body. The decay of a radioisotope results in the emission of positrons. The positrons are absorbed by organs and tissues of the body, and the PET scanner records the energy of the positrons. Areas with high activity appear bright or colored. Different colors or brightness represent various levels of cell or organ activity. Thus PET scans can be used to assess tissue functions such as blood flow, oxygenation, and glucose metabolism. An example is ^{18}F luorine, incorporated into glucose to form fludeoxyglucose. It can be used as a marker of glucose metabolism as well as for detecting tumors. Active tissues in the body including the brain, the heart, and tumors will have a greater uptake of glucose than other tissues. Thus, these tissues can be visualized by the PET system. However, compared to other imaging systems such as magnetic resonance imaging (MRI) or computed tomography (CT), PET has a relatively low resolution, of approximately 2 – 10 mm (15). Some PET systems, including dual modality systems such as PET/CT systems, can achieve 1.4 mm spatial resolution (7, 10). Standard PET systems are also poor at providing anatomic information unless co-registered with other imaging systems such as CT or MRI. Newer PET systems are often paired with CT. CT imaging provides high-resolution anatomic information that standard PET cannot provide. Our studies required structural information at high resolution, so PET scanning would not be useful for our purposes.

MRI uses magnets rather than X-rays. The principle underlying MRI is that tissues contain hydrogen atoms (e.g. in water molecules), which emit a signal when placed in a strong magnetic field. MRI is capable of distinguishing between substances with differing physical properties in the body such as water and fat due to the differing densities of protons (hydrogen nuclei). It can thus produce detailed images of soft tissues. There are two types of basic proton MRI: T1-weighted (anatomical/structural) imaging and T2-weighted (functional) imaging. For T1-weighted images (a structural MRI scan), the darkness of an area in the image is dependent on the density of protons in that area. A greater density of protons

correlates to a darker area on the image. Thus, dark areas of a T1-weighted image correspond to the presence of water, and can therefore be used to detect tumors or edema. Bright areas on a T1-weighted image may correlate to the presence of fat or fatty bone marrow. Magnetic resonance angiography (MRA) is a technique based on MRI to visualize blood vessels. Intravenous contrast agents are commonly used in MRA to visualize the vessels. A limitation of MRI is the cost involved, as it is relatively expensive compared to some other types of imaging. Furthermore the resolution of conventional MRI, although higher than PET scans, is limited to 50 μm – 1 mm (28, 30). However, more recent developments have led to magnetic resonance imaging techniques that reach <10 μm in resolution (8, 19).

CT scanners come in various sizes and resolutions. For example, CT scanners dedicated to small animal imaging (mini-CT) can have a spatial resolution of 100 – 450 μm . Clinical scale CT scanners have a resolution greater than 450 μm . Clinical scale CT scans utilize X-ray images taken at many angles to generate tomographic (cross-sectional) images. The series of X-ray images are then processed and an image is produced. Similar to MRA, CT imaging can also use contrast agents to visualize blood vessels. Modern CT scanners are now capable of generating 3D images. Like CT, micro-CT also uses X-rays to create 3D images. The only difference is that micro-CT has pixel sizes in the micrometer range, resulting in high-resolution 3D images. Due to its complex structure, the geometry of the renal circulation has been difficult to study and quantify. Three-dimensional micro-CT (3D micro-CT) allows imaging of kidney samples in high resolution (up to 5 μm) without the need to section or slice them (5, 14). Furthermore, 3D micro-CT removes limitations commonly found when using 2D histological approaches. Such limitations, detailed earlier in Section 3.4.1, include superimposition, as well as the restriction to a single plane of section (14). These limitations result in analyses that can only capture ‘snapshots’ of the renal circulation. 3D micro-CT allows us to follow the course of the renal circulation, thus enabling the examination of the spatial characteristics of arteries and veins continuously along the vasculature.

3.4.3.2 Advantages and limitations of synchrotron radiation micro-computed tomography

Synchrotron radiation micro-CT has many advantages over conventional micro-CT. Some bench-top CT scanners can provide voxel sizes as small as 5 μm following extensive customization. However, such small voxel sizes result in a limited field of view. Common bench-top CT scanners are not optimized to achieve such resolution. Synchrotron radiation micro-CT has the potential to provide higher resolutions. Synchrotron radiation is produced when high-energy electrons are forced into a circular trajectory. Synchrotron sources provide

monochromatic X-rays of great intensity, high photon flux, and high signal-to-noise ratio, enabling reconstructions of 3D images in high-resolution (1, 6, 9, 17). The increased intensity, orders of magnitude greater than conventional CT, not only improves the quality of the images, but also reduces acquisition time (29). In contrast, a bench-top CT scanner imaging at 5 μm resolution would require more time for image acquisition and reconstruction as such scanners do not incorporate supercomputers as synchrotron imaging systems do. Furthermore, the use of a monochromatic beam in synchrotron radiation micro-CT, as opposed to a polychromatic beam used in conventional CT, avoids hardening artifacts (6) often observed in the latter. The high flux coupled with the small field-of-view also allows for spatial resolution to reach sub-micron levels (1, 6). Thus, we opted for the synchrotron radiation micro-CT technique to visualize the cortical vasculature of the rat. By perfusing Microfil®, which acts as a contrast agent, through the rat renal circulation, we were able to not only visualize the vessels in 3D, but also use the silicone as a means to identify blood vessels in corresponding histological sections.

While there has been immense progress in the field of 3D reconstructions to visualize various objects, a limitation of micro-CT is the resolution that can be achieved in a single object. Relatively low-resolution X-ray projections are capable of imaging whole objects. High-resolution imaging systems that can achieve up to sub-micron resolutions are unable to image whole objects unless they are miniscule. This is due to a smaller field of view associated with high-resolution systems. Array size and pixel dimensions determine the spatial resolution of the sensor. The spatial resolution subsequently determines the size of the field of view that can be captured. High-resolution imaging systems often require optical magnification by fitting a lens in front of the detector sensor, further narrowing the field of view. A typical field of view for micro-CT systems is within 1 – 5 cm, with resolution ranging between 5 μm (smaller field of view) to 100 μm (larger field of view) (3). Lower resolution imaging systems correspond with larger field of views, allowing for larger samples to be imaged. As mentioned above, clinical CT scanners have a spatial resolution of $>450\ \mu\text{m}$ which correlate with field of views greater than 20 cm (3). Therefore, there is no imaging system available that is able to image a whole rat kidney at high resolution. It was thus imperative for us to utilize multiple methods (histology and micro-CT) to visualize renal tissue and the renal vasculature. Small vessels not imaged or detected by the synchrotron beam can be visualized in histological sections. Also, renal tubules cannot be visualized using the synchrotron micro-CT approach because they are not part of the circulation and hence not filled with the contrast agent. A complete model of oxygen transport in the renal cortex should incorporate the oxygen

consumption of tubules as this may influence oxygen transport around artery-vein pairs. Information on the spatial arrangement of tubules in the renal parenchyma can be obtained by analyzing histological tissue sections. Thus, it is apparent that the use of only one of these methods would not generate the multiple levels of information required for the generation of a pseudo-3D model of renal oxygen transport. Therefore, in the studies described in this thesis, we used both approaches.

REFERENCES

1. **Alvarenga de Moura Meneses A, Giusti A, de Almeida AP, Parreira Nogueira L, Braz D, Cely Barroso R, deAlmeida CE.** Automated segmentation of synchrotron radiation micro-computed tomography biomedical images using Graph Cuts and neural networks. *Nucl Instrum Meth A* 660: 121-129, 2011.
2. **Bancroft JD, Stevens A.** *Histopathological Stains and their Diagnostic Uses*. Edinburgh; New York: Churchill Livingstone, 1975, p. 149.
3. **Bartling SH, Stiller W, Semmler W, Kiessling F.** Small animal computed tomography imaging. *Curr Med Imaging Rev* 3: 45-59, 2007.
4. **Bentley MD, Jorgensen SM, Lerman LO, Ritman EL, Romero JC.** Visualization of three-dimensional nephron structure with microcomputed tomography. *Anat Rec* 290: 277-283, 2007.
5. **Bentley MD, Ortiz MC, Ritman EL, Carlos Romero J.** The use of microcomputed tomography to study microvasculature in small rodents. *Am J Physiol Regul Integr Comp Physiol* 282: R1267-R1279, 2002.
6. **Chappard C, Basillais A, Benhamou L, Bonassie A, Brunet-Imbault B, Bonnet N, Peyrin F.** Comparison of synchrotron radiation and conventional x-ray microcomputed tomography for assessing trabecular bone microarchitecture of human femoral heads. *Med Phys* 33: 3568-3577, 2006.
7. **Cherry SR, Yiping S, Siegel S, Silverman RW, Mumcuoglu E, Meadors K, Phelps ME.** Optical fiber readout of scintillator arrays using a multi-channel PMT: a high resolution PET detector for animal imaging. In: *IEEE Nucl Sci Symp Conf Rec (1995)*, p. 1766-1770.
8. **Ciobanu L, Seeber DA, Pennington CH.** 3D MR microscopy with resolution 3.7 μm by 3.3 μm by 3.3 μm . *J Magn Reson* 158: 178-182, 2002.
9. **Cooper DML, Erickson B, Peele AG, Hannah K, Thomas CDL, Clement JG.** Visualization of 3D osteon morphology by synchrotron radiation micro-CT. *J Anat* 219: 481-489, 2011.
10. **Del Guerra A, Belcari N.** State-of-the-art of PET, SPECT and CT for small animal imaging. *Nucl Instrum Meth A* 583: 119-124, 2007.
11. **Fortepiani LA, Ruiz MC, Passardi F, Bentley MD, Garcia-Estan J, Ritman EL, Romero JC.** Effect of losartan on renal microvasculature during chronic inhibition of nitric oxide visualized by micro-CT. *Am J Physiol Renal Physiol* 285: F852-860, 2003.
12. **Garcia-Sanz A, Rodriguez-Barbero A, Bentley MD, Ritman EL, Romero JC.** Three-dimensional microcomputed tomography of renal vasculature in rats. *Hypertension* 31: 440-444, 1998.
13. **Gardiner BS, Smith DW, O'Connor PM, Evans RG.** A mathematical model of diffusional shunting of oxygen from arteries to veins in the kidney. *Am J Physiol Renal Physiol* 300: F1339-1352, 2011.
14. **Gossel M, Bentley MD, Lerman LO.** Review--3D micro CT imaging of renal micro-structural changes. *Nephron Clin Pract* 103: c66-70, 2006.
15. **Harris JC.** *Developmental Neuropsychiatry: Assessment, Diagnosis, and Treatment of Developmental Disorders*. Oxford University Press, 1998.
16. **Lalor GC, Martin SL.** Studies on haematoxylin and haematein, the colouring principles of logwood: i-absorption spectra of pure compounds in various solvents and a spectrophotometric method of analysis for haematoxylin and haematein. *J Soc Dyers Colour* 75: 513-517, 1959.
17. **Larrue A, Rattner A, Peter Z-A, Olivier C, Laroche N, Vico L, Peyrin F.** Synchrotron radiation micro-CT at the micrometer scale for the analysis of the three-dimensional morphology of microcracks in human trabecular bone. *PLoS ONE* 6: e21297, 2011.

18. **Mallory FB.** On certain improvements in histological technique: i. A differential stain for amoebae coli. ii. Phosphotungstic-acid-haematoxylin stain for certain tissue elements. iii. A method of fixation for neuroglia fibres. *J Exp Med* 2: 529-533, 1897.
19. **Mamin HJ, Poggio M, Degen CL, Rugar D.** Nuclear magnetic resonance imaging with 90-nm resolution. *Nat Nanotechnol* 2: 301-306, 2007.
20. **Marshall PN, Horobin RW.** The oxidation products of Haematoxylin and their role in biological staining. *Histochem J* 4: 493-503, 1972.
21. **Nordsletten DA, Blackett S, Bentley MD, Ritman EL, Smith NP.** Structural morphology of renal vasculature. *Am J Physiol Heart Circ Physiol* 291: H296-H309, 2006.
22. **Ortiz MC, Garcia-sanz A, Bentley MD, Fortepiani LA, Garcia-Estan J, Ritman EL, Romero JC, Juncos LA.** Microcomputed tomography of kidneys following chronic bile duct ligation. *Kidney Int* 58: 1632-1640, 2000.
23. **Pannabecker TL.** Loop of Henle interaction with interstitial nodal spaces in the renal inner medulla. *Am J Physiol Renal Physiol* 295: F1744-1751, 2008.
24. **Pannabecker TL, Abbott DE, Dantzler WH.** Three-dimensional functional reconstruction of inner medullary thin limbs of Henle's loop. *Am J Physiol Renal Physiol* 286: F38-F45, 2004.
25. **Pannabecker TL, Dahlmann A, Brokl OH, Dantzler WH.** Mixed descending- and ascending-type thin limbs of Henle's loop in mammalian renal inner medulla. *Am J Physiol Renal Physiol* 278: F202-208, 2000.
26. **Pannabecker TL, Henderson CS, Dantzler WH.** Quantitative analysis of functional reconstructions reveals lateral and axial zonation in the renal inner medulla. *Am J Physiol Renal Physiol* 294: F1306-1314, 2008.
27. **Papanicolaou GN.** A new procedure for staining vaginal smears. *Science* 95: 438-439, 1942.
28. **Pelberg R, Mazur W.** *Cardiac CT Angiography Manual*. Springer London, 2007.
29. **Peyrin F.** Investigation of bone with synchrotron radiation imaging: from micro to nano. *Osteoporos Int* 20: 1057-1063, 2009.
30. **Shapiro EM, Skrtic S, Sharer K, Hill JM, Dunbar CE, Koretsky AP.** MRI detection of single particles for cellular imaging. *Proc Natl Acad Sci USA* 101: 10901-10906, 2004.
31. **Titford M.** The long history of hematoxylin. *Biotech Histochem* 80: 73-78, 2005.
32. **Vij R, Vij H, Rao NN.** Modified technique for soft tissue processing and staining. *J Histochemol* 37: 14-20, 2014.
33. **Yuan J, Pannabecker TL.** Architecture of inner medullary descending and ascending vasa recta: pathways for countercurrent exchange. *Am J Physiol Renal Physiol* 299: F265-272, 2010.

4 | A PILOT STUDY OF THE UTILITY OF IMMUNOHISTOCHEMICAL METHODS FOR IDENTIFICATION OF THE RENAL VASCULATURE

Monash University

Declaration for Thesis Chapter 4

Declaration by candidate

In the case of Chapter 4, the nature and extent of my contribution to the work was the following:

| Nature of contribution | Extent of contribution (%) |
|---|----------------------------|
| Performed experiments, analyzed data, interpreted results, prepared tables and figures, drafted, edited and revised chapter | 70% |

The following co-authors contributed to the work. If co-authors are students at Monash University, the extent of their contribution in percentage terms must be stated:

| Name | Nature of contribution | Extent of contribution (%) for student co-authors only |
|------------------------|---|--|
| John F Bertram | Provided advice regarding the design of the research | 5% |
| Amany Abdelkader | Supervision, provided design of research | 5% |
| Brad R S Broughton | Helped with some experiments, provided design of research | 5% |
| Michelle M Kett | Provided editorial advice | ~1.5% |
| Rebecca Douglas-Denton | Performed some experiments | ~1.5% |
| Victor Puelles | Performed some imaging | ~1.5% |
| Roger G Evans | Supervision, provided advice regarding the design of research, interpreted results, provided editorial advice | 10% |

The undersigned hereby certify that the above declaration correctly reflects the nature and extent of the candidate's and co-authors' contributions to this work*.

| | | |
|-----------------------|--|------------|
| Candidate's Signature |  | Date |
| | | 24/04/2016 |

| | | |
|-----------------------------|---|------------|
| Main Supervisor's Signature |  | Date |
| | | 24/04/2016 |

*Note: Where the responsible author is not the candidate's main supervisor, the main supervisor should consult with the responsible author to agree on the respective contributions of the authors.

4.1 ABSTRACT

It has been proposed that the countercurrent arrangement of afferent and efferent vessels in the renal cortex facilitates diffusional shunting of oxygen from afferent to efferent limbs. Current models of renal oxygenation lack quantitative data on the spatial characteristics of arteries and veins in the kidney. To gather this information we need to be able to first identify and differentiate between the types of vessels in the cortical circulation. In the present study we utilized both histochemical and immunohistochemical methods in an attempt to identify the various vessels in the rat renal cortex: arteries (and arterioles), veins (and venules) and capillaries. Rat kidneys were perfusion fixed and then embedded in paraffin. In order to optimize identification of the blood vessels, five different protocols were carried out: (i) von Willebrand factor (vWF) and diaminobenzidine (DAB) were used to stain endothelial cells, (ii) immunofluorescence was used to visualize vWF, (iii) double-labeling immunofluorescence was used to label vWF and smooth muscle (SM) actin, (iv) immunofluorescence for vWF and histochemical staining were used on serial sections, and (v) immunofluorescence for vWF with antigen retrieval and blocking with bovine serum albumin. Our qualitative analysis revealed relatively little positive staining for blood vessels. An important limitation of immunofluorescence in the case of renal tissue is the autofluorescence of the renal tubules, which hinders visualization of blood vessels. Collectively, our current findings suggest that histochemical and immunohistochemical approaches have limited utility for identification of blood vessels in the rat renal cortex.

4.2 INTRODUCTION

Oxygen shunting between arteries and veins may reduce oxygen delivery to renal tissue (18, 19). The existence of oxygen shunting has been supported by studies from over fifty years ago (11). The finding by Levy *et al* (11) provided evidence that oxygen is transported through the renal circulation more rapidly than erythrocytes. This finding suggested that diffusional oxygen shunting occurs between renal arteries and veins. Further support for the existence of arterial-to-venous (AV) oxygen shunting came from the studies of Welch *et al* (27). They found that the partial pressure of oxygen (PO_2) of renal venous blood exceeded that of efferent arterioles in the outer cortex. It was proposed that the parallel arrangement of the renal vasculature promotes in countercurrent exchange of oxygen between arteries and veins (27).

To aid our understanding of the physiological regulation of kidney oxygenation, our group is developing mathematical models of oxygen transport in the kidney (6). A major limitation of existing models is a lack of quantitative data regarding the barriers of oxygen diffusion between arteries and veins in the kidney (3). To overcome this limitation, we aim to examine the characteristic arrangements of arteries and veins in the rat kidney. In order to examine the relationship between arteries and veins in the kidney, we need to first be able to identify these vessels, as well as differentiate them from other vessels such as capillaries and from the renal tubules.

The current pilot study examined the utility of histochemical and immunohistochemical methods to definitively label and identify the various blood vessels in the rat kidney: the arteries, veins, and capillaries. We hypothesized that the use of histochemical and immunohistochemical methods could enable the identification of renal blood vessels in the rat, as well as differentiation of these vessels from the tubular elements in the kidney.

4.3 METHODS

4.3.1 Experimental approach

In a mathematical model of kidney oxygen transport described by Gardiner *et al* (6), the renal vasculature is represented by eleven compartments of countercurrent systems connected in series. For each compartment, an artery and the corresponding vein are arranged in parallel. These compartments correspond to the Strahler orders (branch levels) identified by Nordsletten *et al* (17) in their structural analysis of the rat renal circulation. Nordsletten *et al* (17) based their analysis on micro-computed tomographic data from vascular casts of the rat renal vasculature provided by Garcia-Sanz *et al* (5). To be consistent with these previous analyses, kidney tissue for histological analysis was prepared using methods similar to those of Garcia-Sanz *et al* (5). Male Sprague-Dawley rats weighing between 250 and 300 g were given an intraperitoneal injection of pentobarbital (60 mg/kg of body weight, i.p; Sigma-Aldrich, St Louis, MO, USA) and their kidneys were obtained after perfusion fixation. The kidneys were sectioned in three planes, processed and histochemical and immunohistochemical analyses were carried out to identify renal arteries, veins and capillaries.

An assessment of the characteristic arrangements and relationships between arteries and veins in the renal cortex was made using standard histological and immunofluorescence analyses. We took an immunohistochemical approach to identify endothelial cells and actin in smooth

muscle of the renal blood vessels. A common biomarker for endothelial cells is von Willebrand factor (vWF), a glycoprotein that is synthesized in endothelial cells. In endothelial cells that produce vWF, it is stored in Weibel-Palade bodies or secreted to the extracellular matrix. In smooth muscle cells, actin filaments form part of the cytoskeleton and play an essential role in regulating cell shape and movement via their molecular interaction with myosin filaments. Hematoxylin and eosin (H & E) staining was performed to better visualize the cellular structure of the renal tissue sections. We reasoned that the presence of endothelial cells would enable identification of arteries and veins from tubules. The detection of actin in smooth muscle would in turn differentiate arteries and veins from capillaries.

4.3.2 Animals

Two male Sprague Dawley rats were used for this study (275 & 256 g).

4.3.3 Kidney Perfusion protocol

Perfusion fixations of rat kidneys were carried out using phosphate buffered saline and 3% paraformaldehyde (PFA; see Appendix 4 of this thesis) as described in the Chapter 3 of this thesis (Section 3.2).

4.3.4 Kidney sectioning

After post-fixation in PFA for 24 hours, the kidneys were removed from the PFA solution, cut into sections as described in Figure 4.1, and placed into 70% v/v ethanol. They were then processed and embedded in paraffin at a histology laboratory (Department of Anatomy and Developmental Biology, Monash University, VIC, Australia). Using a microtome (microTec Laborgeräte GmbH, cut 4060, Germany), the paraffin-embedded kidneys were sectioned at 5 μm , placed on microscope slides (Menzel Glazer, Super frost Plus, Braunschweig, Germany) and left to adhere for 2 hours at 70 °C.

4.3.5 Microscopy and photomicrography

Once all slides were stained, mounted and cover slipped, the sections were observed under a microscope (Olympus BX51; Hamburg, Germany). Using the analysSIS software (Olympus Soft Imaging Solutions), each image was taken at varying magnifications ($\times 2$ to $\times 40$) using the ColorViewIIIu camera (Olympus Soft Imaging Solutions GmbH), and scale bars were calculated in terms of micrometers (μm).

4.3.6 Hematoxylin and eosin staining

Histological analyses were carried out to observe the structures surrounding the blood vessels in the kidney. Hematoxylin (Harris's) and eosin staining was carried out to distinguish the nuclear (blue) and cytoplasmic (pink) components respectively.

The kidney was sectioned in three basic planes with the following reference position:

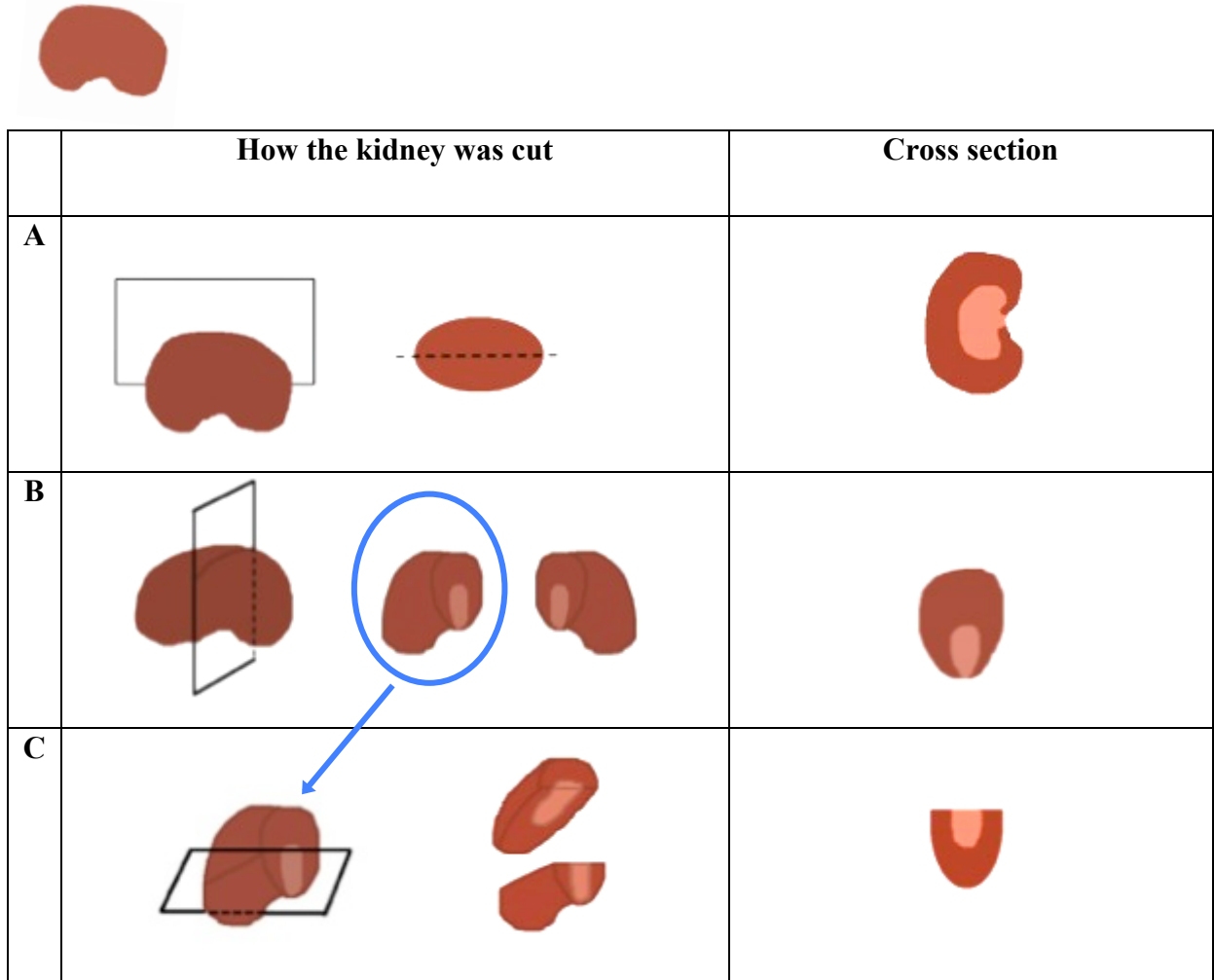


Figure 4.1. Schematic diagram of the three different planes in which the kidneys were sectioned.

The renal arteries and veins branch into interlobar arteries and veins before changing direction and running in an arc-like manner to become arcuate arteries and veins. These vessels then give rise to interlobular arteries and veins located in the outer cortex. Due to the different directions in which the vessels are arranged within the kidney, analyses of the vessels in different planes of the kidney were necessary. The kidney was sectioned in the three basic planes so that analyses could be made on blood vessels in the perpendicular plane to which the vessels run. From each rat, one kidney was cut in the frontal plane (**A**) along the longitudinal axis. The remaining kidney was cut perpendicular to the longitudinal axis in the sagittal plane (**B**), resulting in two halves, one of which was sectioned horizontally in the transverse plane (**C**) and the other was sectioned in the sagittal plane (**B**).

4.3.7 Immunohistochemistry

Immunohistochemistry is a technique commonly used to detect specific proteins in tissue sections. A primary antibody is used to localize the protein of interest. A secondary antibody, directed against the primary antibody, is chemically coupled to an enzyme that converts a colorless substrate into a colored product. The localization of the colored product by light microscopy indicates where the antibody has bound. Horseradish peroxidase (HRP) is commonly used for such applications, with the most widely used substrate being diaminobenzidine (DAB), which forms a brown colored oxidation product. In order to identify the vessels in the kidney, the kidney sections were stained for vWF, a common biomarker for endothelial cells, and then visualized with DAB. Subsequent experiments examined the potential for various fluorescence immunohistochemical protocols to identify blood vessels using antibodies for vWF and/or SM actin. For fluorescence immunohistochemistry, the secondary antibody is coupled with a fluorescent marker.

4.3.7.1 Control slides

A negative control slide was used to ensure that any positive staining or fluorescence was due to the binding of the primary antibody, and not the antibody diluent, autofluorescence, or non-specific binding of the secondary antibody. The control slides were incubated with diluent and secondary antibodies but not the primary antibody in which the experimental slides were incubated.

4.3.7.2 Antisera

All primary and secondary antibodies used for immunohistochemical protocols are listed in Table 4.1.

For all immunohistochemical protocols, unless stated otherwise, a 30-minute incubation in 10% normal goat serum was used to block the sections prior to antibody incubation. The slides were then incubated, in the appropriate primary antibody, overnight at room temperature in an incubation tray. After 24 hours, slides were washed three times in 0.01 M phosphate buffered saline (PBS) before being incubated with the appropriate secondary antibody for 2 hours at room temperature.

4.3.7.3 Protocol 1: Detecting von Willebrand factor using diaminobenzidine

In an attempt to identify the blood vessels of the kidney, staining for vWF was carried out using DAB.

Slides were first heated in a dry oven at 55 – 60 °C for 20 minutes in a position to allow drainage of the paraffin wax. Slides were then immersed in xylene for 10 minutes three times. The slides were then hydrated through gradual ethanol immersions: 100% v/v for 2 minutes, 95% v/v for 1 minute, 70% v/v for 1 minute, 50% v/v for 1 minute, and 30% v/v for 1 minute. This was followed by an immersion in 0.85% w/v sodium chloride (NaCl) for 2 minutes and then in 0.01 M PBS for 5 minutes thrice.

Following the de-waxing protocol (Section 4.3.7.3), slides were blocked as described above (Section 4.3.7.2) and then incubated in rabbit anti-vWF overnight in an incubation tray. After 24 hours, the slides were incubated with goat anti-rabbit conjugated to a peroxidase-labeled polymer for 2 hours. The sections were then immersed in 0.01 M PBS for 5 minutes thrice. Sections were incubated for 5 minutes in a drop of DAB (Envision kit, DAKO North America, Carpinteria, CA, USA) and 1 ml of substrate buffer (Envision kit, DAKO North America, Carpinteria, CA, USA). The slides were then rinsed in distilled water and counterstained with hematoxylin for 1 minute. Before microscopic examination, the slides were rinsed in tap water, 70% v/v ethanol, 100% v/v ethanol, and then xylene for 1 minute each. The slides were then mounted with DPX (dibutyl phthalate in xylene), cover slipped, and viewed under a microscope.

4.3.7.4 *Indirect Immunofluorescence*

Due to inadequate labeling of vWF in Protocol 1, the protocol was changed to immunofluorescence labeling so that fluorescent tags were used to identify vWF instead of DAB as in Protocol 1.

4.3.7.4.1 *Deparaffinization protocol*

Prior to staining, all slides were first deparaffinized and rehydrated through a series of graded alcohol immersions. Slides were immersed in xylene three times for 10 minutes each time, after which the slides were placed in graded concentrations of alcohol: 100% v/v for 2 minutes, 95% v/v for 1 minute, and 70% v/v for 1 minute. The slides were then immersed in 0.85% w/v NaCl solution for 2 minutes, followed by immersion in 0.01 M PBS for 2 minutes.

Table 4.1. Primary and secondary antisera used for immunohistochemical protocols

| Antigen | Code of primary antibody or fluorophore for secondary antibody | Host species | Dilution | Incubation period | Source |
|---|--|--------------|----------|-------------------|---|
| Primary antibodies | | | | | |
| Von Willebrand factor (vWF) | Rabbit anti- vWF | Rabbit | 1:500 | 24 hours | AbCam (Cambridge, MA, USA) |
| Von Willebrand factor (vWF) | Mouse anti- vWF | Mouse | 1:30 | 24 hours | AbCam |
| Von Willebrand factor (vWF) | Rabbit anti-human vWF | Rabbit | 1:200 | 24 hours | DAKO North America (Carpinteria, CA, USA) |
| α smooth muscle actin (SM-actin) | Rabbit anti-SM actin | Rabbit | 1:200 | 24 hours | AbCam |
| Secondary antisera | | | | | |
| Rabbit IgG | Goat anti- rabbit conjugated to a peroxidase-labeled polymer | Goat | 1:200 | 2 hours | Envision kit, DAKO North America |
| Rabbit IgG | Goat anti- rabbit conjugated to Alexa 488 or Alexa 594 | Goat | 1:500 | 2 hours | Invitrogen (Carlsbad, CA, USA) |
| Rabbit IgG | Goat anti- rabbit conjugated to Texas Red | Goat | 1:200 | 2 hours | Invitrogen |
| Mouse IgG | Goat anti- mouse conjugated to FITC | Goat | 1:200 | 2 hours | Invitrogen |
| Rabbit IgG | Goat anti-rabbit conjugated to Alexa 555 | Goat | 1:1000 | 1 hour minimum | Invitrogen |

vWF: von Willebrand factor; SM actin: smooth muscle actin; IgG: Immunoglobulins G; FITC: Fluorescein isothiocyanate

4.3.7.4.2 *Antigen retrieval*

Following deparaffinization, the sections were then placed into a glass container filled with 10 mM citrate buffer (pH 6.0) and microwaved on a low heat for 10 minutes to avoid boiling. The basic mechanism by which tissues are fixed by aldehydes is by the formation of protein cross-links, resulting in some conformational changes of the proteins (15). This process can therefore mask the antigenic sites in tissue specimens. This results in weak or false negative staining for immunohistochemical detection of some proteins (25) because antibodies cannot recognize the antigens (15). This citrate-based solution is designed to break these cross-links, and therefore uncover the antigens and epitopes in fixed and paraffin embedded tissue sections. Hence, the immersion in citrate buffer enhances the fluorescence intensity of the fluorescent dye. The heating process was paused at 5 minutes to ensure the slides were still submerged in citrate buffer. After the slides were heated, the glass container was removed from the microwave and left to cool for 10-20 minutes.

4.3.7.4.3 *Protocol 2: Detecting von Willebrand factor using immunofluorescence*

Following the deparaffinization protocol as above, the kidney sections were blocked and incubated with rabbit anti-vWF antibodies overnight, after which the slides were then incubated in goat anti-rabbit conjugated to Alexa 488 before being rinsed in 0.01 M PBS. Since exposure to light may destroy the fluorophore (Texas Red or Alexa dyes), photobleaching and loss of fluorescence was prevented by the use of Vectashield mounting medium (Vector Laboratories; CA, USA). After the slides were dried, they were mounted with Vectashield, cover slipped, and observed under a fluorescence microscope. Photomicrographs were taken using a ColorViewIIIu camera (Olympus Soft Imaging Solutions GmbH).

4.3.7.4.4 *Protocol 3: Double-labeling immunofluorescence*

In order to examine the co-distribution of two (or more) different antigens in the same sample, a double-labeling immunofluorescence protocol can be used. Because the veins were not positively labeled in Protocol 2, SM actin staining was carried out in an attempt to label veins. Thus, double-labeling immunofluorescence was carried out to visualize both vWF and SM actin on one kidney section. After the deparaffinization and antigen retrieval protocols were carried out, the kidney sections were blocked and incubated in primary antibodies at room temperature overnight. To stain for vWF, mouse anti-vWF was used as the primary antibody.

To stain for actin, the primary antibody was rabbit anti-SM. A negative control slide was incubated only with the antibody diluent overnight.

After 24 hours, the slides were washed in 0.01 M PBS and then incubated in secondary antibodies for 2 hours. For detecting vWF, the secondary antibody was goat anti-mouse conjugated to fluorescein (FITC). The secondary antibody for detecting α SM actin was goat anti-rabbit conjugated to Texas Red. The negative control slide was incubated with both secondary antibodies.

After this incubation period, all sections were washed three times in 0.01 M PBS for 10 minutes per wash. The slides were then mounted with Vectashield, cover slipped, and examined under a fluorescence microscope. Images were taken with a ColorViewIIIu camera (Olympus Soft Imaging Solutions GmbH).

4.3.7.4.5 Protocol 4: Serial sections

To better visualize the labeling of vWF, SM actin, and the cellular structure of the kidney section, immunohistochemical and histological staining was carried out on serial sections. Since the primary mouse antibody (used in Protocol 3) provided weak labeling of vWF, we reverted to the use of rabbit anti-vWF. After deparaffinization of the renal sections, the slides prepared for immunostaining were washed thrice in 0.01 M PBS for 5 minutes each time. The kidney sections were then blocked and incubated in primary antibodies at room temperature overnight. One slide was incubated with rabbit anti-vWF, one slide was incubated with rabbit anti-SM actin, and H & E staining was carried out on another slide (Fig. 4.2).

After 24 hours, the slides were rinsed in 0.01 M PBS and incubated in secondary antibodies for 2 hours. The secondary antibodies used were goat anti-rabbit conjugated to a red fluorescent dye; either Texas-Red or Alexa 594. After this incubation period, all sections were washed three times in 0.01 M PBS for 10 minutes each time. The slides were mounted with Vectashield (Vector Laboratories; CA, USA), cover slipped, and observed under a fluorescence microscope (Olympus BX51; Hamburg, Germany). Images were taken using a ColorViewIIIu camera (Olympus Soft Imaging Solutions GmbH).

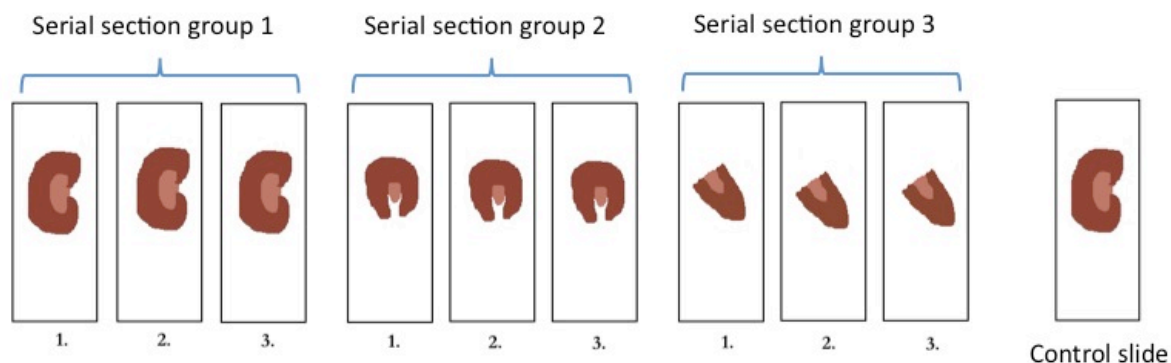


Figure 4.2. A schematic diagram of the serial section method. Each group consisted of 3 consecutive 5 µm sections. One slide per group was stained with an antibody for von Willebrand Factor (vWF; slide 1), one with an antibody for α smooth muscle actin (α SM actin; slide 2), and one with hematoxylin and eosin (H & E; slide 3.). Incubation in primary antibody was omitted for one slide (control slide), which was only incubated with the secondary antibody, giving a total of 10 slides. Serial section group 1 corresponds with the cross sections in Figure 4.1A; group 2 corresponds with Figure 4.1B; group 3 corresponds with Figure 4.1C.

4.3.7.4.6 Protocol 5: Fluorescence immunohistochemistry for von Willebrand factor after antigen retrieval using sodium citrate buffer, and blocking with bovine serum albumin

Prior to antibody incubation, slides were dewaxed in xylene as above, and then rehydrated in 100% v/v and 70% v/v ethanol for 5 minutes each before a wash in PBS for 5 minutes. Slides were then heated in sodium citrate buffer (pH 6.0) for 2 minutes at 1-minute intervals to avoid boiling. Slides were then washed in PBS for 5 minutes prior to blocking with 1% bovine serum albumin (BSA) for a minimum of 1 hour covered in foil at room temperature. Slides were then incubated in rabbit anti-human vWF, covered in foil, and kept at 4 °C overnight.

After 24 hours, the slides were washed in PBS for 5 minutes before being incubated in goat anti-rabbit conjugated to Alexa 555. Slides were covered in foil and kept at room temperature for a minimum of 1 hour. Following incubation, slides were washed in PBS thrice and then incubated with 4', 6-diamidino-2-phenylindole (DAPI; 1:10,000, Sigma-Aldrich) for 5-10 minutes to visualize cell nuclei. After a wash in PBS, slides were dried, coverslipped, and viewed under fluorescence microscopes (Leica SP5, Mannheim, Germany; and Nikon C1 upright, Japan) at Monash Micro Imaging (Clayton, VIC, Australia).

4.4 RESULTS

4.4.1 Detection of renal blood vessels

4.4.1.1 Immunohistochemistry - Diaminobenzidine method

Photomicrographs of renal sections stained with DAB were taken at varying magnifications of $\times 20$ and $\times 40$ (Fig. 4.3). The DAB stain was localized to the endothelial lining of large arteries (Figs 4.3A & B). However, positive staining was not observed in all large arteries (Fig. 4.3D). There was very little or no positive staining in capillaries (e.g. glomerular capillaries) or veins in the kidney sections.

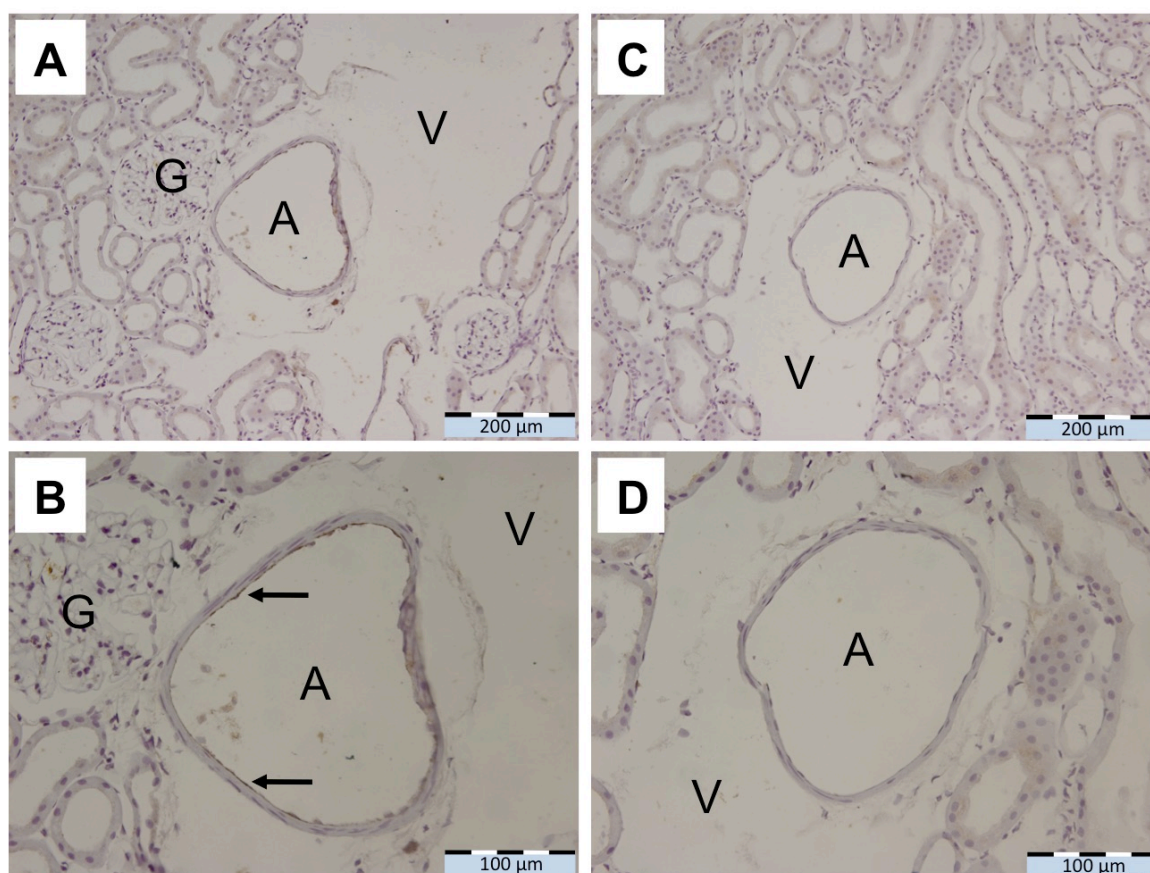


Figure 4.3. Photomicrographs of diaminobenzidine (DAB) staining for von Willebrand factor in sections of the rat kidney. Positive DAB staining was observed in the endothelial lining of some large arteries 'A' (A & B), but not all large arteries (C & D). There was very little or no labeling of the capillaries, glomerular capillaries 'G', or veins 'V'. Images are shown at magnifications of $\times 20$ (A & C) and $\times 40$ (B & D). Images B and D are higher magnifications of images A and C respectively.

4.4.1.2 Fluorescence immunohistochemistry

With inadequate staining of vWF using DAB in the previous protocol, the protocol was modified so that fluorescence immunohistochemistry would be used to label the vascular elements in the kidney. Images of kidney sections stained for von Willebrand factor were taken at a magnification of $\times 10$ (Fig. 4.4). Positive labeling was identified in the larger arteries and glomeruli (Fig. 4.4A). However there was no fluorescence observed in the endothelial lining of veins or capillaries. Furthermore, fluorescence was also observed in renal tubules, which are devoid of endothelial cells and also vWF.

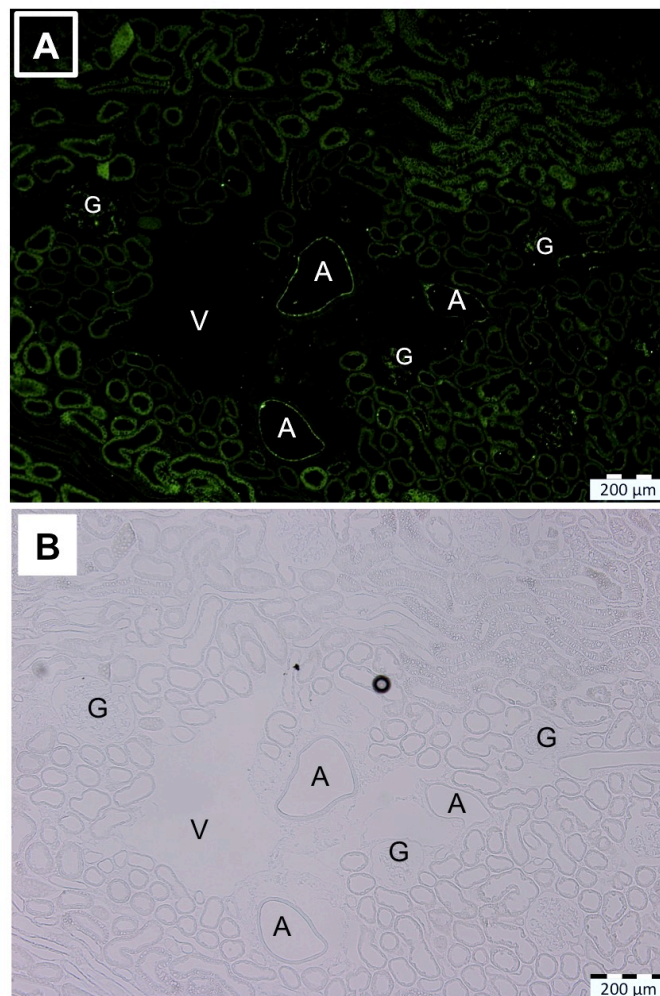


Figure 4.4. Photomicrographs of (A) immunofluorescence for von Willebrand factor (vWF) in sections of the rat kidney and (B) a light micrograph of the same section. In image (A), positive vWF labeling was observed in the endothelial lining of three large arteries 'A'. There was no positive labeling observed in capillaries or veins 'V', demonstrated by the lack of labeling in the large vein to the left of the arteries. There was some positive labeling in three glomeruli 'G' seen to the left and right of the arteries, demonstrating that some labeling of the glomerular capillaries was obtained. Note the autofluorescence from the tubular elements surrounding the vascular structures. All images are at a magnification of $\times 10$.

Double-labeling immunofluorescence (Protocol 3) was used so that both vWF and SM actin could be identified on the same kidney section. To label vWF, mouse anti-vWF was used as the primary antibody and goat anti-mouse conjugated to FITC was used as the secondary antibody. To label actin, rabbit anti-SM actin was used as the primary antibody and goat anti-rabbit conjugated to Texas Red was used as the secondary antibody. For double-labeling immunohistochemical protocols, the primary antibodies must be derived from different species (in this case, mouse and rabbit).

Kidney sections double-labeled for vWF and SM actin were photomicrographed at a magnification of $\times 20$ (Fig. 4.5). There was strong positive staining of actin in the smooth muscle cells of arteries (Fig. 4.5A). In contrast, there was only weak positive labeling for von Willebrand factor in arteries (Fig. 4.5B), and no capillaries were labeled. Furthermore, a high level of autofluorescence by the surrounding tubular elements was observed (Fig. 4.5B). There was no positive labeling for either von Willebrand factor or SM actin in veins.

Due to the considerable autofluorescence arising from renal tubules, and also the weak labeling through the use of a mouse antibody, we chose to investigate the use of serial sections. This allowed us to revert to the use of rabbit anti-vWF as the primary antibody, which provided stronger positive labeling as seen in Protocol 2 compared to Protocol 3 (Figs 4.4 and 4.5 respectively). The secondary antibodies used were goat anti-rabbit conjugated to a red fluorophore (Texas red or Alexa 594). The renal serial sections labeled for von Willebrand factor and SM actin were photomicrographed at a magnification of $\times 20$ and $\times 40$ (Fig. 4.6).

H & E staining enabled the identification of arteries, veins, glomeruli and tubular elements (Fig. 4.6C). Positive staining for vWF was observed only in large arteries and some glomerular capillaries, with no positive labeling observed in veins or capillaries (Fig. 4.6A). Immunofluorescence for SM actin was observed in arteries of the kidney (Fig. 4.6B). However no positive fluorescence was observed for veins.

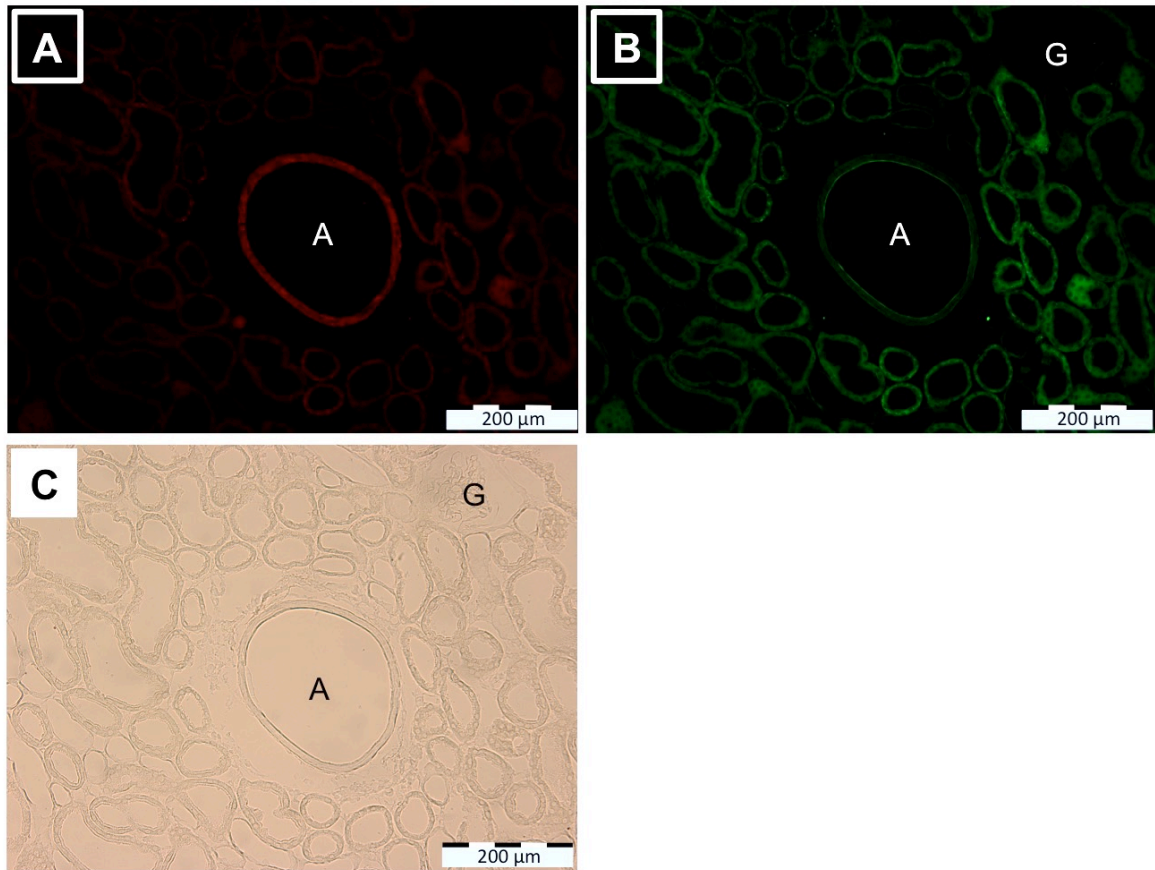


Figure 4.5. Photomicrographs of double-labeling immunofluorescence for (A) smooth muscle actin, and (B) von Willebrand factor (vWF), and also a light micrograph of the same section (C). (A) There was strong positive labeling for smooth muscle actin in large arteries 'A'. (B) vWF was localized to the endothelial lining of large arteries 'A', but was not observed in capillaries or veins. (C) The glomerulus 'G' located in the top right hand corner was not positively labeled for vWF in image B. A high level of autofluorescence by the surrounding tubular elements was observed in the section stained for vWF (B). All images are at a magnification of $\times 20$.

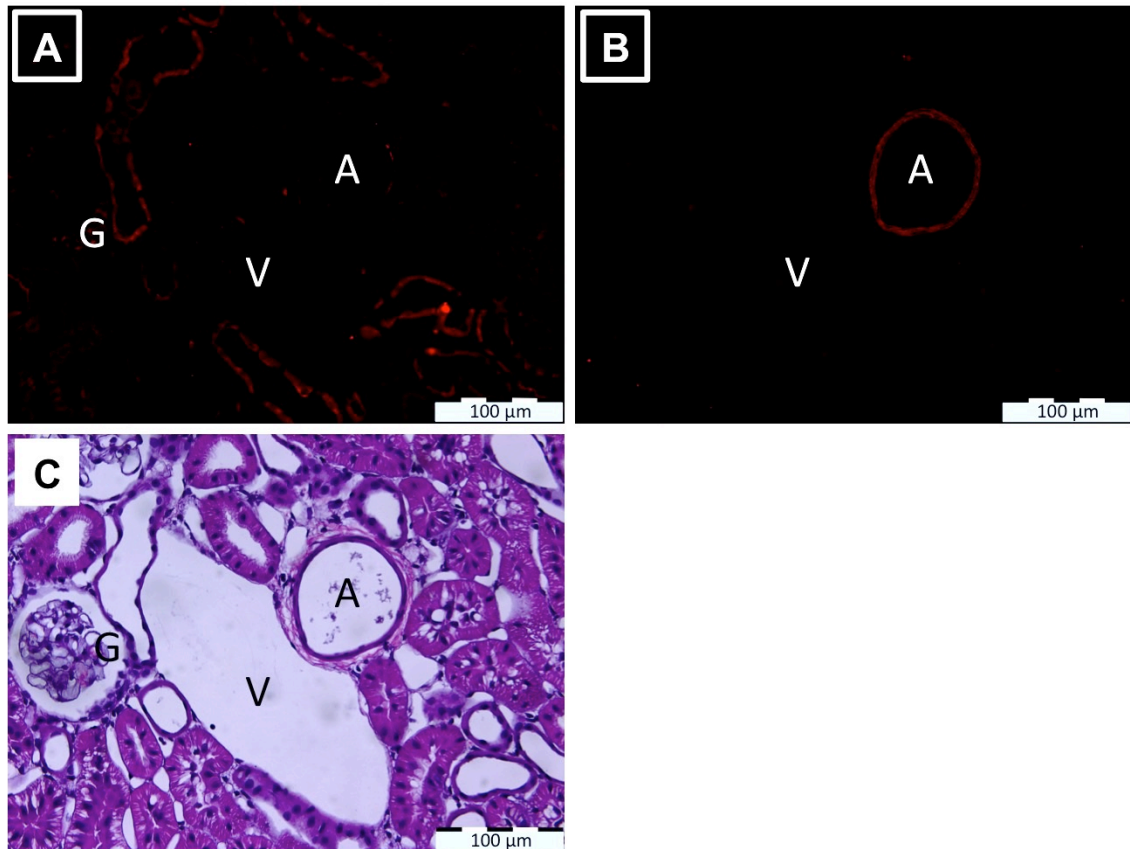


Figure 4.6. Photomicrographs of serial sections. (A) immunofluorescence for von Willebrand factor (vWF), (B) smooth muscle actin, and (C) a photomicrograph of a section stained with hematoxylin and eosin. There was very little vWF labeling in either arteries ‘A’ or glomerular capillaries ‘G’. Note also the non-specific fluorescence in tubular epithelium below the artery (A) in image A. There was strong positive labeling for smooth muscle actin (B) in the arteries ‘A’. Neither vWF nor actin was detected in the vein found directly beside the artery ‘V’. Images are at a magnification of $\times 40$.

Finally we trialed a modified method (See Appendix 4) to that employed by Puelles *et al* (24), which is optimized for human kidney tissue. The main differences between this protocol and Protocol 2 were the different antigen retrieval step (sodium citrate buffer was used instead of citrate buffer), the blocking step (BSA was used instead of goat serum), and the source of the primary antibody (DAKO instead of AbCam). The renal sections stained for von Willebrand factor using this method were photomicrographed at a magnification of $\times 20$ (Fig. 4.7). Positive labeling was observed in the endothelial lining of large (Figs 4.7A & B), as well as small arteries (Fig. 4.7C). Glomerular capillaries also displayed positive labeling (Fig. 4.7A). However, autofluorescence and non-specific labeling was detected in the surrounding tubular elements (Figs 4.7A & B).

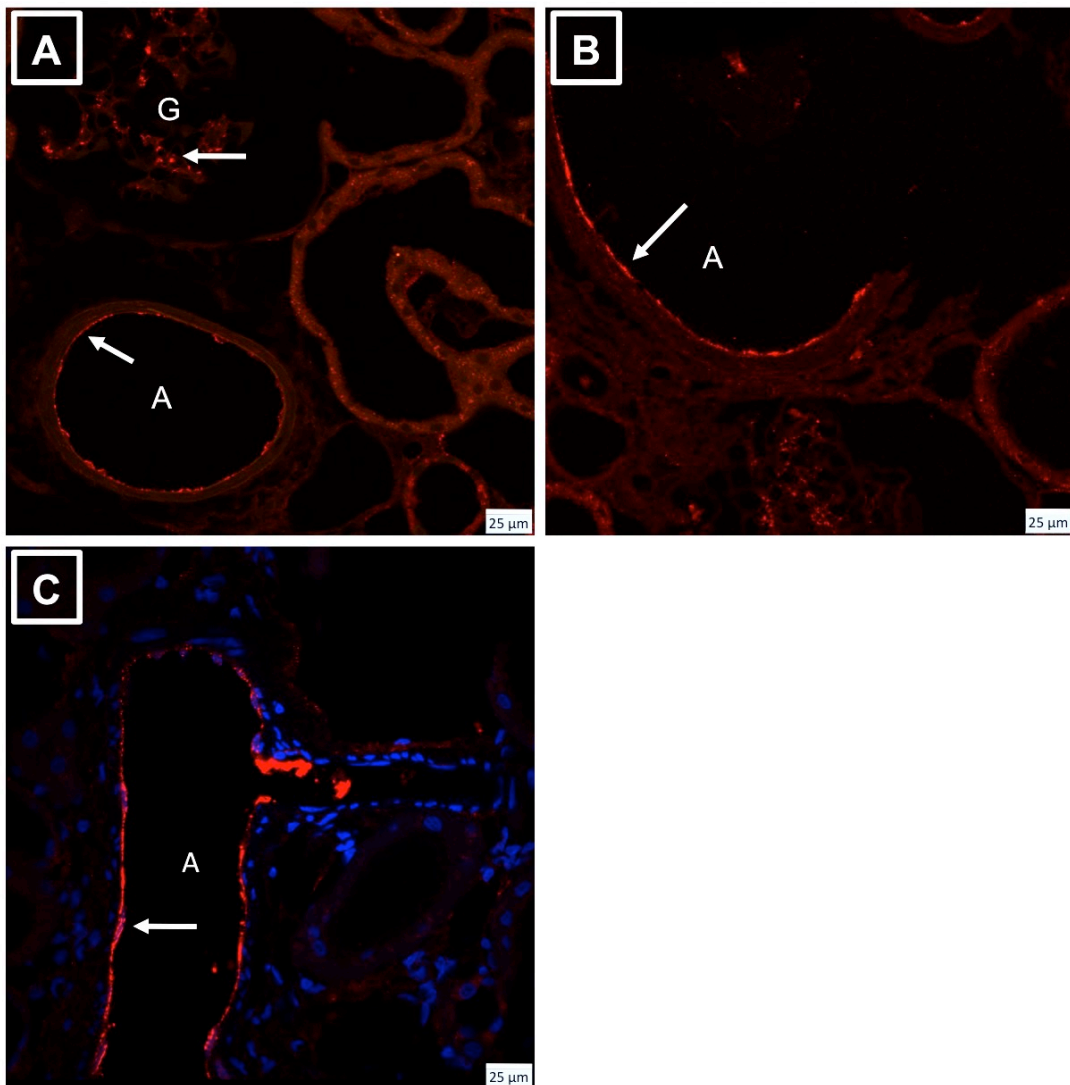


Figure 4.7. Photomicrographs of immunofluorescence for von Willebrand factor (vWF) in sections of the rat kidney. Positive vWF labeling fluoresced red, indicated by the arrows. vWF was observed in large arteries ‘A’ (A & B) and in glomerular capillaries ‘G’. (C) Positive labeling was also observed in small branching arteries ‘A’, demonstrating that this protocol is capable of staining very small arteries down to the level of the afferent arteriole. The blue fluorescence observed (C) is due to DAPI staining of cell nuclei. Images are at a magnification of $\times 20$ to $\times 40$ with an oil lens.

4.5 DISCUSSION

4.5.1 Major findings

We trialed a number of immunohistochemical approaches for identification of the various vascular elements in the kidney, but none proved satisfactory for our purposes. Indeed, none of these methods provided adequate labeling of veins or capillaries. Labeling of vWF and/or SM actin was only observed in large arteries in Protocols 1-3. Even the improved approach used in Protocol 4 was unable to label veins. We conclude that the use of immunohistochemistry as a method for differential labeling of blood vessels in the kidney is problematic for our purposes.

4.5.2 Immunohistochemistry as a technique to distinguish renal arteries, veins, and capillaries.

4.5.2.1 Strengths and limitations

The use of HRP for enzyme-mediated immunodetection is a well-established histochemical technique (14, 26). One of the most widely used HRP substrates for immunohistochemistry is DAB, which produces a brown-colored polymeric oxidation product. Initially, having stained renal sections to detect vWF (DAB staining), the immunostaining protocol was modified from DAB staining to immunofluorescence to better visualize the renal blood vessels. The protocol was changed because the kidney sections stained via the DAB staining protocol did not provide strong visualization of the endothelial lining of blood vessels. As a result, the protocol was changed so that immunofluorescence was used. A potential limitation of this approach is that vWF staining alone would not be able to distinguish small venules from capillaries, as both vessel types are of similar size and structure (4). However, one would expect the media of venules to contain smooth muscle fibers. Thus, the protocol was modified so that double-labeling immunofluorescence was employed, enabling the visualization of both endothelial cells (vWF) and SM actin. A limitation of this protocol was that the mouse anti-vWF used for double-labeling was not as effective as the rabbit anti-vWF used in the previous protocol. Furthermore, a high level of autofluorescence was observed in the surrounding tubular elements, resulting in poor identification and visualization of the blood vessels in the kidney.

The protocol was therefore changed so that 5 μ m serial sections of the kidney would be stained. Use of this protocol allowed improved labeling of vWF because rabbit anti-vWF was used instead of mouse anti-vWF. Each group of serial sections initially contained 2 sections.

One slide from the serial section group was stained for vWF, and the other for actin. Initially, Alexa-488 was used as the secondary antibody for the sections stained with vWF, and Texas Red was used for the sections stained for actin. After examining the slides under the microscope, it was observed that the vessels of the slides stained with vWF and Alexa-488 fluoresced green. However, due to the kidney's autofluorescence in the green portion of the visible spectra, the tubules and surrounding structures also appeared green, making it difficult to visualize the blood vessels of the kidney. SM actin fluoresced red and was only observed in the arteries, not the veins.

Due to the auto-fluorescence of kidney structures, the protocol was modified once more. Both vWF and actin were labeled with Texas Red to better distinguish the vessels. Also, in order to better visualize the renal structure, one slide from each serial section group was stained with H & E. This resulted in three serial sections per group, as opposed to two serial sections per group in the previous protocol. In summary, one slide per group was stained for vWF; one for SM actin, and H & E staining was carried out on a third slide. Although H & E staining provided good visualization of the cellular structure of the kidney sections, fluorescent labeling of veins, and capillaries in the kidney was still not apparent.

Previous studies have demonstrated positive labeling of vWF in fixed paraffin embedded kidney tissue (10). A possible explanation for the lack of positive labeling of vWF in veins relates to the structure of the renal vein wall. The walls of the interlobular and arcuate veins differ to those of most veins in the body (2, 4). Typical veins have walls consisting of a tunica intima, a tunica media, where the smooth muscle cells are located, and the tunica adventitia, which contains fibroblasts and extracellular matrix. In contrast, the walls of the interlobular and arcuate veins in the kidney consist of an extremely thin lining of endothelial cells and a thin basal lamina (2, 4). It can therefore be expected that labeling the arcuate and interlobular veins of the kidney would be difficult due to the extreme thinness of the vessel wall. Similarly, the extremely thin tunica media in the walls of interlobular veins (9) likely explains why these veins could not be positively labeled for actin.

SM actin acted as a label for smooth muscle cells in the kidney. It was only able to label actin located in smooth muscle of arteries. It was expected that the glomeruli in the kidney would also be positively labeled for actin. This is because of the presence of specialized smooth muscle-like cells, known as mesangial cells, which have previously been positively labeled for actin (8). However, no positive staining of the mesangial cells was observed in this study.

We therefore conclude that the immunohistochemical approaches we employed are unlikely to provide definitive identification of arteries, veins and capillaries in the renal cortex.

4.6 CONCLUSIONS AND ALTERNATIVE APPROACHES TO IDENTIFY THE RENAL VASCULATURE

In this project, we attempted to identify and distinguish the various vascular elements in the renal cortex by labeling the vessels using immunohistochemical and immunofluorescence techniques. However, we identified that these techniques, at least as employed in the current study, could not identify all intrarenal blood vessels and thus are not very useful for our studies.

An alternative immunohistochemical approach would be to label the tubular elements of the kidney rather than the vascular elements. Aquaporin-1 (AQP1) is a water channel present in the proximal tubules and descending thin limbs of Henle's loop in the kidney, and aquaporin-2 (AQP2) is a water channel present in the collecting ducts (16). Taking an alternative approach by using antibodies that label these water channels could potentially enable the identification of multiple tubular segments. Furthermore, an antibody against the protein α B-crystallin, which is localized to descending thin limbs, ascending thin limbs, and collecting ducts (7, 13) would allow identification of sections of tubules not labeled by the antibodies against AQP1 and AQP2 (21-23). However, labeling the tubular elements of the kidney instead of the vascular elements would still not allow differentiation of venules from capillaries. While larger arteries and veins could easily be identified, small veins and capillaries would still be unidentifiable.

Another approach that could be considered is the use of frozen sections instead of paraffin embedded tissue. Generally, immunohistochemical protocols provide better results for frozen sections (12) because the antigenic content is well preserved, provided the tissue is frozen rapidly. The advantages of fixation and embedding tissues in paraffin wax are that the morphology is better maintained compared to frozen tissue. A disadvantage of using paraffin blocks is that the processing of the tissue, which requires fixatives such as formalin or formaldehyde-based solutions, leads to formation of cross-links between proteins. Pre-treatment to "unmask" cross-linked antigens is often essential. Such antigen retrieval techniques include microwaving in a citrate-based solution, as was carried out in this study. Although the citrate solution is able to uncover antigens and therefore allow antibody binding,

some antigens are permanently ‘masked’ by the fixative. Thus, immunostaining of paraffin embedded tissues tends to provide less intense labeling and/or more false negatives (12).

Another possible approach to identify the blood vessels of the kidney is to perfuse the kidney with Microfil©, a silicone-based product, which has been previously used to fill the renal vasculature for examination using micro-computed tomography (micro-CT) (20). We could modify our perfusion fixation protocol so that after perfusion fixation, the vasculature is filled with Microfil® silicone rubber, and renal tissue embedded in paraffin or resin. An additional advantage of this approach is that it can also be used in conjunction with micro-CT, since the silicone rubber is radio-opaque (1). Thus, for subsequent experiments, we submitted fixed kidney tissue, filled with silicone rubber, to both light microscopic analysis (Chapters 5-9 of this thesis) and synchrotron-based micro-CT (Chapter 9 of this thesis).

REFERENCES

1. **Bentley MD, Ortiz MC, Ritman EL, Carlos Romero J.** The use of microcomputed tomography to study microvasculature in small rodents. *Am J Physiol Regul Integr Comp Physiol* 282: R1267-R1279, 2002.
2. **Bertram J.** Structure of the renal circulation. In: *The Renal Circulation*, edited by Anderson WP, Evans RG, and Stevenson KM. Elsevier, 2000.
3. **Evans RG, Smith DW, Khan Z, Ngo JP, Gardiner BS.** Letter to the editor: "The plausibility of arterial-to-venous oxygen shunting in the kidney: it all depends on radial geometry". *Am J Physiol Renal Physiol* 309: F179-180, 2015.
4. **Frank M, Kriz W.** The luminal aspect of intrarenal arteries and veins in the rat as revealed by scanning electron microscopy. *Anat Embryol (Berl)* 177: 371-376, 1988.
5. **Garcia-Sanz A, Rodriguez-Barbero A, Bentley MD, Ritman EL, Romero JC.** Three-dimensional microcomputed tomography of renal vasculature in rats. *Hypertension* 31: 440-444, 1998.
6. **Gardiner BS, Smith DW, O'Connor PM, Evans RG.** A mathematical model of diffusional shunting of oxygen from arteries to veins in the kidney. *Am J Physiol Renal Physiol* 300: F1339-1352, 2011.
7. **Iwaki T, Kume-Iwaki A, Goldman JE.** Cellular distribution of α B-crystallin in non-lenticular tissues. *J Histochem Cytochem* 38: 31-39, 1990.
8. **Johnson RJ, Iida H, Alpers CE, Majesky MW, Schwartz SM, Pritzi P, Gordon K, Gown AM.** Expression of smooth muscle cell phenotype by rat mesangial cells in immune complex nephritis. Alpha-smooth muscle actin is a marker of mesangial cell proliferation. *J Clin Invest* 87: 847-858, 1991.
9. **Jurčić V, Jeruc J, Marić S, Ferluga D.** Histomorphological assessment of phlebitis in renal allografts. *Croat Med J* 48: 327-332, 2007.
10. **Kuin A, Citarella F, Oussoren YG, Van der Wal AF, Dewit LGH, Stewart FA.** Increased glomerular Vwf after kidney irradiation is not due to increased biosynthesis or endothelial cell proliferation. *Radiat Res* 156: 20-27, 2001.
11. **Levy MN, Imperial ES.** Oxygen shunting in renal cortical and medullary capillaries. *Am J Physiol* 200: 159-162, 1961.
12. **Mera SL, Young EW, Bradfield JW.** Direct immunofluorescence of skin using formalin-fixed paraffin-embedded sections. *J Clin Pathol* 33: 365-369, 1980.
13. **Michl M, Ouyang N, Fraek ML, Beck FX, Neuhofer W.** Expression and regulation of α B-crystallin in the kidney in vivo and in vitro. *Pflugers Arch* 452: 387-395, 2006.
14. **Milde P, Merke J, Ritz E, Haussler MR, Rauterberg EW.** Immunohistochemical detection of 1,25-dihydroxyvitamin D₃ receptors and estrogen receptors by monoclonal antibodies: comparison of four immunoperoxidase methods. *J Histochem Cytochem* 37: 1609-1617, 1989.
15. **Montero C.** The antigen-antibody reaction in immunohistochemistry. *J Histochem Cytochem* 51: 1-4, 2003.
16. **Nielsen S, Frokiaer J, Marples D, Kwon TH, Agre P, Knepper MA.** Aquaporins in the kidney: from molecules to medicine. *Physiol Rev* 82: 205-244, 2002.
17. **Nordsletten DA, Blackett S, Bentley MD, Ritman EL, Smith NP.** Structural morphology of renal vasculature. *Am J Physiol Heart Circ Physiol* 291: H296-H309, 2006.
18. **O'Connor PM, Anderson WP, Kett MM, Evans RG.** Renal preglomerular arterial-venous O₂ shunting is a structural anti-oxidant defence mechanism of the renal cortex. *Clin Exp Pharmacol Physiol* 33: 637-641, 2006.
19. **O'Connor PM, Evans RG.** Structural antioxidant defense mechanisms in the mammalian and nonmammalian kidney: Different solutions to the same problem? *Am J Physiol Regul Integr Comp Physiol* 299: R723-R727, 2010.

20. **Ortiz MC, Garcia-sanz A, Bentley MD, Fortepiani LA, Garcia-Estan J, Ritman EL, Romero JC, Juncos LA.** Microcomputed tomography of kidneys following chronic bile duct ligation. *Kidney Int* 58: 1632-1640, 2000.
21. **Pannabecker TL, Abbott DE, Dantzler WH.** Three-dimensional functional reconstruction of inner medullary thin limbs of Henle's loop. *Am J Physiol Renal Physiol* 286: F38-F45, 2004.
22. **Pannabecker TL, Dantzler WH.** Three-dimensional architecture of inner medullary vasa recta. *Am J Physiol Renal Physiol* 290: F1355-1366, 2006.
23. **Pannabecker TL, Dantzler WH.** Three-dimensional lateral and vertical relationships of inner medullary loops of Henle and collecting ducts. *Am J Physiol Renal Physiol* 287: F767-F774, 2004.
24. **Puelles VG, Douglas-Denton RN, Cullen-McEwen L, McNamara BJ, Salih F, Li J, Hughson MD, Hoy WE, Nyengaard JR, Bertram JF.** Design-based stereological methods for estimating numbers of glomerular podocytes. *Ann Anat* 196: 48-56, 2014.
25. **Shi SR, Key ME, Kalra KL.** Antigen retrieval in formalin-fixed, paraffin-embedded tissues: An enhancement method for immunohistochemical staining based on microwave oven heating of tissue sections. *J Histochem Cytochem* 39: 741-748, 1991.
26. **Shi ZR, Itzkowitz SH, Kim YS.** A comparison of three immunoperoxidase techniques for antigen detection in colorectal carcinoma tissues. *J Histochem Cytochem* 36: 317-322, 1988.
27. **Welch WJ, Baumgartl H, Lubbers D, Wilcox CS.** Nephron pO₂ and renal oxygen usage in the hypertensive rat kidney. *Kidney Int* 59: 230-237, 2001.

5 | ANALYSIS OF THE SPATIAL GEOMETRY OF ARTERY-VEIN PAIRS IN THE KIDNEY

Monash University

Declaration for Thesis Chapter 5

Declaration by candidate

Some content of this chapter was published in the *American Journal of Physiology – Renal Physiology*:

Gardiner BS, Thompson SL, Ngo JP, Smith DW, Abdelkader A, Broughton BR, Bertram JF, Evans RG. Diffusive oxygen shunting between vessels in the preglomerular renal vasculature: anatomic observations and computational modeling. *Am J Physiol Renal Physiol* 303: F605-618, 2012.



In the case of Chapter 5, the nature and extent of my contribution to the work was the following:

| Nature of contribution | Extent of contribution (%) |
|--|----------------------------|
| Provided design of research, performed experiments, analyzed data, interpreted results, prepared tables and figures, drafted, edited and revised chapter | 70% |

The following co-authors contributed to the work. If co-authors are students at Monash University, the extent of their contribution in percentage terms must be stated:

| Name | Nature of contribution | Extent of contribution (%) for student co-authors only |
|-------------------------|--|--|
| Bruce S Gardiner | Provided design of research, analyzed data, interpreted results, drafted, edited and revised manuscript | 3% |
| Sarah L Thompson | Performed experiments, interpreted results, prepared figures, drafted, edited and revised manuscript | 10% |
| David W Smith | Provided design of research, interpreted results, edited and revised manuscript | 3% |
| Amany Abdelkader | Supervision, performed experiments, analyzed data, edited and revised manuscript | 2% |
| John F Bertram | Provided design of research, performed experiments, edited and revised manuscript | 2% |
| Roger G Evans | Supervision, provided design of research, performed experiments, interpreted results, drafted, edited and revised manuscript | 10% |

The undersigned hereby certify that the above declaration correctly reflects the nature and extent of the candidate's and co-authors' contributions to this work*.

| | | |
|-----------------------------|--|--------------------|
| Candidate's Signature |  | Date 24/04/2016 |
| Main Supervisor's Signature |  | Date 24/04/2016 |

*Note: Where the responsible author is not the candidate's main supervisor, the main supervisor should consult with the responsible author to agree on the respective contributions of the authors.

5.1 ABSTRACT

Both acute kidney injury (AKI) and chronic kidney injury (CKD) are major causes of morbidity and mortality. There is accumulating evidence to suggest that tissue hypoxia is a major factor in the pathogenesis of both AKI and CKD. However, renal oxygenation is complicated by a phenomenon known as arterial-to-venous (AV) oxygen shunting. Thus, our group is developing a mathematical model of oxygen transport in the kidney in order to aid our understanding of the physiological regulation of oxygen in the kidney. A major limitation of the current model is a lack of quantitative information pertaining to the barriers of oxygen diffusion between arteries, veins, and the renal parenchyma. To overcome this limitation, we examined the spatial association of arteries and veins in the kidney using histologically stained sections from the rat kidney.

Six rat kidneys were perfusion-fixed at physiological pressure and embedded in paraffin and glycolmethacrylate (2 kidneys and 4 kidneys respectively). In addition, kidneys that were embedded in glycolmethacrylate (GMA) had the vasculature filled with Microfil® so that microvessels could be easily visualized. The kidneys were then sectioned and histochemically stained. Paraffin-embedded kidney sections were stained with hematoxylin and eosin. GMA-embedded kidney sections were stained with toluidine blue. The spatial association and diffusion distances of the renal vasculature was first qualitatively analyzed, and then quantitatively analyzed using the open source program ImageJ.

The initial qualitative analysis provided evidence that the spatial association between arteries and veins changes along the course of the renal circulation. The analysis showed that larger arteries are surrounded for much of the circumference by a vein wall. In contrast, this arrangement is rarely seen for smaller vessels. Our subsequent quantitative analysis, based on data from both light microscopy and data derived from our colleagues (University of Western Australia) from micro-computed tomography (micro-CT) of a vascular cast of the rat renal circulation, provided preliminary evidence that diffusion distances, between arteries and veins, do not remain constant through the circulation.

Peritubular capillary density was least in the immediate vicinity of the artery, and this was apparent for arteries of all sizes. Capillary density was greater near smaller arteries than larger arteries. Capillaries and tubules were frequently observed between smaller artery-vein pairs, but were not observed between wrapped artery-vein pairs. A U-shaped relationship was found between arterial diameter and diffusion distance, suggesting that AV oxygen shunting could be favored in vessels common to both the cortical and medullary circulations. Thus, AV

oxygen shunting within the renal cortex may act to limit oxygen delivery to the medulla. This mechanism may contribute to rendering the medulla vulnerable to developing hypoxia.

Some of the results from this study were incorporated in the paper titled ‘Diffusive oxygen shunting between vessels in the preglomerular renal vasculature: anatomic observations and computational modeling’ (8). This paper can be found in Appendix 1.

5.2 INTRODUCTION

Oxygen transport in the kidney is of interest because hypoxia is thought to be a critical factor in the pathogenesis of both acute and chronic kidney disease. There are a number of respects in which oxygen regulation in the kidney is unique. One of these is the impact of AV oxygen shunting (3, 16). The intimate relationship between some arteries and veins in the kidney facilitates the diffusion of oxygen down its concentration gradient from the arterial blood to the venous blood. Thus, variation in the spatial relationships between arteries and veins would be expected to affect the amount of oxygen that is shunted. Perhaps more importantly, such variation might occur progressively along the course of the branching network of the cortical circulation. This putative phenomenon would be expected to have a major impact on the relative amounts of oxygen shunted in vessels that deliver blood to both the cortical and medullary circulations versus that shunted in vessels that only supply blood to the cortex.

Experimental evidence (17) and the results of preliminary modeling studies (7) suggest that AV oxygen shunting in vessels upstream from the divergence of the cortical and medullary circulations could render the medulla susceptible to hypoxia in cortical ischemia, even if medullary perfusion is perfectly maintained. For example, O’Connor *et al* showed that tissue oxygenation of the cortex is independent of medullary perfusion; while medullary oxygenation is dependent on both cortical and medullary perfusion (17). Medullary oxygenation was reduced as expected when medullary perfusion was reduced. Interestingly, reduced cortical blood flow also resulted in reduced medullary oxygenation, even when medullary perfusion was maintained. Reductions in medullary perfusion were found to have no significant effect on cortical oxygenation. O’Connor *et al* proposed that the observed dependence of medullary oxygenation on cortical perfusion reflects the ability of deoxygenated venous blood in cortical veins to ‘steal’ oxygen from arteries containing blood destined for the medullary circulation (17). This proposition was supported by the findings of Gardiner *et al* using a computational model of oxygen transport in the preglomerular circulation (7).

Gardiner *et al* (7) recently produced a mathematical model of oxygen transport in the kidney which incorporates the phenomenon of AV oxygen shunting. The model predicted that most AV oxygen shunting occurs in the distal parts of the cortical circulation, after its divergence from the medullary circulation. Nevertheless, in agreement with the experimental findings of O'Connor *et al* (17), the model did predict that severe cortical hypoxia would reduce the oxygen content of arterial blood destined for the medullary circulation (7). However, the utility of the model was limited by the fact that there are currently no quantitative data on the barriers to oxygen diffusion between arteries and veins. Consequently, the diffusion coefficients in their model were set at a constant value throughout the cortical circulation. It remains to be determined whether this assumption is justified.

In the current study we investigated the nature of the spatial association of intrarenal arteries and veins of varying sizes and branching levels in order to provide information regarding the potential sites of AV oxygen shunting in the kidney. Gardiner *et al* (7) identified four factors that would be expected to have a significant impact on the quantity of oxygen shunting that might occur at any specific point along the preglomerular circulation. These were (i) the presence of oxygen 'sinks' (capillaries and tubules) between the artery and vein, (ii) the distance between the lumen of an artery and the lumen of its associated vein, (iii) the spatial arrangement of the vessel pairs, in particular the degree at which the vein partially surrounds the circumference of the artery, and (iv) the oxygen tension (PO_2) gradient between blood in the artery and vein. In the current study we investigated the first three of these factors.

One technical challenge for these studies was to develop methods to allow unequivocal identification of arteries and veins in the kidney. As described in detail in Chapter 4, preliminary studies were performed to assess the potential use of immunohistochemical methods for this purpose. None of the immunohistochemical protocols we employed allowed identification of all vascular elements in the kidney. Yet, over the course of these studies it became apparent that arteries within the kidney could be identified by their characteristic structure. Veins could also often be identified by their extremely thin walls (6). Therefore, a preliminary study was conducted to assess the relationships between arterial caliber and the distances separating the lumens of the arteries and veins. In conjunction with these studies, our colleagues at the School of Computer Science and Software Engineering of the University of Western Australia (UWA) conducted an analysis of the micro-computed tomographic data generated by Nordsletten *et al* (15), to generate analogous data to ours. Our aim was to compare the utility of the light microscopy approach with that of the micro-CT approach for quantification of artery-vein relationships in the kidney. We also aimed to: (i) determine the

typical arrangement of arteries and veins of various sizes, (ii) determine the relationship between arterial diameter and separation distance, and finally (iii) determine whether capillary density around artery-vein pairs varies by arterial caliber. The micro-CT data are presented in the Discussion section of this thesis, since the raw data were generated by our colleagues at UWA. Some of the data presented in this Chapter were published, together with a mathematical model of oxygen diffusion from arteries to veins (8). This paper is presented in Appendix 1 in this thesis.

5.3 METHODS

5.3.1 Experimental approach

As for the initial immunohistochemical (Chapter 4) and light microscopic studies, perfusion-fixed kidneys from Sprague Dawley rats were cut into three different sections as described in Figure 5.1. Perfusion-fixed skeletal muscle was also studied. The kidneys and skeletal muscle were then processed, stained, and analyses were carried out to identify arteries, veins, and capillaries. The characteristic arrangements and relationships between arteries and veins in the renal cortex were assessed using histological methods.

For tissues stained with hematoxylin and eosin (H & E), the kidneys and skeletal muscle from two male Sprague Dawley rats and one female Sprague Dawley rat were retrieved after perfusion fixation. Furthermore, an additional four kidneys of male Sprague Dawley rats were retrieved after perfusion fixation and filling of the vasculature with silicone rubber material (Microfil®). All kidneys were sectioned in three planes, processed, stained, and analyses were carried out to identify the characteristic arrangements of renal arteries, veins, and capillaries.

We experienced difficulty identifying the smaller vessels such as arterioles and capillaries using only H & E staining. Thus our approach was to use Microfil®, a silicone based compound, to fill the renal vasculature, which allowed us to identify not only the small arteries, but also capillaries. The diffusion distances between artery-vein pairs from both H & E stained and Microfil®-filled tissue sections were measured.

5.3.2 Hematoxylin and eosin stained tissue

5.3.2.1 Perfusion protocol

The kidneys were perfusion-fixed with phosphate buffered saline and 3% paraformaldehyde (3% PFA; Appendix 4) as described in the General Methods section (Chapter 3, Section 3.2). Furthermore, in a single male rat, hind limb skeletal muscle (biceps femoris) was fixed via

orthograde perfusion of the abdominal aorta. The tissue was kept in fixative overnight at 4 °C prior to histological analyses.

5.3.2.2 Tissue processing, embedding in paraffin and sectioning

After overnight immersion in fixative, the kidneys were cut into sections as described in Figure 5.1, and then placed in 70% ethanol. The biceps femoris tissue was cut in such a manner to provide a cross section perpendicular to the direction in which the muscle fibers ran. Both kidney and biceps femoris tissues were then processed and embedded in paraffin at a histology laboratory (Department of Anatomy and Developmental Biology, Monash University, VIC, Australia). Using a microtome (MicroTec Laborgeräte GmbH, cut 4060, Germany), the paraffin sections were sectioned at 5 µm, placed on microscope slides (Menzel Glazer, Super frost Plus, Braunschweig, Germany) and left to adhere for 2 hours at 70 °C.

5.3.2.3 Microscopy

Unless otherwise stated, once all slides were stained, mounted, and coverslipped, the sections were observed under a microscope (Olympus BX41; Hamburg, Germany). Using the Leica Application Suite (Leica Microsystems CMS GmbH), images were taken at varying magnifications using the Leica DFC450C camera (Leica Microsystems CMS, GmbH, Germany), and scale bars were calculated in terms of micrometers (µm).

5.3.2.4 Hematoxylin and eosin staining

Harris's hematoxylin and eosin was used in this study to stain the tissues.

The kidney was sectioned in three basic planes with the following reference position:

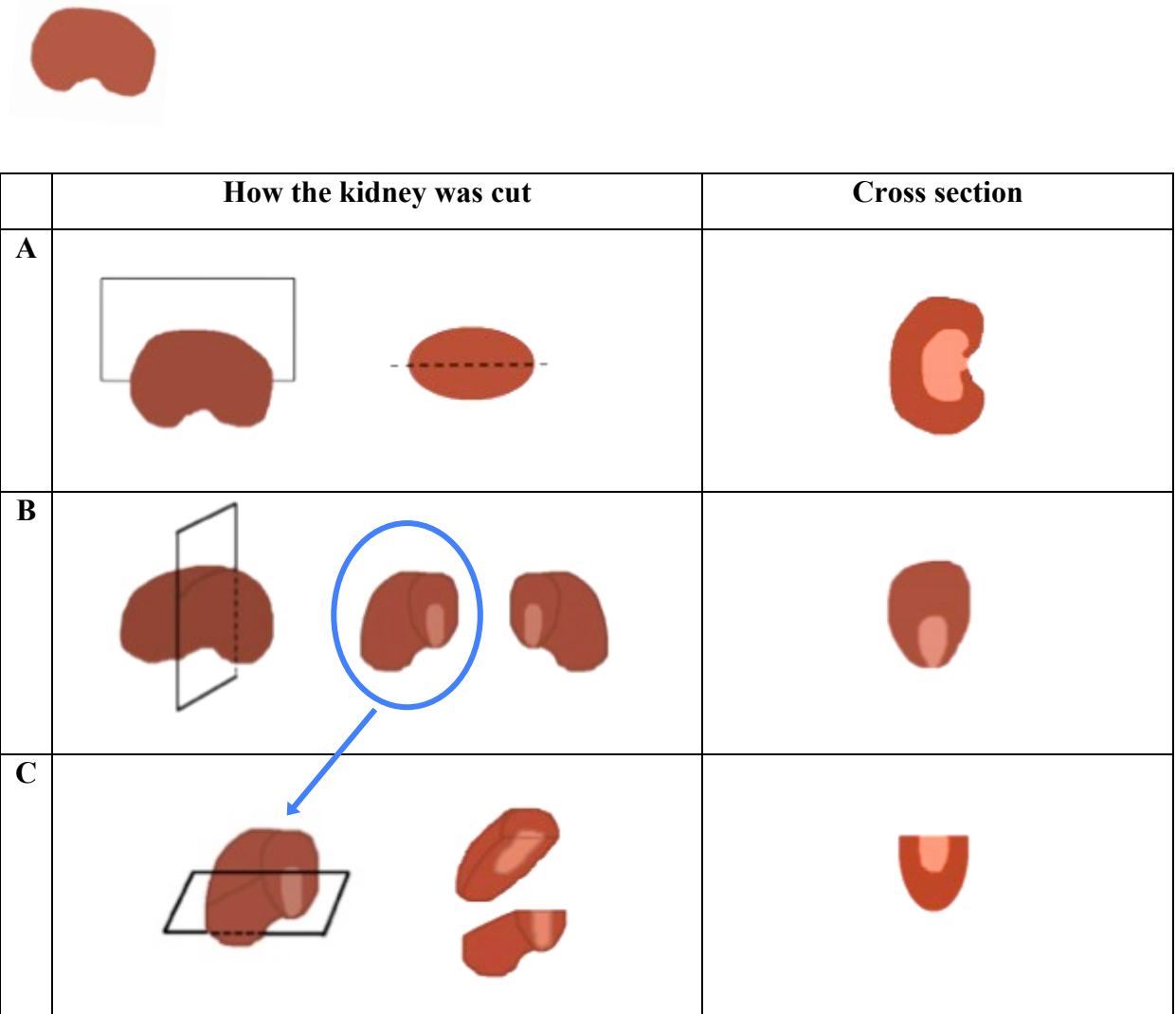


Figure 5.1. Schematic diagram of the three different planes in which the kidneys were sectioned. The renal arteries and veins branch into interlobar arteries and veins before changing direction and running in an arc-like manner to become arcuate arteries and veins. These vessels then give rise to interlobular arteries and veins located in the outer cortex. Due to the different directions in which the vessels are arranged within the kidney, analyses of the vessels in different planes of the kidney were necessary. The kidney was sectioned in the three basic planes so that analyses could be made on blood vessels in the perpendicular plane to which the vessels run. From each rat, one kidney was cut in the frontal plane (**A**) along the longitudinal axis. The remaining kidney was cut perpendicular to the longitudinal axis in the sagittal plane (**B**), resulting in two halves, one of which was then sectioned horizontally in the transverse plane (**C**).

5.3.2.5 Analysis of diffusion distances between arteries and veins

The software package ImageJ (<http://imagej.nih.gov/ij/>) was used for analysis of the distances between arteries and veins. Artery-vein profiles were selected when arteries had a circular profile, indicating that the artery was sectioned at a near perpendicular plane. Images from both hematoxylin & eosin stained tissue and Microfil®-filled tissue were imported into ImageJ. The scale was set so that measurements could be made in μm . Once the scale was adjusted, a line selection was made to measure the artery's diameter. All line selections were made with the naked eye to select the shortest length of the arterial diameter or artery-vein separation. The line was drawn so that it began from one end of the arterial lumen and ended at the other side of the lumen. Using the analysis 'Measure', the length of the line was quantified, providing the arterial diameter in μm . Once the arterial diameter was found, the diffusion distance between the lumens of the artery and vein was measured in a similar fashion. A line selection was made, with the line starting at the lumen of the artery and ending at the lumen of the vein. Diffusion distance was defined as the shortest distance between the arterial and venous lumens.

5.3.3 Microfil® - filled tissue

5.3.3.1 Kidney perfusion protocol

The kidneys of male Sprague Dawley rats were perfusion-fixed with 3% PFA in a similar fashion to the protocol described in Chapter 3 (Section 3.2). Once approximately 50-150 ml of fixative had been delivered, the solution being perfused was switched to the Microfil® compound (MV-122; Flow Tech Inc., MA, USA). The kidneys were slowly filled with 10-30 ml of Microfil® using a syringe that was attached to the three-way valve. While the pressure of 150 mmHg was maintained, the kidneys were tied off at the renal artery and vein, removed, and immersed in fixative overnight at 4 °C.

5.3.3.2 Kidney tissue processing, embedding in glycol methacrylate and sectioning

After overnight immersion in fixative, the kidneys were decapsulated and cut into three different planes as described in Figure 5.1.

To prepare the kidney tissue for embedding in glycolmethacrylate resin, the kidneys were then subjected to two 70% v/v ethanol washes and a final rinse in 70% v/v ethanol overnight. The tissues were then dehydrated and embedded in glycolmethacrylate resin (Technovit 7100 Kit; Heraeus Kulzer GmbH, Wehrheim, Germany). The dehydration process was as follows: 100% ethanol for 2 hours thrice and then 100% butanol for 2 hours before immersion of the tissues in 100% butanol overnight.

Following the overnight immersion in butanol, the tissues were incubated with infiltration solution (Technovit 7100 kit) for 2-3 days. After processing, the kidneys were embedded in resin, and sectioned (1-3 sections in each plane) using a microtome (Leica RM 2165, Mt Waverley, VIC, Australia) at 5 μm , before being stained.

5.3.3.3 *Staining and microscopy*

Slides were stained with toluidine blue for ~2 seconds, coverslipped and viewed under a microscope (Olympus BX41; Hamburg, Germany). Photomicrographs were captured using the Leica DFC450C camera and the Leica Application Suite program (Leica Microsystems CMS, GmbH).

5.3.3.4 *Analysis of diffusion distances between arteries and veins*

As with the tissue sections stained with H & E, ImageJ was used for analyzing the distances between arteries and veins for the tissue filled with Microfil®. The method is described earlier in section 5.3.2.5 of this thesis. ImageJ was also used to measure the minimum width of adventitia around arteries, using the same ‘Measure’ function.

5.3.3.5 *Analysis of capillary density*

In order to determine capillary density in the vicinity of artery-vein pairs, and thus determine the effect of oxygen sinks located around arteries within the rat kidney, four separate analyses were carried out. These analyses were only carried out on the kidneys that were filled with Microfil® because the silicone compound enabled us to identify the capillaries, which was not possible for the tissues stained with H & E. In each analysis, the number of capillaries observed within four concentric circles (zones) around arteries was determined. Four analyses were carried out to analyze the capillary density for arteries within defined ‘arterial diameter groups’. We defined these groups based on the various types of arteries and their known sizes. The smallest arterial elements are arterioles, with a size of <15 μm . Arteries with internal diameters of 15-50 μm were assumed to be distal interlobular arteries. Arteries with internal diameters of 100-150 μm were assumed to be proximal interlobular arteries. Vessels with internal diameters of ~200 μm were most likely the large arcuate arteries, and those with internal diameters of 150-200 μm were assumed to be distal interlobar arteries. Arteries with an internal diameter of 200-300 μm were assumed to be proximal interlobar arteries. Hence, our six diameter groups were: <15 μm , 15-25.9 μm , 26-50.9 μm , 51-100.9 μm , 101-200 μm , >200 μm . In each analysis, the widths of the four concentric rings (‘zone diameters’) were varied so as to provide different information about capillary density in the vicinity of artery-vein pairs, as described below.

For the first analysis (Analysis A) of the 49 Microfil-filled arteries, the radii of these four zones were selected to take into account the likelihood that oxygen could diffuse further from large arteries than from smaller arteries. We reasoned that this would be the case because the PO_2 and the total oxygen content should be greater in larger arteries than smaller arteries. Four concentric circles were drawn around the center of the artery. Thus, for arteries $<16.0\ \mu\text{m}$ in diameter, these zones were defined by steps of $20\ \mu\text{m}$, so that the capillary density was calculated from 0-20, 20-40, 40-60 and 60-80 μm from the center of the artery. For arteries 16.0-25.9 μm , 26.0-50.9 μm , 51.0-100.9 μm , 101-200 μm and $>200\ \mu\text{m}$ in diameter, the zones were defined by steps of 25, 50, 75, 100 and 250 μm respectively (Table 5.1). The zones in this analysis represent distances from the center of the artery and not from the arterial lumen (Fig. 5.2; Table 5.1).

For the second analysis (Analysis B), we estimated that in renal tissue, oxygen could diffuse a distance of approximately 100 μm (19). Hence, capillary density was determined using four consistent concentric rings, each 30 μm in width, commencing from the margin of the arterial lumen (Fig. 5.2B; Table 5.1). Arterial diameter was measured as part of the analysis of diffusion distance. Subsequently, a circle that represented the artery was drawn so that concentric circles could be drawn around it (Fig. 5.2).

The third analysis (Analysis C) took into account the size of the artery as well as the width of the adventitia surrounding the arteries. For each arterial diameter group, the smallest distance from the arterial lumen to the adventitia (outer side) was measured for the 49 arteries. From these measurements, the mean distance from the arterial lumen to the adventitia was calculated for each arterial diameter group (Table 5.2). We reasoned that as arterial diameter increased, so should the width of the zones. As with the second analysis, the zones represent the distance from the arterial lumen, not from the center of the artery.

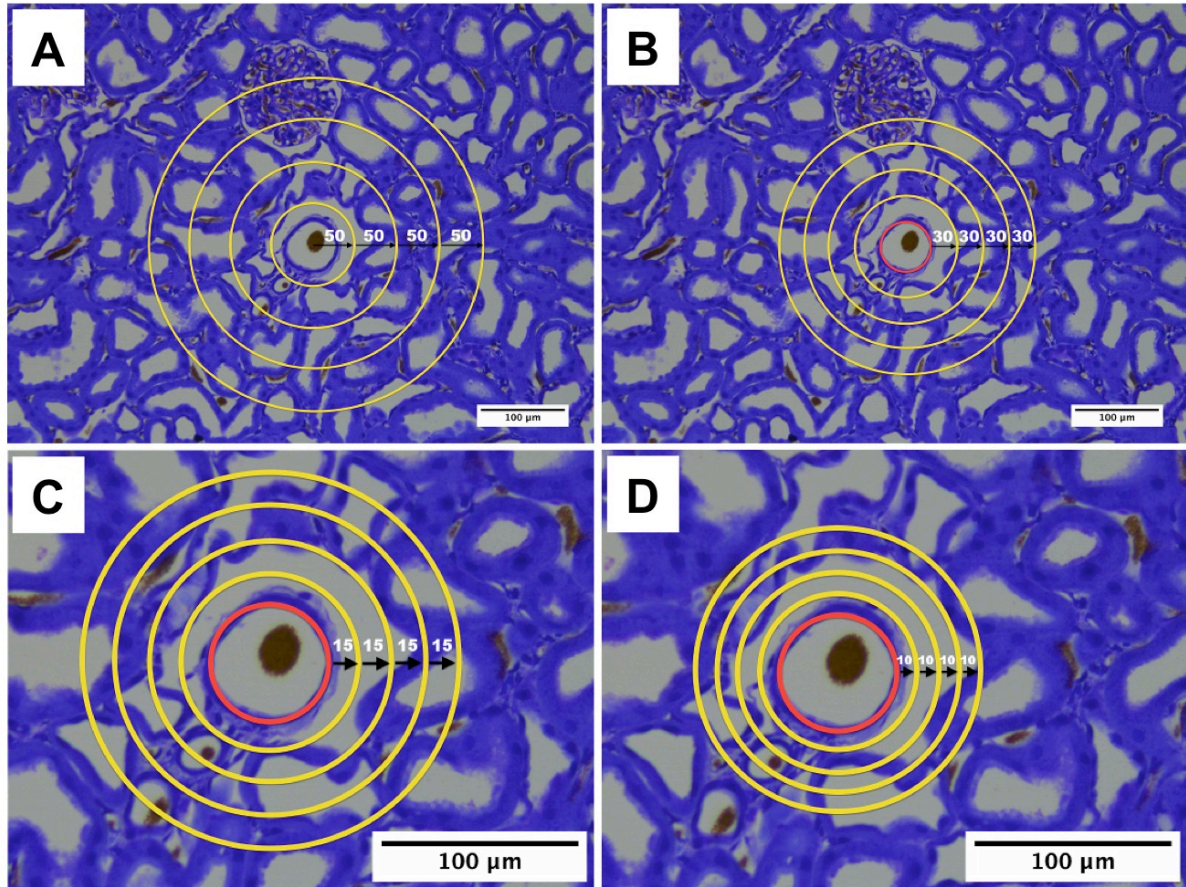


Figure 5.2. A section of rat kidney stained with toluidine blue and examples of concentric zones used for the three different capillary analyses. Panel (A) represents the first analysis (Analysis A) in which the concentric rings were defined with respect to the size of the artery. The artery in panel A is 50 μm in diameter, and thus the widths of the zones from the center of the artery were 50, 100, 150, and 200 μm . Panel (B) represents the second analysis (Analysis B) where it was assumed that oxygen diffuses approximately 100 μm through kidney tissue. The width of each zone from the arterial lumen was in steps of 30 μm . Panel (C) demonstrates the zones for the third analysis (Analysis C). Here, the size of the artery, as well as the width of the adventitia was used to define the zone widths. For this particular artery, zones were created in steps of 15 μm . Panel (D) represents the fourth analysis (Analysis D) where only the width of adventitia defined the width of the concentric zones.

The fourth analysis (Analysis D) took into account only the width of the adventitia surrounding the arteries. As for the third analysis (Analysis C), the mean widths of the adventitia for each arterial diameter group (Table 5.2) were used to define the widths of the concentric circles, and thus the zones were defined as presented in Table 5.1. Arterial diameter groups were given the same zone width as another diameter group according to the mean distance of arterial lumen to adventitia (Tables 5.1 and 5.2). Again, the zones represent the distance from the arterial lumen, not from the center of the artery.

Table 5.1. The varying zone widths for each arterial diameter group across the four different analyses.

| Analysis | Arterial diameter group (μm) | Zone width (μm) | Zones (μm) |
|----------------|---|------------------------------|-------------------------|
| A ^a | <16.0 | 20 | 20, 40, 60, 80 |
| | 16.0 - 25.9 | 25 | 25, 50, 75, 100 |
| | 26.0 - 50.9 | 50 | 50, 100, 150, 200 |
| | 51.0 - 100.9 | 75 | 75, 150, 225, 300 |
| | 101.0 – 199.9 | 100 | 100, 200, 300, 400 |
| | >200.0 | 250 | 250, 500, 750, 1000 |
| B ^b | <16.0 | 30 | 30, 60, 90, 120 |
| | 16.0 - 25.9 | 30 | 30, 60, 90, 120 |
| | 26.0 - 50.9 | 30 | 30, 60, 90, 120 |
| | 51.0 - 100.9 | 30 | 30, 60, 90, 120 |
| | 101.0 – 199.9 | 30 | 30, 60, 90, 120 |
| | >200.0 | 30 | 30, 60, 90, 120 |
| C ^b | <16.0 | 5 | 5, 10, 15, 20 |
| | 16.0 - 25.9 | 10 | 10, 20, 30, 40 |
| | 26.0 - 50.9 | 15 | 15, 30, 45, 60 |
| | 51.0 - 100.9 | 20 | 20, 40, 60, 80 |
| | 101.0 – 199.9 | 25 | 25, 50, 75, 100 |
| | >200.0 | 30 | 30, 60, 90, 120 |
| D ^b | <16.0 | 5 | 5, 10, 15, 20 |
| | 16.0 - 25.9 | 5 | 5, 10, 15, 20 |
| | 26.0 - 50.9 | 10 | 10, 20, 30, 40 |
| | 51.0 - 100.9 | 10 | 10, 20, 30, 40 |
| | 101.0 – 199.9 | 20 | 20, 40, 60, 80 |
| | >200.0 | 20 | 20, 40, 60, 80 |

a = zones originating from the center; b = zones originating from the arterial lumen

Table 5.2. The mean minimum distance from the arterial lumen to the adventitia for the arterial diameter groups, and the corresponding zone width assigned to the arterial diameter.

| Arterial diameter (μm) | Mean distance from arterial lumen to adventitia (μm) | Zone width (μm) | n |
|-------------------------------------|---|------------------------------|----|
| <16.0 | 6.6 ± 0.7 | 5 | 12 |
| 16.0 - 25.9 | 6.8 ± 0.9 | 5 | 10 |
| 26.0 - 50.9 | 8.1 ± 1.0 | 10 | 8 |
| 51.0 - 100.9 | 11.1 ± 1.4 | 10 | 7 |
| 101.0 – 199.9 | 18.5 ± 1.5 | 20 | 9 |
| >200.0 | 22.2 ± 2.9 | 20 | 3 |

Distance measured from the arterial lumen to the adventitia are represented as mean \pm SEM. This distance is to the outer limit of the adventitia. ‘n’ represents the number of arteries observed for each arterial diameter group.

5.3.3.6 Statistical analyses

Data are presented as mean \pm standard error of the mean (SEM) of n observations. Independent variables were partitioned into categories according to arterial diameter, and the data subjected to repeated measures analysis of variance. P values from the within-subjects factor (vessel) were conservatively adjusted using the Greenhouse-Geisser method (12). Two-tailed $P \leq 0.05$ was considered statistically significant.

5.4 RESULTS

For this study, a combination of measurements from one approach (H & E staining) and additional data from the Microfil® approach were used (described above). Approximately 250 artery profiles were observed for this qualitative analysis (H & E stained only and Microfil®-filled tissue). Artery-vein pairs from these artery profiles were selected based on the artery appearing circular in shape. This indicated that the section was cut almost perpendicular to the direction in which the artery travels. A total of 81 artery-vein pairs conformed to this criterion. These were used for the quantitative analysis of the spatial relationships between arteries and veins.

Although we cannot definitively categorize each renal blood vessel into specific vessel types based merely on their diameters, it is generally accepted that arteries with luminal diameters greater than 300 μm are mostly interlobar arteries (15). Arteries with luminal diameters of 130-300 μm are likely mostly interlobar and arcuate arteries. Arteries with luminal diameters between 30-100 μm are most likely interlobular vessels, and those with luminal diameters less than 30 μm are most likely afferent and efferent arterioles.

5.4.1 Typical arrangement of arteries and veins vary according to arterial diameter

Initial qualitative analysis of the separation distance between the lumens of the arteries and veins suggested that for very large arteries (e.g. interlobar arteries), veins often surround a considerable proportion of the total arterial circumference, with a typical separation distance of 100 μm or less, composed almost entirely of connective tissue (Fig. 5.3A). This also appears to be the case for proximal interlobular and arcuate arteries (Figs 5.3B-E). Some large arteries were separated by a distance greater than 100 μm (Fig. 5.3F). Smaller artery-vein pairings were often observed to be less intimate, with the vein no longer surrounding the artery, and the space between the two vessels filled with tubules and capillaries (Fig. 5.4). Likewise, microscopic observation of even smaller vessels indicated that the vessels shared a less intimate relationship, and also that the pathway for oxygen diffusion from the artery to

the vein appeared to be blocked by tubular elements (Figs 5.4C, D, F). The separation distances for the smaller vessels appeared to vary (Figs 5.4C-E) much more than for the larger vessels.

In biceps femoris tissue, arteries and veins were often found to be spatially intimate. However, veins did not surround arteries to the same extent as that observed in the kidney (Fig. 5.5).

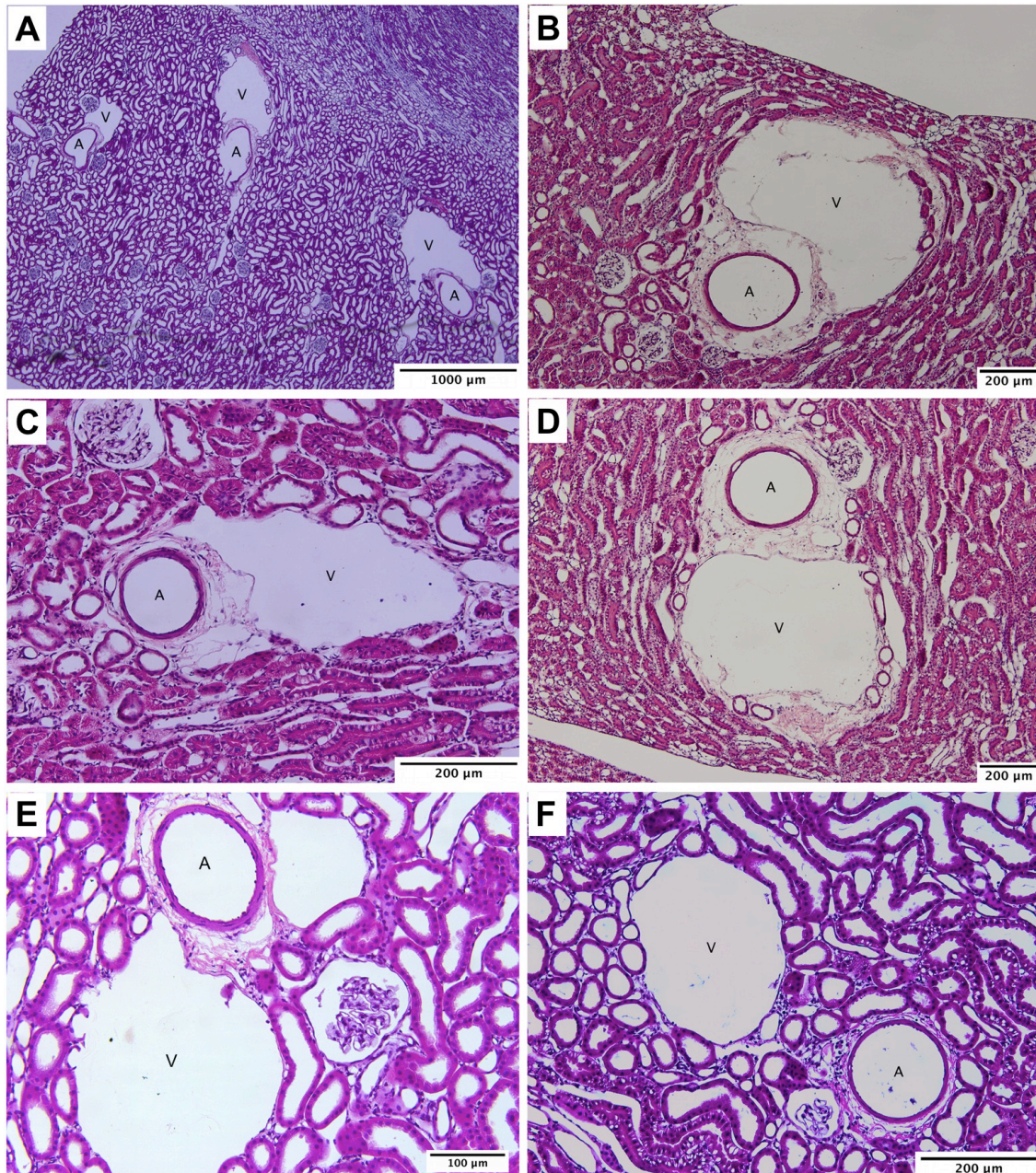


Figure 5.3. Photomicrographs of hematoxylin and eosin stained sections displaying large arteries in the renal cortex of the rat. Arteries are indicated by ‘A’, and veins are indicated by ‘V’. The vein wall partially surrounds a considerable proportion of the arterial profile for very large arteries (A) with only connective tissue between the artery and vein. Similarly, for arteries $\geq 100\ \mu\text{m}$ in diameter (B-E), the association was often seen to be similar to that of (A). Some large arteries were separated by a distance of $100\ \mu\text{m}$ or more (F). Images are at a magnification of $\times 4$ (A), $\times 10$ (B, D), $\times 20$ (C, E & F).

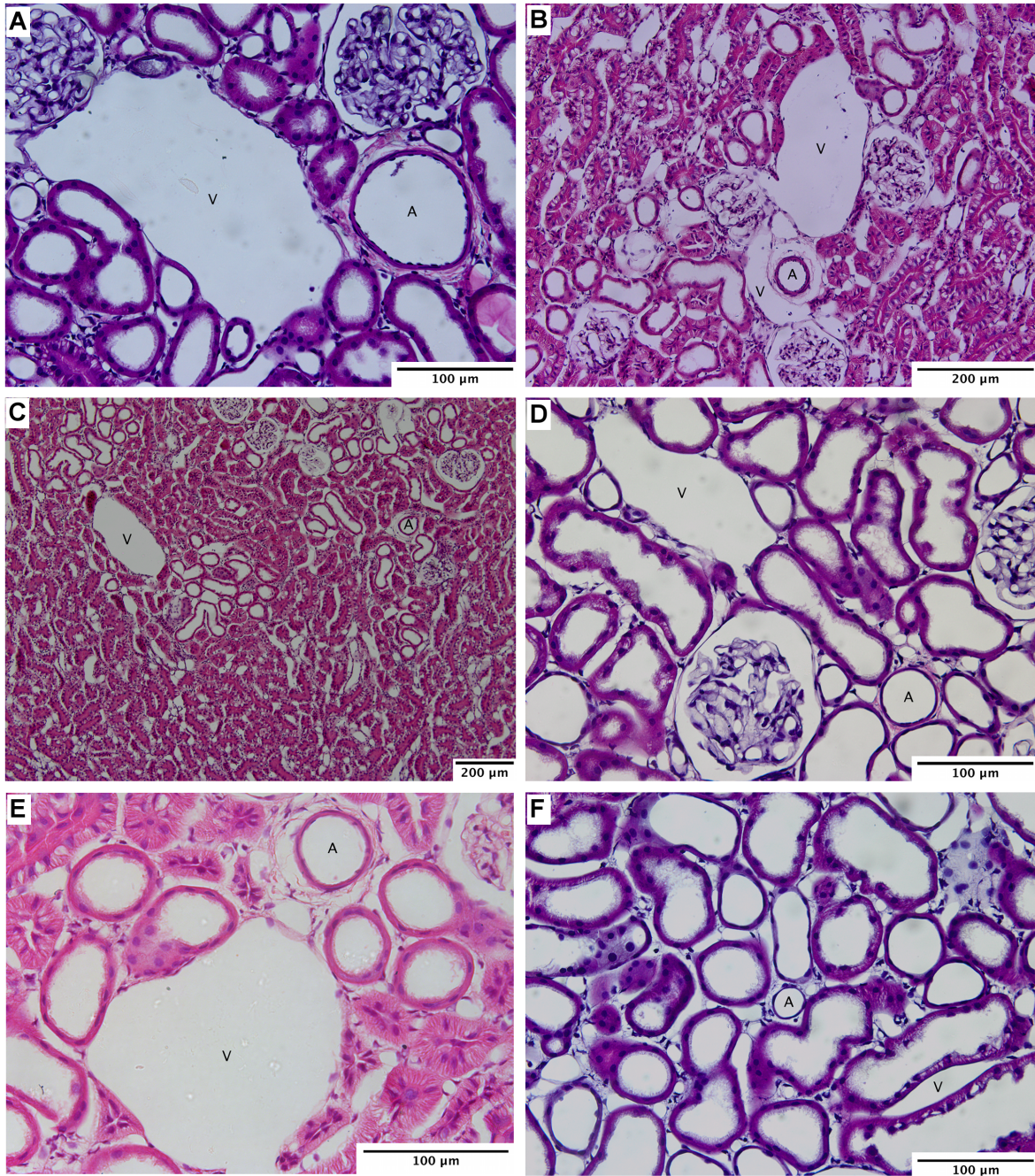


Figure 5.4. Photomicrographs of hematoxylin and eosin stained sections displaying small arteries in the renal cortex of the rat Arteries are indicated by ‘A’, and veins are indicated by ‘V’. Often, for an artery $<100\ \mu\text{m}$ in diameter (A), the vein wall did not surround the arterial profile. Instead the vessels appeared to be separated with some tubular elements within the space between. Some smaller arteries (B) had an intimate relationship with the corresponding vein. For other small vessels (C, D, E), the distance between the artery and vein varied widely. For images (C, D, E), the distance between the artery and vein was approximately $800\ \mu\text{m}$, $200\ \mu\text{m}$, and $50\ \mu\text{m}$ respectively. Also, for vessel pairings that were less intimately associated, the pathway between the vessels was completely filled by tubules (C, D, F). Images are of magnification $\times 40$ (A, D & F), $\times 20$ (B & E) and $\times 10$ (C).

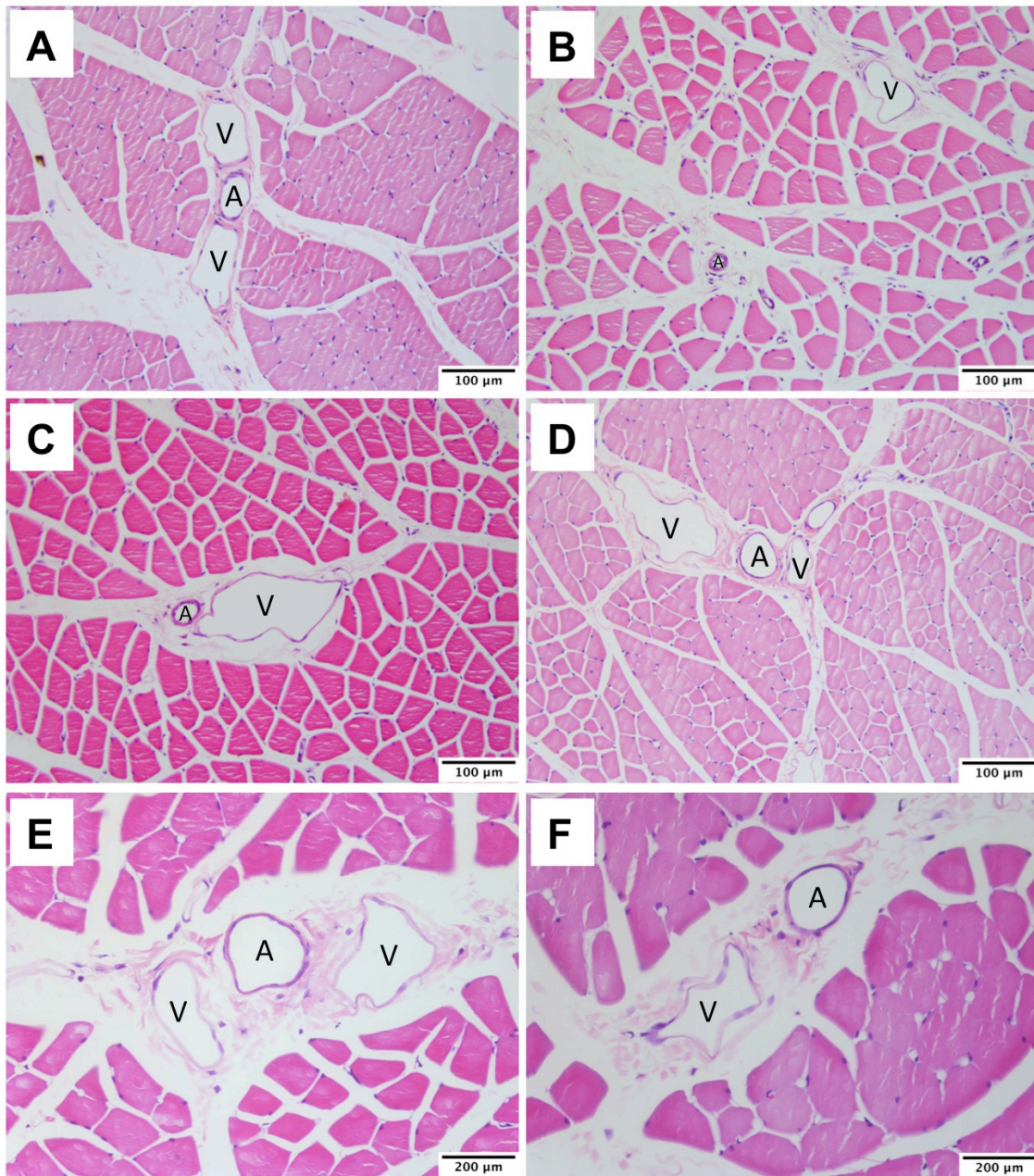


Figure 5.5. Arrangements of artery and veins in hematoxylin and eosin stained sections of biceps femoris tissue of the rat. The arrangement of arteries ‘A’ and veins ‘V’ in biceps femoris was often observed to be intimate (**A, C, D, E, F**), in that only adventitia lay between the artery and vein. In other cases the arteries and veins were found to be separate (**B**), in that muscle tissue lay between the two vessels. However, veins were never observed to ‘wrap’ around the artery as was observed in renal tissue. Images are of magnification $\times 20$ (**A, B, C, D**) and $\times 40$ (**E & F**).

5.4.2 The relationship between arterial caliber and separation distance and wrapping

A quantitative analysis of the diffusion distances between the 81 intrarenal artery-vein pairs indicated fairly constant diffusion distances between the arterial and venous lumen (Fig. 5.6). Nevertheless, for arteries of small diameter the separation distances were more variable than for vessels of medium to large diameter (Fig. 5.6). Also, arteries that were ‘wrapped’ were observed to have consistently smaller separation distances compared to those that were not ‘wrapped’ by a vein.

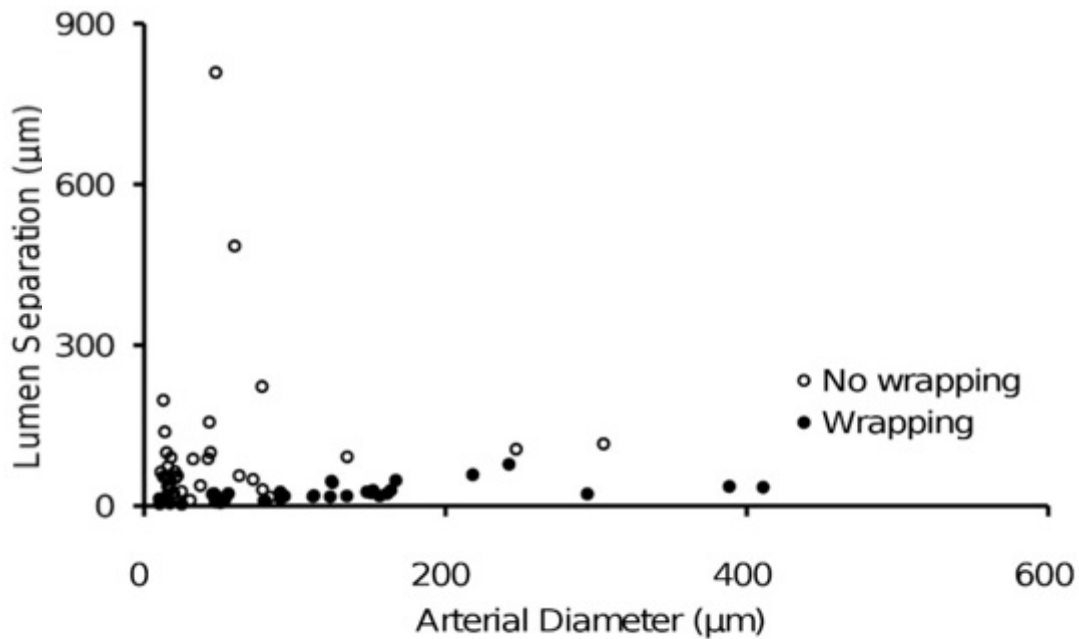


Figure 5.6. Scatter plot of arterial diameter against diffusion distance (lumen-to-lumen). Artery-vein pairings were selected on the basis that circular arteries indicate the tissue was sectioned perpendicular to the direction in which the artery travels. The majority of the 81 vessel pairs had a diffusion distance of ≤ 100 μm , and all but three had diffusion distances of less than 200 μm . Open circles represent arteries where the closest vein did not surround their profile. Black circles represent arteries where the closest vein surrounded a portion of their profile. Image reproduced, with permission, from Gardiner *et al* (8).

Connective tissue was observed to surround each artery, as expected from previous observations by Frank and Kriz (6). The minimum distance from the arterial lumen to the connective tissue was found to vary with arterial diameter. The average thickness of the connective tissue for arterial diameters is provided in Table 5.2 in the Methods section of this chapter.

5.4.3 Capillary density around artery-vein pairs varies by arterial caliber

5.4.3.1 Capillary density within large zones around the artery

In analysis A, zones commencing from the center of the artery were relatively large (20 – 250 μm) and increased in size in proportion to arterial diameter (Fig. 5.7A). There was a clear trend for capillary density to reduce as arterial caliber increased. In the case of the smallest arterial diameter groups ($\leq 25.9 \mu\text{m}$), capillary density tended to be greatest near the arterial wall. In contrast, for the largest vessels ($\geq 101 \mu\text{m}$ in diameter) capillary density was least near the arterial wall. Capillary density remained relatively constant across the various zones in the case of arteries of intermediate diameter (26 – 100.9 μm).

In analysis B, the zones were constant increments of 30 μm , commencing at the luminal border of the artery (Fig. 5.7B). There was a tendency for capillary density to vary inversely with arterial caliber, although this effect was less clear than in analysis A. As in analysis A, capillary density around small arteries ($< 16 \mu\text{m}$) was greatest close to the arterial wall, whereas it was least near the wall of large arteries ($> 101 \mu\text{m}$).

In analysis C, the zones varied in proportion to the combined thickness of the arterial wall and adventitia. The zones were consistently smaller (5 – 30 μm) than was the case in analysis A. Moreover, the zones commenced at the luminal border of the artery (Fig. 5.7C). There was a strong trend for capillary density to decrease as the arterial caliber increased. Furthermore, in all but one case (arteries 16 – 25.9 μm in diameter), capillary density was least in the immediate vicinity of the arterial wall.

In analysis D, the zones varied according to the combined thickness of the arterial wall and adventitia for that arterial diameter group, rounded to the nearest 5 μm (Fig. 5.7D). This approach produced a pattern very similar to that derived from analysis C, except that in this case, capillary density was least in the immediate vicinity at the arterial wall for all arterial diameter groups.

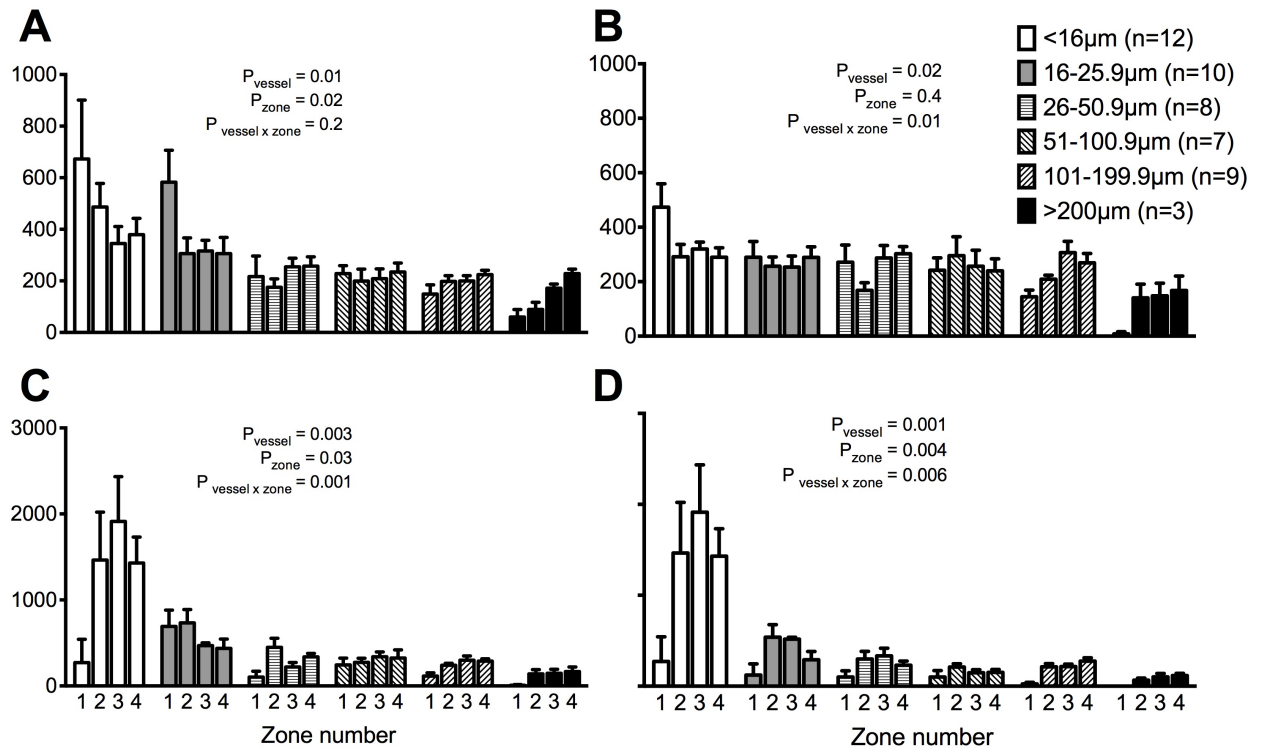


Figure 5.7. Peritubular capillary density around arteries of varying diameters. Capillary density (per mm²) was calculated for varying zones around arteries of interest and plotted according to arterial diameter. Four different analyses were carried out, each varying in zone width, as described in the Methods section. Analysis A had four zones in steps of 20, 25, 50, 75, 100 and 250 µm from the center of the vessel for the six arterial diameter groups (A). Analysis B had zones varying in steps of 30 µm from the arterial lumen for all arterial diameters (B). Analysis C had zones in steps of 5, 10, 15, 20, 25, 30 µm from the arterial lumen for the six arterial diameter groups (C). Analysis D had zones in steps of 5, 5, 10, 10, 20, 20 µm from the arterial lumen for the six arterial diameter groups (D). Image reproduced, with permission, from Gardiner *et al* (8).

5.5 DISCUSSION

5.5.1 Major findings

Our quantitative analysis of vessel separation distance indicates that the average diffusion distances between arteries to veins are quite small, with more variability in the smaller than larger arteries. Also, larger arteries were more commonly surrounded partially by an adjacent vein than were smaller arteries. Furthermore, some small artery-vein pairs appeared to be separated by larger distances than was the case for larger vessels. Larger artery-vein pairs mostly lacked the presence of oxygen ‘sinks’ lying between the vessels. In contrast, in the case of smaller artery-vein pairs, both tubules and capillaries, which can act as oxygen sinks, were observed in the space between the arterial and venous walls. Finally, capillary density in the immediate vicinity of arteries was less than that of areas further away from the arteries. There was also a greater density of capillaries around smaller arteries compared to larger arteries. Collectively, these observations indicate that the spatial characteristics of artery-vein pairs that would be expected to facilitate AV oxygen shunting are observed more often in the larger than the smaller vessels in the renal cortex.

A subsequent analogous analysis was generated by our colleagues at UWA, based on data generated by Nordsletten *et al* (15) from a micro-CT reconstruction of the rat renal circulation. These analyses, which will be presented in detail later in this Discussion (Section 5.5.3), indicate a U-shaped relationship between arterial diameter and separation distance (Fig. 5.9). At first sight these two data sets appear to be inconsistent with each other. However, as discussed in detail later (Section 5.5.6), these apparent inconsistencies likely arise from limitations in both approaches. Taken together, we believe these data provide evidence that the nature of the barriers to diffusion of oxygen from arteries to veins changes along the course of the cortical circulation. This, in turn, likely has a profound impact on the nature of the vascular elements where the bulk of AV oxygen shunting occurs. Our current observations therefore justify the generation of quantitative data regarding the axial and radial geometry of artery-vein pairs in the renal preglomerular circulation. Incorporation of such data into the mathematical model of kidney oxygen transport developed by Gardiner *et al* (7) should allow future studies to assess the inter-relationships between cortical and medullary oxygenation.

5.5.2 Analysis of the characteristic association of arteries and veins using hematoxylin and eosin stained sections

An initial qualitative analysis of the characteristic arrangements of arteries and veins in the kidney suggested that large arteries are intimately associated with their corresponding vein. Moving downstream along the arterial circulation, vessels appeared to be less intimately associated, with less of the total circumference of the artery surrounded by the vein. However, our quantitative analysis provided evidence that the spatial relationship between artery and vein pairings is not as simple as suggested by this initial qualitative analysis.

A quantitative analysis was carried out, in which measurements were made of the diffusion distances (lumen-to-lumen) of the various vessel pairings observed in hematoxylin and eosin stained sections, and later in the Microfil®-filled tissue sections. These data provided preliminary evidence that the diffusion distances between arteries and veins remain relatively constant throughout the renal circulation, albeit with a few outliers. It was only possible to generate a relatively small sample size using this method. However, our colleagues at UWA, using an automated approach, were able to generate a large data set using the micro-CT data of Nordsletten *et al* (15). It is therefore instructive for us to consider these data and how they affect interpretation of the data generated by light microscopy.

5.5.3 Analysis of data generated by micro-CT

The data set created using data from Nordsletten *et al* (15) was produced using a program that calculated the center-to-center and lumen-to-lumen diffusion distances using known measurements of arterial and venous diameters. The program essentially took these measurements and estimated the site of the center of each vessel. While it can be easy to establish the center of circular arteries, there is difficulty in determining the center of irregular shaped veins (Fig. 5.8). The resulting dataset provided data on arterial diameter and diffusion distance, which were used to plot the relationship between the two (Fig. 5.9). It was noted, however, that when the program calculated the lumen-to-lumen diffusion distances, some values were negative (Fig. 5.9B). This is because the data generated by Nordsletten *et al* (15) were based on the centerline of each vessel and approximate radii were calculated. This means that if a vessel was elliptical in shape, the average of the two axes was used to determine the diameter. Hence, all vessels were estimated to have a circular shape. However, veins in particular are not always circular in shape and as a result, there are errors with the calculations of the distances (Fig. 5.8). The center-to-center separation distance is correct, but the lumen-to-lumen diffusion distance has error. Wherever a negative lumen-to-lumen

distance is observed, it suggests that the vein is not circular but elliptical or surrounding the artery, meaning they are intimately associated. Consequently, the more negative the lumen-to-lumen distance, the higher the degree of intimacy between a paired artery and vein.

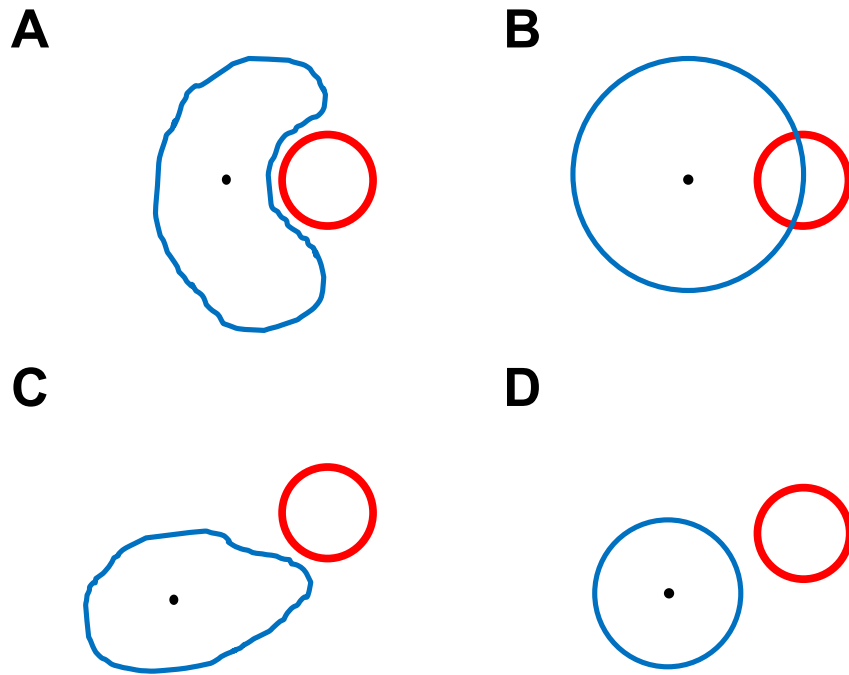


Figure 5.8. Critical error in the method used to measure diffusion distances in the data analysis of Nordsletten *et al* (15). A program was used to calculate the centre-to-centre and lumen-to-lumen diffusion distances. Arteries are shown in red, and veins are shown in blue. For a vessel arrangement such as (A), the analysis is based on the assumption that the centre of the vein is located at the dot. Thus, in the calculation of the lumen-to-lumen distance, the analysis generates an artery-vein arrangement similar to that shown in (B). This will therefore underestimate the lumen-to-lumen diffusion distance, and result in negative values as presented in Figure 5.9. Similarly, for a vessel arrangement such as (C), the analysis generates an artery-vein arrangement similar to that shown in (D). This will therefore overestimate some diffusion distances.

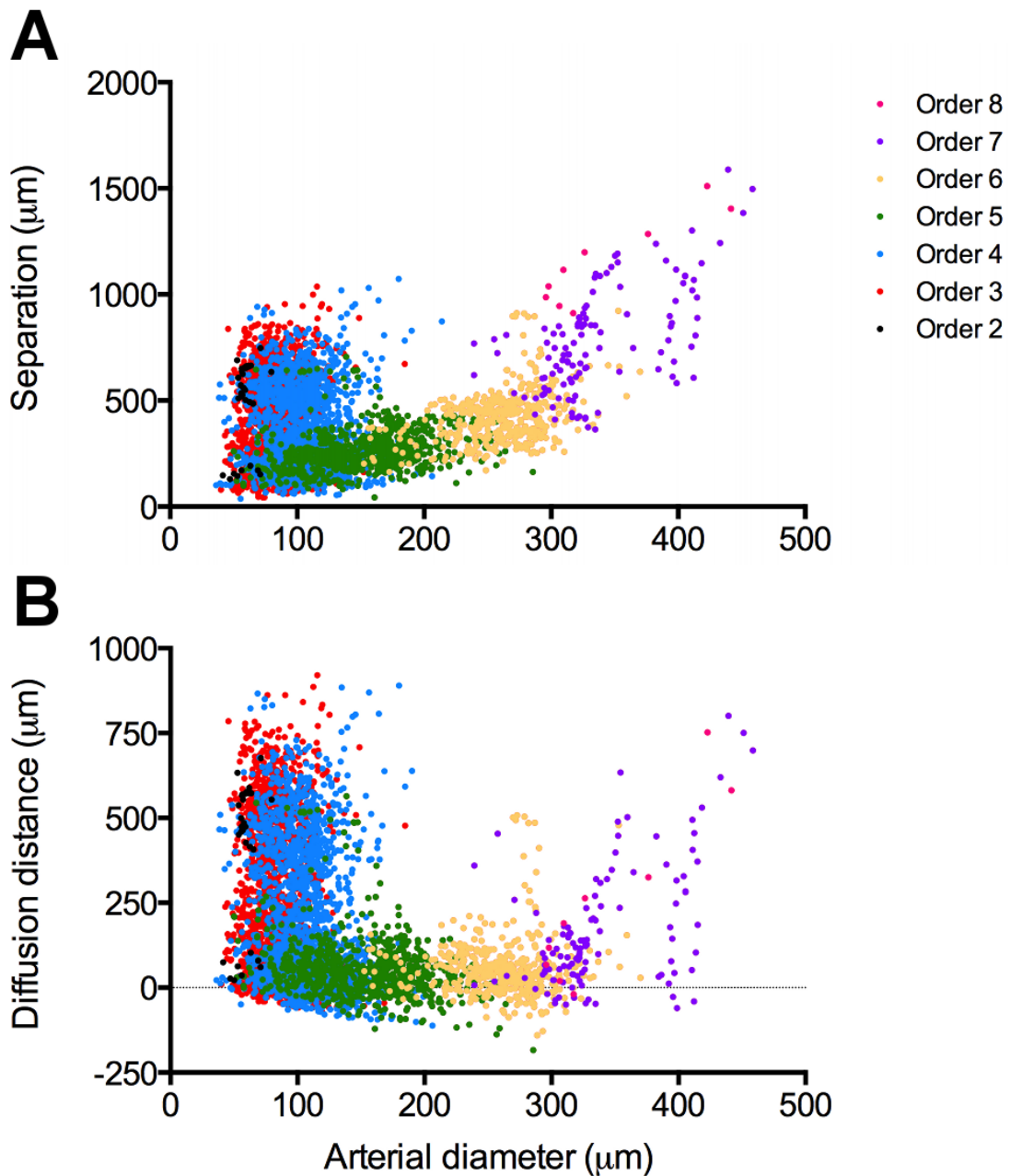


Figure 5.9. Scatter plots illustrating the relationship between arterial diameter and diffusion distance in terms of Strahler order, generated from the data-set of Nordsletten *et al* (15). Plot (A) illustrates the relationship between arterial diameter and separation distance (centre-to-centre). Plot (B) demonstrates the relationship between arterial diameter and diffusion distance (lumen-to-lumen). Note the negative values in plot (B), which indicate some error in the calculation of the distances by the program (See Fig. 5.8). Nevertheless, the more negative the lumen-to-lumen distance, the greater the degree of intimacy between the artery and vein.

5.5.4 Analysis of peritubular capillary density in the vicinity of arteries

Capillaries can deliver oxygen to tissue, but they can also remove oxygen from tissue. Capillaries would remove oxygen from tissue if the PO_2 of blood in the capillary is lower than that of the tissue. This phenomenon might be expected in the vicinity of arteries (11). The majority of oxygen consumption in the kidney is due to the metabolic cost of sodium reabsorption (3, 4). A considerable amount of energy is required by the kidney tubules for the activity of Na^+/K^+ -ATPase (14). It is therefore considered that if capillaries or tubules are present between an artery-vein pair, such oxygen ‘sinks’ would effectively ‘steal’ oxygen that could have otherwise been shunted from the artery to the vein.

A total of four analyses were carried to quantify capillary density around the 49 arteries filled with Microfil®. It was possible to quantify capillary density in the vicinity of these arteries because the silicone-based Microfil® enabled identification of the capillaries. A total of four analyses were carried out in order to identify whether capillary density varied in location and distance from an artery, and whether this variation was consistent across all arterial sizes or only present for arteries of a certain diameter. Each analysis was based on quantifying the number of capillaries observed within four concentric circles (zones) around the artery. To analyze the capillary density for each arterial diameter group (5-15 μm , 15-25 μm , 26-50 μm , 51-100 μm , 101-200 μm , >200 μm), four different analyses were carried out, each with varying zone distances. Analyses using wider zones presented similar results to each other, in that capillary density appeared uniform when the area analyzed was large. In contrast, once we analyzed capillary density in smaller zones, it was apparent that capillary density was much greater for smaller arteries compared to larger arteries.

In arrangements where the vein surrounded part of the circumference of the artery, capillaries and tubules were found to be absent from the space between the vessels. This is expected due to the presence of connective tissue (adventitia), as previously described by Frank and Kriz (6). Capillary density was least in the area in the immediate vicinity of the arterial wall, and this was the case for arteries of all sizes in the kidney. This observation was particularly prominent in analysis D, reflecting the virtual absence of capillaries in the adventitia surrounding arteries.

Peritubular capillary density in larger ‘zones’ around arteries appeared to be relatively constant. Capillary density around arteries was particularly low for larger vessels, and this was observed in all four analyses. On closer inspection, capillary density in the area immediately surrounding larger arteries ($\geq 26 \mu m$ in diameter) was less compared to that in

smaller arteries ($\leq 25.9 \mu\text{m}$ in diameter). This suggests that differences in capillary density are only detectable when smaller ‘zones’ of influence are analyzed.

Furthermore, low capillary density was not only observed in the ‘adventitial space’, but also in the renal parenchyma. This was particularly the case in analysis A for arteries $\leq 25.9 \mu\text{m}$, where relatively large zones generated lower peritubular capillary density with increasing distance from the artery.

Observations of capillaries and tubules between the larger vessel pairs were uncommon. This is because larger artery-vein pairs were observed to be more intimately associated. In contrast, capillaries and tubules were often observed between and also around smaller arteries and veins. Such an arrangement would be expected to retard AV oxygen shunting between these smaller vessels because, as previously mentioned, capillaries are capable of ‘stealing’ oxygen from tissue or arteries with a higher oxygen tension than the capillaries (10).

5.5.5 Potential sites of AV oxygen shunting

Consideration of the data sets obtained by light microscopy and micro-CT provides insight into the potential sites of oxygen shunting in the kidney. The data suggest a U-shaped relationship between arterial diameter and diffusion distance (Fig. 5.9). The presence of large diffusion distances between large arteries ($>300 \mu\text{m}$ diameter) and their associated veins were not detected in the analysis of data obtained by light microscopy. This is likely attributable to the fact that few arteries $>300 \mu\text{m}$ in diameter were observed in the light microscopic study (Fig. 5.6). Nevertheless, the frequency distributions of diffusion distance for the two methods (micro-CT and light microscopy) were similar in shape, with most diffusion distances $\leq 100 \mu\text{m}$ (Fig. 5.10).

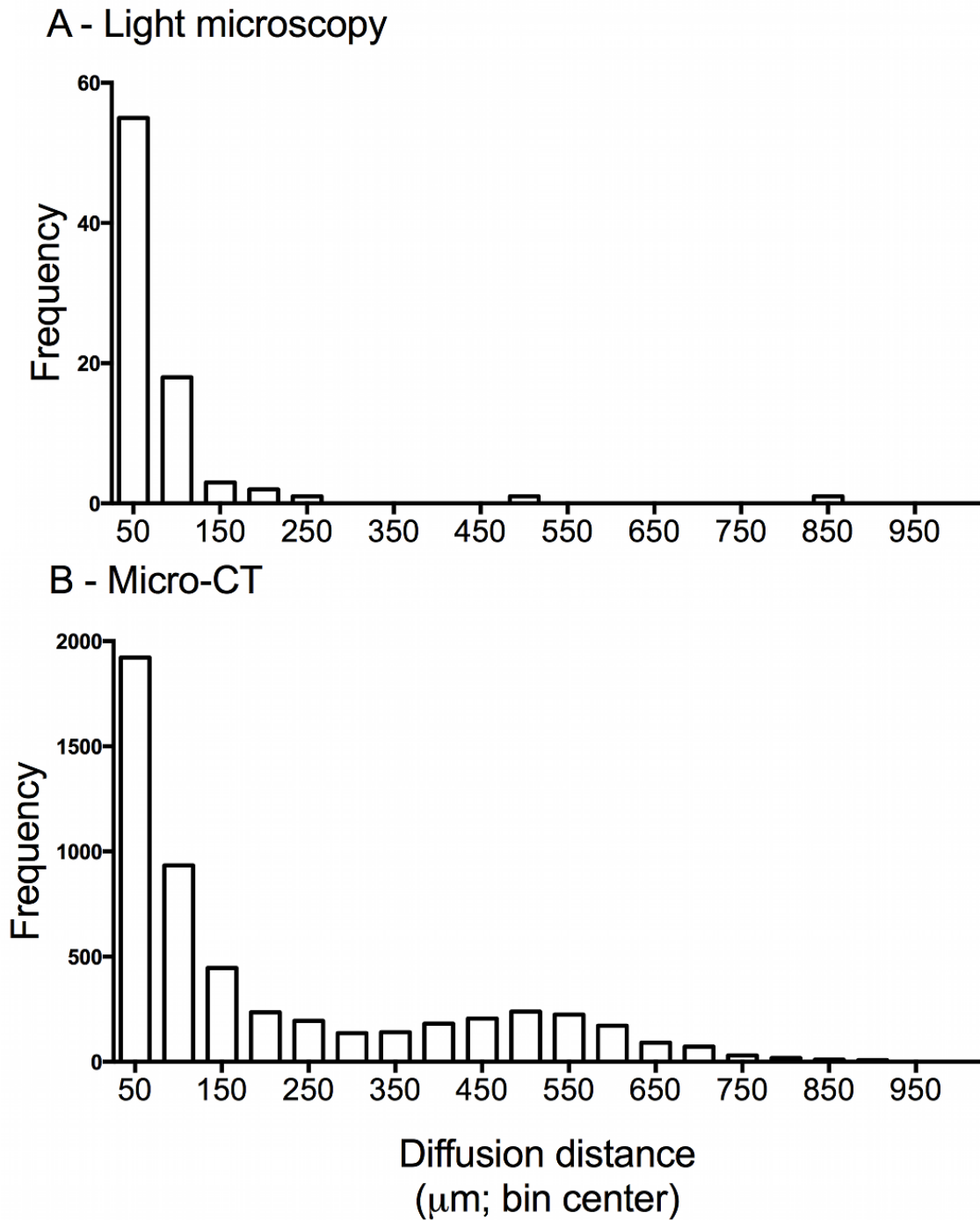


Figure 5.10. Frequency histograms of diffusion distances of (A) our data based on light microscopy and (B) data generated by micro-computed tomography (micro-CT) (15). In both data sets, most diffusion distances were $\leq 100 \mu\text{m}$.

An additional analysis of the relationship between arterial branching order (Strahler order) and average artery-vein separation distances (center-to-center and lumen-to-lumen) also suggests a U-shaped relationship between vessel order and the intimacy of arteries and veins (Fig. 5.11), as was the case for vessel caliber (Fig. 5.6). The lumen-to-lumen diffusion distance was relatively small for arteries of order 4 to 7 (Fig. 5.11B). This analysis complements that seen in Figure 5.9, where arteries of Strahler order 2-4 and 7-8 had variable diffusion distances, but the arteries of Strahler order 5-6 had shorter distances to the nearest vein. Arteries of order 7 are likely mainly arcuate arteries (15), which run parallel to the corticomedullary border (Fig. 5.12), suggesting that shunting may be favored between arteries and veins common to cortical and medullary circulations.

The medullary circulation arises from the efferent arterioles of juxtamedullary glomeruli, whose afferent arterioles arise from the proximal interlobular arteries, near their junction with arcuate arteries (1, 5, 13, 18). The efferent arterioles of the juxtamedullary nephrons divide to form the vasa recta. The vasa recta travel down into the medulla and return to the corticomedullary junction and empty into the arcuate vein (Fig. 5.12). Thus, if AV shunting is favored between vessels located in the corticomedullary junction, high levels of oxygen would be expected to diffuse from the arcuate and proximal interlobular arteries into the corresponding veins, so reducing the oxygen content of blood destined for the medullary circulation (Fig. 5.12).

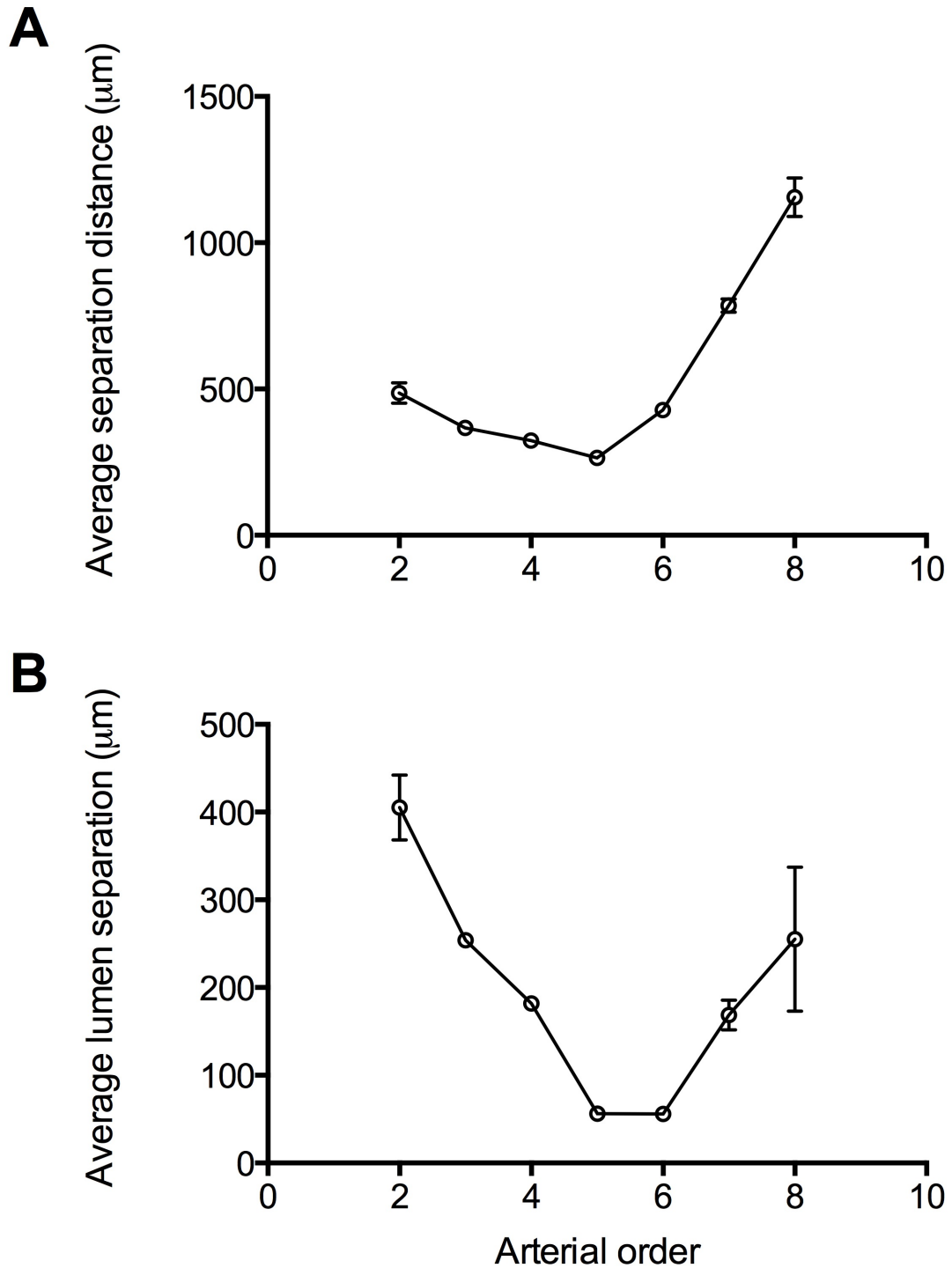


Figure 5.11. Relationships between arterial order and diffusion distance. Panel (A) demonstrates centre-to-centre distances and panel (B) illustrates lumen-to-lumen distances. Symbols and error bars are mean \pm standard error of the mean. Data are from an analysis of the data-set generated by Nordsletten *et al* (15). Note that the greater the arterial (Strahler) order, the more proximal the vessels are in the renal circulation.

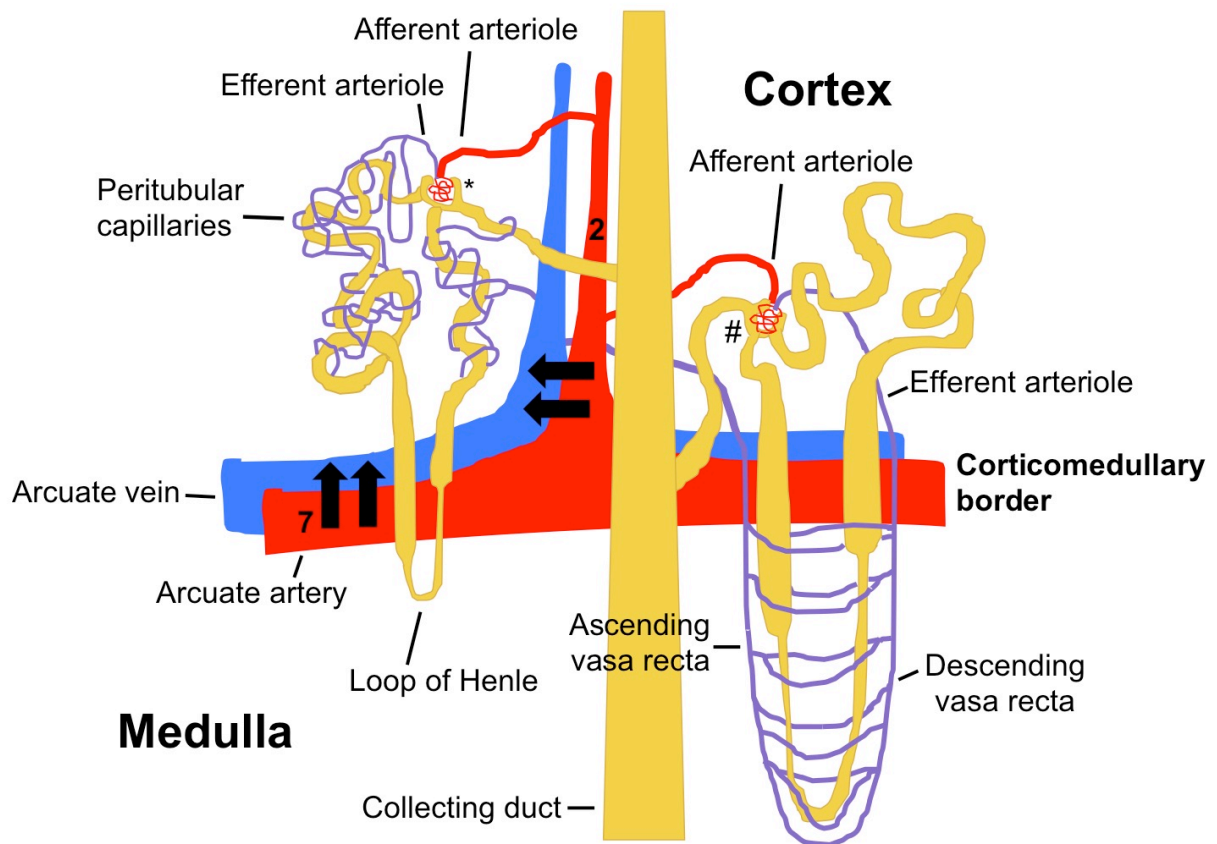


Figure 5.12. A schematic of the renal circulation. Arcuate arteries run parallel to the corticomedullary border, branching into interlobular arteries that radiate towards the cortical surface. Arcuate arteries correspond roughly to arteries of Strahler order 7 and our data analysis suggests that the diffusion distance (lumen-to-lumen) is relatively small for this arterial order (Fig. 5.11). From the interlobular arteries [2] arise afferent arterioles, which then form the capillary network in the glomerulus (* & #). The capillaries then form an efferent arteriole which leaves the glomerulus and divides into two types of capillary networks: peritubular capillaries (stemming from cortical nephrons; *), or vasa recta (arising from juxtaglomerular nephrons; #). It is the vasa recta that run down through the medulla and then return to the corticomedullary junction to the arcuate vein. The parallel arrangement of arteries and veins provides the opportunity for oxygen to diffuse from the artery into the vein, thereby reducing the amount of oxygen in the blood destined for the renal capillaries. Directional arrows indicate the proposed direction of diffusion of oxygen from arteries to veins. The very close association of vessels of order 7 (mainly arcuate arteries and veins) and 6 and 5 (likely corresponding to the proximal segments of interlobular arteries and veins) supports the hypothesis that oxygen shunting is favoured in vessels common to the cortical and medullary circulations. Numbers represent arterial Strahler orders.

Interlobular arteries are mainly vessels of orders 2-6. Interlobular arteries taper and branch as they radiate into the renal cortex (2, 9). Thus, one would expect the proximal segments of interlobular arteries (before separation of the cortical and medullary circulation) to correspond to vessels of higher Strahler order (e.g. order 6). Furthermore, vessels specific to the cortical circulation would be expected to be of a lesser Strahler order (e.g. orders 2-5). Thus, the data presented in Figure 5.11 support the notion that AV oxygen shunting is favored in the vessels at the corticomedullary border, which are common to the cortical and medullary circulations, because there are relatively short distances for oxygen to diffuse.

Schurek *et al* previously proposed that most AV shunting occurs in the interlobular arteries (20). Our data are not entirely consistent with this notion. We propose instead that AV oxygen shunting may become diminished as arterial blood flows from the corticomedullary junction into the cortex. To better test this preposition, we need to incorporate quantitative data regarding the radial geometry of artery-vein pairs into the mathematical model of kidney oxygen transport developed by Gardiner *et al* (7). The provision of these data will be the major aim of the studies described in Chapter 6 of this thesis.

5.5.6 Strengths and limitations of the light microscope and micro-CT methods

Both methods have strengths and limitations. Firstly, our light microscope analysis used observations that were biased due to the fact that the kidneys were sectioned in three chosen planes rather than from randomly generated sections. Moreover, the fact that the identification, and therefore differentiation, of small veins from capillaries was not a simple process, resulted in the need for some assumptions regarding the location of the vein corresponding to each arterial vessel. Similarly, in the case of the data generated by micro-CT, the algorithm was forced to calculate the distance between vessel pairings that were most closely associated. However, for some arteries, the program still selected veins that were located further away than another vein that would have otherwise been selected as the corresponding vein if the analysis was done manually. That is, the algorithm was not always able to find the corresponding/closest vein. Furthermore, by using the naked eye to identify vessels in the kidney from light microscopy, we could not distinguish small veins from capillaries, or indeed small veins from lymphatic vessels. It is possible therefore, that in our light microscope analysis, lymphatic vessels were mis-identified as veins.

Another limitation in our light microscope method is that it generated only a limited number of observations. This is in part due to microscopic examination being a time consuming

process, as well as the difficult identification of veins mentioned above. For our analysis, a total of 81 observations were made (32 via H & E stained tissue, 49 via Microfil®-filled and toluidine blue stained tissue). In contrast, the micro-CT analysis, because it was automated, provided 5260 observations. Such a large data set provided the level of statistical power required for us to examine the typical diffusion distances from arteries to veins. In the studies described in Chapter 6 we attempt to overcome this limitation by performing a more extensive and less biased analysis of the radial geometry of artery-vein pairs, using light microscopy.

Importantly, the light microscope and micro-CT methods provided a similar profile of changes in diffusion distance with changes in arteriolar caliber (Fig. 5.9). However, we did not generate any observations of arteries with a diameter greater than 300 μm using light microscopy, providing an explanation for the apparent discrepancy between the two data sets.

An additional limitation of the dataset of Nordsletten *et al* arises from the fact that the vessels have been rendered in such a way that their profiles were assumed to be circular (15). Consequently, some values for lumen-to-lumen distance were negative. In reality, the lumen-to-lumen distance between arteries and veins cannot be less than zero. Thus the light microscope provides a less biased estimate of diffusion distance than does the micro-CT analysis. As briefly described above, the program used for analysis of the micro-CT data did not measure the absolute diffusion distance between arteries and veins. Rather the algorithm calculated the lumen-to-lumen distance based on vessel diameter and center-to-center distances. Thus, due to the method by which the lumen-to-lumen distances were calculated, we can expect that the micro-CT analysis to be associated with some error (Fig. 5.8). Although the estimates of lumen-to-lumen distances have some error, the estimates of center-to-center distances should not. The fact that both analyses generated a similar U-shaped relationship between arterial diameter and diffusion distances provides some confidence in our conclusions. Overall, while both methods (light microscopy and micro-CT) have their limitations, when taken together, they provide us with growing confidence that the spatial relationship between arteries and veins changes considerably throughout the renal circulation. Nevertheless, it should be possible to generate micro-CT data sets in which information about the radial geometry of artery-vein pairs is retained. This issue is addressed in the studies described in Chapter 9 of this thesis.

5.5.7 Implications for a mathematical model of oxygen transport in the kidney

In Gardiner *et al*'s (7) one-dimensional mathematical model, a constant 'shunting coefficient' was applied across all branch levels of the renal circulation, based on the assumption assuming that the artery-vein diffusion barrier is constant throughout the circulation. This assumption is not appropriate as our studies demonstrate that the barriers to diffusion vary along the renal circulation. By removing this assumption, and instead integrating the various degrees of spatial association between artery-vein pairs, it should be possible to generate more precise estimates of the magnitude of shunting that occurs between artery-vein pairs on the basis of their specific spatial geometry. Based on the data generated from the current study, a two-dimensional model was developed which showed the profound effects of wrapping and diffusion distance on oxygen flux between artery-vein pairs (7). Therefore, there is a need to generate data that can be used to construct a pseudo three-dimensional (3D) model, which is the aim of the experiments and studies described in Chapters 6 and 7 of this thesis.

5.6 SUMMARY AND CONCLUSIONS

In our current study, we examined the diffusion distances between arteries and veins in the kidney through histologically stained kidney sections and light microscopy. An analogous analysis was conducted using data generated by micro-CT (15) and the findings using the two methods were compared. A U-shaped relationship was found between arterial diameter and diffusion distance. Taking the two analyses together, we believe these data provide evidence that the nature of the barriers to diffusion of oxygen from arteries to veins changes along the course of the cortical circulation. This phenomenon is likely to have a profound impact on the nature of the vascular elements where the bulk of AV oxygen shunting occurs. The data generated in this study are not in a form that would allow them to be incorporated into a pseudo-3D model of AV oxygen shunting. The overall aim of the studies described in Chapters 6 and 7 was to generate data that can be used in this manner.

REFERENCES

1. **Bankir L, Kaissling B, de Rouffignac C, Kriz W.** The vascular organization of the kidney of *Psammomys obesus*. *Anat Embryol (Berl)* 155: 149-160, 1979.
2. **Chilton L, Smirnov SV, Loutzenhiser K, Wang X, Loutzenhiser R.** Segment-specific differences in the inward rectifier K⁺ current along the renal interlobular artery. *Cardiovasc Res* 92: 169-177, 2011.
3. **Evans RG, Gardiner BS, Smith DW, O'Connor PM.** Intrarenal oxygenation: Unique challenges and the biophysical basis of homeostasis. *Am J Physiol Renal Physiol* 295: F1259-F1270, 2008.
4. **Evans RG, Harrop GK, Ngo JP, Ow CP, O'Connor PM.** Basal renal O₂ consumption and the efficiency of O₂ utilization for Na⁺ reabsorption. *Am J Physiol Renal Physiol* 306: F551-560, 2014.
5. **Evans RG, Head GA, Eppel GA, Burke SL, Rajapakse NW.** Angiotensin II and neurohumoral control of the renal medullary circulation. *Clin Exp Pharmacol Physiol* 37: e58-69, 2010.
6. **Frank M, Kriz W.** The luminal aspect of intrarenal arteries and veins in the rat as revealed by scanning electron microscopy. *Anat Embryol (Berl)* 177: 371-376, 1988.
7. **Gardiner BS, Smith DW, O'Connor PM, Evans RG.** A mathematical model of diffusional shunting of oxygen from arteries to veins in the kidney. *Am J Physiol Renal Physiol* 300: F1339-1352, 2011.
8. **Gardiner BS, Thompson SL, Ngo JP, Smith DW, Abdelkader A, Broughton BR, Bertram JF, Evans RG.** Diffusive oxygen shunting between vessels in the preglomerular renal vasculature: anatomic observations and computational modeling. *Am J Physiol Renal Physiol* 303: F605-618, 2012.
9. **Hayashi K, Epstein M, Loutzenhiser R.** Enhanced myogenic responsiveness of renal interlobular arteries in spontaneously hypertensive rats. *Hypertension* 19: 153-160, 1992.
10. **Kobayashi H, Pelster B, Piiper J, Scheid P.** Significance of the Bohr effect for tissue oxygenation in a model with counter-current blood flow. *Respir Physiol* 76: 277-288, 1989.
11. **Kobayashi H, Takizawa N.** Imaging of oxygen transfer among microvessels of rat cremaster muscle. *Circulation* 105: 1713-1719, 2002.
12. **Ludbrook J.** Repeated measurements and multiple comparisons in cardiovascular research. *Cardiovasc Res* 28: 303-311, 1994.
13. **Mattson DL.** Importance of the renal medullary circulation in the control of sodium excretion and blood pressure. *Am J Physiol Regul Integr Comp Physiol* 284: R13-27, 2003.
14. **Nangaku M, Nishi H, Miyata T.** Role of chronic hypoxia and hypoxia inducible factor in kidney disease. *Chin Med J* 121: 257-264, 2008.
15. **Nordsletten DA, Blackett S, Bentley MD, Ritman EL, Smith NP.** Structural morphology of renal vasculature. *Am J Physiol Heart Circ Physiol* 291: H296-H309, 2006.
16. **O'Connor PM.** Renal oxygen delivery: Matching delivery to metabolic demand. *Clin Exp Pharmacol Physiol* 33: 961-967, 2006.
17. **O'Connor PM, Kett MM, Anderson WP, Evans RG.** Renal medullary tissue oxygenation is dependent on both cortical and medullary blood flow. *Am J Physiol Renal Physiol* 290: F688-F694, 2006.
18. **Pallone TL, Zhang Z, Rhinehart K.** Physiology of the renal medullary microcirculation. *Am J Physiol Renal Physiol* 284: F253-266, 2003.
19. **Pittman RN.** The Circulatory System and Oxygen Transport. Morgan & Claypool Life Sciences. <http://www.ncbi.nlm.nih.gov/books/NBK54112/>. [January 20, 2016].
20. **Schurek HJ, Jost U, Baumgartl H, Bertram H, Heckmann U.** Evidence for a preglomerular oxygen diffusion shunt in rat renal cortex. *Am J Physiol* 259: F910-915, 1990.

6 | VASCULAR GEOMETRY AND OXYGEN DIFFUSION IN THE VICINITY OF ARTERY-VEIN PAIRS IN THE KIDNEY

Monash University

Declaration for Thesis Chapter 6

Declaration by candidate

This chapter was published as is, in the *American Journal of Physiology – Renal Physiology*

Ngo JP, Kar S, Kett MM, Gardiner BS, Pearson JT, Smith DW, Ludbrook J, Bertram JF, and Evans RG (2014). “Vascular geometry and oxygen diffusion in the vicinity of artery-vein pairs in the kidney”, *Am J Physiol Renal Physiol*, 305: F1111-F1122.

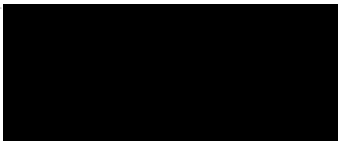
In the case of Chapter 6, the nature and extent of my contribution to the work was the following:

| Nature of contribution | Extent of contribution (%) |
|--|----------------------------|
| Provided design of research, performed experiments, analyzed data, interpreted results, prepared figures, drafted, edited and revised manuscript | 60% |

The following co-authors contributed to the work. If co-authors are students at Monash University, the extent of their contribution in percentage terms must be stated:

| Name | Nature of contribution | Extent of contribution (%) for student co-authors only |
|-------------------------|---|--|
| Saptarshi Kar | Performed experiments, analyzed data, interpreted results, prepared figures, drafted, edited and revised manuscript | 15% |
| Michelle M Kett | Supervision, provided design of research, performed experiments, interpreted results, edited and revised manuscript | 5% |
| Bruce S Gardiner | Provided design of research, interpreted results, edited and revised manuscript | 4% |
| James T Pearson | Supervision, provided design of research, interpreted results, edited and revised manuscript | 4% |
| David W Smith | Provided design of research, interpreted results, edited and revised manuscript | 4% |
| John Ludbrook | Analyzed data, edited and revised manuscript | 2% |
| John F Bertram | Provided design of research, edited and revised manuscript | 2% |
| Roger G Evans | Supervision, provided design of research, interpreted results, drafted, edited and revised manuscript | 6% |

The undersigned hereby certify that the above declaration correctly reflects the nature and extent of the candidate's and co-authors' contributions to this work*.

| | | |
|------------------------------|--|---------------------------|
| Candidate's Signature |  | Date 24/04/2016 |
|------------------------------|--|---------------------------|

| | | |
|------------------------------------|---|---------------------------|
| Main Supervisor's Signature |  | Date 24/04/2016 |
|------------------------------------|---|---------------------------|

*Note: Where the responsible author is not the candidate's main supervisor, the main supervisor should consult with the responsible author to agree on the respective contributions of the authors.

CALL FOR PAPERS | Renal Hypoxia

Vascular geometry and oxygen diffusion in the vicinity of artery-vein pairs in the kidney

Jennifer P. Ngo,¹ Saptarshi Kar,⁴ Michelle M. Kett,¹ Bruce S. Gardiner,⁴ James T. Pearson,^{1,3} David W. Smith,⁴ John Ludbrook,⁵ John F. Bertram,² and Roger G. Evans¹

¹Department of Physiology, Monash University, Melbourne, Australia; ²Department of Anatomy and Developmental Biology, Monash University, Melbourne, Australia; ³Monash Biomedical Imaging Facility, Monash University, Melbourne, Australia; ⁴School of Computer Science and Software Engineering, The University of Western Australia, Perth, Australia; and ⁵The University of Adelaide, Adelaide, Australia

Submitted 7 July 2014; accepted in final form 8 September 2014

Ngo JP, Kar S, Kett MM, Gardiner BS, Pearson JT, Smith DW, Ludbrook J, Bertram JF, Evans RG. Vascular geometry and oxygen diffusion in the vicinity of artery-vein pairs in the kidney. *Am J Physiol Renal Physiol* 307: F1111–F1122, 2014. First published September 10, 2014; doi:10.1152/ajprenal.00382.2014.—Renal arterial-to-venous (AV) oxygen shunting limits oxygen delivery to renal tissue. To better understand how oxygen in arterial blood can bypass renal tissue, we quantified the radial geometry of AV pairs and how it differs according to arterial diameter and anatomic location. We then estimated diffusion of oxygen in the vicinity of arteries of typical geometry using a computational model. The kidneys of six rats were perfusion fixed, and the vasculature was filled with silicone rubber (Microfil). A single section was chosen from each kidney, and all arteries ($n = 1,628$) were identified. Intrarenal arteries were largely divisible into two “types,” characterized by the presence or absence of a close physical relationship with a paired vein. Arteries with a close physical relationship with a paired vein were more likely to have a larger rather than smaller diameter, and more likely to be in the inner-cortex than the mid- or outer cortex. Computational simulations indicated that direct diffusion of oxygen from an artery to a paired vein can only occur when the two vessels have a close physical relationship. However, even in the absence of this close relationship oxygen can diffuse from an artery to periarteriolar capillaries and venules. Thus AV oxygen shunting in the proximal preglomerular circulation is dominated by direct diffusion of oxygen to a paired vein. In the distal preglomerular circulation, it may be sustained by diffusion of oxygen from arteries to capillaries and venules close to the artery wall, which is subsequently transported to renal veins by convection.

arterial-to-venous oxygen shunting; arteries; blood vessels; counter-current diffusion; hypoxia; oxygen transport to tissue

EVIDENCE FROM EXPERIMENTAL (25, 40, 47) and computational (14, 15) studies indicates that diffusional shunting of oxygen from arteries to veins acts to limit oxygen delivery to the renal cortex. The results of a one-dimensional computational model of arterial-to-venous (AV) oxygen shunting indicate that this phenomenon is quantitatively significant, being on the same order of magnitude as total oxygen consumption under normal physiological conditions (14). The adaptive feature of renal AV oxygen shunting may be that it acts as a structural antiox-

idant defense mechanism. That is, by limiting oxygen delivery to renal tissue it may prevent cortical tissue hyperoxia, and thus oxidative stress, that would otherwise occur due to the high level of renal blood flow (33, 34). However, it likely also renders the renal cortex susceptible to hypoxia when renal oxygen delivery is threatened by ischemia or hemodilution (14). In the kidney, AV oxygen shunting is facilitated by the intimate spatial association of arteries and veins, characterized by the walls of some veins partially enveloping the arterial wall (33, 34). Herein, we define this phenomenon as “wrapping.”

AV oxygen shunting also has the potential to limit oxygen delivery to the renal medulla, if a significant amount of oxygen is shunted in arterial vessels that supply oxygen to the renal medulla (interlobar, arcuate and proximal interlobular arteries, and/or juxtamedullary glomerular arterioles) (11). It was assumed that most oxygen shunting occurs in the outer cortex, beyond the point where the arterial supply to the medullary circulation diverges from that of the bulk of the renal cortex (40). This assumption has been based on the fact that the surface area for diffusion of oxygen from arteries increases exponentially along the course of the renal circulation (30, 40). However, the factors that govern diffusion of oxygen between intrarenal arteries and veins and the renal parenchyma have not been quantified, so this assumption cannot be justified based on current knowledge.

We recently developed a two-dimensional (2D) computational model of diffusion of oxygen in the vicinity of a single artery-vein pair in cross section, in which we could alter geometric and other factors that might influence oxygen transport (15). The model predicted that four factors, associated with the spatial geometry of artery-vein pairs, have major effects on the diffusion of oxygen from paired arteries and veins. These are 1) the distance separating the lumen of the artery from the lumen of the vein, 2) the proportion of the vein wall that wraps around the wall of the artery (wrapping), 3) the thickness of the artery wall and associated adventitia, and 4) the presence of oxygen sinks (capillaries or tubules) between the artery and vein walls. Qualitative analysis of the spatial arrangements of arteries and veins in the renal cortex indicated that these factors change along the course of the renal circulation, in a way that might promote diffusional oxygen shunting in more proximal vascular elements. However, such qualitative information cannot be used as the basis for predicting

Address for reprint requests and other correspondence: R. Evans, Dept. of Physiology, PO Box 13F, Monash Univ., Victoria 3800, Australia.

the relative quantities of oxygen shunting along the course of the preglomerular circulation.

In the current study, we performed a quantitative analysis of the spatial association of arteries and veins in the renal cortex. We determined how the four factors identified by computational modeling (15), that determine diffusion of oxygen from arteries to veins and the renal parenchyma, change along the course of the renal circulation. Specifically, we determined the diffusion (separation) distance between an artery and its closest vein, as well as the degree to which the venous wall surrounds

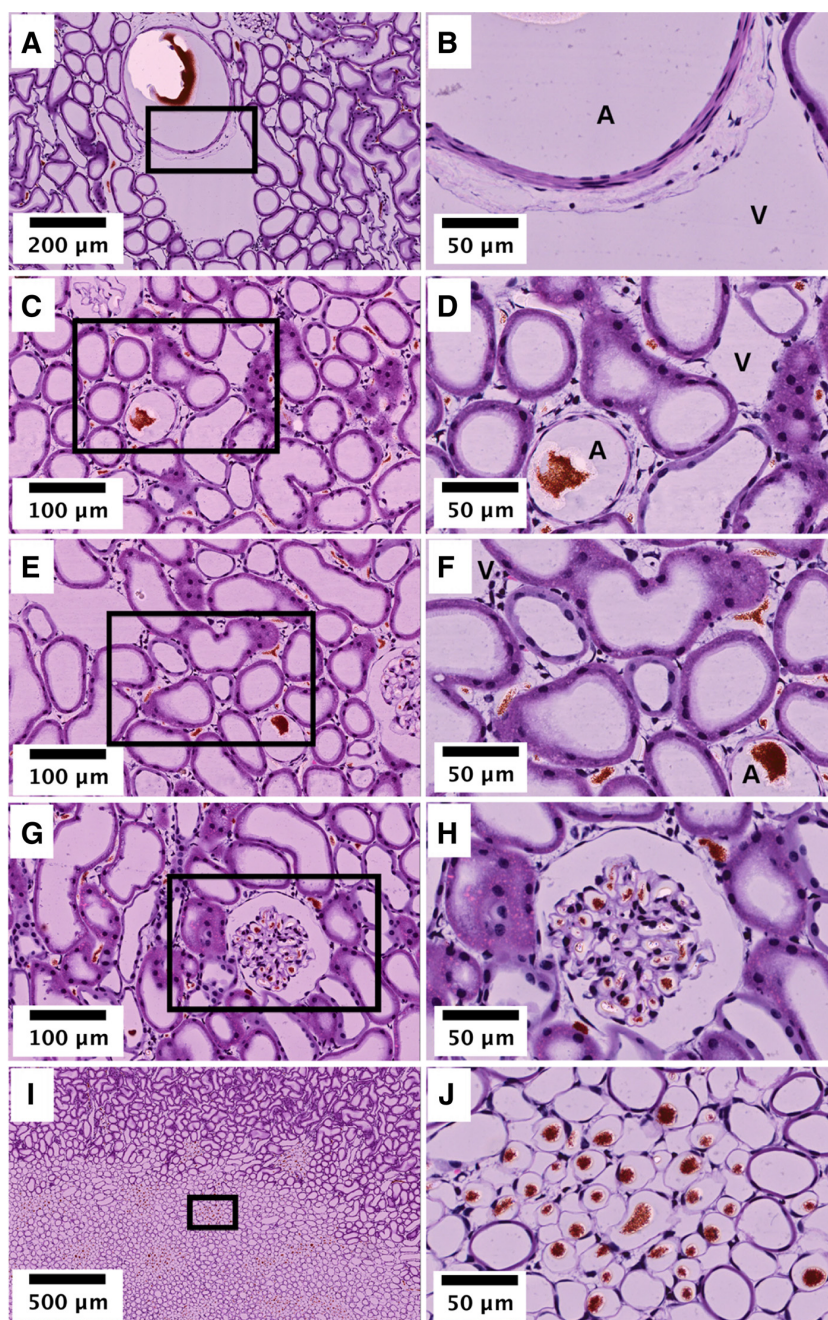
the artery (termed wrapping throughout the paper). We then used a computational model to determine the pathways of oxygen diffusion in the vicinity of typical artery-vein pairs.

METHODS

Anatomic Observations

Animal ethics. All procedures involving animals were approved by the Animal Ethics Committee of the Monash University School of Biomedical Sciences and were in accordance with the Australian

Fig. 1. Representative micrographs of renal tissue in which the vasculature was visualized by Microfil. Images on the left-hand side are of lower power. Images on the right-hand side are higher power images of the outlined areas in the panels on the left-hand side. *A* and *B*: artery-vein pair typical of that for arteries of diameter $>100\ \mu\text{m}$. *C*–*F*: typical arrangements of arteries with diameters $<100\ \mu\text{m}$. *B* demonstrates that larger artery-vein pairs are void of any tubular or capillary elements between the pair. Note, however, the presence of lymphatic vessels. *D* and *E* demonstrate that smaller arteries often have tubular and capillary elements between the artery-vein pair. *G*–*J*: Microfil in glomerular capillaries and vasa recta. A, artery; V, vein.



Code of Practice for the Care and Use of Animals for Scientific Purposes.

Preparation of tissues for morphometric analyses. Male Sprague-Dawley rats (250–300 g) were anesthetized with pentobarbital sodium (60 mg/kg ip). A large-bore catheter was inserted into the aorta below the level of the kidneys. Heparin (50 IU, Pfizer, West Ryde, NSW, Australia) was then administered, and the kidneys retrogradely perfused at physiological pressure. The kidneys were first cleared with phosphate buffer (0.2 M) containing sodium nitroprusside (0.24 mg/ml) and then perfusion fixed with Karnovsky's fixative (4% paraformaldehyde and 4% glutaraldehyde in 0.2 M phosphate buffer). Once fixed, the kidneys were filled with Microfil compound (MV-122; Flow Tech) at a rate of 1 ml/min. Once 10–12 ml of Microfil had been infused, the renal artery and vein were ligated and the kidneys removed and immersed in fixative overnight at 4°C.

Sampling of renal tissue. Following overnight fixation, both kidneys were decapsulated, weighed, and prepared for slicing. In brief, kidneys were embedded in 2% agarose gel and sliced into 1.25-mm slices using a slicing device (3, 18), generating 10–20 slices/kidney. Three kidneys were sliced perpendicular to the longitudinal axis in the sagittal plane. Another three kidneys were sliced along the longitudinal axis. Left and right kidneys were used in an alternating fashion so that not all right/left kidneys were sliced in the same direction. This approach minimized bias in our sampling method. Whole kidney volume was estimated from these slices using Cavalieri's principle (32).

Kidney slices were numbered in order and separated into "odd" slices and "even" slices. All morphometric analyses were carried out on the slices in the odd group. One slice from the odd group of each kidney was systematically chosen, processed, and embedded for morphometric analyses. For the kidneys sliced in the sagittal plane, the three options were odd slices numbered 1, 5, and 9. For the kidneys sliced along the longitudinal axis, the three choices were slices numbered 1, 3, and 5. Once a slice was chosen from one kidney, the same option (e.g., slice 1) was omitted from the other kidneys so that that slice number would not be chosen again. Thus morphometric analyses were carried out on sections obtained from one of three different areas of the kidney. That is, a slice near the edge of the kidney, a slice near the midline, and a slice in an intermediate position in each of the two planes, generating six slices in total.

Whole kidney slices were embedded in glycolmethacrylate (Technovit 7100; Heraeus Kulzer, Wehrheim, Germany), sectioned at 3 μm , and stained with hematoxylin and eosin. Sections were scanned with Aperio Scan Scope (Aperio, Vista, CA), providing a digital representation of the entire section. Representative images are shown in Fig. 1.

Morphometric studies. Morphometric studies were carried out using Image Scope (v. 11.2.0.780, Aperio Technologies), a digital slide viewer. All arteries within each section were identified and labeled. For each artery, we manually measured arterial diameter, the shortest diffusion distance from the artery to its nearest vein, the percentage of the arterial adventitia in direct contact with the vein wall (wrapping), the thickness of the adventitia around the artery (shortest width), the thickness of the arterial wall, the shortest distance from the artery to its nearest artery, and the diameter of this second artery.

Analysis of spatial relationships of artery-vein pairs by region of the kidney. In conjunction with our analyses by arterial diameter, we also analyzed the spatial geometry of artery-vein pairs in terms of their anatomic location within the kidney. Of the six kidney sections used in our morphometric analyses, four of these, which had a distinct medulla, were used in this analysis. The two kidney sections that contained only cortical tissue were not included.

For each of the four kidney sections, the corticomedullary junction was identified (22, 24). In brief, juxtamedullary glomeruli were identified as glomeruli located closest to the medulla. Using these glomeruli, as well as the large arteries situated nearby and the overall

shape of the kidney section as a guide, a line of best fit was drawn manually. The region from this line to the surface of the cortex was then divided into thirds, outer cortex, midcortex, and inner cortex, while the region inward of this line was defined as the corticomedullary region. All arteries that were intersected by a line were assigned to the region that was closer to the medulla rather than the cortical surface.

Statistical methods. Continuous data were summarized as group means \pm SE, together with group size (n). Continuous variables were analyzed by one-way ANOVA, followed by the Tukey-Kramer test for all possible pairwise contrasts (to control the type I error rate) (27). Categorical variables were analyzed by the exact Cochran-Armitage test for trends (2, 8). To protect against excessive type I error, P values were adjusted by the Ryan-Holm step-down Bonferroni procedure (26). Analyses were performed with either SYSTAT v.13 (Systat, San Jose, CA) or StatXact v.9 (Cytel Software, Cambridge, MA). Two-sided $P \leq 0.05$ was considered statistically significant.

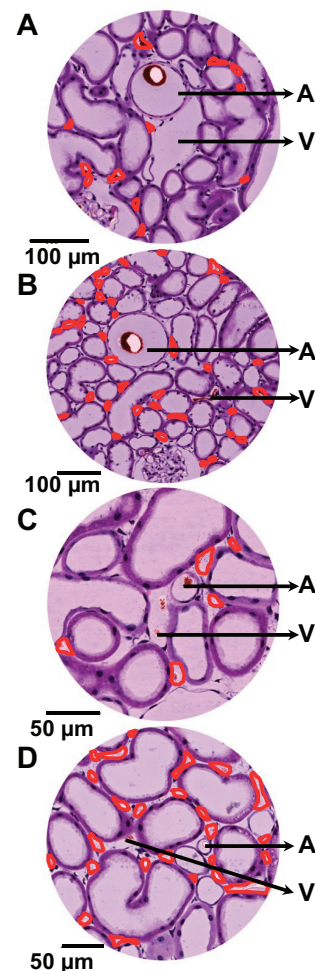


Fig. 2. Characteristic cross sections of tissue in the vicinity of an artery. The figure displays typical arrangements for a large "wrapped" artery [internal diameter (D_A) = 89 μm ; A], a large "not-wrapped" artery (D_A = 133 μm ; B), a small wrapped artery (D_A = 25 μm ; C), and a small not-wrapped artery (D_A = 18 μm ; D). A and V denote arteries and veins, respectively. The zones containing capillaries or venules are demarcated by red lines. The minimum luminal wall separation distances (diffusion distances) between the main artery and vein are 7 μm (A), 149 μm (B), 5 μm (C), and 71 μm (D).

Table 1. *Model parameters*

| Parameter | Values and Units | Reference(s) |
|--|---|--------------|
| Arterial PO ₂ (PO _{2A}) | 85 mmHg | 47 |
| Venous PO ₂ (PO _{2V}) | 52 mmHg | 14, 47 |
| Capillary PO ₂ (PO _{2cap}) | 50 mmHg | 47 |
| Renal tissue oxygen diffusion coefficient (<i>D</i>) | 2.8×10^{-9} m ² /s | 5, 6, 15 |
| Oxygen solubility (σ) | 1.34×10^{-3} mol·m ⁻³ ·mmHg ⁻¹ | 14 |
| Tubule oxygen consumption rate ($\dot{V}O_2$) | 0.103, mol·m ⁻³ ·s ⁻¹ | 14, 15 |

Capillary oxygen tension (PO_{2cap}) should have a value in between the PO₂ of afferent (55 mmHg) (14) and efferent (45 mmHg) (47) arteriolar PO₂. As a conservative estimate, we chose PO_{2cap} to be the average of the reported PO₂ in the afferent and efferent arteriole. This is consistent with experimentally measured microvascular PO₂ in the rat renal cortex (31).

Computational Modeling

Utilization of anatomic information. We have previously used computational methods to investigate the impact of the microanatomy of artery-vein pairs on AV oxygen shunting and oxygen transport in the parenchyma surrounding an artery-vein pair (15). However, the anatomic configurations of artery-vein pairs and the patterns of distribution of parenchymal oxygen sinks (tubules and capillaries) in the earlier study were highly idealized (15). In the current study, we generated more physiologically relevant information by simulating oxygen diffusion in an actual representation of the microanatomy of an artery-vein pair and its associated oxygen sinks. We selected four representative images (Fig. 2) on the basis that they represented large wrapped (Fig. 2A), large not-wrapped (Fig. 2B), small-wrapped (Fig. 2C), and small not-wrapped arteries (Fig. 2D). An additional criterion was that the chosen arteries were nearly circular, indicating that the plane of section was perpendicular to the plane of the artery. The histological images clearly show the heterogeneous distribution of capillaries and venules (red boundaries) and tubule segments across the parenchyma.

The selected images were imported to an image-processing software (GIMP v2.8), and the boundaries of the arteries, veins, capillaries/venules and tubule segments were traced. The traced images were converted into a vector format to make them compatible with the finite-element computer software used for modeling the oxygen transport process (COMSOL Multiphysics, v. 4.2, COMSOL, Burlington, MA). Specifically, the vector format conversion was performed using a raster-to-vector conversion program (Magic Tracer V 2.0.012, Elgorithms, Pryor, OK). During the vector conversion process, the cross-sectional areas of putative capillaries (i.e., small vessels containing Microfil) <50 μm^2 were adjusted to 50 μm^2 . Small vessels containing Microfil, but with cross-sectional areas >150 μm^2 , were designated as venules due to their relatively high ratio of luminal diameter to vascular wall thickness, a characteristic that distinguishes venules from capillaries (39). The images imported into the computational domain were scaled to match the dimensions calculated from the scales in the captured photomicrographs (Fig. 2).

Computational model. Details of the 2D model of oxygen transport between artery-vein pairs have been described previously (15). Oxygen transport across a cross section of renal tissue located in a Cartesian 2D (*x*, *y*) plane is a combination of diffusion and consumption and can be mathematically represented by a diffusion equation with a source/sink term:

$$D \left(\frac{\partial^2 c}{\partial x^2} + \frac{\partial^2 c}{\partial y^2} \right) = S \quad (1)$$

In Eq. 1, *c* (mol/m³) denotes the concentration of free oxygen. It is related to the partial pressure of oxygen (PO₂; mmHg) by the following equation

$$c = \sigma \text{PO}_2 \quad (2)$$

where σ is the solubility coefficient of oxygen (mol·m⁻³·mmHg⁻¹), which was assumed to be constant (Table 1), *D* (m²/s) is the effective diffusion coefficient of oxygen across the renal tissue, and *S* (mol·m⁻³·s⁻¹) represents either oxygen generation (*S* > 0) or oxygen consumption (*S* < 0).

Model parameters. The values of the geometrical and transport parameters used in the computational analysis are shown in Table 1. The source term *S* is set to a fraction of $\dot{V}O_2$ in the tubule segments, depending upon the aspect ratio of the tubule cross section as shown in Fig. 3. The aspect ratio of the individual tubule cross sections depends on the angle of the sectioning plane relative to the orientation of the tubular lumen. In most cases, not all capillaries servicing an obliquely cut tubule appear in the tissue slice (see circular tubule labeled T₁ and oblique tubule labeled T₂ in Fig. 3A). This is due to the tortuosity of capillaries and tubules located in the renal cortex (1, 46). A second consideration, on which we based the reduction in $\dot{V}O_2$ with respect to the aspect ratio of the tubules, is shown in Fig. 3. The schematic in Fig. 3 shows that oblique sectioning of parallel capillar-

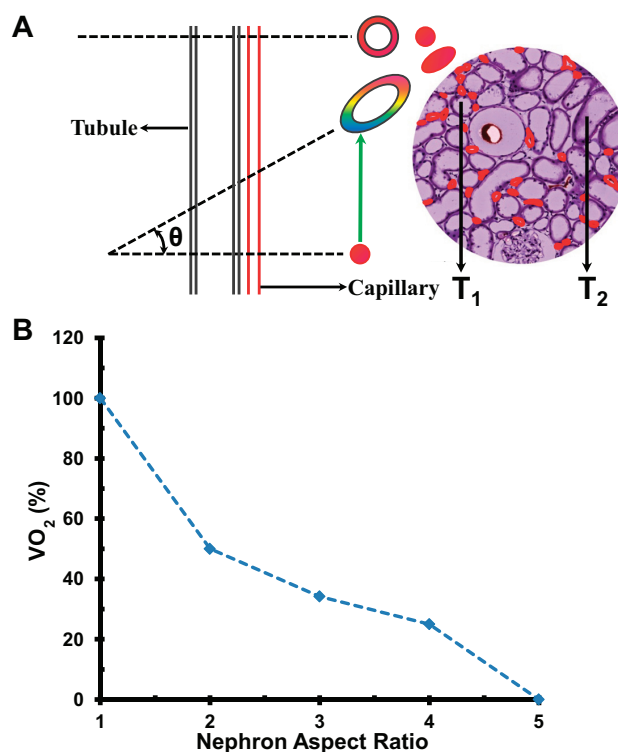


Fig. 3. Theoretical effects of the plane of sectioning on estimation of the metabolic oxygen demand of tubules. A: effect of orientation of the sectioning plane (dotted lines) on the 2-dimensional (2D) cross-sectional geometry of tubules (black boundaries) and capillaries (red boundaries). Also shown is an actual photomicrograph of a typical cortical tissue slice. As the plane of sectioning becomes steeper with respect to the horizontal, the capillary adjoining the tubule only services a fraction of the tubular epithelium. This can lead to a gradient in oxygen tension (normoxic: red, hypoxic: blue/green/yellow) along the tubular epithelium. The gradient in the tubular oxygen tension is minimized by oxygen supply from a capillary located outside the sectioning plane (green arrow). T₁ and T₂ in the photomicrograph show the 2D representation of a circular and oblique proximal tubule, respectively. Capillaries are virtually absent in the vicinity of T₂ indicating that it was obtained by sectioning of a tortuous segment of the tubule. Consequently, the contribution of individual capillaries in the 2D field to the delivery of oxygen to the tubule is only a fraction of total tubule oxygen demand ($\dot{V}O_2$) defined in Table 1. This fraction becomes smaller as the aspect ratio of the tubule becomes greater, as shown in B.

ies and tubules increases the mass transfer distance of oxygen from the capillary to the tubular epithelium. The mass transfer distance increases with an increase in the aspect ratio of the tubules. In such cases, the capillaries captured in the sectioning plane only service a fraction of the tubular epithelium. The rest of the tubular epithelium is serviced by a capillary located outside the sectioning plane (green arrow in Fig. 3).

Allocating a fraction of \dot{V}_{O_2} along the epithelium of oblique tubules corrects the net imbalance between the oxygen sources and sinks in a 2D representation of the actual 3D geometry. For perfectly horizontal sectioning planes, the capillary can service the entire tubular epithelium. Therefore, a capillary can service tubular epithelium located at distances below or equal to the actual tubule diameter. The larger diameter of oblique tubular sections prevents oxygen in the capillary, captured in the 2D plane, servicing the entire tubular epithelium. The increase in the tubular cross-sectional diameter is dependent on the cosine of the angle (Θ) of the sectioning plane relative to the horizontal. Under such circumstances, it is reasonable to assume that the capillary cross section captured in the 2D micrographs only contributes a fraction of the metabolic oxygen demand (\dot{V}_{O_2}) of the tubule, as shown in Fig. 3B. The tortuous segments of tubules and their servicing peritubular capillaries demonstrate a high degree of geometrical complexity in 3D (46). This makes it difficult to correlate the aspect ratio and \dot{V}_{O_2} for tubules obtained by sectioning of tissue along the tortuous segments of the tubules. In such cases, we assume that the relationship between \dot{V}_{O_2} and tubule aspect ratio in Fig. 3B is a reasonable approximation. For other elements, within the tissue (excluding the cross sections of tubules), S was set to zero. This decision was based on the fact that $\sim 80\%$ of the oxygen consumed within the kidney under physiological conditions is used to power tubular sodium reabsorption (13). \dot{V}_{O_2} ($\text{mol} \cdot \text{m}^{-3} \cdot \text{s}^{-1}$) thus represents the rate of oxygen consumption by the tubular epithelium.

Boundary conditions. A zero-flux condition was applied along the boundary of the tissue image (Fig. 2), assuming spatial repetition of the tissue geometry. The radius of each image in Fig. 2 was set at half the average distance between arteries of that size and the nearest artery (Table 2). Therefore, each image approximates the area of influence, on diffusive transport of oxygen to the tissue, of the artery-vein pair depicted in it. We propose that such areas of influence are periodically repeated throughout the renal parenchyma. Consequently, a no-flux boundary condition is reasonable. The concentration of oxygen at the boundaries of the artery, vein, and capillaries was set at c_A , c_V , and c_{cap} , respectively (Table 1). It was assumed that the oxygen is radially well mixed within the blood vessels (artery, vein, and capillaries) and no oxygen concentration gradients exist within these vessels.

Numerical solution. The governing equations pertaining to the four models with the appropriate boundary conditions were solved numerically using COMSOL Multiphysics. The “fine” meshing scheme as defined by the “physics-control” settings was used for all the simulations. This resulted in generation of 21,172, 73,208, 12,778, and 29,412 mesh elements for the computational domains generated from processing the photomicrographs represented in Fig. 2A, B, C, and D, respectively. The relative accuracy for all simulations was set at 0.0001.

RESULTS

Anatomic Observations

Kidney weight and volume. The weight of the six kidneys processed for morphometry averaged 1.83 ± 0.06 g (range = 1.55–1.94 g). Their volume averaged $1,671 \pm 94$ mm^3 (range = 1,480–2,095 mm^3).

Microfil as a means of identifying the renal vasculature. Microfil could be seen as dark brown staining inside the lumen of most arteries, glomerular and peritubular capillaries, vasa recta, and venules (Fig. 1). Microfil was often not seen in larger veins, presumably reflecting incomplete filling of the vasculature. Nevertheless, these veins were easily identified because of their thin walls. Thus we were able to easily distinguish between the vascular and tubular elements in the renal cortex and medulla.

Characteristics of arteries. A total of 1,628 arteries from 6 kidneys were analyzed. The lumen diameter of arteries in the juxtamedullary and inner cortical region tended to be >40 μm (Table 2), consistent with a predominance of interlobar (>200 μm), arcuate (>100 μm), and proximal interlobular (>60 μm) vessels in these regions (19, 42). The lumen diameter of arteries in the mid- and outer cortex tended to be <25 μm , consistent with the tapering of interlobular arteries as they extend toward the cortical surface, to a diameter of ~ 30 μm at the terminal segment (19) and 10–25 μm at the level of afferent and efferent arterioles (10). As described previously (42), the thickness of the arterial wall and associated adventitia progressively diminished as vessel diameter reduced (Table 2). Consistent with the relatively thin arterial wall of all vessels studied (29), there was little evidence of vasa vasorum. The mean distance to the nearest artery varied according to both

Table 2. Characteristics of arteries according to internal diameter and anatomic region

| | Mean Arterial Diameter, μm | Arterial Wall,* μm | Adventitia, μm | Total Wall Thickness (Arterial Wall and Adventitia), μm | Distance to Nearest Artery, μm |
|---|---------------------------------------|-------------------------------|---------------------------|--|--|
| <i>Smallest arterial diameter, μm</i> | | | | | |
| <20 ($n = 810$) | 14.03 ± 0.15^a | 2.32 ± 0.08^a | $1.64 \pm 0.07^{a,b}$ | 3.97 ± 0.11^a | 167.54 ± 4.93^a |
| 20–49.9 ($n = 561$) | 29.47 ± 0.36^b | 2.25 ± 0.06^a | 1.39 ± 0.06^a | 3.65 ± 0.11^a | 147.48 ± 5.79^b |
| 50–99.9 ($n = 210$) | 66.16 ± 0.87^c | 3.04 ± 0.12^b | 1.87 ± 0.13^b | 4.91 ± 0.21^b | $185.24 \pm 11.76^{a,b}$ |
| >100 ($n = 45$) | 166.52 ± 11.22^d | 5.73 ± 0.46^c | 4.22 ± 0.54^c | 9.95 ± 0.77^c | $231.24 \pm 38.88^{a,b}$ |
| <i>Region of the kidney</i> | | | | | |
| CM ($n = 147$) | 57.46 ± 6.46^a | 3.93 ± 0.35^a | 2.22 ± 0.16^a | 6.15 ± 0.44^a | 176.20 ± 16.75^a |
| IC ($n = 226$) | 41.15 ± 2.04^b | 2.86 ± 0.10^b | 1.99 ± 0.14^b | 4.85 ± 0.19^b | 198.30 ± 12.50^b |
| MC ($n = 429$) | 21.45 ± 0.70^c | $2.46 \pm 0.11^{b,c}$ | 1.96 ± 0.14^c | $4.41 \pm 0.18^{b,c}$ | 172.40 ± 6.61^c |
| OC ($n = 243$) | 16.26 ± 0.51^d | 2.30 ± 0.15^c | 1.65 ± 0.08^d | 3.76 ± 0.13^c | 191.10 ± 10.39^d |

Values are means \pm SE of mean arterial diameter, mean thickness of the arterial wall (media and endothelium only)*, and associated adventitia, as well as the mean distance to the nearest artery. Arteries were partitioned by vessel diameter and by anatomic region of the kidney. Letters represent bins of arterial diameter or region of the kidney for which the independent variables did not differ significantly (Tukey's test). CM, corticomedullary; IC, inner cortex; MC, midcortex; OC, outer cortex.

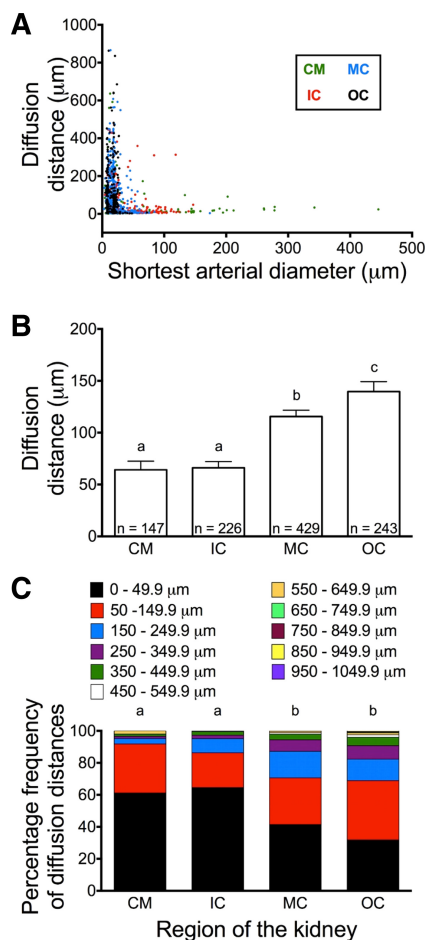


Fig. 4. Distance between the arterial and venous lumens as a function of arterial diameter in various regions of the kidney. *A*: scattergram in which measurements are plotted against arterial diameter. The various colors represent the 4 different regions of the kidney: corticomedullary (CM), inner cortex (IC), midcortex (MC), outer cortex (OC). *B*: independent variable is bins of the 4 regions of the kidney. Values are means \pm SE. *C*: relative frequencies of diffusion distances in each of the 4 regions of the kidney. The same lower case letters represent bins of anatomic region for which diffusion distance (Tukey's test; *B*) or percentage frequency of categories of diffusion distance (Cochran-Armitage test for trends; *C*) did not differ significantly.

arterial diameter and anatomic location (Table 2). Across all arteries, this distance averaged 164.6 ± 3.7 μ m.

Spatial relationships between arteries and veins in the renal cortex. Visual inspection of the range of spatial arrangements of artery-vein pairs confirmed the finding of our previous qualitative analysis (15) that larger arteries tend to be more closely associated with their corresponding veins than are smaller arteries (Fig. 1). Capillaries or tubules were rarely found between these larger artery-vein pairs. In most cases, only adventitia separated the larger artery/vein pairs (Fig. 1*B*). Smaller arteries were more often found at longer distances from their veins, with tubules and capillaries in between the artery-vein pair (Fig. 1, *C-F*).

The scattergram plotting artery-vein diffusion distance against arterial diameter was L-shaped. That is, the diffusion distances for arteries of a diameter ≥ 100 μ m were uniformly

short (<100 μ m) whereas there was considerable variation in the diffusion distances for smaller vessels (Fig. 4*A*). On average, large arteries had shorter diffusion distances than smaller arteries (Fig. 5*A*). The distribution of artery-vein diffusion distances progressively shifted to longer distances as arterial diameter reduced (Fig. 5*B*). For example, 89.4% of arteries ≥ 50 μ m in diameter were closer than 50 μ m to the nearest vein, whereas this was the case for only 28.3% of arteries <20 μ m in diameter.

Arteries located in the corticomedullary and inner cortical regions tended to be relatively large and close to their corresponding veins. Arteries found in the mid- and outer cortex tended to be small and more distant to the closest vein (Fig. 4, *A* and *B*). For example, 63.3% of arteries found in the corticomedullary and inner cortical regions had diffusion distances of <50 μ m, whereas this was the case for only 37.9% of arteries found in the mid- and outer cortex (Fig. 4*C*).

When analyzed by vessel caliber, arteries with diameters >200 μ m consistently displayed a close physical relationship with their corresponding vein. That is, at least part of the arterial wall was wrapped by the corresponding vein (Fig. 6*A*). Consequently, the diffusion distance between the arterial and venous lumen was short. On average, the proportion of arterial wall wrapped by the vein progressively decreased from the larger to smaller vessels (Fig. 7*A*). Consistent with this finding, our frequency analysis showed that larger vessels were more likely to be wrapped by a vein than were smaller vessels (Fig. 7*B*). For example, 33.3% of arteries of diameter >100 μ m had 30% or more of their wall wrapped by the vein, while this was the case for only 6.0% of arteries of diameter <50 μ m.

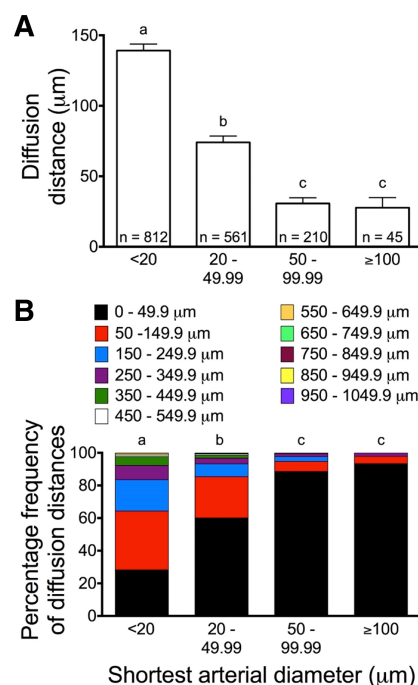


Fig. 5. Distance between the arterial and venous lumens as a function of arterial diameter. *A*: independent variable (arterial lumen diameter) is binned into 4 categories: <20 , 20-49.99, 50-99.99, and ≥ 100 μ m. Values are means \pm SE. *B*: dependent variable is binned into ranges of diffusion distance. The statistical analysis is as for Fig. 4.

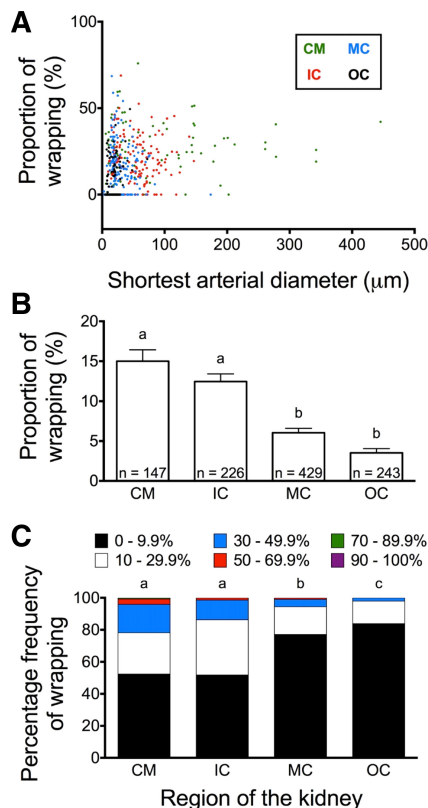


Fig. 6. Proportion of the arterial lumen wrapped by the venous wall in various regions of the kidney. *A*: scattergram in which all measurements were plotted against arterial diameter. The various colors represent the 4 different regions of the kidney: CM, IC, MC, and OC. *B*: independent variable is binned into the 4 regions of the kidney. Values are means \pm SE. *C*: relative frequencies of the proportion of the arterial profile wrapped in each of the 4 regions of the kidney. Statistical analysis is as for Fig 4.

Arteries found at the corticomedullary and inner cortical regions had a greater proportion of their profile surrounded by the vein than did those in the mid- and outer cortex (Fig. 6). For example, 16.9% of arteries found in the corticomedullary and inner cortical regions had their profiles wrapped by 30% or more, while this was the case for only 4.3% of arteries in the mid- and outer cortex (Fig. 6C).

We performed a separate analysis in which the data were partitioned according to whether any of the arterial profile was wrapped by a vein (Fig. 8). The arteriovenous diffusion distance was approximately 10-fold less for those arteries wrapped to any extent by a vein, than for “not wrapped” arteries. Furthermore, the relationship between arterial diameter and diffusion distance, seen when the data were amalgamated (Fig. 5), was completely lost when the data were partitioned into wrapped and not-wrapped vessels (Fig. 8, *A* and *B*). Similarly, the variation in diffusion distance by anatomic region (Fig. 6) was also largely lost when the data were partitioned in this way (Fig. 8, *C* and *D*). A scatterplot of arteriovenous diffusion distance against the proportion of wrapping for individual artery-vein pairs showed that the data clustered into two distinct categories of 1) wrapped vessels, which by definition have short arteriovenous diffusion dis-

tances; and 2) not-wrapped vessels with consistently long diffusion distances (Fig. 9). Both “types” of arteries can have large or small diameters, and can be present in any region of the cortex. However, the proportion of vessels of the two types varies with arterial diameter and cortical region.

Computational Modeling

Spatial variations in renal tissue P_{O_2} . As would be expected, our simulations of P_{O_2} in the vicinity of the four typical artery-vein pairs shown in Fig. 2 demonstrated, in all cases, a region of high P_{O_2} (60–82 mmHg) around the artery (Fig. 10A). Oxygen diffuses from this region to nearby tubules, veins, venules, and capillaries. The P_{O_2} in the tubules outside the region of high P_{O_2} varied from 40 to 50 mmHg. The slightly lower P_{O_2} in the periphery of the field around the larger AV pairs is due to a lesser capillary density around the larger arteries, which we have previously quantified (15). The predicted P_{O_2} in the capillaries and their immediate vicinity was \sim 50 mmHg. The range of tissue P_{O_2} predicted by our model is consistent with that measured experimentally (12, 47, 48).

Oxygen flux in the vicinity of artery-vein pairs. Consistent with an area of relatively high P_{O_2} around all four typical artery-vein pairs, there was significant flux of oxygen from the artery in all cases (Fig. 10B). The oxygen flux from the artery was greatest when there were nearby veins, venules, and capillaries, as shown by the presence of red (high flux) and pale blue (moderate flux) “sparks” around the artery against the dark blue (low flux) background of the renal parenchyma (Fig. 10C). The oxygen flux from wrapped arteries was mainly to the closely associated vein. The oxygen flux from not-wrapped arteries was mainly to capillaries and venules in the immediate vicinity of the artery (compare Figs. 2 and 10, *B* and *C*).

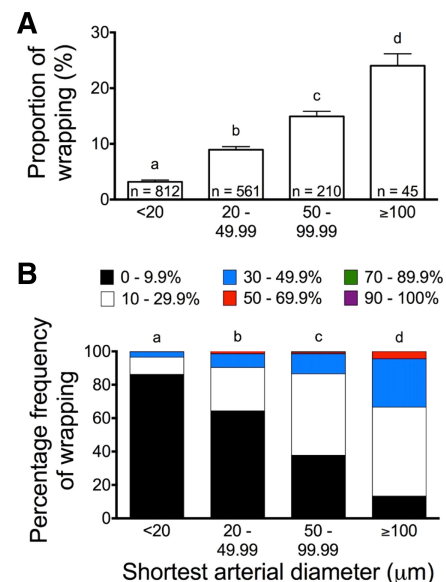
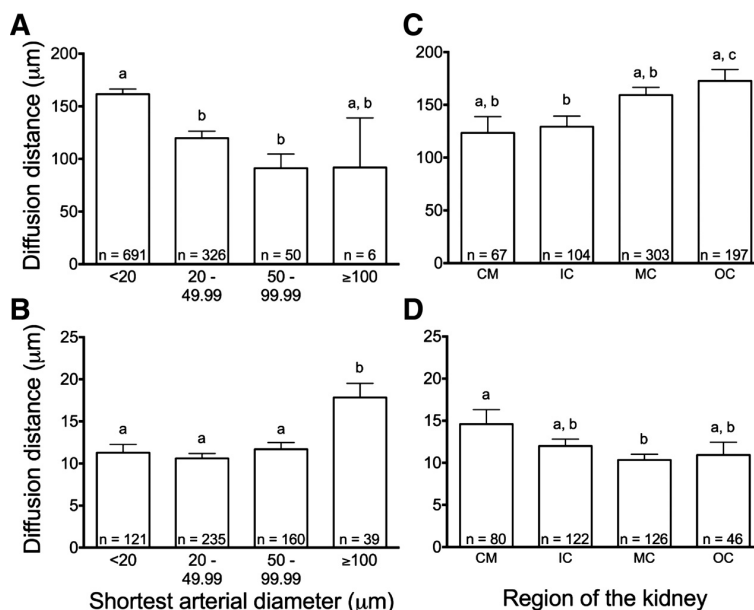


Fig. 7. Proportion of the arterial lumen wrapped by the venous wall as a function of arterial diameter. *A*: independent variable (arterial lumen diameter) is binned in 4 categories: <20, 20–49.9, 50–99.9, and \geq 100 μ m. *B*: relative frequencies of the proportion of the arterial profile wrapped in each of the 4 regions of the kidney. Values are means \pm SE. The statistical analysis is as for Fig 4.

Fig. 8. Diffusion distance for not-wrapped (A and C) and wrapped (B and D) arteries of various sizes and regions of the kidney. A and B: data binned by arterial diameter. C and D: data binned by anatomic region: CM, IC, MC, and OC. Values are means \pm SE. The statistical analysis is as for Fig. 4 (Tukey's test).



Consistent with the predictions from our earlier simulations of oxygen fluxes from idealized artery-vein pairs (15), a significant flux of oxygen from an artery to its closest vein (i.e., AV oxygen shunting) was only observed when at least some of the wall of the artery was wrapped by the wall of the vein (Fig. 11A).

The analysis described above has an important limitation. The results of the simulation shown in Fig. 11A are based on the (unrealistic) assumption that all of the oxygen that diffuses from arteries to nearby capillaries and venules will diffuse back into the tissue further downstream. However, it is likely that some proportion of the oxygen that diffuses from arteries to capillaries, and an even larger proportion of the oxygen that diffuses to venules, will instead be transported to veins by convection. The results of the simulation shown in Fig. 11B are based on the (unrealistic) assumption that all of the oxygen that diffuses from arteries to nearby capillaries and venules is transported to veins by convection. Under these theoretical conditions, wrapped and not-wrapped arteries show similar patterns and magnitudes of oxygen flux (Fig. 11B). When this flux is added to that which occurs directly to the paired vein, significant AV oxygen shunting is observed in all four examples, regardless of whether the artery is wrapped or

not-wrapped (Fig. 11B). The real answer must lie somewhere between these two extreme examples.

Our analysis also indicates that AV oxygen flux is greater (~2-fold), and oxygen flux from vein to tissue is greater (~5-fold, although still negligible) for larger (50–150 μm) than smaller (<50 μm) arteries. The oxygen flux from arteries to the tissue is similarly greater (~2-to 5-fold) for larger (50–150 μm) than smaller (<50 μm) arteries.

DISCUSSION

Previously, we developed a 2D computational model of oxygen flux between artery-vein pairs of idealized geometry (15). Simulations derived from this model provided evidence that diffusion of oxygen from an artery to its paired vein can only be of significant magnitude if the arteriovenous diffusion distance is short (i.e., <50 μm) and at least some of the arterial wall is wrapped by the venous wall (15). Our current anatomic observations indicate that artery-vein pairs with these characteristics are present throughout the preglomerular circulation. However, such close physical relationships between arteries and veins were observed in a much greater proportion of larger arteries than smaller arteries, and arteries in the inner cortex and juxtamedullary region rather than the mid- or outer cortex. Thus conditions required for oxygen to diffuse directly from an artery to its associated vein appear to be predominantly observed in segments of the preglomerular circulation proximal to the divergence of the medullary and cortical circulations. However, our current model simulations provide evidence of another route via which oxygen in renal arterial blood could be shunted to renal venous blood, even in the absence of a close physical relationship between artery-vein pairs. That is, in both small and large arteries that are not wrapped by a vein of similar size, oxygen appears to diffuse to peritubular capillaries and venules in the vicinity of the artery. Some of this oxygen is likely to be delivered to veins by convection. The distinction between wrapped and not-wrapped arteries may therefore not

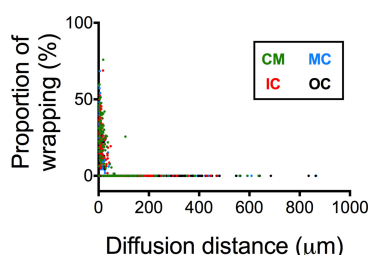


Fig. 9. Scattergram of diffusion distance against proportion of wrapping (%) for arteries in various regions of the kidney.

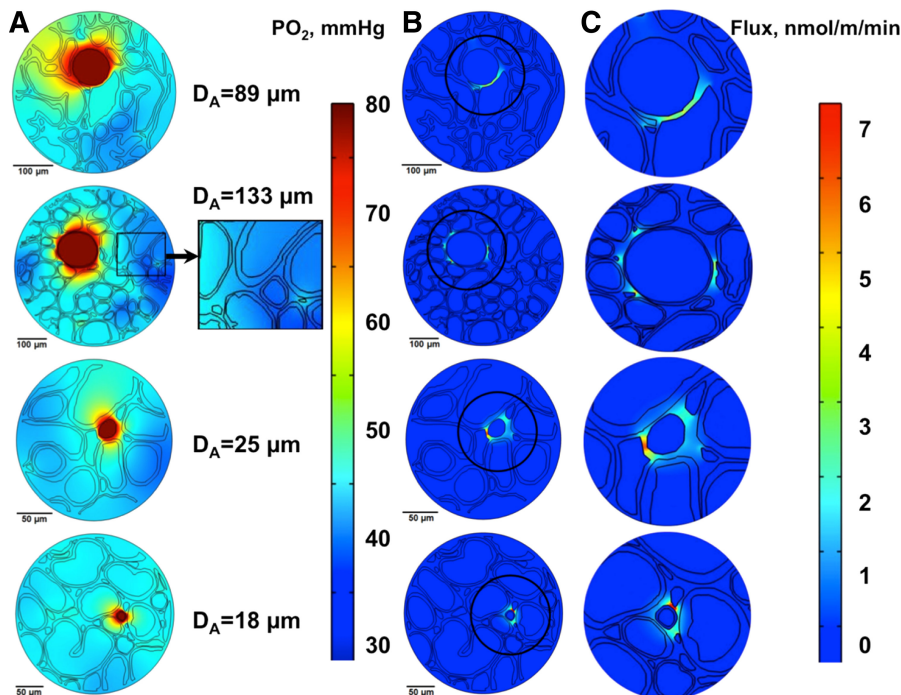


Fig. 10. Variation in tissue oxygen tension (PO_2) and oxygen fluxes for artery-vein pairs of different length scales (based on D_A) and spatial configurations (wrapped/not-wrapped). The vessel pairs correspond to those shown in Fig. 2. From top to bottom, these are large wrapped, large not-wrapped, small wrapped, and small not-wrapped arteries (see Fig. 2). A: variation in tissue PO_2 . B: variation in oxygen flux. Inset on the right of panel A shows a magnified view of a tissue region containing tubules and capillaries as outlined in the PO_2 plot of the large not-wrapped artery. C: magnified views of regions of tissue in the vicinity of the artery as outlined by the circular boundaries (black) in the oxygen flux plots shown in B. COMSOL scaling factors: large wrapped, $\times 59$ (1st row), large not-wrapped, $\times 60$ (2nd row), small wrapped, $\times 30$ (3rd row), and small not-wrapped, $\times 30$ (4th row).

be as important as we initially proposed (15). Thus anatomic conditions favorable to AV oxygen shunting may be present throughout the cortical circulation. We propose that in more proximal vessels, mainly those common to the cortical and medullary circulations, AV oxygen shunting may be dominated by direct diffusion of oxygen from an artery to its closely associated vein. In more distal parts of the cortical circulation, mainly after its divergence from the medullary circulation, oxygen shunting may be dominated by diffusion of oxygen from arteries to capillaries and venules.

Our current anatomic observations confirm and extend those of our previous study (15). In that study, we measured arteriovenous diffusion distance by light microscopy in a relatively small sample of 82 artery-vein pairs. This approach was limited both in terms of the small sample size and by the fact that identification of veins was hindered by the lack of a method to specifically label all vascular elements. To overcome the limitation of sample size, our previous study also employed the data set generated by Nordsletten and colleagues (30) from microcomputed tomography of the vasculature of a rat kidney that had been filled with Microfil. This allowed us to determine arteriovenous diffusion distances across 5,260 vessel profiles. However, these data were limited both because of the potential confounding effects of shrinkage of Microfil (28), and because the radial geometry of this data set had been converted to circular profiles (15). To overcome these limitations, in the current study we were able to identify 1,628 artery-vein pairs from six different kidneys using light microscopy. Importantly, vascular elements were clearly labeled by the presence of Microfil. The size and resolution of these data set allow us to draw conclusions, regarding the characteristic arrangements of arteries and veins in the kidney, with considerable confidence.

The present findings demonstrate that the mean absolute diffusion distance, between arteries and veins, progressively increased as arterial diameter decreased. Furthermore, the mean percentage of the arterial wall wrapped by the wall of the corresponding vein progressively diminished as arterial diameter decreased. Taken at face value, these data might suggest that the intimacy of arteries and veins progressively decreases from proximal to distal segments of the preglomerular circulation. However, we believe these mean data may be potentially misleading. Rather, our interpretation is that the geometric relationships between arteries and veins in the kidney may be simplified into two types of vessel pairs, the relative abundance of which differs according to arterial diameter and anatomic region of the kidney. The first type is characterized by arteries that are at least partially wrapped by their corresponding vein and so by definition have short arteriovenous diffusion distances (~ 10 – $15 \mu\text{m}$). The second type is characterized by arteries that are not wrapped by their corresponding vein and uniformly have much longer arteriovenous diffusion distances (~ 100 – $200 \mu\text{m}$). Our argument relies on the following logic. First, even 13.8% of arteries of $<20 \mu\text{m}$ diameter had $>10\%$ of their circumference wrapped by the corresponding vein. Consistent with this observation, the arteriovenous diffusion distance was $<50 \mu\text{m}$ for 28.3% of arteries with a diameter of $<20 \mu\text{m}$. Second, when arteries were binned into those that were wrapped and those that were not, the relationship between arterial diameter and diffusion distance, and the relationship between anatomic region of the kidney and diffusion distance, that were clearly evident in the amalgamated dataset, were both largely lost. Third, a scatterplot of the relationship between diffusion distance and proportion of wrapping revealed two distinct clusters of data.

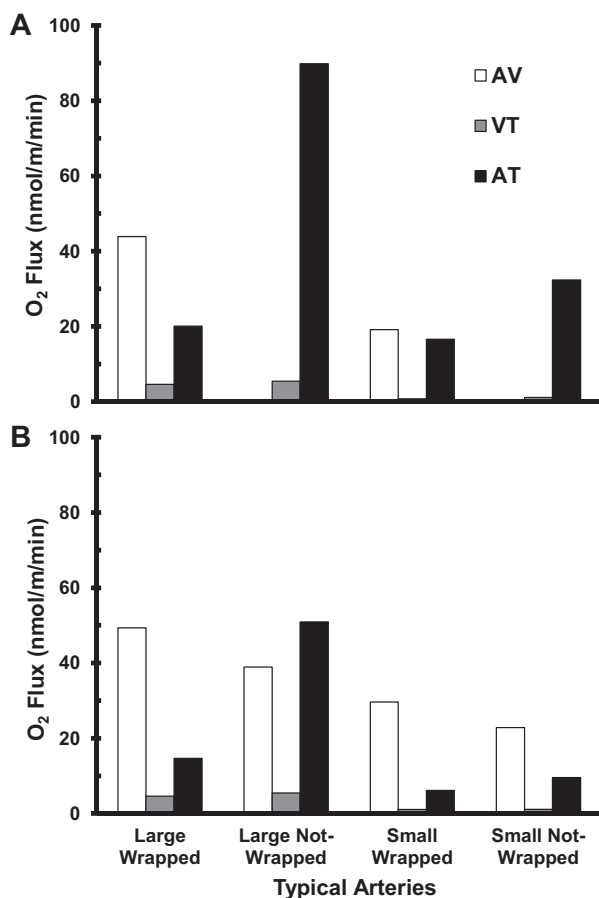


Fig. 11. Quantification of oxygen diffusion in the vicinity of the 4 typical arteries shown in Figs 2 and 10. *A*: effects of typical geometries of artery-vein pairs on the flux of oxygen from artery to vein (AV), vein to tissue (VT), and artery to tissue (AT), when all the capillaries and venules in the computational domain are a part of the renal tissue for post-process calculations of oxygen fluxes. *B*: predicted oxygen fluxes, when in addition to the representative vein, the capillaries and venules receiving high oxygen fluxes from the representative artery are considered as part of the representative venous vasculature for post-process calculations of oxygen fluxes.

Our longer-term aim is to generate a pseudo-3D model of oxygen transport in the renal cortex that can quantify oxygen diffusion from arteries to veins and tissue along the course of the circulation, and thus convection of oxygen to the cortical peritubular capillaries and vasa recta of the medulla. Our ability to now simplify our understanding of the geometry of artery-vein pairs in the kidney to a concept of two types of arrangements has important implications for the generation of such a model. Critically, it should allow us to quantify oxygen diffusion in only a limited number of tissue cross sections. In a multiscale model, we could then vary the relative proportions of these cross sections at the various branching levels of the renal circulation. As a first step in this process, we modeled oxygen diffusion in four typical artery-vein pairs that differed according to arterial diameter (small, large) and degree of wrapping (wrapped, not wrapped).

As we might have expected from our previous study of oxygen diffusion between idealized artery-vein pairs (15),

significant diffusion of oxygen from an artery to its associated paired vein only occurred if the vein wrapped at least part of the wall of the artery. This phenomenon was largely independent of arterial diameter, although oxygen flux from artery to vein was greater for larger than smaller vessels. We also observed significant diffusion of oxygen from not-wrapped arteries to capillaries and venules in the immediate vicinity of the arterial wall. This phenomenon has been observed experimentally in skeletal muscle (9, 23) and subjected to considerable scrutiny through development of computational models (16, 21, 38, 41). In the renal cortex, it may sustain oxygen shunting in smaller arteries in the mid- and outer cortex because 1) these are less likely to be wrapped by a vein than their larger counterparts in the inner cortex and corticomedullary border, and 2) capillary density in the immediate vicinity of renal arteries is greater for smaller than larger arteries (15). We are currently unable to quantify the contribution of this putative mechanism to AV oxygen shunting. This limitation arises because we cannot determine the relative proportions, of the oxygen that diffuses from arteries to capillaries and venules, that diffuse back into renal tissue vs. that which is transported by convection to renal veins.

We must acknowledge some further limitations of our current study. Our computational model is limited by the presence of some unknown quantities. For example, there is considerable controversy as to the level of oxygen consumption by the arterial wall and its consequent impact on the delivery of oxygen from arteries to surrounding vessels and tissue (36, 43–45). In the current study, we do not include oxygen consumption in the vascular wall. In supplementary analyses (data not shown), we examined the impact of oxygen consumption by the arterial wall on AV shunting and oxygen fluxes in the four tissue cross sections shown in Figs. 2 and 10. This was done by incorporating, in our model, the vascular wall oxygen consumption term from earlier computational studies of vascular oxygen transport (4, 7). Incorporation of arterial wall oxygen consumption had minimal impact on the distributions of tissue oxygen concentration and oxygen flux (<0.05% difference). It should also be noted that oxygen fluxes from arterioles that have been measured experimentally tend to be an order of magnitude greater than those generated by computational models (37). Furthermore, our model does not incorporate the potential for heterogeneity of oxygen diffusion coefficients across various renal tissues, due to lack of reliable experimental data. It has been suggested that tissue microstructure plays a crucial role in tissue oxygenation (17). We also assumed that oxygen is well mixed in the intravascular space, so our model neglects intraluminal resistance to oxygen transport (20). Additional analysis of intraluminal resistances to oxygen transport (data not shown) revealed negligible intraluminal gradients in P_{O_2} (~2% difference between the average luminal and vessel wall P_{O_2}). Finally, we cannot exclude the possibility of incomplete filling of capillaries and venules by Microfil, which may have led to underestimation of oxygen flux from arteries. Thus the oxygen fluxes computed in our current work, although they provide qualitative insights into the diffusion of oxygen in the vicinity of artery-vein pairs in the renal cortex, may not be quantitatively accurate.

We must also concede that our measures of vascular geometry could be biased. The model does not use any specific geometrical approach to account for the complex 3D capillary

networks that service the tortuous sections of the tubules represented in 2D. Instead, it relies on a relationship between VO_2 and tubule aspect ratio shown in Fig. 3B. This relationship is based on a simple geometrical arrangement of a parallel capillary and tubule to account for the imbalance in oxygen source and sink in a 2D representation of the actual 3D geometry. Ideally, we would have used 3D reconstructions of the entire circulation of the rat kidney to quantify the intimacy of artery-vein pairs. This would enable us to follow the circulation and be certain of which vein corresponds to which artery. Furthermore, we would not be limited by plane of section as we are with light microscopy. Such information could, at least theoretically, be obtained from microcomputed tomography of the renal vasculature after perfusion with Microfil. Our ongoing studies are aimed at generating this information using synchrotron radiation. Nevertheless, such 3D reconstructions of the rat renal circulation would be limited to only the vasculature; parenchymal elements such as tubules would not be visualized. Thus, to model oxygen flux between vessel pairs, as well as oxygen flux from vessels to renal tissue, we required information regarding the spatial arrangement of tubular elements, which is best generated by light microscopy.

In conclusion, our current findings suggest that the close physical relationship between arteries and veins in the kidney, that is obligatory for direct diffusion of oxygen from arterial to venous blood, is far more prominent in the proximal than distal segments of the renal circulation. These proximal segments likely include arteries that supply blood to the renal medulla (i.e., interlobar, arcuate, and proximal interlobular arteries). Quantitatively significant AV oxygen shunting in the proximal preglomerular circulation could explain the phenomenon of medullary hypoxia during cortical ischemia, even when medullary perfusion is well maintained (35). However, our current findings also suggest that, in the absence of a close physical relationship between an artery and a paired vein, oxygen can diffuse from arterial blood to surrounding periarteriolar capillaries and venules. Some of this oxygen will diffuse back into renal tissue, but some will likely be transported to veins by convection and so contribute to AV oxygen shunting. Our current and previous (15) anatomic observations indicate that this phenomenon is likely to be most prominent in the smaller arteries in the distal cortical circulation, after the divergence of the medullary circulation (e.g., distal interlobular arteries and perhaps afferent and/or efferent arterioles). Our findings do not allow us to estimate the relative quantities of oxygen that are shunted by these two related mechanisms, or their impact on renal oxygenation under physiological and pathological conditions. However, they have allowed us to develop a simplified understanding of the nature of the relationships between afferent (arteries) and efferent (veins, venules, and periarteriolar capillaries) vessels in the kidney. That is, arteries appear to be largely divisible into two “types,” characterized by the presence or absence of a close physical relationship with a paired vein. Our current findings show how the relative proportions of these vessel types change throughout the renal circulation. They also provide an assessment of diffusive oxygen transport in the vicinity of arteries of these types. Armed with this information, and a 1D model of oxygen convection and diffusion in the preglomerular circulation that we developed previously (14), we can now turn our attention to the construction of a pseudo-3D computational model of oxygen diffusion from

arteries in the rat kidney. Such a model should allow quantification of AV oxygen shunting along the course of the preglomerular circulation and estimation of how this changes under physiological and pathophysiological conditions.

ACKNOWLEDGMENTS

The authors thank the staff at the Monash Histology Platform for assistance.

GRANTS

This work is supported by grants from the National Health and Medical Research Council of Australia (606601 and 1024575), the Australian Research Council (DP140103045), and the National Heart Foundation of Australia (CR 07M3337).

DISCLOSURES

No conflicts of interest, financial or otherwise, are declared by the authors.

AUTHOR CONTRIBUTIONS

Author contributions: J.P.N., M.M.K., B.S.G., J.T.P., D.W.S., J.F.B., and R.G.E. provided conception and design of research; J.P.N., S.K., and M.M.K. performed experiments; J.P.N., S.K., and J.L. analyzed data; J.P.N., S.K., M.M.K., B.S.G., J.T.P., D.W.S., and R.G.E. interpreted results of experiments; J.P.N. and S.K. prepared figures; J.P.N., S.K., and R.G.E. drafted manuscript; J.P.N., S.K., M.M.K., B.S.G., J.T.P., D.W.S., J.L., J.F.B., and R.G.E. edited and revised manuscript; J.P.N., S.K., M.M.K., B.S.G., J.T.P., D.W.S., J.L., J.F.B., and R.G.E. approved final version of manuscript.

REFERENCES

1. Aird WC. Phenotypic heterogeneity of the endothelium: II. Representative vascular beds. *Circ Res* 100: 174–190, 2007.
2. Armitage P. Tests for linear trends in proportions and frequencies. *Biometrics* 11: 375–386, 1955.
3. Bertram JF. Analyzing renal glomeruli with the new stereology. *Int Rev Cytol* 161: 111–172, 1995.
4. Buerk DG, Lamkin-Kennard K, Jaron D. Modeling the influence of superoxide dismutase on superoxide and nitric oxide interactions, including reversible inhibition of oxygen consumption. *Free Radic Biol Med* 34: 1488–1503, 2003.
5. Chen J, Edwards A, Layton AT. A mathematical model of O_2 transport in the rat outer medulla. II. Impact of outer medullary architecture. *Am J Physiol Renal Physiol* 297: F537–F548, 2009.
6. Chen J, Layton AT, Edwards A. A mathematical model of O_2 transport in the rat outer medulla. I. Model formulation and baseline results. *Am J Physiol Renal Physiol* 297: F517–F536, 2009.
7. Chen X, Jaron D, Barbee KA, Buerk DG. The influence of radial RBC distribution, blood velocity profiles, and glycocalyx on coupled NO/O_2 transport. *J Appl Physiol* 100: 482–492, 2006.
8. Cochran WG. Some methods for strengthening the common χ^2 tests. *Biometrics* 10: 417–451, 1954.
9. Ellsworth ML, Pittman RN. Arterioles supply oxygen to capillaries by diffusion as well as by convection. *Am J Physiol Heart Circ Physiol* 258: H1240–H1243, 1990.
10. Evans RG, Eppel GA, Anderson WP, Denton KM. Mechanisms underlying the differential control of blood flow in the renal medulla and cortex. *J Hypertens* 22: 1439–1451, 2004.
11. Evans RG, Gardiner BS, Smith DW, O'Connor PM. Intrarenal oxygenation: unique challenges and the biophysical basis of homeostasis. *Am J Physiol Renal Physiol* 295: F1259–F1270, 2008.
12. Evans RG, Goddard D, Eppel GA, Connor PM. Factors that render the kidney susceptible to tissue hypoxia in hypoxemia. *Am J Physiol Regul Integr Comp Physiol* 300: R931–R940, 2011.
13. Evans RG, Harrop GK, Ngo JP, Ow CP, O'Connor PM. Basal renal O_2 consumption and the efficiency of O_2 utilization for Na^+ reabsorption. *Am J Physiol Renal Physiol* 306: F551–F560, 2014.
14. Gardiner BS, Smith DW, O'Connor PM, Evans RG. A mathematical model of diffusional shunting of oxygen from arteries to veins in the kidney. *Am J Physiol Renal Physiol* 300: F1339–F1352, 2011.
15. Gardiner BS, Thompson SL, Ngo JP, Smith DW, Abdelkader A, Broughton BR, Bertram JF, Evans RG. Diffusive oxygen shunting between vessels in the preglomerular renal vasculature: anatomic obser-

- variations and computational modeling. *Am J Physiol Renal Physiol* 303: F605–F618, 2012.
16. **Goldman D.** Theoretical models of microvascular oxygen transport to tissue. *Microcirculation* 15: 795–811, 2008.
 17. **Goldman D, Popel AS.** A computational study of the effect of capillary network anastomoses and tortuosity on oxygen transport. *J Theor Biol* 206: 181–194, 2000.
 18. **Gundersen HJ, Bagger P, Bendtsen TF, Evans SM, Korbo L, Marcussen N, Møller A, Nielsen K, Nyengaard JR, Pakkenberg B, Sørensen FB, Vesterby A, West MJ.** The new stereological tools: disector, fractionator, nucleator and point sampled intercepts and their use in pathological research and diagnosis. *APMIS* 96: 857–881, 1988.
 19. **Hayashi K, Epstein M, Loutzenhiser R.** Enhanced myogenic responsiveness of renal interlobular arteries in spontaneously hypertensive rats. *Hypertension* 19: 153–160, 1992.
 20. **Hellums JD, Nair PK, Huang NS, Ohshima N.** Simulation of intraluminal gas transport processes in the microcirculation. *Ann Biomed Eng* 24: 1–24, 1996.
 21. **Hsu R, Secomb TW.** Analysis of oxygen exchange between arterioles and surrounding capillary-perfused tissue. *J Biomech Eng* 114: 227–231, 1992.
 22. **Kett MM, Alcorn D, Bertram JF, Anderson WP.** Enalapril does not prevent renal arterial hypertrophy in spontaneously hypertensive rats. *Hypertension* 25: 335–342, 1995.
 23. **Kobayashi H, Takizawa N.** Imaging of oxygen transfer among microvessels of rat cremaster muscle. *Circulation* 105: 1713–1719, 2002.
 24. **Kriz W, Bankir L.** A standard nomenclature for structures of the kidney. The Renal Commission of the International Union of Physiological Sciences (IUPS). *Kidney Int* 33: 1–7, 1988.
 25. **Levy MN, Imperial ES.** Oxygen shunting in renal cortical and medullary capillaries. *Am J Physiol* 200: 159–162, 1961.
 26. **Ludbrook J.** Multiple comparison procedures updated. *Clin Exp Pharmacol Physiol* 25: 1032–1037, 1998.
 27. **Ludbrook J.** On making multiple comparisons in clinical and experimental pharmacology and physiology. *Clin Exp Pharmacol Physiol* 18: 379–392, 1991.
 28. **Møller J, Robertsen K, Hansen ES.** Severe shrinkage of Microfil during tissue clearing with the Spalteholz technique. *J Microsc* 174: 125–127, 1994.
 29. **Mulligan-Kehoe MJ, Simons M.** Vasa vasorum in normal and diseased arteries. *Circulation* 129: 2557–2566, 2014.
 30. **Nordsletten DA, Blackett S, Bentley MD, Ritman EL, Smith NP.** Structural morphology of renal vasculature. *Am J Physiol Heart Circ Physiol* 291: H296–H309, 2006.
 31. **Norman JT, Stidwill R, Singer M, Fine LG.** Angiotensin II blockade augments renal cortical microvascular pO₂ indicating a novel, potentially renoprotective action. *Nephron Physiol* 94: 39–46, 2003.
 32. **Nyengaard JR.** Stereologic methods and their application in kidney research. *J Am Soc Nephrol* 10: 1100–1123, 1999.
 33. **O'Connor PM, Anderson WP, Kett MM, Evans RG.** Renal preglomerular arterial-venous O₂ shunting is a structural anti-oxidant defence mechanism of the renal cortex. *Clin Exp Pharmacol Physiol* 33: 637–641, 2006.
 34. **O'Connor PM, Evans RG.** Structural antioxidant defense mechanisms in the mammalian and nonmammalian kidney: different solutions to the same problem? *Am J Physiol Regul Integr Comp Physiol* 299: R723–R727, 2010.
 35. **O'Connor PM, Kett MM, Anderson WP, Evans RG.** Renal medullary tissue oxygenation is dependent on both cortical and medullary blood flow. *Am J Physiol Renal Physiol* 290: F688–F694, 2006.
 36. **Pittman RN.** Oxygen gradients in the microcirculation. *Acta Physiol (Oxf)* 202: 311–322, 2011.
 37. **Pittman RN.** Oxygen transport in the microcirculation and its regulation. *Microcirculation* 20: 117–137, 2013.
 38. **Popel AS, Pittman RN, Ellsworth ML.** Rate of oxygen loss from arterioles is an order of magnitude higher than expected. *Am J Physiol Heart Circ Physiol* 256: H921–H924, 1989.
 39. **Rhodin JA.** Ultrastructure of mammalian venous capillaries, venules, and small collecting veins. *J Ultrastruct Res* 25: 452–500, 1968.
 40. **Schurek HJ, Jost U, Baumgartl H, Bertram H, Heckmann U.** Evidence for a preglomerular oxygen diffusion shunt in rat renal cortex. *Am J Physiol Renal Fluid Electrolyte Physiol* 259: F910–F915, 1990.
 41. **Secomb TW, Hsu R.** Simulation of O₂ transport in skeletal muscle: diffusive exchange between arterioles and capillaries. *Am J Physiol Heart Circ Physiol* 267: H1214–H1221, 1994.
 42. **Smeda JS, Lee RM, Forrest JB.** Structural and reactivity alterations of the renal vasculature of spontaneously hypertensive rats prior to and during established hypertension. *Circ Res* 63: 518–533, 1988.
 43. **Tsai AG, Friesenecker B, Cabrales P, Hangai-Hoger N, Intaglietta M.** The vascular wall as a regulator of tissue oxygenation. *Curr Opin Nephrol Hypertens* 15: 67–71, 2006.
 44. **Tsai AG, Friesenecker B, Mazzoni MC, Kerger H, Buerk DG, Johnson PC, Intaglietta M.** Microvascular and tissue oxygen gradients in the rat mesentery. *Proc Natl Acad Sci USA* 95: 6590–6595, 1998.
 45. **Vadapalli A, Pittman RN, Popel AS.** Estimating oxygen transport resistance of the microvascular wall. *Am J Physiol Heart Circ Physiol* 279: H657–H671, 2000.
 46. **Weinstein SW, Szyjewicz J.** Superficial nephron tubular-vascular relationships in the rat kidney. *Am J Physiol Renal Fluid Electrolyte Physiol* 234: F207–F214, 1978.
 47. **Welch WJ, Baumgartl H, Lubbers D, Wilcox CS.** Nephron pO₂ and renal oxygen usage in the hypertensive rat kidney. *Kidney Int* 59: 230–237, 2001.
 48. **Wilcox CS, Palm F, Welch WJ.** Renal oxygenation and function of the rat kidney: effects of inspired oxygen and preglomerular oxygen shunting. *Adv Exp Med Biol* 765: 329–334, 2013.

7 | POTENTIAL IMPACT OF VASCULAR GEOMETRY ON ARTERIAL- TO-VEIN OXYGEN SHUNTING ACROSS THE BRANCHING LEVELS OF THE RENAL CORTICAL CIRCULATION

7.1 ABSTRACT

Arterial-to-venous (AV) oxygen shunting in the kidney might limit oxygen delivery to renal tissue. However, the significance of AV shunting remains a matter of controversy, chiefly because of the limited quantitative information regarding the geometry of artery-vein pairs in the kidney, and how this varies throughout the various branching levels of the cortical vasculature. We previously developed a dataset defining the relationship between characteristics of the cross-sectional geometry of artery-vein pairs and arterial diameter in the kidney of the rat. The key parameters that quantify the cross-sectional anatomy of artery-vein pairs include the separation (diffusion) distance (h) between the artery and its neighboring vein and the degree to which the venous wall wraps around the arterial wall (wrapping factor γ). A so-called mass transfer coefficient (MTC) can be used to capture the combined effect of these two geometrical parameters, along with the diffusion coefficient. Thus the MTC quantifies how easily diffusive transport of oxygen can occur between neighboring vessels. In the current study, we first estimated the degree of shrinkage of Microfil® expected to arise from the processing of kidney tissue for micro-computed tomography (micro-CT), as employed in the generation of the dataset, of 11 branching (Strahler) orders of the pre-glomerular circulation of the rat kidney, by Nordsletten and colleagues (22%). This allowed us to harmonize their dataset with our dataset derived from light microscopy. We then compared two methods for assigning arteries to Strahler orders. A statistical approach was employed initially, based on 95% tolerance limits. The second method defined the limits of each Strahler order as the mid-point between the mean diameters of each Strahler order. The statistical approach permitted each artery to be categorized into one or more Strahler orders. The ‘mid-point method’ provided a unique assignment to a Strahler order for each vessel, while the statistical approach led to some overlap in Strahler orders, so some vessels were assigned two or more Strahler order labels. These data were then used to quantify the shunting capacity of various cross-sectional anatomy of artery-vein pairs, by calculating MTCs, for each of these branching orders, both for individual artery-vein pairs and for the entire network of artery-vein pairs at each Strahler order. We employed two methods for calculating MTCs. The first was the standard product of the diffusion coefficient of oxygen and the proportion of the arterial profile wrapped by a vein, divided by diffusion distance. The second method removed the effect of vessel length at each branching level on surface area. Once individual MTCs were calculated, we then calculated the effective mass transfer area ($SA_{\text{effective}}$) at each Strahler order, which takes into account the total number of vessels in each Strahler order. We took two approaches in the analysis of MTCs and $SA_{\text{effective}}$: either (i) all vessels were analyzed or (ii) only wrapped arteries were analyzed. The data reveal a trend for

a biphasic relationship between the MTCs for individual artery-vein pairs and Strahler order. $SA_{\text{effective}}$ increased as Strahler order increased. Total mass flux per unit driving force, which is dependent on the product of MTC, the $SA_{\text{effective}}$, and the total number of vessels, was calculated to determine the mass transferred at each Strahler order for a unit difference in concentration between arteries and veins. Whether all or only ‘wrapped’ vessels were analyzed, estimated total mass flux per unit driving force was almost the same, and found to be highest at Strahler order 1. Apart from Strahler orders 0 and 1, there was a trend for total mass flux per unit driving force to decrease as Strahler order increased. Total mass flux per unit driving force was consistently and significantly higher in orders 0-4 compared to orders 5-9. Thus, if AV oxygen shunting is quantitatively significant, it most likely occurs in the mid-to-distal parts of the renal circulation (i.e. Strahler orders 0-4), which includes the middle portions of the interlobular arteries and efferent arterioles. The quantification of the actual mass flux at each Strahler order depends on knowing the AV concentration difference driving oxygen mass transfer.

7.2 INTRODUCTION

A number of lines of experimental evidence indicate that a proportion of the oxygen delivered to the kidney in the renal artery never reaches renal tissue, but instead diffuses from arterial to venous segments of the cortical vasculature (9, 10, 22). Nevertheless, the biological significance of arterial-to-venous (AV) oxygen shunting in the renal cortex remains a matter of controversy (4). It is not currently possible to determine the quantitative significance of AV oxygen shunting experimentally. Thus, we must rely on computational models of renal oxygen transport to study this phenomenon.

Gardiner *et al* (6) and more recently Olgac and Kurtcuoglu (16) used the eleven defined branching orders of the renal circulation of the rat, described by Nordsletten *et al* (14), to generate mathematical models of oxygen transport in the renal cortex. These representative branching levels of arteries and veins are termed ‘Strahler orders’. The model by Gardiner *et al* (6) was calibrated by adjusting the mass transfer coefficient (MTC), such that the predicted cortical tissue oxygen tension was consistent with experimental measurements by Welch *et al* (22). The model by Gardiner *et al* (6) was based on the assumption that the AV pair cross-sectional anatomy (i.e. separation distance and proportion of arterial profile wrapped by a vein) is uniform along all the branching levels of the cortical circulation. The simulations of Gardiner *et al* predicted that AV oxygen shunting is quantitatively significant, being of the same order of magnitude as total renal oxygen consumption (6). In contrast, Olgac and Kurtcuoglu’s model, which employed the homogeneous tissue model of Salathé (18), predicted

that AV oxygen shunting is quantitatively insignificant (16). Oxygen transport in these models (6, 16) is mathematically represented by advection-diffusion equations, which satisfy mass conservation requirements. Oxygen shunting in these models is represented by the diffusion term. Mathematically, the diffusion term is in the form of Fick's first law of diffusion (1). Critically, both models are limited by the fact that they do not include realistic representations of the cross sectional geometry of artery-vein pairs (4), which is likely a critical determinant of peri-arteriolar diffusion of oxygen (7, 21). For example, our computational model predicted that direct diffusion of oxygen from an artery to a vein can be significant only if the distance across which oxygen must diffuse is exceedingly small ($< 50 \mu\text{m}$) and there is a complete absence of oxygen sinks (i.e. capillaries and tubules) between the two vessels (13). Indeed, in the kidney, there is a proportion of artery-vein pairs that are intimately associated, such that the arterial wall is partially enveloped by the associated vein (termed 'wrapping'), and no capillaries or tubules are found in the space between the two vessels. If AV oxygen shunting is quantitatively significant, it likely occurs predominantly between these 'wrapped' vessels.

We recently quantified the proportion of wrapped and non-wrapped vessels within the cortical circulation, and how these proportions vary according to arterial caliber (13). The objective of the current study was to obtain a realistic quantitative representation of artery-vein pair cross-sectional geometry, which can subsequently be incorporated into computational models. Therefore, we developed and compared two methods for assigning arteries of known diameter, identified in our previous study (Chapter 6) (13), to the Strahler orders defined by Nordsletten *et al* (14). We also used two equations for determining the MTC for individual vessel pairs. We then generated estimates of effective mass transfer area ($\text{SA}_{\text{effective}}$) at each Strahler order. The data we generate can subsequently be incorporated into computational models of oxygen transport in the rat renal circulation (e.g. the model by Gardiner *et al* (6)) to permit estimation of the magnitude of AV oxygen diffusion along each order of vascular branching.

7.3 METHODS

7.3.1 Overview

The dataset generated by Nordsletten *et al* (14) characterized arteries and veins within the renal cortical circulation according to their branching level, with Strahler order 0 representing the very smallest vessels (e.g. afferent arterioles) and Strahler order 10 representing the main renal artery/vein (14). The dataset was derived from a micro-computed tomographic (micro-

CT) analysis of a single kidney of a rat in which the vasculature was filled with a radio-opaque silicon rubber material (Microfil®) (5). In preparation for micro-CT, the kidney was incubated in 70% ethanol, graded solutions of glycerol, and then acetone, before being embedded in resin (5). This process would be expected to result in shrinkage of Microfil® (12). Therefore, we first performed a bench-top analysis, in which cylinders of Microfil® were exposed to the solutions used by Garcia-Sanz *et al* (5), to allow determination of the degree of shrinkage expected in their studies. This procedure enabled us to adjust the mean and standard deviation of the radius for each arterial Strahler order, to account for this shrinkage. Ranges for the radius of each Strahler order were then generated, using two different methods (see below), so that each of the 1,628 arteries identified in our previous light microscopic analysis (13) could be binned into Strahler orders. MTCs were then calculated, again using two different methods, for individual vessel pairs. Then, $SA_{\text{effective}}$ was also calculated for each Strahler order.

7.3.2 Shrinkage of Microfil® following exposure to ethanol, glycerol and acetone

To account for the shrinkage of Microfil®, the values reported by Nordsletten *et al* (14) were divided by a correction factor to obtain an estimate of the original radius of Microfil® before shrinkage. To determine the correction factor, polyethylene (PE) catheters of various sizes were filled with Microfil® (MV-120, Flow Tech Inc., MA, USA). The catheter sizes included PE 55 (nominal inner diameter (ID) = 0.80 mm) (Critchley Electrical Products Pty, NSW, Australia), 20 (nominal ID = 0.38 mm), 90 (nominal ID = 0.86 mm), 160 (nominal ID = 1.14 mm) and 200 (nominal ID = 1.40 mm) (Becton Dickinson and Company, MD, USA). Once the Microfil® was prepared, the silicone solution was injected through the PE tubing and the ends of the tubing were then clamped. The Microfil® was left to set for at least 3 days, after which the catheters were cut into smaller segments, each 5 cm in length. The Microfil® cylinders were carefully removed from the PE tubing using a syringe and needles (gauges 18, 21, 23, and 25; Terumo, Tokyo, Japan) to expel them from the tubes. Then, the diameter of the Microfil® cylinders were measured. Mimicking the methods used by Garcia-Sanz *et al* (5), the Microfil® cylinders were immersed in 70% ethanol, and 30%, 50%, 75% and 100% glycerol for 24 hours each. The Microfil® cylinders were then immersed in 100% acetone for 1 minute. Following immersion in 100% acetone, the diameter of Microfil® cylinders were re-measured. Measurements of diameter were obtained by taking photographs of the Microfil® cylinders using a microscope (Leica DFC450C). The diameter of each Microfil® cylinder was then measured using ImageJ (<https://imagej.nih.gov/ij/>). Care was taken to keep

the Microfil® cylinders slack when measuring the diameter since any stretching would affect our measurements. Note that this analysis is based on the assumption that Microfil® is a homogeneous medium, so shrinks equally in all directions.

7.3.3 Estimation of the shrinkage of Microfil®

To calculate the original mean radius of each Strahler order, we used the following equation obtained from regression analysis (See Results section):

$$\text{Original radius} = \text{measured radius} / 0.78 \mu\text{m}$$

where *original radius* is the arterial radius corrected for shrinkage (i.e. true vessel radius), and *measured radius* is the radius of the vessel after shrinkage (i.e. the radius reported by Nordsletten *et al* (14)).

For example, if Nordsletten *et al* (14) stated that a vessel was 100 μm in radius, the corrected radius would be:

$$\text{Original radius} = 100 / 0.78 \mu\text{m}$$

$$\text{Original radius} = 128.21 \mu\text{m}$$

7.3.4 Methods for assigning arteries to Strahler orders

Two approaches were used. We first used a statistical approach based on 95% tolerance limits. Thus, this method employed overlapping ranges for each Strahler order, so each of the 1,628 arteries could be binned into one or more Strahler orders. The second approach (the ‘mid-point method’) was more stringent in that there was no overlap in the ranges defining each Strahler order. Thus, each of the 1,628 arteries could be binned into only one Strahler order.

7.3.4.1 Statistical method:

Each of the 1,628 arteries identified in our previous study (13) was assigned to one or more Strahler order(s), according to the ranges of radii specified by Nordsletten *et al* (14). Assuming a normal population distribution, 95% tolerance limits were used to identify the likelihood that a single experimental value (greater than 5% probability), was drawn from the population of interest (Table 7.1).

Using the means and standard deviations reported by Nordsletten *et al* (14), we calculated ‘tolerance intervals’ for each Strahler order using the following equation:

$$\bar{x} \pm k_7s$$

where \bar{x} is the mean, s is the standard deviation and k_7 is found in Geigy Scientific Tables (1982), p. 52-53 (3). Table 7.1 in the Results section shows the mean radii for each Strahler order as reported by Nordsletten *et al* (14), as well as the k_7 value for each sample and the calculated tolerance limits.

Using the 7th column of Table 7.1 (tolerance limits & arterial radius corrected for shrinkage), a code was used to scan through the arterial radii provided by our light microscopic study to allocate each arterial vessel to one or more Strahler order(s). Essentially, an artery of radius R would be allocated into a Strahler order provided the following is true:

$$R_{\text{mean-tol}} \leq R \leq R_{\text{mean+tol}}$$

where $R_{\text{mean-tol}}$ and $R_{\text{mean+tol}}$ define the 95% tolerance limits for a given Strahler order in Table 7.1. Using this method, arteries were categorized into one or more Strahler orders.

7.3.4.2 Mid-point method:

Ranges of arterial radius were defined by the radii halfway between the values of corrected arterial radii for each Strahler order (Table 7.1). There were two exceptions to this rule. First, we set the minimum radius as 8.60 μm . Thus any artery with a radius of $\geq 8.60 \mu\text{m}$ but less than the upper limit of Strahler order 0 was assigned to Strahler order 0 (see below). Any arteriole with a radius of $< 8.60 \mu\text{m}$ was excluded from the analysis. Second, the upper limit of Strahler order 9 was not defined because we reasoned that any arterial radii greater than the lower limit of Strahler order 9 has to be assigned to Strahler order 9.

Therefore, calculations of the upper limits for Strahler order 0 and subsequent orders were as follows:

$$\text{Upper limit}_{(\text{SO})} = \frac{\text{Radius}_{(\text{SO}+1)} - \text{Radius}_{(\text{SO})}}{2} \mu\text{m}$$

where SO is the Strahler order of interest and ‘Radius’ is in μm .

For example, to calculate the upper limit for Strahler order 0, we find the mid-point between arterial radii 12.92 and 17.82 μm (the corrected arterial radii for Strahler orders 0 and 1 respectively, found in Table 7.1). Thus:

$$\text{Upper limit}_{(\text{SO}=0)} = \frac{\text{Radius}_{(\text{SO}=1)} + \text{Radius}_{(\text{SO}=0)}}{2} \mu\text{m}$$

$$\text{Upper limit}_{(\text{SO}=0)} = \frac{17.82 + 12.92}{2} \mu\text{m}$$

$$\text{Upper limit}_{(0)} = 15.37 \mu\text{m}$$

The new upper limit for SO = 0 is also the lower limit for SO = 1. Likewise, the upper limit of SO = 1 is also the lower limit of SO = 2 etc.

7.3.5 Calculation of mass-transfer coefficients

The renal circulation, like other vascular beds, includes arterial and venous vessels. These vessels progressively decrease in diameter along the course of the renal cortical circulation while the level of vascular branching increases (6, 14). The variation in vessel diameter and branching along the course of the renal circulation can be represented in a simplified form by a hierarchy of paired cylindrical compartments arranged in a counter-current fashion and connected in series (6). Each compartment consists of an artery and vein. Thus, it was assumed that (i) each arterial compartment has a corresponding venous compartment and (ii) the lengths of the arterial and venous compartments are equal. Both assumptions were also made in our initial modeling study (6). At each compartment, some oxygen diffuses from the artery to its corresponding vein. This phenomenon, also known as AV oxygen shunting, can be characterized by a lumped constant known as the mass transfer coefficient (MTC).

To define MTC, we first considered a cylindrical shaped arterial compartment from a specific branching level with radius 'R' and length 'L' as shown in Figure 7.1.

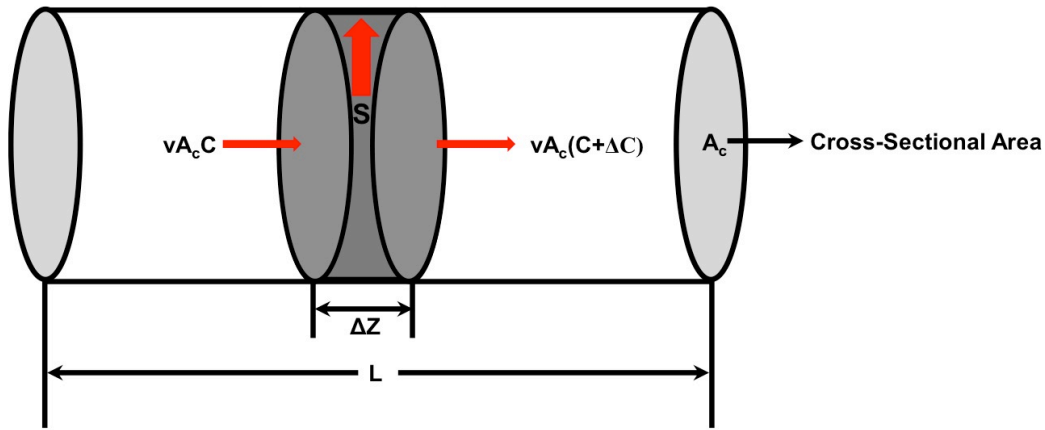


Figure 7.1. A simplified geometrical schematic of a vascular (arterial or venous) compartment corresponding to a specific branching level in the renal cortical circulation. The compartment is in the form of a cylindrical blood vessel with cross-sectional area, A_c and length, L . The parameters v (m/s) and C (moles/m³) represent the average velocity of blood flow in the vascular compartment and the concentration of oxygen, respectively. The red arrows indicate the direction of the blood flow (thin) or oxygen diffusion (thick). The law of mass conservation was applied over a volume element of thickness ΔZ (shaded dark grey region) to derive the governing equation of oxygen transport across the vascular compartment. S (moles/m³/s) represents the amount of oxygen lost (shunted) from the unit volume of the vascular compartment to a paired vascular compartment nearby.

Application of mass conservation over a volume element of thickness ΔZ within the arterial compartment (Fig. 7.1) leads to:

$$vAC|_Z - vAC|_{Z+\Delta Z} = SAA\Delta Z \quad [1]$$

where v (m/s) is the average blood velocity in the arterial compartment, C (moles/m³) is the oxygen concentration and S (moles/m³/s) is the amount of oxygen lost per unit volume of blood per unit time, which is diffused from the curved surface of the volume element. The parameter A (m²) represents the cross sectional area of the arterial compartment and is represented as:

$$A = \pi R^2 \quad [2]$$

where R represents the radius of the arterial vessels (m). Equation [1] can be re-written as:

$$\frac{v(C|_Z - C|_{Z+\Delta Z})}{\Delta Z} = S \quad [3]$$

Equation [3] can be represented in the following form when ΔZ approaches zero:

$$v \frac{\partial C}{\partial Z} = S \quad [4]$$

Equation [4] can be used to calculate the amount of oxygen shunted from one artery to its paired vein. In this case, the term S (moles/m³/s) represents the amount of oxygen shunted per unit volume of blood per unit time from the curved surface of the arterial compartment to its

paired venous compartment. This equivalence can be expressed mathematically represented as (2):

$$S = \frac{D}{hV} A_c \gamma (C_A - C_V) \quad [5]$$

where D (m^2/s) represents the diffusion coefficient of oxygen and A_c (m^2) represents the curved surface area of the arterial compartment. In equation [4] it is assumed that oxygen is shunted through the whole surface area of the arterial compartment. However, from experimental observations, we predict that oxygen is shunted only through a proportion of the arterial wall that is closely wrapped by its paired venous compartment. Here, we introduced a new term γ , which represents the proportion of wrapping of the arterial wall surface by its paired venous compartment. The variable h (m) represents the luminal wall separation distance between the paired arterial and venous compartment. C_A and C_V (moles/m^3) represents the average oxygen concentration of the arterial and its paired venous compartment, respectively. V (m^3) represents the volume of the arterial/venous compartment as applicable.

Multiplying both sides of equation [5] by the volume of the arterial/venous compartment gives the amount of oxygen shunted per unit time (i.e. mass flux expressed in moles/s):

$$S_1 = \frac{D}{h} A_c \gamma (C_A - C_V) \quad [6]$$

where S_1 is the amount of oxygen shunted per unit time. Here, we defined MTC as a diffusion rate constant that relates the oxygen transfer rate (i.e. diffusion coefficient D), the proportion of wrapping (γ) and the luminal separation distance (h) as a single variable. Therefore, for a particular Strahler order at the i^{th} level, MTC can be expressed as:

$$k_{mi} = \frac{D\gamma}{h} \quad [7]$$

where k_{mi} (m/s) is the mass transfer coefficient, D represents the diffusion coefficient for oxygen ($2.8 \times 10^{-9} \text{ m}^2/\text{s}$), γ is the proportion of wrapping (the proportion of arterial lumen surrounded by the vein wall, which is a dimensionless number between 0 and 1), and h is the separation distance (the shortest distance from the arterial lumen to venous lumen in meters). Clearly this MTC (k_{mi}) is high when the proportion of wrapping (γ) is large or when the separation distance (h) is small, as is evident from equation [7].

By replacing relevant terms with k_m , Equation [6] can now be re-written as:

$$S_1 = k_m A_c (C_A - C_V) \quad [8]$$

where k_m (m/s) is the mass transfer coefficient.

The mass transfer coefficient (k_{mi}) in equation [7] takes into account the transport property of oxygen (diffusion coefficient) and geometrical factors representing the artery-vein pair cross-sectional anatomy (γ and h). It can also be advantageous to define MTC independent of the vessel length (i.e. MTC per unit vessel length).

To calculate the mass transfer coefficient per unit length of the arterial compartment (k_{li}) we can simply divide both sides of equation [8] by L :

$$k_{li} = \frac{D\gamma}{hL} \quad [9]$$

where k_{li} (s^{-1}) represents the effective mass transfer coefficient per unit vessel length, while L (m) represents the length of an arterial/venous compartment corresponding to a particular branching level i . The advantage of calculating k_{li} is it allows one to assess the MTC at each Strahler order independent of vessel length. Both equations [7] and [9] were applied to evaluate both MTCs (k_{mi} and k_{li}) for all vessels in Strahler orders 0-9 as defined by the mid-point method. Data on radial geometry of artery-vein pairs from Ngo *et al* (13) were used in the calculations of both k_{mi} and k_{li} .

Alternatively, MTCs between artery-vein pairs can be back-calculated using equation 8 provided the amount of oxygen shunted along the different branching levels of the cortical circulation is known *a priori*. Unfortunately, experimental methods to measure the amount of AV oxygen shunting along the cortical circulation have so far remained elusive. However, Gardiner *et al* (7) developed a two-dimensional computational model to evaluate oxygen mass fluxes (and so MTCs) for oxygen shunting across idealized cross-sectional configurations of artery-vein pairs. These results were employed to estimate the MTCs for the actual artery-vein pairs, based on the actual cross-sections established by our previous light microscopic work (13). These MTCs (calculated from equation [11] below) were then used to validate the MTCs calculated using equation [9].

To do this, all artery-vein pairs from Ngo *et al* (13) were first classified into one of the six configurations presented in Gardiner *et al* (7) (Figs 9C, E, G, H, I & J in Gardiner *et al* (7)). We estimated the amount of AV oxygen shunting for these artery-vein pairs using simulations from a model of oxygen flux shown in Figs 10 and 12 in Gardiner *et al* (7).

To back-calculate k_{li} , the term k_m in equation [8] is replaced with k_{li} and is re-arranged as follows:

$$k_{li} = \frac{S_2}{A_c(C_A - C_V)} \quad [10]$$

Here, S_1 in Equation [8], which is in moles/s, is replaced with S_2 , which is in moles/m/s. The oxygen flux is given per unit vessel length because the model is defined in two-dimensional form (i.e. is independent of vessel length). Equation [10] can be rewritten for a specific artery-vein pair as follows:

$$k_{li} = \frac{S_2}{2\pi RL(C_A - C_V)} \quad [11]$$

where S_2 represents the amount of oxygen shunted over a unit length of an arterial/venous compartment in moles/m/s, as estimated from the results of Gardiner *et al* (7).

7.3.6 Effective mass transfer area

The effective mass transfer area for a particular Strahler order ($SA_{\text{effective}}$) can be calculated by multiplying together: (i) the number of arteries (presented by Nordsletten *et al* (14)), (ii) the length of arteries in that Strahler order (presented by Nordsletten *et al* (14), and applying the correction for shrinkage in this study), (iii) the fraction of vessels in a Strahler order that are ‘wrapped’ (determined from our light microscopic data and based on a non-zero MTC), and (iv) the cross-sectional area of an individual vessel ($2\pi R$, where ‘R’ is the arterial radius).

7.3.7 Statistical analysis

Student’s paired t-test was used to determine whether the diameters of cylinders of Microfil® were altered by chemical processing (i.e. to test the hypothesis that exposure to chemicals led to shrinkage). To quantify the shrinkage, ordinary least products (model II) regression analysis was used to provide a line of best fit forced through the origin (11). Ordinary least products regression was used since this method takes into account experimental error in both the independent (x -axis) and dependent (y -axis) variable (11). The Shapiro-Wilk test was used to determine whether, within each Strahler order, the distributions of arterial diameter, wrapping, and MTC violated normality (20). Because normality was often violated, both the Kruskal-Wallis (non-parametric) (8) and one-way analysis of variance (ANOVA) were employed to determine whether arterial diameter, wrapping or MTC varied with Strahler order. Unless otherwise stated, measures of central tendency and dispersion are presented as mean \pm standard deviation (SD), or median and interquartile range. Statistical analyses were performed using SYSTAT v.13 (Systat Inc, San Jose, CA, USA). In all cases, two-tailed $P \leq 0.05$ was considered statistically significant.

7.4 RESULTS

7.4.1 Shrinkage of Microfil®

Microfil® shrunk as a result of treatment in alcohols. Across 30 Microfil® cylinders of varying diameter, mean diameter reduced from 0.89 ± 0.34 mm to 0.68 ± 0.30 mm (Fig. 7.2A; paired t-test, $P < 0.001$), representing a mean shrinkage of $25.3 \pm 7.8\%$. A line of best fit determined by ordinary least squares regression analysis, forced through the origin, gave a slope of 0.78 with 95% confidence limits (0.76 – 0.81) (Fig. 7.2B). This slope was then used to correct the arterial radii reported by Nordsletten *et al* (14), for each Strahler order, to the arterial radius expected prior to processing of the tissue for micro-CT.

Tolerance limits were generated so that the data we generated by light microscopy could be binned into one or more Strahler order using the statistical method (Table 7.1). The data of Nordsletten *et al* (14) contain information from imaging at both 4- μ m and 20- μ m resolution. Because the 4- μ m dataset is incomplete, we used the 20- μ m data set to calculate tolerance limits and to assign arteries into Strahler orders.

7.4.2 Frequency distribution patterns for the characteristics of arteries binned into Strahler orders

7.4.2.1 Statistical method

For the statistical method for assigning arteries to Strahler orders, a total of 3,973 arteries were binned across 10 Strahler orders. A total of 1,103 arteries were binned into Strahler order 0, 1,603 in Strahler order 1, 7 in Strahler order 3, 12 in Strahler order 4, 153 in Strahler order 5, 124 in Strahler order 6, 189 in Strahler order 7, 27 in Strahler order 8, and 366 in Strahler order 9. Due to the assignment of some arteries into two or more Strahler orders, the total number of binned arteries was considerably greater than the 1,628 original observations in our light microscopic study.

Analyses of distribution patterns were conducted for vessels assigned to Strahler orders using tolerance limits. The distribution patterns for all of the measured characteristics of artery-vein pairs deviated significantly from normality. For example, the distribution of arterial diameter within each Strahler order deviated significantly from normality ($P \leq 0.001$) for all Strahler orders but Strahler orders 3 ($P = 0.27$) and 4 ($P = 0.20$). Similarly, the distribution of diffusion distance deviated from normality for all 10 Strahler orders ($P \leq 0.02$) and the distribution of wrapping deviated from normality ($P \leq 0.001$) for all but Strahler orders 3 ($P = 0.44$), 4 ($P = 0.20$), and 8 ($P = 0.08$).

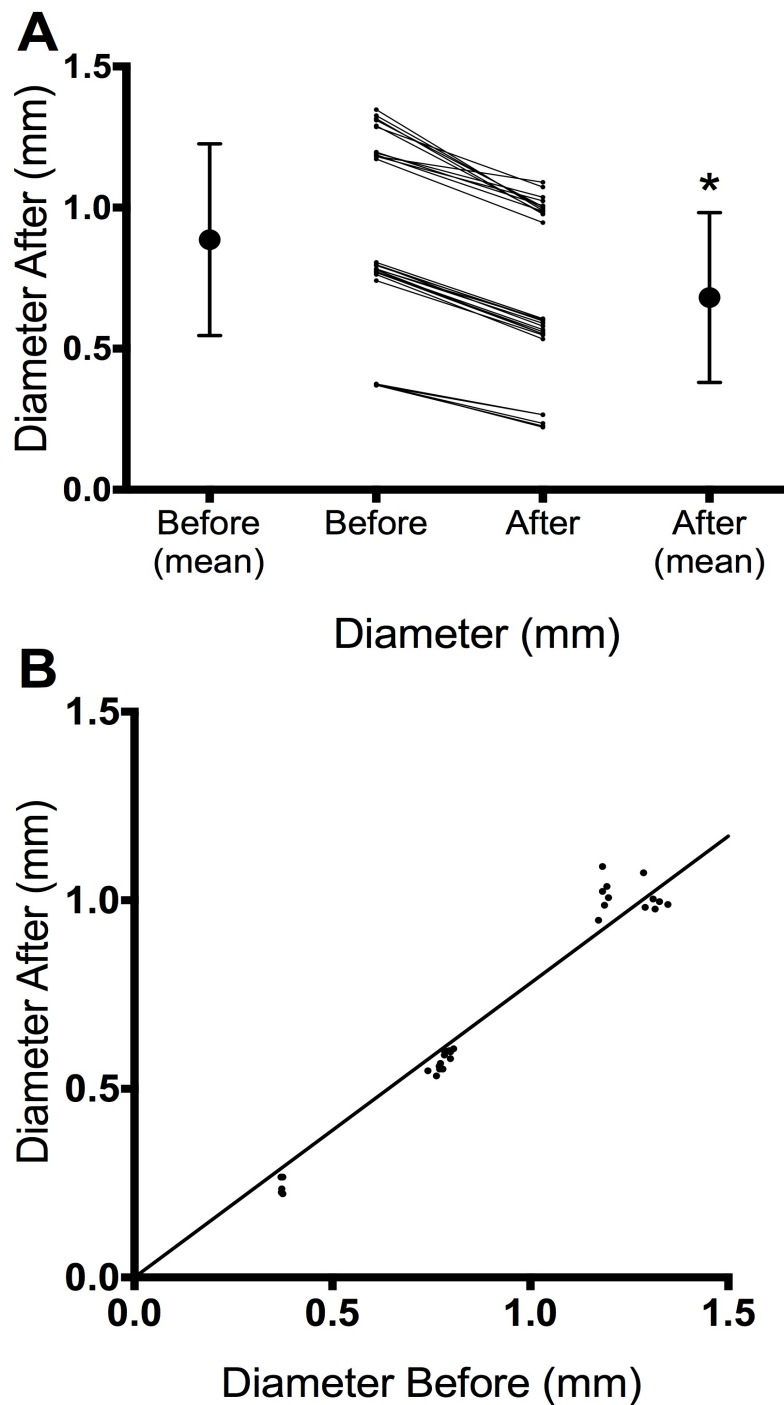


Figure 7.2. Degree of Microfil® shrinkage. (A) The diameter of cylinders of Microfil® before and after treatment. Data for individual cylinders are shown by lines. Mean \pm standard deviation is shown by the filled circles and error bars. (B) Scatterplot of the relationship between the diameters of the Microfil® cylinders before and after treatment. The ordinary least products method (11) (line forced through the origin) gave a line of best fit with the equation $y = 0.78x$.

Table 7.1. Arterial radii corrected for shrinkage and the range of arterial radii used for categorizing data into Strahler orders via the ‘statistical’ and ‘mid-point’ methods.

| Strahler order | n^\dagger | k_7 | 20 μm image data | | | | Statistical method | | Mid-point method | | |
|----------------|-------------------|-------|--|--------------|------------------------------|--|-----------------------|---------------------------|---|-----------------------|---------------------------|
| | | | Mean arterial radius $(\mu\text{m})^\dagger$ | SD^\dagger | SD corrected for shrinkage | Mean arterial radius corrected for shrinkage with 95% tolerance limits $(\mu\text{m})^*$ | n of wrapped arteries | n of non-wrapped arteries | Radius range $(\mu\text{m}; \text{mid-point method})$ | n of wrapped arteries | n of non-wrapped arteries |
| 0 | 29,566 \pm 5965 | 1.96 | 10.08 | 0.14 | 0.18 | 12.92 (12.57-13.27) | 216 | 887 | 11.46 – 15.37 | 180 | 484 |
| 1 | 13,070 \pm 2293 | 1.96 | 13.9 | 3.80 | 4.87 | 17.82 (8.27-27.37) | 325 | 604 | 15.37 – 21.77 | 81 | 57 |
| 2 | 4,373 \pm 664 | 1.96 | 20.06 | 6.90 | 8.85 | 25.72 (8.38-43.06) | 435 | 628 | 21.77 – 32.01 | 110 | 56 |
| 3 | 1,245 \pm 198 | 2.036 | 29.87 | 0.35 | 0.45 | 38.29 (37.38-39.20) | 6 | 1 | 32.01 – 44.33 | 67 | 17 |
| 4 | 578 \pm 71 | 2.062 | 39.29 | 1.08 | 1.38 | 50.37 (47.51-53.23) | 11 | 1 | 44.33 – 53.54 | 21 | 3 |
| 5 | 247 \pm 23 | 2.123 | 44.23 | 9.81 | 12.58 | 56.71 (30.01-83.41) | 127 | 26 | 53.54 – 62.89 | 10 | 1 |
| 6 | 90 \pm 6 | 2.251 | 53.87 | 12.51 | 16.04 | 69.06 (32.96-105.16) | 103 | 21 | 62.89 – 89.76 | 12 | 3 |
| 7 | 24 \pm 1 | 2.651 | 86.15 | 24.06 | 30.85 | 110.45 (28.68-192.22) | 159 | 30 | 89.76 – 144.76 | 9 | 1 |
| 8 | 6 | 4.414 | 139.83 | 20.11 | 25.78 | 179.27 (65.47-293.07) | 23 | 4 | 144.76 – 212.24 | 2 | 0 |
| 9 | 3 | 9.916 | 191.42 | 17.79 | 22.81 | 245.41 (19.25-471.57) | 258 | 108 | \geq 212.24 | 1 | 0 |
| 10 | 1 | - | 216.1 | 4.74 | - | 277.05 | - | - | - | - | - |

SD = standard deviation.

* The formula used to correct arterial radius for shrinkage was as follows: Corrected arterial radius = (Mean arterial radius)/0.78. The 95% tolerance limits defined the range of diameters for each Strahler order according to the ‘statistical method’.

k_7 values were taken from Geigy Scientific Tables (3).

† Data from Nordsletten *et al* (14).

7.4.2.2 Mid-point method

For the mid-point method of assigning arteries to Strahler orders, a total of 1,115 arteries were binned across the 10 Strahler orders. There were 664 arteries in Strahler order 0, 138 in Strahler order 1, 166 in Strahler order 2, 84 in Strahler order 3, 24 in Strahler order 4, 11 in Strahler order 5, 15 in Strahler order 6, 10 in Strahler order 7, 2 in Strahler order 8, and 1 in Strahler order 9. For the mid-point method there is no overlap of the ranges for each Strahler order, so each artery was assigned to only one Strahler order.

After categorizing our data into Strahler orders using the mid-point method, the distribution patterns were analyzed in the same manner as they were for the statistical method. The distribution patterns for all of the measured characteristics of artery-vein pairs mostly deviated significantly from normality. For example, the distribution of arterial diameter within each Strahler order deviated significantly from normality ($P \leq 0.05$) for all but Strahler orders 4 and 5 ($P = 0.06$ and $P = 0.24$ respectively). Similarly, the distribution of diffusion distance deviated from normality for all Strahler orders ($P \leq 0.001$). Also, the distribution of wrapping deviated from normality ($P \leq 0.001$) for all but Strahler orders 4 ($P = 0.08$), 5 ($P = 0.48$), 6 ($P = 0.32$), and 7 ($P = 0.07$). Because the distributions of the data deviated significantly from normality, subsequent analyses were performed using both parametric and non-parametric methods.

7.4.3 Mean and median separation distance, and wrapping

7.4.3.1 Statistical method

Regardless of whether parametric (ANOVA) or non-parametric (Kruskal-Wallis) methods were used, separation distance (Fig. 7.3A; $P < 0.001$, and Fig. 7.4A; $P < 0.001$) and wrapping (Fig. 7.3B; $P \leq 0.02$, and Fig. 7.4B; $P \leq 0.008$) were all found to vary significantly according to Strahler order.

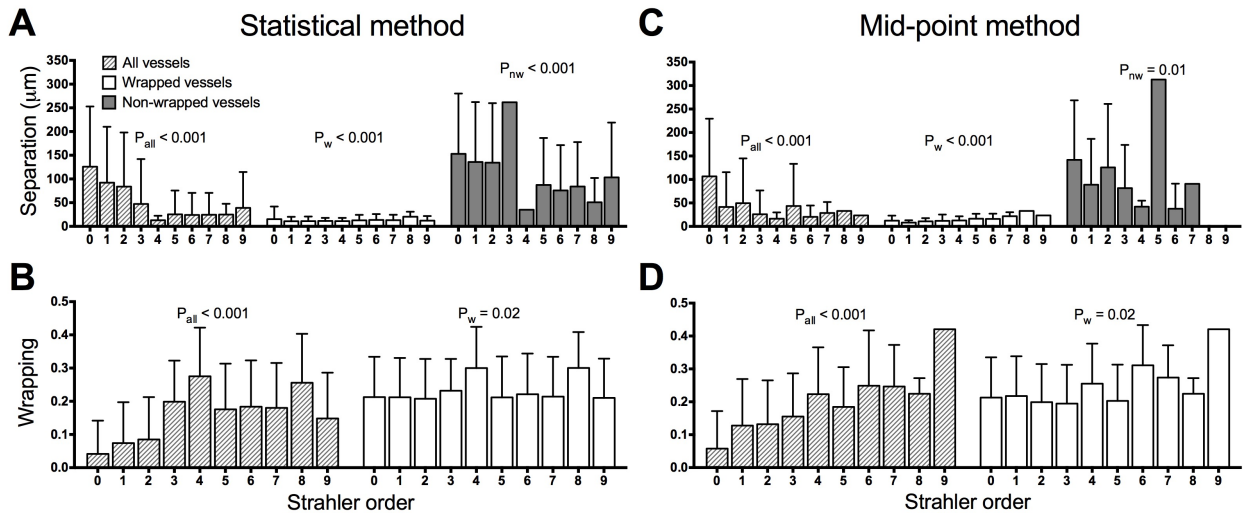


Figure 7.3. Mean separation distance and wrapping according to Strahler order. Data are the light microscopic data set of Ngo *et al* (13). Data were categorized into Strahler orders via the ‘statistical’ method (A & B) and ‘mid-point’ method (C & D). Mean separation distance within each Strahler order is shown for all, wrapped, and non-wrapped arteries (A & C). Mean proportion of the circumference of the arterial wall in direct contact with the wall of the associated vein (wrapping) is shown for all arteries and only those arteries showing some degree of wrapping (B & D). P values were derived from one-way ANOVA. P_{all} = all vessels, P_w = wrapped vessels, P_{nw} = non-wrapped vessels. Columns and error bars represent means and standard deviations.

When all arterial vessels were included in the analysis, separation distance progressively reduced as Strahler order increased (Figs 7.3A and 7.4A). Similarly, the proportion of arterial wall in direct contact with the vein wall (Figs 7.3B and 7.4B) also increased at higher Strahler orders. However, when arteries were separated into those that were wrapped by a proportion of the wall of the accompanying vein, and those that were not, a more uniform pattern was observed. For example, even though separation distance varied significantly according to Strahler order in wrapped vessels (Figs 7.3A and 7.4A), they were always much shorter (mean 10.84 – 20.37 μm ; median 7.90 – 18.26 μm) than the separation distances for non-wrapped vessels (both mean and median 35.02 – 261.80 μm) (Figs 7.3A and 7.4A). Similarly, although the proportion of wrapping progressively increased with Strahler order (Figs 7.3B and 7.4B), the proportion of the arterial wall in contact with the vein wall varied little by Strahler order when the analysis was confined to wrapped vessels (mean 0.21 – 0.30; median 0.19 – 0.35) (Figs 7.3B and 7.4B).

7.4.3.2 Mid-point method

We determined whether the method of assigning arteries to Strahler order (i.e. the statistical method versus the mid-point method) influences the predicted relationship between Strahler order and vascular geometry. As was the case for the statistical method, when the mid-point method was used, separation distance (Figs 7.3C; $P \leq 0.01$, and 7.4C; $P < 0.001$) and wrapping (Figs 7.3D; $P \leq 0.02$, and 7.4D; $P \leq 0.02$) varied significantly according to Strahler order, irrespective of whether parametric or non-parametric methods were used for hypothesis testing.

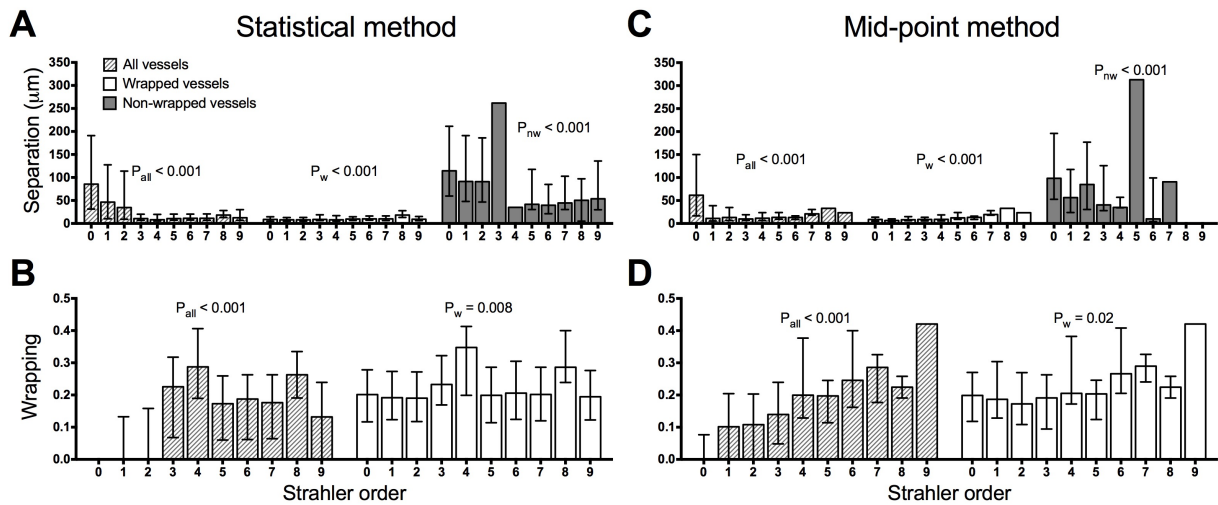


Figure 7.4. Median separation distance and wrapping according to Strahler order. Data are the light microscopic data set of Ngo *et al* (13). Data were categorized into Strahler orders via the ‘statistical’ method (A & B) and ‘mid-point’ method (C & D). Median separation distance within each Strahler order is shown for all, wrapped, and non-wrapped arteries (A & C). Median proportion of the circumference of the arterial wall in direct contact with the wall of the associated vein (wrapping) is shown for all arteries and only those arteries showing some degree of wrapping (B & D). P values derived from the Kruskal-Wallis test. P_{all} = all vessels, P_w = wrapped vessels, P_{nw} = non-wrapped vessels. Columns and error bars represent medians and interquartile ranges.

As was the case for the statistical method, when the mid-point method was used and all arterial vessels were included in the analysis, separation distance progressively reduced as Strahler order increased (Figs 7.3C and 7.4C). Furthermore, proportion of wrapping (Figs 7.3D & 7.4D) also increased at higher Strahler orders. As was the case when arteries were categorized into Strahler orders via the statistical method, when arteries were separated into those that were partially wrapped by a vein, and those that were not, a more uniform pattern was observed. For example, even though separation distance varied significantly according to Strahler order in wrapped vessels (Figs 7.3C & 7.4C), these distances were always much shorter (mean 9.39 – 28.65 μm ; median 7.12 – 30.64 μm) than the separation distances for

non-wrapped vessels (mean 0 – 144.24 μm ; median 0 – 99.27 μm) (Figs 7.3C & 7.4C). Similarly, although the proportion of wrapping progressively increased with Strahler order (Figs 7.3D & 7.4D), the proportion of the arterial wall in contact with the vein wall for wrapped arteries varied little by Strahler order (mean 0.19 – 0.42; median 0.17 – 0.42) (Figs 7.3D & 7.4D).

Thus, even though the statistical method for assigning arteries to Strahler orders generated anomalous numbers of arteries in each branching order, the overall patterns of changes in vascular geometry throughout the branching network of the pre-glomerular circulation closely resembled that generated using the mid-point method.

Nevertheless, the branching nature of the renal circulation produces an exponential increase in the number of vessels at progressively lesser Strahler orders. Anomalies appear to arise from use of the statistical method for assigning arteries into Strahler orders. Presumably this is partly attributable to the fact that there is significant overlap of the ranges of diameter for each Strahler order determined using this method. Consequently, each artery can be categorized into many Strahler orders. The statistical method is further confounded by the disparity in the magnitude of the ranges generated for each Strahler order, which is a consequence of the disparity on standard deviations of arterial radius across the various Strahler orders (Table 7.1). Consequently, when the statistical approach was used, the number of vessels assigned to each Strahler order did not reflect the expected exponential relationship. In contrast, this expected pattern was replicated when the mid-point method was used. Thus we reasoned that the mid-point method for assigning arteries to Strahler orders is more valid than the statistical method. Therefore, MTCs were only calculated for the artery-vein pairs categorized via the mid-point method.

7.4.4 The impact of vascular geometry on barriers to oxygen diffusion across Strahler orders

The mid-point method provides a better representation of the branching nature of the renal cortical circulation, so in this respect is more valid than the statistical method. Thus, arteries categorized into Strahler orders using the mid-point method were subjected to the two methods for calculating MTCs (MTC vs MTC per unit vessel length). Here, again, we compared two approaches (all vessels vs wrapped vessels). Thus a total of four approaches were used: (i) an analysis of the MTC for all arterial vessels in the analysis (both wrapped, that is, where the arterial wall was in direct contact with the vein wall, and not-wrapped), (ii) an analysis of the MTC for only wrapped vessels, on the basis that diffusion of oxygen

between paired arteries and veins is only feasible when wrapping is present, (iii) an analysis of the MTC per unit vessel length and all arterial vessels, and (iv) an analysis of the MTC per unit vessel length and only wrapped vessels.

Although Nordsletten presented both arterial and venous lengths (14), only the lengths of arteries were considered in our calculations of $SA_{\text{effective}}$ because our computational models are based on arterial Strahler order, not venous Strahler order. Furthermore, Nordsletten and colleagues observed that venous Strahler orders were often paired with arteries two orders lower (14). Thus we reasoned that our calculations of $SA_{\text{effective}}$ should only consider the length of arteries reported by Nordsletten *et al* (14), corrected for shrinkage.

7.4.4.1 Mass transfer coefficients

Two forms, and thus two equations were used to estimate MTCs. The MTC (k_{mi}) was calculated by using equation [7], and MTC per unit vessel length (k_{li}) was calculated by using Equation [9]. K_{li} from equation [9] was validated against another MTC per unit vessel length (k_{li}) calculated from using equation [11]. The difference between the two methods of calculating MTCs per unit vessel length (equation [9] vs equation [11]) was minimal, with the mean percentage difference in MTC calculated between the two methods being 12.0%. Thus, the approach of using equation [9] as an estimate of MTC per unit vessel length was deemed to be valid.

We first examined the distribution of MTCs. Here, we observed that the distribution of MTCs deviated from normality ($P \leq 0.04$) for all but Strahler order 5 ($P = 0.53$). Similarly, the distribution of MTCs per unit vessel length also deviated from normality ($P \leq 0.04$) for all but Strahler order 5 ($P = 0.53$). Because the distributions of MTCs and MTCs per unit vessel length deviated significantly from normality, subsequent analyses were performed using both parametric and non-parametric methods.

7.4.4.2 k_{mi} vs k_{li}

Equation [7] was used to calculate mass transfer coefficients (k_{mi}) (Figs 7.5A & B and Figs 7.6A & B). Equation [9] was used to calculate the mass transfer coefficients per unit vessel length (k_{li}) (Figs 7.5C & D and Figs 7.6C & D). When all arteries were considered in the analysis, there was a trend for a biphasic relationship between Strahler order and mean k_{mi} (Fig. 7.5A), median k_{mi} (Fig. 7.6A), and median k_{li} (Fig. 7.6C). In contrast, there was a trend for mean k_{li} to decrease as Strahler order increased (Fig. 7.5C). When only wrapped arteries were analyzed (Figs 7.5B & D, and Figs 7.6B & D), there was a trend for a biphasic

relationship between Strahler order and both k_m (Fig. 7.5B) and k_{li} (Figs 7.6B &D). An exception was for mean k_{li} , which decreased as Strahler order increased (Fig. 7.5D).

7.4.4.3 Effective mass transfer area

The effective mass transfer area for a particular Strahler order ($SA_{\text{effective}}$) was calculated by multiplying (i) the surface area of an individual vessel ($2\pi R$, where 'R' is the arterial radius), and (ii) the length of arteries in that Strahler order (presented by Nordsletten *et al* (14), and corrected for shrinkage in this study), and if required, (iii) the fraction of vessels in a Strahler order that are 'wrapped' (determined from our light microscopic data). We calculated both the mean (and standard error of the mean) and median (and interquartile range) $SA_{\text{effective}}$ for each Strahler order. Both mean (Fig. 7.5) and median (Fig. 7.6) $SA_{\text{effective}}$ increased as Strahler order increased.

7.4.4.4 Impact of vascular geometry on the diffusion of oxygen

To visualize the impact of vascular geometry on the transfer of oxygen between artery-vein pairs at each Strahler order, we plotted the product of MTC (k_m or k_{li}), $SA_{\text{effective}}$, and the number of vessels at each Strahler order. We term this value 'total mass flux per unit driving force'. For a particular Strahler order, the combination of a low k_m (or k_{li}) and a low effective surface area is predicted to result in relatively little diffusive flux of oxygen between an artery-vein pair belonging to this Strahler order. Likewise, the combination of a high k_m (or k_{li}) and high effective surface area is predicted to result in significant diffusive flux of oxygen between an artery-vein pair belonging to that Strahler order. When analyzing mean total mass flux per unit driving force, regardless of whether all vessels or only 'wrapped' vessels were analyzed, there was a trend for a biphasic relationship between Strahler order and total mass flux per unit driving force (Fig. 7.7). Total mass flux per unit driving force peaked at Strahler order 1 before decreasing as Strahler order increased. Likewise, median total mass flux per unit driving force, regardless of how the data were analyzed, peaked at Strahler order 1 and decreased as Strahler order increased (Fig. 7.8). A significantly higher total mass flux per unit driving force was observed in Strahler orders 0-4 compared to orders 5-9 (Figs 7.7 and 7.8).

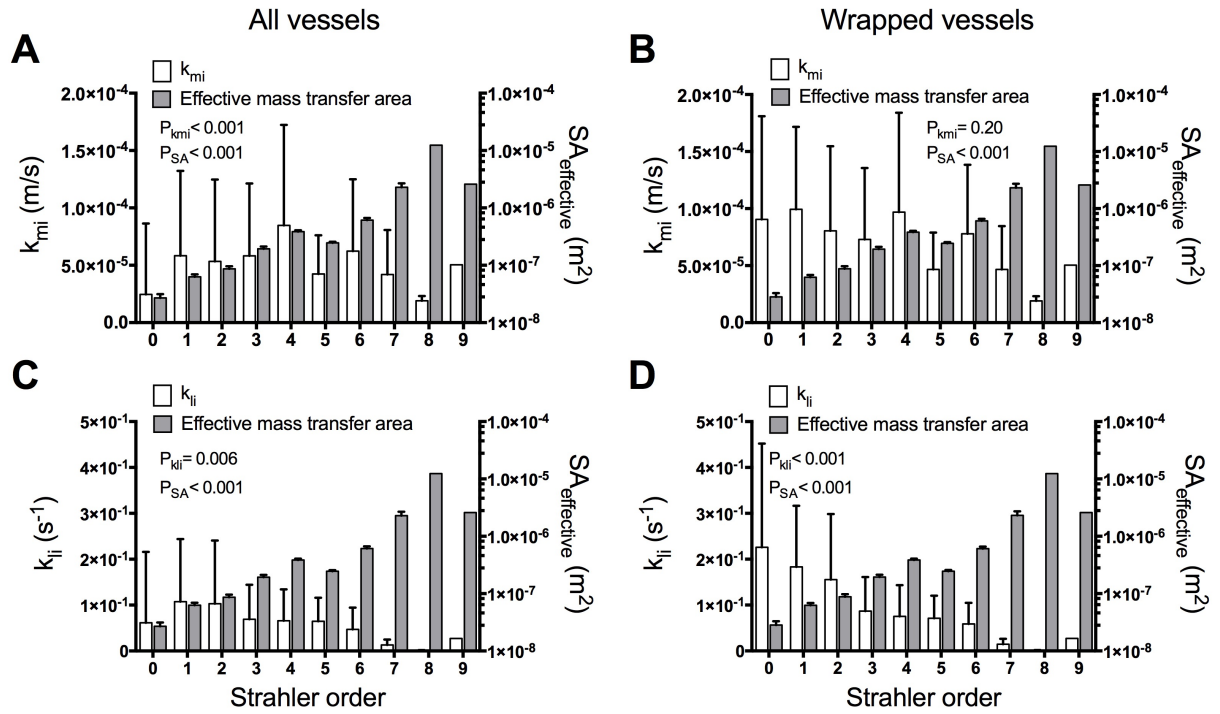


Figure 7.5. Mean mass transfer coefficients and mean effective mass transfer areas across Strahler orders. Mass transfer coefficient (k_{mi} ; A & B) and mass transfer coefficient per unit vessel length (k_{li} ; C & D) are plotted on the left y-axis. Effective mass transfer area ($SA_{effective}$) is plotted against the right y-axis. The ‘mean effective mass transfer area’ is defined as the area for one vessel, multiplied by the number of vessels. P values were derived from one-way ANOVA. Columns and error bars represent the as mean \pm SD.

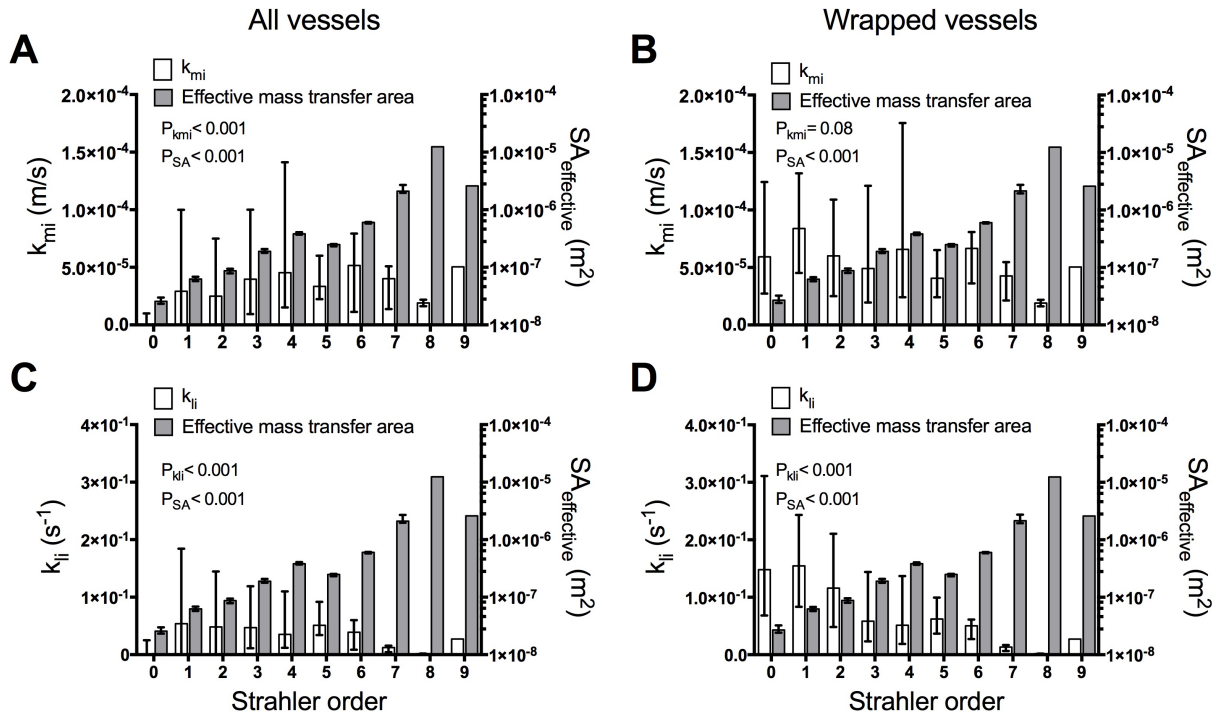


Figure 7.6. Median mass transfer coefficients and median effective mass transfer areas across Strahler orders. Mass transfer coefficient (k_{mi} ; A & B) and mass transfer coefficient per unit vessel length (k_{li} ; C & D) are plotted on the left y-axis. Effective mass transfer area ($SA_{effective}$) is plotted against the right y-axis. The ‘median effective mass transfer area’ is defined as the area for one vessel, multiplied by the number of vessels. P values were derived from the Kruskal-Wallis test. Columns and error bars represent medians and interquartile ranges.

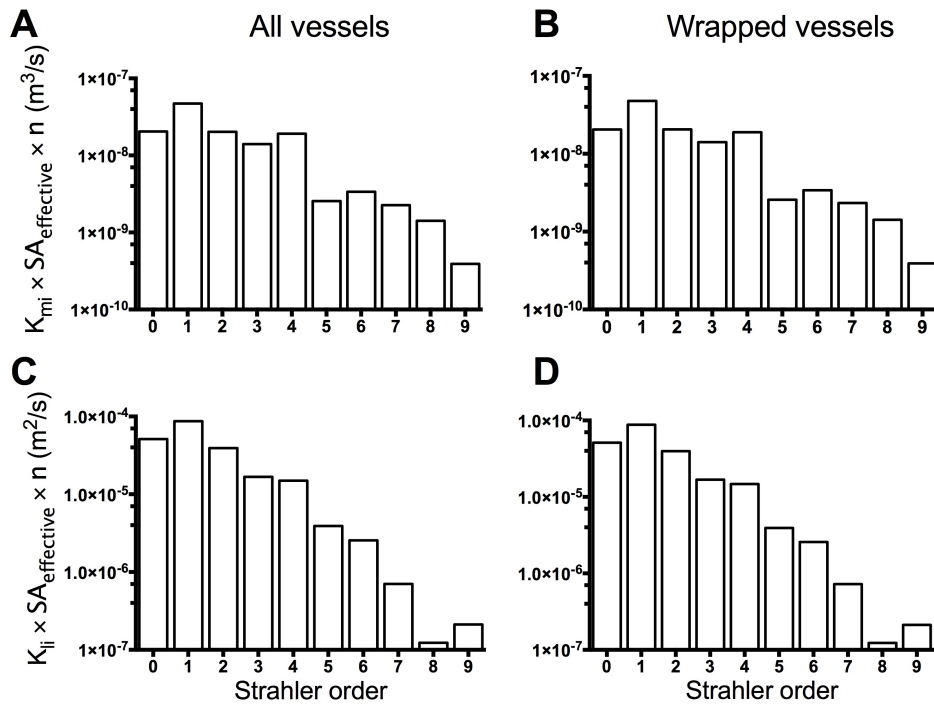


Figure 7.7. Mean total mass flux per unit driving force across Strahler orders. Total mass flux per unit driving force is defined by the product of mass transfer coefficient (k_{mi}), effective mass transfer area ($SA_{effective}$), and the number of vessels at a particular Strahler order as presented by Nordsletten *et al* (14) (A and B). Total mass flux per unit driving force can also defined by the product of mass transfer coefficient per unit vessel length (k_{li}), $SA_{effective}$, and the number of vessels at a particular Strahler order as presented by Nordsletten *et al* (14) (C and D).

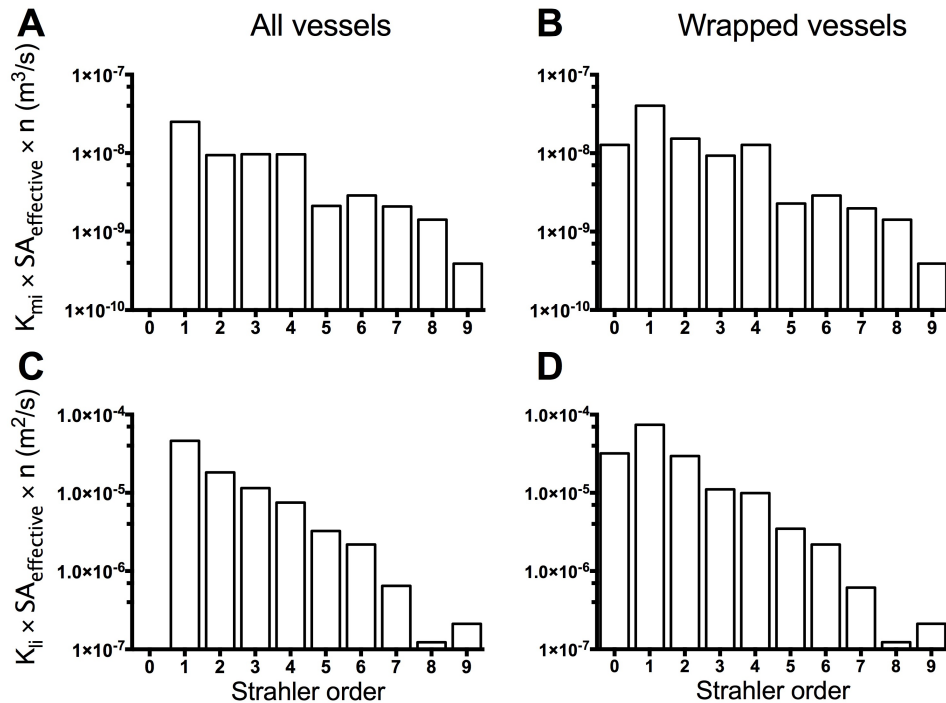


Figure 7.8. Median total mass flux per unit driving force across Strahler orders. Total mass flux per unit driving force is defined by the product of mass transfer coefficient (k_{mi}), effective mass transfer area ($SA_{effective}$), and the number of vessels at a particular Strahler order as presented by Nordsletten *et al* (14) (A and B). Total mass flux per unit driving force can also defined by the product of mass transfer coefficient per unit vessel length (k_{li}), $SA_{effective}$, and the number of vessels at a particular Strahler order as presented by Nordsletten *et al* (14) (C and D).

7.5 DISCUSSION

7.5.1 Main findings

We harmonized our previous light microscopic observations (13) with observations generated by Nordsletten *et al* from a micro-CT dataset (14). Consequently, by applying predictions from the computational model of Gardiner *et al* (7), we were able to examine the impact of vascular geometry on the potential for oxygen to diffuse between artery-vein pairs across 10 of the 11 branching levels of the renal circulation, originally defined by Nordsletten *et al* (14). It has been predicted that most AV oxygen shunting should occur at the most distal branches of the cortical circulation, since these vessels provide the greatest total cross sectional area for oxygen diffusion from arteries (19). Our current findings indicate that this prediction may only be partially true. Whether or not AV oxygen shunting is quantitatively significant remains a matter of controversy (4, 17). But if it is, our current findings indicate that oxygen diffusion to veins from interlobar arteries (Strahler orders 8-9) or arcuate arteries (Strahler orders 6-7) is unlikely to be significant. However, oxygen diffusion to veins from interlobular arteries (Strahler orders 1-4), including proximal interlobular arteries, is more likely to be significant.

A strength of our study was the use of multiple approaches to categorize our light microscopic data into Strahler orders. These two approaches tested two extremes: (i) a statistical approach that allowed for overlapping of arteries into one or more Strahler orders and (ii) an approach that did not allow for overlapping (mid-point method). Both approaches generated similar patterns in distribution, and means and medians of separation distance and wrapping. We also applied two different equations to the determination of MTCs. Importantly, similar patterns of MTCs were generated irrespective of the equation used to calculate MTCs. Finally, the trends of total mass flux per unit driving force were similar across the various approaches taken. That is, regardless of whether the MTCs were in the form of k_{mi} or k_{li} , and regardless of whether all or only wrapped vessels were used in the analysis of MTCs, we observed a decrease in total mass flux per unit driving force as Strahler order increased. Collectively our multiple approaches lead to a similar conclusion, that interlobular arteries are the most likely site of AV oxygen shunting.

7.5.2 Analysis of shrinkage of Microfil®

Vascular casts of the rat renal circulation were imaged at high resolution by Garcia-Sanz *et al* using micro-CT (5). The data were subsequently analyzed by Nordsletten *et al* (14) to define 11 Strahler orders of the cortical circulation. In order to categorize our light microscopic data

into 10 of these Strahler orders, we first determined the degree of shrinkage associated with Microfil® following exposure to the solutions used by Garcia-Sanz *et al* (5). We observed 22% shrinkage in Microfil® following exposure to ethanol, glycerol and acetone. Previous studies have also shown that Microfil® shrinks considerably following immersion in graded alcohols (12). In line with the findings of Møller *et al* (12), the degree of shrinkage determined in our study indicates that caution must be applied when Microfil® is used for quantitative studies, particularly those that involve dehydration of tissue in alcohols. By quantifying the degree of shrinkage of Microfil® we were able to harmonize our light microscopic data with the micro-CT data presented by Nordsletten *et al* (14). Thus we were able to first categorize our light microscopic data into Strahler orders using two extreme approaches: a statistical approach and a mid-point method. Then, we determined the $SA_{\text{effective}}$ for each Strahler order to estimate the impact of vascular geometry on the ability of oxygen to diffuse from arteries to veins in the cortical circulation. This was achieved using two different equations to calculate individual MTCs for each individual artery-vein pair.

7.5.3 Categorizing light microscopic data into Strahler orders

7.5.3.1 Statistical method

We first took a statistical approach to categorize our light microscopic data into Strahler orders. We chose to calculate tolerance limits to estimate the likelihood that a single experimental value would have come from the population of vessels of individual Strahler orders using 95% tolerance limits. These were chosen to provide an inclusive estimate of the range of arterial diameter in each Strahler order that we are confident would contain at least 95% of the population. The strength of this approach is that it is objective and inclusive. That is, we can be confident that the data-set for each Strahler order excluded only vessels with a less than 5% chance of belonging to that order. However a limitation of this approach is that it results in overlapping ranges of arterial radius. Some values of arterial radius are thus assigned to two or more Strahler orders. This resulted in a large number of observations for some orders. However, some Strahler orders had a small number of observations because some standard deviations reported by Nordsletten *et al* (14), and consequently the tolerance limits calculated, were small (Table 7.1).

7.5.3.2 Mid-point method

The second approach taken to categorize our light microscopic work into Strahler orders was based on the mid-point method. This method of binning did not require tolerance limits, but instead was based on calculations of radii halfway between the mean arterial radii, corrected for shrinkage, of two consecutive Strahler orders. An advantage of this method is that any

particular arterial radius can only be assigned to one Strahler order; there was no overlapping of arterial radii into two or more Strahler orders. Thus, MTCs were only calculated for arteries categorized into Strahler orders via this method.

7.5.4 Two different approaches for calculating mass transfer coefficients

7.5.4.1 k_{mi} vs k_{ji}

Once our light microscopic data were categorized into Strahler orders using the mid-point method, two methods for calculating the individual MTC for each artery-vein pair were used. The first method was via equation [7], which considered the diffusion coefficient of oxygen, proportion of wrapping, and diffusion distance. The second method used equation [9], which also considered all three factors in equation [7], but in addition took into consideration the length of the branching level. Therefore, by comparing k_{mi} and k_{ji} , we observed the effect of vessel length on MTC (k_{mi}).

7.5.5 Impact of vascular geometry on the barriers to diffusion of oxygen

Overall, our findings indicate greater ability for diffusion of oxygen between artery-vein pairs in the smaller, distal vessels (proximal and middle portions of the interlobular arteries) rather than the larger, proximal vessels (interlobar, arcuate and proximal interlobular arteries). This is a consequence of the larger number of vessels in Strahler orders 0-4 (ranging from 578 to 29,566 vessels) compared with orders 5-9 (ranging from 3 to 247 vessels). The total mass flux per unit driving force is a product of MTC, the $SA_{\text{effective}}$, and the number of vessels. But to estimate the impact of vascular geometry on the diffusion of oxygen, we should also consider the concentration gradient between the paired vessels. If this gradient is taken as a unit concentration difference, then we can interpret the data presented in Figures 7.7 and 7.8 as the ‘unit total mass transferred’ at each Strahler order. However, in order to complete this, we require a mathematical model to calculate the AV concentration difference at each Strahler order. Only then can we calculate the mass transfer at each Strahler order and thus determine the total oxygen shunted between an afferent and efferent vessel. Nevertheless, we interpret the data presented in this study to suggest AV oxygen shunting is most likely quantitatively insignificant, at least under normal physiological conditions, at the level of interlobar and arcuate arteries (Strahler Orders 5-9), despite our previous observations suggesting the spatial arrangement of the proximal vessels of the cortical circulation likely facilitate the shunting of oxygen (13). The work presented in the current study suggests there may be more quantitatively significant shunting of oxygen at the mid-portions of the interlobular arteries (orders 3-4). However it is important to note that the interlobular vessels taper as they travel towards the cortical surface. Thus, assigning a particular portion of an interlobular artery to

one Strahler order is not feasible. Nevertheless, it is plausible that Strahler orders 4 and 5 represent mid-to-proximal interlobular arteries.

The findings in the present study provide further insight into the mechanisms underlying the observations by O'Connor *et al* (15). The interlobar and arcuate arteries and veins, found before the divergence of the cortical and medullary circulations, have a close physical association (13). O'Connor and colleagues postulated, based on experimental findings in anesthetized rabbits and rats, that this association facilitates the shunting of oxygen from the interlobar/arcuate artery to the corresponding vein. They used renal nerve stimulation and angiotensin II infusion to selectively reduce cortical perfusion. They found that cortical perfusion and oxygenation reduced as expected, but also that medullary oxygenation reduced despite medullary perfusion being maintained (15). They reasoned that the close physical association of the proximal vessels, before the branch-points that define the separation of the cortical and medullary circulations, could provide an explanation for their findings. This close association would assist the diffusive shunting of oxygen down its concentration gradient from the artery and into the vein. Thus, medullary oxygenation was found to be dependent on cortical oxygenation (15). The data presented in the current study are not consistent with the hypothesis presented by O'Connor and colleagues. Instead, our data suggest more AV flux of oxygen is likely to occur at Strahler orders 0-4, which correspond to afferent arterioles (orders 0-1) and mid-to-distal interlobular arteries (orders 2-3), than Strahler orders 5-9, which likely represent proximal-to-mid interlobular (orders 4-5), arcuate (orders 6-7) and interlobar arteries (orders 8-9). Our findings, therefore, also suggest comparatively high diffusive shunting of oxygen may occur at the proximal interlobular arteries (Strahler order 4). Thus it is possible that significant AV shunting of oxygen occurs at portions of the interlobular arteries prior to the divergence of the cortical and medullary circulations, at least under conditions of cortical ischemia, consistent with the proposition of O'Connor *et al* (15). Unfortunately, the data presented here, in isolation, cannot support definitive conclusions regarding the magnitude of AV oxygen shunting at various sites within the cortical circulation under physiological and pathophysiological conditions. However, computational modeling studies, that incorporate the MTCs calculated in this study, could provide this information.

7.5.6 Future perspectives

In order to generate a valid model of oxygen transport in the kidney, it is imperative that the data that the model is based on are accurate. Previous models of oxygen transport between afferent and efferent limbs of the renal cortical circulation were based on unrealistic geometry and vessel arrangement (6, 16). Thus, the quantitative significance of AV oxygen shunting

remains unresolved (4, 17). Although the current study does not provide explicit insight into the quantitative significance of AV oxygen shunting, the work presented here provides the basis for future computational modeling studies to resolve this. MTCs and flux presented in this chapter only provides a prediction of the oxygen shunting capacity at each Strahler Order. We need to know the AV concentration difference in order to determine the total amount of oxygen shunted. Thus, the data generated here may be integrated into our previous mathematical model (6) to provide insight into the relative magnitudes of AV oxygen diffusion between arteries and veins along the branches of the renal cortical circulation. The MTCs calculated in this study are based on the diffusion coefficient of oxygen, and not other molecules. However, the manner in which we have calculated the MTC for oxygen can be applied to other molecules provided we know the diffusion coefficients for these molecules.

7.5.7 Strengths and limitations

Our findings and conclusions are strengthened by the large dataset, which was corrected for shrinkage, and is thus based on realistic vessel dimensions. A limitation in this study is that the conversion of arterial diameter to Strahler order may be inexact. To overcome this limitation, we are currently developing a technique that automatically assigns Strahler orders to a three-dimensional reconstruction of the renal cortical circulation. In its current form, the application is also able to automatically measure the diameters along an arterial branch and subsequently determine the median diameter for a particular arterial branch. But the approach is not without its own limitations (see Chapter 9). As described earlier, another limitation of our current study arises from the small number of observations for some Strahler orders, in particular Strahler orders 3 and 4 when analyzed via the statistical approach, and Strahler orders 4-9 when analyzed via the mid-point method. So although we found that the total mass flux per unit driving force was consistently greater for Strahler order 4 compared to orders 5-9, it is worth noting that the small number of observations for this Strahler order likely affected the mean and median MTC calculated for this order. Thus, the mean and median total mass flux per unit driving force for Strahler orders 3 and 4, in particular, may be inexact.

7.6 CONCLUSIONS

In the present study, we have estimated the relative impact of vascular geometry on the ability of oxygen to diffuse from the afferent to efferent vessels in the rat renal cortex. Our estimations suggest that although vessels in Strahler orders 5-9 tend to have a close physical relationship, as determined from our previous work (13), there seems to be overall, greater ability for oxygen to diffuse from an artery to a corresponding vein in the mid-to-distal cortical circulation (Strahler orders 0-4) than in the proximal cortical circulation (Strahler

orders 5-9). The data presented in the current study do not show if and where there is significant AV oxygen shunting, only that if it were, it would likely occur predominantly in Strahler orders 0-4 (mid-to-distal and possibly proximal interlobular arteries). To determine the significance of AV oxygen shunting, the next step required is to integrate our findings into mathematical models of renal oxygen transport such as that of Gardiner *et al* (6). This will allow us to (i) evaluate our interpretations of the data in the present study, (i) determine if and where AV diffusive shunting of oxygen occurs, and (iii) determine if AV oxygen shunting is quantitatively significant under physiological and pathological conditions.

REFERENCES

1. **Bird RB, Stewart WE, Lightfoot EN.** *Transport Phenomena*. New York: John Wiley & Sons, 2007.
2. **Cussler EL.** *Diffusion: Mass Transfer in Fluid Systems*. Cambridge University Press, 2009.
3. **Diem K, Seldrup J.** Introduction to statistics, statistical tables, mathematical formulae. In: *Geigy Scientific Tables*, edited by Lentner C. Basle, Switzerland: CIBA-GEIGY, 1982, p. 52-53.
4. **Evans RG, Smith DW, Khan Z, Ngo JP, Gardiner BS.** Letter to the editor: "The plausibility of arterial-to-venous oxygen shunting in the kidney: it all depends on radial geometry". *Am J Physiol Renal Physiol* 309: F179-180, 2015.
5. **Garcia-Sanz A, Rodriguez-Barbero A, Bentley MD, Ritman EL, Romero JC.** Three-dimensional microcomputed tomography of renal vasculature in rats. *Hypertension* 31: 440-444, 1998.
6. **Gardiner BS, Smith DW, O'Connor PM, Evans RG.** A mathematical model of diffusional shunting of oxygen from arteries to veins in the kidney. *Am J Physiol Renal Physiol* 300: F1339-1352, 2011.
7. **Gardiner BS, Thompson SL, Ngo JP, Smith DW, Abdelkader A, Broughton BR, Bertram JF, Evans RG.** Diffusive oxygen shunting between vessels in the preglomerular renal vasculature: anatomic observations and computational modeling. *Am J Physiol Renal Physiol* 303: F605-618, 2012.
8. **Kruskal WH, Wallis WA.** Use of ranks in one-criterion variance analysis. *J Am Stat Assoc* 47: 583-621, 1952.
9. **Levy MN, Imperial ES.** Oxygen shunting in renal cortical and medullary capillaries. *Am J Physiol* 200: 159-162, 1961.
10. **Levy MN, Saucedo G.** Diffusion of oxygen from arterial to venous segments of renal capillaries. *Am J Physiol* 196: 1336-1339, 1959.
11. **Ludbrook J.** A primer for biomedical scientists on how to execute model II linear regression analysis. *Clin Exp Pharmacol Physiol* 39: 329-335, 2012.
12. **Møller J, Robertsen K, Hansen ES.** Severe shrinkage of Microfil during tissue clearing with the Spalteholz technique. *J Microsc* 174: 125-127, 1994.
13. **Ngo JP, Kar S, Kett MM, Gardiner BS, Pearson JT, Smith DW, Ludbrook J, Bertram JF, Evans RG.** Vascular geometry and oxygen diffusion in the vicinity of artery-vein pairs in the kidney. *Am J Physiol Renal Physiol* 307: F1111-1122, 2014.
14. **Nordsletten DA, Blackett S, Bentley MD, Ritman EL, Smith NP.** Structural morphology of renal vasculature. *Am J Physiol Heart Circ Physiol* 291: H296-H309, 2006.
15. **O'Connor PM, Kett MM, Anderson WP, Evans RG.** Renal medullary tissue oxygenation is dependent on both cortical and medullary blood flow. *Am J Physiol Renal Physiol* 290: F688-F694, 2006.
16. **Olgac U, Kurtcuoglu V.** Renal oxygenation: preglomerular vasculature is an unlikely contributor to renal oxygen shunting. *Am J Physiol Renal Physiol* 308: F671-688, 2015.
17. **Olgac U, Kurtcuoglu V.** Reply to "Letter to the editor: 'The plausibility of arterial-to-venous oxygen shunting in the kidney: it all depends on radial geometry'". *Am J Physiol Renal Physiol* 309: F181-182, 2015.
18. **Salathé EP.** Mathematical modeling of oxygen transport in skeletal muscle. *Math Biosci* 58: 171-184, 1982.
19. **Schurek HJ, Jost U, Baumgartl H, Bertram H, Heckmann U.** Evidence for a preglomerular oxygen diffusion shunt in rat renal cortex. *Am J Physiol* 259: F910-915, 1990.
20. **Shapiro SS, Wilk MB.** An analysis of variance test for normality (complete samples). *Biometrika* 52: 591-611, 1965.
21. **Sharan M, Popel AS.** A mathematical model of countercurrent exchange of oxygen between paired arterioles and venules. *Math Biosci* 91: 17-34, 1988.

22. **Welch WJ, Baumgartl H, Lubbers D, Wilcox CS.** Nephron pO_2 and renal oxygen usage in the hypertensive rat kidney. *Kidney Int* 59: 230-237, 2001.

8 | SURFACE AREA OF PERITUBULAR CAPILLARIES IN THE RAT RENAL CORTEX

8.1 ABSTRACT

A computational model of oxygen transport in the renal cortex requires an accurate measure of the surface area of cortical peritubular capillaries. Therefore, we employed stereological methods to determine the density of peritubular capillaries in the renal cortex of the rat. The kidneys of six rats were perfusion fixed and the vasculature filled with Microfil®. Using a single section from each kidney, the surface area density of peritubular capillaries was calculated to be $239.7 \text{ cm}^2/\text{cm}^3$ of cortex. This information will be useful for generation of computational models of oxygen transport in the renal cortex.

8.2 INTRODUCTION

Capillaries are major sites of oxygen transport (12, 13). In the kidney, peritubular capillaries appear capable not only of delivering oxygen to tissue, but can also act as sinks that remove oxygen from the vicinity of the walls of arteries (10). A valid computational model of kidney oxygenation must therefore depend upon the provision of quantitative information regarding the distribution of peritubular capillaries. We have previously quantified the variations in capillary density in the vicinity of artery-vein pairs in the kidney of the rat (4). However, to the best of our knowledge, information on peritubular capillary surface area in the parenchyma of the renal cortex is scarce. In one report, in German, peritubular capillary surface area in the dog kidney was estimated at 350 cm^2 per gram kidney weight (7). This work has been cited by others in the field (3). In a separate report, the surface area of capillaries in the rat kidney was estimated at 400 cm^2 per gram kidney weight (9). However, no information was provided regarding the methods that were used to generate these data. Therefore, in the current study, we used stereological methods to estimate the surface area of peritubular capillaries in the renal cortex of the rat.

8.3 METHODS

8.3.1 Tissue preparation

The tissues used in this study were produced in a previous study (10) (described in Chapter 6 of this thesis). In brief, the kidneys of six rats were perfusion fixed and the vasculature filled with a silicone compound (Microfil®) to visualize the blood vessels. One kidney was used from each rat. Three of the kidneys were sectioned in the longitudinal plane. For the other three kidneys, the plane chosen was perpendicular to the longitudinal plane. The kidneys were embedded in glycolmethacrylate and for each kidney, $3 \mu\text{m}$ sections were cut. Only one

histological section was used from each kidney for analysis, resulting in a total of six sections. The sections were stained with hematoxylin and eosin.

8.3.2 Sampling

All six micrographs were first visualized on ImageScope (version 11.2.0.780, Aperio Technologies). Image tiles were then extracted from each micrograph, providing between 800 – 2000 image tiles depending on the size of the tissue section. Pilot studies employed running means and allowed us to determine the appropriate method of sampling. Following this we chose to sample every 20th image tile that consisted of renal cortex. This resulted in an analysis of between 35 – 184 tiles for each tissue section. The images were analyzed in ImageJ, an open source software package (<http://imagej.nih.gov/ij/>). Using the cycloid arc plugin (<http://rsb.info.nih.gov/ij/plugins/grid-cycloid-arc.html>), a cycloid test system was overlaid on each image tile. The number of intersections and test points was then counted using the methods described below.

8.3.3 Estimation of surface area

The surface area of two-dimensional sections can be estimated using isotropic line probes. The common method is to use a cycloid test system (1, 11). The number of intersections (I) between the test lines and the surface of interest, in this case capillary walls, and the number of test points (P) which hit the area of interest (i.e. renal cortical tissue) were counted. The formula used to estimate surface area density S_v was:

$$S_v = 2(p/l) \frac{\Sigma I}{\Sigma P}$$

where ΣI is the total number of intersections for all micrographs, ΣP is the total number of test points, and (p/l) is the ratio of test points to test curve length.

Total surface area (TSA) of peritubular capillaries in the renal cortex was estimated by multiplying the surface area density of peritubular capillaries by the volume of the renal cortex. Therefore, the formula for the total surface area of peritubular capillaries in the renal cortex is:

$$\text{TSA} = S_v \times \text{volume of the renal cortex}$$

The volume of the renal cortex was determined by multiplying the kidney volume from our previous study (1.67 cm³; (10)) with known percentages of cortical tissue in the rat kidney (2).

Four different percentages of cortical tissue were used for determining the total surface area of peritubular capillaries. The four percentages were obtained via four different methods (2). These included three morphometric approaches: the ‘arcuate arteries method’, the ‘curved line method’, and the ‘medullary rays method’. The fourth method was the ‘magnetic resonance imaging (MRI) *in vivo* method’. For the morphometric approaches, the corticomedullary border was defined in three different ways using: (i) the arcuate arteries, (ii) a curved line that traced the glomeruli located closest to the medulla (juxtamedullary glomeruli), and (iii) the medullary rays approach where the corticomedullary border was defined to a line at the top of the medullary rays. For the MRI *in vivo* approach, images were obtained following injection of contrast agent (gadolinium) and the volume was calculated via automatic interpolation of marked areas of the kidney (2).

Data are presented as mean \pm standard error of the mean.

8.4 RESULTS

Total surface area density of peritubular capillaries was calculated to be $239.65 \text{ cm}^2/\text{cm}^3$ of cortex. The mean surface area density of peritubular capillaries was $250.40 \pm 24.68 \text{ cm}^2/\text{cm}^3$ of cortex across the six tissue sections. Calculated total surface area of peritubular capillaries depended on the method used for determining the proportion of kidney volume taken up by renal cortex (Table 8.1). It ranged from $209.21 \pm 20.62 \text{ cm}^2$ to $292.89 \pm 28.87 \text{ cm}^2$.

Table 8.1. Calculated total surface area (mean \pm SEM) of cortical peritubular capillaries.

| | Arcuate arteries | Curved line | Medullary rays | MRI <i>in vivo</i> |
|--|---------------------|--------------------|--------------------|--------------------|
| Proportion of kidney volume that is cortex | 0.65 | 0.70 | 0.50 | 0.50 |
| Volume of cortex using previous data * (cm^3) | 1.09 | 1.17 | 0.84 | 0.84 |
| Total surface area (cm^2) | 271.97 ± 26.81 | 292.89 ± 28.87 | 209.21 ± 20.62 | 209.21 ± 20.62 |

* Previous data from Ngo *et al* (10) (mean kidney volume = 1.67 cm^3) multiplied by the proportion of kidney volume that is cortex.

8.5 DISCUSSION

In our study, we provide an estimate of the surface area density and the total surface area of peritubular capillaries in the rat kidney. Surface area density was found to be $239.65 \text{ cm}^2/\text{cm}^3$ of renal cortex. Total surface area of cortical peritubular capillaries ranged from 209.21 to 292.89 cm^2 depending on which percentage of cortical volume in the rat kidney (based on data in the literature) was used in the calculations. Comparing our estimations to earlier estimations, our estimations of surface area density are less than that of estimations by others ($\sim 240 \text{ cm}^2/\text{cm}^3$ of cortex vs 350-400 cm^2 per gram of kidney weight).

It is important to note that this is a preliminary study with a number of limitations. Firstly, the sampling method used in this study was not ideal for our purposes. A total of only six tissue sections were analyzed across six rats. A different sampling approach would be required in future studies to confirm or refute our current findings. One approach that could be taken is that of Madsen *et al* who quantified peritubular capillaries in postnatal kidney development (8). Their work consisted of a more ideal sampling method: the kidney was cut in 1 mm thick sections and every second slice was used for stereologic measurements. These kidney sections were further cut into 1 mm x 1 mm pieces, mixed, and then systematically randomly chosen to embed in paraffin. Then, the sections were cut and peritubular capillaries were stained via immunohistochemical methods (cell marker CD31) to correctly identify as many capillaries as possible. Thus, their approach in both sampling and identifying peritubular capillaries is more suitable for our purposes than the approach taken in our present study. Secondly, we used Microfil® together with morphometry to identify peritubular capillaries. Although the Microfil® compound was allowed to flow freely prior to tying off the renal artery and vein, we acknowledge that there may be incomplete filling of the capillaries. This is because there are varying degrees of resistance in the renal circulation. Incomplete filling of the peritubular capillaries would hinder our ability to identify all objects of interest, in this case the lumen of peritubular capillaries. Thus, it is most probable that our estimates of surface area in this study represent an underestimation of the true surface area. Previous studies have used endothelial cell markers or electron microscopy to label and/or identify glomerular and peritubular capillaries (5, 6, 8). Endothelial cell markers, such as CD31, label endothelial cells (platelet endothelial cell adhesion molecule-1) and would thus enable identification of peritubular capillaries. Future studies should employ such methods for a more valid approach to identifying all (or as many as possible) cortical peritubular capillaries. Our preliminary study has provided estimations of peritubular capillary surface area in the rat kidney. These estimations can now be used in computational models of renal oxygenation.

REFERENCES

1. **Baddeley AJ, Gundersen HJ, Cruz-Orive LM.** Estimation of surface area from vertical sections. *J Microsc* 142: Pt 3/, 1986.
2. **Christiansen T, Rasch R, Stodkilde-Jorgensen H, Flyvbjerg A.** Relationship between MRI and morphometric kidney measurements in diabetic and non-diabetic rats. *Kidney Int* 51: 50-56, 1997.
3. **Crone C.** The permeability of capillaries in various organs as determined by use of the 'Indicator diffusion' method. *Acta Physiol Scand* 58: 292-305, 1963.
4. **Gardiner BS, Thompson SL, Ngo JP, Smith DW, Abdelkader A, Broughton BR, Bertram JF, Evans RG.** Diffusive oxygen shunting between vessels in the preglomerular renal vasculature: anatomic observations and computational modeling. *Am J Physiol Renal Physiol* 303: F605-618, 2012.
5. **Guo M, Ricardo SD, Deane JA, Shi M, Cullen-McEwen L, Bertram JF.** A stereological study of the renal glomerular vasculature in the db/db mouse model of diabetic nephropathy. *J Anat* 207: 813-821, 2005.
6. **Kaukinen A, Lautenschlager I, Helin H, Karikoski R, Jalanko H.** Peritubular capillaries are rarefied in congenital nephrotic syndrome of the Finnish type. *Kidney Int* 75: 1099-1108, 2009.
7. **Kügelgen A Von KB, Kuhlo W, Otto K-J.** Die Gefässarchitektur der Niere. In: *Zwangslose Abhandlungen aus dem Gebiet der normalen und pathologischen Anatomie*, edited by Bargmann W DWS. Stuttgart: Georg Thieme Verlag, 1959.
8. **Madsen K, Marcussen N, Pedersen M, Kjaersgaard G, Facemire C, Coffman TM, Jensen BL.** Angiotensin II promotes development of the renal microcirculation through AT₁ receptors. *J Am Soc Nephrol* 21: 448-459, 2010.
9. **Navar LG, Evan AP, Rosivall L.** Microcirculation of the Kidneys. In: *The Physiology and Pharmacology of the Microcirculation*, edited by Mortillaro N. New York: Academic Press, 1983, p. 397-488.
10. **Ngo JP, Kar S, Kett MM, Gardiner BS, Pearson JT, Smith DW, Ludbrook J, Bertram JF, Evans RG.** Vascular geometry and oxygen diffusion in the vicinity of artery-vein pairs in the kidney. *Am J Physiol Renal Physiol* 307: F1111-1122, 2014.
11. **Nyengaard JR.** Stereologic methods and their application in kidney research. *J Am Soc Nephrol* 10: 1100-1123, 1999.
12. **Pittman RN.** Oxygen gradients in the microcirculation. *Acta Physiol (Oxf)* 202: 311-322, 2011.
13. **Pittman RN.** Oxygen transport in the microcirculation and its regulation. *Microcirculation* 20: 117-137, 2013.

9 | MICRO-COMPUTED TOMOGRAPHIC ANALYSIS OF THE RADIAL GEOMETRY OF ARTERY-VEIN PAIRS IN THE KIDNEY OF THE RAT

9.1 ABSTRACT

We aimed to utilize synchrotron-based micro-computed tomography to quantify radial geometry of artery-vein pairs in the rat kidney. The kidneys of six rats were perfusion fixed and the renal circulation was filled with Microfil®, a radio-opaque compound. Firstly, in order to assess shrinkage of Microfil®, the kidneys were imaged at the Australian Synchrotron immediately upon tissue preparation, and also 24 hours after the first micro-computed tomographic acquisition, following post-fixation for 24 hours in paraformaldehyde. We determined that Microfil® shrinks 2-5% over the 24 hours after sample preparation. Secondly, vessel geometry was manually quantified from three-dimensional (3D) images. Radial geometry quantified by manual analysis of micro-computed tomographic images corresponded closely to data generated by histological analysis. However, because of the resolution we could achieve, only arteries $\geq 100\ \mu\text{m}$ in diameter were analyzed. Thus it is feasible and valid to use micro-computed tomography (micro-CT) to analyze vascular geometry in the proximal renal circulation. Finally, software was produced to provide an automated and rapid method for analysis of vessel geometry. The automated method, at least in its current form, underestimates arterial diameter and the proportion of the arterial wall ‘wrapped’ by the wall of its nearest vein, and overestimates diffusion distance. We conclude that a combination of light microscopic and micro-CT approaches are required to evaluate the spatial relationships of intrarenal arteries and veins over an extensive range of vessel sizes.

9.2 INTRODUCTION

There is experimental evidence that oxygen delivery to renal tissue may be limited by diffusive arterial-to-venous (AV) oxygen shunting (13, 14, 26). However, the quantitative significance of this phenomenon remains a matter of controversy (5, 22, 23). Currently, it is not possible to measure AV oxygen shunting experimentally. Thus, we rely on mathematical modeling to investigate this phenomenon by simulating diffusion and convection of oxygen within the renal cortex.

In collaboration with mathematicians at the University of Western Australia, we have generated models of oxygen transport in the renal cortex (8, 9, 20). Our initial model (8) was based on eleven branching orders, termed ‘Strahler orders’, of the rat renal circulation defined by Nordsletten *et al* (21). It was ‘calibrated’ with experimental measurements of the oxygen tension of blood in the efferent arterioles and renal vein of anesthetized rats (26). The model simulations predicted that AV oxygen shunting is quantitatively significant. More recently, Olgac and Kurtuoglu developed a model that predicts AV oxygen shunting to be

quantitatively insignificant (22). Importantly, neither model incorporated detailed information regarding the radial geometry of artery-vein pairs in the renal cortex (5, 23). Analyses of the impact of radial geometry (9, 20), predict that AV oxygen shunting is negligible unless the artery-vein pair are very closely associated. That is, AV shunting can only occur if the arterial wall is partially surrounded by the vein ('wrapped'). As a result of this phenomenon of wrapping, diffusion distances between the arterial and venous lumen are short and oxygen sinks (tubules and capillaries) are excluded from the pathway of AV oxygen diffusion.

Our analyses of the spatial arrangements of arteries and veins in the renal cortex, presented in Chapters 5-7 of this thesis, suggest that the radial geometry of artery-vein pairs changes along the course of the circulation. That is, at the level of individual vessel pairs, conditions for shunting are most favorable in the proximal renal circulation. When considering the renal circulation as a network, however, AV oxygen shunting is probably most favored in interlobular arteries because of their large number (see Chapter 7). Importantly, the phenomenon of wrapping was seen more frequently in the larger, more proximal vessels located at the corticomedullary region of the renal circulation. The data we based these conclusion on were generated from histological sections so only provide 'snapshots' of the radial geometry of artery-vein pairs. Synchrotron-based micro-computed tomography (micro-CT) has the potential to generate 3D reconstructions of the renal vasculature. Thus, it can be used to obtain information on axial geometry and thus convection, as well as radial geometry, and thus diffusion. Such 3D geometric information is vital for development of a realistic model of oxygen transport in the cortical circulation.

Micro-CT has been used previously to generate quantitative information regarding the geometry of the renal vasculature (21). One of the limitations of this approach is the potential for Microfil® to shrink (1, 18), particularly when exposed to solvents such as ethanol (18), as was the case in the studies of Garcia-Sanz and colleagues (7) which generated the material used in the previous analysis by Nordsletten and colleagues (21). Therefore, in the current study we avoided these processing steps to minimize shrinkage. However, there is still the potential for Microfil® to shrink, both during curing and after curing. Therefore we first determined whether Microfil® could be used without addition of the curing agent. We also determined whether, in the 24 hours after preparation of the tissue, there was appreciable shrinkage and/or deterioration of vascular casts generated with either cured or uncured Microfil®. Subsequently we compared the spatial characteristics of the cortical circulation determined by light microscopy and micro-CT. We then developed a method for automated

analysis of the radial geometry of artery vein pairs in micro-CT images, to examine the spatial relationships between arteries and veins at the corticomedullary region.

9.3 METHODS

9.3.1 Overview

To assess the effects of the curing process on shrinkage, rat kidneys were perfusion fixed and filled with Microfil®. Some component of the shrinkage of Microfil® is known to be due to the curing process (3, 10, 12). Thus, rat kidneys were perfusion fixed and filled with Microfil® that either included ($n = 6$) or excluded ($n = 3$) the curing agent, and then scanned to produce micro-CT images at two time points; immediately upon tissue preparation, and 24 hours later. Diameters of vessels were measured by manual analysis at both time points to determine the degree of shrinkage. An automated method was also used to analyze the spatial characteristics (diameter, diffusion distance, wrapping) of AV pairs in 3D reconstructed rat kidneys. Following the micro-CT scans, 3 μm sections were cut from four regions of each kidney, stained with hematoxylin and eosin, imaged by Scan Scope (Aperio, Vista, CA, USA) and viewed by a virtual microscope (Image Scope, version 11.2.0.780, Aperio Technologies).

9.3.2 Animal ethics

All procedures involving animals were approved by the Animal Ethics Committee of the Monash University School of Biomedical Sciences and were in accordance with the Australian Code of Practice for the Care and Use of Animals for Scientific Purposes.

9.3.3 Preparation of tissues for morphometric analyses

Tissue preparation was analogous to our previous study (20), as described in Chapter 6 of this thesis. In brief, male Sprague Dawley rats (weighing between 250 – 300 g) were anesthetized with pentobarbital (60 mg/kg. i.p; Sigma-Aldrich, St Louis, MO, USA). The kidneys were then cleared with phosphate buffer and perfusion fixed at physiological pressure with Karnovsky's fixative (4% paraformaldehyde and 4% glutaraldehyde in 0.2 M phosphate buffer). Once 10-12 ml of Microfil® (MV-122; Flow Tech, Carver, MA, USA) was infused, the renal artery and vein were ligated. The kidneys were removed, then immersed in fixative and transported immediately to the Imaging and Medical Therapy Beam Line (IMBL) at the Australian Synchrotron.

9.3.4 Micro-CT scanning and imaging

There were two application rounds of ‘beam-time’ in our study. In the first round of beam-time, we aimed to determine whether phase-contrast could enhance the edges of the vessel. To do this, whole kidney samples were placed 3.24 m away from the detector as the distance between a sample and the detector affects the edges of the object being imaged. However, as described in further detail later, the enhanced edges interfered with the fidelity of the algorithm we later developed for automated analysis of vessel geometry. Thus, in the second round of beam-time, whole kidneys were placed 0.38 m away from the detector. Thus in the second round we removed the edge enhancement by placing the kidneys closer to the detector.

Whole kidney imaging was carried out using the Ruby Detector at the IMBL. High-resolution images were captured using an X-ray source of 32 KeV at a voxel resolution of 6.3 μm in the object plane and 6.1 μm in the sample plane. To complete the scans, each tissue specimen was placed in an upright vial on a stage. The stage was rotated 180° in 0.25° increments, resulting in 720 projections. Routine background correction of all projections for X-ray beam instability and detector noise was performed. Twenty dark field (detector noise) and twenty bright field (excluding sample) images were obtained for background correction, both before and after each sample was scanned. To determine the amount of shrinkage within a 24-hour period, two scans were completed for each kidney; one immediately after tissue preparation and one 24 hours later.

9.3.5 Three-dimensional volume reconstruction of whole kidneys

Prior to rendering the whole kidney in 3D, each of the 5000+ image slices were visually inspected in ImageJ (<http://imagej.nih.gov/ij/>). Cross sectional images were reconstructed by the (Linear-Ramp) Filtered Back-Projection algorithm in XLI-XTRACT software (<http://www.ts-imaging.net/Services/AppInfo/X-TRACT.aspx>; CSIRO, Australia). The reconstructed slices were stored as 8-bit TIFF volumetric images. Images were then rendered using Drishti (version 2.4, <http://anusf.anu.edu.au/Vizlab/drishti/>) (15). Visualization and manipulation of whole kidneys were achieved using both Drishti and Avizo (VSG Inc., Burlington, MA, USA). ImageJ, Drishti and Avizo were accessed via the MASSIVE network (Multi-modal Australian ScienceS Imaging and Visualization Environment; National Computational Infrastructure, Australian National University, Australia).

9.3.6 Selection of artery-vein pairs and image analysis

We quantified the shrinkage of Microfil® over a period of 24 hours, between the first scan and second scan. The widths of artery-vein pairs were measured using Drishti and Avizo (MASSIVE network). Using Drishti, the measurements were taken at the same region in each reconstruction; at the base of branching of vessels (Fig. 9.1A & B). In total, 244 branching junctions were located in 6 kidneys. Using Avizo, a smaller subset of vessels was assessed by measuring diameters of only arteries (Fig. 9.1C & D). Two arterial ‘lines’ were analyzed in each kidney, one from the middle and one from the pole of the kidney. This resulted in a total of 66 measurements.

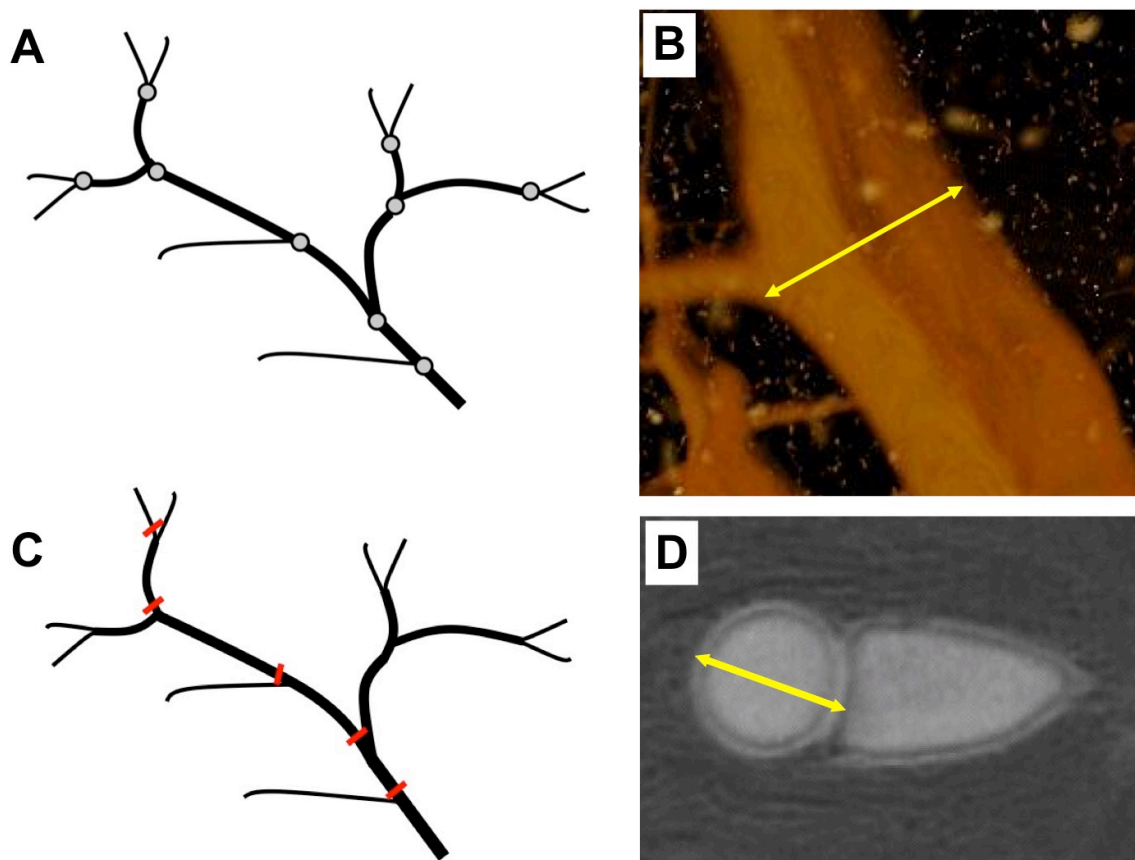


Figure 9.1. Selection of artery-vein pairs for determining shrinkage after 24 hours of tissue preparation. *Approach 1:* Beginning at the proximal vessels, a vessel pair was followed until another branching point was reached (A). Measurements were taken at the base of branching points (circles and B). At a branch point, one branch was chosen and followed. This was repeated until the most distal vessels were reached. The path was retraced back to previous branching points so that measurements were made along the other branches of the circulation that were not chosen before. *Approach 2:* Measurements were also taken in a smaller subset (C). In this subset, diameters of only arteries were measured (D) as opposed to the entire artery-vein pair (B). Measurements were generated from two arterial ‘lines’ in each of the six kidneys.

9.3.7 Histological tissue sections

Three kidneys were used to assess whether radial geometry of the cortical vasculature determined by micro-CT is similar to that determined by light microscopy. Once micro-CT images were obtained, the kidneys were removed from the vials and four regions of each kidney were cut. Each kidney was first cut in the sagittal plane, leaving two halves. One half was then cut in the longitudinal plane. For each plane, 1-2 mm thick sections from two different areas of the kidney were obtained; a slice near the midline and a slice in an intermediate position between the midline and the edge of the kidney (Fig. 9.2). A total of 12 sections (four from each kidney) were used for the qualitative morphometric analyses. The sections were then embedded in glycol methacrylate (Technovit 7100; Heraeus Kulzer GmbH, Wehrheim, Germany), sectioned at 3 μm and stained with Weigert's hematoxylin and eosin. Sections were scanned with Aperio Scan Scope (Aperio, Vista, CA, USA), providing a digital representation of the entire section.

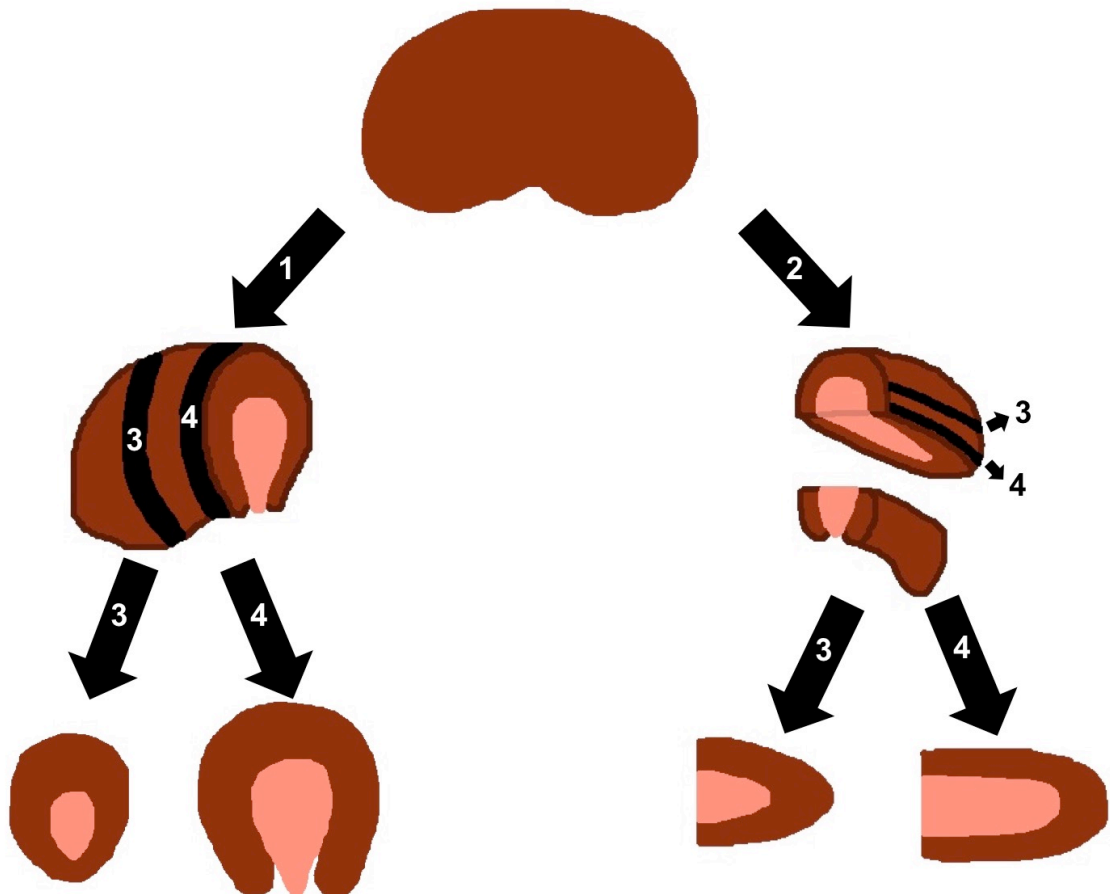


Figure 9.2. Sampling of renal tissue. For three rat kidneys, the kidneys were first cut in half. One half was cut in the transverse plane (1), and the other half in the longitudinal plane (2). For each half, two sections were cut. One piece was cut in the intermediate position between the midline and the end of the kidney (3). The other piece was cut at the midline (4). Each kidney thus resulted in four specimens.

9.3.8 Qualitative analysis: matching histological sections with corresponding micro-CT slices

ImageScope and Avizo were used to match histological and micro-CT sections. With the histological section viewed on ImageScope (version 11.2.0.780, Aperio Technologies), and the micro-CT 3D volume viewed concurrently on Avizo, large distinctive vessel pairs were first identified on the histological section. Large vessel pairs were of interest because their intimate spatial association may facilitate the diffusional shunting of oxygen (see Chapter 6). By knowing the approximate location where the histological section was derived, a two-dimensional (2D) slice could be manually moved through the 3D volume to first obtain an approximate match. Once this was achieved, we moved, rotated, and angled the plane of section to visualize the same distinctive vessels and any nearby glomeruli that could be identified on the histological section.

9.3.9 Quantitative analysis: Comparison of vascular geometry generated by micro-CT and light microscopy

Arterial diameter, diffusion distance, and proportion of wrapping were manually measured for vessel pairs, that were matched in both the light micrographs and micro-CT images, in a blinded manner. Artery-vein pairs were identified, matched in both micro-CT and light microscopy images, and then labeled. Measurements were first made for the artery-vein pairs in the light micrographs. Then, measurements were made for the artery-vein pairs in the micro-CT images. A total of 25 vessel pairs were identified across two kidney volumes.

9.3.10 Automated analysis of the radial geometry of artery-vein pairs

Sub-volumes of the 3D whole-kidney reconstructions were generated, that included large arteries ($> 100 \mu\text{m}$) that were expected to be partially wrapped by their corresponding veins. Across three kidneys, sub-volumes were selected in two regions of the kidney: a region in the midline of the kidney (mid-region), and a region between the mid-region and a pole of the kidney (outer region). For two of the kidneys, the selection of mid-region sub-volumes was based on the large distinctive vessels that were matched with the corresponding histological section (Section 9.3.8). For example, four distinctive vessel pairs in a section resulted in four sub-volumes. Because we could not match the micro-CT image with its corresponding histological image for one kidney, the selection of sub-volumes was based on large vessels at the mid-region. The selection of outer region sub-volumes was based on large distinct vessels in that region. This resulted in a total of 30 sub-volumes. The dimensions of each sub-volume were $512 \times 512 \times 512$ voxels. To validate the automated analysis software, smaller sub-

volumes were generated for some artery-vein pairs. The size of these smaller sub-volumes was restricted so that branches were excluded, thus allowing the software to compute measurements for a single ‘vessel’ between branch points.

Data processing and analysis of the 8-bit TIFF images (generated as described in Section 9.3.5) were performed using the commercial software package MATLAB (version 4.5.2, The Mathworks Inc., Natick, MA, USA). All voxels were then subjected to a threshold to distinguish the vascular voxels from the non-vascular (background) voxels (Fig. 9.3A). A multi-seed region growing process was performed for segmentation of arterial and venous voxels. At least one seed voxel was manually identified in each vascular region (arterial and venous; Fig. 9.3B). Once identified, each region was designated a vessel-type (artery or vein). Geodesic distances of vascular voxels from the nearest seed voxel were then generated. Each vascular voxel was then assigned a vessel-type. The vessel-type was the type of its nearest seed voxel. A volumetric atlas was then produced to map the vascular voxels to either ‘artery’ or ‘vein’. The atlas was then smoothed via an averaging filter. A 3D vascular geometry was produced using isosurface generation. The isosurface geometry was generated as a triangulated mesh. The geometry was simplified but still preserved vascular shape. A centerline (skeleton) was extracted from the 3D geometry using mesh contraction (2) (Fig. 9.3C) before the results of the automated analyses were generated (Fig. 9.3D).

One ‘vessel’ was defined as a segment of an artery between two branch points. A total of 339 vessels were identified and analyzed. The variables measured included radius, diffusion distance, and proportion of wrapping. These variables were measured at 6.3 μm intervals along the length of each vessel. For each vessel, the software generated the median radius (μm), the median diffusion distance (the shortest distance from the arterial and its nearest venous vessel), and the proportion of wrapping by the vein (%). Wrapping was based on the percentage of arterial surface area within a specified angle and proximity of a concave venous surface. An artery was defined as ‘wrapped’ only if it satisfied two rules. First, for any particular artery, the software produced lines that stem perpendicularly from the arterial surface. A semi-circular ‘pie’ was drawn at the point where the line radiating from the artery intersected the venous surface (Fig. 9.4A).

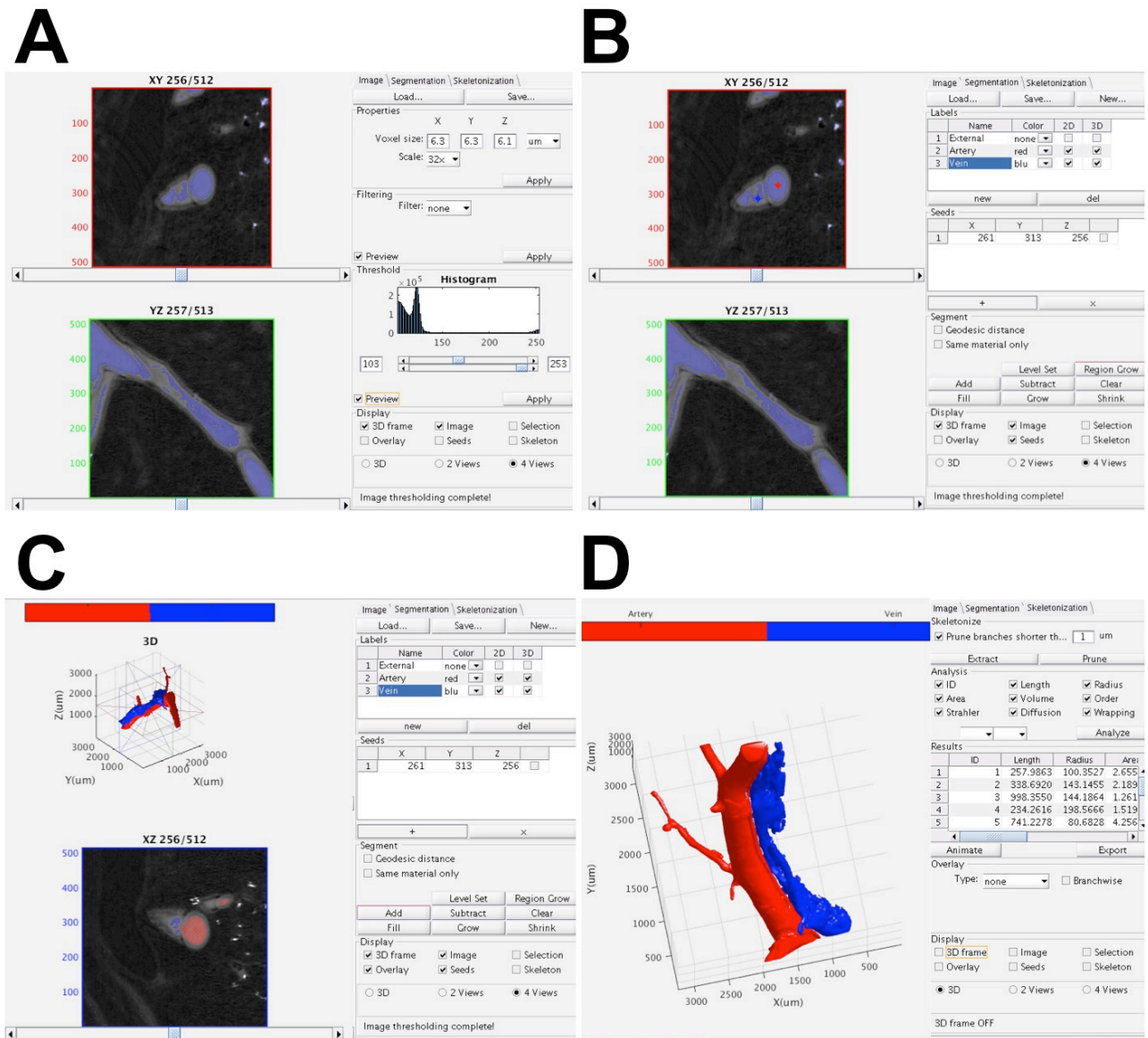


Figure 9.3. Generating automated analyses of artery-vein geometry via MATLAB. (A) An optimum threshold to distinguish the vascular elements from the background was first selected. (B) The arterial and venous regions were identified and a ‘seed’ was planted in each region (red seed = arterial, blue seed = venous). (C) Three-dimensional vascular geometry was generated and a centerline skeleton was extracted (red = arterial vessel, blue = venous vessel). (D) Automated analyses were generated and the data output exported to Microsoft Excel.

If the line passed through the smaller portion of the ‘pie’, this indicated the presence of ‘wrapping’ (Fig. 9.4A). If the line did not pass through this section, the software recognized this as the absence of wrapping (Fig. 9.4A). Thus, the size of the smaller portion of the ‘pie’ dictates the likelihood that the algorithm will detect ‘wrapping’ (Fig. 9.4B). Consequently, following some trials and observations, the specified angle was set at 45° (Fig. 9.4C). The trials to determine a valid angle involved changing the specified angle until it agreed well with visual inspection of wrapping. Second, wrapping was only considered where the venous surface was concave (negative curvature; Fig. 9.4D). Curvature was thus set at less than 0.

Hence, if the venous surface was convex (Fig. 9.4E), the software did not recognize this as wrapping despite satisfying the first requirement. ‘Proximity’ was based on diffusion distance being less than infinity. Thus all diffusion distances were included.

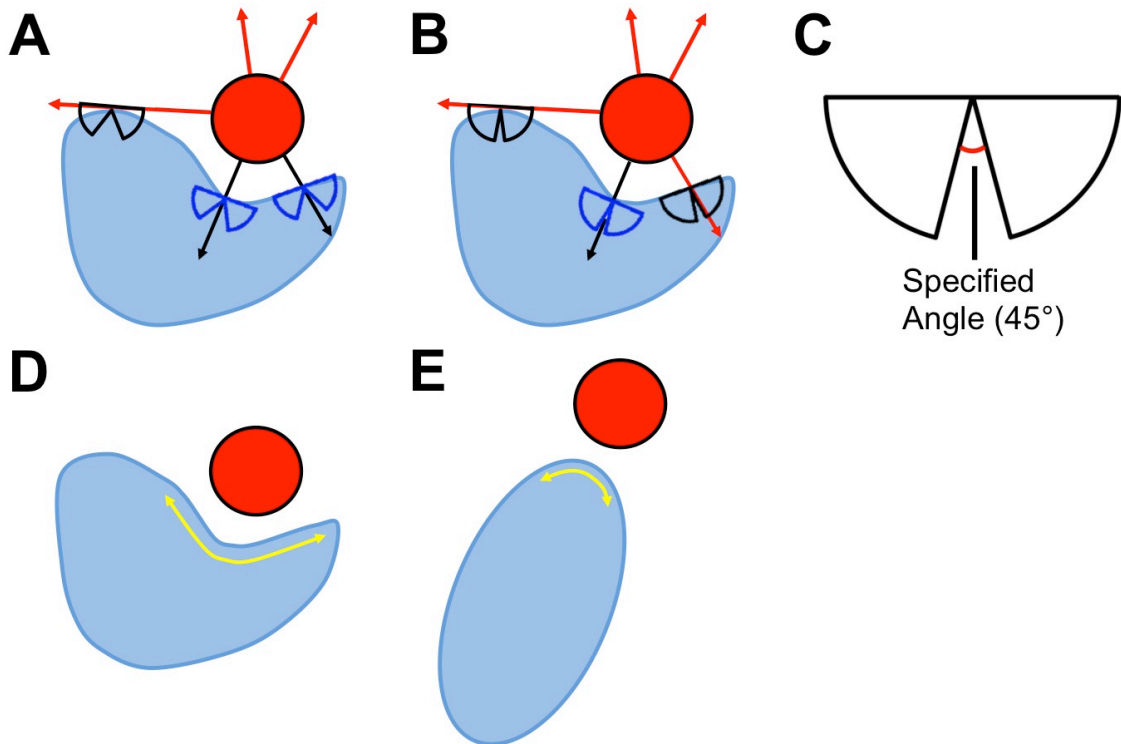


Figure 9.4. A schematic representing the method determining wrapping for an artery. (A) Lines radiate perpendicularly from the arterial surface towards the venous surface. A ‘pie’ is drawn perpendicularly at the point where the line intersects the venous surface. If the line passes through the smaller ‘portion’ of the pie, the application will recognize this as ‘wrapping’ (black arrows and blue pies). If the line does not pass through this smaller portion, it is classified as ‘non-wrapping’ (red arrows and black pie). **(B)** The size of the smaller portion of the pie will dictate the likelihood of the application recognizing ‘wrapping’. Here, the size of the smaller portion is reduced compared to **(A)** such that only one line now passes through (black arrow and blue pie). **(C)** The specified angle for our purposes was set at 45°. **(D)** Wrapping was only considered if the venous surface was concave. Convex venous surfaces were excluded and thus artery-vein pairs with this arrangement were classified as non-wrapped **(E)**. Red circle = artery, blue = vein.

9.3.11 Statistics

Data are presented as mean \pm standard error of the mean (SEM) unless stated otherwise. Ordinary least products regression was used to generate lines of best fit (16). Regression analyses were performed using SYSTAT v.13 (Systat Inc, San Jose, CA, USA). Paired t-tests were performed for matched data using Microsoft Excel. For all comparisons, two-tailed $P \leq 0.05$ was considered statistically significant.

9.4 RESULTS

9.4.1 Quality of Micro-CT reconstructions

There was a clear difference in the quality of visualization of the renal circulation depending on whether curing agent had been added to the Microfil® compound (Fig. 9.5). The vasculature of kidneys containing Microfil® and curing agent could be clearly visualized in the scans taken both immediately after (Figs 9.5G, I, K) and 24 hours after (Figs 9.5H, J, L) sample preparation. There was very little evidence of changes in the morphology of the Microfil® across the 24 h period. In contrast, while the three kidneys prepared without curing agent had reasonable, albeit somewhat patchy, visualization in the immediate scan (Figs 9.5A, C, E), visualization was poor in the scans 24 hours after sample preparation (Figs 9.5B, D, F). Consequently, subsequent analyses only included the 6 kidneys containing Microfil® and its curing agent.

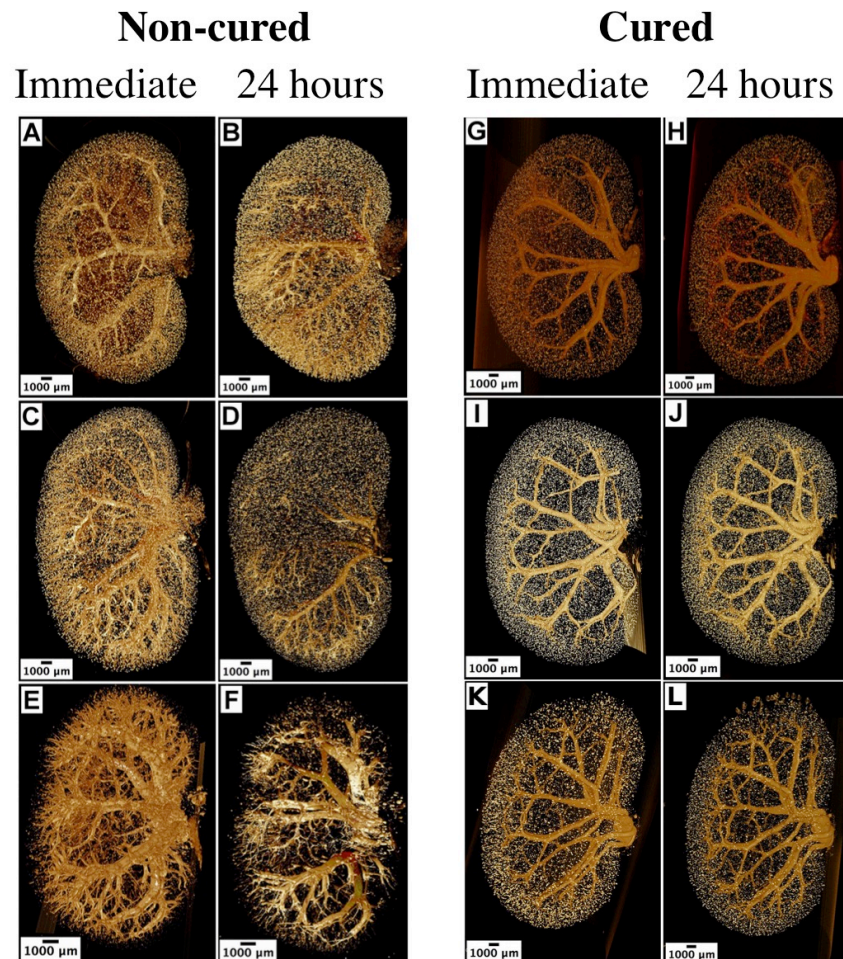


Figure 9.5. A comparison of kidneys with and without curing agent added to Microfil®. Left hand images are scans of the three whole kidneys with Microfil® excluding curing agent. Right hand images are scans of three of the six whole kidneys with Microfil® including the curing agent. ‘Immediate’ represents scans immediately upon tissue preparation, and ‘24 hours’ represents scans taken 24 hours following the first scan.

9.4.2 Shrinkage of Microfil

A quantitative analysis of the shrinkage of Microfil® demonstrated a small but statistically significant degree of shrinkage over the 24 hours between the two scans. The widths of a total of 244 vessel pairs (approach 1) in the six micro-CT reconstructions were compared. The overall mean width 24 hours after sample preparation ($594 \pm 16 \mu\text{m}$) was $3.27 \pm 0.63\%$ less than that determined immediately after sample preparation ($621 \pm 18 \mu\text{m}$; $P < 0.001$ by Student's paired t-test; Fig. 9.6A). When only arterial diameter was measured (approach 2), it was found to reduce by $2.2 \pm 0.4\%$, from $377 \pm 13 \mu\text{m}$ to $368 \pm 13 \mu\text{m}$ over the 24 h period ($P < 0.001$; Fig. 9.6B).

In order to better characterize the degree of shrinkage across the 24 hours after sample preparation, regression analysis was performed. Because the relationships between vessel diameter at the two time-points should theoretically pass through the origin, the ordinary least products method was used to generate a line in the form of $y = bx$, where y = the diameter of vessels 24 hours after sample preparation, x = diameter of vessels from the immediate scan, and b = the slope of the relationship between x and y .

For the analysis of the widths of vessel pairs (approach 1), the line of best fit was $y = 0.95x$, with 95% confidence limits of the slope that excluded unity (95% CI: 0.94 – 0.96). Thus, this regression analysis suggests that Microfil® shrinks ~5% following 24 hours of tissue preparation (Fig. 9.7A).

In the analysis of changes in arterial diameter across the 24 hours after sample preparation, ordinary least products regression (Fig. 9.7B) provided a line of best fit with the equation $y = 0.98x$. The 95% confidence intervals of the slope excluded unity (0.97 – 0.99). This analysis suggests that Microfil® shrinks by ~2% during the 24 hours after tissue preparation.

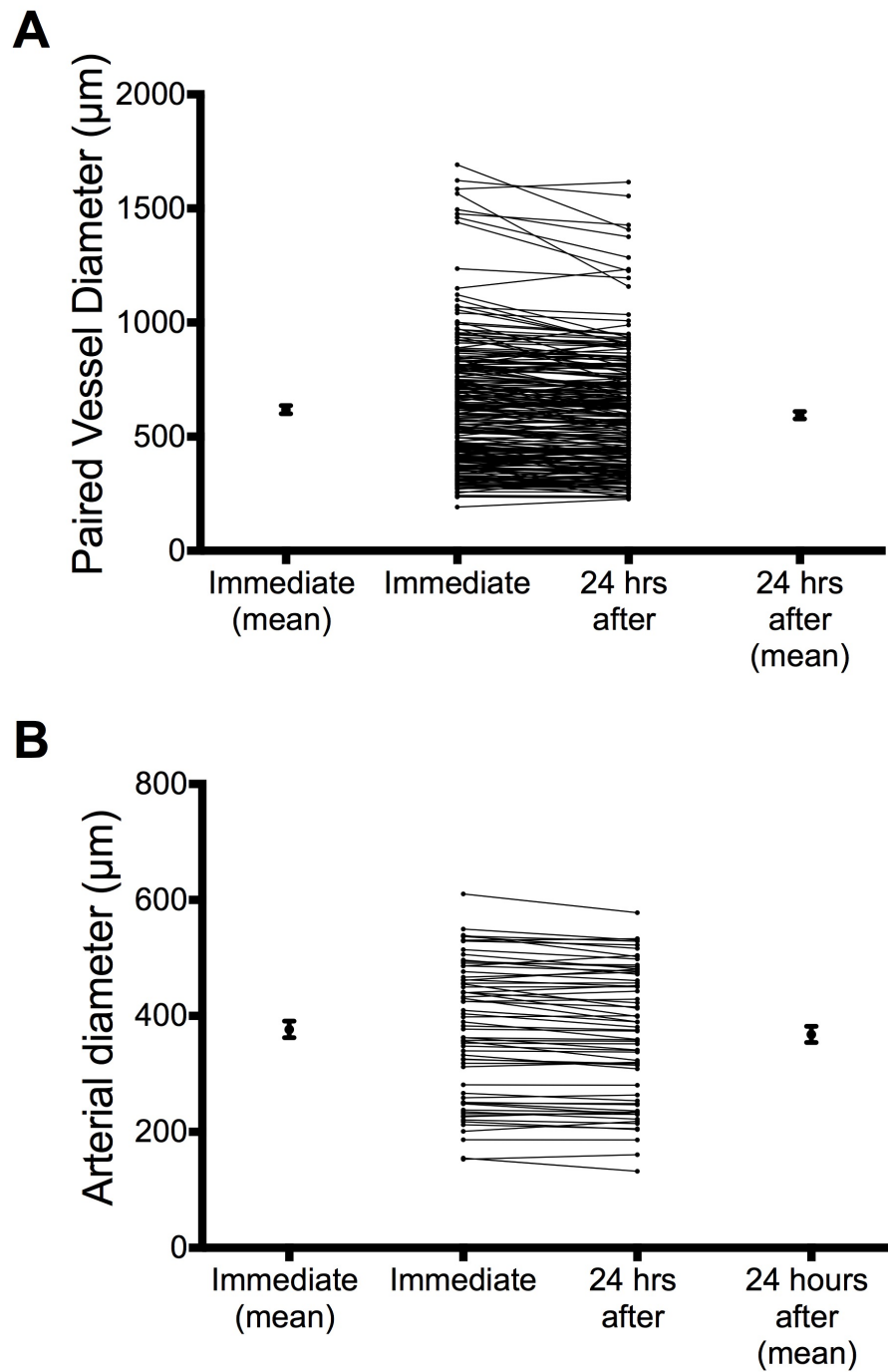


Figure 9.6. Vessel diameters from scans generated immediately after and 24 hours after tissue preparation. Panel A represents measurements of paired vessels (approach 1; $n = 244$) before and after 24 hours. Panel B represents the measurements of arterial diameter only (approach 2; $n = 66$). ‘Immediate (mean)’ represents the mean of all measurements taken in the initial scan. ‘24 hours after (mean)’ represents the mean of all measurements in the scan generated 24 hours after sample preparation. Symbols represent mean \pm standard error of the mean.

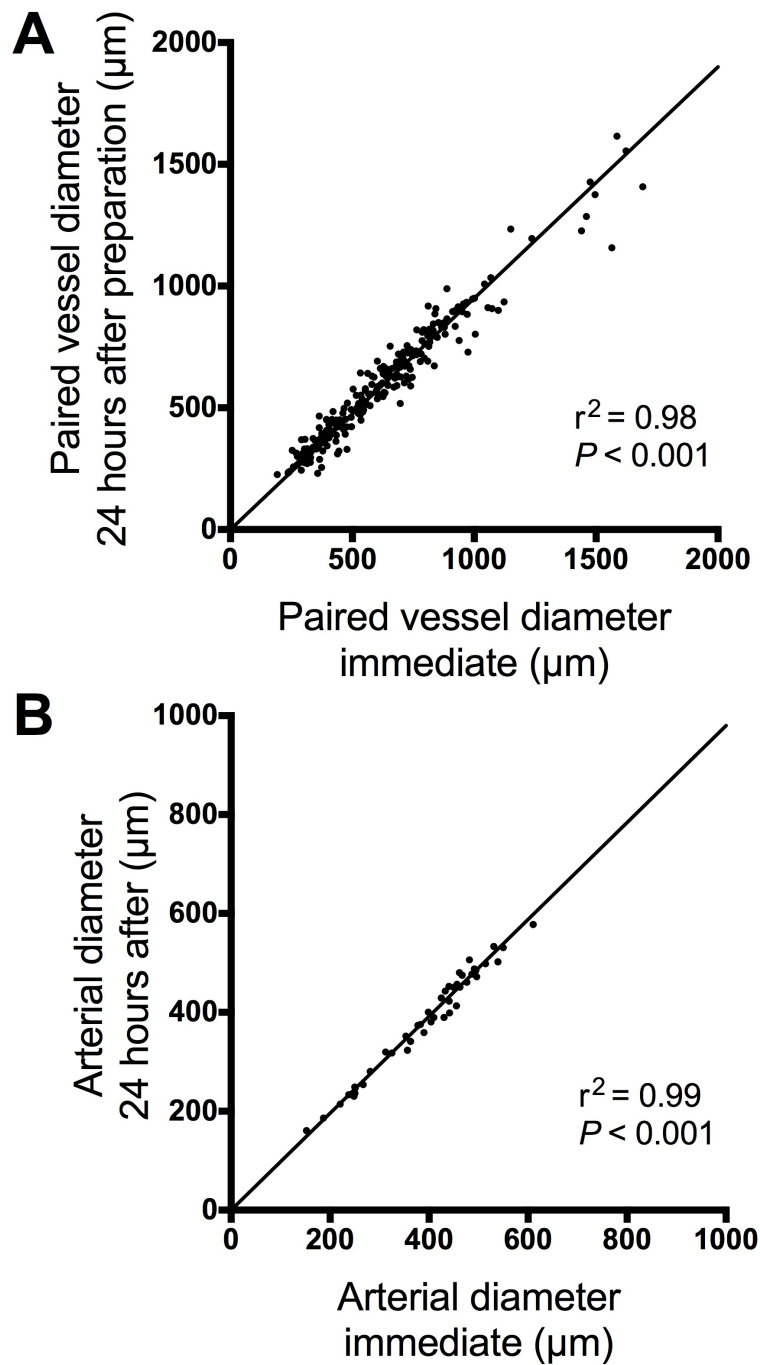


Figure 9.7. Ordinary least products regression analyses of the diameters of vessels determined from scans generated immediately after sample preparation and 24 hours later. **(A)** Paired vessel diameter before and 24 hours after preparation. **(B)** Arterial diameter in the immediate scan plotted against arterial diameter determined from scans taken 24 hours after sample preparation.

9.4.3 Qualitative comparison of vessel geometry using micro-CT and light microscopy

A qualitative comparison between histological and micro-CT sections demonstrated that vessels identified in the histological sections could be identified in the sections obtained by micro-CT (Fig. 9.8). Due to the difficulty of matching artery-vein pairs in light micrographs and micro-CT images, only a total of 17 artery-vein pairs were matched with artery-vein pairs in corresponding histological images. Glomeruli seen in the histological sections (Figs 9.8C, E, G, M, O, Q, S), were for the most part also observed in the micro-CT images as bright white dots (Figs 9.8D, F, H, N, R, T). In the light micrographs, Microfil® could be identified in most arteries and veins, as well as capillaries. The rings observed in the micro-CT images are artifacts due to phase-contrast. The rings are part of the true diameter of the vessels (as determined by the quantitative analysis below).

9.4.4 Quantitative comparison of light microscopy and micro-CT using manual analyses

Measurements of arterial diameter, diffusion distance, and wrapping determined from micro-CT images correlated strongly with corresponding measurements determined by light microscopy (Fig. 9.9).

Because the relationship between measurements generated using the two approaches might not necessarily pass through the origin, the ordinary least products method was used to generate a line of the form $y = bx + c$, where y = the variable measured in the micro-CT images, x = the variable measured in the histological images, b = the proportional bias, and c = the fixed bias.

For the analysis of arterial diameter (Fig. 9.9A), the line of best fit when including the ring artifact was $y = 1.10x + 14.35$. The 95% confidence limits of the slope included unity (95% CI: 0.93 – 1.27). The 95% confidence limits of the y -intercept included zero (95% CI: -37.52 – 66.21). For the analysis of arterial diameter excluding the ring artifact observed in the micro-CT images, the line of best fit was $y = 0.96x - 55.77$. The 95% confidence limits of the slope included unity (95% CI: 0.81 – 1.11). The 95% confidence limits of the y -intercept excluded zero (95% CI: -101.56 to -9.98). Thus, we could detect fixed bias in the micro-CT method compared with light microscopy only if the ring artifact was excluded. Importantly, no proportional bias could be detected, regardless of whether the ring artifact was included in the analysis. Nevertheless, arterial diameter was on average $11.2 \pm 4.9 \mu\text{m}$ less when the ring was excluded than when it was included ($P < 0.001$, paired t-test).

On average, diffusion distance was $45.55 \pm 2.98 \mu\text{m}$ greater when measurements included the ring artifact than when it was excluded ($P < 0.001$, paired t-test). Also, diffusion distance measured by micro-CT, including the ring artifact, did not differ significantly from that measured by light microscopy ($P = 0.89$, paired t-test). However, both fixed and proportional bias were detected by ordinary least products regressions analysis (Fig. 9.9B). The line of best fit could be described by the equation $y = 0.76x + 5.71$. The 95% confidence intervals of the slope excluded unity (95% CI: 0.53 – 0.98). The 95% confidence limits of the y-intercept excluded zero (95% CI: 0.20 – 11.22). Thus, manual measurements of diffusion distance from micro-CT images may generate an overestimate when diffusion distance is small, but may underestimate larger diffusion distances. For the analysis of diffusion distance excluding the ring artifact, the line of best fit was $y = 2.11x + 20.62$. The 95% confidence limits of the slope excluded unity (95% CI: 1.13 – 3.09). The 95% confidence limits of the y-intercept included zero (95% CI: -3.11 – 44.34). Thus, we detected proportional but not fixed bias, indicating an overestimation of diffusion distance when the ring artifact was excluded in our measurements.

In the analysis of wrapping, including and excluding the ring artifact, wrapping measured by the manual micro-CT method did not differ significantly from measurement via the light microscopic method ($P = 0.18$ and $P = 0.09$ respectively, paired t-test). When including the ring artifact, ordinary least products regression (Fig. 9.9C) provided a line of best fit with the equation $y = 1.08x - 4.13$. The 95% confidence intervals of the slope included unity (0.80 – 1.37). The 95% confidence limits of the y-axis included zero (95% CI: -14.22 – 5.97). Analysis of wrapping excluding the ring provided a line of best fit described by $y = 1.01x - 2.65$. The 95% confidence intervals of the slope included unity (0.68 – 1.35). The 95% confidence intervals of the y-intercept included zero (-14.51 – 9.21). On average, wrapping was $0.94 \pm 0.87\%$ greater when including the ring artifact than when the ring artifact was excluded ($P = 0.29$, paired t-test). Thus, we were unable to detect significant fixed or proportional bias in measurements of wrapping obtained from micro-CT images, regardless of whether the ring artifact was included or excluded.

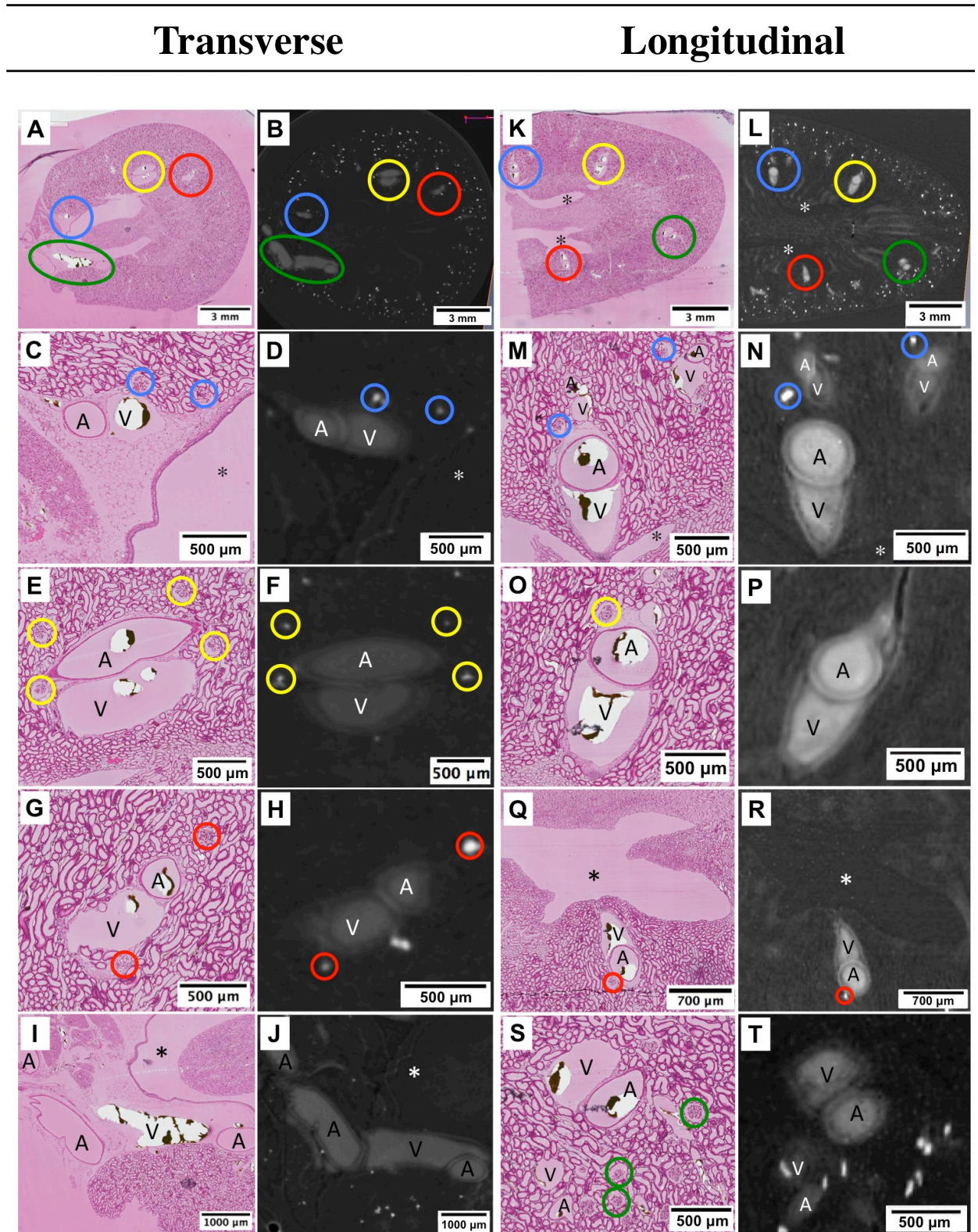


Figure 9.8. Sections of rat cortical tissue as observed by light microscopy and in corresponding micro-computed tomographic slices. Left and right pairs of images show sections in the transverse and longitudinal plane respectively. Histological images were stained with hematoxylin and eosin, photographed at $\times 0.7$ (A & K), $\times 2$ (I), $\times 3$ (Q), $\times 4$ (C, E, G, M, O), or $\times 5$ (S) magnification. Objects identified by color circles in A, B, K & L are shown at higher magnification in the lower panels. A = artery, V = vein, * = empty space.

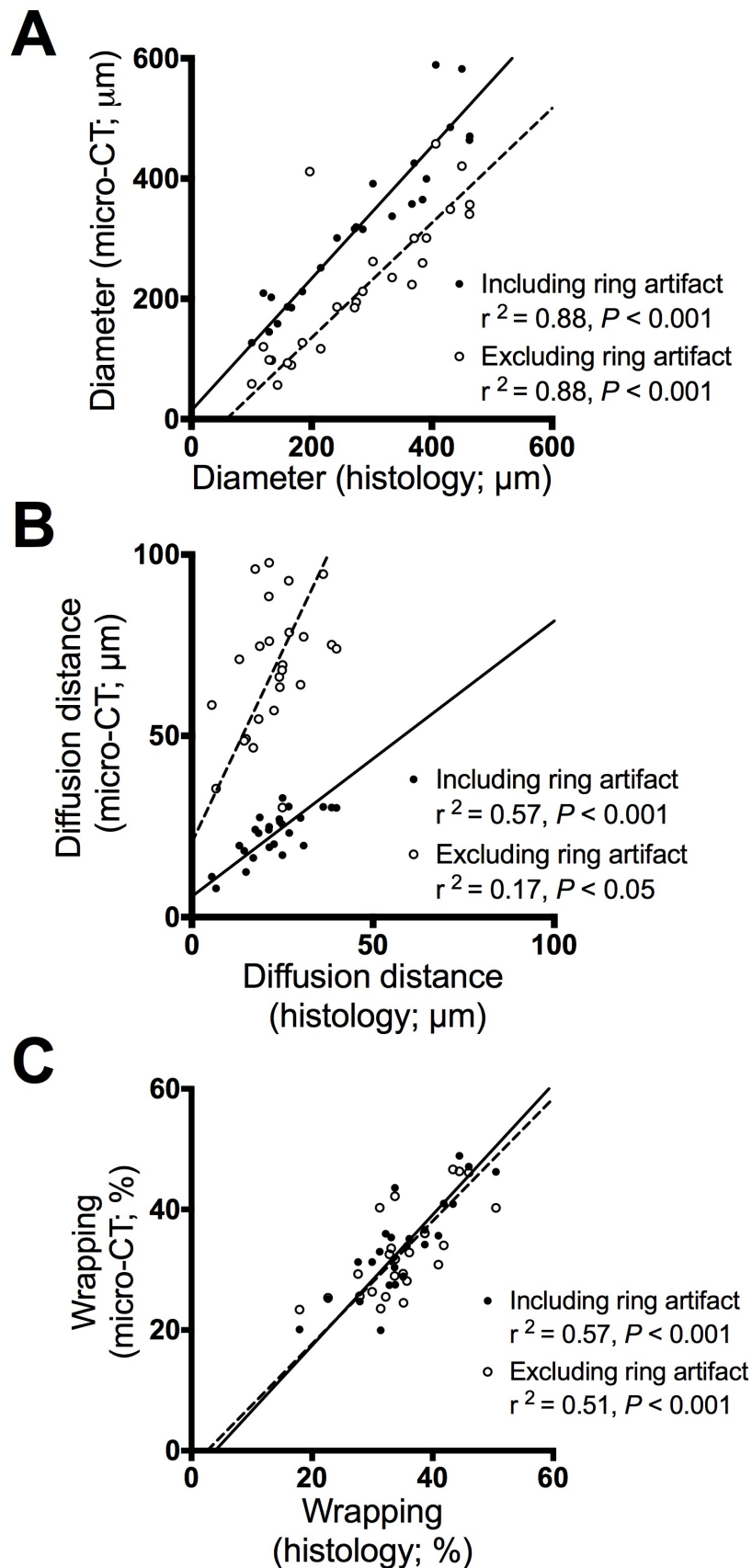


Figure 9.9. Relationships between measures of renal vascular geometry determined by light microscopy and micro-computed tomography (micro-CT) when the ring artifact was included and excluded. (A) Scatter-plot of arterial diameter. (B) Scatter-plot of diffusion distance. (C) Scatter-plot of proportion of wrapping. Lines of best fit were determined by ordinary least products regression analysis (16).

9.4.5 Quantitative comparison of light microscopy and automated analyses via micro-CT

There appeared to be major differences between measurements of diameter and diffusion distance between the manual and automated approaches. The automated method systematically underestimated arterial diameter and wrapping, while overestimating diffusion distance, relative to the manual method (Fig. 9.10). Compared to the manual method, arterial diameter was mostly smaller when using the automated approach (Fig. 9.10A). Ordinary least products regression (Fig. 9.10A) provided a line of best fit with the equation $y = 1.11x - 106.60$. The 95% confidence intervals of the slope included unity (0.64 – 1.57). The 95% confidence limits of the fixed bias included zero (95% CI: -269.76 – 56.57). Thus we could not detect significant proportional or fixed bias in the automated method compared to the light microscopic method. Nevertheless on average arterial diameter was $70.87 \pm 18.51 \mu\text{m}$ less when determined using the automated method than when determined by light microscopy ($P = 0.005$, paired t-test).

Diffusion distance was systematically greater in the automated measurements than those generated manually from either the micro-CT images or the corresponding light micrographs (Fig. 9.10B). On average, diffusion distance was $43.39 \pm 8.75 \mu\text{m}$ greater in the automated measurements than in the manual measurements ($P < 0.001$, paired t-test). Ordinary least products regression of the relationship between measurements of diffusion distance obtained by the automated method and by light microscopy, provided an equation $y = 5.43x - 74.17$. The 95% confidence intervals of the slope excluded unity (1.36 – 9.49). The 95% confidence limits of the y -intercept included zero (95% CI: -185.20 – 36.86). Thus we detected significant proportional bias, but not fixed, in automated measurements of diffusion distance.

Proportion of wrapping tended to be less in the automated measurements than those generated manually or from either the micro-CT images or the corresponding light micrographs (Fig. 9.10C). Ordinary least products regression provided an equation $y = 0.92x - 18.73$. The 95% confidence intervals of the slope included unity (0.14 – 1.70). The 95% confidence limits of the y -intercept included zero (95% CI: -47.12 – 9.67). Thus, we could not detect significant fixed or proportional bias in automated measurements of wrapping relative to those determined by light microscopy. Nevertheless, there was a clear trend for the line of best fit for the automated method to be shifted to the right of the line of best fit for the manual method. On average, wrapping was $21.55 \pm 2.36\%$ less when determined using the automated method compared to the manual method ($P < 0.001$, paired t-test).

Collectively, these data indicate that the automated approach underestimates arterial diameter (Fig. 9.10A) and wrapping (Fig. 9.10C), and overestimates diffusion distance (Fig. 9.10B).

9.4.6 Automated analysis of vessel geometry

Our current automated analysis of micro-CT images generated a data set of the relationships between arterial diameter and both diffusion distance and proportion of wrapping that could be compared with our previous data set generated by light microscopy in the experiments described in Chapter 6 (Fig. 9.11). The two data sets are clearly different, attributable in part to the fact that the automated method overestimates diffusion distances and underestimates proportion of wrapping. It is also relevant to note that larger arteries are relatively over-represented in the micro-CT data set relative to the data set from light microscopy.

The micro-CT data-set provides evidence of greater variation among larger artery-vein pairs (arterial diameter $>100\ \mu\text{m}$), in both diffusion distance and wrapping, than was evident from our previous light microscopic analysis (Chapter 6 of this thesis). Taken at face value, this analysis suggests that a considerable number of larger arteries do not show wrapping (Fig. 9.10B).

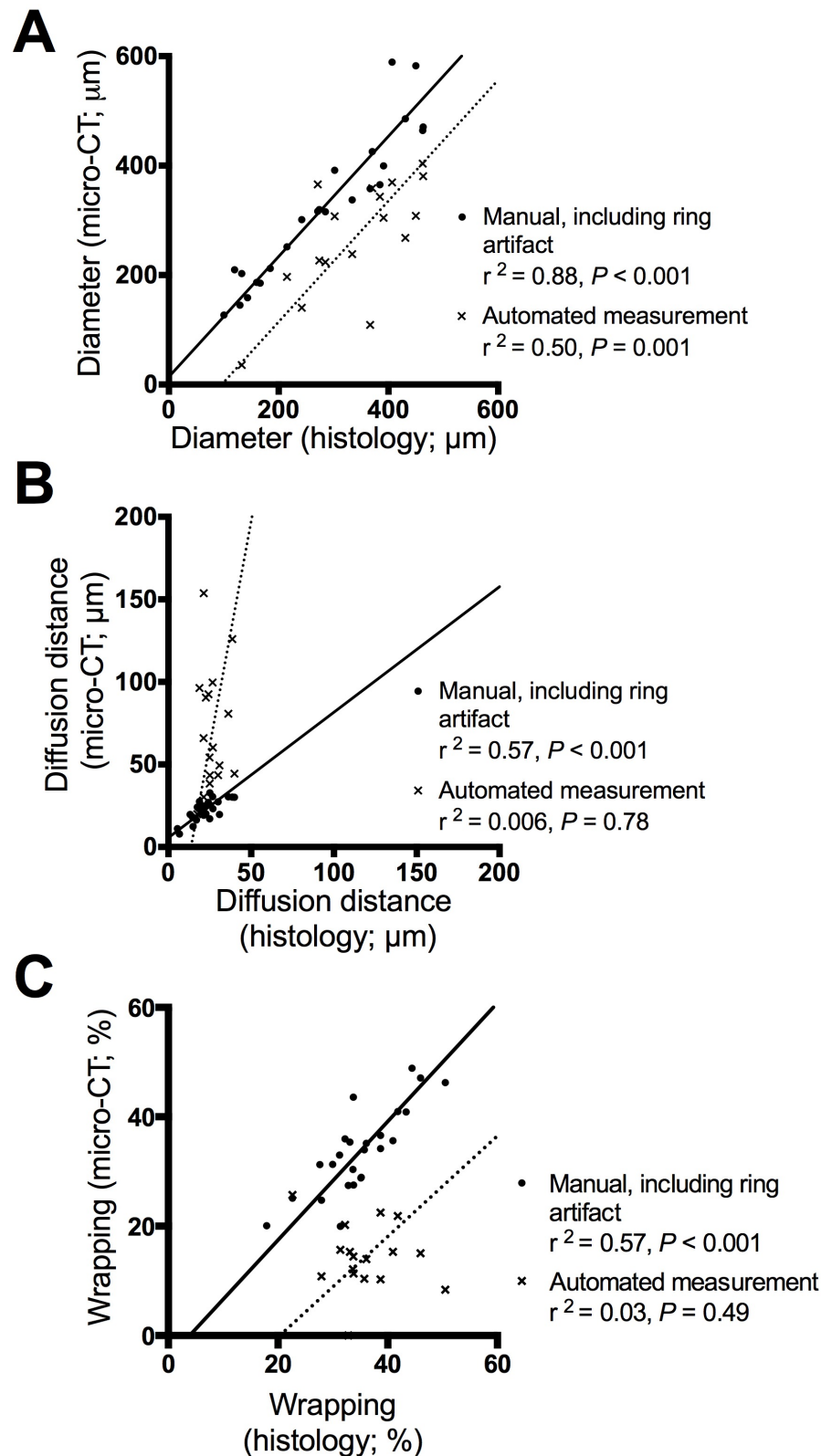


Figure 9.10. Relationships between manual and automated measures of renal vascular geometry determined by light microscopy and micro-computed tomography (micro-CT). (A) Scatter-plot of arterial diameter. (B) Scatter-plot of diffusion distance. (C) Scatter-plot of proportion of arterial profile wrapped by the vein. Lines of best fit were determined by ordinary least products regression analysis (16).

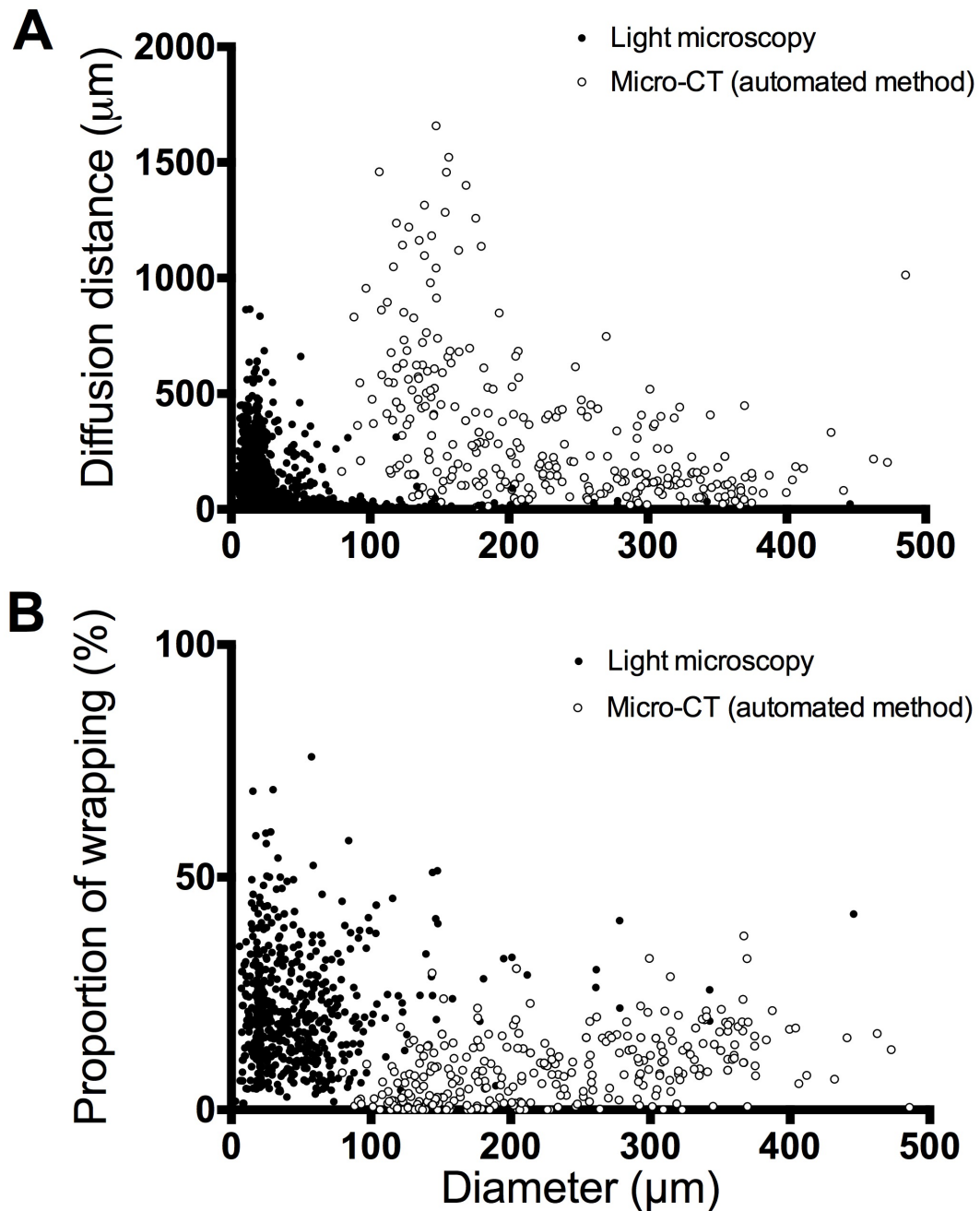


Figure 9.11. Scatter plots of the relationships of diffusion distance (A) and proportion of wrapping (B) with arterial diameter. Each plot shows data from 207 vessel pairs from micro-CT and 1648 vessel pairs from light microscopy. The light microscopic data are reproduced from data presented in Chapter 6 of this thesis.

9.5 DISCUSSION

9.5.1 Main findings

We have determined that measurements of vascular geometry derived from micro-CT images correspond closely with those derived from histological images. To the best of our knowledge, previous renal vascular imaging studies utilized techniques that would have resulted in shrinkage of the polymer. Thus our new method enables observations of ‘real’ vessel geometry. We have also determined that there is insignificant shrinkage of Microfil® following 24 hours after tissue preparation for micro-CT imaging. Thus micro-CT images can be used for analysis of vascular geometry. We also developed an automated method to analyze the geometry of artery-vein pairs, in the rat renal cortex, from micro-CT images. However, in its current form, this automated method does not provide accurate measures of arterial diameter, diffusion distance, and wrapping. Specifically, this method underestimates arterial diameter and wrapping, and overestimates diffusion distance compared to measurements determined from histological analysis or from manual analysis of micro-CT images.

9.5.2 Analysis of the quality of cured and non-cured Microfil®

By omitting the curing agent in three of the rat kidneys, we aimed to generate a 3D reconstruction of the renal cortical vasculature free of the effects of shrinkage or breakage of the polymer. However, it was apparent that the kidneys that excluded curing agent were not adequate for analysis following 24 hours. These kidneys had many missing vessels 24 hours after infusion of the Microfil®. There were regions of vessel sparseness, suggesting that the Microfil® solution had separated into two components; the MV-Compound and the MV-Diluent. These compounds are mixed before infusion. However, it is highly likely that the heavier component (MV-Compound), which contains lead chromate and can thus be visualized by synchrotron radiation, sinks to the bottom while the MV-Diluent disperses to the top. This is especially since the compounds were not polymerized. On the basis of these findings, we recommend that cured Microfil® should always be used in preference to non-cured Microfil®, unless the micro-CT scans are conducted immediately upon tissue preparation. Furthermore, as a consequence of these preliminary observations, subsequent analyses focused only on those kidneys that were filled with Microfil® and curing agent.

9.5.3 Analysis of shrinkage of Microfil®

An important consequence of the requirement for curing agent in studies using Microfil® is that we cannot account for shrinkage that might occur in our samples during the curing process. However, this effect is likely small, since we demonstrated close agreement between measures of vascular geometry obtained manually from micro-CT images and those obtained from light microscopy. Furthermore, shrinkage of only 2-5% was observed over the 24 hours following tissue preparation. Nevertheless, this shrinkage could potentially in-part explain the overestimation of diffusion distance when estimated from manual analysis of micro-CT images compared with estimation from light microscopic images.

A major limitation of previous studies in which renal vascular geometry was quantified by micro-CT (21) was that the tissues were exposed to organic solvents which would promote shrinkage of Microfil®. Indeed, we have estimated that the processing of the tissues analyzed by Nordsletten and colleagues would have led to ~22% shrinkage (see Chapter 7 of this thesis). Therefore, in the current study we avoided use of such solvents. Using this approach, we were also able to show minimal shrinkage in the 24 hours after tissue fixation and filling of the vasculature with Microfil®. Using multiple analytical approaches, we found only 2-5% shrinkage of Microfil® in the 24 hours after preparation of the tissue for micro-CT. This knowledge can be used in future quantitative studies and the shrinkage of Microfil® can be accounted for. Furthermore, due to time constraints, some studies require a delay between tissue preparation and scanning. Thus some scans may be completed a day after the tissue has been prepared for micro-CT. Our current findings provide confidence that data from such studies are unlikely to be greatly confounded by shrinkage. Unfortunately, a limitation is that we do not know how much shrinkage there is beyond 24 hours, so our findings cannot be applied to micro-CT scans completed more than 24 hours after tissue preparation.

9.5.4 The validity of manual analysis of renal vascular geometry from micro-CT

The morphology of the vasculature determined from micro-CT images closely resembled that from light microscopy. However, the histological and micro-CT sections did not match completely. Some glomeruli were not apparent in the histological section despite being clearly visible in the micro-CT image. This is most likely due to two factors: (i) the angle of the sections, and (ii) the final position the tissue was embedded in for histological analyses. Some tissues were embedded at a slight angle, despite care being taken in attempting to embed the tissues completely flat in the mold. This was likely a result of the use of thin tissue

sections. Nevertheless, we observed that the micro-CT images in large part accurately mirrored the corresponding histological images. Thus, the micro-CT approach appears to accurately reflect true vascular geometry.

To assess whether the ring artifact should be included in our manual micro-CT measurements, we compared measurements of arterial diameter, diffusion distance and proportion of wrapping generated from micro-CT images with those of light microscopy. We found that when the ring artifact was excluded, arterial diameter was underestimated, and diffusion distance overestimated. However, we could not detect a difference in the proportion of wrapping between the two ring artifact methods. The similarity in the lines of best fit for proportion of wrapping, regardless of whether the ring artifact was included or not, was a result of the consistent width of the ring artifact in both the artery and vein (Fig. 9.12). An analysis of the proportion of wrapping excluding the ring was predicted to generate similar results to those when the ring artifact was included (Fig. 9.12). Indeed, we could not detect a significant difference in proportion of wrapping regardless of whether the ring artifact was included or not.

To quantitatively assess the validity of the micro-CT approach, we determined the relationships between spatial characteristics determined by the two approaches. There was a strong correlation between the two methods, demonstrating that micro-CT is a valid approach in accurately quantifying the spatial characteristics of the renal circulation. Indeed, no fixed or proportional bias, for micro-CT relative to light microscopy, was detected for measurements of arterial diameter or proportion of wrapping. However, we did detect proportional bias for diffusion distance. Nevertheless, the mean estimate of diffusion distance did not differ between the two methods, and the level of bias was small. Thus micro-CT appears to be particularly useful for analysis of larger vessels, which tend to be underrepresented in data sets generated by light microscopy. Thus, micro-CT and light microscopy appear to complement each other. By combining these approaches, information on the radial geometry of both large and small vessel-pairs can be generated.

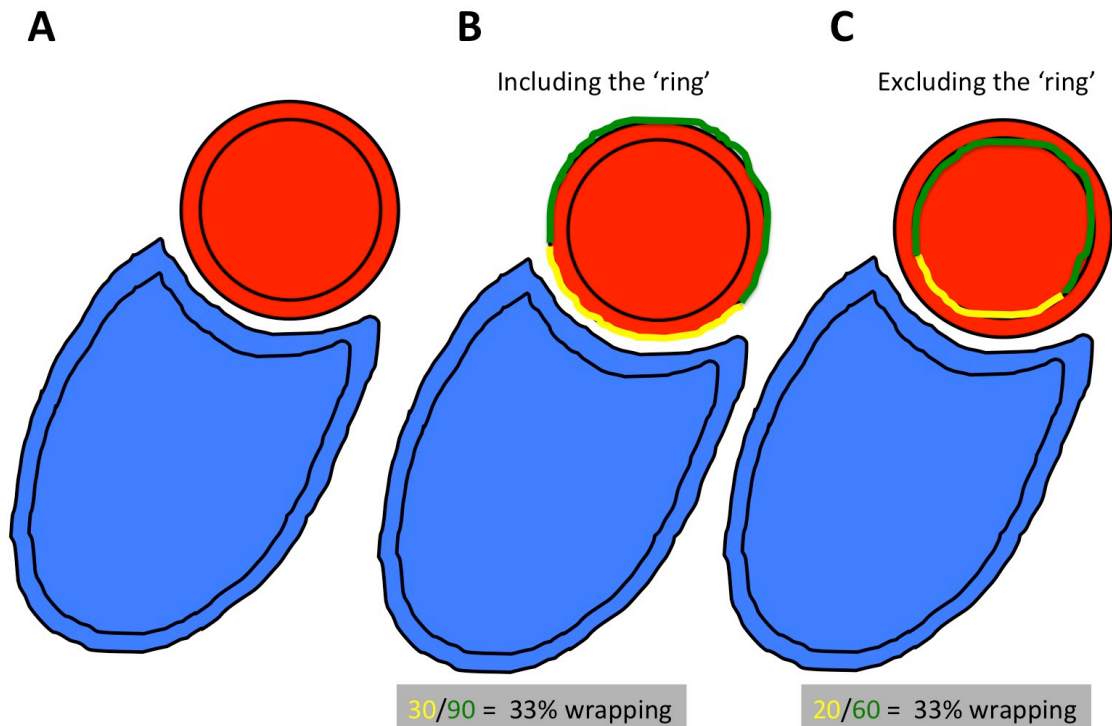


Figure 9.12. A schematic of artery vein pairs with ring artifacts and a possible explanation for the results shown in Figure 9.9C. Proportion of wrapping is calculated by dividing the arterial lumen wrapped by the vein (yellow) by the arterial lumen not wrapped by the vein (green). (A) An example of an artery vein pair with ring artifacts. (B) An example of how wrapping including the ring artifact was calculated. (C) An example of how wrapping excluding the ring artifact was calculated. Although the raw numbers are different, calculations of proportion using either method provides similar results (33% wrapping).

9.5.5 Automated analysis of micro-CT volumes

Our approach to generate quantitative information regarding the spatial characteristics of the renal cortical circulation requires multiple techniques. A 3D reconstruction of the renal vasculature along with automated image analysis software could potentially provide a rapid, automated approach. An automated method could greatly increase the efficiency of data collection from micro-CT.

To determine if micro-CT and image analysis software can provide a valid method for analysis of the radial and axial geometry of artery-vein pairs, we first extracted sub-volumes of the 3D micro-CT volumes. Unfortunately, the current formulation of the automated method systematically underestimates arterial diameter and proportion of wrapping and overestimates diffusion distance.

The precise explanation for the inaccuracy of the automated method could not be determined. However, one potential factor is the presence of ring artifacts in the images we used for automated analysis. These rings impede the efficiency of the algorithm we used. The algorithm uses grey scale contrast to identify the beginning and end of a vessel. The presence of the ring artifacts could therefore lead the algorithm to underestimate vessel diameter and overestimate diffusion distance. This was evident in our quantitative analyses (section 9.4.5).

The ring artifact is caused by edge enhancement, which is a consequence of phase contrast. Snigirev *et al* were the first to explore the concept of phase contrast X-ray imaging (24). It is now a technique used to image various soft tissues. Phase contrast imaging, more specifically propagation based imaging (PBI), produces ‘edge effects’. PBI employs the same equipment as conventional radiography: an X-ray source, sample and X-ray detector. The major difference is the distance between the sample and detector. The detector is placed at some distance away from the sample, not immediately behind the sample. Our initial samples (first round of beam-time) were placed at a distance of 3.24 m away from the detector. Our second group of samples (second round of beam-time) were placed 0.38 m away from the detector.

PBI is based on the same principle as that of in-line holography (24), where radiation refracted by the sample can interfere with the beam. The distance between the sample and the detector affects the scatter of radiation by the sample (Fig. 9.13). If the detector is placed too far behind the sample, distortions in the waves produced by the sample will subsequently generate edge effects or ‘interference fringes’ (6).

Phase contrast is a technique that can be exploited in imaging of soft tissue due to its ability to improve contrast for samples of ‘lighter elements’ (6). Indeed, numerous studies have examined the advantages of phase-contrast imaging in soft biological tissues (4, 11, 17, 19, 25). Thus, it appears that phase contrast radiography has potential for use in biological soft tissue as it generates images with stronger contrast outlining the surface or edges. The stronger contrast consequently allows for greater definition at the edges.

An early objective of the first round of ‘beam-time’ was to determine whether we could improve soft-tissue definition by phase-contrast while simultaneously obtaining absorption images of the renal vasculature. However the interference fringes created by phase-contrast prevented us from fully exploiting the then-yet-to-be-generated software algorithm developed by our colleagues. Thus, our initial imaging method confounded accurate measurements of vessels, particularly when there is ‘wrapping’ by the vein. Our studies in the second round of beam-time consisted of samples that were placed much closer to the detector. In these images

no edge effects were observed. However, the rat kidneys were poorly filled with Microfil® and could not be used in the automated vessel segmentation analysis. The kidneys from this group, however, were used for determining the shrinkage of Microfil® 24 hours after tissue preparation.

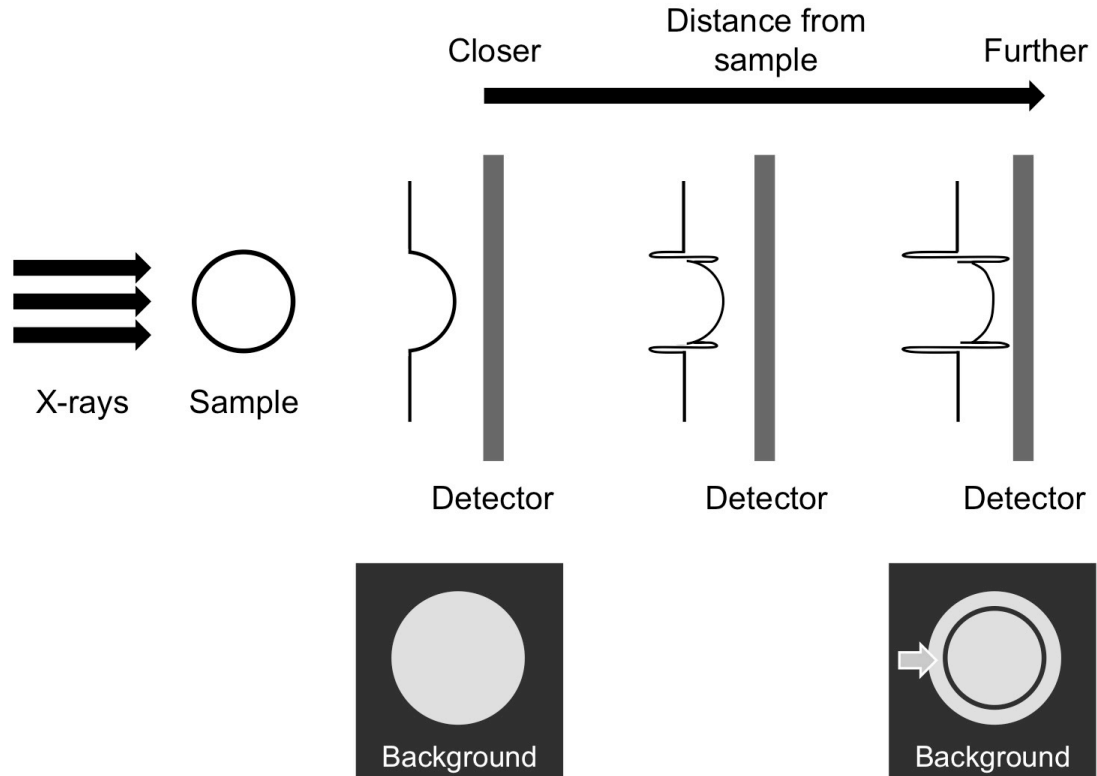


Figure 9.13. Schematic of the concept of propagation-based imaging. Interference fringes are generated if the distance between the sample and detector is increased sufficiently. The different wavelength patterns generated result in different images captured by the detector (bottom of the schematic). If the distance between the sample and detector is short, the fringes in the resulting image will be absent. If the sample is placed further away from the detector then the fringes will be present (arrow).

An additional factor that could confound automated analysis of micro-CT images arises from the fact that the algorithm requires an adequate separation distance between the paired vessels in order for it to calculate separation. This represents an important caveat to our approach. If the grey scale threshold is set at a low level, the shape of the afferent and efferent vessels are close to their true geometry but will ‘leak’ into each other in the process of image analysis. Thus the threshold must be increased sufficiently to remove the opportunity for the vessels to leak into each other. However, increasing the threshold reduces arterial diameter since the vessels are brightest at the center and, as we move radially outwards, gradually ‘fade’ to the background. Consequently both vessel diameter and wrapping would be underestimated, whereas diffusion distance would be overestimated.

Additionally, because the software only applies ‘wrapping’ to concave venous surfaces, smaller degrees of wrapping cannot be computed by the software. Our previous work using histological sections included both concave and convex venous surfaces in the determination of the proportion of wrapping of arteries by veins (see Chapter 6; (20)). Our only condition for ‘wrapping’ in that study was that there had to be no oxygen sinks (veins, arteries, capillaries, glomeruli or tubular structures) between an artery-vein pair. The exclusion of convex venous surfaces from analysis for wrapping would lead the software to again underestimate wrapping for artery-vein pairs with this particular spatial arrangement. However, the results in our previous study suggest that convex venous surfaces are more frequent in smaller artery-vein pairs (20). The larger artery-vein pairs, such as those analyzed in the present study, commonly consist of the afferent vessel being partially enveloped by the efferent vessel. Thus a concave venous surface frequently exists in these larger artery-vein pairs.

Another limitation in our approach is the inability for the software, in its current form, to segment and thus analyze a large volume of the renal cortical circulation. Thus, in the present time we cannot use the automated approach to determine how the spatial relationships that likely favor AV shunting of oxygen change along the course of the circulation. We are also further limited by the resolution of the images. The images we have captured can resolve up to the proximal interlobular vessels at best. Vessels smaller than these are indistinguishable, apart from glomerular capillaries, which appear as a ‘ball’ or dot. In an attempt to visualize smaller interlobular vessels, we imaged biopsies of kidney cortex with a higher resolution beam at the Swiss Light Source (Paul Scherrer Institute, Villigen, Switzerland). However the beam was not appropriate for the kidney biopsies (see a more detailed discussion in Chapter 10 of this thesis). Thus we currently are yet to resolve smaller vessels via micro-CT. We should aim to image more rat kidneys in the future and then use the software on ideal images that do not include ring artifacts.

While light microscopy allows for visualization of the smaller vessels, we are limited by 2D images. A significant advantage of using a 3D image is the ability for us to potentially follow the course of the circulation. The method developed in this study can also provide information on the axial geometry of the circulation, important information that cannot be obtained using 2D images generated from light microscopy.

9.5.6 Conclusions

It is feasible to utilize micro-CT techniques to gather information on the spatial relationships of arteries and veins in the rat kidney. Manual analysis of micro-CT data appears to be a valid approach. However, the automated method we developed, in its current form, shows promise but is not completely valid. It overestimates diffusion distance and underestimates vessel diameter and wrapping. However, we believe that once the method has been refined, there is great potential for this approach to provide a rapid analysis of the spatial associations of artery-vein pairs in the kidney. An alternative image-processing technique may be required to resolve smaller vessels. Indeed, both light microscopy and micro-CT approaches are required to assess the spatial relationships over a wide range of vessel diameter. An automated method has potential to be applied to analyses of the vascular geometry of various species and disease states, but our current method will require considerable refinement.

REFERENCES

1. **Bentley MD, Jorgensen SM, Lerman LO, Ritman EL, Romero JC.** Visualization of three-dimensional nephron structure with microcomputed tomography. *Anat Rec* 290: 277-283, 2007.
2. **Cao J, Tagliasacchi A, Olson M, Zhang H, Su Z.** Point cloud skeletons via laplacian based contraction. *Shape Modeling International Conference (SMI)*.
3. **Cortell S.** Silicone rubber for renal tubular injection. *J Appl Physiol* 26: 158-159, 1969.
4. **Elodie P, Stefan F, Peter C, Alberto B, Paola C, Kamel F, José B, Jürgen H.** Quantitative comparison between two phase contrast techniques: diffraction enhanced imaging and phase propagation imaging. *Phys Med Biol* 50: 709, 2005.
5. **Evans RG, Smith DW, Khan Z, Ngo JP, Gardiner BS.** Letter to the editor: "The plausibility of arterial-to-venous oxygen shunting in the kidney: it all depends on radial geometry". *Am J Physiol Renal Physiol* 309: F179-180, 2015.
6. **Fitzgerald R.** Phase-sensitive X-ray imaging. *Phys Today* 53: 23-27, 2000.
7. **Garcia-Sanz A, Rodriguez-Barbero A, Bentley MD, Ritman EL, Romero JC.** Three-dimensional microcomputed tomography of renal vasculature in rats. *Hypertension* 31: 440-444, 1998.
8. **Gardiner BS, Smith DW, O'Connor PM, Evans RG.** A mathematical model of diffusional shunting of oxygen from arteries to veins in the kidney. *Am J Physiol Renal Physiol* 300: F1339-1352, 2011.
9. **Gardiner BS, Thompson SL, Ngo JP, Smith DW, Abdelkader A, Broughton BR, Bertram JF, Evans RG.** Diffusive oxygen shunting between vessels in the preglomerular renal vasculature: anatomic observations and computational modeling. *Am J Physiol Renal Physiol* 303: F605-618, 2012.
10. **Ghanavati S, Yu LX, Lerch JP, Sled JG.** A perfusion procedure for imaging of the mouse cerebral vasculature by X-ray micro-CT. *J Neurosci Methods* 221: 70-77, 2014.
11. **Gureyev TE, Mayo SC, Ya IN, Mohammadi S, Lockie D, Menk RH, Arfelli F, Pavlov KM, Kitchen MJ, Zanconati F, Dullin C, Tromba G.** Investigation of the imaging quality of synchrotron-based phase-contrast mammographic tomography. *J Phys D Appl Phys* 47: 365401, 2014.
12. **Hafez SA, Freeman LE, Caceci T, Smith BJ.** Study of the vasculature of the caprine reproductive organs using the tissue-clearing technique, with special reference to the angioarchitecture of the utero-ovarian vessels and the adaptation of the ovarian and/or vaginal arteries to multiple pregnancies. *Anat Rec (Hoboken)* 290: 389-405, 2007.
13. **Levy MN, Imperial ES.** Oxygen shunting in renal cortical and medullary capillaries. *Am J Physiol* 200: 159-162, 1961.
14. **Levy MN, Saucedo G.** Diffusion of oxygen from arterial to venous segments of renal capillaries. *Am J Physiol* 196: 1336-1339, 1959.
15. **Limaye A.** Drishti: a volume exploration and presentation tool. *Proc SPIE 8506, Developments in X-Ray Tomography VIII*. 85060X
16. **Ludbrook J.** A primer for biomedical scientists on how to execute model II linear regression analysis. *Clin Exp Pharmacol Physiol* 39: 329-335, 2012.
17. **Martin B, Torben HJ, Robert FI, Oliver B, Christian D, Franz P.** Soft-tissue phase-contrast tomography with an x-ray tube source. *Phys Med Biol* 54: 2747, 2009.
18. **MØller J, Robertsen K, Hansen ES.** Severe shrinkage of Microfil during tissue clearing with the Spalteholz technique. *J Microsc* 174: 125-127, 1994.
19. **Momose A, Takeda T, Itai Y, Hirano K.** Phase-contrast X-ray computed tomography for observing biological soft tissues. *Nat Med* 2: 473-475, 1996.

20. **Ngo JP, Kar S, Kett MM, Gardiner BS, Pearson JT, Smith DW, Ludbrook J, Bertram JF, Evans RG.** Vascular geometry and oxygen diffusion in the vicinity of artery-vein pairs in the kidney. *Am J Physiol Renal Physiol* 307: F1111-1122, 2014.
21. **Nordsletten DA, Blackett S, Bentley MD, Ritman EL, Smith NP.** Structural morphology of renal vasculature. *Am J Physiol Heart Circ Physiol* 291: H296-H309, 2006.
22. **Olgac U, Kurtcuoglu V.** Renal oxygenation: preglomerular vasculature is an unlikely contributor to renal oxygen shunting. *Am J Physiol Renal Physiol* 308: F671-688, 2015.
23. **Olgac U, Kurtcuoglu V.** Reply to "Letter to the editor: 'The plausibility of arterial-to-venous oxygen shunting in the kidney: it all depends on radial geometry'". *Am J Physiol Renal Physiol* 309: F181-182, 2015.
24. **Snigirev A, Snigireva I, Kohn V, Kuznetsov S, Schelokov I.** On the possibilities of x-ray phase contrast microimaging by coherent high-energy synchrotron radiation. *Rev Sci Instrum* 66: 5486-5492, 1995.
25. **Sztrókay A, Diemoz PC, Schlossbauer T, Brun E, Bamberg F, Mayr D, Reiser MF, Bravin A, Coan P.** High-resolution breast tomography at high energy: a feasibility study of phase contrast imaging on a whole breast. *Phys Med Biol* 57: 2931, 2012.
26. **Welch WJ, Baumgartl H, Lubbers D, Wilcox CS.** Nephron pO₂ and renal oxygen usage in the hypertensive rat kidney. *Kidney Int* 59: 230-237, 2001.

10 | FINAL DISCUSSION AND CONCLUSIONS

10.1. DO THE SPATIAL RELATIONSHIPS BETWEEN ARTERIES, VEINS AND BARRIERS TO DIFFUSION CHANGE ALONG THE COURSE OF THE RENAL CIRCULATION?

The possibility that oxygen could diffuse from arteries to veins in the kidney was first raised more than 50 years ago (11, 12). Nevertheless, there is still considerable debate regarding the quantitative significance of this phenomenon (7, 15). Early experimental observations provided evidence that the countercurrent arrangement of the renal cortical circulation allows for the diffusive shunting of oxygen between afferent and efferent limbs. A critical piece of evidence for diffusive shunting of oxygen in the renal cortex is the lower oxygen tension (PO_2) observed in the efferent arteriole compared to the renal vein (23). Furthermore, observations in rats and rabbits have shown that, during cortical ischemia, renal medullary oxygenation is dependent on cortical oxygenation, even if medullary perfusion is maintained (14). Thus the collective aim of the studies presented in this thesis was to determine the mechanistic basis of these experimental findings, and subsequently determine the locations of countercurrent oxygen shunting. This issue is of considerable importance due to the susceptibility of the medulla to hypoxia during cortical ischemia. That is, a more quantitative understanding of arterial-to-venous (AV) oxygen shunting in the kidney could underpin more evidence-based approaches to management of renal hemodynamics in patients at risk of acute kidney injury (AKI).

The results of our studies using light microscopy to quantify radial vascular geometry (described in Chapters 5, 6 & 7) suggest that the spatial relationships of arteries and veins change along the course of the renal circulation. When examined closely, arteries could be further classified into those that were ‘wrapped’ and those that were ‘non-wrapped’. The data demonstrate that arterioles and arteries of various sizes are wrapped. However, it seems that the proportion of arteries that are wrapped differs at various levels of the circulation. A greater proportion of larger arteries are wrapped compared to their smaller counterparts. Thus it appears that the spatial arrangements that would favor diffusive shunting between individual paired vessels are more likely present in the larger proximal vessels than in the distal preglomerular circulation. Such vessels are located in the corticomedullary region. Taken at face value, this finding provides a potential explanation for the observations made by O’Connor *et al* (14). However, it did not take into account the branching of the renal circulation.

In light of these findings, as well as to minimize computational costs involved in generating a three-dimensional (3D) model of oxygen transport in the renal cortex, we categorized the data

into Strahler orders (Chapter 7). Here, the aim was to calculate the total mass transfer coefficients for each Strahler order and so effectively estimate the magnitude of oxygen transferred at each level of the cortical circulation. Collectively, our calculations predict that despite the fact that larger, proximal vessels are more likely to having an intimate relationship (Chapter 6), the smaller interlobular arteries (Strahler orders 2-5) provide a greater opportunity for oxygen to diffuse into veins than do the interlobar arteries (Strahler orders 8-9), arcuate arteries (Strahler orders 6-7), and afferent arterioles (Strahler orders 0-1). Thus, in contrast to our original interpretation of our light microscopic findings, it seems that if AV oxygen shunting is quantitatively significant, it likely occurs mainly in the more distal regions of the renal circulation. This is due to the branching of the renal circulation. Because of this branching, there are far more vessels at the distal regions compared to the proximal regions of the renal circulation. Consequently, the total mass transfer coefficients for more distal vessel-types is far greater than that for more proximal vessel-types.

10.2. PERITUBULAR CAPILLARIES ACT AS BOTH OXYGEN SOURCES AND SINKS

Cortical capillaries can act as both oxygen sources and oxygen sinks. Thus in order to generate a computational model of oxygen transport in the kidney, it is imperative that the distribution of peritubular capillaries is included. We were not aware of previous reports of estimates of peritubular capillary surface area density in adult rat kidneys. Therefore the aim of the study presented in Chapter 8 was to provide such information. An estimation of peritubular capillary surface area density was calculated.

The total surface area density of peritubular capillaries was calculated to be $239.65 \text{ cm}^2/\text{cm}^3$ of cortex. Total surface area of peritubular capillaries was estimated to be between 209 – 293 cm^2 . However, we must consider that there could be incomplete filling of the microcirculation in the rat kidney tissues we studied. Although we infused Microfil® until it was flowing freely out of the renal vein, we cannot be certain that all peritubular capillaries were filled. Thus we acknowledge that the values reported here likely underestimate peritubular capillary density.

To determine a better estimation of peritubular capillary surface area density, future studies should use established histological and immunohistochemical methods to stain the endothelial cells of peritubular capillaries. We could compare the findings with those in the study described in Chapter 8 of this thesis.

We also generated information on the distribution of capillaries in the vicinity of artery-vein pairs (Chapter 5). Peritubular capillary density around artery-vein pairs progressively reduced with increasing arterial diameter. Capillaries were frequently observed between smaller artery-vein pairs, while they were rarely observed in larger artery-vein pairs. Thus, it is expected that such vascular arrangements would reduce AV oxygen shunting between the smaller vessels. Indeed, capillaries around an artery (Chapter 6) could act as oxygen sinks. Some of the oxygen will diffuse into the renal tissue, but some will also be transported to the renal vein and thus contribute to AV shunting.

10.3. MICRO-COMPUTED TOMOGRAPHY AS A POTENTIAL AUTOMATED ANALYSIS APPROACH FOR DETERMINING THE SPATIAL RELATIONSHIPS OF THE CORTICAL CIRCULATION

One of the longer-term goals of this program of research is to generate quantitative information regarding renal vascular geometry in a range of species. The light-microscopic methods used in the studies described in Chapters 4-8 are limited both by the fact that they provide information in two-dimensions only, and also because they provide little scope for automation of analysis. To overcome these limitations, and so generate a method that could be applied in multiple species, in my final experimental study (Chapter 9), I tested the feasibility of micro-computed tomography (micro-CT) as a faster and automated approach to determining the spatial characteristics of the rat cortical circulation. Our findings indicate that the micro-CT approach is valid. Vascular geometry in micro-CT images resembled that seen in histological images. Furthermore, there was relatively good agreement, with respect to quantitative measures of vascular geometry (arterial diameter, diffusion distance and proportion of wrapping) between the micro-CT and light microscopic methods. However, the algorithm developed by our colleagues at the University of Western Australia, for quantitative and automated analysis of micro-CT images, were unable to replicate the data we generated by manual analysis of these images. Nevertheless, a major advantage of the micro-CT approach is that it allows the course of the renal circulation to be visualized in 3D. Thus, once the current limitations of the algorithm are overcome, micro-CT may provide a technique for automated analyses of the spatial arrangement of the renal circulation in multiple species. Our current method requires refinement, but we conclude it is feasible to use an automated method to extract quantitative information on the spatial relationships of arteries and veins from micro-CT reconstructions.

10.4. USE OF STRUCTURAL INFORMATION IN MATHEMATICAL MODELS

Some hypotheses cannot be answered by experimental approaches. An example is the quantitative significance of oxygen that is shunted from an afferent to an efferent vessel in the kidney, which was an area of interest in my project. Thus, in the absence of suitable experimental methods, we rely on mathematical models to aid our understanding of this and other phenomena. The validity of any model depends heavily on the information upon which it is based. Thus, a model can only provide accurate predictions if the information used to generate the model is detailed and accurate.

Layton and colleagues (3, 4, 8) have based their models on detailed structural information on the arrangement of tubules and vasa recta in the rat inner medulla provided in large part by Pannabecker *et al* (16-19). For example, in order to examine the impact of the architecture of the rat outer medulla on oxygen delivery, Chen *et al* generated detailed models of oxygen transport in the rat outer medulla (3, 4). They used a ‘region-based’ approach to represent the known distribution of tubules and vessels relative to the positions of vascular bundles (18, 19). The model predicted that the isolation of descending vasa recta at the center of the vascular bundles results in significant PO₂ gradients but also helps conserve oxygen delivery to the inner medulla. Similarly, in a model of solute transport in the renal medulla, Fry *et al* (8) accounted for the 3D arrangement of the renal medulla using a region-based approach. This included specifying the distribution of tubules and vasa recta in the inner medulla. This information came from comprehensive analyses on the tubular structure of the rat inner medulla (16-19). Their model predicts that the structural organization of the vascular bundles may function to aid the preservation of oxygen delivery to the renal papilla.

Thus modeling approaches can provide great insight into the physiological or functional significance of the specific structural organization of tubular and vascular elements in the kidney. Therefore incorporating detailed structural information on the renal circulation into mathematical models of the renal cortex can predict the significance of the unique spatial arrangement of the renal vasculature.

10.5. CLINICAL IMPLICATIONS

From a clinical perspective, the overall aim of this project was to develop structural information that will inform mathematical models of renal oxygenation that can be used to study the potential causes of AKI. The impetus for our studies was the evidence for a role of

hypoxia in the development of AKI (10, 13, 20). The observations by O'Connor *et al* (14) imply that we need to develop techniques that prevent or minimize the potential for renal ischemia to lead to medullary hypoxia. Patients who have thoracic surgery requiring cardiopulmonary bypass often develop AKI in the post-operative period (1, 21). AKI following cardiac surgery is associated with a four-fold increase in risk of death (9). The work and techniques presented in this thesis provide the foundation for development of computational approaches to management of renal oxygenation, and thus risk of AKI that can, in the future, be applied to clinical conditions including cardiac surgery performed on cardiopulmonary bypass. The work in this thesis will therefore aid our understanding of the types of interventions that could be used to prevent hypoxia and thus AKI.

10.6. FUTURE DIRECTIONS

The findings presented in this thesis are not without limitations. With regard to our micro-CT studies (Chapter 9), a major limitation was the limited resolution. A potential solution that would allow visualization of the kidney of the rat is to image at a facility capable of sub-micron resolution. The Swiss Light Source (SLS) is such a facility. We did trial imaging of some biopsies of rat renal tissue (filled with Microfil®) at the SLS to determine whether the facility is capable of generating high-resolution images of the smaller cortical vessels. Unfortunately the rat kidney biopsies were not able to withstand the heat from the light source. Thus, generating high-resolution images of the whole rat renal circulation remains to be achieved by our group. However, there are desktop micro-CT scanners available (SkyScan 1272 and SkyScan 1172) that are able to image up to 0.4 and 0.5 μm resolutions respectively (Bruker microCT, SkyScan, Kontich, Belgium). Indeed, by employing the SkyScan 1172, Ehling and colleagues have imaged at a resolution of 3 μm in the whole rat kidney, and visualized vessel diameters as small as 3.4 μm in lung tumors of mice (6). Furthermore, Wagner and colleagues used nano-CT to generate high-resolution images of vascular casts of the whole mouse kidney (22). They were able to visualize vasa recta, peritubular capillaries, and whole glomeruli at a resolution of 0.5 μm voxels. Thus it seems possible to image a whole rat kidney at high-resolution if there is access to suitable equipment. Nevertheless, micro-CT and nano-CT would not be able to provide information on the distribution of tubular structures. This indicates that using light microscopy (capable of visualizing smaller vessels and surrounding tubules; Chapters 5 & 6) in conjunction with micro-CT techniques (capable of visualizing larger vessels as well as length of vessels; Chapter 9) can provide accurate spatial information of the whole cortical circulation and surrounding parenchymal elements.

In order to build upon this project, it is critical that we also investigate different species. Our laboratory has to date studied renal vascular geometry in the rat (studies presented in this thesis) and rabbit (unpublished). The rat and rabbit kidney is unilobar and human kidneys are multilobar. Although unilobar kidneys share common traits with multilobar kidneys, it is imperative that we compare our findings with those generated from studies of multilobar kidneys. Thus we plan to investigate the kidneys of sheep in the future. Sheep kidneys are multilobar and thus resemble and exhibit many characteristics of human kidneys (2). By interrogating the spatial relationships between arteries and veins in the sheep kidney, we are likely to get closer to understanding these relationships in the human kidney. A limitation to using human kidneys is the availability of healthy whole kidneys. While biopsies may be obtainable, whole human kidneys are unlikely to be freely available. Thus it is imperative that we use animals with kidneys that have similar characteristics to kidneys in humans.

There are significant anatomical and functional differences between mammalian and non-mammalian kidneys. The kidneys of reptiles, birds, and some fish contain a portal circulation (5). Thus it is also important to investigate kidneys of non-mammalian species where AV shunting is likely absent. Therefore we plan to examine the relationships of afferent and efferent vessels in the chicken (avian) kidney in the future.

Collectively, the studies presented in this thesis have identified a way forward for modeling oxygen transport in the renal cortex using quantitative anatomical information. Using light microscopic methods, we have demonstrated the locations where AV oxygen shunting is most likely to occur, as well as the spatial characteristics that would favor diffusive shunting of oxygen between afferent and efferent vessels. Our micro-CT approach, while valid, is currently unable to provide automated analysis of vascular geometry. Importantly, we now have information to create a pseudo-3D model of oxygen transport and can eventually apply these techniques to models of renal disease, as well as various species.

REFERENCES

1. **Bagur R, Webb JG, Nietlispach F, Dumont E, De Larochelliere R, Doyle D, Masson JB, Gutierrez MJ, Clavel MA, Bertrand OF, Pibarot P, Rodes-Cabau J.** Acute kidney injury following transcatheter aortic valve implantation: predictive factors, prognostic value, and comparison with surgical aortic valve replacement. *Eur Heart J* 31: 865-874, 2010.
2. **Buys-Gonçalves GF, De Souza DB, Sampaio FJB, Pereira-Sampaio MA.** Anatomical relationship between the kidney collecting system and the intrarenal arteries in the sheep: Contribution for a new urological model. *Anat Rec (Hoboken)* 299: 405-411, 2016.
3. **Chen J, Edwards A, Layton AT.** A mathematical model of O₂ transport in the rat outer medulla. II. Impact of outer medullary architecture. *Am J Physiol Renal Physiol* 297: F537-F548, 2009.
4. **Chen J, Layton AT, Edwards A.** A mathematical model of O₂ transport in the rat outer medulla. I. Model formulation and baseline results. *Am J Physiol Renal Physiol* 297: F517-F536, 2009.
5. **Dantzler WH.** Comparative physiology of the kidney. In: *Comprehensive Physiology*. John Wiley & Sons, Inc., 2011, p. 415-474.
6. **Ehling J, Theek B, Gremse F, Baetke S, Mockel D, Maynard J, Ricketts SA, Grull H, Neeman M, Knuechel R, Lederle W, Kiessling F, Lammers T.** Micro-CT imaging of tumor angiogenesis: Quantitative measures describing micromorphology and vascularization. *Am J Pathol* 184: 431-441, 2014.
7. **Evans RG, Smith DW, Khan Z, Ngo JP, Gardiner BS.** Letter to the editor: "The plausibility of arterial-to-venous oxygen shunting in the kidney: it all depends on radial geometry". *Am J Physiol Renal Physiol* 309: F179-180, 2015.
8. **Fry BC, Edwards A, Sgouralis I, Layton AT.** Impact of renal medullary three-dimensional architecture on oxygen transport. *Am J Physiol Renal Physiol* 307: F263-272, 2014.
9. **Karkouti K, Wijeyesundera DN, Yau TM, Callum JL, Cheng DC, Crowther M, Dupuis JY, Fremes SE, Kent B, Laflamme C, Lamy A, Legare JF, Mazer CD, McCluskey SA, Rubens FD, Sawchuk C, Beattie WS.** Acute kidney injury after cardiac surgery: focus on modifiable risk factors. *Circulation* 119: 495-502, 2009.
10. **Legrand M, Mik EG, Johannes T, Payen D, Ince C.** Renal hypoxia and dysoxia after reperfusion of the ischemic kidney. *Mol Med* 14: 502-516, 2008.
11. **Levy MN, Imperial ES.** Oxygen shunting in renal cortical and medullary capillaries. *Am J Physiol* 200: 159-162, 1961.
12. **Levy MN, Saucedo G.** Diffusion of oxygen from arterial to venous segments of renal capillaries. *Am J Physiol* 196: 1336-1339, 1959.
13. **Nangaku M, Eckardt KU.** Hypoxia and the HIF system in kidney disease. *J Mol Med* 85: 1325-1330, 2007.
14. **O'Connor PM, Kett MM, Anderson WP, Evans RG.** Renal medullary tissue oxygenation is dependent on both cortical and medullary blood flow. *Am J Physiol Renal Physiol* 290: F688-F694, 2006.
15. **Olgac U, Kurtcuoglu V.** Reply to "Letter to the editor: 'The plausibility of arterial-to-venous oxygen shunting in the kidney: it all depends on radial geometry'". *Am J Physiol Renal Physiol* 309: F181-182, 2015.
16. **Pannabecker TL, Abbott DE, Dantzler WH.** Three-dimensional functional reconstruction of inner medullary thin limbs of Henle's loop. *Am J Physiol Renal Physiol* 286: F38-F45, 2004.
17. **Pannabecker TL, Dantzler WH.** Three-dimensional architecture of collecting ducts, loops of Henle, and blood vessels in the renal papilla. *Am J Physiol Renal Physiol* 293: F696-704, 2007.

18. **Pannabecker TL, Dantzler WH.** Three-dimensional architecture of inner medullary vasa recta. *Am J Physiol Renal Physiol* 290: F1355-1366, 2006.
19. **Pannabecker TL, Dantzler WH.** Three-dimensional lateral and vertical relationships of inner medullary loops of Henle and collecting ducts. *Am J Physiol Renal Physiol* 287: F767-F774, 2004.
20. **Rosenberger C, Rosen S, Heyman SN.** Renal parenchymal oxygenation and hypoxia adaptation in acute kidney injury. *Clin Exp Pharmacol Physiol* 33: 980-988, 2006.
21. **Rosner MH, Okusa MD.** Acute kidney injury associated with cardiac surgery. *Clin J Am Soc Nephrol* 1: 19-32, 2006.
22. **Wagner R, Van Loo D, Hossler F, Czymmek K, Pauwels E, Van Hoorebeke L.** High-resolution imaging of kidney vascular corrosion casts with Nano-CT. *Microsc Microanal* 17: 215-219, 2011.
23. **Welch WJ, Baumgartl H, Lubbers D, Wilcox CS.** Nephron pO₂ and renal oxygen usage in the hypertensive rat kidney. *Kidney Int* 59: 230-237, 2001.

| APPENDIX 1

DIFFUSIVE OXYGEN SHUNTING BETWEEN VESSELS IN THE PREGLOMERULAR RENAL VASCULATURE – ANATOMIC OBSERVATIONS AND COMPUTATIONAL MODELING

Bruce S. Gardiner,¹ Sarah L. Thompson,¹ Jennifer P. Ngo,² David W. Smith,¹ Amany Abdelkader,² Brad R. S. Broughton,³ John F. Bertram,⁴ and Roger G. Evans²

¹School of Computer Science and Software Engineering, The University of Western Australia, Perth, Australia; ²Department of Physiology, Monash University, Melbourne, Australia; ³Department of Pharmacology, Monash University, Melbourne, Australia; and ⁴Department of Anatomy and Developmental Biology, Monash University, Melbourne, Australia

Submitted 30 March 2012; accepted in final form 30 May 2012

Monash University

Declaration for Thesis Appendix 1

Declaration by candidate

The following manuscript was published, as is, in the American Journal of Physiology Renal Physiology.

Gardiner BS, Thompson SL, Ngo JP, Smith DW, Abdelkader A, Broughton BR, Bertram JF, Evans RG. Diffusive oxygen shunting between vessels in the preglomerular renal vasculature: anatomic observations and computational modeling. *Am J Physiol Renal Physiol* 303: F605-618, 2012.

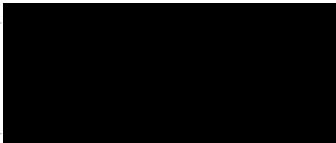
In the case of Appendix 1, the nature and extent of my contribution to the work was the following:

| Nature of contribution | Extent of contribution (%) |
|--|----------------------------|
| Performed experiments, analyzed data, interpreted results, prepared figures, edited and revised manuscript | 10% |

The following co-authors contributed to the work. If co-authors are students at Monash University, the extent of their contribution in percentage terms must be stated:

| Name | Nature of contribution | Extent of contribution (%) for student co-authors only |
|--------------------------|---|--|
| Bruce S Gardiner | Provided design of research, analyzed data, interpreted results, drafted, edited and revised manuscript | 50% |
| Sarah L Thompson | Analyzed data, interpreted results, prepared figures, drafted, edited and revised manuscript | 15% |
| David W Smith | Provided design of research, interpreted results, edited and revised manuscript | 5% |
| Amany Abdelkader | Performed some experiments | ~1% |
| Brad RS Broughton | Performed some experiments, edited and revised manuscript | ~2% |
| John F Bertram | Provided design of research and performed some experiments | ~2% |
| Roger G Evans | Provided design of research, performed some experiments, analyzed data, interpreted results, drafted, edited and revised manuscript | 15% |

The undersigned hereby certify that the above declaration correctly reflects the nature and extent of the candidate's and co-authors' contributions to this work*.

| | | |
|------------------------------|--|---------------------------|
| Candidate's Signature |  | Date 24/04/2016 |
|------------------------------|--|---------------------------|

| | | |
|------------------------------------|---|---------------------------|
| Main Supervisor's Signature |  | Date 24/04/2016 |
|------------------------------------|---|---------------------------|

*Note: Where the responsible author is not the candidate's main supervisor, the main supervisor should consult with the responsible author to agree on the respective contributions of the authors.

CALL FOR PAPERS | *Mathematical Modeling of Renal Function*

Diffusive oxygen shunting between vessels in the preglomerular renal vasculature: anatomic observations and computational modeling

Bruce S. Gardiner,¹ Sarah L. Thompson,¹ Jennifer P. Ngo,² David W. Smith,¹ Amany Abdelkader,² Brad R. S. Broughton,³ John F. Bertram,⁴ and Roger G. Evans²

¹School of Computer Science and Software Engineering, The University of Western Australia, Perth, Australia;

²Department of Physiology, Monash University, Melbourne, Australia; ³Department of Pharmacology, Monash University, Melbourne, Australia; and ⁴Department of Anatomy and Developmental Biology, Monash University, Melbourne, Australia

Submitted 30 March 2012; accepted in final form 30 May 2012

Gardiner BS, Thompson SL, Ngo JP, Smith DW, Abdelkader A, Broughton BR, Bertram JF, Evans RG. Diffusive oxygen shunting between vessels in the preglomerular renal vasculature: anatomic observations and computational modeling. *Am J Physiol Renal Physiol* 303: F605–F618, 2012. First published June 6, 2012; doi:10.1152/ajprenal.00186.2012.—To understand how geometric factors affect arterial-to-venous (AV) oxygen shunting, a mathematical model of diffusive oxygen transport in the renal cortex was developed. Preglomerular vascular geometry was investigated using light microscopy (providing vein shape, AV separation, and capillary density near arteries) and published micro-computed tomography (CT) data (providing vessel size and AV separation; Nordsletten DA, Blackett S, Bentley MD, Ritman EL, Smith NP. IUPS Physiome Project. http://www.physiome.org.nz/publications/nordsletten_blackett_ritman_bentley_smith_2005/folder_contents). A “U-shaped” relationship was observed between the arterial radius and the distance between the arterial and venous lumens. Veins were found to partially wrap around the artery more consistently for larger rather than smaller arteries. Intrarenal arteries were surrounded by an area of fibrous tissue, lacking capillaries, the thickness of which increased from ~5 μm for the smallest arteries (<16- μm diameter) to ~20 μm for the largest arteries (>200- μm diameter). Capillary density was greater near smaller arteries than larger arteries. No capillaries were observed between wrapped AV vessel pairs. The computational model comprised a single AV pair in cross section. Geometric parameters critical in renal oxygen transport were altered according to variations observed by CT and light microscopy. Lumen separation and wrapping of the vein around the artery were found to be the critical geometric factors determining the amount of oxygen shunted between AV pairs. AV oxygen shunting increases both as lumen separation decreases and as the degree of wrapping increases. The model also predicts that capillaries not only deliver oxygen, but can also remove oxygen from the cortical parenchyma close to an AV pair. Thus the presence of oxygen sinks (capillaries or tubules) near arteries would reduce the effectiveness of AV oxygen shunting. Collectively, these data suggest that AV oxygen shunting would be favored in larger vessels common to the cortical and medullary circulations (i.e., arcuate and proximal interlobular arteries) rather than the smaller vessels specific to the cortical circulation (distal interlobular arteries and afferent arterioles).

hypoxia; kidney circulation; oxygen tension; renal oxygenation

FIFTY YEARS AGO Levy et al. (17, 18) provided evidence that oxygen is transported more rapidly than erythrocytes through

the renal circulation, suggesting the existence of diffusional oxygen shunting between intrarenal arteries and veins. Shunting reduces the delivery of oxygen to renal tissue (26, 27). In further support of the existence of arterial-to-venous (AV) oxygen shunting, Welch et al. (29) observed that the Po_2 of renal venous blood exceeds that of blood in the efferent arterioles of the outer cortex. In common with other countercurrent systems in biology and chemical engineering, it is thought that the parallel architecture of the renal artery and vein facilitates countercurrent oxygen exchange. It has also been noted by several groups (8, 23, 24, 26) that the arteries and veins in the kidney are intimately associated, and we will later show that the available data suggest this intimacy varies with distance along the cortical circulation. Despite general acceptance of the existence of AV oxygen shunting in the kidney, little is known about the effects of AV oxygen shunting on renal parenchymal oxygenation or the quantity of oxygen shunted at the various levels of the renal circulation (e.g., interlobar, arcuate, and interlobular arteries). In this paper, we focus on a quantitative analysis of diffusive oxygen shunting between vessels in the preglomerular renal vasculature of the rat.

Gardiner et al. (14) developed a one-dimensional (1D) mathematical model of AV oxygen shunting along the preglomerular renal vasculature. This model has a hierarchy of 11 countercurrent systems in series, representing the various levels of branching of the preglomerular renal vasculature described by Nordsletten et al. (22, 23). Reactive-advection equations were solved at each branch level. The model predicted that AV oxygen shunting is quantitatively significant, being of the same order of magnitude as total kidney oxygen consumption. However, this model has several limitations, the most important being that the cross-sectional geometry of typical vessel pairs at each branch level was unknown. To overcome this lack of information, the model (14) used a single “shunting coefficient” between arteries and veins that was calibrated using the measurements made by Welch et al. (29) for Po_2 within microdomains of the rat superficial cortex. Our current study focuses on clarifying how the cross-sectional geometry of typical vessel pairs at each branch level affects the amount of AV oxygen shunting occurring along the preglomerular renal vasculature.

Clearly, the cross-sectional geometry of the renal vasculature is of critical importance for the quantification of AV oxygen shunting. We hypothesized that the two critical geometric factors were the mean distance between the arterial and venous wall (so-called “lumen separation”) and the degree to

Address for reprint requests and other correspondence: B. Gardiner, School of Computer Science and Software Engineering, The Univ. of Western Australia, M002, 35 Stirling Highway, Crawley, WA 6009, Australia (e-mail: bruce.gardiner@uwa.edu.au).

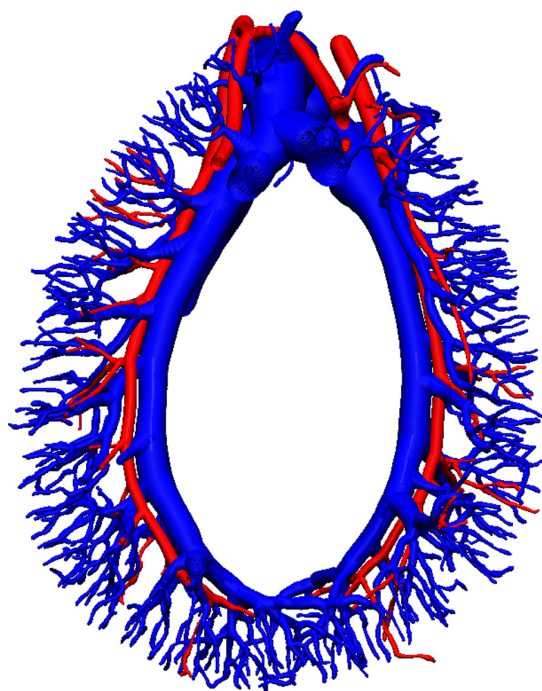


Fig. 1. A slice through the data set of Nordsletten et al. (22, 23) allows us to see the intimate relationship between arterial (red) and venous (blue) networks in the rat kidney.

which the vein wall surrounds the arterial wall (so-called “wrapping”). We also viewed the presence of other vessels, particularly capillaries, as a potentially important factor in oxygen transport in the tissue, as oxygen binding to hemoglobin is reversible, implying that capillaries may deliver oxygen to a region of tissue or remove oxygen from a region of tissue, depending on oxygen gradients between the tissue and capillary. Therefore, we first used standard histological methods to perform qualitative and quantitative analyses of the spatial relationships among arteries, veins, and capillaries in the rat renal cortex. To independently confirm conclusions drawn from these data, we then used a data set produced by Nordsletten and colleagues (22, 23) using micro-computed tomography (micro-CT) of vascular casts of the rat renal circulation (Fig. 1), to estimate how distances between arteries and veins differ across the course of the renal circulation. Together, these data sets led to the formulation of a computational model of oxygen transport at various AV-tissue cross sections.

The model was then employed for a series of “computational experiments” to assess how variations, typically observed or expected in the kidney based on data from light microscopy and micro-CT, influence AV oxygen shunting. We tested the specific hypotheses that oxygen shunting in the preglomerular vasculature is critically dependent upon 1) the distance separating arteries and veins, 2) the degree to which the venous wall wraps around the arterial wall, and 3) the presence of capillaries and tubules, which act as oxygen sinks, around and between artery-vein pairs. We have quantified the relative oxygen flux from artery to vein vs. the flux from these vessels to the surrounding cortical parenchyma.

METHODS

Histological Studies

All experimental procedures were approved by the Animal Ethics Committee of the School of Biomedical Sciences, Monash University (reference 2009/84) and were in accordance with the Australian Code of Practice for the Care and Use of Animals for Scientific Purposes. Sprague-Dawley rats (7 males and 1 female, 250–300 g) were anesthetized with pentobarbital sodium (60 mg/kg ip; Sigma, St Louis, MO). The kidneys of seven of these rats (including the female) were perfused via retrograde perfusion of the abdominal aorta at 150 mmHg. Perfusion commenced with a 0.1 M phosphate-buffered saline solution (pH 7.4) containing 0.2 mg/ml lidocaine (Xylocard 2000, Astra Pharmaceuticals, North Ryde, NSW, Australia). Once the kidneys were blanched (~60 s), they were perfused with ~300 ml of ice-cold 3% wt/vol paraformaldehyde in 0.1 M phosphate-buffered saline. In four rats, the vasculature was then filled with Microfil (MV-122; Flow Tech, Carver, MA) by slowly injecting 20–30 ml of the compound via the abdominal aorta. The 14 kidneys were decapsulated and postfixed in paraformaldehyde overnight before being placed in 70% vol/vol ethanol. In a single male rat, a hindlimb skeletal muscle (biceps femoris) was fixed by orthograde perfusion of the abdominal aorta, in an analogous manner to renal perfusion.

The six kidneys in which Microfil was not injected were divided and embedded in paraffin, while the eight Microfil-treated kidneys were embedded in methacrylate (technovit 3040 resin). In all cases, the kidneys were embedded to provide cross sections 1) in the frontal plane along the longitudinal axis, 2) perpendicular to the longitudinal axis, and 3) horizontally to the transverse plane. The biceps femoris muscle was embedded to provide sections perpendicular to the orientation of the muscle fibers. Microtome sections (1–3 in each plane) were then cut at 5 μ m and stained with either hematoxylin and eosin or toluidine blue before being viewed and photographed using an Olympus BX51 microscope. Arteries were chosen with near-circular profiles, indicating that they had been sectioned at a near-perpendicular plane. A total of 200–250 arterial profiles were considered in a qualitative analysis of typical vessel geometry. We then retained only those images in which arteries had a circular cross section ($n = 81$), indicating an image slice perpendicular to the

Table 1. Variables used in the formulation of the diffusive oxygen transport model

| Description | Name | Value/Expression | Units | Source/Ref. |
|--|---------------------------|-----------------------------|---|-------------|
| Perfusion constant | α_{cap} | –15 | s^{-1} | This study |
| Venous PO_2 | $\text{PO}_2 \text{ v}$ | 52 | mmHg | 29 |
| Tissue PO_2 | $\text{PO}_2 \text{ cap}$ | 42 | mmHg | 29 |
| Arterial PO_2 | $\text{PO}_2 \text{ A}$ | $m * \text{PO}_2 \text{ v}$ | mmHg | 29 |
| Oxygen consumption rate | S_0 | –0.1 | $\text{mol} \cdot \text{s}^{-1} \cdot \text{m}^{-3}$ | 14 |
| Diffusion coefficient of oxygen in kidney tissue | D | 2.8×10^{-9} | m^2/s^{-1} | 6 |
| Arterial radius | R_A | 75×10^{-6} | m | 6 |
| Solubility coefficient of oxygen | σ | 1.34×10^{-3} | $\text{mol} \cdot \text{m}^{-3} \cdot \text{mmHg}^{-1}$ | 14 |
| Hill coefficient | n | 4 | | This study |
| Ratio of arterial to venous PO_2 | m | 1.6 | | 29 |

arterial wall, for a quantitative analysis of the radial geometry of arteries and veins. The minimum distance between arterial and venous wall (lumen separation), in each case, was determined using ImageJ software (<http://rsbweb.nih.gov/ij/>).

In addition, for the eight Microfil-treated kidneys, the number of capillaries per unit image area (so-called “capillary density”) within four zones, defined by concentric circles around the center of the artery, was determined. The radii of these zones were increased with vessel size. That is, for arteries $<16.0\text{ }\mu\text{m}$ in diameter ($n = 12$), these zones were defined by steps of $5\text{ }\mu\text{m}$ from the arterial wall, so that capillary density was determined at 0–5, 5–10, 10–15, and 15–20 μm

from the arterial wall. For arteries 16.0–25.9 ($n = 10$), 26.0–50.9 ($n = 8$), 51.0–100.9 ($n = 7$), 101–200 ($n = 9$), and $>200\text{ }\mu\text{m}$ ($n = 3$) in diameter, the zones were defined by steps of 10, 15, 20, 25, and 30 μm from the arterial wall, respectively. These data were analyzed by repeated measures analysis of variance (19). The between-subjects factor was vessel category, and the within-subjects factor was zone.

Analysis of Micro-CT Data Generated by Nordsletten and Colleagues

Nordsletten et al. (23) presented an analysis of the three-dimensional (3D) quantitative morphology of the rat renal circulation based

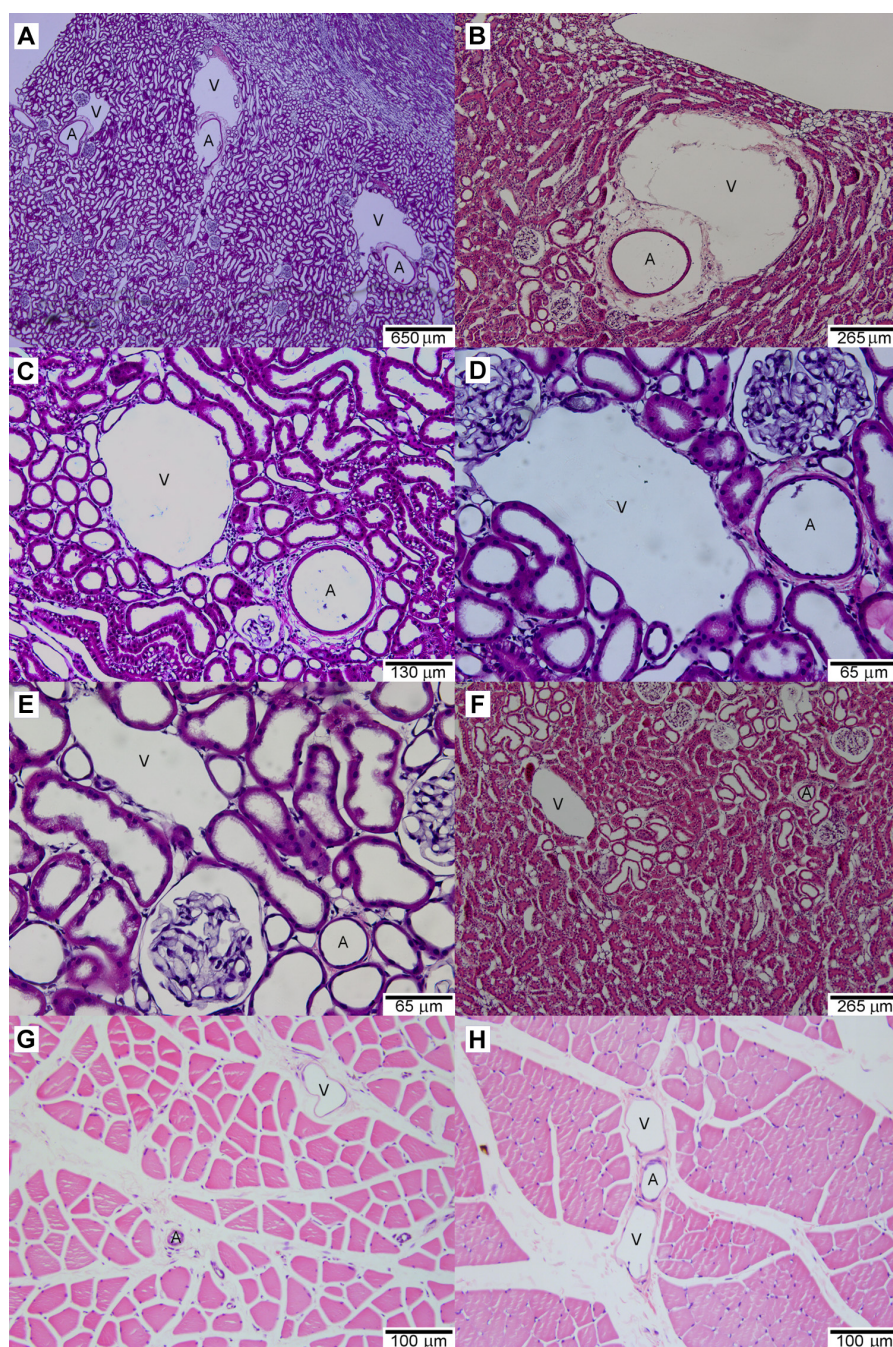


Fig. 2. Micrographs of hematoxylin and eosin stained rat renal cortex (A–F) and skeletal muscle (biceps femoris; G and H) showing different arrangements of arteries (A) and veins (V).

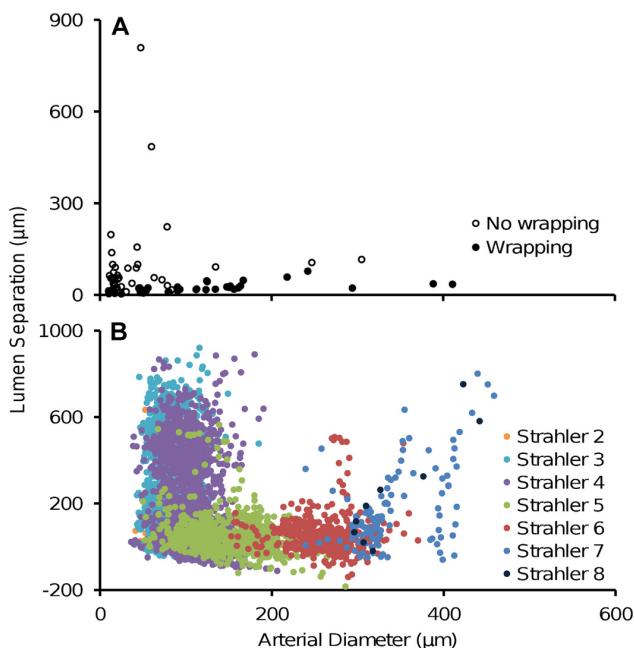


Fig. 3. Relationship between arterial diameter and the distance between the arterial and venous wall (lumen separation). Data were generated both from light microscopy ($n = 81$; A) and analysis of the micro-computed tomography (micro-CT) data set generated by Nordsletten et al. (22); $n = 5,260$; B.

on 20- μm resolution CT data (Fig. 1). The 3D geometrical model generated by Nordsletten et al. (22) was obtained and analyzed in this study. This model consists of a series of points in 3D space (nodal points) connected by straight lines (elements). The nodal points belong to one of two networks, either the arterial tree or the venous tree. A Perl script was written so that for each nodal point in the arterial network, its closest neighbor in the venous network was calculated according to Eq. 1

$$d = \sqrt{((A_x - V_x)^2 + (A_y - V_y)^2 + (A_z - V_z)^2)} \quad (1)$$

where d is distance between arterial and venous nodes, (A_x , A_y , A_z) are the nodal (x , y , z) coordinates of the arterial node, and (V_x , V_y , V_z) are the nodal (x , y , z) coordinates of the venous node.

Nordsletten et al. (23) found that arteries are likely to pair with veins typically two orders higher; therefore, in this analysis a condition was set to find the closest vein within two Strahler orders of the artery. Once the closest vein had been found for each artery, the following parameters were extracted and calculated: the ratio of the arterial to venous radius, arterial diameter, venous diameter, lumen separation, and the ratio of the lumen separation to arterial diameter.

Computational Model

Here, we developed computational models of oxygen transport in the preglomerular renal vasculature based on the well-known diffusion equation (2). Parameters in the models such as the diffusion coefficient and oxygen consumption are appropriate for a volume of tissue contained in a low-magnification view of the renal parenchyma. That is, they represent a smoothing over of a small volume of tissue such that the discrete structures are averaged out. Vessel arrangements were based on the light microscope and micro-CT data obtained as described above. Each model consisted of a cross-sectional view of an artery and a vein lying parallel to each other. The arterial and venous radii corresponded to average vessel dimensions from analysis of

micro-CT of vascular casts of the rat renal cortical circulation, reported by Nordsletten et al. (23).

Two dimensional (2D) steady-state oxygen transport by diffusion within a cross section of renal tissue (i.e., regions broadly characterized as everything other than blood vessels) can be described mathematically using the well-known diffusion equation

$$D \left(\frac{\partial^2 c}{\partial x^2} + \frac{\partial^2 c}{\partial y^2} \right) = S \quad (2)$$

Here, c is the concentration of free oxygen defined by $c = \sigma \text{Po}_2$, where σ is the solubility coefficient of oxygen and Po_2 is the partial pressure of oxygen. D is the effective "average" diffusion coefficient within this heterogeneous tissue, and S describes oxygen production or loss per volume of tissue (e.g., if S refers to an oxygen loss, then $S < 0$). The derivatives are with respect to spatial coordinates (x , y). In this study, it was assumed that D is not a function of (x , y) within any defined tissue regions (i.e., D is spatially constant).

It was assumed that there are two contributions to the term S in Eq. 2. The first is consumption of oxygen per volume of tissue, corresponding to kidney $\dot{V}\text{O}_2$, and was given the symbol S_0 . The second contribution comes from a potential source (or sink) of oxygen offered by capillaries, depending on any concentration difference between c and an assumed concentration within the capillaries, i.e., c_{cap} . That is, oxygen may be lost or gained by the tissue through transport along the capillaries. We did not model this capillary transport explicitly. Rather, we treated it as a spatially homogenized contribution to S which is proportional to $(c_{\text{cap}} - c)$, with a proportionality constant α_{cap} . Specifically,

$$S = S_0 - \alpha_{\text{cap}}(c_{\text{cap}} - c) \quad (3)$$

Boundary conditions. Boundary conditions are required to solve Eq. 2 in each model. Here, it was assumed that oxygen concentration at the vessel wall is fixed, with $c = c_A$ on the artery wall and $c = c_V$ on the venous wall. That is, we assumed that oxygen is radially well mixed within each vessel such that there are no oxygen concentration gradients within each vessel. The vessel pair was assumed to be sitting at the center of a square of tissue, the boundaries of which were assigned a zero-flux boundary condition, consistent with a vessel-tissue organization that it spatially repeated. The width of the tissue under consideration was assumed to be 20 times the arterial radius, based on our light imaging results.

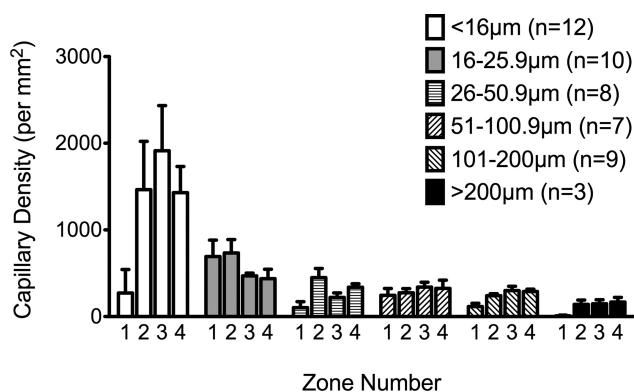


Fig. 4. Capillary density in concentric zones around arteries of various calibres. The concentric zones were in steps of 5, 10, 15, 20, 25, and 30 μm from the arterial wall, respectively, for arteries <16 , 16–25.9, 26–50.9, 51–100.9, 101–200, and >200 μm in diameter. Values are means \pm SE. The number of observations (n) for each arterial vessel class is shown in the figure. Statistical analysis of these data, using repeated measures analysis of variance (19), showed that capillary density around arteries varied significantly according to the arterial caliber ($P_{\text{vessel}} = 0.003$) and across the various concentric zones ($P_{\text{zone}} = 0.03$).

Parameter selection. Values used for the model parameters and their sources are shown in Table 1, unless otherwise stated. Welch et al. (29), using Clark-type microelectrodes, measured *in vivo* the renal venous and tissue Po_2 . They reported a renal venous Po_2 of 52 mmHg for a known renal blood flow of ~ 5 ml/min with an arterial Po_2 of 85 mmHg. Furthermore, the average tissue Po_2 in the superficial cortex, the most oxygenated part of the kidney, was found to be 42 mmHg (referred to here as the tissue Po_2).

The diffusion coefficient of oxygen has been reported in the literature for a variety of mediums and tissues, from water to plasma, arterioles, and smooth muscle, etc. (4, 5, 9, 11, 20). Typically, the values fall within the range of 1.2×10^{-9} to 3.1×10^{-9} m^2/s . Here, a value of 2.8×10^{-9} m^2/s was chosen to be consistent with that used by Chen et al. (6) in their mathematical model of the rat outer medulla.

In the Wistar-Kyoto rat kidney, $\dot{V}\text{O}_2$ per weight of renal tissue has been reported to be $7.6 \mu\text{mol}\cdot\text{min}^{-1}\cdot\text{g}^{-1}$ (29). Assuming a tissue density of $1 \text{ g}/\text{cm}^3$, we then estimate S_0 to be $-0.1 \text{ mol}\cdot\text{s}^{-1}\cdot\text{m}^{-3}$.

The mass transfer coefficient α_{cap} for oxygen transport through the capillary wall is unknown but can be estimated. For tissue far from the AV pair, the oxygen consumed by the tissue must be provided by the capillaries. In this case, from Eq. 3, $S_0 = \alpha_{\text{cap}}(c_{\text{cap}} - c)$. If the difference between the Po_2 in the capillary and the tissue is in the range 1 to 10 mmHg, then this corresponds to α_{cap} varying between -80 and -8 s^{-1} , respectively. Here, a value of $\alpha_{\text{cap}} = -15 \text{ s}^{-1}$ was chosen and corresponds to a Po_2 difference of 5 mmHg between the capillary and the average value in the tissue.

Arterial diameter was selected based on our analysis of the model of Nordsletten et al. (22), in which an artery of Strahler order 5, typically considered an arcuate artery (23), had an average diameter of $150 \mu\text{m}$.

All models were implemented in the commercial computer simulation package COMSOL (version 4.2) and solved as steady-state problems with a "parameter sweep" on a Dell PC with an Intel Core 2.67-GHz CPU running Windows 7 Enterprise. Diffusive transport in each vessel pair was considered with oxygen consumption defined in the tissue, as described above. For each of these models, we ran parametric studies varying arterial radius, separation, wrapping, and Po_2 in the tissue, vein, and artery.

RESULTS

Light Microscopy

A total of 200–250 intrarenal arteries were surveyed. The relationships between arteries and veins varied markedly throughout the rat kidney. In the case of larger arteries (e.g., interlobar arteries ~ 200 – $300 \mu\text{m}$ in diameter), the corresponding vein tended to surround a considerable proportion of the total arterial circumference, with a typical lumen separation of $<100 \mu\text{m}$ (Fig. 2A). A similar arrangement was observed for vessels presumed to be arcuate arteries (~ 200 – μm diame-

ter; Fig. 2B). In both cases (interlobar and arcuate arteries), the space between the artery and vein walls was mostly filled with loose connective tissue, with a notable absence of capillaries and tubules. In the case of smaller artery-vein pairings (<150 – μm diameter), presumed to be mainly interlobular arteries and glomerular arterioles, a less intimate relationship was often observed (Fig. 2, C–F). That is, veins less often "wrapped" around the artery, and the space between the artery and vein was often filled by tubular elements and/or capillaries. However, there were some exceptions in which smaller arteries were found to be closely associated with veins, as for larger vessels. In biceps femoris, although arteries and veins were sometimes found in close proximity, veins were never found to wrap arteries (Fig. 2, G and H).

For these quantitative analyses, all artery-vein cross sections in which the artery approached a circular shape, indicating a section approximately perpendicular to the artery, were included, while those in which the artery appeared oval shaped were excluded. Of the 81 profiles examined from kidney tissue, in all but 3 the distance between the artery and vein wall was $<200 \mu\text{m}$ (Fig. 3A). Forty percent of the profiles showed wrapping of the vein around the artery. The ratio of lumen separation to arterial radius averaged 0.5 ± 0.1 in the wrapped vessels, compared with 5.7 ± 1.0 in the nonwrapped vessel pairs, indicating that oxygen diffusion should be favored between wrapped vessels rather than those where wrapping was not present.

In many of the light microscope images, an area of loose connective tissue surrounded each artery, as has been described previously by Frank and Kriz (13) (Fig. 2). The minimum thickness of this area varied with arterial diameter, being $6.6 \pm 0.7 \mu\text{m}$ for arteries $<16.0 \mu\text{m}$ in diameter, $6.8 \pm 0.9 \mu\text{m}$ for arteries 16.0 – $25.9 \mu\text{m}$ in diameter, $8.1 \pm 1.0 \mu\text{m}$ for arteries 26.0 – $50.9 \mu\text{m}$ in diameter, $11.1 \pm 1.4 \mu\text{m}$ for arteries 51.0 – $100.9 \mu\text{m}$ in diameter, $18.5 \pm 1.5 \mu\text{m}$ for arteries 101 – $200 \mu\text{m}$ in diameter, and $22.2 \pm 2.9 \mu\text{m}$ for arteries $>200 \mu\text{m}$ in diameter.

Peritubular capillary density in the zones surrounding the arterial wall progressively reduced with increasing arterial diameter ($P_{\text{vessel}} = 0.003$). Peritubular capillary density also appeared to be less in the zones immediately surrounding vessels compared with those further away, at least in the case of vessels $<16 \mu\text{m}$, 26.0 – $50.9 \mu\text{m}$, 101 – $200 \mu\text{m}$, and $>200 \mu\text{m}$ ($P_{\text{zone}} = 0.03$). The pattern of changes in capillary density, across the four zones, differed significantly according to vessel caliber ($P_{\text{vessel}\cdot\text{zone}} < 0.001$) (Fig. 4).

Table 2. Results from the mathematical analysis of the 3D (micro-CT) model of rat renal vasculature of Nordsletten et al. (22)

| Strahler | D_A , μm | LS, μm | R_V/R_A | LS/ R_A | LS/ R_A | | | | n |
|----------|-----------------------|-------------------|-----------|-----------|-----------|------|------|------|-------|
| | | | | Overall | Q1 | Q2 | Q3 | Q4 | |
| 2 | 58.1 | 474.0 | 1.8 | 13.6 | 2.1 | 14.8 | 18.2 | 19.6 | 32 |
| 3 | 80.4 | 177.0 | 1.8 | 6.4 | 0.2 | 2.5 | 8.3 | 14.7 | 1,803 |
| 4 | 102.8 | 90.4 | 1.8 | 3.8 | −0.1 | 1.1 | 3.9 | 10.5 | 2,103 |
| 5 | 150.7 | 45.3 | 1.8 | 0.9 | −0.3 | 0.4 | 0.9 | 2.7 | 768 |
| 6 | 263.7 | 44.1 | 1.8 | 0.4 | −0.2 | 0.2 | 0.5 | 1.3 | 429 |
| 7 | 325.6 | 115.3 | 2.7 | 0.9 | 0.0 | 0.5 | 1.0 | 2.3 | 116 |
| 8 | 317.4 | 189.4 | 4.4 | 1.3 | 0.0 | 0.6 | 1.4 | 2.6 | 9 |

3D, three-dimensional; CT, computed tomography; D_A , median arterial diameter; LS, median lumen separation; R_V/R_A , ratio of venous to arterial radius; LS/ R_A , average ratio of lumen separation to arterial radius defined over all vessels within an order (Overall) and over each quartile in an order (Q1–Q4); n is the number of observations at each order. See text for further details.

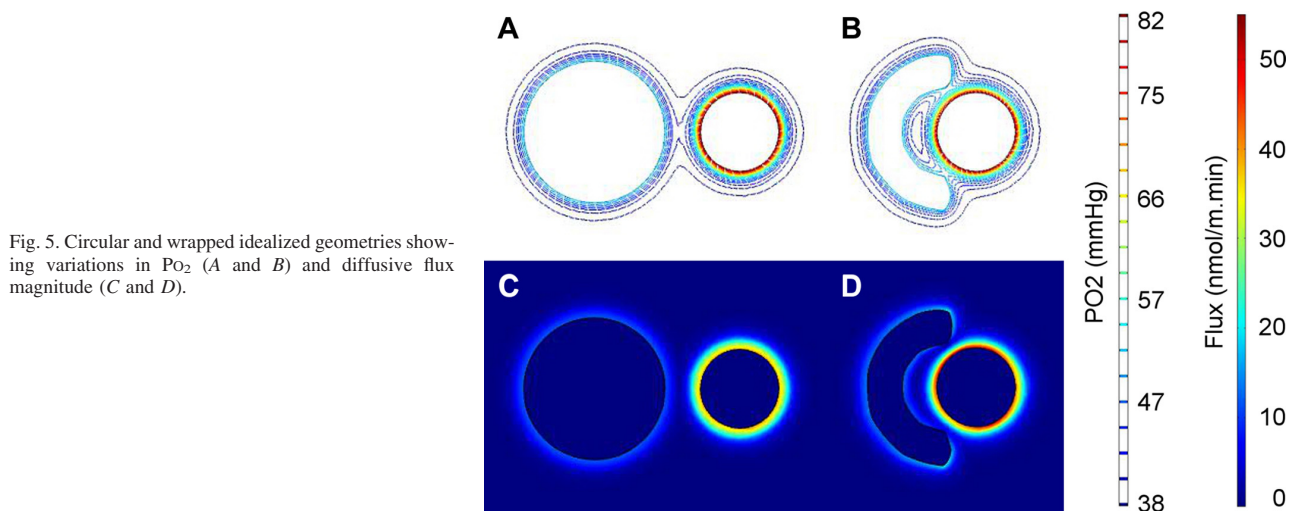


Fig. 5. Circular and wrapped idealized geometries showing variations in PO_2 (A and B) and diffusive flux magnitude (C and D).

Quantification of Spatial Variations in the Renal Preglomerular Vasculature

A mathematical analysis was conducted of the micro-CT model of the rat renal vasculature (Table 2) by Nordsletten et al. (22). The center-to-center distance between arterial and venous vessels in the model, along with lumen separation, was calculated. First, across each Strahler order, the lumen separation of an artery-vein pair decreased with increasing diameter, to a point (Strahler order 7) where it then started to increase. Prima facie, this suggests that the quantity of AV shunting per vessel pair will vary along the various levels of branching. This U-shaped relationship was also observed with the light microscopic data set (Fig. 3). This relationship points to a structural variation in which vessel pairs with an intermediate arterial diameter of 150–350 μm tend to consistently have a smaller lumen separation than larger or smaller vessels. It is noteworthy that some data points (Fig. 3B) have a negative value for lumen separation. This is because the data we used

in this analysis were not raw data but instead came from an existing model where an equivalent vessel radius was assigned to each vessel node according to the vessel cross-sectional area observed in micro-CT images. Importantly, the negative values indicate that there was some degree of overlap or wrapping between the vessels.

The next step was to look more closely at the distribution within each Strahler order. For each Strahler order, the median, lower, and upper quartiles for lumen separation were determined. This analysis demonstrated that although vessels in the first three quarters of orders 5–7 had a wide range of size (median arterial diameter 150.7–325.6 μm) and separation (median lumen separation 44.1–115.3 μm), they had an average lumen separation to arterial radius ratio of 1.0 or less (Table 2).

Computational Results

Idealized geometries. The imaging studies conducted here have quantified the spatial associations of arteries and veins at

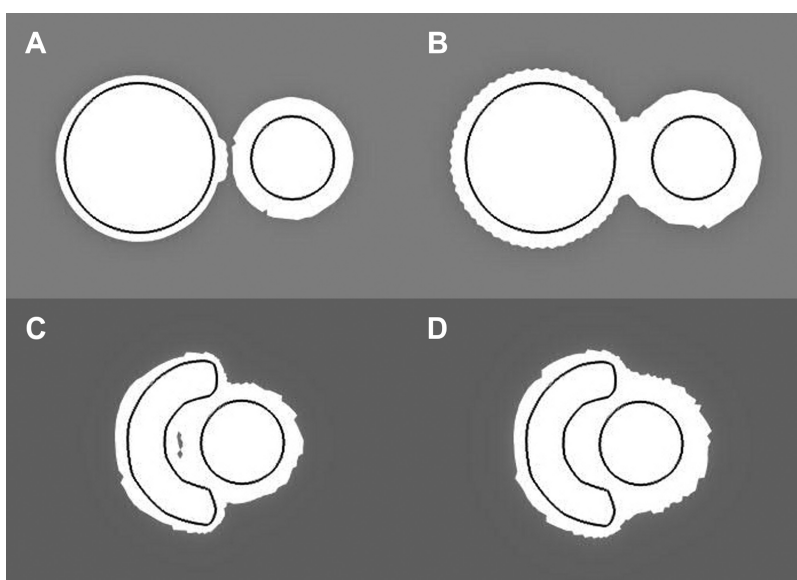


Fig. 6. Incorporating the capillary switch (CS) into the models (B and D) creates a larger PO_2 exclusion zone around the vessels compared with the idealized models (A and C). The grey area indicates $PO_2 < 42$ mmHg, while the white region indicates $PO_2 \geq 42$ mmHg.

various discrete locations within the preglomerular network. A number of different vessel arrangements were observed in the histological images, including circular veins, elliptical veins, and veins that partially wrap around the artery they paired with. Our analysis provided information on vessel pair separation for a range of vessel sizes. Based on these two sources of information, we created two representative configurations of vessel pairs for our subsequent computational modeling. The first contains a circular artery and vein ("circular" geometry) with the venous radius set to be 1.8 times that of the arterial radius, as determined from our analysis of Nordsletten's micro-CT model (Table 2). The wrapped geometry comprised a circular artery with a vein wrapped around 50% of its circumference. Due to the difficulty in defining the radius of this wrapped vein, its perimeter was set to be equal to that of the vein in the idealized circular geometry. Lumen separation for both models was initially set at nine-tenths of the arterial radius, as this was the average lumen separation calculated for a 5th order artery (Table 2). From a qualitative analysis of histological images, it was noted that the separation between adjacent AV pairs was <20 times the arterial radius (R_A). Thus the representative volume in which a single artery-vein pair was considered had length of $20R_A$. Unless otherwise stated, all simulations used these geometric parameters.

The diffusion equation was solved for the two idealized geometries to predict the steady-state distribution of oxygen through the tissue. The concentration of oxygen dropped off rapidly with distance from the vessels (Fig. 5). The diffusive flux normal to the surface of each vessel was numerically integrated around the boundary of each vessel and used to calculate AV flux (shunting), artery-to-tissue (AT) flux, and vein-to-tissue (VT) flux. Specifically, total oxygen flux directed into the vein provides AV flux. The oxygen flux directed out of the vein was VT flux. Subtracting the AV flux from the total oxygen flux from the artery provides the AT flux. The idealized models showed that AT flux (circular = $128 \text{ nmol} \cdot \text{m}^{-1} \cdot \text{min}^{-1}$, wrapped = $149 \text{ nmol} \cdot \text{m}^{-1} \cdot \text{min}^{-1}$) was about twice that of VT flux (circular = $66 \text{ nmol} \cdot \text{m}^{-1} \cdot \text{min}^{-1}$, wrapped = $78 \text{ nmol} \cdot \text{m}^{-1} \cdot \text{min}^{-1}$), but that no shunting was predicted to occur in either configuration (AV flux = $0 \text{ nmol} \cdot \text{m}^{-1} \cdot \text{min}^{-1}$) (Fig. 5). That is, these standard configurations, based on median values observed in the images predict that AV shunting is not significant. Assuming that AV shunting is significant, this result suggests that the majority of shunting is occurring in a subset of vessels in which the conditions (e.g., degree of wrapping, lumen separation) are more favorable and/or the computational model is poorly parameterized or incomplete. Therefore, our attention turned to the impact of the observed absence of capillaries and tubules between and around the AV pair.

Oxygen sinks around intrarenal arteries. Our histological analysis demonstrated that an area of loose connective tissue, lacking capillaries or tubules, immediately surrounds intrarenal arteries. Furthermore, in vessel pairs in which the vein partially wrapped the artery, neither capillaries nor tubules were seen in the space between the two vessels. In addition, peritubular capillary density around arteries $\geq 26 \mu\text{m}$ in diameter was relatively low. This indicates that there is a zone around arteries, and particularly around closely associated AV pairs (the "exclusion zone") relatively devoid of oxygen sinks. From our simulations (Fig. 5, A and B), we know that Po_2 is relatively high between and near the AV pair. In development,

hypoxia is known to induce vasculogenesis and angiogenesis (7), whereas hyperoxia inhibits angiogenesis. We therefore made the model assumption that the observed lack of capillaries is related to Po_2 and simulated this zone using a numerical "switch" in the oxygen source/sink term, S , of Eq. 2. The switch operated so that when the oxygen concentration of tissue is high (such as in the immediate vicinity of the blood vessels), oxygen removal (either by metabolic consumption or by capillaries) is shut down, creating the exclusion zone. Further from the vessels, the oxygen concentration decreases, and this effect is inhibited, allowing capillaries to supply/remove oxygen in addition to the metabolic consumption of oxygen from kidney Vo_2 .

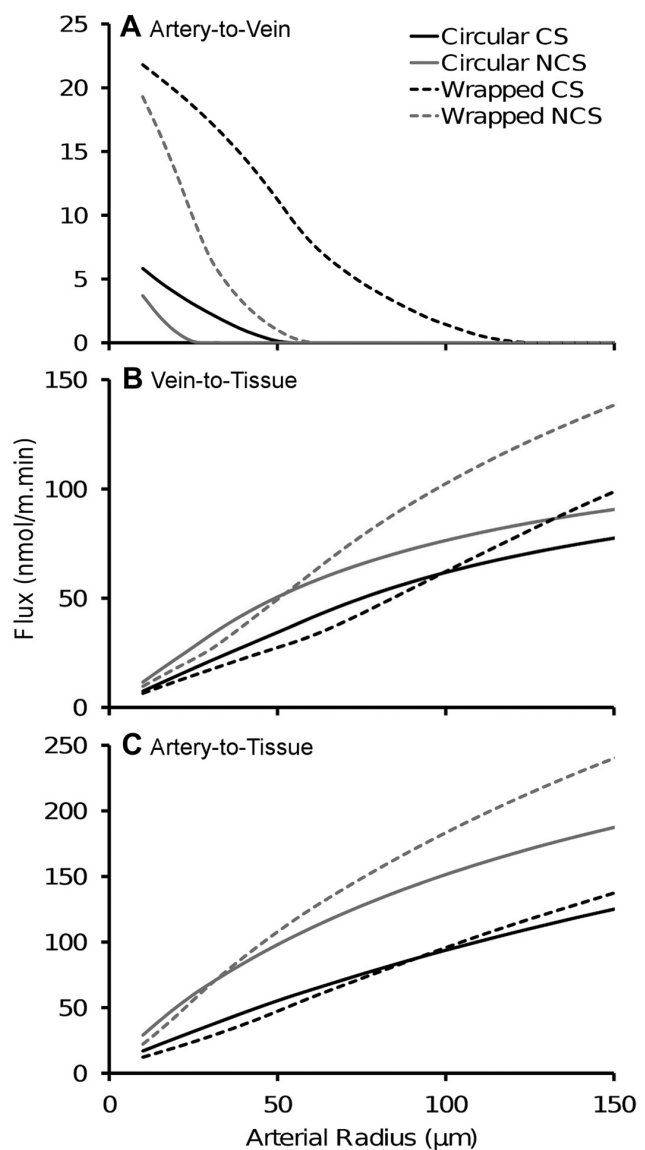


Fig. 7. Effect of applying (CS) or not applying (NCS) the capillary switch on arterial-to-venous (AV) shunting (A), vein-to-tissue (VT) flux (B), and artery-to-tissue (AT) flux (C) is shown as arterial radius changes in the circular and wrapped idealized configurations. Note different scales for flux.

$$\frac{\partial^2 c}{\partial x^2} + \frac{\partial^2 c}{\partial y^2} = \left(\frac{S}{D}\right) \left(\frac{1}{1 + \left(\frac{c}{c_{\text{cap}}}\right)^n} \right) \quad (4)$$

In Eq. 4, c_{cap} is the oxygen concentration at which the oxygen sink has been reduced by 50%, and the parameter n changes the oxygen sensitivity of the switch. We set $n = 4$, to have a relatively sharp change in the oxygen sink, reflecting the observed distinct region of connective tissue devoid of capillaries and tubules. We also assumed that $c_{\text{cap}} = 0.056 \text{ mol/m}^3$ (corresponding to a Po_2 of 42 mmHg) to have the oxygen sink transition to occur at the average tissue Po_2 recorded by Welch et al. (29) of 42 mmHg. Qualitatively, we can see how this capillary switch (CS) creates an exclusion zone around the vessels (Fig. 6). In both the wrapped and circular geometries, the effect of including the CS was compared with the idealized scenario in which consumption is always active, i.e., no capillary switch (NCS). It was found that AV shunting was greater over a wider range of arterial radii when the exclusion zone was incorporated, by use of the CS, than in the idealized NCS geometries (Fig. 7). That is, a lack of oxygen consumption between the AV pair aided shunting efficiency.

These findings, from both imaging and computational predictions, led to the incorporation of the CS into the model for both circular and wrapped geometries. Parametric studies vary-

ing lumen separation, Po_2 , arterial radius, and wrapping were then conducted. The geometries used in these analyses, along with corresponding fields of Po_2 and oxygen flux, are shown in Figs. 8 and 9. Note that the geometries we used in the parametric analysis included more than just the typical geometries observed by light microscopy, so that we could examine the impact of specific features of vessel geometry (e.g., degree of wrapping, vein aspect ratio, etc.). The results of the parametric studies are discussed below.

Length scale. Simulations were performed for the circular and wrapped geometries for a range of arterial radii, while keeping the relative proportions (e.g., vein radius and lumen separation) constant to evaluate the influence of length scale on various fluxes (Figs. 10 and 11; also, see Fig. 13). In all cases, AV shunting decreased and VT flux and AT flux increased, as the length scale (R_A) increased. The gradient in oxygen concentration was less steep for smaller length scales than larger (see Fig. 8, K–M), with oxygen moving further into the tissue before being removed by the oxygen sink.

Lumen separation. Due to the large variation observed in lumen separation (Table 2), it was important to determine how this parameter affected AV shunting. We found that when the lumen separation between the artery and vein was reduced to one-tenth of the arterial radius, the flux between the artery and vein increased, particularly in the wrapped configuration (Figs.

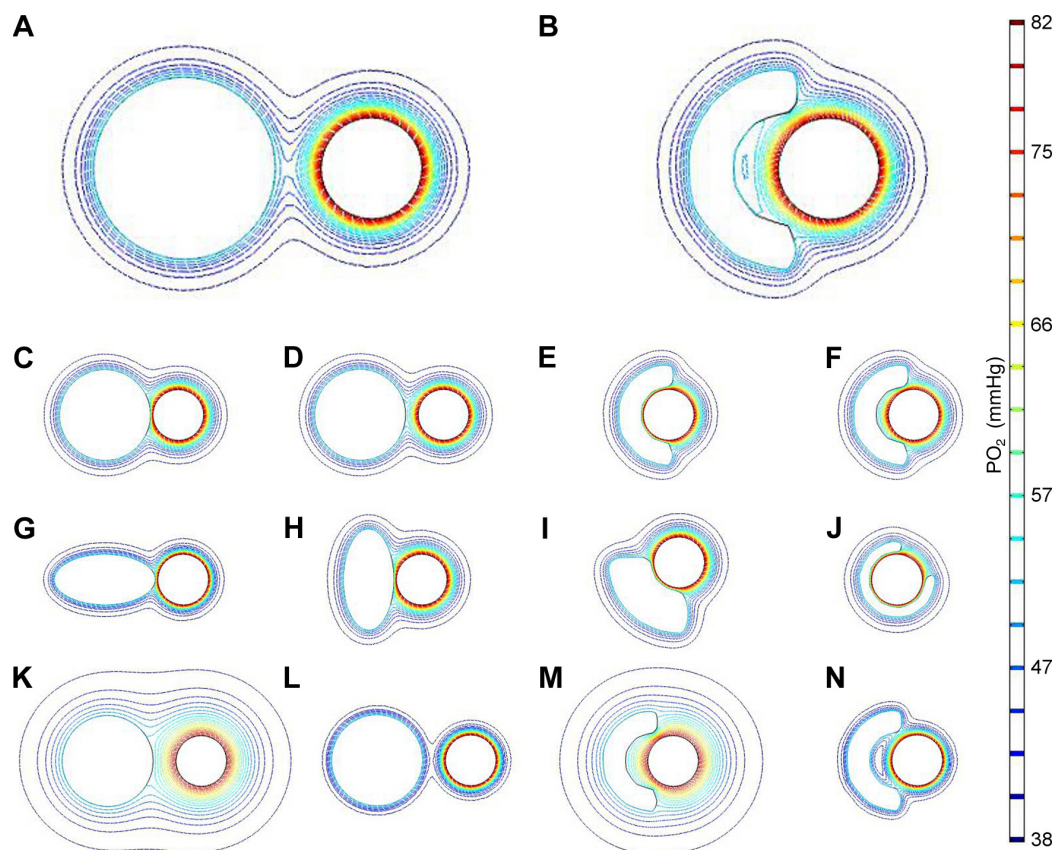


Fig. 8. Po_2 profiles of vessels in the parametric study. Circular (A) and wrapped (B) idealized models have an arterial radius (R_A) of $75 \mu\text{m}$ and lumen separation (LS) of $0.9R_A$. LS is reduced to $0.1R_A$ (C and E) and $0.5R_A$ (D and F). Orientation of vessels is altered in G–J. Geometry was rescaled to have R_A of 25 (K and M) and $125 \mu\text{m}$ (L and N).

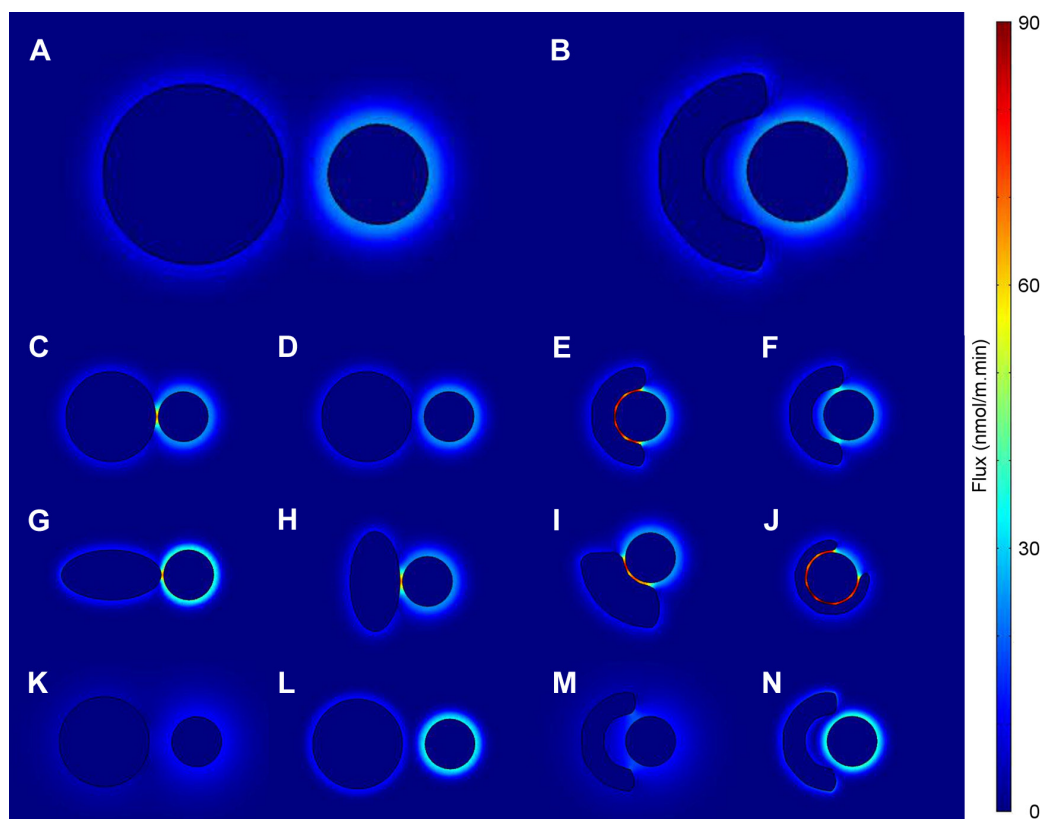


Fig. 9. Diffusive flux magnitude profiles corresponding to the geometries used in Fig. 8 for Po_2 . Shown are profiles specifically for circular (A) and wrapped (B) idealized models. Reducing LS to $0.1R_A$ (C and E) and $0.5R_A$ (D and F) increased flux. Vessel orientation (G–J) affected flux, with wrapped vessels showing greater flux. Geometry was rescaled to have R_A of 25 (K and M) and 125 μm (L and N).

9, C–F, and 10, A and D). Conversely, the flux from the vessels to the tissue (VT flux and AT flux) decreased as lumen separation was reduced (Fig. 10, B, C, E, and F). AV shunting was compared between the circular and wrapped configurations across a range of lumen separations. Results show the same qualitative patterns of change in flux between the two configurations. However, in the wrapped configuration AV shunting was about five times greater than the circular configuration across all lumen separations. This was due to a longer “contact” surface area between the artery and the vein in the wrapped configuration compared with the circular configuration. This finding indicates that the closeness of the vessels as well as their spatial arrangement is critically important in facilitating AV shunting. For the smallest lumen separation, AV shunting was largely independent of length scale, particularly in the case of wrapping. This is because the 2D diffusion begins to be approximated by a 1D diffusion model, particularly in the case of wrapping, and the arterial radius dependence of vessel surface area is cancelled by the arterial radius dependence of separation distance, such that the AV flux is independent of the arterial radius (and length scale). The smallest lumen separation also reduced the vessel-to-tissue fluxes (AT flux and VT flux). As lumen separation decreased, the drop in Po_2 occurred between the artery and vein over a shorter distance, thus increasing the concentration gradient (Fig. 8, C–F) and oxygen flux.

Radius. The mathematical analysis of Nordsletten’s micro-CT model (22) showed that the ratio of the venous to arterial radius (R_V/R_A) increases with vessel size. Therefore, R_V/R_A was altered in the circular configuration, with constant arterial radius, to determine the effect of this ratio (Fig. 11). Increasing R_V/R_A increased AV shunting in the model and VT flux, but had little effect on AT flux.

Wrapping. We hypothesized that the degree to which the vein wall wraps around the arterial wall profile greatly influences the amount of AV shunting. Therefore, diffusion was solved in six different vessel configurations where the spatial association between artery and vein changed (Fig. 12). The first orientation was a vein wrapped 75% around an artery (Fig. 9J). The second orientation was one of our idealized geometries with the vein wrapped 50% around the artery (Fig. 9E). The third orientation was similar to the first but with a lesser degree of wrapping; the vein only wrapped around 25% of the artery (Fig. 9I). The fourth orientation had an elliptical vein with its long edge parallel to the circular artery (Fig. 9H). The fifth orientation also had an elliptical vein, but with its short edge parallel to the circular artery (Fig. 9G). The sixth orientation was the second of our idealized geometries; a circular vein and artery (Fig. 9C). All configurations were investigated with a $0.1R_A$ lumen separation and with an arterial radius of 75 μm . When moving from the wrapped to circular arrangement (i.e., as the degree of wrapping decreased), AV shunting decreased

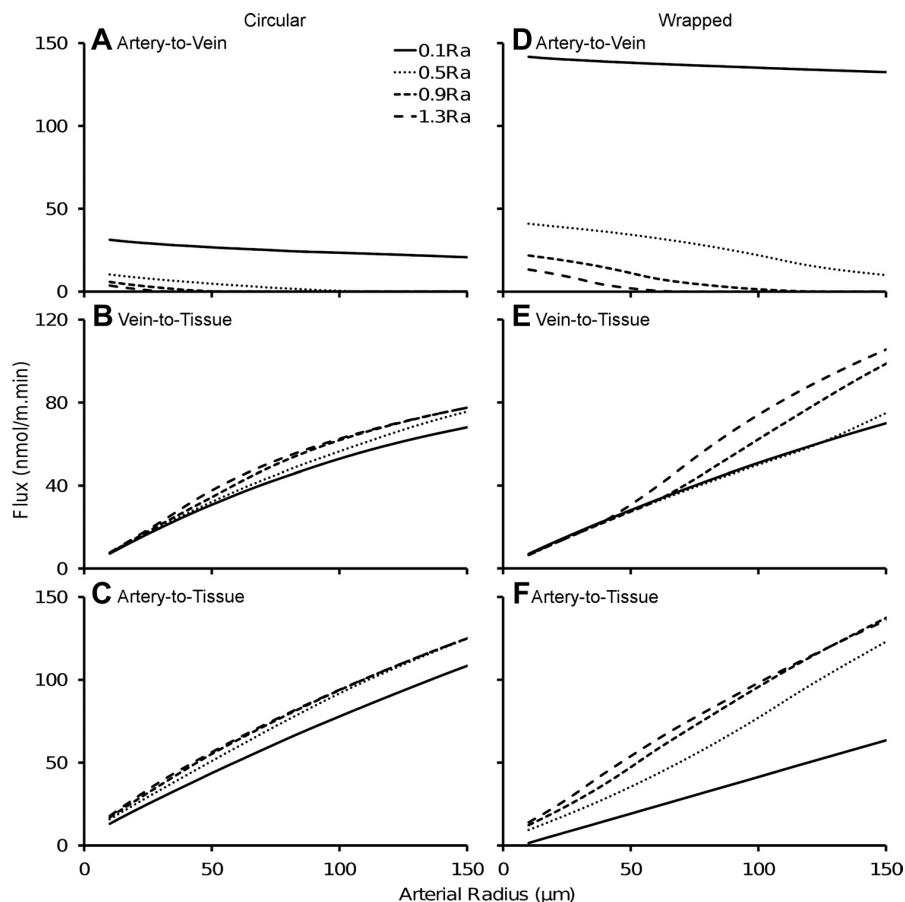


Fig. 10. Effect on flux of altering LS from $0.1R_A$ to $1.3R_A$ in the circular (A–C) and wrapped (D–F) configurations.

significantly, while AT flux and VT flux increased slightly (Fig. 12). AV shunting in the 25% wrapped vessel was about one-third of that in the 75% wrapped vessel, indicating a roughly linear relationship between the proportion of wrapping and AV shunting.

AV P_{O_2} ratio. The measurements of P_{O_2} within microdomains of the superficial cortex by Welch et al. (29) indicate that AV P_{O_2} must vary along the course of the renal preglomerular circulation. Unfortunately, it is not technically feasible to directly measure P_{O_2} at specific locations within the arterial and venous vessel networks, only at the entry/exit of the kidney. Therefore, in the majority of these simulations we have used arterial and venous P_{O_2} values measured at the renal artery/vein level. To assess how variations in P_{O_2} expected at the different representative levels of the vasculature may affect shunting, the AV P_{O_2} ratio was varied. As the AV P_{O_2} ratio was increased from 1.2 to 2, by changing the arterial P_{O_2} , AV shunting in both the wrapped and circular vessels increased, with a much steeper gradient of increase in the former (Fig. 13, A and D). For example, AV shunting at an arterial radius of 50 μm was nine times greater when the AV P_{O_2} ratio was set at 2 than when it was set at 1.2. AT shunting steadily increased as the AV P_{O_2} ratio was increased in both the wrapped and circular geometries (Fig. 13, C and F). In the experiment of Welch et al. (29), the AV P_{O_2} ratio was ~ 1.6 (85/52 mmHg) for the main renal artery/vein pair. If we assume equilibration of tissue P_{O_2} with

venular P_{O_2} , the ratio is likely to be ~ 1.1 (45/42) at the level of efferent arterioles and venules. Thus the change in the AV P_{O_2} ratio along the course of the renal circulation is likely to favor shunting in larger vessels.

DISCUSSION

The factors controlling oxygen shunting in the kidney are not well understood. It is assumed that the parallel architecture of the renal circulation facilitates countercurrent oxygen exchange. Experimental data have shown that renal venous P_{O_2} exceeds P_{O_2} in the efferent arterioles (29), which means that some of the oxygen in the renal arteries diffuses to adjacent veins. It is not known whether this occurs throughout all levels of the vasculature in the kidney or only in certain regions. This question is not just of academic interest. In particular, knowledge of the impact of AV oxygen shunting on oxygen delivery to the medullary circulation has important implications for our understanding of the causes of medullary hypoxia in ischemic acute kidney injury (25). It has been assumed, since the seminal work of Schureck (28), that most AV oxygen shunting occurs in vessels downstream from the divergence of the cortical and medullary circulation. This conclusion was based on the fact that, in a branching vascular network such as that in the renal cortex, the overall surface area for diffusion of oxygen from arteries increases geometrically at each order of

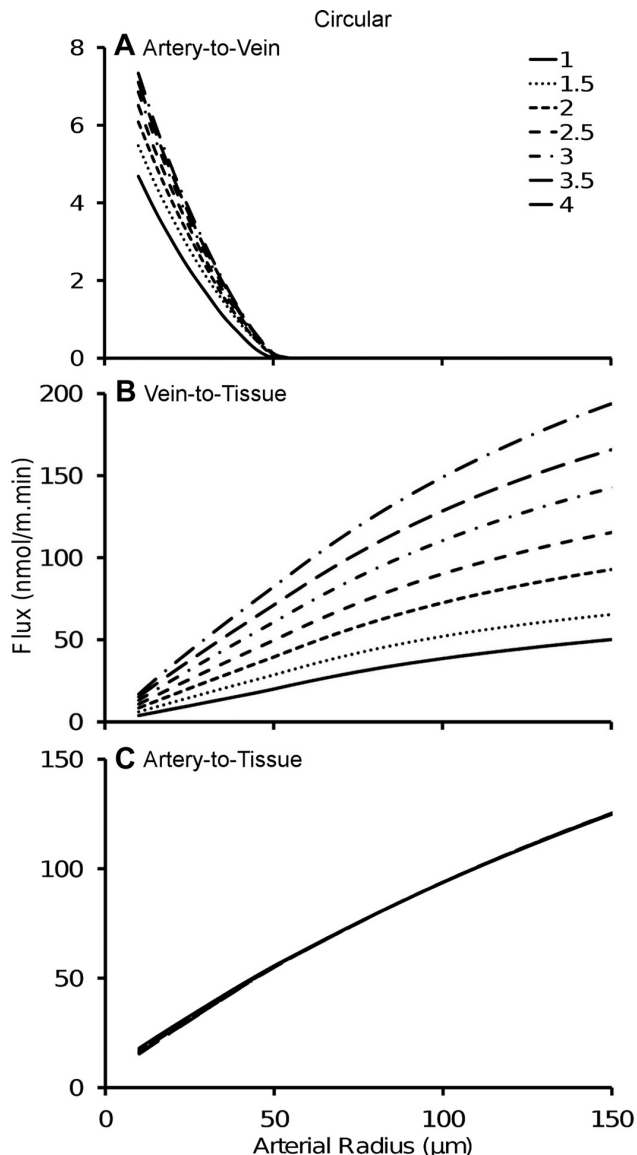


Fig. 11. Effect of R_A/R_V ratio on AV shunting (A), VT flux (B), and AT flux (C) in the circular configuration.

branching (23). But this conclusion is based on the assumption that the driving force for oxygen shunting (i.e., AV P_{O_2} difference) and the barriers to AV diffusion (e.g., lumen separation, wrapping) do not change appreciably across the course of the preglomerular circulation. Our current findings indicate that such an assumption is unwarranted.

We identified four factors that have a critical impact on the quantity of oxygen shunted between individual artery and vein vessel pairs. These are 1) the presence of oxygen sinks (capillaries or tubules) between the artery and the vein walls; 2) the distance separating the lumen of the artery and vein; 3) the spatial geometry of AV pairs, especially the degree to which the vein wall wraps around the wall of the artery; and 4) the ratio of P_{O_2} of blood in the artery and vein. In all four cases,

these factors favor AV oxygen shunting in vessels that are likely common to the cortical and medullary circulations.

Our model predicts that the efficiency of oxygen shunting from arteries to veins is significantly enhanced and that the flux of oxygen from arteries to tissue and veins to tissue is reduced, if the kidney parenchyma is not treated as an homogeneous oxygen sink. That is, AV oxygen shunting is facilitated by the absence of oxygen sinks, in the form of capillaries and tubules, between and around artery and vein pairs. As previously shown by Frank and Kriz (13), there is a zone in the immediate vicinity of intrarenal arteries of loose connective tissue in which neither capillaries nor tubules are present. Capillaries not only deliver oxygen but may also remove oxygen from tissue if they are in close vicinity to arteries or arterioles where oxygen concentrations are above those in nearby capillaries (16). Renal tubules account for the vast majority of oxygen consumption within the kidney through the utilization of ATP to drive sodium reabsorption (10). Thus capillaries and tubules, if they were to appear between the AV pair would "rob" oxygen that might have otherwise contributed to AV shunting. In short, our modeling shows that AV oxygen shunting could not operate if there were any kind of oxygen sink removing significant quantities of oxygen from the region between the artery and vein.

Importantly, we found a virtually complete absence of capillaries and tubules in the space between arteries and veins in which the vein partially wrapped the artery, and a reduced capillary density in the vicinity of larger ($\geq 26\text{-}\mu\text{m}$ diameter) compared with smaller ($< 26\text{-}\mu\text{m}$ diameter) arteries. Furthermore, while capillaries and/or tubules were rarely observed between large artery and vein pairs, they were frequently observed between and around smaller arteries and veins, presumably corresponding to distal interlobular arteries and glomerular arterioles. This arrangement would be expected to reduce AV oxygen shunting in these smaller vessels. Interestingly, the lack of capillaries and tubules we observed around large arteries and veins also serves to reduce the oxygen transport from the artery to the tissue. Fick's 1st law (2) states that oxygen diffusive flux is driven by the oxygen concentration gradient. The reduction in the strength of the oxygen sinks close to the vessel wall reduces the oxygen gradient near the wall and the oxygen flux from the vessel to the tissue.

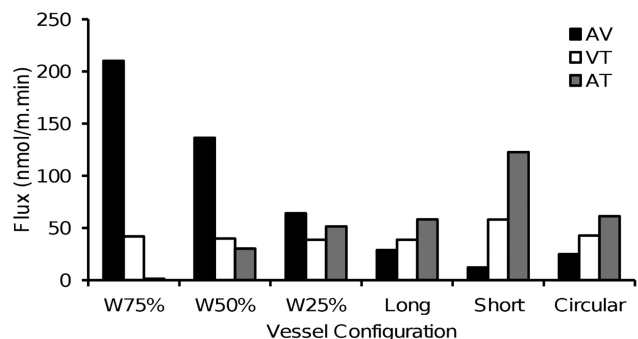


Fig. 12. Effect of vessel orientation on flux. W75%, W50%, and W25% refer to veins surrounding 75, 50, and 25%, respectively, of the arterial circumference. Long and short refer to elliptical veins with either their long or short axis in close contact with the paired artery. Columns show oxygen flux from artery to vein (AV; black), vein to tissue (VT; white), and artery to tissue (AT; grey).

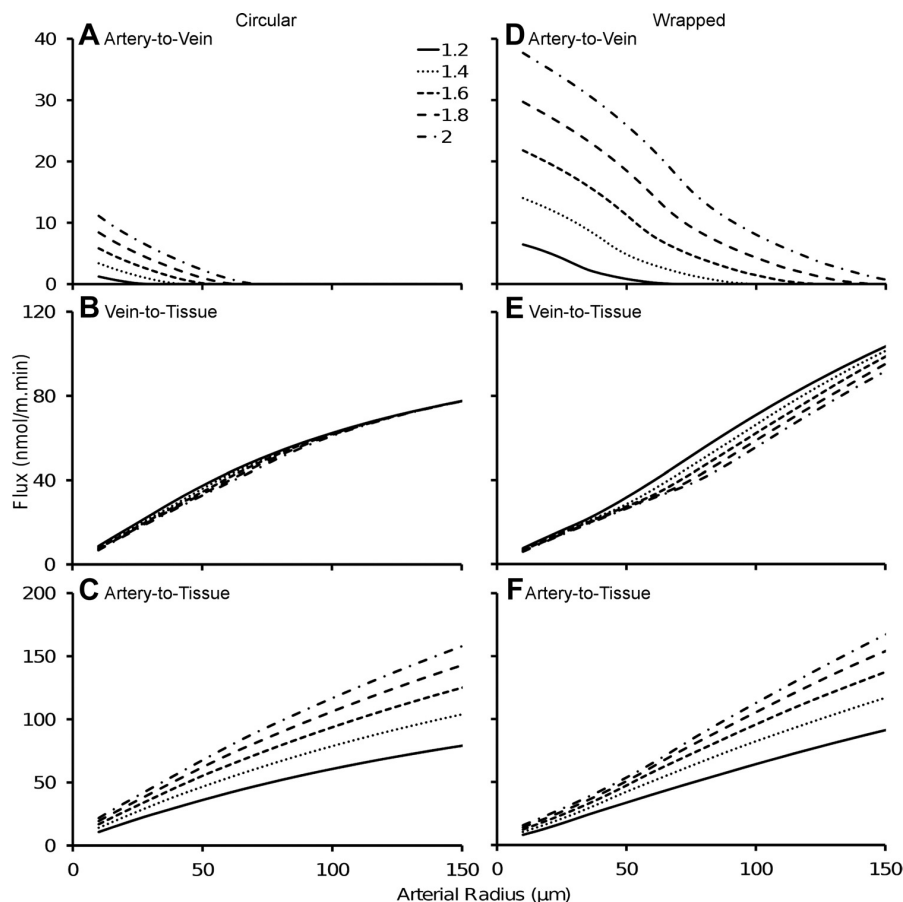


Fig. 13. Effect of the ratio of arterial to venous P_{O_2} on AV shunting (A and D), VT flux (B and E), and AT flux (C and F) in circular (A–C) and wrapped (D–F) configurations.

As might be expected from first principles (i.e., from Fick's 1st law), our model predicts that AV oxygen shunting diminishes as the distance between the lumens of adjacent arteries and veins increases. Interestingly, our analysis of Nordsletten's micro-CT model suggests that there is a U-shaped relationship between arterial diameter (or Strahler order) and lumen separation. The smallest separation distances were found for vessels of Strahler orders 5 and 6, and a proportion of vessels of Strahler orders 4 and 7, roughly corresponding to arteries of 130- to 300- μ m diameter. Larger (>300 μ m) and smaller (<130 μ m) arteries tended to be associated with more distant veins. The findings of this analysis were supported by a smaller data set of observations from light microscopy. It is not possible to definitively assign anatomic classifications to arteries based on lumen diameter or level of branching. Nevertheless, it is generally accepted that arteries of 130- to 300- μ m diameter or Strahler orders 4–7 would include interlobar, arcuate, and interlobular arteries (12, 23). The interlobular arteries taper as they radiate out from the juxtamedullary cortex, so an interlobular artery of 130- μ m diameter is likely to be proximal rather than distal (12), and so potentially before the divergence of the cortical and medullary circulations.

Our model predicts that AV oxygen shunting is facilitated in vessel pairs where a considerable proportion of the circumference of the artery is wrapped by the corresponding vein. Our light microscopic analysis suggested that the phenomenon of

wrapping was particularly prominent in larger arteries. Indeed, as arterial radius diminished there was a tendency not just for the vein to wrap less around its corresponding artery but also for the lumen separation distance to increase. Our analysis of the micro-CT model of Nordsletten et al. (23) provided further support for this notion. Analysis of these data produces a negative separation distance after CT image analysis for some vessel pairs, which can be explained by the phenomenon of veins wrapping around the arterial wall. These negative separation distances were most frequent for arteries ranging from ~100 to 300 μ m, corresponding once again to vessels likely to be common to the cortical and medullary circulations.

Our model predicts that the ratio of P_{O_2} in the blood of AV pairs (AV P_{O_2} gradient) is critical in determining AV flux. The AV P_{O_2} gradient is generated by tissue oxygen consumption, but it is also modulated by diffusive transport of oxygen among the arterial, venous, and tissue compartments (including AV oxygen shunting). The current model does not allow us to definitively predict the precise AV P_{O_2} ratio at each point along the preglomerular circulation. However, it must fall from a value of ~1.6 at an arterial P_{O_2} of 85 mmHg at the main renal artery-vein pair to a value much closer to unity (~1.1) at the level of the efferent arteriole and smallest venules. Thus the driving force for AV oxygen shunting diminishes along the course of the preglomerular circulation.

Our previous model provided a conservative estimate of the quantity of oxygen shunted between arteries and veins in the rat preglomerular circulation (14), but it provided no insight into the sites within the preglomerular circulation where shunting occurs. Our current study has identified four factors which should promote AV oxygen shunting in preglomerular vessels common to the cortical and medullary circulation (see above). These findings challenge the accepted view that most AV oxygen shunting occurs in distal vascular elements. However, there is another critical factor, not assessed in the current model, which would be expected to promote AV oxygen shunting in more distal cortical vessels, downstream from the divergence of the cortical and medullary circulation. That is, because of the branching nature of the renal circulation, the total surface area for diffusion of oxygen from arteries increases geometrically at each branch level. How, then, might we make quantitative predictions regarding the amount of oxygen shunted between arteries and veins at each representative level of the renal preglomerular circulation? To do this, we require information regarding the lengths and calibers of vessels at each representative level [as provided by the micro-CT model of Nordsletten and colleagues (22, 23)]. However, our current study shows that we also require quantitative information about the radial geometry of AV pairs at each representative level, and knowledge of the density of oxygen sinks (tubules and capillaries) in the vicinity of these vessels. Unfortunately, the data set generated by Nordsletten et al. (23) does not have the level of resolution required for provision of such information. Nevertheless, generation of high-resolution data is feasible (21), and our current findings provide justification for such studies.

In its current form, our mathematical model only deals with diffusion of oxygen in discrete cross sections of tissue. An important area for model improvement would be to combine the results from this oxygen transport model with the Gardiner et al. (14) model of countercurrent exchange of oxygen to create a 3D model of diffusive and advective oxygen transport in the kidney. In the model of Gardiner et al. (14), the diffusion barrier to oxygen shunting was assumed to be constant throughout the kidney. Relaxing this assumption, to incorporate the variation in AV spatial intimacy along the preglomerular renal vasculature, will help estimate the degree to which shunting occurs in the vessels common to the cortical and medullary circulation, and how variations in oxygen delivery and \dot{V}_{O_2} alter this shunting along the length of the vasculature. Development of such a model will require precise quantitative information regarding the radial geometry of arteries and veins at each branching level of the renal circulation, rather than the mostly qualitative analysis we have provided herein. However, once such data are available it will be possible to model changes in kidney oxygen transport in disease states associated with, for example, renal fibrosis. Our current model also does not account for the impact of PCO_2 on the affinity of hemoglobin for oxygen, or for local variations in parenchymal oxygen consumption, both of which are known to vary across various regions of the renal cortex (1, 15).

Perspectives

The susceptibility of the renal medulla to hypoxia is thought to be a critical factor in the pathogenesis of acute kidney injury

of multiple etiology (3). It is known to arise from multiple factors. These factors include the countercurrent shunting of oxygen between descending and ascending vasa recta (6). Furthermore, the predominant tubular elements in the outer medulla, the thick ascending limbs of Henle's loop, are highly metabolically active, yet their main oxygen supply is from the relatively deoxygenated blood within ascending vasa recta (3). Our current findings raise the possibility that an additional factor, AV oxygen shunting in the renal preglomerular circulation, may also limit oxygen delivery to the medullary circulation, since multiple factors appear to favor oxygen shunting in vessels upstream from the point where the cortical and medullary circulations diverge. This proposition is supported by our experimental findings in anesthetized rabbits and rats, in which we found that cortical ischemia can induce medullary hypoxia even when medullary perfusion is maintained (25). It is not currently feasible to measure the PO_2 or oxygen content of blood in arteries deep within the renal cortex. However, our current and previous (14, 25) findings predict that when such methods become available, the PO_2 of blood in the arcuate and proximal interlobular arteries, some of which is destined for the medullary circulation, may be found to be considerably lower than that of arterial blood. The loss of oxygen from arterial blood before it reaches the medullary circulation is likely exacerbated by cortical ischemia.

GRANTS

This work was supported by a grant from the National Health and Medical Research Council of Australia (606601). B. R. S. Broughton is supported by a Foundation for High Blood Pressure Research Postdoctoral Fellowship.

DISCLOSURES

No conflicts of interest, financial or otherwise, are declared by the authors.

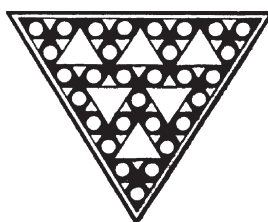
AUTHOR CONTRIBUTIONS

Author contributions: B.S.G., D.W.S., J.F.B., and R.G.E. provided conception and design of research; B.S.G., S.L.T., J.P.N., and R.G.E. analyzed data; B.S.G., S.L.T., J.P.N., D.W.S., and R.G.E. interpreted results of experiments; B.S.G., S.L.T., and R.G.E. drafted manuscript; B.S.G., S.L.T., J.P.N., D.W.S., B.R.B., and R.G.E. edited and revised manuscript; B.S.G., S.L.T., D.W.S., and R.G.E. approved final version of manuscript; S.L.T., J.P.N., A.A., B.R.B., J.F.B., and R.G.E. performed experiments; S.L.T. and J.P.N. prepared figures.

REFERENCES

1. Atherton LJ, Maddox DA, Gennari FJ, Deen WM. Analysis of PCO_2 variations in the renal cortex. II. Countercurrent exchange. *Am J Physiol Renal Physiol* 255: F361–F371, 1988.
2. Bird RB, Stewart WE, Lightfoot EN. *Transport Phenomena*. New York: Wiley, 2002.
3. Brezis M, Rosen S. Hypoxia in the renal medulla—its implications for disease. *N Engl J Med* 332: 1995.
4. Buerk DG, Lamkin-Kennard K, Jaron D. Modeling the influence of superoxide dismutase on superoxide and nitric oxide interactions, including reversible inhibition of oxygen consumption. *Free Radic Biol Med* 34: 1488–1503, 2003.
5. Chen J, Edwards A, Layton AT. Effects of pH and medullary blood flow on oxygen transport and sodium reabsorption in the rat outer medulla. *Am J Physiol Renal Physiol* 298: F1369–F1383, 2010.
6. Chen J, Layton AT, Edwards A. A mathematical model of O_2 transport in the rat outer medulla. I. Model formulation and baseline results. *Am J Physiol Renal Physiol* 297: F517–F536, 2009.
7. Dunwoodie SL. The role of hypoxia in development of the mammalian embryo. *Dev Cell* 17: 755–773, 2009.
8. Eckardt KU, Bernhardt WM, Weidemann A, Warnecke C, Rosenberger C, Wiesener MS, Willam C. Role of hypoxia in the pathogenesis of renal disease. *Kidney Int* 68: S46–S51, 2005.

9. Evans NTS, Naylor PFD, Quinton TH. The diffusion coefficient of oxygen in respiring kidney and tumour tissue. *Respir Physiol* 43: 179–188, 1981.
10. Evans RG, Gardiner BS, Smith DW, O'Connor PM. Intrarenal oxygenation: unique challenges and the biophysical basis of homeostasis. *Am J Physiol Renal Physiol* 295: F1259–F1270, 2008.
11. Federspiel WJ, Popel AS. A theoretical analysis of the effect of the particulate nature of blood on oxygen release in capillaries. *Microvasc Res* 32: 164–189, 1986.
12. Fourman J, Moffat D. *The Blood Vessels of the Kidney*. Oxford, UK: Blackwell, 1971.
13. Frank M, Kriz W. The luminal aspect of intrarenal arteries and veins of the rat as revealed by scanning electron microscopy. *Anat Embryol* 177: 371–375, 1988.
14. Gardiner BS, Smith DW, O'Connor PM, Evans RG. A mathematical model of diffusional shunting of oxygen from arteries to veins in the kidney. *Am J Physiol Renal Physiol* 300: F1339–F1352, 2011.
15. Gullans SR, Hebert SC. *Metabolic Basis of Ion Transport*. Philadelphia, PA: Saunders, 1996, p. 211–246.
16. Kobayashi H, Takizawa N. Imaging of oxygen transfer among microvessels of rat cremaster muscle. *Circulation* 105: 1713–1719, 2002.
17. Levy MN, Imperial ES. Oxygen shunting in renal cortical and medullary capillaries. *Am J Physiol* 200: 159–162, 1961.
18. Levy MN, Saucedo G. Diffusion of oxygen from arterial to venous segments of renal capillaries. *Am J Physiol* 196: 1336–1339, 1959.
19. Ludbrook J. Repeated measurements and multiple comparisons in cardiovascular research. *Cardiovasc Res* 28: 303–311, 1994.
20. MacDougall JDB, McCabe M. Diffusion coefficient of oxygen through tissues. *Nature* 215: 1173–1174, 1967.
21. Mader K, Marone F, Hintermuller C, Mikuljian G, Isenegger A, Stamparoni M. High throughput full-automatic synchrotron-based tomographic microscopy. *J Synchrotron Radiat* 18: 117–124, 2011.
22. Nordsletten DA, Blackett S, Bentley MD, Ritman EL, Smith NP. IUPS Physiome Project. http://www.physiome.org.nz/publications/nordsletten_blackett_ritman_bentley_smith_2005/folder_contents.
23. Nordsletten DA, Blackett S, Bentley MD, Ritman EL, Smith NP. Structural morphology of renal vasculature. *Am J Physiol Heart Circ Physiol* 291: H296–H309, 2006.
24. O'Connor PM. Renal oxygen delivery: matching delivery to metabolic demand. *Clin Exp Pharmacol Physiol* 33: 961–967, 2006.
25. O'Connor PM, Anderson WP, Kett MM, Evans RG. Medullary oxygenation is dependent on both cortical and medullary blood flow. *Am J Physiol Renal Physiol* 290: F688–F694, 2006.
26. O'Connor PM, Anderson WP, Kett MM, Evans RG. Renal preglomerular arterial-venous O₂ shunting is a structural anti-oxidant defence mechanism of the renal cortex. *Clin Exp Pharmacol Physiol* 33: 637–641, 2006.
27. O'Connor PM, Evans RG. Structural antioxidant defense mechanisms in the mammalian and non-mammalian kidney: different solutions to the same problem? *Am J Physiol Regul Integr Comp Physiol* 299: R723–R727, 2010.
28. Schurek HJ, Jost U, Baumgartl H, Bertram H, Heckmann U. Evidence for a preglomerular oxygen diffusion shunt in rat renal cortex. *Am J Physiol Renal Fluid Electrolyte Physiol* 259: F910–F915, 1990.
29. Welch WJ, Baumgartl H, Lubbers D, Wilcox CS. Nephron pO₂ and renal oxygen usage in the hypertensive rat kidney. *Kidney Int* 59: 230–237, 2001.



| APPENDIX 2

BASAL RENAL O₂ CONSUMPTION AND THE EFFICIENCY OF O₂ UTILIZATION FOR Na⁺ REABSORPTION

Roger G. Evans,¹ Gerard K. Harrop,¹ Jennifer P. Ngo,¹ Connie P. C. Ow,¹ and Paul M. O'Connor²

¹*Department of Physiology, Monash University, Melbourne, Victoria, Australia; and*

²*Department of Physiology, Georgia Regents University, Augusta, Georgia*

Submitted 20 August 2013; accepted in final form 8 January 2014

Monash University

Declaration for Thesis Appendix 2

Declaration by candidate

The following manuscript was published, as is, in the American Journal of Physiology Renal Physiology.

Evans RG, Harrop GK, Ngo JP, Ow CP, O'Connor PM. Basal renal O₂ consumption and the efficiency of O₂ utilization for Na⁺ reabsorption. *Am J Physiol Renal Physiol* 306: F551-560, 2014.

In the case of Appendix 2, the nature and extent of my contribution to the work was the following:

| Nature of contribution | Extent of contribution (%) |
|-------------------------------|----------------------------|
| Edited and revised manuscript | 5% |

The following co-authors contributed to the work. If co-authors are students at Monash University, the extent of their contribution in percentage terms must be stated:

| Name | Nature of contribution | Extent of contribution (%) for student co-authors only |
|------------------------|--|--|
| Roger G Evans | Provided design of research, performed experiments, analyzed data, interpreted results, prepared figures, drafted, edited and revised manuscript | 60% |
| Gerard K Harrop | Provided design of research, analyzed data, interpreted results, drafted, edited and revised manuscript | 20% |
| Connie P Ow | Edited and revised manuscript | 5% |
| Paul M O'Connor | Provided design of research, interpreted results, edited and revised manuscript | 10% |

The undersigned hereby certify that the above declaration correctly reflects the nature and extent of the candidate's and co-authors' contributions to this work*.

| | | |
|------------------------------|--|-------------|
| Candidate's Signature | | Date |
| | | 24/04/2016 |

| | | |
|------------------------------------|--|-------------|
| Main Supervisor's Signature | | Date |
| | | 24/04/2016 |

*Note: Where the responsible author is not the candidate's main supervisor, the main supervisor should consult with the responsible author to agree on the respective contributions of the authors.

Basal renal O₂ consumption and the efficiency of O₂ utilization for Na⁺ reabsorption

Roger G. Evans,¹ Gerard K. Harrop,¹ Jennifer P. Ngo,¹ Connie P. C. Ow,¹ and Paul M. O'Connor²

¹Department of Physiology, Monash University, Melbourne, Victoria, Australia; and ²Department of Physiology, Georgia Regents University, Augusta, Georgia

Submitted 20 August 2013; accepted in final form 8 January 2014

Evans RG, Harrop GK, Ngo JP, Ow CP, O'Connor PM. Basal renal O₂ consumption and the efficiency of O₂ utilization for Na⁺ reabsorption. *Am J Physiol Renal Physiol* 306: F551–F560, 2014. First published January 15, 2014; doi:10.1152/ajprenal.00473.2013.—We examined how the presence of a fixed level of basal renal O₂ consumption ($\dot{V}O_2^{\text{basal}}$; O₂ used for processes independent of Na⁺ transport) confounds the utility of the ratio of Na⁺ reabsorption (T_{Na^+}) to total renal $\dot{V}O_2$ ($\dot{V}O_2^{\text{total}}$) as an index of the efficiency of O₂ utilization for T_{Na^+} . We performed a systematic review and additional experiments in anesthetized rabbits to obtain the best possible estimate of the fractional contribution of $\dot{V}O_2^{\text{basal}}$ to $\dot{V}O_2^{\text{total}}$ under physiological conditions (basal percent renal $\dot{V}O_2$). Estimates of basal percent renal $\dot{V}O_2$ from 24 studies varied from 0% to 81.5%. Basal percent renal $\dot{V}O_2$ varied with the fractional excretion of Na⁺ (FE_{Na^+}) in the 14 studies in which FE_{Na^+} was measured under control conditions. Linear regression analysis predicted a basal percent renal $\dot{V}O_2$ of 12.7–16.5% when $FE_{\text{Na}^+} = 1\%$ ($r^2 = 0.48$, $P = 0.001$). Experimentally induced changes in T_{Na^+} altered $T_{\text{Na}^+}/\dot{V}O_2^{\text{total}}$ in a manner consistent with theoretical predictions. We conclude that, because $\dot{V}O_2^{\text{basal}}$ represents a significant proportion of $\dot{V}O_2^{\text{total}}$, $T_{\text{Na}^+}/\dot{V}O_2^{\text{total}}$ can change markedly when T_{Na^+} itself changes. Therefore, caution should be taken when $T_{\text{Na}^+}/\dot{V}O_2^{\text{total}}$ is interpreted as a measure of the efficiency of O₂ utilization for T_{Na^+} , particularly under experimental conditions where T_{Na^+} or $\dot{V}O_2^{\text{total}}$ changes.

oxygen consumption; renal metabolism; efficiency of oxygen utilization for sodium reabsorption

THE KIDNEY derives chemical energy from O₂, which it then uses to reabsorb Na⁺ and to perform functions that are independent of Na⁺ reabsorption (T_{Na^+}). The relationship between total renal O₂ consumption ($\dot{V}O_2^{\text{total}}$) and T_{Na^+} is quasilinear. It is often depicted by a straight line that intersects the ordinal ($\dot{V}O_2$) axis at a point representing the cost of “basal metabolism” ($\dot{V}O_2^{\text{basal}}$). $\dot{V}O_2^{\text{basal}}$ can thus be defined as the sum of all of $\dot{V}O_2$ that remains after accounting for that used for (T_{Na^+}) ($\dot{V}O_2^{\text{Na}^+}$) (19). There is general agreement that, under physiological conditions, $\dot{V}O_2^{\text{basal}}$ comprises <20% of $\dot{V}O_2^{\text{total}}$. This quantity ($100 \times \dot{V}O_2^{\text{basal}}/\dot{V}O_2^{\text{total}}$), which we define herein as “basal percent renal $\dot{V}O_2$,” can be estimated experimentally in intact animals. However, these estimates have varied widely (Table 1), indicating that this parameter is highly susceptible to experimental conditions.

The actual magnitude of basal percent renal $\dot{V}O_2$ has important implications for our understanding of the mechanisms underlying renal hypoxia in acute and chronic kidney disease. It has become widely accepted that the quotient of T_{Na^+} to renal $\dot{V}O_2^{\text{total}}$ (or its reciprocal) represents an index of the efficiency

(or inefficiency) of O₂ utilization for T_{Na^+} (6, 7, 35, 55). $T_{\text{Na}^+}/\dot{V}O_2^{\text{total}}$ is reduced in acute kidney injury (6, 7, 35, 55), chronic kidney disease (8), diabetes (51), and hypertension (8). These observations have been interpreted as evidence that inefficient utilization of O₂ for T_{Na^+} contributes to the renal tissue hypoxia characteristic of these pathological states. Furthermore, Laycock and colleagues showed that blockade of nitric oxide synthase reduced the glomerular filtration rate (GFR) and T_{Na^+} but increased renal $\dot{V}O_2^{\text{total}}$, so that $T_{\text{Na}^+}/\dot{V}O_2^{\text{total}}$ was more than halved (35). These observations were interpreted as evidence that nitric oxide normally acts to enhance the “renal efficiency for transportation of sodium.” Changes in transport efficiency, which can be defined as the rate of change in T_{Na^+} per unit change in $\dot{V}O_2^{\text{total}}$ ($dT_{\text{Na}^+}/d\dot{V}O_2^{\text{total}}$) could result from changes in mitochondrial function, shifts in T_{Na^+} along the nephron to sites of differing efficiency for O₂ utilization, altered Na⁺ backleak through paracellular pathways, or changes in the function of mechanisms of secondary active transport (19). However, the denominator of $T_{\text{Na}^+}/\dot{V}O_2^{\text{total}}$ is composed of a component dependent on T_{Na^+} ($\dot{V}O_2^{\text{Na}^+}$) as well as a component independent of T_{Na^+} ($\dot{V}O_2^{\text{basal}}$). Consequently, the use of $T_{\text{Na}^+}/\dot{V}O_2^{\text{total}}$ as an index of the efficiency of T_{Na^+} (transport efficiency = $dT_{\text{Na}^+}/d\dot{V}O_2^{\text{total}} \approx T_{\text{Na}^+}/\dot{V}O_2^{\text{Na}^+}$) rests on the assumption that $\dot{V}O_2^{\text{basal}}$ is negligible and does not vary much under physiological or pathophysiological conditions. Therefore, in the present study, we set out to test the hypotheses that 1) under physiological conditions, $\dot{V}O_2^{\text{basal}}$ makes up a substantial proportion of $\dot{V}O_2^{\text{total}}$ and 2) estimates of basal percent renal $\dot{V}O_2$ and $T_{\text{Na}^+}/\dot{V}O_2^{\text{total}}$ depend on the natriuretic state of the kidney and, thus, vary with the fractional excretion of Na⁺ (FE_{Na^+}) and T_{Na^+} . To assess basal percent renal $\dot{V}O_2$, we first performed a systematic review of published reports of studies of intact animals in which basal percent renal $\dot{V}O_2$ was estimated or that contained data from which it could be estimated. We also performed an experiment to assess the effects of ureteral ligation on renal $\dot{V}O_2$, since this approach has been little used (Table 1). We then reviewed published reports in which $T_{\text{Na}^+}/\dot{V}O_2^{\text{total}}$ was measured or that contained data from which it could be calculated to determine whether it varies with FE_{Na^+} and/or T_{Na^+} . Patterns arising in these data were then compared with theoretical relationships between these variables, generated for varying levels of $\dot{V}O_2^{\text{basal}}$.

METHODS

Systematic Review: Search Criteria

In a Medline search, we used as Medical Subject Headings (MESH) and keywords “oxygen consumption” (105,389 results) AND “kidney” (652,799 results) AND either “glomerular filtration rate” (38,655 results) OR the MESH “sodium” OR the keyword “sodium reabsorption” (127,115 results), giving a combined return of 553

Address for reprint requests and other correspondence: R. G. Evans, Dept. of Physiology, PO Box 13F, Monash Univ., Victoria 3800, Australia.

Table 1. Available estimates of $\dot{V}O_2^{basal}$ as a percentage of $\dot{V}O_2^{total}$ (basal percent renal $\dot{V}O_2$)

| Author(s) | Reference | Species and Number of Animals/Patients Studied | Anesthetic | FE _{Na+} , % | T _{Na+} / $\dot{V}O_2^{total}$ ^a | Basal Percent Renal $\dot{V}O_2$ |
|-----------------------|-----------|--|--|--|--|--|
| Lassen et al. | 34 | Dog (<i>n</i> = 14) | Pentobarbital | 1.51 ± 0.42 | 23.0 ± 0.6 | 11.6% by extrapolation ^b ; 18.6% when GFR = 0 (hemorrhage) |
| Thaysen et al. | 69 | Dog (<i>n</i> = 10) | NR | NR | 23.0 ± 0.6 | 18.0% when GFR = 0 (hemorrhage); note the likely overlap of data with Lassen et al. (34) |
| Thureau | 72 | Dog (<i>n</i> = 12) | Pentobarbital or thiobutabarbital | 1.19 | NR | 17.9% by extrapolation ^b |
| Fujimoto et al. | 16 | Dog (<i>n</i> = 21) | Pentobarbital | NR | 21.5 ± 2.3 ^d | 0% by extrapolation ^b |
| Knox et al. | 30 | Dog (<i>n</i> = 42) | Chloralose or pentobarbital | Control: 2.40 ± 0.52; mannitol diuresis: 8.8 ± 0.3 | Control: 26.4 ± 3.8; mannitol diuresis: 15.6 ± 1.7 | 3.7% by extrapolation ^c ; T _{Na+} reduced by hemorrhage and increased ureteral pressure and infusion of Ringer solution or mannitol solution; 15% by extrapolation ^c during ethacrynic acid-induced diuresis if total $\dot{V}O_2$ is considered the value before ethacrynic acid administration; 20% by extrapolation ^c during ethacrynic acid-induced diuresis if total $\dot{V}O_2$ is considered the value after ethacrynic acid administration. |
| Wolf et al. | 81 | Dog (<i>n</i> = 15) | Chlorpromazine/pentobarbital/chloralose | Control: ~4; after ethacrynic acid: ~29 | Control: ~33; after ethacrynic acid: ~21 | 30.5% by extrapolation ^b |
| Sadowski and Torun | 58 | Dog (<i>n</i> = 16) | <i>N</i> -methyl- β -bromoallylisopropyl barbiturate | NR | NR | 30.6% by extrapolation ^b ; 63.9% when GFR = 0 (hypertonic mannitol infusion); 81.5% when GFR = 0 (tubular blockade with oil) |
| Sejerssted et al. | 60 | Dog (<i>n</i> = 7) | Pentobarbital | 20.8 during mannitol-Ringer infusion | 16.5 | 33.6% by extrapolation ^c before ouabain treatment; T _{Na+} reduced by aortic constriction; 28.4% by extrapolation ^c after ouabain treatment |
| Stecker et al. | 65 | Dog (<i>n</i> = 8) | Pentobarbital | NR | NR | 35.6% 3 h after complete ureteral obstruction |
| Theye and Maher | 70 | Dog (<i>n</i> = 13) | Lightly anesthetized with 0.1% (vol/vol) halothane (plus neuromuscular blockade) | NR | 19.4 | 35.0% by extrapolation ^c ; T _{Na+} reduced by 1% (vol/vol) expired halothane; 38.1% when GFR = 0 [3% (vol/vol) expired halothane] |
| Melchiorri et al. | 45 | Dog (<i>n</i> = 6) | Pentobarbital and phenobarbital | NR | NR | ~10% when GFR = 0 (intravenous bombesin) |
| Dies et al. | 9 | Dog (<i>n</i> = 19) | Pentobarbital | ~10 (7–13) | 33.9 | 30.4% by extrapolation ^c ; T _{Na+} reduced by ouabain, acetazolamine, ethacrynic acid, and furosemide |
| Steen et al. | 66 | Dog (<i>n</i> = 6) | Pentobarbital | 16.6 | 21.0 | 39.0% by extrapolation ^c ; T _{Na+} reduced by graded doses of ethacrynic acid |
| Rosenbaum and DiScala | 57 | Dog (<i>n</i> = 5) | Pentobarbital | NR | 23.2 ± 2.2 | 24% by extrapolation ^c ; T _{Na+} reduced by intravenous infusion of Ringer solution |
| Ostensen and Stokke | 49 | Dog (<i>n</i> = 10) | Pentobarbital | NR | NR | All dogs were pretreated with acetazolamide; 15.1% by extrapolation ^c ; T _{Na+} reduced by bumetanide and ouabain |
| Torelli et al. | 73 | Rabbit (<i>n</i> = 24) | Pentobarbital and urethane | NR | 8.8 ± 1.1 | 64.6% by extrapolation ^b ; 40.5% when GFR = 0 (hemorrhage) |
| Evans et al. | 13 | Rabbit (<i>n</i> = 6) | Pentobarbital | 12.1 ± 1.6 | 13.0 ± 0.7 ^e | 47.2 ± 5.5% when GFR = 0 (reduced renal artery pressure) |
| Present study | | Rabbit (<i>n</i> = 6) | Pentobarbital | 14.8 ± 4.0 | 11.3 ± 1.1 | 60 ± 8% when GFR = 0 (90 min after ligation of the ureter) |

Continued

Table 1.—Continued

| Author(s) | Reference | Species and Number of Animals/Patients Studied | Anesthetic | FE _{Na+} , % | T _{Na+} /V̇O ₂ ^{total} ^a | Basal Percent Renal V̇O ₂ |
|------------------------------|-----------|---|-----------------------|---------------------------------------|--|---|
| Juillard et al. | 27 | Pig (n = 8) | Ketamine and xylazine | 8.1 ± 2.7 | 19.6 | 15% when GFR = 0 (reduced renal artery pressure) ^f |
| Parekh and Veith | 52 | Rat (n = 22) | Thiobutabarbital | 0.66 ± 0.19 | 25.8 | 19.9% by extrapolation ^c ; T _{Na+} reduced by subjecting some rats to ischemia-reperfusion injury 40 days before the experiment |
| Elinder and Aperia | 12 | Rat (n = 24) | Thiobutabarbital | 1.05 | 14.9 | 12.3% by extrapolation ^c ; T _{Na+} reduced by intravenous infusion of isotonic saline |
| Welch et al. | 80 | Rat (n = 10 Wistar-Kyoto rats + n = 10 spontaneously hypertensive rats) | Thiobarbital | NR | 15.1 ± 1.6 | Wistar-Kyoto rats: 43.4% by extrapolation ^b ; spontaneously hypertensive rats: 21.1% by extrapolation ^b |
| Brodwall; Brodwall and Laake | 2, 3 | Human (n = 24) | Unanesthetized | NR | 43.4 | 19.8% by extrapolation ^{b,g} |
| Ofstad et al. | 48 | Human (n = 10) | Unanesthetized | Control: 1.96; after furosemide: 14.4 | Control: 13.7; after furosemide: 12.1 | 0.1% by extrapolation ^b before furosemide treatment; 30.8% by extrapolation ^b after furosemide treatment |
| Kurnik et al. | 33 | Human (n = 60) | Unanesthetized | 1.9 ± 0.3 ⁱ | NR | 29.4% by extrapolation ^{b,h} |

V̇O₂^{basal}, basal renal O₂ consumption; V̇O₂^{total}, total renal V̇O₂; FE_{Na+}, fractional excretion of Na⁺ under control conditions; T_{Na+}, Na⁺ reabsorption; GFR, glomerular filtration rate; NR, not reported. ^aT_{Na+}/V̇O₂^{total} results, including V̇O₂^{basal}. "Extrapolation" refers to the estimation of V̇O₂ when either GFR or T_{Na+} = 0 from regression analysis of the relationships between V̇O₂ and T_{Na+} or GFR. ^bFrom the relationship between GFR or T_{Na+} and V̇O₂ determined in the absence of any specific interventions to alter these variables. ^cFrom the relationship between GFR or T_{Na+} and V̇O₂ determined using specific interventions to alter these variables. ^dThis is the slope of the line of best fit between T_{Na+} and V̇O₂ and can be used in this case because the line of best fit passed through the origin. ^eDue to a calculation error, the values of T_{Na+}/V̇O₂^{total} presented in this study (13) were twice the true value, which is presented here. ^fApproximated by reading off Fig. 3 in their study. ^gPatients with normal renal function or chronic kidney disease were studied before cardiac catheterization. ^hThe ordinal intercept of the relationship between T_{Na+} and V̇O₂ was estimated by inspection. ⁱNo measure of FE_{Na+} was available for normal subjects, so values for patients with chronic renal failure (with and without diabetes) are presented.

results (from 1946 to November 1, 2013). Two authors (G. K. Harrop and R. G. Evans) then performed an initial screen and excluded 478 articles that lacked data from which basal percent renal V̇O₂ or T_{Na+}/V̇O₂^{total} might be estimated. The remaining 75 articles formed the basis of the literature search. Additional articles were sourced from the references of articles obtained from the search and from an examination of articles that cited the papers identified in our search. The final analysis included only original studies with at least an abstract written in English. Thus, four potentially relevant articles written in German were excluded (5, 17, 31, 82).

Basal Percent Renal V̇O₂

Overview of available methods for estimating basal percent renal V̇O₂. Basal renal metabolism can be assessed in vivo in a number of ways. One approach might be to pharmacologically inhibit Na⁺-K⁺-ATPase using an agent such as ouabain. However, not all isoforms of Na⁺-K⁺-ATPase are ouabain sensitive, particularly in rodents (39), and ouabain is arrhythmogenic. Consequently, caution must be applied to the interpretation of data derived from such studies. Another approach is to plot the relationship between T_{Na+} and renal V̇O₂^{total} observed under relatively normal physiological conditions or in response to maneuvers that alter T_{Na+} and then calculate the ordinal intercept, where T_{Na+} = 0 (or GFR = 0). This approach has been used widely (Table 1). Nevertheless, this does require the assumption that the relationship between T_{Na+} and renal V̇O₂^{total} is linear [or log linear (58)] and could be confounded by changes in renal metabolism, independent of T_{Na+}, that might occur in response to experimental maneuvers used to alter T_{Na+}. Another approach, which has also been used widely, is to lower arterial pressure below the point at which glomerular filtration ceases. This approach is, of course, limited by the potential for neurohumoral activation, particularly if arterial pressure is lowered by hemorrhage, to alter V̇O₂^{basal} or the efficiency of O₂ uti-

lization for Na⁺ transport (dT_{Na+}/dV̇O₂^{total}). Finally, ureteric obstruction will also abolish Na⁺ excretion, but it has not been definitively established that ureteric obstruction abolishes Na⁺ transport.

Inclusion and exclusion criteria for published data. Some studies of the effects of maneuvers that reduced T_{Na+} [e.g., reduced arterial pressure and/or renal blood flow (RBF) or the administration of diuretics] were excluded because of the unavailability of information on GFR and/or T_{Na+} (10, 11, 18, 20, 26, 32, 36, 37, 59, 75, 78). Others were excluded because GFR was not reduced to zero and T_{Na+} was not measured or because there was no analysis of the relationship between GFR or T_{Na+} and V̇O₂^{total} from which basal percent renal V̇O₂ could be derived (1, 21, 22, 25, 28, 46, 50, 53, 56, 63, 64, 67, 76, 77) or because no significant correlation was observed between T_{Na+} and V̇O₂^{total} (47). We also excluded studies in which both renal V̇O₂^{total} and T_{Na+} were measured, but the latter were not varied sufficiently to allow the ordinal intercept of the relationship(s) between V̇O₂^{total} and T_{Na+} or GFR to be determined (7, 38), or because the data were not presented in a form to allow this relationship to be extracted (29, 42, 54). Studies in which T_{Na+} and V̇O₂^{total} were varied by the induction of acute renal failure (23, 24) or clinical studies in patients with acute kidney injury (55) were excluded on the basis that these pathophysiological conditions might be associated with increased renal V̇O₂^{basal}. Studies in which agents were administered that are known to alter the efficiency of O₂ utilization for T_{Na+} were also excluded (6, 35). Studies in isolated perfused kidneys (44, 62, 68, 74) were excluded, in part because of the nonphysiological nature of these experimental conditions but also because of the difficulty in defining an appropriate denominator for the calculation of basal percent renal V̇O₂ under what might be considered "physiological" conditions. Thus, we restricted our analysis to in vivo studies in which renal V̇O₂^{total} was measured under relatively normal physiological conditions as well as under conditions in which it was established that glomerular filtration had

ceased and/or in which the apparently linear relationship between T_{Na^+} and renal $\dot{V}O_2^{total}$ could be extrapolated to the ordinal intercept (i.e., T_{Na^+} or GFR = 0; Table 1).

Experimental studies. Male New Zealand White rabbits ($n = 6$, 2.83 ± 0.11 kg) were studied according to the Australian Code of Practice for the Care and Use of Animals for Scientific Purposes. Experimental conditions were similar to those we have previously reported (13). Catheters were placed in the central arteries and marginal veins of both ears under local analgesia (1% lidocaine, Xylocaine, AstraZeneca, North Ryde, NSW, Australia). Rabbits were then anesthetized with pentobarbital sodium (90–150 mg plus 30–50 mg/h iv, Sigma Chemical, St. Louis, MO) and artificially ventilated. Throughout the surgery and experiment, the extracellular fluid volume was maintained by an intravenous infusion ($0.15 \text{ ml} \cdot \text{kg}^{-1} \cdot \text{min}^{-1}$) of a 4:1 mixture of compound sodium lactate and polygeline/electrolyte solution. Body temperature was maintained between 37.0 and 38.0°C throughout the surgery and subsequent experiment by means of a heated table and infrared heating lamp. Baseline arterial P_{O_2} (90–110 mmHg) and P_{CO_2} (30–45 mmHg) were maintained within the desired ranges by altering the respiratory rate and volume and the level of positive end-expiratory pressure. The kidney was denervated, and a transit time ultrasound flowprobe (type 2SB, Transonic Systems, Ithaca, NY) was placed around the renal artery for the measurement of RBF. A catheter was placed in the renal vein (13). A 90-min equilibration period was allowed between the completion of the surgical procedures and commencement of the experimental procedures.

Arterial pressure was measured via an ear artery catheter connected to a pressure transducer (Cobe, Arvada, CO) and bridge amplifier (model QA1, Scientific Concepts, Mount Waverley, VIC, Australia). The transit time ultrasound flowprobe was connected to a compatible flowmeter (model T206, Transonic Systems). Values of mean arterial pressure (MAP), heart rate (triggered by the arterial pressure pulse), RBF, and core body temperature were digitized as 2-s averages. Blood gas analysis was performed on 0.5-ml samples of arterial and renal venous blood, collected simultaneously, using an ABL 700 series blood gas analyzer (Radiometer, Copenhagen, Denmark). Kidney O₂ delivery (DO_2) was calculated as the product of RBF and the O₂ content of arterial blood. $\dot{V}O_2$ was calculated as the product of RBF and the arteriovenous O₂ concentration difference. Comparisons between the measured variables at baseline relative to those 90 min after ureter ligation were made using Student's paired *t*-test. Two-sided *P* values of ≤ 0.05 were considered statistically significant.

$$T_{Na^+}/\dot{V}O_2^{total}$$

From the published reports identified in our systematic review, we identified studies in which both FE_{Na^+} and $T_{Na^+}/\dot{V}O_2^{total}$ were reported, both T_{Na^+} and $T_{Na^+}/\dot{V}O_2^{total}$ were reported, or that provided data from which these variables could be calculated. For the most part, we confined our analysis to reports in which $T_{Na^+}/\dot{V}O_2^{total}$ was or could be calculated from T_{Na^+} and $\dot{V}O_2^{total}$ measured in individual animals or humans. However, in seven cases, we calculated $T_{Na^+}/\dot{V}O_2^{total}$ from between-animal mean values of T_{Na^+} and $\dot{V}O_2^{total}$ (9, 27, 33, 50, 52, 61, 66).

Theoretical Predictions for the Rat Kidney

We assumed that 28 mol of Na⁺ are reabsorbed for every 1 mol of O₂ consumed (43), as follows:

$$\frac{dT_{Na^+}}{d\dot{V}O_2^{total}} = \frac{T_{Na^+}}{\dot{V}O_2^{Na^+}} = \beta = 28 \quad (1)$$

We also assumed a linear relationship between $\dot{V}O_2^{total}$ and T_{Na^+} , as follows:

$$\dot{V}O_2^{total} = \dot{V}O_2^{basal} + \dot{V}O_2^{Na^+} = \dot{V}O_2^{basal} + \frac{T_{Na^+}}{\beta} \quad (2)$$

In addition, we assumed that a rat kidney reabsorbs 100 μmol of Na⁺ each minute under normal physiological conditions ($\alpha = 100 \mu\text{mol}/\text{min}$), based on a value of T_{Na^+} of $115 \mu\text{mol} \cdot \text{min}^{-1} \cdot \text{g kidney wt}^{-1}$ in Wistar-Kyoto rats whose kidneys weighed ~ 1.1 g (80). $\dot{V}O_2^{basal}$ was set as a constant (i.e., independent of the actual rate of T_{Na^+}), defined as a proportion (γ) of the O₂ required to reabsorb 100 $\mu\text{mol}/\text{min}$ of Na⁺, as follows:

$$\dot{V}O_2^{basal} = \gamma \times \frac{\alpha}{\beta} \quad (3)$$

Basal percent $\dot{V}O_2$ was then defined as follows:

$$\text{Basal percent } \dot{V}O_2 = 100 \times \frac{\dot{V}O_2^{basal}}{\dot{V}O_2^{total}} \quad (4)$$

First, we set the filtered load of Na⁺ at 100 $\mu\text{mol}/\text{min}$ and at various levels of γ (0–0.6); we then calculated how changes in FE_{Na^+} would affect basal percent $\dot{V}O_2$ and $T_{Na^+}/\dot{V}O_2^{total}$. We then examined the effects of changes in γ on the way $T_{Na^+}/\dot{V}O_2^{total}$ varies with T_{Na^+} within the range from 0 to 200 $\mu\text{mol}/\text{min}$. Finally, we examined the effects on estimates of basal percent $\dot{V}O_2$ of the presence of an additional source of renal $\dot{V}O_2$ for functions other than T_{Na^+} but that nevertheless varies in proportion to T_{Na^+} . We defined this additional source of $\dot{V}O_2$, distinct from both $\dot{V}O_2^{basal}$ and $\dot{V}O_2^{Na^+}$, as ($\kappa \times \dot{V}O_2^{Na^+}$), so that:

$$\dot{V}O_2^{total} = \dot{V}O_2^{basal} + \dot{V}O_2^{Na^+} + (\kappa \times \dot{V}O_2^{Na^+}) \quad (5)$$

RESULTS

Basal Percent Renal $\dot{V}O_2$

Systematic review. The text below summarizes the experimental procedures and major findings of the 23 published studies included in our final analysis (Table 1).

We identified 10 publications that presented estimates of basal percent renal $\dot{V}O_2$ determined by extrapolation to the ordinal intercept of the relationship between GFR or T_{Na^+} and $\dot{V}O_2^{total}$ (i.e., when GFR or $T_{Na^+} = 0$) in experiments in which no specific interventions were applied to alter GFR or T_{Na^+} . In anesthetized dogs (16, 34, 58, 72, 81) and rats (80) and unanesthetized humans (2, 3, 33, 48), estimates of basal percent renal $\dot{V}O_2$ ranged from 0% to 43.4% (Table 1).

We identified 12 publications reporting estimates of basal percent renal $\dot{V}O_2$ derived from an extrapolation of the relationship between GFR or T_{Na^+} and $\dot{V}O_2^{total}$ from experiments in which specific treatments were applied to alter GFR or T_{Na^+} . These treatments included progressive hemorrhage (30, 73), suprarenal aortic constriction (60), administration of diuretic agents (9, 30, 49, 79, 81), expansion of extracellular fluid volume (12, 57), inhibition of ouabain-sensitive Na⁺-K⁺-ATPase (9), halothane inhalation (70), and chronic recovery from ischemia-reperfusion injury (52). These estimates of basal percent renal $\dot{V}O_2$, from studies in anesthetized dogs, rabbits, and rats, ranged from 15% to 64.6% (Table 1).

We identified nine published reports including estimates of basal percent renal $\dot{V}O_2$ determined by comparison of $\dot{V}O_2^{total}$ under control conditions with $\dot{V}O_2$ when glomerular filtration was abolished. The specific interventions included hemorrhage (27, 34, 69, 73), suprarenal aortic constriction (13), high-dose halothane (70), administration of bombesin (45), administra-

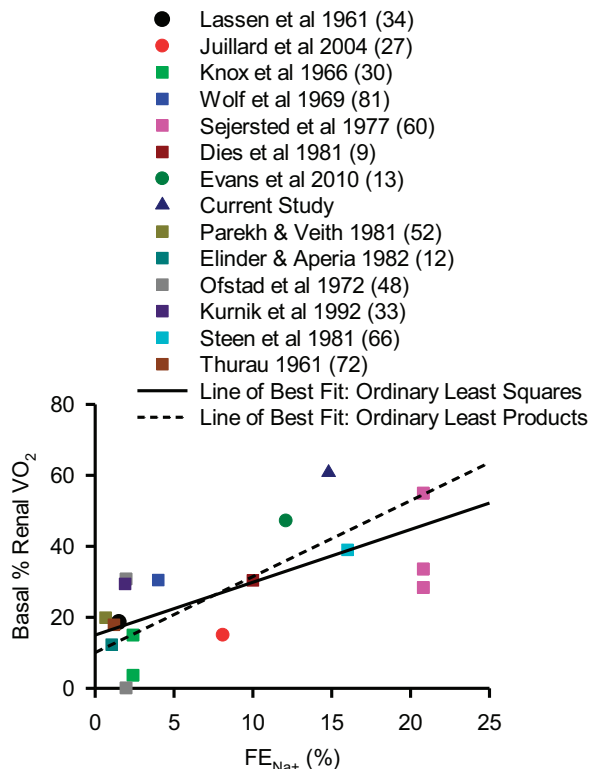


Fig. 1. Relationship between the fractional excretion of Na⁺ (FE_{Na^+}) under control conditions and the estimate of basal renal O₂ consumption ($\dot{V}O_{2\text{basal}}$) as a percentage of total renal $\dot{V}O_2$ ($\dot{V}O_{2\text{total}}$) (basal percent renal $\dot{V}O_2$). Each study is represented by a different color. Circles represent data obtained from studies where glomerular filtration was reduced to zero by reducing renal perfusion pressure. Triangles represent data from studies in which the ureter was ligated to abolish glomerular filtration. Squares represent data from studies in which basal percent renal $\dot{V}O_2$ was estimated by extrapolation of the relationship between Na⁺ reabsorption (T_{Na^+}) and $\dot{V}O_2$ to the ordinal intercept. Regression analysis ($r^2 = 0.483$, $P = 0.001$) by the ordinary least-squares method (solid line) (40, 41) provided a line of best fit of $\dot{V}O_2 = 15.0 + 1.488 \times FE_{Na^+}$. The ordinary least-products method (dashed line) provided a line of best fit of $\dot{V}O_2 = 10.1 + 2.141 \times FE_{Na^+}$. Numbers in parentheses refer to specific references.

tion of hypertonic mannitol (58), blockade of tubular flow by retrograde filling of the lower urinary tract with oil (58), or complete ureteral occlusion (65). These estimates of basal percent renal $\dot{V}O_2$, from studies in anesthetized dogs, pigs, and rabbits, ranged from 10% to 81.5% (Table 1).

New experimental studies. Baseline levels of MAP (73 ± 1 mmHg), heart rate (256 ± 6 beats/min), RBF (23.0 ± 2.3 ml/min), arterial blood PO_2 (107 ± 4 mmHg) and hemoglobin saturation ($99.5 \pm 0.2\%$), renal venous blood PO_2 (60 ± 3 mmHg) and hemoglobin saturation ($77.2 \pm 2.0\%$), renal DO_2 (183 ± 17 $\mu\text{mol/min}$) and $\dot{V}O_2$ (42 ± 5 $\mu\text{mol/min}$), fractional O₂ extraction ($22.8 \pm 1.9\%$), and FE_{Na^+} ($14.8 \pm 4.0\%$) were similar to those we have observed in previous studies using this experimental preparation (13–15).

Ureteral ligation did not significantly alter MAP, RBF, arterial blood PO_2 or saturation, or renal DO_2 , but renal venous PO_2 was increased by $11 \pm 4\%$ and hemoglobin saturation increased to $84.6 \pm 2.2\%$. Consequently, fractional O₂ extraction was reduced to $15.6 \pm 2.2\%$ and renal $\dot{V}O_{2\text{total}}$ was reduced

by $40 \pm 8\%$. Thus, this experiment provided an estimate of basal percent renal $\dot{V}O_2$ of $60 \pm 8\%$.

Patterns in the data. Published estimates of basal percent renal $\dot{V}O_2$ have been highly variable. In general, calculated basal percent $\dot{V}O_2$ appears to be greater when estimated using treatments that abolish glomerular filtration by blockade of tubular flow (Refs. 58 and 65 and the present study) than by methods that abolish glomerular filtration by lowering renal perfusion pressure (Refs. 27, 34, 69, and 73). Linear regression analysis established a positive relationship between FE_{Na^+} and the estimate of basal percent renal $\dot{V}O_2$ ($P = 0.001$; Fig. 1). Indeed, this linear relationship accounted for 48.3% of the variance in estimates of basal percent renal $\dot{V}O_2$. The theoretical relationships we constructed (Fig. 2A) were a family of curves that deviated only slightly from linearity within the range of $FE_{Na^+} = 0$ –70%. The relationships predict that basal percent renal $\dot{V}O_2$ increases with increasing FE_{Na^+} . The slope of the relationship increases as FE_{Na^+} or $\dot{V}O_{2\text{basal}}$ increase.

The experimental data and theoretical relationships shown in Figs. 1 and 2A indicate that estimates of basal percent renal $\dot{V}O_2$ from studies performed in animals in a natriuretic state likely overestimate basal percent renal $\dot{V}O_2$ under truly physiological conditions. This likely includes estimates of basal percent $\dot{V}O_2$ from studies in pentobarbital-anesthetized rabbits (Refs. 13 and 73 and the present study), since our experience is that this anesthetic tends to inhibit T_{Na^+} . Estimates of basal percent renal $\dot{V}O_2$ derived from studies of dogs in a natriuretic state are also likely to be overestimates (9, 60, 66, 81). If we

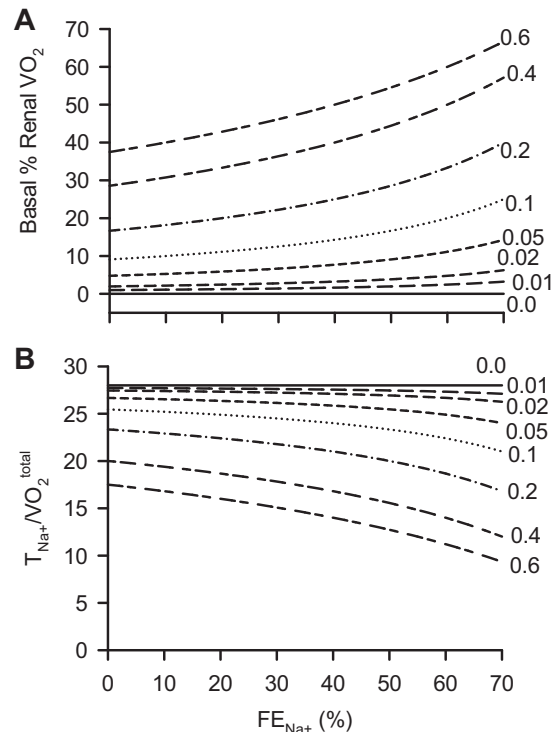


Fig. 2. Predicted effects of altered $\dot{V}O_{2\text{basal}}$ in the rat kidney on the relationships between FE_{Na^+} and basal percent renal $\dot{V}O_2$ (A) and the molar ratio of T_{Na^+} to $\dot{V}O_2$ ($T_{Na^+}/\dot{V}O_{2\text{total}}$; B). $\dot{V}O_{2\text{basal}}$ was set at a proportion ($\gamma = 0, 0.01, 0.02, 0.05, 0.1, 0.2, 0.4$, and 0.6) of the O₂ required to reabsorb 100 μmol of Na⁺ per minute, assuming 28 mol of Na⁺ are reabsorbed for every 1 mol of O₂ consumed.

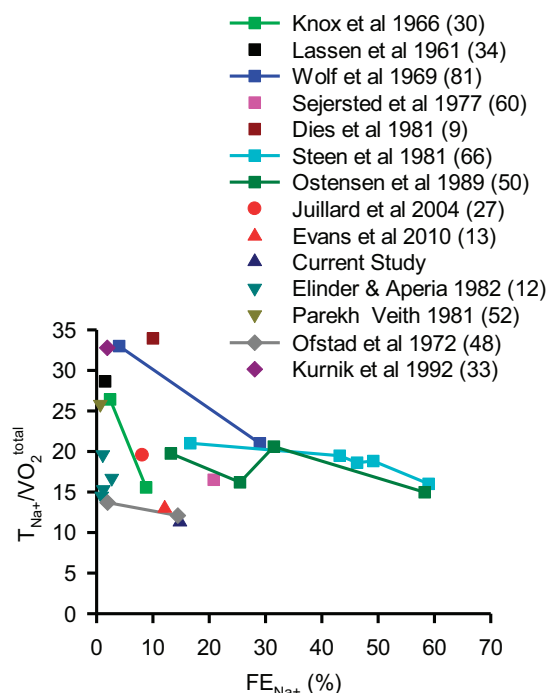


Fig. 3. Relationship between FE_{Na^+} and $T_{Na^+}/\dot{V}O_2^{total}$. Each study is represented by a different color. The various symbols represent different species: squares are dogs, circles are pigs, triangles are rabbits, inverted triangles are rats, and diamonds are humans. Observations made in a within-subject fashion are linked by lines. Linear regression analysis across the entire data set failed to detect a significant relationship between the two variables ($r^2 = 0.12$, $P = 0.07$). Numbers in parentheses refer to specific references.

assume a physiological value of FE_{Na^+} of 1%, the data shown in Fig. 1 provide an estimate of basal percent renal $\dot{V}O_2$ of 16.5% under physiological conditions according to the line of best fit determined by ordinary least-squares regression. When the line of best fit was determined by the ordinary least-products method (40, 41), basal percent renal $\dot{V}O_2$ was predicted to be 12.7%.

$$T_{Na^+}/\dot{V}O_2^{total}$$

The theoretical relationships we constructed (Fig. 2B) between FE_{Na^+} and $T_{Na^+}/\dot{V}O_2^{total}$ were a family of curves that deviated only slightly from linearity within the range of $FE_{Na^+} = 0$ –70%. They predict that $T_{Na^+}/\dot{V}O_2^{total}$ decreases with increasing FE_{Na^+} . The slope of the relationship increases as FE_{Na^+} or $\dot{V}O_2^{basal}$ increase.

We identified 13 published reports, of studies in anesthetized dogs, rats, and pigs as well as unanesthetized humans, from which we could retrieve paired values of FE_{Na^+} and $T_{Na^+}/\dot{V}O_2^{total}$. These data were also available for the present study of anesthetized rabbits. Overall, $T_{Na^+}/\dot{V}O_2^{total}$ tended to vary inversely with FE_{Na^+} (Fig. 3), in a manner consistent with the theoretical relationships we generated (Fig. 2B). Linear regression analysis demonstrated that this apparent effect was not quite statistically significant ($P = 0.07$) and only explained 12% of the variance in the data set. However, in four of the five experiments in which data were collected in a within-subject fashion, $T_{Na^+}/\dot{V}O_2^{total}$ was reduced by treatments that increased FE_{Na^+} .

We identified eight published reports, of studies in anesthetized dogs, rats, rabbits, and pigs in which T_{Na^+} was manipulated, from which we could retrieve paired values of T_{Na^+} and $T_{Na^+}/\dot{V}O_2^{total}$. T_{Na^+} was manipulated by reducing renal perfusion pressure, altering renal vascular tone by electrical stimulation of the renal nerves or renal arterial infusion of vasoactive agents, by increasing ureteral pressure, or by administration of a range of diuretic agents. In some reports, the effects of more than one maneuver and/or of graded stimuli were presented. These data were normalized by expressing both variables as percent changes from their control level (Fig. 4). We observed a strong positive relationship between percent changes in T_{Na^+} (x) and $T_{Na^+}/\dot{V}O_2^{total}$ (y), which was consistent across species exposed to similar stimuli. For example, the observations of Warner et al. (76) of the effects of progressively reduced renal artery pressure in anesthetized pigs were virtually superimposable on those of Evans et al. (13) of the effects of this maneuver in anesthetized rabbits. There was also remarkably little variation in this relationship between maneuvers that altered T_{Na^+} , chiefly by altering GFR through effects on renal hemodynamics, and those in which T_{Na^+} was more directly manipulated by administration of diuretic agents.

The theoretical relationships we constructed between T_{Na^+} (or the percent change in T_{Na^+}) and $T_{Na^+}/\dot{V}O_2^{total}$ (or the percent change in $T_{Na^+}/\dot{V}O_2^{total}$) were curvilinear (Fig. 5). They predicted that $T_{Na^+}/\dot{V}O_2$ in the rat kidney falls steeply as T_{Na^+} is reduced below the physiological level of 100 $\mu\text{mol}/\text{min}$ and increases in a less steep manner when T_{Na^+} is increased above

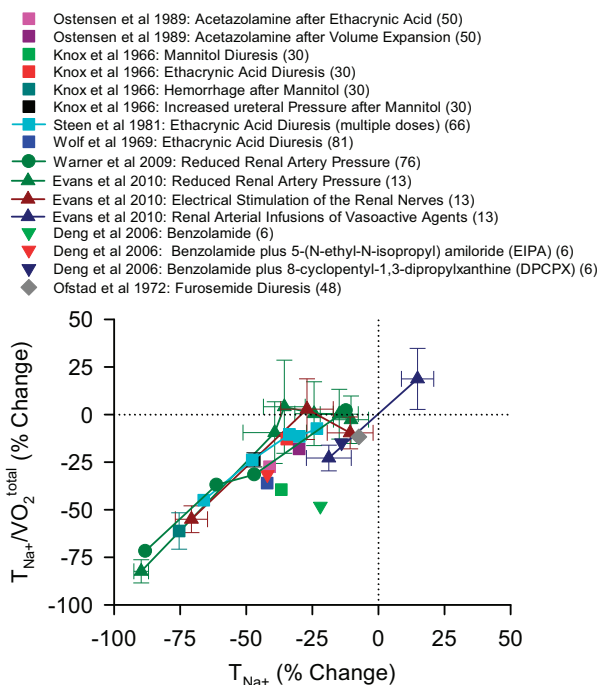


Fig. 4. Relationship between percent changes in T_{Na^+} and percent changes in $T_{Na^+}/\dot{V}O_2^{total}$. Each specific treatment is represented by a different color. The various symbols represent different species: squares are dogs, circles are pigs, triangles are rabbits, inverted triangles are rats, and diamonds are humans. Observations made in a within-subject fashion are linked by lines. Error bars represent SEs in cases where these were available. Numbers in parentheses refer to specific references.

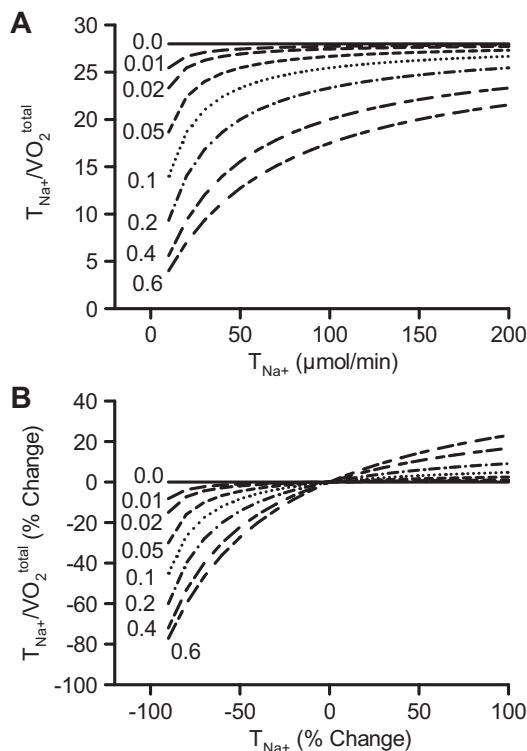


Fig. 5. Predicted effects of altered $\dot{V}O_2^{basal}$ in the kidney of the rat on the relationship between T_{Na^+} and the quotient of $T_{Na^+}/\dot{V}O_2^{total}$. $\dot{V}O_2^{basal}$ was set at a proportion ($\gamma = 0, 0.01, 0.02, 0.05, 0.1, 0.2, 0.4$, and 0.6) of the O₂ required to reabsorb 100 μmol of Na⁺ per minute, assuming 28 mol of Na⁺ are reabsorbed for every 1 mol of O₂ consumed. Note that B, which shows the relationships between percent changes in these variables, is essentially a logarithmic transformation of the data in A.

this level. The range of variations increased with increasing $\dot{V}O_2^{basal}$. Importantly, the experimental data (Fig. 4) followed a similar trend to the theoretical relationships between percent changes in T_{Na^+} and $T_{Na^+}/\dot{V}O_2^{total}$ (Fig. 5B).

Theoretical Impact of T_{Na^+} -Dependent Changes in $\dot{V}O_2$ for Processes Other Than T_{Na^+}

As would be expected, the imposition of an additional source of $\dot{V}O_2$ used for functions other than T_{Na^+} , but nevertheless linearly dependent on T_{Na^+} , increases the slope of the relationship between T_{Na^+} and $\dot{V}O_2^{total}$. As a result, estimates of basal percent renal $\dot{V}O_2$ that would be predicted to arise from experimental studies are reduced (Fig. 6).

DISCUSSION

Why is it important to know what basal percent $\dot{V}O_2$ is? Primarily, its importance lies in the interpretation of $T_{Na^+}/\dot{V}O_2^{total}$ as a measure of the efficiency of O₂ utilization for T_{Na^+} . The denominator of this ratio comprises at least two components: a “variable” cost of O₂ utilization for Na⁺ transport ($\dot{V}O_2^{Na^+}$) and a presumed “fixed” cost of $\dot{V}O_2^{basal}$. To make things even more complicated, it is possible that O₂ utilization for functions other than T_{Na^+} may vary with T_{Na^+} (see below and Refs. 4, 62, and 68). To better understand how $\dot{V}O_2^{basal}$ confounds the use of $T_{Na^+}/\dot{V}O_2^{total}$ as an index of the efficiency

of O₂ utilization for T_{Na^+} , we analyzed the available data regarding the magnitude of $\dot{V}O_2^{basal}$ as a percentage of $\dot{V}O_2^{total}$ (basal percent renal $\dot{V}O_2$). We also examined how estimates of basal percent renal $\dot{V}O_2$ and $T_{Na^+}/\dot{V}O_2^{total}$ vary with the physiological state of the kidney.

We are able to draw two important conclusions. First, although available estimates of basal percent renal $\dot{V}O_2$ vary widely, ranging from 0% to 81.5%, nearly half of this variation can be accounted for by variations in FE_{Na^+} . Consequently, regression analysis of available experimental data provided a “consensus” estimate of basal percent renal $\dot{V}O_2$ of 12.7–16.5% when FE_{Na^+} is 1%, depending on the method used to perform linear regression (40, 41). Our analysis of these experimental observations is in accordance with the results of our theoretical analysis, which predicted a positive curvilinear relationship between FE_{Na^+} and basal percent renal $\dot{V}O_2$.

If basal percent renal $\dot{V}O_2$ varies with the natriuretic state of the kidney, it follows that $T_{Na^+}/\dot{V}O_2^{total}$ should too, as demonstrated by our theoretical analysis. Our finding of a positive relationship between experimentally induced changes in T_{Na^+} and $T_{Na^+}/\dot{V}O_2^{total}$ supports this prediction. Thus, our second conclusion is that the use of $T_{Na^+}/\dot{V}O_2^{total}$ as an index of the efficiency of O₂ utilization for T_{Na^+} is confounded by the presence of $\dot{V}O_2^{basal}$. Consequently, caution should be applied when this variable is used as a quantitative index of the efficiency of O₂ utilization for T_{Na^+} , especially when experimental manipulations result in changes in T_{Na^+} . Our observations reflect the fact that renal $\dot{V}O_2^{total}$ includes a component that does not vary with T_{Na^+} ($\dot{V}O_2^{basal}$) as well as a component that does vary with T_{Na^+} ($\dot{V}O_2^{Na^+}$). Consequently, $T_{Na^+}/\dot{V}O_2^{total}$ can change independently of the efficiency of T_{Na^+} ($dT_{Na^+}/d\dot{V}O_2$), especially when T_{Na^+} changes.

Three caveats must be applied to our conclusions. The first caveat relates to the assumption that the $\dot{V}O_2$ for functions other

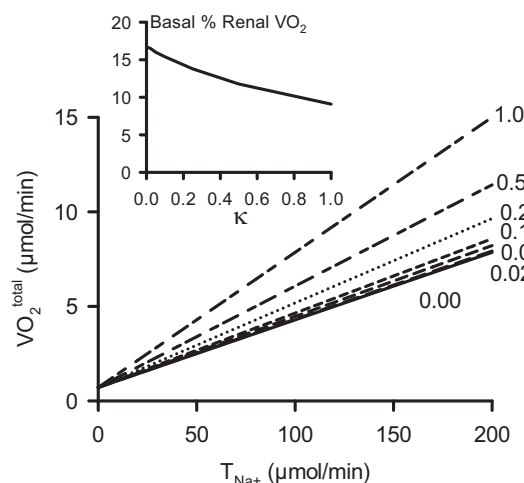


Fig. 6. Predicted effects of altered T_{Na^+} on $\dot{V}O_2^{total}$ when $\dot{V}O_2$ for functions other than T_{Na^+} varies as a linear function of T_{Na^+} . True $\dot{V}O_2^{basal}$, defined as renal $\dot{V}O_2$ when $T_{Na^+} = 0$, was set at 20% of the cost of reabsorption of 100 μmol/min Na⁺. $\dot{V}O_2^{total}$ was calculated as the sum of $\dot{V}O_2^{basal}$, $\dot{V}O_2$ for T_{Na^+} ($\dot{V}O_2^{Na^+}$; assuming 28 mol of Na⁺ are reabsorbed for each 1 mol of O₂ consumed), and an additional proportion ($\kappa = 0, 0.02, 0.05, 0.1, 0.25, 0.5$, or $1.0 \times \dot{V}O_2^{Na^+}$). The inset shows how this additional O₂ utilization would affect an estimate of basal percent $\dot{V}O_2$ determined experimentally by a maneuver that abolishes tubular T_{Na^+} .

than T_{Na^+} is relatively constant. There is evidence that this quantity, which theoretically could include true " $\dot{V}O_{2\text{basal}}$," as well as a component of $\dot{V}O_2$ for functions other than T_{Na^+} but that nevertheless varies with T_{Na^+} , is not static (4, 62, 68). For example, Cohen and colleagues (4) provided evidence, using the isolated perfused kidney, that the rate at which lactate enters into O₂-dependent biochemical pathways (e.g., glucose production) increases as T_{Na^+} increases. Our theoretical analysis indicates that the presence of this additional source of $\dot{V}O_2$ would lead to an underestimation of the efficiency of direct O₂ utilization for T_{Na^+} and reduce basal percent $\dot{V}O_2$ when determined experimentally by abolition of T_{Na^+} .

Second, it should be acknowledged that some of the variation in estimates of basal percent renal $\dot{V}O_2$ likely arises from the confounding influence of the maneuvers used to alter T_{Na^+} . For example, the greatest estimates of basal percent renal $\dot{V}O_2$ came from the present study, in which the ureter was ligated (60%), and from an earlier study (58), in which tubular flow was blocked by a retrograde infusion of oil (81.5%). It has been proposed that damage to the tubular epithelium induced by blockade of tubular flow at a downstream site may lead to increased renal $\dot{V}O_2$ (58). It is also possible that ligation of the ureter does not cause the complete cessation of Na⁺ transport. Finally, it is also likely that the presence and mode of anesthesia used in these studies could have influenced estimates of basal percent renal $\dot{V}O_2$. For example, pentobarbital is known to influence mitochondrial function by inhibition of complex 1 (NADH dehydrogenase) of the respiratory chain (71), thus leading to reduced cellular ATP availability. This action might at least partly explain the relatively high FE_{Na^+} observed in experiments performed under pentobarbital anesthesia.

The third caveat that must be applied to our conclusions relates to the possibility that some of the treatments that altered T_{Na^+} in the studies shown in Fig. 3 may have really altered the efficiency of O₂ utilization for T_{Na^+} (i.e., $dT_{Na^+}/d\dot{V}O_{2\text{total}}$). Such effects might be expected if active Na⁺ transport is shifted from the proximal tubule to less efficient tubular segments (19), if the efficiency of mitochondrial function is reduced, as is known to occur when the bioavailability of nitric oxide is reduced (35), or by factors that inhibit passive Na⁺ transport and/or secondary active transport. For example, Deng et al. (6) provided strong evidence that inhibition of carbonic anhydrase can reduce the efficiency of O₂ utilization for T_{Na^+} . They showed that the carbonic anhydrase inhibitor benzolamide increased renal $\dot{V}O_{2\text{total}}$ by ~50% despite a concomitant reduction in T_{Na^+} of ~25%. They proposed that this effect was mediated by increased active Cl⁻ transport in the proximal tubule. Similarly, Knox et al. (30) found that the slope of the relationship between T_{Na^+} and renal $\dot{V}O_{2\text{total}}$ was increased during diuresis induced by an infusion of mannitol, implying that the metabolic cost of T_{Na^+} was increased by mannitol, at least under the conditions of their experiment. However, the fact that the experimental observations shown in Fig. 4 are consistent with the theoretical relationships shown in Fig. 5B, despite the fact that T_{Na^+} was manipulated by a wide range of maneuvers, suggests that effects of the maneuvers on the efficiency of O₂ utilization for T_{Na^+} have not undermined our conclusions. Interestingly, the one obvious outlier shown in Fig. 4 represents the effects of benzolamide observed by Deng et al. The fact that $T_{Na^+}/\dot{V}O_{2\text{total}}$ was reduced more by benzolamide than any of the other maneuvers, for a given reduction in

T_{Na^+} , provides some level of confidence that the ability of benzolamide to alter the efficiency of O₂ utilization for T_{Na^+} is the exception rather than the rule.

In conclusion, renal $\dot{V}O_{2\text{basal}}$ accounts for a significant proportion of renal $\dot{V}O_{2\text{total}}$. Estimates based on the literature vary from 0% to 81.5% of renal $\dot{V}O_{2\text{total}}$. Our best estimate based on linear regression equations relating estimates of $\dot{V}O_{2\text{basal}}$ to the natriuretic state of the experimental preparation is 12.7–16.5% of renal $\dot{V}O_{2\text{total}}$ when $FE_{Na^+} = 1\%$ (i.e., standard physiological conditions). We also conclude that $T_{Na^+}/\dot{V}O_{2\text{total}}$ should be interpreted cautiously, because $\dot{V}O_{2\text{basal}}$ is not negligible and may vary in ways we cannot predict. Consequently, significant changes in $T_{Na^+}/\dot{V}O_{2\text{total}}$ can occur when T_{Na^+} changes, even if the efficiency of O₂ utilization for T_{Na^+} remains unaltered. One way to at least partially overcome the limitations of $T_{Na^+}/\dot{V}O_{2\text{total}}$ as an index of the efficiency of O₂ utilization for T_{Na^+} would be for experimenters to directly determine renal $\dot{V}O_{2\text{basal}}$ under the conditions of their experiments. This would allow $\dot{V}O_{2\text{basal}}$ to be removed from the denominator of $T_{Na^+}/\dot{V}O_{2\text{total}}$. Another, perhaps better, approach would be to subject experimental animals to maneuvers that progressively alter T_{Na^+} , so that the slope of the relationship between $T_{Na^+}/\dot{V}O_{2\text{total}}$ ($dT_{Na^+}/d\dot{V}O_{2\text{total}}$) can be determined. This approach, of course, does not overcome the potentially confounding effects of potential changes in $\dot{V}O_{2\text{basal}}$ induced by the maneuvers used to abolish T_{Na^+} . These methods were used in earlier investigations of the physiology of renal O₂ utilization but have fallen out of favor as we have moved from large-animal to small-animal experimental models. Finding ways to use more rigorous methods to assess the efficiency of O₂ utilization for T_{Na^+} in small animals, such as rats and mice, represents an important technical challenge for investigators studying the physiology and pathophysiology of renal oxygenation.

ACKNOWLEDGMENTS

The authors thank Dr. Prabhleen Singh for providing information regarding relevant publications from her research group, but absolve her of any responsibility for any errors we might have made.

GRANTS

This work was supported by National Health and Medical Research Council of Australia Grants 606601 and 1024575 (to R. G. Evans) and American Heart Association Grant 10SDG4150061 (to P. M. O'Connor).

DISCLOSURES

No conflicts of interest, financial or otherwise, are declared by the author(s).

AUTHOR CONTRIBUTIONS

Author contributions: R.G.E., G.K.H., and P.M.O. conception and design of research; R.G.E. performed experiments; R.G.E. and G.K.H. analyzed data; R.G.E., G.K.H., and P.M.O. interpreted results of experiments; R.G.E. prepared figures; R.G.E. and G.K.H. drafted manuscript; R.G.E., G.K.H., J.P.N., C.P.O., and P.M.O. edited and revised manuscript; R.G.E., G.K.H., J.P.N., C.P.O., and P.M.O. approved final version of manuscript.

REFERENCES

1. Bragadottir G, Redfors B, Nygren A, Sellgren J, Ricksten SE. Low-dose vasopressin increases glomerular filtration rate, but impairs renal oxygenation in post-cardiac surgery patients. *Acta Anaesthesiol Scand* 53: 1052–1059, 2009.
2. Brodwall EK. The relation between the renal oxygen consumption and the transport of sodium, clearance of inulin and the renal extraction of PAH. *Scand J Clin Lab Invest* 16: 287–291, 1964.

3. Brodwall EK, Laake H. The relation between oxygen consumption and transport of sodium in the human kidney. *Scand J Clin Lab Invest* 16: 281–286, 1964.
4. Cohen JJ, Merckens LS, Peterson OW. Relation of Na⁺ reabsorption to utilization of O₂ and lactate in the perfused rat kidney. *Am J Physiol Renal Fluid Electrolyte Physiol* 238: F415–F427, 1980.
5. Deetjen P, Kramer K. [The relation of O₂ consumption by the kidney to Na re-resorption]. *Pflügers Arch Gesamte Physiol Menschen Tiere* 273: 636–650, 1961.
6. Deng A, Miracle CM, Lortie M, Satriano J, Gabbai FB, Munger KA, Thomson SC, Blantz RC. Kidney oxygen consumption, carbonic anhydrase, and proton secretion. *Am J Physiol Renal Physiol* 290: F1009–F1015, 2006.
7. Deng A, Miracle CM, Suarez JM, Lortie M, Satriano J, Thomson SC, Munger KA, Blantz RC. Oxygen consumption in the kidney: effects of nitric oxide synthase isoforms and angiotensin II. *Kidney Int* 68: 723–730, 2005.
8. Deng A, Tang T, Singh P, Wang C, Satriano J, Thomson SC, Blantz RC. Regulation of oxygen utilization by angiotensin II in chronic kidney disease. *Kidney Int* 75: 197–204, 2009.
9. Dies F, Valdez JM, Vilet R, Garza R. Lactate oxidation and sodium reabsorption by dog kidney in vivo. *Am J Physiol Renal Fluid Electrolyte Physiol* 240: F343–F351, 1981.
10. Dole VP, Emerson KJ, Phillips RA, Hamilton P, Van Slyke DD. The renal extraction of oxygen in experimental shock. *Am J Physiol* 145: 337–345, 1946.
11. Edlund A, Sollevi A. Renal effects of i.v. adenosine infusion in humans. *Clin Physiol* 13: 361–371, 1993.
12. Elinder G, Aperia A. Renal oxygen consumption and sodium reabsorption during isotonic volume expansion in the developing rat. *Pediatr Res* 16: 351–353, 1982.
13. Evans RG, Eppel GA, Michaels S, Burke SL, Nematbakhsh M, Head GA, Carroll JF, O'Connor PM. Multiple mechanisms act to maintain kidney oxygenation during renal ischemia in anesthetized rabbits. *Am J Physiol Renal Physiol* 298: F1235–F1243, 2010.
14. Evans RG, Goddard D, Eppel GA, O'Connor PM. Factors that render the kidney susceptible to tissue hypoxia in hypoxemia. *Am J Physiol Regul Integr Comp Physiol* 300: R931–R940, 2011.
15. Evans RG, Goddard D, Eppel GA, O'Connor PM. Stability of tissue Po₂ in the face of altered perfusion: a phenomenon specific to the renal cortex and independent of resting renal oxygen consumption. *Clin Exp Pharmacol Physiol* 38: 247–254, 2011.
16. Fujimoto M, Nash FD, Kessler RH. Effects of cyanide, Qo, and dinitrophenol on renal sodium reabsorption and oxygen consumption. *Am J Physiol* 206: 1327–1332, 1964.
17. Fulgraff G, Wolf K, Adelman J, Krieger AK. [On the mode of action of diuretics. Action of furosemide on renal O₂ consumption]. *Naunyn Schmiedebergs Arch Exp Pathol Pharmacol* 263: 485–495, 1969.
18. Gadano A, Moreau R, Heller J, Chagneau C, Vachieri F, Trombino C, Elman A, Denie C, Valla D, Lebrech D. Relation between severity of liver disease and renal oxygen consumption in patients with cirrhosis. *Gut* 45: 117–121, 1999.
19. Gullans SR, Hebert SC. Metabolic basis of ion transport. In: *Brenner and Rector's The Kidney*, edited by Brenner BM. Philadelphia, PA: WB Saunders, 1996, p. 211–246.
20. Halpenny M, Markos F, Snow HM, Duggan PF, Gaffney E, O'Connell DP, Shorten GD. Effects of prophylactic fenoldopam infusion on renal blood flow and renal tubular function during acute hypovolemia in anesthetized dogs. *Crit Care Med* 29: 855–860, 2001.
21. Halperin ML, Vinay P, Gougoux A, Pichette C, Jungas RL. Regulation of the maximum rate of renal ammoniogenesis in the acidotic dog. *Am J Physiol Renal Fluid Electrolyte Physiol* 248: F607–F615, 1985.
22. Hayes DF, Werner MH, Rosenberg IK, Lucas CE, Westreich M, Bradley V. Effects of traumatic hypovolemic shock on renal function. *J Surg Res* 16: 490–497, 1974.
23. Heemskerk AE, Huisman E, van Lambalgen AA, van den Bos GC, Hennekes MW, Thijs LG, Tangelder GJ. Influence of fluid resuscitation on renal function in bacteremic and endotoxemic rats. *J Crit Care* 12: 120–131, 1997.
24. Herminghuysen D, Welbourne CJ, Welbourne TC. Renal sodium reabsorption, oxygen consumption, and gamma-glutamyltransferase excretion in the postischemic rat kidney. *Am J Physiol Renal Fluid Electrolyte Physiol* 248: F804–F809, 1985.
25. Iwamoto HS, Oh W, Rudolph AM. Renal metabolism in fetal and newborn sheep. *Pediatr Res* 19: 641–644, 1985.
26. Juillard L, Lemoine S, Janier MF, Barthez PY, Bonnefoi F, Laville M. Validation of renal oxidative metabolism measurement by positron-emission tomography. *Hypertension* 50: 242–247, 2007.
27. Juillard L, Lerman LO, Kruger DG, Haas JA, Rucker BC, Polzin JA, Riederer SJ, Romero JC. Blood oxygen level-dependent measurement of acute intra-renal ischemia. *Kidney Int* 65: 944–950, 2004.
28. Kessler RH, Weinstein SW, Nash FD, Fujimoto M. Effects of chlormerodrin, *p*-chloromercuribenzoate and dichlorophenamide on renal sodium reabsorption and oxygen consumption. *Nephron* 1: 221–229, 1964.
29. Kiil F, Aukland K, Refsum HE. Renal sodium transport and oxygen consumption. *Am J Physiol* 201: 511–516, 1961.
30. Knox FG, Fleming JS, Rennie DW. Effects of osmotic diuresis on sodium reabsorption and oxygen consumption of kidney. *Am J Physiol* 210: 751–759, 1966.
31. Kramer K, Deetjen P. [Relation of renal oxygen consumption to blood supply and glomerular filtration during variations of the blood pressure]. *Pflügers Arch Gesamte Physiol Menschen Tiere* 271: 782–796, 1960.
32. Kramer K, Winton FR. The influence of urea and of change in arterial pressure on the oxygen consumption of the isolated kidney of the dog. *J Physiol* 96: 87–103, 1939.
33. Kurnik BR, Weisberg LS, Kurnik PB. Renal and systemic oxygen consumption in patients with normal and abnormal renal function. *J Am Soc Nephrol* 2: 1617–1626, 1992.
34. Lassen NA, Munck O, Thaysen JH. Oxygen consumption and sodium reabsorption in the kidney. *Acta Physiol Scand* 51: 371–384, 1961.
35. Laycock SK, Vogel T, Forfia PR, Tuzman J, Xu X, Ochoa M, Thompson CI, Nasjletti A, Hintze TH. Role of nitric oxide in the control of renal oxygen consumption and the regulation of chemical work in the kidney. *Circ Res* 82: 1263–1271, 1998.
36. Levy MN. Effect of variations of blood flow on renal oxygen extraction. *Am J Physiol* 199: 13–18, 1960.
37. Levy MN. Influence of variations in blood flow and of dinitrophenol on renal oxygen consumption. *Am J Physiol* 196: 937–942, 1959.
38. Lie M, Johannesen J, Kiil F. Glomerulotubular balance and renal metabolic rate. *Am J Physiol* 225: 1181–1186, 1973.
39. Loreaux EL, Kaul B, Lorenz JN, Lingrel JB. Ouabain-sensitive α₁ Na,K-ATPase enhances natriuretic response to saline load. *J Am Soc Nephrol* 19: 1947–1954, 2008.
40. Ludbrook J. Linear regression analysis for comparing two measurers or methods of measurement: but which regression? *Clin Exp Pharmacol Physiol* 37: 692–699, 2010.
41. Ludbrook J. A primer for biomedical scientists on how to execute model II linear regression analysis. *Clin Exp Pharmacol Physiol* 39: 329–335, 2012.
42. Mathisen O, Monclair T, Kiil F. Oxygen requirement of bicarbonate-dependent sodium reabsorption in the dog kidney. *Am J Physiol Renal Fluid Electrolyte Physiol* 238: F175–F180, 1980.
43. McDonough AA, Thomson SC. Metabolic basis of solute transport. In: *Brenner & Rector's The Kidney*, edited by Taal MW, Chertow GM, Marsden PA, Skorecki KL, Yu ASL, Brenner BM. Philadelphia, PA: Elsevier Saunders, 2012, p. 138–157.
44. McTigue M, Ting GO, Weiner MW. Relationship between sodium transport and oxygen consumption in the isolated perfused rat kidney. *Ren Physiol* 6: 112–129, 1983.
45. Melchiorri P, Sopranzi N, Roseghini M. Effects of bombesin on erythropoietin production in the anaesthetized dog. *Naunyn Schmiedebergs Arch Pharmacol* 294: 193–197, 1976.
46. Nath KA, Croatt AJ, Hostetter TH. Oxygen consumption and oxidant stress in surviving nephrons. *Am J Physiol Renal Fluid Electrolyte Physiol* 258: F1354–F1362, 1990.
47. Nitter-Hauge S, Brodwall EK. Influence of variations in blood flow on renal A-V oxygen difference and renal oxygen consumption in heart failure. A clinical study. *Am Heart J* 90: 445–450, 1975.
48. Ofstad J, Willassen Y, Gjengsto H. The effect of furosemide upon renal oxygen consumption in the human kidney. *Acta Med Scand* 192: 95–97, 1972.
49. Ostensen J, Stokke ES. Energy requirement of sodium reabsorption in the thick ascending limb of Henle's loop in the dog kidney: effects of bumetanide and ouabain. *Acta Physiol Scand* 157: 275–281, 1996.
50. Ostensen J, Stokke ES, Hartmann A, Wensell K, Kiil F. Low oxygen cost of carbonic anhydrase-dependent sodium reabsorption in the dog kidney. *Acta Physiol Scand* 137: 189–198, 1989.

51. **Palm F, Fasching A, Hansell P, Kallskog O.** Nitric oxide originating from NOS1 controls oxygen utilization and electrolyte transport efficiency in the diabetic kidney. *Am J Physiol Renal Physiol* 298: F416–F420, 2010.
52. **Parekh N, Veith U.** Renal hemodynamics and oxygen consumption during postischemic acute renal failure in the rat. *Kidney Int* 19: 306–316, 1981.
53. **Pate JW, Estes JW.** Effects of elevated venous pressures on kidney function. *Am Surgeon* 34: 729–735, 1968.
54. **Persson P, Hansell P, Palm F.** NADPH oxidase inhibition reduces tubular sodium transport and improves kidney oxygenation in diabetes. *Am J Physiol Regul Integr Comp Physiol* 302: R1443–R1449, 2012.
55. **Redfors B, Bragadottir G, Sellgren J, Sward K, Ricksten SE.** Acute renal failure is NOT an “acute renal success”—a clinical study on the renal oxygen supply/demand relationship in acute kidney injury. *Crit Care Med* 38: 1695–1701, 2010.
56. **Redfors B, Sward K, Sellgren J, Ricksten SE.** Effects of mannitol alone and mannitol plus furosemide on renal oxygen consumption, blood flow and glomerular filtration after cardiac surgery. *Intensive Care Med* 35: 115–122, 2009.
57. **Rosenbaum B, DiScala VA.** Renal tubular sodium reabsorption and oxygen consumption in the hypothyroid dog. *Metabolism* 31: 247–251, 1982.
58. **Sadowski J, Torun L.** Oxygen consumption of nonfiltering dog kidneys. *Pflügers Arch* 349: 351–358, 1974.
59. **Schlichtig R, Kramer DJ, Boston JR, Pinsky MR.** Renal O₂ consumption during progressive hemorrhage. *J Appl Physiol* 70: 1957–1962, 1991.
60. **Sejersted OM, Mathisen O, Kiil F.** Oxygen requirement of renal Na-K-ATPase-dependent sodium reabsorption. *Am J Physiol* 232: 152–158, 1977.
61. **Sejersted OM, Steen PA, Kiil F.** Energetics of tubular sodium reabsorption sensitive to ethacrynic acid and ouabain. *Am J Physiol Renal Fluid Electrolyte Physiol* 242: F254–F260, 1982.
62. **Silva P, Ross B, Spokes K.** Competition between sodium reabsorption and gluconeogenesis in kidneys of steroid-treated rats. *Am J Physiol Renal Fluid Electrolyte Physiol* 238: F290–F295, 1980.
63. **Solling C, Christensen AT, Krag S, Frokiaer J, Wogensen L, Krog J, Tonnesen EK.** Erythropoietin administration is associated with short-term improvement in glomerular filtration rate after ischemia-reperfusion injury. *Acta Anaesthesiol Scand* 55: 185–195, 2011.
64. **Solling C, Christensen AT, Nygaard U, Krag S, Frokiaer J, Wogensen L, Krog J, Tonnesen EK.** Erythropoietin does not attenuate renal dysfunction or inflammation in a porcine model of endotoxemia. *Acta Anaesthesiol Scand* 55: 411–421, 2011.
65. **Stecker JF Jr, Vaughan ED Jr, Gillenwater JY.** Alteration in renal metabolism occurring in ureteral obstruction in vivo. *Surg Gynecol Obstet* 133: 846–848, 1971.
66. **Steen PA, Hartmann A, Kiil F.** Ethacrynic acid inhibits transcellular NaCl reabsorption in dog kidneys in doses of 1 to 10 mg·kg⁻¹ and proximal bicarbonate-dependent reabsorption at higher doses. *J Pharmacol Exp Ther* 219: 505–509, 1981.
67. **Sward K, Valsson F, Sellgren J, Ricksten SE.** Differential effects of human atrial natriuretic peptide and furosemide on glomerular filtration rate and renal oxygen consumption in humans. *Intensive Care Med* 31: 79–85, 2005.
68. **Swartz RD, Silva P, Hallac R, Epstein FH.** The relation between sodium transport and oxygen consumption in isolated perfused rat kidney. *Curr Probl Clin Biochem* 8: 123–132, 1977.
69. **Thaysen JH, Lassen NA, Munck O.** Sodium transport and oxygen consumption in the mammalian kidney. *Nature* 190: 919–921, 1961.
70. **Theye RA, Maher FT.** The effects of halothane on canine renal function and oxygen consumption. *Anesthesiology* 35: 54–60, 1971.
71. **Thorniley MS, Lane NJ, Manek S, Green CJ.** Non-invasive measurement of respiratory chain dysfunction following hypothermic renal storage and transplantation. *Kidney Int* 45: 1489–1496, 1994.
72. **Thureau K.** Renal Na-reabsorption and O₂-uptake in dogs during hypoxia and hydrochlorothiazide infusion. *Proc Soc Exp Biol Med* 106: 714–717, 1961.
73. **Torelli G, Milla E, Faelli A, Costantini S.** Energy requirement for sodium reabsorption in the in vivo rabbit kidney. *Am J Physiol* 211: 576–580, 1966.
74. **Torelli G, Milla E, Kleinman LI, Faelli A.** Effect of hypothermia on renal sodium reabsorption. *Pflügers Arch* 342: 219–230, 1973.
75. **Van Slyke DD, Rhoads CP, Hiller A, Alving AS.** Relationships between urea excretion, renal blood flow, renal oxygen consumption, and diuresis. The mechanism of urea excretion. *Am J Physiol* 109: 336–374, 1934.
76. **Warner L, Gomez SI, Bolterman R, Haas JA, Bentley MD, Lerman LO, Romero JC.** Regional decreases in renal oxygenation during graded acute renal arterial stenosis: a case for renal ischemia. *Am J Physiol Regul Integr Comp Physiol* 296: R67–R71, 2009.
77. **Weinstein SW, Klose R, Szyjewicz J.** Proximal tubular Na, Cl, and HCO₃ reabsorption and renal oxygen consumption. *Am J Physiol Renal Fluid Electrolyte Physiol* 247: F151–F157, 1984.
78. **Weinstein SW, Klose RM.** Micropuncture studies on energy metabolism and sodium transport in the mammalian nephron. *Am J Physiol* 217: 498–504, 1969.
79. **Weinstein SW, Szyjewicz J.** Individual nephron function and renal oxygen consumption in the rat. *Am J Physiol* 227: 171–177, 1974.
80. **Welch WJ, Baumgartl H, Lubbers D, Wilcox CS.** Nephron Po₂ and renal oxygen usage in the hypertensive rat kidney. *Kidney Int* 59: 230–237, 2001.
81. **Wolf K, Bieg A, Fulgraff G.** On the mode of action of diuretics. II. Effects of ethacrynic acid on renal oxygen consumption and tubular sodium reabsorption in dogs. *Eur J Pharmacol* 7: 342–344, 1969.
82. **Wolf K, Fulgraff G.** [Renal O₂ consumption and Na resorption after furosemide]. *Naunyn Schmiedeberg Arch Pharmacol* 264: 325–326, 1969.

| APPENDIX 3

LETTER TO THE EDITOR: "THE PLAUSIBILITY OF ARTERIAL-TO-VENOUS OXYGEN SHUNTING IN THE KIDNEY: IT ALL DEPENDS ON RADIAL GEOMETRY"

Roger G. Evans,¹ David W. Smith,² Zohaib Khan,² Jennifer P. Ngo,¹ and Bruce S. Gardiner²

¹Department of Physiology, Monash University, Melbourne, Australia; and ²School of Computer Science and Software Engineering, The University of Western Australia, Perth, Western Australia

Monash University

Declaration for Thesis Appendix 3

Declaration by candidate

The following manuscript was published, as is, in the American Journal of Physiology Renal Physiology.

Evans RG, Smith DW, Khan Z, Ngo JP, Gardiner BS. Letter to the editor: "The plausibility of arterial-to-venous oxygen shunting in the kidney: it all depends on radial geometry". *Am J Physiol Renal Physiol* 309: F179-180, 2015.

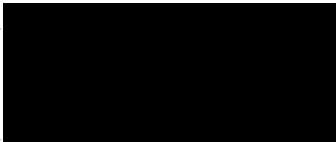
In the case of Appendix 3, the nature and extent of my contribution to the work was the following:


| Nature of contribution | Extent of contribution (%) |
|---|----------------------------|
| Prepared figures, edited and revised manuscript | 10% |

The following co-authors contributed to the work. If co-authors are students at Monash University, the extent of their contribution in percentage terms must be stated:

| Name | Nature of contribution | Extent of contribution (%) for student co-authors only |
|-------------------------|---|--|
| Roger G Evans | Drafted, edited and revised manuscript | 70% |
| David W Smith | Edited and revised manuscript | 5% |
| Zohaib Khan | Prepared figures, edited and revised manuscript | 10% |
| Bruce S Gardiner | Edited and revised manuscript | 5% |

The undersigned hereby certify that the above declaration correctly reflects the nature and extent of the candidate's and co-authors' contributions to this work*.

| | | |
|-----------------------|--|------------|
| Candidate's Signature |  | Date |
| | | 24/04/2016 |

| | | |
|-----------------------------|---|------------|
| Main Supervisor's Signature |  | Date |
| | | 24/04/2016 |

*Note: Where the responsible author is not the candidate's main supervisor, the main supervisor should consult with the responsible author to agree on the respective contributions of the authors.

Letter to the editor: “The plausibility of arterial-to-venous oxygen shunting in the kidney: it all depends on radial geometry”

Roger G. Evans,¹ David W. Smith,² Zohaib Khan,² Jennifer P. Ngo,¹ and Bruce S. Gardiner²

¹Department of Physiology, Monash University, Melbourne, Australia; and ²School of Computer Science and Software Engineering, The University of Western Australia, Perth, Western Australia

TO THE EDITOR: we read with great interest the recent paper by Olgac and Kurtcuoglu (5) entitled “Renal oxygenation: pre-glomerular vasculature is an unlikely contributor to renal oxygen shunting.” We commend the authors on their careful approach to the problem of oxygen transport in the renal cortex. The authors’ model simulations support an important contribution of oxygen delivery to tissue from the pre-glomerular vasculature, particularly under conditions of hyperoxemia and hemodilution, or when oxygen consumption is high in relation to oxygen delivery. This phenomenon has been well documented in other tissues, but this appears to be the first attempt at the problem in the kidney. We also believe that the concept of advection-facilitated diffusion, which appears to allow the simulations of the model to be reconciled with the experimental observations of Schurek and colleagues (6) and Johannes and colleagues (1), represents an important concept to explore in the field.

The authors also conclude from their simulations that “the amount of pre-glomerular arterial-to-venous (AV) oxygen shunting is negligible.” We believe that the authors have overinterpreted their findings. It is not surprising to us that the authors’ model did not provide any evidence of AV oxygen shunting, since the “checkboard pattern” of arteries and veins adapted for the vascular geometry would be expected to preclude this phenomenon (Fig. 1). In our recent analysis of oxygen diffusion in the vicinity of artery-vein pairs, over a range of cross-sectional configurations, we concluded that the presence of oxygen sinks of any kind (e.g., tubules or capillaries) between an artery-vein pair should prevent AV oxygen shunting (4) and that shunting would be strongly dependent on the degree of wrapping by veins on arteries. Without wrapping, our models predicted little to no shunting. The model of Olgac and Kurtcuoglu (5) is generally based on an assumption that there are oxygen sinks between all artery-vein pairs. Yet, the critical feature of the renal cortical circulation, unlike the circulation of skeletal muscle, is that a proportion of arteries are partially

wrapped by their associated vein, so that oxygen sinks (tubules and capillaries) are excluded from intervening space across which oxygen might diffuse and diffusion distances are very short ($\sim 15\ \mu\text{m}$) (Fig. 1). The phenomenon of wrapping is particularly prominent in larger vessels ($\geq 50\ \mu\text{m}$ in diameter), although wrapped vessels can be observed, with variable frequency, throughout the cortical circulation (4). We propose that any model aimed toward testing the plausibility of AV oxygen shunting should include the phenomenon of wrapping, and certainly should not rely on a lumped average of diffusion distances between artery-vein pairs.

The seminal observations that relate to the concept of AV oxygen shunting were obtained more than 50 years ago by Matthew Levy and colleagues (3). They found that the transit time for oxygen across the renal circulation was considerably shorter than that for labelled erythrocytes (3). Olgac and Kurtcuoglu (5) state that “Levy and Saucedo pointed to either the peritubular capillaries in the cortex or the vasa recta in the medulla as the location of potential oxygen shunting, favoring the latter on the basis of their anatomic arrangement.” However, Levy and Imperial (2) later found that the difference in transit time between oxygen and labeled erythrocytes was maintained when the renal medulla was cooled, thus greatly reducing medullary perfusion and the driving force for oxygen shunting in the medulla, medullary oxygen consumption. Thus we maintain that the experimental findings of Levy and colleagues can only be satisfactorily explained by diffusive shunting of oxygen between arteries and veins in the renal cortex.

We believe the jury must remain out on the question of whether AV oxygen shunting is an important phenomenon in the regulation of intrarenal oxygenation. Two lines of research are required to resolve this issue. First, we must develop experimental methods, perhaps along the lines of Levy and colleagues’ pulse experiments, to quantify this phenomenon. At the very least, we need to quantify the cross-sectional geometry of the artery-vein pairs throughout the kidney. Second, we must develop computational models, based on realistic

Address for reprint requests and other correspondence: R. Evans, Dept. of Physiology, PO Box 13F, Monash Univ., Victoria 3800, Australia.

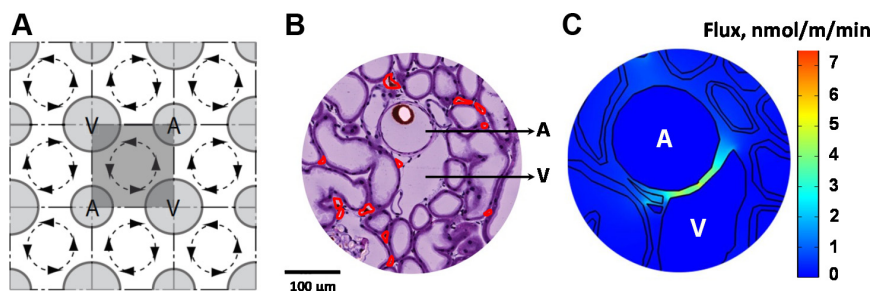


Fig. 1. Effects of the close association between arteries and veins (wrapping) on oxygen flux between artery-vein pairs. A: Olgac and Kurtcuoglu's (5) vascular arrangement consists of 2 one-quarter artery-vein pairs and the adjoining tissue. The layout of oxygen advection pathways is depicted by arrows. The absence of wrapping leads to the exclusion of arteriovenous (AV) oxygen shunting. B: histological cross sections of renal tissue in the vicinity of a wrapped artery (4). C: oxygen flux plots of regions of tissue in the vicinity of the artery in B (4).

vascular geometry, to generate realistic estimates of the magnitude of AV oxygen shunting.

GRANTS

The authors' work is funded by a grant from the Australian Research Council (DP140103045).

DISCLOSURES

No conflicts of interest, financial or otherwise, are declared by the authors.

AUTHOR CONTRIBUTIONS

Author contributions: R.G.E. drafted manuscript; R.G.E., D.W.S., Z.K., J.P.N., and B.S.G. edited and revised manuscript; R.G.E., D.W.S., Z.K., J.P.N., and B.S.G. approved final version of manuscript; Z.K. and J.P.N. prepared figures.

REFERENCES

1. Johannes T, Mik EG, Nohe B, Unertl KE, Ince C. Acute decrease in renal microvascular PO_2 during acute normovolemic hemodilution. *Am J Physiol Renal Physiol* 292: F796–F803, 2007.
2. Levy MN, Imperial ES. Oxygen shunting in renal cortical and medullary capillaries. *Am J Physiol* 200: 159–162, 1961.
3. Levy MN, Saucedo G. Diffusion of oxygen from arterial to venous segments of renal capillaries. *Am J Physiol* 196: 1336–1339, 1959.
4. Ngo JP, Kar S, Kett MM, Gardiner BS, Pearson JT, Smith DW, Ludbrook J, Bertram JF, Evans RG. Vascular geometry and oxygen diffusion in the vicinity of artery-vein pairs in the kidney. *Am J Physiol Renal Physiol* 307: F1111–F1122, 2014.
5. Olgac U, Kurtcuoglu V. Renal oxygenation: pre-glomerular vasculature is an unlikely contributor to renal oxygen shunting. *Am J Physiol Renal Physiol* 308: F671–F688, 2015.
6. Schurek HJ, Jost U, Baumgartl H, Bertram H, Heckmann U. Evidence for a preglomerular oxygen diffusion shunt in rat renal cortex. *Am J Physiol Renal Fluid Electrolyte Physiol* 259: F910–F915, 1990.



| APPENDIX 4

PROTOCOLS

Phosphate buffered saline (PBS, 0.1 M; 1 L solution)

1. In distilled H₂O, the following were dissolved:
 - 9 g of NaCl
 - 8.7 g of Na₂HPO₄ (anhydrous)
 - 5.44 g of NaH₂PO₄•H₂O (monohydrate)
2. Adjust pH to 7.4 using NaOH
3. Make up to required volume

Phosphate buffer (0.2 M; 1 L solution)

- Add 7.18 g of NaH₂PO₄•2H₂O (dihydrate) to 900 ml distilled water until dissolved
- Add 21.86 g of Na₂HPO₄ (anhydrous) until dissolved
- Adjust pH to 7.4 using NaOH
- Make up to 1 L
- Add 240 mg of sodium nitroprusside

3% Paraformaldehyde (1 L)

- 30 g of paraformaldehyde powder dissolved in 900 ml of 0.1 M PBS
- Heated and stirred (~60 °C)
- Add drops of 10 M NaOH to adjust pH to 7.4
- Make up to 1 L
- When solution is clear, cool to room temperature

4% Paraformaldehyde (1 L)

- 40 g of paraformaldehyde powder dissolved in 900 ml of 0.2 M of phosphate buffer
- Heated and stirred (~60 °C)
- Cool to room temperature
- Add 40 ml of 25% stock glutaraldehyde
- Make up to 1 L
- Adjust pH as required using 10 M NaOH

Toluidine Blue (100 ml)

- 0.5 g Toluidine Blue
- 0.5 g Borax
- 100 ml H₂O
- Stir on a mechanical stirrer until dissolved
- Filter solution before use

Immunohistochemical protocol (Chapter 4)

1. Dewax with Xylene:
2. Rehydration:
 - 100% ethanol (ETOH) (5 mins), 70% ETOH (5 mins) and PBS (5 mins).
3. Antigen Retrieval:
 - 10× Sodium Citrate Buffer (Microwave for 2 min, 1 min at a time, AVOID boiling).
 - Fresh PBS for 5 mins
4. Blocking with 1% bovine serum albumin (BSA)
 - Leave covered in foil for a minimum of 1 hour
5. Primary Antibody:
 - Polyclonal rabbit anti-human von Willebrand Factor (vWF); 1:200 dilution
 - Cover with foil and place in the fridge overnight
6. Wash 1× 5 mins in PBS
7. Secondary Antibody:
 - Goat anti-rabbit 555 (1:1000 dilution)
 - Cover with foil and leave on the bench at room temperature for a minimum of 1 hour
8. Wash 3× 5 mins
9. 4', 6-diamidino-2-phenylindole (DAPI):
 - 1:10,000 dilution
 - Incubate for 5-10 minutes.
10. Wash 1× 5 mins
11. Dry and coverslip slides

Agarose gel preparation

Prior to slicing the kidneys, they were first embedded in agarose gel. The preparation for the gel was as follows:

1. Pour 100 ml distilled water into a beaker and add 3 grams of agarose powder (Sigma-Aldrich, St Louis, MO, USA)
2. Stir the solution and heat in a microwave for 4 minutes until the cloudy solution turns into a clear and viscous liquid.
3. Take out of microwave and cool to ~60 °C.
4. Once the solution reaches 60 °C, it is ready to be poured into the mold to embed the kidney(s).
5. The gel and kidneys were left to set at room temperature.

Hardened agar was stored in the refrigerator for later re-use. When needed, the hardened agar was heated on high heat for ~2 minutes, after which it was left to cool to ~60 °C and ready for re-use.